Power Systems

Vasily Y. Ushakov et al.

Impulse Breakdown of Liquids

Vasily Y. Ushakov et al.

Impulse Breakdown of Liquids

With 202 Figures and 23 Tables

Vasily Y. Ushakov
Tomsk Polytechnik University
Lenin Ave. 30
TOMSK
russische föderation 634034
icd@tpu.ru

The main physical processes and phenomena in pulsed electric breakdown of liquids are described. The nature of charge carriers, mechanisms of formation and evolution of the gas phase, and their role in charge ignition (initiation) and development are considered. Spatiotemporal laws of propagation and parameters of charge channels are described. The basic mechanisms of liquid breakdowns and boundary conditions of their initiation are formulated. The monograph will be useful to experts in high-voltage pulsed technology, physics of dielectrics, and electrical insulation as well as to students of the corresponding speciality.

Contents

Preface

Recently there has been a remarkable surge of interest in the phenomenon of pulsed electric breakdown in liquids in connection with the rapid development of high-voltage pulsed power. High-voltage micro- and nanosecond pulses find wide application in experimental physics, electrodischarge technology, physics of dielectrics, radar detection and ranging, high-speed photography, etc.

In the last decades, a new direction of science and technology – pulsed power – has been originated from electrical power engineering and physics.

Sources of high pulsed currents (10^5–10^6 A) and voltages (10^6–10^7 V) with nanosecond front duration are required to carry out the experiments on superfast plasma heating in laser and accelerating technologies and in a number of other cases. In such generators, a high-voltage pulse is first generated without stringent requirements on its shape; then this pulse is transformed with the use of low-inductive energy storages and dischargers. Extremely high values of the parameters of generated pulses impose a number of stringent requirements on the insulation medium of storages and switches and on configurations of these elements in actual circuits. The requirements on insulation can be briefly formulated as follows: 1) high electric strength, 2) high permittivity, 3) low electrical conduction, 4) low rate of decomposition in electric discharges, and 5) fast restoration of the dielectric properties after breakdowns. The experience on application of various dielectric media as insulation in high-voltage pulsed power accumulated by the present time demonstrates that purified water and dielectric liquids, in particular, transformer oil meet the above-listed requirements. An increase in working electric field gradients required of insulation of pulse generators with the state-of-the-art parameters obligatory calls for reduction of their overall dimensions and hence parasitic parameters in order to shape and use nanosecond pulses.

To simplify the design of high-voltage high-current nanosecond generators with liquid insulation, to reduce their inductance, and to make a solution of the insulation problem easier, it is expedient to switch currents using liquid dielectric dischargers. Moreover, in many cases controllable dischargers, which allow a current to be switched to several parallel spark channels thereby

increasing the power transferred to a load (a vacuum diode, solenoid, etc.), must be used because of the requirements imposed on generated pulse power. Thus, two problems – the problem of insulation and creation of high-voltage high-current high-speed dischargers – determine in many respects an increased interest in the phenomenon of pulsed electric breakdowns in liquids.

The start of the intensive development of pulsed power have coincided with the expansion of works on the application of high-voltage spark discharge energy in industrial technologies. When spark is a working tool, the development of the discharge in a liquid is the first stage of the complex technological process, and the liquid itself plays the role of an insulating and working medium. In this case, the pulsed discharge characteristics influence the laws of energy liberation in the spark channel and finally, the formation of various pulsed disturbances (hydrodynamic, thermal, acoustic, light, etc.) used in the technology.

At the same time, interest in the liquid breakdown under lightning pulses and in particular, internal surges has quickened in connection with an expansion of working voltages of electric power transmission lines and substations and the tendency to a decrease in the insulation level of high-power electrical equipment systems.

The knowledge of the electric breakdown of liquids has not kept pace with this increasing interest and more and more stringent requirements on liquid dielectric insulation design. In the literature, 20 or so different models of liquid breakdown were considered equivalent, thereby testifying to the absence of reliable experimental data on the laws of discharge propagation and their dependence on the liquid properties and breakdown conditions.

The foregoing gave impetus to investigations of the electric breakdown in liquids in the laboratories of the leading countries in the early 60s.

The main results of these investigations obtained till 1972–73 have been generalized in monograph [1]. In the next 30 years, investigations of the electrical conduction and breakdown in liquid in the USSR (later in Russia), France, the USA, Great Britain, Norway, Japan, Poland, India, China, and in other countries were characterized not only by a wide variety of works but also by the most advanced experimental technology and modern methodical procedures.

The present book is devoted to a description of physical mechanisms of initiation and propagation of pulsed discharges in liquids as well as to the basic laws describing impulse electric strength of liquids. The book is based mainly on the investigations carried out at Tomsk Polytechnic University, Novosibirsk State University, Siberian Scientific-Research Institute of Power Engineering, Novosibirsk State Technical University, Saint-Petersburg State Technical University, Nuclear Physics Institute of the Siberian Branch of the Russian Academy of Sciences (Novosibirsk), and All-Russian Electrical Engineering Institute. The results obtained in foreign laboratories and institutes and necessary for the integrated presentation of the problem formulated in the title of the monograph have also been included.

In the process of writing, we have generalized the results of modern research and re-analyzed and re-examined a large volume of data on liquid dielectric breakdown obtained in the last decades. This has provided their deeper understanding and interpretation.

We especially wish to thank the Rector of Tomsk Polytechnic University Prof. Yury P. Pokholkov for financial and moral support in preparation of the English version of this monograph.

We would like to acknowledge all our colleagues who took part in investigations that provided the basis of the monograph. Their names are presented in References.

The authors are grateful to E. V. Bogdanova and S.V. Barabin for help in preparation of the manuscript for printing.

The Foreword, Introduction, Conclusions, Chapters 4, 6, and 8, and the introductory part of Chapter 7 have been written by V. Y. Ushakov; Sections 7.3 and 8.2 has been written by V. Y. Ushakov and V. F. Klimkin.

Chapters 3 and 5 and Section 7.2 have been written by V. F. Klimkin.

Chapters 1 and 2 and Section 7.1 have been written by S. M. Korobeynikov.

The translation of monograph have been made by Ph.D. L.G. Shamonaeva, Institute of Atmosphere Optic of the Siberian Branch of Russian Academy of Sciences, Tomsk.

Introduction. Brief Historical Review

The concept of the physical mechanism of liquid electric breakdown in has run a very complex course. Even in the early 20th century, two radically different approaches to the phenomenon of liquid electric discharge were clearly distinguished. According to one of them, the electric discharge in a liquid is the discharge in gas cavities either already presented in the liquid and on the electrodes or newly formed under voltage exposure (by electrolysis, boiling, cavitation, and decomposition under electron bombardment). This discharge mechanism is conventionally called the bubble discharge. According to the other approach, the discharge is a consequence of avalanche multiplication of free charge carriers in the liquid and is described by the gas discharge model generalized to the liquid phase. It implies that electrons in strong fields are accelerated in liquids and ionize molecules and atoms. The electric strength of the liquid is related to the molecular liquid structure through the electron free path, interaction cross section, and ionization energy. This discharge mechanism is further called the ionization discharge.

Macfarlane [2] pointed out in 1880 that under long-term voltage exposure, four processes simultaneously participate in the liquid breakdown: formation of filaments from suspended particles, liquid flow, formation and motion of gas bubbles, and finally, spark discharge. This point of view was confirmed by experimental investigations that provided the basis for a number of non-ionization theories of liquid breakdown: thermal, gas-thermal, voltaic, polarization, etc. A detailed review of these theories can be found in [3–6]. This point of view prevailed till the middle 40s.

At the same time, external analogs in the phenomena accompanying the electric discharge in liquids and gases as well as similarity in the laws describing the electric strength of liquids and gases provided the basis for the attempts to develop the theory of liquid breakdown starting from the Townsend theory [3, 7–9]. In more recent investigations it was established that the liquid impurity, temperature, and gas pressure above the liquid affect the breakdown under impulse voltage much weaker than under long-term voltage exposure. This fact together with small delay times of breakdowns in liquids ($\sim 10^{-8}$ s)

established by A. F. Valter and L. D. Inge [10] and other authors were interpreted as the proof of the ionization breakdown mechanism. These results have demonstrated that the Townsend breakdown mechanism has only limited application to a description of the discharge phenomena in liquids.

A. F. Valter and L. D. Inge put forward a hypothesis that initial electrons causing the collision ionization in the ionization breakdown mechanism are emitted into the liquid from the cathode. Baker and Boltz [11] accepted this hypothesis, and more recently it provided the basis for a number of theories of liquid breakdown [12–17].

Goodwin and Macfadyen [12] tried to find an analytical expression for the criterion of liquid breakdown with allowance for the field emission from the cathode described by the Fowler–Norgdheim equation and for the collision ionization described by the Löbe equation [18]. The field strength at which a current instability arises due to emission and ionization is taken to be the breakdown field strength. In [6, 19] it was demonstrated that this model has many mistakes and incorrect initial premises; therefore, the coincidence of theoretical and experimental values of the electric strength was only random.

In the Bragg–Sharbaugh–Crowe model [15], the relationship of the emission current density, space charge, and field intensities at the cathode and anode is established in the absence of ionization. Assuming that the breakdown occurs when the field strength in the entire liquid volume is no less than a certain fixed value, the authors derive the breakdown criterion from the condition of electron emission from the cathode. Three cases corresponding to the cathodes with strong, intermediate, and weak emissivities were considered. In the first case, the current obeys the emission law with allowance for the space charge; this dependence is observed until the average field strength in the gap reached $2/3E_{br} = 2/3E_{av}$. At E_{br}, the field at the anode is 1.5 times greater than E_{av}, that is, it reaches the breakdown value. In the second case, the field at the anode reaches E_{br} for E_{av} lying between $2/3E_{br}$ and E_{br}. Finally, the space charge is not formed for the weak emitter, and the breakdown is initiated at $E_{av} = E_{br}$. Only in the third case the process depends on the conditions on the cathode.

According to the Swan hypothesis [16], the breakdown is formed mainly due to the field emitted from the cathode and amplified by positive ions accumulated on the dielectric or semiconductor film on the cathode surface. The collision ionization is considered only as a reason of field distortion at the cathode. The field strength at which positive ions at the cathode cause the emission current to increase continuously until the breakdown initiation in the liquid is taken to be the breakdown field strength. For well-fitted empirical coefficients in the equation for the criterion, the calculated dependence $E_{br} = f(d)$ for liquid argon was in good agreement with the experimental dependence.

On the contrary, in the Lewis model [13] the electron emission from the cathode was not considered at all. It was assumed that for high enough electric field strengths, a number of electrons acquire more energy from the field than lose in the process of non-ionization collisions with molecules of the

liquid. These electrons are accelerated up to the ionization energy and give rise to electron avalanches. From all collision types causing the electron energy losses, only the energy losses on the excitation of molecular vibrations in the medium were taken into account. The breakdown condition was derived from the Hippel criterion [20] for solid dielectrics based on the energy balance condition:

$$[qE\lambda = C \cdot h \cdot \nu,]$$ (1)

where E is the electric field intensity, λ is the electron free path, C is an arbitrary constant, $h\nu$ the quantum of energy the electron loses by excitation of molecules. The satisfactory agreement between the calculated and experimental E_{br} was obtained for a number of hydrocarbons.

In the Kuchinsky model [17] developed for thin layers (10^{-4}–10^{-2} cm) of mineral oil, the initial low-intensive partial discharges are attributed to the processes of collision ionization, and the occurrence of critical discharges is attributed to a sharp increase in the gassing intensity and formation of gas bubbles. The condition of the non-stationary mode in the gap leading to an increase in the positive charge at the cathode that causes a fast increase in the emission current density thereby progressively increasing the space charge density until a breakdown of the oil layer is initiated is taken as the breakdown criterion. Based on the study of the characteristics of individual partial discharge pulses, Kuchinsky [17] estimated the collision ionization coefficient α and found a dependence of α on E. This allowed him to calculate E_{br} of thin mineral oil layers.

Not dwelling on a detailed analysis of the above-mentioned theories considered in [5, 6, 19, 21], we must note the following. In many careful investigations of the dependence of static and pulsed electric strength of very pure liquids and conduction currents in strong electric fields on cathode material, gap length, molecular structure of the liquid, etc. [5, 6, 19–22], the main points of these models were not confirmed. The cathode material and temperature, that is, the cathode emissivity had essentially no effect on the electric strength of even micron gaps, though emission played the main role in the high-voltage electrical conduction of dielectric liquids. Moreover, the initial concept of ionization breakdown models for liquids that the discharge in a uniform field always develops from the cathode due to initiation by emitted electrons was violated for pulsed breakdowns.

The collision ionization as a basis of the ionization mechanism of breakdown in liquids was not convincingly confirmed with experiments as well. A decrease in E_{br} and an increase in the pre-breakdown current with increasing interelectrode distance pointed out in a number of early experimental works and used to prove the collision ionization mechanism in liquids were interpreted in more recent works as a consequence of imperfection of the experiments and, in particular, of application of spherical rather than flat electrodes. A decrease in E_{br} and an increase in current with increasing distance between

the hemispherical electrodes can be caused by an increased area of electrodes located in the strong field and hence, an increased number of effective weak sections and emitting centers [21].

Thus, the authors would have to consider the coincidence of the calculated and experimental data on the electric strength the only criterion for model reliability. However, the experimental data on the electric strength of even so-called extremely pure liquids are highly diversified; therefore, their coincidence with the calculated results is mostly random.

Because of lacking of the direct experimental proof of the correctness of ionization liquid breakdown models developed in [12, 13, 23, 24] and the dependence of electric strength on hydrostatic pressure established in a number of works even for degassed liquids under short-term voltage exposure, a rebirth of interest in the non-ionization (bubble) liquid breakdown mechanism reveals itself in models [21, 23–25] developed in the 60s. Moreover, conditions of realization of this discharge model were generalized to short-term voltage exposure down to pulses of nanosecond duration.

The Kao model [25] suggests that a gas bubble that already existed or was newly formed in the liquid under voltage exposure is extended along the field lines. To find a mathematical expression for the breakdown criterion, Kao has made the following assumptions: a) the volume of the deformed bubble remains unchanged and b) the breakdown occurs when the voltage drop inside the bubble is equal to the minimum of the Paschen curve (for the gas inside the bubble). The theoretical dependence of electric strength of the liquid on hydrostatic pressure was analogous to the experimental one. However, calculations of the electric strength for this model are difficult, because the model does not describe the process of gas bubble formation, and it is necessary to know the initial bubble radius, the state of the gas in the bubble, and some other parameters that are difficult to measure. In addition, the model is inapplicable when the condition of constancy of the deformed bubble volume is violated or the interelectrode distance is much greater than the deformed bubble length.

Gassing due to local (near geometrical cathode inhomogeneities) liquid heating by emission currents provides the basis for the Watson–Scharbaugh model [21]. The breakdown condition is the violation of equality between the energy necessary for boiling up of a certain liquid mass and the energy W liberated in the liquid as well as the gas bubble extension up to the critical length or complete bubble crossover of the interelectrode distance. The energy W is determined as

$$[W = A \cdot E^n \cdot \tau_r,] \tag{2}$$

where E is the field intensity, n is the power determined by the emission current, space charge, and applied field strength, and τ_r is the time during which the liquid mass can be located near the microtip without its replacement by a colder liquid. If voltage pulse duration is longer than τ_r, the electric strength

of the liquid must be independent of the pulse duration. The uncertainty of almost all factors entering into Eq. (2) gives no way of quantitative calculations for this model, and the experimentally established fact of preferable pulsed discharge ignition on the anode rather than on the cathode calls into question the correctness of the initial premises of this model.

The well-known phenomenon of the decreased electric strength of liquids in the presence of suspended solid particles provides the basis for the Kok–Corbey model [23]. It suggests that the suspended particles – polarized spheres whose permittivity is much greater than the permittivity of the liquid – move toward the strong field region under voltage exposure. The diffusion and viscous friction hinder the particle motion. The field strength at which particles are progressively accumulated near a field amplification center forming a bridge along which a breakdown occurs is taken as a breakdown field strength. The model suggests an increase in E_{br} with increasing temperature, which contradicts the available experimental data. Moreover, the formation of bridges from suspended particles seems unrealistic under impulse voltages.

Thus, the non-ionization breakdown models are also based on premises that in most cases were not confirmed experimentally.

In conclusion of our brief analysis of theoretical liquid breakdown models, it should be noted that no one of these models considers the discharge evolution which in many respects determines the breakdown characteristics, especially under short-term voltage exposure. The ionization theories consider only the conditions of the build-up of collision ionization or electron emission that are identified with the breakdown criterion. Skanavi [5] emphasized that the condition of the build-up of collision ionization is insufficient criterion of electric breakdown even if its nature is purely ionization. In the non-ionization models, conditions of progressive gassing, gas bubble deformations, formation of the bridge from impurity particles, etc. are identified with the breakdown criterion.

The history of gas discharge physics demonstrates that a reliable breakdown theory can be elaborated only based on a detailed physical pattern of the phenomenon, including a description of all discharge phases developing in time and space. This approach to the study of breakdown is especially promising for liquids, taking into account a wide variety and complexity of the discharge formation and development processes. Even in the most favorable case of breakdown in a simple carefully purified liquid, it is impossible to establish a reliable relationship between the electric strength and the molecular structure of the liquid that could be used as a basis of the theory. Despite careful purification by different methods and decontamination, the liquids used in experiments on breakdown were still far from being ideal. For example, in [12] it was demonstrated that the electrical conduction of the liquid continuously purified and decontaminated for five months decreased but did not reach the limit which could be considered as the physical-chemical constant of this liquid. In addition, the situation is complicated by lacking of a well-developed theory of material in the liquid phase.

Komelkov [26, 27] first described the propagation of the discharge in a liquid using a high-speed camera for photographic registration of the discharge channel and simultaneously an oscillograph for registration of voltage and current accompanying the discharge propagation.

The discharge in transformer oil and distilled water in tip-plane and tip-tip gaps of length $d =$ 12–20 cm was photographed with the Boys rotating lens-type camera. Satisfactory streak photograph were obtained with the help of artificial discharge retardation using a high ohmic resistance R_{ret} (10^4–$1.5 \cdot 10^6\ \Omega$) connected into the discharge circuit. It was established that the breakdown of the gap was similar to the leader process in long air gaps followed by a bright burst considered by Komelkov as a main (return) discharge in long air gaps; after the burst, an arc was observed. At high R_{ret}, repeated breakdowns were observed after the main discharge. It was pointed out that breaks in leader propagation were caused by voltage relaxation whose time was determined by the circuit parameters (R, L, C), electron capture by molecules and atoms of the liquid that led to aging of the leader channel and decreasing its electrical conduction and electric field gradient in the region of ionization, and the leader deceleration by the space charge barrier formed in the gap by the ionization zone. The length of the ionization zone was 1–2 cm, and the effective velocities of the leader channel propagation in transformer oil were $1.7 \cdot 10^5$ and $6 \cdot 10^4$ cm/s for positive and negative leaders. Based on the results of these investigations, Komelkov has made a very important conclusion that the main concept that provided the basis for the classical theories, namely, the concept that the breakdown is the build up of pre-breakdown currents in the gap or the single-avalanche process was incorrect. Actually, a qualitatively new phenomenon, involving the formation of a conduction channel and an ionization zone, takes place, and the processes of collision ionization proceed in a local moving region. He also pointed out that the development of the leader from the tip electrode of positive polarity demonstrated that the electron emission from the cathode is not the governing factor of the discharge mechanism in long gaps. He emphasized that the discharge in liquids was similar to the breakdown of long rather than short gas gaps similar to a lightning and hence it can be used to model the lightning.

More recently, Liao and Andersen [28, 29] carried out analogous investigations. To clip currents and glow in the final stage of the discharge, they put an insulation plate on the flat electrode. The linear film framing speed in the Boys camera was about $4 \cdot 10^3$ cm/s. The discharge parameters (velocity, current, and duration of pauses between bursts) were the same as in [26, 27], but the discharge evolution was treated differently. According to Liao and Andersen, it includes five rather than three stages: 1) initiating streamer, 2) equivalent pilot-streamer, 3) stepped streamer, 4) return discharge, and 5) arc. At the moment of voltage application to the discharge gap, the initiating streamer develops from the tip electrode. It passes half the interelectrode distance (3–4 cm) in 1 µs. From the end of the initial negative streamer, continuous diffusion glow – the pilot-streamer – is observed. It is reached by a

series of streamers with intervals between bursts 1–5 µs. After the next burst (step), a pause in streamer propagation is observed during which the streamer channel does not glow. For the negative discharge, the pilot-streamer develops after the stepped streamer from its head; it propagates with a velocity of $2.5 \cdot 10^5$ cm/s. For the positive streamer, jumps in the potential and bursts in the streamer channel corresponding to them are also observed; however, a smooth increase of the potential in this case is absent. Based on these results, the authors concluded that the pilot-streamer was absent in this case. When the stepped streamers reached the opposite electrode, the inception of the main discharge stage was observed followed by the arc.

Because of artificial clipping of the discharge current (the discharge retardation), the lack of the data on the discharge channel parameters (cross section, longitudinal electric field gradients, current density, electrical conduction, etc.), and different discharge schemes used in [26–29], the leader liquid breakdown mechanism in long intervals has been recognized not by all researchers of this phenomenon. For example, Balygin [30] on the basis of investigations of the discharge in liquids with an oscillograph concluded that the leader process in the liquid reported in [26] was due to the presence of the high retarding resistance in the discharge circuit. Without resistance, the discharge is developed as a single avalanche. The unjustified character of these conclusions was discussed in [31], and their inaccuracy was demonstrated in [32, 33].

The first experimental investigations of the discharge in liquids by the methods of high-speed photography have demonstrated with all evidence that they are promising. However, technical imperfection of cameras available at that time with mechanical framing did not allow one to develop this direction of research further and to detail the physical pattern of the discharge in liquids. In the next decade (approximately from 1953 until 1963), the great number of efforts had been made to create a breakdown pattern and theory based only on the dependence of the electric strength and electrical conduction of carefully purified liquids on various factors.

In the foregoing historical review, we have briefly considered the works published approximately until the middle 60s.

By the early 60s, the opportunity appeared to study the discharge in liquids using high-speed photographic devices equipped with electron-optical image intensifiers (Image Converter Camera-ICC) having time resolution of $\sim 10^{-12}$ s with light amplification coefficient of $\sim 10^6$ together with the methods and means of nanosecond pulsed power, including high-speed oscillographs.

The first studies of electric breakdown in liquids with the use of ICC were carried out by Ushakov [1] in the Laboratory of High-Voltage Gas Discharge and Lightning Protection of the G. M. Krzhizhanovskii Institute of Power Engineering in 1962–1964 (Moscow); then they were continued at Tomsk Polytechnic Institute (University). In these studies of the physical processes initiating pulsed breakdown of liquids, the main methodical procedure was integrated synchronous registration of spatiotemporal patterns and electric

parameters of discharges with high-speed electronic, electron-optical, and optical equipment by methods of high-voltage pulsed power including nanosecond one.

The application of these methods allowed the basic laws of formation and propagation of pulsed discharges in liquids to be investigated for a wide range of pulse durations and discharge gaps covering a significant part of the range of their variations in actual designs.

Results of these investigations were generalized in [1]. The hypotheses about two main breakdown mechanisms in liquids, namely, bubble and ionization ones were confirmed, and their basic characteristics were elucidated. The approximate boundary conditions of realization of these mechanisms were also indicated.

In the bubble model, the main sources of charge carriers creating the plasma discharge channel are the processes inside of the gas bubbles (voids) that have already existed in the liquid or have been newly formed in a strong electric field.

In the second model, it is accepted that plasma in the initial stages of channel development (in "fresh" sections of the channel) is created as a result of collision or autoionization (field ionization) processes in the liquid. The charge carriers that are formed in this case and move in the electric field cause warming and boiling up of the liquid and forming gas channels. Ionization can develop in these channels in accordance with the gas discharge laws, converting them into highly conductive channels (into the leader channels in long gaps).

In [1], the voltage exposure time and the electrical conduction of liquids were chosen as the key parameters of one or another breakdown mechanism.

Investigations carried out in the leading laboratories all over the world in the next 2.5–3 decades have demonstrated that the actual situation is much more complicated. It was found that the nature and sequence of the discharge processes depend not only on these actually most important factors but also on a number of other factors including the curvature radius of the electrode initiating the discharge, discharge polarity, viscosity of the liquid, interelectrode gap length, and hydrostatic pressure.

Further progress in the study of the electric discharge mechanism in liquids was mainly due to application of laser technology. Laser light sources used in optical methods (schlieren photography, interpherometry, etc.) allowed one to obtain high temporal and spatial resolution. This is especially important for studying the initial discharge stages. It should be noted that the high temporal resolution provided by ICC was accompanied by deterioration of the image quality at nanosecond exposure times. This limits their application for the study of microobjects changing with high rates.

In the USSR, the first studies of the physical pattern of the electric discharge in liquids with the use of a ruby laser as an illumination source in high-speed schlieren photography were carried out at the Nuclear Physics Institute of the Siberian Branch of the Russian Academy of Sciences (NPI SB RAN) in 1970–1971 [34, 35]. They allowed some important details of the

discharge initiation and development in water to be elucidated. The results obtained demonstrated that the given direction of research, intensively developed over the next few years, was promising. The application of multiframe systems allowed one to study the dynamics of the processes more reliably. Further development of the new experimental approach to the study of the electric discharge mechanism in liquids was connected with the refinement of methods and modernization of means for ultrahigh-speed optical registration.

The special features of the electric discharge in liquids (a great variety and complexity of the phenomena itself and its small characteristic dimensions ≤ 10 μm, high propagation rates $\sim 10^5$–10^7 cm/s allowed us to formulate a number of requirements on the methods of high-speed optical measurements: 1) illumination pulse duration no longer than ~ 10–0.1 ns, 2) frequency of shooting in the frame-by-frame mode $\sim 10^9$–10^8 frames/s, 3) time interval between the frames changing in a wide range (~ 1–100 ns), 4) high accuracy of frame synchronization and the desirable frame number no less than 4–7, 5) light beam energy sufficient for registration of subsequent frames with the necessary time delay, and 6) high beam quality to obtain reliable quantitative data. Systems of multiframe photography based on light delay lines with a laser illumination source were developed and used at the Institute of Applied Mechanics of the Siberian Branch of the Russian Academy of Sciences and Novosibirsk State University [36, 37].

In the early 80s, the interference and schlieren methods of laser diagnostics of the phenomena from changes in the complex refractive index of the examined medium, including algorithms of reconstruction of the permittivity profiles in perturbed media from the amplitude and phase of a probing wave with allowance for the diffraction, refraction, and absorption were developed at the High-Voltage Research Institute at Tomsk Polytechnic University. The diagnostic complex comprised:

– a laser with active mode synchronization providing the following parameters per pulse: duration of 1 ns, energy of 40 mJ, wavelength of 0.69 μm, and instability of pulse of discharger triggering < 1 ns

– a synchronization system that allows gap sensing to be performed within 0.1–10000 μs of the start of the high-voltage pulse

– a two-frame system with spatial division of probing beams

– a two-frame system with a common camera angle and polarization division of beams

– a Sagnac interferometer with triangular beam path outside of the examined object [38].

Approximately at the same time, two other research groups from Siberian Scientific Research Institute of Power Engineering (Novosibirsk) [39, 40] and Saint Petersburg State Technical University [41] developed optical methods of registration of the dynamics of electric field re-distribution and (or) changes in the liquid density based on the Kerr effect and used these methods to study the pre-breakdown and breakdown processes in liquids.

In [39,40], optical registration was carried out using a SFR ultrahigh-speed photodetector operating in the chronographic mode. Multiframe photographs were obtained using a pulsed ruby laser in the Q-switched mode. In this case, a series of light pulses with 50–80 ns duration was generated with time interval between pulses changing from 1 to 40 μs. During the pause between pulses (exposure time), the image moved along the film by the frame width, and the frame was illuminated by the next light pulse. The number of subsequent photographs was 10–20, that is, the method allowed the events that lasted from a few tens to a few hundreds of microseconds to be registered.

The Mach–Zehnder laser interferometer with registration of interference patterns in the photochronographic mode on an electron-optical photochronograph was used in [41]. It was capable of registering short-term phenomena, including nanosecond high-voltage pulses.

The experimental data obtained by more sophisticated experimental methods enabled us to address again the problem of integrated study of the nature of electric breakdown in liquids on a new higher level.

References to Preface and Introduction

1. V. Y. Ushakov, Pulsed Electric Breakdown in Liquids [in Russian], Publishing House of Tomsk State University, Tomsk (1975).
2. Mac Farlane, Philos. Mag., No. 10, 389 (1880).
3. A. Nikuradze, Das Flüssige Dielktrikum (Isolierende Flüssigkeiten). Berlin,Verlag von Julius Springer, 1934.
4. F. F. Volkenshtein, Liquid Dielectric Breakdown [in Russian], Moscow-Leningrad, (1934).
5. G. I. Skanavi, Physics of Dielectrics (Area of the Strong Fields). [in Russian], State Ph. and Math. Press, Moscow (1958).
6. I. E. Balygin, Electric Strength of Liquid Dielectrics [in Russian], Energiya, Leningrad (1964).
7. S. Whitehead, Dielectric Phenomena. Vol. 2. Electrical Discharges in Liquids, E. B. Wedmore, ed., London (1928).
8. W. Rogowski, Der elektrische Durchschlag von gasen, festen und fluessigen Isolatoren, Arch. Elektr., **23**, 569–578 (1930).
9. F. W. Peeck, Dielektric Phenomena in High-Voltage Engineering, New York, 1930.
10. A. F.Valter and L. L. Inge, Electric breakdown in liquid dielectrics, Zh. Tekh. Fiz., **4**, No. 9, 1669–1687 (1934).
11. E. B. Baker and H. A. Boltz, Thermionic emission into dielectric liquids, Phys. Rev., **51**, No. 11, 989 (1937).
12. D. W. Goodwin and K. A. Macfadyen, Electrical conduction and breakdown in liquid dielectrics, Proc. Phys. Soc. London, **66**, No. 398, 85–96 (1953).
13. T. J. Lewis, The dependence of the dielectric strength of pure liquids on cathode material, Proc. Phys. Soc. London, **B66**, No. 5, 425–428 (1953).
14. T. J. Lewis, The electric strength and molecular structure of liquids, Br. J. Appl. Phys., **9**, No. 1, 30–33 (1958).

15. J. K. Bragg, A. H. Sharbaugh, and R. W. Crowe, Cathode effects in the dielectric breakdown of liquids, Appl. Phys., **25**, No. 3, 382–391 (1954).

16. D. W. Swan, Electrical breakdown of liquid dielectrics, Proc. Roy. Soc. London, No. 3, 423–432 (1961).

17. G. S. Kuchinskii, Theory of breakdown of thin liquid dielectric layers, Zh. Tekh. Fiz., **36**, No. 7, 1297–1304 (1966).

18. L. B. Loebe, Fundamental Pracesses of Electrical Discharge in Gases, N.Y. , 1939.

19. T. Lewis, in: Progress in Dielectrics, Part 1, J. Berks and J. Shulman, **6,** (1965).

20. A. Hippel, Electric breakdown of solid and liquid insulators, Physics, **8**, No. 12, 816–832 (1937).

21. A. H. Scharbaugh and P. K. Watson, in: Progress in Dielectrics, Claredon Press, Oxford (1962), pp. 201–248.

22. I. Adamczewski, Ionization, Conductivity and Breakdown in Dielectric Liquids, Taylor and Francis Ltd. London, (1969).

23. J. A. Kok and M. M. G. Corbey, Testing the electric strength of liquid dielectric or insulating material, Appl. Sci. Res., **6**, No. 4, 285–295 (1957).

24. K. D. Metzmacher and J. E. Brignell, Application of the statistical model for liquid breakdown, Colloq. Int. CNRS, No. 179, 145–159 (1970).

25. K. C. Kao, Theory of high-field electrical conduction and breakdown in dielectric liquids, IEEE Trans., **EI-11**, 121–128 (1976).

26. V. S. Komelkov, Mechanism of pulsed breakdown in liquids, Dokl. Akad. Nauk SSSR, **47**, No. 4, 269–272 (1945).

27. V. S. Komelkov, Propagation of pulsed discharge in a liquid, Zh. Tekh. Fiz., **31**, No. 8, 948–960 (1961).

28. T. W. Liao and I. G. Anderson, Propagation mechanism of impulse corona and breakdown in oil, AIEE Trans., **72**, No. 1, 641–648 (1953).

29. I. G. Anderson and T. W. Liao, The propagation mechanism of impulse creepage discharges over oil immersed surfaces, AIEE Trans., No.1, 74 (1955).

30. I. E. Balygin, On the discharge duration in liquid insulating materials, Zh. Tekh. Fiz., **24**, No. 2, 337–347 (1954).

31. G. A. Vorobjev, Comments to the paper of I. E. Balygin "Pre-breakdown currents in a liquid," Zh. Tekh. Fiz., **27**, No. 6, 761 (1954).

32. I. S. Stekolnikov and V. Y. Ushakov, Study of the discharge phenomena in liquids, Zh. Tekh. Fiz., **35**, No. 9, 1692–1700 (1965).

33. V. Y. Ushakov, Optical and oscillographic studies of a pulsed discharge in liquids, Candidate's Dissertation, Tomsk Polytechnic Institute, Tomsk (1965).

34. A. P. Alkhimov, V. V. Vorobjev, V. F. Klimkin, et al., On the propagation of electric discharge in water, Dokl. Akad. Nauk SSSR, **194**, No. 5, 1052–1054 (1970).

35. E. A. Abramyan, V. A. Kornilov, V. M. Lagunov, et al., Megavolt Energy Concentrator, Dokl. Akad. Nauk SSSR, **201**, No. 1, 56–59 (1971).

36. V. F. Klimkin and A. G. Ponomarenko, Study of pulsed electric breakdown in liquids by the method of optical interferometry, Zh. Tekh. Fiz., **49**, No. 9, 1896–1904 (1979).

37. V. F. Klimkin, A multiframe ultraspeed laser shlieren photography system for observation of nanosecond pre-breakdown phenomena in liquids, Zh. Tekh. Fiz., **61**, No. 9, 15–19 (1991).

38. V. R. Kukhta, V. V. Lopatin, and P. G. Petrov, Reconstruction of permittivity profiles for symmetric microobjects from the interferometric data, Opt. Spektrosk., **56**, No. 1, 179–181 (1984); A setup for investigation of the initial stage of the electric discharge in dielectrics, Elektronn. Obrab. Mater., No. 3, 66–68 (1986).
39. I. T. Ovchinnikov, K. V. Yanshin, and E. V. Yanshin, Study of electric field distributions in water using the Kerr effect, Zh. Tekh. Fiz., **44**, No. 2, 472–474 (1974); Experimental investigations of pulsed electric fields in water at the tip electrode using the Kerr effect, Zh. Tekh. Fiz., **48**, No. 2, 2596–2598 (1978).
40. S. M. Korobeynikov, K. V. Yanshin, and E. V. Yanshin, Study of pre-breakdown fields in nitrobenzene using the Kerr effect, in: Abstracts of Reports at the All-Union Conf. on Physics of Dielectrics and New Areas of Their Application, Ser. 2 [in Russian], Karaganda (1978), pp. 18–19.
41. G. S. Kuchinskii and E. A. Morozov, Study of the physical phenomena in water in pre-discharge electric fields, Pisma Zh. Tekh. Fiz., **8**, No. 24, 1526–1531 (1982); Registration of electric fields in liquid dielectrics with the Mach–Zehnder interferometer using the Kerr effect, Zh. Tekh. Fiz., **53**, No. 6, 1215–1220 (1983).

1

Behavior of Liquids in Strong Electric Fields

We shall restrict our consideration of the problem indicated in the title of the chapter to a description of the processes that, in our opinion, play the key role in breakdown initiation and have been covered insufficiently in the literature.

1.1 Liquid Pressure under an Electric Field

1.1.1 Liquid pressure under conditions of impulse breakdown

The influence of a strong electric field on a liquid is noticeable when the electric field energy density is comparable with the external pressure $\varepsilon_0\varepsilon E^2/2 \geq P$. It is clear that this condition is usually satisfied in fields characteristic of electric discharge initiation. In this case, it is important to reveal mechanisms of influence of the electric field and arising pressure. The effects of a strong pulsed field are important not only for discharge ignition but also for electro-physics of liquids. The hydrostatic pressure arising in the liquid under exposure to pulses, in particular, at the expense of electrostriction and forces acting on the liquid in uniform and non-uniform fields should be examined in more detail. Forces acting on the liquid in the vicinity of the electrodes with allowance for the actual field structure near the electrodes having double electric layers and emission of charge carriers should also be analyzed.

   As is well known, the hydrostatic pressure influences significantly the electric strength of liquid dielectrics [1–4]. Qualitative explanation of this experimental fact was one of the main evidences for the bubble breakdown mechanism. It is commonly considered that pre-breakdown bubbles are formed in the liquid due to boiling up, and since the boiling point depends on the pressure, its variations change the boiling point and hence the electric strength. However, the circumstance that bubbles are formed in the region exposed to the electric field was not taken into account. Since the electric field renders the mechanical action on any dielectric body and this action in the uniform field can cause volume compression or expansion and deformation of

the body, this should influence the thermodynamic stability of the bubble facilitating or hindering its growth. To consider the mechanical action of the electric field, we first calculate the hydrostatic pressure of the liquid when the electric field is switched on. The formation of pre-breakdown bubbles was examined in [5–9], where the electrostriction pressure of the liquid was set equal to $P_{\text{str}} = \varepsilon_0(\varepsilon - 1)(\varepsilon + 2)E^2/6$. Experiments [10] in n-hexane demonstrated that the additional hydrostatic pressure caused by an increase in the liquid density was actually registered. At the same time, calculations of the bubble deformation with allowance for electrostriction gave incorrect results. Namely, from the calculated results it followed that the bubble should oblate along the field direction [11, 12], whereas experiments [11–14] demonstrated that bubbles and drops elongate along the field force lines. To eliminate this contradiction, in [11] it was suggested to consider the electrostriction pressure to be image one. The incorrectness of this assumption was pointed out in [12]; the necessity of an analysis of the electrostriction influence on bubble formation was repeatedly indicated in [15, 16].

An attempt to invoke electrostriction in the explanation of the formation of a pre-breakdown shock wave near the tip cathode in the field with a strength of $\sim 25\,\text{MV/cm}$ was made in [17], where it was established that initial luminescence was preceded by the formation of the electrostriction shock wave at the tip cathode. It was pointed out that the ionization processes arise most probably in cavitations voids formed behind the shock wave front; the assumption of Yanshin et al. [17] about the electrostriction nature of the shock wave was conjectural. Nevertheless, the absence of ionization phenomena in water upon exposure to the field with a strength of $25\,\text{MV/cm}$ for 30–$100\,\text{ns}$ pointed out in [17] is of theoretical and practical importance; it should be analyzed in more detail.

Since the electrostriction pressure is caused by changes in the liquid density, a transition process of density redistribution and establishment of pressure should be observed which will be terminated when the electrostriction forces are compensated by the arising pressure gradient. An analytical solution to the problem on pressure dynamics and its influence on bubbles faces significant difficulties and can be derived only for a limited class of electrode systems. No consideration has been given to this problem. A formal similarity of the equations gives us grounds to consider the aero-hydrodynamic problem of atmospheric fluctuations accompanying the gravitational force change to be the closest analog of the problem of the electrostriction pressure dynamics [18]. However, before proceeding to a study of the electrostriction pressure dynamics, we must study the conditions of static equilibrium of the liquid in the electric field and then consider the relaxation process of establishing pressure for two important types of the electrode system admitting analytical solutions, namely, a single sphere and coaxial electrode system.

1.1.2 Nature of the electrostriction pressure

The electrostriction pressure is formed in the liquid because of the dependence of its permittivity on the density:

$$\Delta P_{\mathrm{es}} = \varepsilon_0 \rho \frac{\partial \varepsilon}{\partial \rho} \frac{E^2}{2} \, . \tag{1.1}$$

This dependence is different for gases and liquids. Moreover, for polar and non-polar liquids it also has different forms.

For non-polar liquids, the dependence of the permittivity ε on the liquid density ρ (for convenience, in this chapter we omit the subscript "l" of the liquid density) is described by the well-known Clausius–Mossotti equation from which it follows that

$$\rho \frac{\partial \varepsilon}{\partial \rho} = \frac{(\varepsilon - 1)(\varepsilon + 2)}{3} \, . \tag{1.2}$$

For polar liquids, we take advantage of the Onsager–Kirkwood–Fröhlich equation [19, 20]; after differentiation, we obtain [21, 22]

$$\rho \frac{\partial \varepsilon}{\partial \rho} = \varepsilon - \varepsilon_\infty \, , \tag{1.3}$$

where ε_∞ is the permittivity in the infrared range. Experiments [10] demonstrated that (1.2) for non-polar liquids is obeyed with high accuracy. For polar liquids, experimental results of Jacobs and Lowson [23] are well described by the formula

$$\rho \frac{\partial \varepsilon}{\partial \rho} \approx k \cdot \varepsilon \, , \tag{1.4}$$

where k is a coefficient of the order of unity, and for most examined liquids $k < 1.5$.

1.1.3 Pressure in electro-hydrostatic equilibrium

As is well known, equilibrium of liquid in the absence of mass forces corresponds to the absence of dependence of pressure, temperature, and chemical potential on coordinates. In an electric field, the chemical potential is independent of coordinates when the condition [24]

$$P(\rho(x, y, z)) - \varepsilon_0 \rho \frac{\partial \varepsilon}{\partial \rho} \frac{E^2(x, y, z)}{2} = \mathrm{const} = P_0 \tag{1.5}$$

is satisfied in the entire liquid volume. Here P_0 is the equilibrium pressure which coincides with P where the field is small.

In addition to condition (1.5) of liquid equilibrium in the volume, equilibrium conditions must be satisfied on the volume boundaries. These conditions unambiguously determine the P_0 value and hence, according to condition (1.4), the pressure in the entire volume.

Let us consider some types of boundary conditions and determine P_0 and P for them.

a) *Closed volume.* In this case, the liquid inflow into the volume is impossible; therefore, the average density and pressure remain constant: $\rho_{av} = \rho_0$ and $P_{av} = P_0$. After averaging of (1.5) over the volume, we obtain that

$$P_0 = P_{out} - \varepsilon_0 \rho \frac{\partial \varepsilon}{\partial \rho} \frac{\int E^2\,(x,y,z)\,dV}{2V} = P_{out} - \varepsilon_0 \rho \frac{\partial \varepsilon}{\partial \rho} E_{av}^2/2 \,, \qquad (1.6)$$

where P_{out} is the external pressure and E_{av} is the average field strength inside the volume.

In a uniform field, $E_{av} = E_0$ and hence, $P(x,y,z)$ and $\rho(x,y,z)$ remain unchanged when the field is switched on, whereas in a sharply non-uniform field, $E_{av} \sim 0$ and the P value is described by the expression

$$P\,(x,y,z) = P_{out} + \varepsilon_0 \rho \frac{\partial \varepsilon}{\partial \rho} E^2\,(x,y,z)\,/2\,. \qquad (1.7)$$

Thus, the sharply non-uniform field in a closed volume causes the pressure in the region of field amplification to increase, whereas the uniform field does change the hydrostatic pressure.

b) *Boundary with the atmosphere.* In this case, the equilibrium boundary condition [24]

$$P_b - P_{out} = \varepsilon_0 \rho \frac{\partial \varepsilon}{\partial \rho} E_b^2/2 - \varepsilon_0\,(\varepsilon - 1)\,\left(\varepsilon E_{n.b}^2 + E_{t.b}^2\right)/2 \qquad (1.8)$$

should be considered additionally, where $E_{n.b}$ is the normal field component and $E_{t.b}$ is the tangential field component at the liquid boundary. From here it immediately follows that

$$P_0 = P_{out} - \varepsilon_0\,(\varepsilon - 1) \cdot \left(\varepsilon E_{n.b}^2 + E_{t.b}^2\right)/2\,,$$

$$P\,(x,y,z) = P_{out} + \varepsilon_0 \rho \frac{\partial \varepsilon}{\partial \rho} E^2/2 - \varepsilon_0\,(\varepsilon - 1)\,\left(\varepsilon E_{n.b}^2 + E_{n.b}^2 + E_{t.b}^2\right)/2\,. \quad (1.9)$$

1.2 Transient Processes of Establishing Pressure

Let us consider the transient process of establishing pressure in a liquid under voltage application to the electrode system. In the region of action of the non-uniform electric field, a bulk force arises whose density is given by the expression

$$f = -\nabla P_0 = -\nabla \left(P - \varepsilon_0 \rho \frac{\partial \varepsilon}{\partial \rho} \frac{E^2}{2} \right)\,. \qquad (1.10)$$

Under the action of this force, the pressure is redistributed with the rate depending on the degree of field non-uniformity, electrode system dimensions, and liquid viscosity. In calculations of pressure establishing, we restrict ourselves to an examination of low-viscosity liquids. For viscous liquids, we present only estimates.

1.2.1 Electrostriction wave near the spherical electrode under impulse voltage

Let us consider the dynamics of establishing the electrostriction pressure when the voltage is instantaneously applied to a sphere placed in a liquid dielectric [25, 26]. The choice of the electrode system is caused by the circumstance that the sphere of small radius is the conventional model of the tip electrodes. To describe the motion of liquid and its pressure, we now write down the acoustics equations with the density of force specified by (1.10):

$$\frac{\partial W}{\partial t_1} + c\frac{\partial U}{\partial r_1} = -\varepsilon_0 \frac{\partial \varepsilon}{\partial \rho} \frac{2E_0^2 r_0^4}{cr_1^5} ,$$
$$\frac{\partial U}{\partial t_1} + 2c\frac{W}{r_1} + c\frac{\partial W}{\partial r_1} = 0 ,$$
(1.11)

where $W = v/c$ is the ratio of the liquid to sound velocities, $u = \Delta\rho/\rho$ specifies the relative density change, and E_0 is the field strength near the sphere. The initial conditions of this system of equations have the form

$$U\mid_{t_1=0}\rangle = 0 , \ W\mid_{r_1=r_0} = 0 ,$$
$$W\mid_{t_1=0} = 0 , \ U\mid_{r_1=\infty} = 0 .$$
(1.12)

For convenience of solution, we now write down the equations in a dimensionless form, replacing

$$r = r_1/r_0 , \ \ t = t_1 \cdot c/r_0 , \alpha = \varepsilon_0\rho\frac{\partial \varepsilon}{\partial \rho}E_0^2 / \left(\rho \cdot c^2\right) .$$

Then (1.1) assumes the form

$$\frac{\partial W}{\partial t} + \frac{\partial U}{\partial r} = \frac{2\alpha}{r} ,$$
$$\frac{\partial U}{\partial t} + \frac{W}{r} + \frac{\partial W}{\partial r} = 0 .$$
(1.13)

Hyperbolic system of equations (1.13) with boundary conditions (1.12) is invertible, and taking advantage of the Laplace transform [27], it can be reduced to the form

$$pW(r,p) + \frac{dU(r,p)}{dr} = -\frac{2\alpha}{pr^5} ,$$
$$pU(r,p) + \frac{dW}{dr} + \frac{2W}{r} = 0 .$$
(1.14)

From the above system of equations, we obtain the second-order equation for U

$$\frac{d^2U}{dr^2} + \frac{2dU}{rdr} - p^2U = -\frac{6\alpha}{pr^6}$$
(1.15)

with the boundary conditions $U(\infty, p) = 0$ and $\dfrac{dU(1,p)}{dr} = -\dfrac{2\alpha}{p}$. The function

$$U_0\left(r,p\right) = C_1 \frac{e^{pr}}{r} + C_2 \frac{e^{-pr}}{r} \tag{1.16}$$

is the general solution of the homogeneous equation. A partial solution of the inhomogeneous equation can be found by variation of constants:

$$U'\left(r,p\right) = \frac{3\alpha e^{pr}}{p^2 r} \int \frac{e^{-px} dx}{x^5} - \frac{3\alpha e^{-pr}}{p^2 r} \int \frac{e^{px} dx}{x^5}. \tag{1.17}$$

The constants C_1 and C_2 are determined from the boundary conditions: $C_1 = 0$ from the condition at infinity, and

$$C_2 = \frac{2\alpha e^p}{p\left(p+1\right)} + 3\alpha \int\limits^1 \frac{e^{-p(x-2)} dx}{p\left(p+1\right) x^5} - 3\alpha \int\limits^1 \frac{e^{-p(x+2)} dx}{p^2 \left(p+1\right) x^5} - 3\alpha \int\limits^1 \frac{e^{px} dx}{p^2 x^5}. \tag{1.18}$$

Unity for the upper integration limit means that indefinite integrals are taken at this point. For convenience of further calculations, we formally transform the indefinite integrals into definite ones, and set the lower integration limit so that the integral value at this point was equal to zero:

$$U\left(r,p\right) = \frac{2\alpha e^{-p(r-1)}}{p\left(p+1\right) r} - \frac{3\alpha}{r} \left(\int\limits_r^\infty \frac{e^{-p(x-r)} dx}{p^2 x^5} + \int\limits_1^\infty \frac{e^{-p(x-2+r)} dx}{p\left(p+1\right) x^5} \right.$$
$$\left. - \int\limits_1^\infty \frac{e^{-p(x+2+r)} dx}{p^2\left(p+1\right) x^5} + \int\limits_r^1 \frac{e^{p(x-r)} dx}{p^2 x^5} + \int\limits_r^1 \frac{e^{p(x-r)} dx}{p^2 x^5} \right). \tag{1.19}$$

Because the integrals everywhere converge, at least in the sense of the principal Cauchy value, we can change the order of the inverse Laplace transformation and integration. Omitting details of calculations, we present the final solution.

For $r_1 \geq r_0 + ct_1$,

$$U\left(r_1,t_1\right) = \frac{\varepsilon_0 \rho \frac{d\varepsilon}{d\rho} E_0^2 r_0^4}{2\rho \cdot c^2 \cdot r_1} \left[\frac{1}{r_1^3} - \frac{1}{2\left(r_1 + ct_1\right)^3} - \frac{1}{2\left(r_1 - ct_1\right)^3} \right], \tag{1.20}$$

and for $r_1 < r_0 + ct_1$,

$$U\left(r_1,t_1\right) = \frac{\varepsilon_0 \rho \frac{d\varepsilon}{d\rho} E_0^2 r_0^4}{2\rho \cdot c^2 \cdot r_1} \left[\frac{1}{r_1^3} - \frac{1}{2\left(r_1 + ct_1\right)^3} - \frac{1}{2\left(2r_0 + ct_1 - r_1\right)^3} \right.$$
$$- \frac{1}{2r_0\left(2r_0 + ct_1 - r_1\right)^2} - \frac{1}{2r_0^2\left(2r_0 + ct_1 - r_1\right)}$$
$$\left. + \frac{e^{-\frac{\left(2r_0 + ct_1 - r_1\right)}{r_0}}}{2r_0^3} \left\{ \mathrm{Ei}\left(\frac{2r_0 + ct_1 - r_1}{r_0}\right) - \mathrm{Ei}\left(1\right) + 2\exp\left(1\right) \right\} \right], \tag{1.21}$$

where Ei(x) is the integral exponent [28]. From the solutions obtained it can
be seen that when the electric field is switched on, two rarefaction waves of
the form $f(r_1 - ct_1)$ and $f(r_1 + ct_1)$ are generated. The first wave propa-
gates toward the sphere and after reflection from it is transformed into the
compression wave $g(ct_1 - r_1 - 2r_0)$; the second wave goes to infinity. The pres-
sure distribution near the sphere is shown in Fig. 1.1 for the transient period.
From the figure it can be seen that the region in which density and pressure
decrease, that is, $\Delta\rho \leq 0$ and $\Delta P_{es} = \Delta\rho c^2 \leq 0$, has the size $\Delta r \sim r_0$ and
moves from the electrode with the sound velocity. The displacement of the
spatial pressure minimum is described by solutions (1.20) and (1.21), and the
absolute pressure minimum is observed at $t_1 = 1$.

The pressure is always positive at $r = r_0$. It first increases from zero to
$0.7\varepsilon_0\rho\frac{\partial\varepsilon}{\partial\rho}E_0^2$ during $t_1 \sim 2 \cdot r_0/c$ and then decreases to a stationary value

$$\Delta P_{es} = \varepsilon_0\rho\frac{\partial\varepsilon}{\partial\rho}\frac{E^2(r)}{2}. \tag{1.22}$$

This stationary pressure, as expected, coincides with the stationary elec-
trostriction pressure distribution characterized by (1.7).

We emphasize that the space-time electrostriction pressure distribution
$\Delta P(r,t)$ can be derived for voltage pulses of arbitrary form $\varphi(t)$. The simplest
method is to take advantage of the Duhamel integral
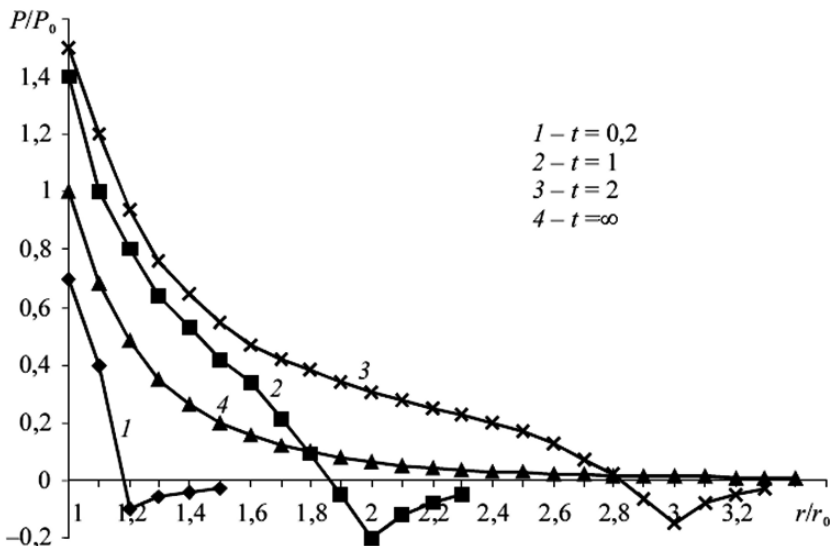
Fig. 1.1. Dependence of the normalized electrostriction pressure on the radius at
the indicated time moments from the impulse voltage application to the spherical
electrode

$$\Delta P_{\text{es}}\left(r,t\right) = \rho \cdot c^2 \int\limits_0^t \varphi\left(t\right) U\left(r, t - \tau\right) d\tau, \tag{1.23}$$

in which the role of the transient function is played by the solution obtained.

Among the factors that specify the applicability limits of the above expressions are the sound wave attenuation, dipole saturation of liquid molecules, and violation of the conditions of acoustic approximation.

The distance at which the monochromatic wave with circular frequency ω attenuates in the medium having viscosity η, adiabatic exponent γ, thermal conduction κ, and heat capacity c_p is determined by the classical attenuation coefficient [29]

$$l \approx \frac{2\rho c^3}{\omega^2} \frac{1}{\left(\gamma - 1\right)\kappa/c_p + 4\eta/3} . \tag{1.24}$$

In our case, $\omega \sim c/r_0 \sim 10^7$ Hz, and l is large for low-viscosity liquids; for example, $l = 1\,\text{m}$ for water and nitrobenzene. For slower processes with characteristic frequencies in the kilohertz range, the attenuation length can be even greater.

We note that for viscous liquids with $l < r_0$, the character of electrostriction waves changes, the pressure is established more slowly, and the negative pressure region is absent.

Let us estimate the applicability limits of the acoustic approximation from the condition $U_{\max} << 1$ from which it follows that $\alpha << 1$ or

$$E_0 \ll E_{\text{cr}} = \frac{c}{\sqrt{\varepsilon_0 \dfrac{\partial \varepsilon}{\partial \rho}}} . \tag{1.25}$$

For nitrobenzene, $E_{\text{cr}} = 27\,\text{MV/cm}$, and for water $E_{\text{cr}} = 18\,\text{MV/cm}$. For $E_0 << E_{\text{cr}}$, the acoustic approximation is applicable, and for $E_0 \sim E_{\text{cr}}$, the establishment of pressure must have some special features.

The complexity of calculations is aggravated by the dipole saturation that occurs in these fields and consists of the dominant orientation of molecules along the field. After achievement of the saturation field strength, the dipole moment of unit volume cannot increase any more with further increase of the field strength. This is equivalent to a decrease in the permittivity of the polar liquid. The saturation field strength can be estimated from the following reasons [26]. If we neglect the deformation polarization component in comparison with the orientation component, the maximum dipole moment of unit volume will be determined from the expression $P_{\max} = d \cdot n$, where d is the dipole moment of the molecule and n is the number of molecules in unit volume. On the other hand, by definition the dipole moment of unit volume is the polarization $P = (\varepsilon - 1)\varepsilon_0 \cdot E$. Considering that values of ε and density n are constant at the beginning of saturation and equating the expressions for polarization, we obtain

$$E_{\mathrm{s}} = dn/\left(\left(\varepsilon - 1\right)\varepsilon_0\right) . \tag{1.26}$$

For nitrobenzene $E_{\mathrm{s}} = 2\,\mathrm{MV/cm}$, and for water $E_{\mathrm{s}} = 3\,\mathrm{MV/cm}$. The accuracy of the estimation based on (1.2) and (1.3) considerably decreases at $E \sim E_{\mathrm{s}}$.

We now consider qualitatively the pattern of establishing the electrostriction pressure. It is obvious that the wave character of the process will be kept unchanged in strong electric fields when the acoustic approximation is inapplicable and the ε value will decrease in the region of maximum field. We note that the last circumstance must cause the field in this region to increase, thereby leading to further decrease in ε, field amplification, and so on. The increase in the field strength does not lead to the electrostatic catastrophe, and the field remains bounded due to a finite electrode potential. Since values of the field strength E and field gradient E^2 increase, the force acting on the liquid at the initial moment of time also increases according to (1.10). Under the action of mass forces, the liquid starts to move toward the electrode and passes by the equilibrium position by inertia; then the liquid gradually returns to the equilibrium position. In the case of significant pressure drop, the reflected wave can be transformed into a shock wave propagating from the electrode.

Let us qualitatively analyze the influence of the electrostriction pressure on the dependence of impulse electric strength on the external pressure. According to [30–32], for tip electrodes this dependence becomes pronounced when the acting voltage duration is greater than $1\,\mu s$; it is not observed for shorter voltage pulses. A qualitative understanding of the electrostriction contribution to this phenomenon is possible even without consideration of the discharge mechanism. If we accept that the electric strength increases for shorter voltage pulses and the electrostriction pressure exceeds stationary value (1.22), a decrease in the voltage pulse duration should result in a significant increase in the hydrostatic pressure near the electrode and hence, the role of the external factor (pressure) should decrease. In addition, as demonstrated below, in order that deformed bubbles with sizes of $10\,\mu m$ be formed in $t \sim 100\,\mathrm{ns}$, forces considerably exceeding the external pressure used in experiments [2, 30–32] must be applied; exactly the breakdown of these bubbles initiates a discharge.

1.2.2 Dipole saturation effect in water and its influence on pre-breakdown processes in the system of tip electrodes

In experiments with the tip electrodes under nanosecond voltage pulses, the field strength in liquid dielectrics exceeds $10^7\,\mathrm{V/cm}$ [17, 33, 34]. It is assumed that such fields are created at micro-tips of the flat electrode surface, thereby initiating an electric discharge in the gap under relatively low average field $E \sim 10^5\,\mathrm{V/cm}$. When analyzing the initial ionization phenomena and conditions of bubble formation, it is implicitly assumed that the liquid keeps the structure and dielectric and thermodynamic properties unchanged. These assumptions

are not evident at least for polar liquids, because the influence of strong fields must result in an orientation of virtually all dipole molecules in the liquid. For non-uniform electric fields, the spatial distribution of the degree of orientation of molecules will change with field non-uniformity and will redistribute the field thereby increasing the degree of field non-uniformity. Simultaneously with the field redistribution, the electrostriction pressure itself will be redistributed.

Let us consider this effect for water having the differential permittivity described by the well-known empirical formula [35]:

$$\frac{dD}{dE} = \varepsilon_0 \frac{\varepsilon(0) - n_0^2}{1 + bE^2} , \qquad (1.27)$$

where $\varepsilon(0)$ is the permittivity of water at $E = 0, n_0^2 = 1.78$, and $b = 1.2 \cdot 10^{-13} \mathrm{m}^2 \cdot \mathrm{V}^{-2}$. After integration of this expression, we obtain

$$\varepsilon(E) = \frac{\varepsilon - n^2}{bE^2} ar \cot\left(bE^2\right) + n_0^2 . \qquad (1.28)$$

A decrease in ε of water with increasing E results in an additional amplification of the field $E = k_E E_0$ and electrostriction pressure $P_{es} = k_P P$ on the sphere surface. Figure 1.2 shows the calculated amplification coefficients k_E and k_P. From the figure it can be seen that the effect of dipole saturation becomes pronounced when $E_0 > 2\,\mathrm{MV/cm}$. At $E_0 \sim 20\,\mathrm{MV/cm}$, the actual field strength on the sphere is by 5 times greater that the calculated one, that is, $E_0 = 100\,\mathrm{MV/cm}$. Since the increase in the electric field is caused by the decrease in ε, the rate of increase of the electrostriction pressure slows down, and its maximum amplification coefficient $k_P = 3$ at $E_0 = 6\,\mathrm{MV/cm}$ decreases to $k_P \sim 1.5$ with further increase in the voltage applied to the electrode.

The dipole saturation causes the field and pressure to concentrate near the electrode (Fig. 1.3), thereby accelerating the transient process. We note that ε changes in the process of orientation of water molecules during $10^{-11} - 10^{-10}\,\mathrm{s}$, that is, practically inertia less. The force acting on the volume element of water
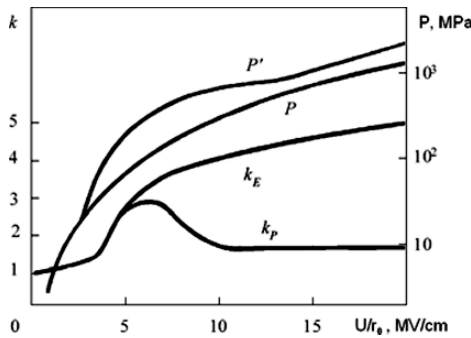
Fig. 1.2. Dependences of the pressure and field amplification coefficient on U/r_0 near the sphere with (P' and k_E) and without allowance for the dipole saturation (P and k_p)
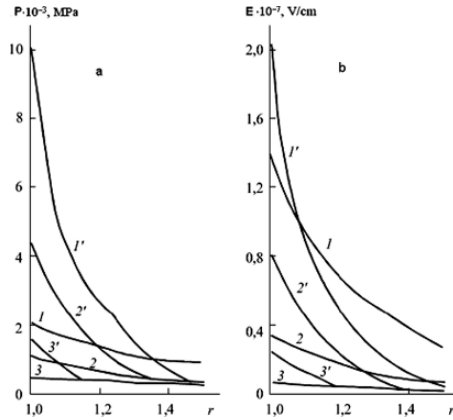
Fig. 1.3. Distributions of the electric field strength (**a**) and electrostriction pressure near the electrode (**b**) with (without primes) and without allowance for the dipole saturation effect (with primes) for $U/r_0 = 20$ (*curves 1 and 1′*), 10 (*curves 2 and 2′*), and 5 MV/cm (*curves 3 and 3′*)

when the field is switched on can be expressed through the stationary pressure gradient. The increase of forces acting on the near-electrode water layers in the initial stage of the transient process and the spatial localization of these forces will result in a sharp pressure drop in the vicinity of electrodes. In this case, the stress wave in water can be followed by a shock wave engendered by a large pressure gradient near the sphere.

In experiments [17,33,36] with the tip cathode ($r_0 = 30\,\mu m$), a jump of the water density propagating from the cathode approximately with the sound velocity was recorded for a voltage amplitude of 250 kV when the field strength near the tip end calculated disregarding saturation was 25 MV/cm (Fig. 1.4). The voltage front pulse duration was less than the characteristic time $r_0/c = 20$ ns, and hence the pressure at the tip was established in the wave regime.
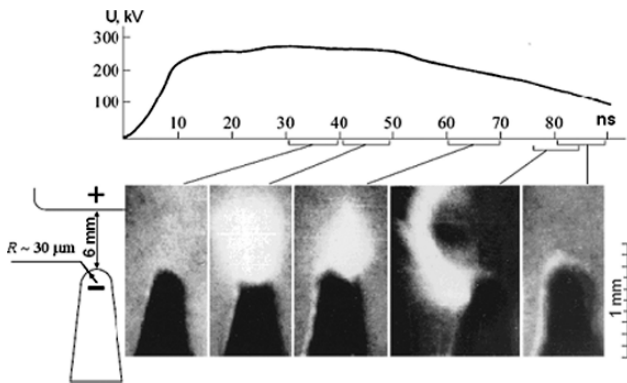
Fig. 1.4. Photographs illustrating the shock wave formation in water near the tip electrode under a strong electric field

The above analysis demonstrates that the observed density jump could be due to a stress pulse or shock wave.

Let us emphasize that the breakdown from the positive tip is initiated on the pulse front; therefore, the electrostriction pressure had no time to become stationary for $t < \tau_{\text{fr}} = 5 \cdot 10^{-9}$ s. It seems likely that the electrostriction plays no role in the pre-breakdown processes near the tip anode.

The important circumstance in an analysis of pre-breakdown processes is that the electrostriction pressure near the tip electrodes considerably exceeds the external pressure in pre-breakdown fields. When E_0 increases from 1 to 20 MV/cm, the water pressure increases from 3.5 MPa to 2.2 GPa (Fig. 1.3b). We note that water changes to ice VI at room temperature under pressure $P_n = 1$ GPa. It is not clear whether water changes to ice under the action of the electrostriction pressure, because it is not known how the dipole saturation affects the P_n value and the lifetime of water molecules in the meta-stable state (the normal state of water molecules under this pressure is metastable).

The following is of interest. Estimates demonstrate that in experiments [33, 36,37], the stress wave amplitude in water reached 10^8 Pa, which corresponded to its theoretical tensile strength and hence, conditions for instantaneous water cavitation had been realized. The special features of this electrostriction cavitation, as follows from the above analysis, are short microbubble lifetime determined by the stress action duration at the observation point in the liquid (which in [36] was $< 10^{-8}$ s) and the liquid layer separating the cavitation zone from the electrode (see Fig. 1.1).

Based on an analysis of the experimental results [33, 36], a conclusion can be made that the electrostriction stress wave, even though it caused cavitation of water, did not decrease its electric strength. This is indicated, in particular, by the long lag time (10^{-7} s) of discharge ignition from the tip cathodes observed in experiments. The absence of ionization phenomena inside cavitation microbubbles can be explained by the absence of free electrons, because the cavitation zone is separated from the electrode by the liquid layer as well as by the short microbubble lifetime (less than 10^{-8} s from the moment of bubble formation to the arrival of the positive pressure wave). Estimates demonstrate that the probability of electron generation by autoionization of water molecules in the cavitation zone was insignificantly small under conditions of experiments [33, 36]. The background free electrons of cosmic origin with a frequency of 10^9 m$^{-3} \cdot$ s^{-3} in water can also be neglected [40].

The electrostriction pressure near the microtips on the electrode surface is established in the quasistationary regime even under application of nanosecond voltage pulses because of small microtip dimensions. The existence of pre-breakdown bubbles near the electrode under these conditions must be directly connected with emission of charge carriers. The formation of a monopolar space charge near the electrode decreases the electrostriction pressure component in the vicinity of the electrode surface due to the effect of field screening, and the liquid density also decreases under the action of the Coulomb forces. Below this problem is considered in more detail.

Thus, the dipole saturation effect in pre-breakdown electric fields can lead to a significant increase in the electrostriction pressure, thereby hindering the microbubble formation and increasing the pre-breakdown period.

1.2.3 Electrostriction waves in a coaxial line

Coaxial lines with liquid insulation are widely used in high-voltage engineering for shaping and transfer of voltage pulses [39, 41, 56]. When analyzing reasons for the electric breakdown of insulation of these lines, the opportunity of forming electrostriction waves was not considered. It was assumed that during passage of a high voltage pulse, the pressure at any point of the liquid remains unchanged and equal to the external pressure. However, taking into account the influence of the pulsed field on liquid insulation, by analogy with the spherical electrode examined above, we can expect that under certain conditions, the electrostriction waves will be formed in coaxial lines as well and will influence significantly the pressure both in the liquid volume and near the electrodes.

As in the previous case, we consider a step influence of voltage and neglect the time of electromagnetic wave propagation. That is, we consider that the potential difference between the electrodes is established instantaneously in the entire coaxial line.

In this case, the initial equations in cylindrical coordinates have the form

$$\frac{\partial U_1}{\partial t_1} + c\frac{W}{r_1} + c\frac{\partial W}{\partial r_1} = 0\,,$$
$$\frac{\partial W}{\partial t_1} + c\frac{\partial U_1}{\partial r_1} = -\frac{1}{c}\cdot\frac{\partial \varepsilon}{\partial \rho}\cdot\frac{E_0^2\cdot r_0^2}{r_1^3} \tag{1.29}$$

with initial and boundary conditions

$$U_1\left|_{t_1=0}\right. = 0,\ \ W\left|_{r_1=R_0}\right. = 0,\ \ W\left|_{t_1=0}\right. = 0,\ \ W\left|_{r_1=r_0}\right. = 0\,. \tag{1.30}$$

Here $U_1 = \frac{\delta\rho}{\rho}$, $W = \frac{V}{C}$, E_0 is the field strength at the internal electrode of radius r_0, and R_0 is the external electrode radius.

After replacement of variables $r = \frac{r_1}{r_0}$ and $t = t_1\cdot c/r_0$, we eliminate W from (1.29) and express the unknown U_1 in the form $U_1 = U + \frac{\alpha}{2r^2}$. We arrive to the equation

$$\frac{\partial^2 U}{\partial t^2} + \frac{\partial^2 U}{\partial r^2} + \frac{1}{r}\cdot\frac{\partial U}{\partial t} = 0 \tag{1.31}$$

with boundary and initial conditions

$$U\left|_{t=0}\right. = \frac{\alpha}{2r^2},\ \ \frac{\partial U}{\partial r}\left|_{r=1}\right. = 0,\ \ \frac{\partial U}{\partial t}\left|_{t=0}\right. = 0,\ \ \frac{\partial U}{\partial r}\left|_{r=b}\right. = 0\,, \tag{1.32}$$

where $b = R_0/r_0$. Homogeneous (1.31) with homogeneous boundary conditions (1.32) can be solved by the method of variable separation:

$$U(r,t) = R(r) \cdot T(t),$$

$$\frac{\dfrac{\partial^2 R}{\partial r^2} + \dfrac{1}{r} \cdot \dfrac{\partial R}{\partial r}}{R} = \frac{\dfrac{\partial^2 T}{\partial t^2}}{T} = -\lambda^2. \tag{1.33}$$

Partial solutions of this equation have the form

$$T_\lambda(t) = a_1 \cos \lambda t + a_2 \sin \lambda t, \tag{1.34}$$

$$R_\lambda(t) = a_3 J_0(\lambda r) + a_4 N_0(\lambda r),$$

where $J_0(x)$ and $N_0(x)$ are the zero-order Bessel and Neumann functions. Substituting the partial solutions to the initial and boundary conditions, we find that $a_2 = 0$ and eigenvalues λ_k obey the equation

$$N_1(\lambda_k) \cdot J_0(b\lambda_k) = N_0(b\lambda_k) \cdot J_1(\lambda_k), \tag{1.35}$$

where $J_1(x)$ and $N_1(x)$ are the first-order Bessel and Neumann functions.

In this case, a solution is written as

$$U(r,t) = \sum_{k=0}^{\infty} C_k \left[N_1(\lambda_k) \cdot J_0(\lambda_k r) + N_0(\lambda_k r) \cdot J_1(\lambda_k) \right], \tag{1.36}$$

where C_k is found by expanding the initial condition in eigenfunctions (1.34):

$$C_k = \frac{1}{N_k^2} \int_1^b \frac{\alpha dr}{2r} \left[N_1(\lambda_k) \cdot J_0(\lambda_k r) + N_0(\lambda_k r) \cdot J_1(\lambda_k) \right]. \tag{1.37}$$

The squared norm of the function is determined from the formula [42]

$$N_k^2 = \frac{2}{\pi \lambda_k^2} \left[\frac{J_1^2(\lambda_k)}{J_1^2(b\lambda_k)} - 1 \right]. \tag{1.38}$$

For the eigenvalue $\lambda = 0$, the partial solution can be found analytically:

$$U_0 = \frac{\alpha \cdot \ln b}{b^2 - 1}, \tag{1.39}$$

For other partial solutions, the coefficients C_k are expressed through the integral Bessel functions

$$\int_x^{\infty} \frac{1 - J_0(t)}{t} dt, \quad \int_x^{\infty} \frac{N_0(t)}{t} dt. \tag{1.40}$$

Function (1.35) was calculated on a computer under a specially developed program.
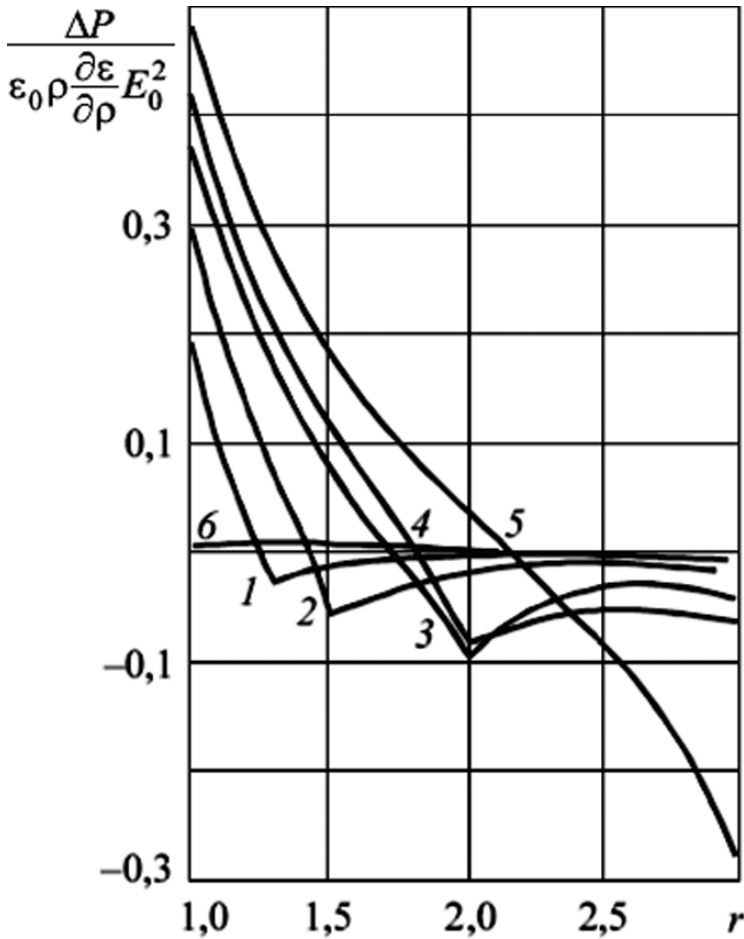
Fig. 1.5. Electrostriction wave in the coaxial system at different time moments after switching of the voltage $t = 0.25$ (*curve 1*), 0.5 (*curve 2*), 1.0 (*curve 3*), 2.0 (*curve 4*), 3.0 (*curve 5*), and 4.0 (*curve 6*)

Figure 1.5 shows the calculated (dimensionless) electrostriction pressure versus the spatial coordinate at the indicated time moments. The ratio of the coaxial electrodes radii b was equal to 3. This value was close to $b = 2.718$ at which the cable had a maximum breakdown voltage [41]. It can be seen that the electrostriction wave is no less clearly pronounced for the coaxial electrode system than for the spherical electrode. In particular, there is a pressure minimum which is displaced from the central electrode with the sound velocity. An absolute pressure minimum of $-0.27\varepsilon_0\varepsilon E_0^2$ is recorded near the external electrode at $t = 2$. The dissimilarity from the spherical electrode is caused by the presence of the second boundary. Near this boundary, the

pressure decreases below its stationary value due to inertia; then it increases again. At the moment of time $t = 4$, zero excess pressure is established in the entire region; then the above-described process is repeated again. As a result, undamped oscillations arise in the coaxial electrode system (Fig. 1.6). The above-described character of the electrostriction pressure dynamics in liquids is confirmed by the experimental results obtained in the study of pre-breakdown processes in water and trichlordiphenyl [42, 43].

Experimental setup [42, 43] comprised a voltage-pulse generator, LG-75 laser, Mach–Zehnder interferometer, blade-blade electrode system, and photorecorder. The generator comprised a charged cable 40 m long connected to a measuring cell. The voltage applied to the cell changed periodically: a 400-ns voltage pulse was followed by a voltage pulse of opposite polarity through the time interval of the same duration. The pulse front duration did not exceed 50 ns. The cell was inserted in one of the interferometer arms; the same cell but without electrodes was inserted into the second arm. The stainless steel electrodes were shaped as wedges with edge 20 mm long, 45°-angle between the wedge planes, and curvature radius of 0.45 mm. The interelectrode gap was 2 mm long. The photorecorder operated in the slit scanning regime. In the absence of voltage on the electrodes, an optical image was formed on the photorecorder photocathode due to different optical path lengths of beams caused by different mirror rotation angles. Under application of voltage, this image was transformed due to the Kerr and elasto-optical effects.

Figure 1.7 shows the typical chronogram of interference bands registered under a voltage pulse with an amplitude of 120 kV applied to the cell filled with deionized water, and Fig. 1.8 shows variations of the water refractive index at the indicated moments of time reconstructed from this chronogram. Since variations of the refractive index are determined by both the Kerr and elasto-optical effects [44]
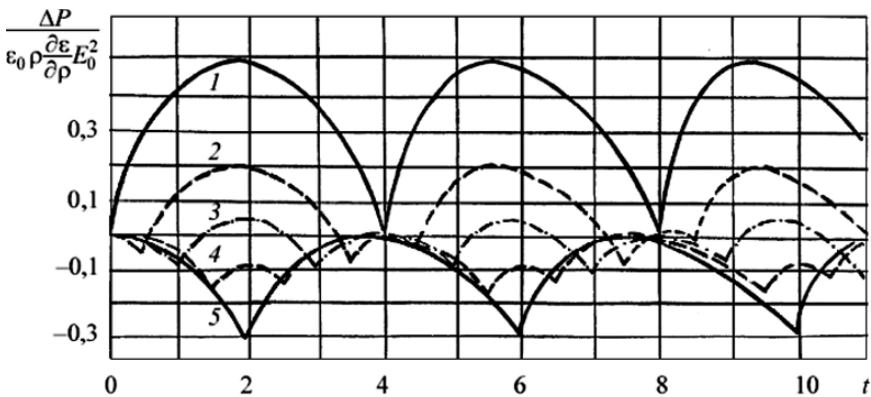
Fig. 1.6. Electrostriction pressure for the coaxial electrode system when the voltage is switched on at zero time moment at distances from the central electrode $r = 1$ (*curve 1*), 1.5 (*curve 2*), 2 (*curve 3*), 2.5 (*curve 4*), and 3 (*curve 5*)
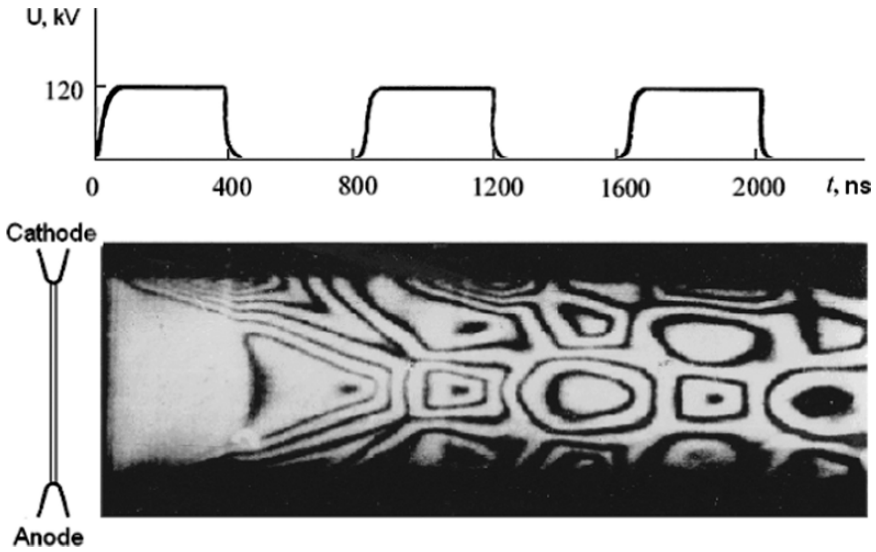
Fig. 1.7. Experiment on electrostriction wave excitation in water in the system of extended electrodes. Slit scanning regime
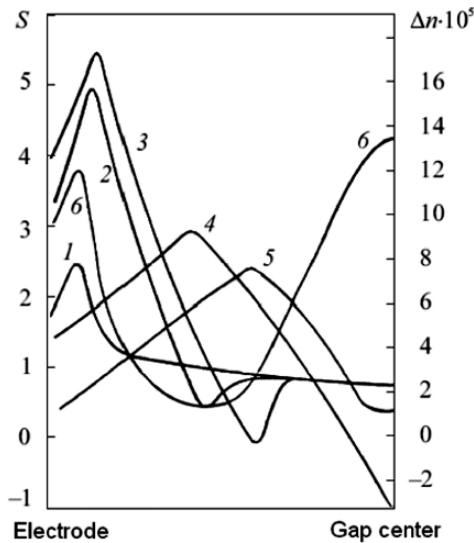
Fig. 1.8. Experiment on excitation of the electrostriction wave in the system of extended electrodes. Data were processed at time moments $t_1 = 150$ (*curve 1*), 300 (*curve 2*), 400 (*curve 3*), 700 (*curve 4*), 800 (*curve 5*), and 1000 ns (*curve 6*)

$$\Delta n = \frac{2}{3}\lambda BE^2 + \kappa\Delta P \,, \tag{1.41}$$

where λ is the wavelength, B is the Kerr constant, and κ is the elasto-optical coefficient, to analyze the pressure variations, we must subtract the term caused by the Kerr effect from the total refractive index. From Fig. 1.8 it can be seen that the pressure near the electrode first increases and then decreases. The spatial pressure minimum is displaced from the electrode toward the gap center with the sound velocity. The pressure in the region the wave has not yet reached decreases. From here we conclude that the registered physical phenomenon can be identified with the wave of electrostriction origin. The predicted behavior differs from that actually observed near the electrode by the characteristic bending of the interference bands and occurrence of closed bands. In our opinion, this fact is explained by interference of the incident beam with the beam reflected from the surface and is purely optical effect. In studies of the electric fields of a blade-plane electrode system, we observed analogous patterns of light intensity distribution in nitrobenzene [44].

Figure 1.9 shows the light intensity distribution under a voltage pulse with an amplitude of $100\,\text{kV}$ applied to a cell filled with trichlordiphenyl. It can be seen that the interference band distribution is mainly caused by the Kerr effect. This follows from the fact that the band shape virtually coincides with the voltage pulse waveform. Slight reorganization of pressure distribution is also testified by the fact that the band near the electrode is detached from the electrode under exposure to a flat part of the pulse, whereas the Kerr band must be fixed under constant voltage. The voltage on the cell is absent between voltage pulses, but the band displacement caused by the pressure relaxation is still registered. This experimental result differs from the previous
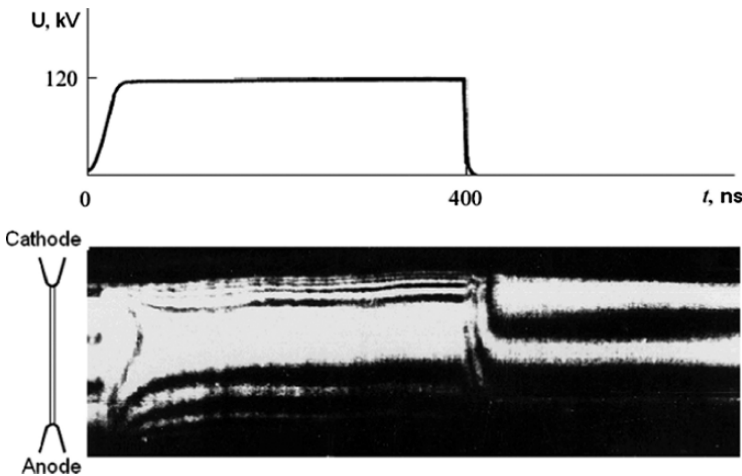
Fig. 1.9. Weak pressure variations under voltage pulses applied to the cell with trichlordiphenyl ($\lambda \ll R_0 - r_0$) borrowed from [43]

one due to the circumstance that the viscosity of trichlordiphenyl is 5 orders of magnitude greater than the viscosity of water. According to (1.24), the wave in trichlordiphenyl is attenuated at the distance $l \sim 10^{-5}$ m, that is, $l << r_0$. Therefore, the stable electrostriction pressure is determined by the liquid viscosity rather than by inertia, and the wave regime of establishing pressure is transformed into the viscous one.

Let us study the influence of the electrostriction wave on possible failures of electric equipment with liquid electric insulation. In cables of electric power transmission and shaping lines with liquid insulation, excitation of electrostriction waves under exposure to lightning or switching pulses is highly improbable. If we consider that only a liquid, for example, transformer oil or any cable oil with low permittivity is used in the cable and choose the working field strength to be equal to 150 kV/cm, we obtain a maximum pressure

$$\Delta P_{\max} = \frac{\varepsilon_0\,(\varepsilon - 1)\,(\varepsilon + 2)}{6} E^2 \approx 0.0025 \, \text{MPa}\,. \qquad (1.42)$$

Owing to surges, the field strength in the cable can increase 3–4 times; then the maximum amplitude of the stress wave will be 0.04 MPa. It is obvious that a single action of the wave of this amplitude is safe for the cable. However, if reflections are present in the line and thereof pulse influence has a periodic character, a resonance can arise resulting in disruption of the electric strength. However, in cables with paper-oil insulation, paper prevents oil motion. It can be demonstrated that the electrostriction in solid dielectrics should also initiate electrostriction waves of various types; however, these effects are impossible in composite paper-oil dielectrics with high effective viscosity. Thus, the electrostriction waves in cables are highly improbable.

In pulsed capacitive energy storages, the energy density reaches 0.5 J/cm^3 [39] at which the electrostriction pressure is ~ 0.5 MPa. These parameters are reached under exposure to nanosecond voltage pulses, and the electrostriction waves are only initiated under these conditions. The distance covered by a relief wave in 100 ns is about $100 \, \mu$m. Because it is much less than the interelectrode distance (1–10 cm), the negative pressure has no time to be formed, though the equivalent pressure on the bubble will be negative. This case will be considered below.

The electrostriction waves are most likely formed in the intermediate energy storages operating in the microsecond range. In this case, $W \sim 0.1$ J/cm^3, and the electrostriction pressure is ~ 0.1 MPa. When the voltage is switched on, a force starts to act in the region of electric field nonuniformity, and a zone with decreased pressure arises in the same region. The lifetime of this zone is determined by the geometry of the electrode system. In particular, the rarefaction zone will be formed in a strip line at the edge of the electrode system, and its lifetime will be determined by the travel time of the sound wave to the gap center and back. Taking into account that for actual electrode systems this time lies in micro- or even millisecond range, it is expected that within the time over which the pulse acts the region with reduced density will

exist near the electrode edges where the processes of electric strength disruption are most probable. On the other hand, in low-viscosity liquids like water, the electrostriction waves can be reflected from boundaries and interfere with each other, thereby leading to the occurrence of local low-frequency minima, etc. This can be one of the reasons for the reduction of the electric strength of liquids in the case of rough pulses, that is, pulses with high-frequency components when the electrostriction resonance is observed at frequencies of parasitic components.

We note that the zone with reduced pressure in actual electrode systems having significant dimensions can be one of the reasons for the so-called effect of the electrode area, that is, a dependence of the pulsed electric strength on the electrode dimensions (see Sect. 6.6.4).

One more circumstance connected with the electrostriction waves should be mentioned. The electrode system configuration can be adjusted and periodic voltage pulses can be applied so that to organize specially a pressure resonance. This enables one to produce controllable nonmechanical devices for generation of pressure pulses.

1.3 High-Voltage Electric Conduction of Liquids

The problem of electric conduction of liquids in strong electric fields is too complicated, and many studies are devoted to it. This problem is of interest to us primarily from the viewpoint of elucidation of the influence of the electrical conduction on the liquid pressure and bubbles, more precisely, on the pressure inside the bubbles, field strength in them, generation of charge carriers, and so on.

The greatest progress in studying the electric conduction of dielectric liquids, in our opinion, has been made in studies of the Laboratory of Electrostatics of Dielectrics Materials (LEMD) of the CNRS/UJE, Grenoble (France). The presentation of the material rests mainly upon [45, 46].

The capability of any materials to conduct electric current is determined by the presence of charges and their mobility. The most general formula for the current density j correct for any medium except vacuum has the form

$$j = \sum n_i q_i \mu_i E . \tag{1.43}$$

Here i is the charge type (for example, electrons, ions of various molecules, molions, charged macroparticles, etc.), n_i is the concentration of charges of the ith type, q_i is the charge, and μ_i is the mobility of charge carriers.

1.3.1 Generation of charge carriers

In not too strong fields, the charge carriers (mainly electrons and ions) are generated primarily by thermal ionization of molecules of the main substance

or impurity or by emission from the electrodes. The most important role in (1.43) is played by n_i, which can be estimated from the general energy considerations. Changes of charge carrier concentration are determined by the expression

$$\frac{dn_i}{dt} \sim n \cdot \nu \cdot e^{-W/kT} , \qquad (1.44)$$

where n is the density of molecules, ν is the frequency of electron vibrations in the molecule ($\sim 10^{14}\,\text{s}^{-1}$), W is the ionization energy, k is the Boltzmann constant, and T is the temperature. At room temperature, $kT \sim 1/40\,\text{eV}$. Mechanisms of charge losses are the electron-ion recombination and attachment to surfaces and electrodes. For recombination, we can take advantage of the expression [50–52]

$$\frac{dn_i}{dt} = k_{\text{r}} n_i^2 , \qquad (1.45)$$

where k_{r} is the recombination coefficient. For volume recombination in liquid, $k_{\text{r}} = 10^{-9}\,\text{cm}^3/(\text{s} \cdot \text{ion})$ [47]. In equilibrium, the number of charge carriers remains unchanged with time. Combining (1.44) and (1.45), we obtain the final expression:

$$n_i = (n \cdot \nu / k_{\text{r}})^{1/2} \cdot e^{-W/2kT} . \qquad (1.46)$$

Modern concept of the electric conduction of *dielectric liquids* is the following. The charge carriers here are practically always ions, because electrons are easily attached to neutral liquid molecules and cannot exist in a free state. Ionization is facilitated in comparison with gases due to higher permittivity; their potential barrier (ionization energy) is reduced ε times. This can be demonstrated by considering the Coulomb energy of interaction of two charges ($+e$ and $-e$) spaced at distance r:

$$W = e^2 / (4\pi\varepsilon_0\varepsilon \cdot r) . \qquad (1.47)$$

The commonly accepted mechanisms of ion generation are electrolytic dissociation of impurity or basic substance molecules and electrochemical reactions in the double electric layer. These reactions are specific enough for each electrode-liquid system. The recombination of charge carriers in the liquid is hindered, because charges are easily surrounded (solvated) by the neighboring molecules oriented by their corresponding constant or induced dipole ends to the ions. The molecules of the basic liquid or impurity, if they are *ionophores*, that is, have mainly ionic bonds between molecular fragments, can be ionized. The NaCl molecule comprising Na^+ and Cl^- ions is the characteristic example of the ionophores. The NaCl molecule can be dissolved in liquid; it exists simultaneously as ions, weakly bonded ionic pairs (Na + Cl), and complexes of ionic pairs. In addition to ionophores, *ionogens*, that is, substances forming ions only in the process of interaction with each other can exist in liquid. For example, water dissolved in a dielectric liquid can facilitate ionization of other impurities dissolved in the liquid.

Estimate of the ionization degree of the impurity with a $4\,V$ ionization potential (in a gas) dissolved to concentration of 1% in the liquid having $\varepsilon = 2$ from (1.46) with allowance for recombination (with the recombination coefficient $k_r \sim 10^{-15}\,m^3/s$) gives the charge carrier concentration exceeding $10^{10}\,cm^{-3}$, which yields the electric conduction of the liquid $\sigma_E \geq 10^{-12}\,\Omega^{-1}\cdot cm^{-1}$.

1.3.2 Motion of charge carriers

Electrohydrodynamic processes

The mobility of charge carriers in strong electric fields is determined by liquid motion. In this case, mobility values of different ions are close to each other since ions have been frozen into the liquid and are transferred by liquid microflows. These considerations and theoretical estimates of the conditions of forming electrohydrodynamic (EHD) flows were presented in [45, 46].

The occurrence of EHD flows is directly related to space charges generated in the liquid. Theoretical estimates and experimental data [50] demonstrate that in the presence of space charge, the EHD flows in nonpolar liquids are observed under a voltage of several hundred volts, whereas in polar liquids they are observed under a voltage of several ten volts. Flows in liquid dielectrics are effectively manifested at resistances in the range $10^{14} - 10^8\,\Omega\cdot cm$ [51–54]. For high electric conduction, the space charge virtually does not arise due to a small time of dielectric relaxation of the charge. Too small conduction in the absence of injection does not provide the required charge. The EHD flows in liquids considerably increase the mobility of charge carriers and contribute to nonlinearity of the current-voltage characteristic. The EHD mobility is approximately 10 times greater than the mobility of ions in weak fields and is virtually independent of the ion type. In strong fields, the liquid motion is transformed from laminar into turbulent regime.

Electrohydrodynamics can play different roles in breakdown of liquids. In addition to the fact that flows are indicative of the presence of space charge, they cause additional local field amplifications. There are data [55, 56] on a decrease in E_{br} of liquids moving with velocities $> 10\,cm/s$.

Our investigations of motion of charge carriers and microbubbles in nitrobenzene under the action of strong pulsed electric fields [57–62] demonstrated that bubbles and ions moved with practically identical velocities (Fig. 1.10). This means that they move together with the liquid. Moreover, flows are formed on the pulse front, that is, for exposure periods of about $1\,\mu s$. From here we conclude that charge carriers are transferred by microflows which are formed for time periods less than $1\,\mu s$.

The motion of charge carriers was registered with an ultrahigh speed photoregister in the slit scanning regime. The motion of charge carriers emitted near the electrode resulted in a redistribution of the field strength registered with the help of the Kerr effect technique. Lines of equal phase difference
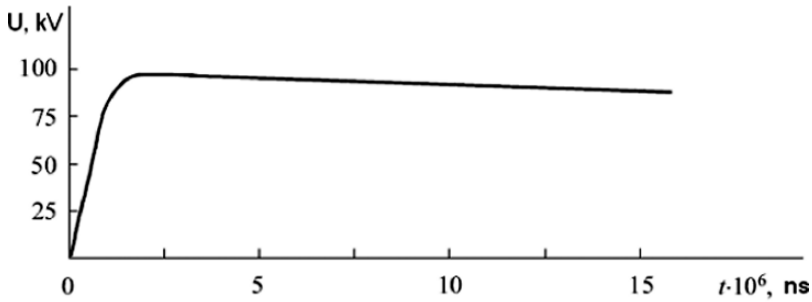
Fig. 1.10. A fragment of chronographic scanning of the optical image near the cathode. Tracks show moving bubbles. Bands whose shapes are close to voltage pulse waveforms show the Kerr bands. Bending of these bands shows the motion of injected charges

(Kerrograms) can be roughly considered as lines of equal field strength. The line position is determined by the applied voltage and injected space charge. Since both these parameters cannot change abruptly, these lines are smooth enough; they begin and end at the electrode. The front of charge carrier motion is clearly pronounced as bends in Kerrogram lines. The bubble motion is displayed by dark lines that can appear or disappear as bubbles appear or disappear as well as escape from the slit field of view. The bubble velocity is determined from the line tilts, and the velocity of charge carriers is determined from the front motion.

The motion of different charge carriers and bubbles with approximately identical velocities registered by the optical method in combination with electrooptical one proves the formation of flows. The typical mobility caused by the liquid motion, according to calculations performed in [45, 63] is

$\mu_{ehd} \sim (3 \cdot 10^{-7} - 10^{-8})\,\mathrm{m}^2/(\mathrm{V \cdot s})$, that is, three-four orders of magnitude less than the mobility of ions in gases. It depends mainly on the permittivity of liquid. Estimates of the mobility of charge carriers in our experiments yielded $\mu_{ehd} \sim (5 \pm 2) \cdot 10^{-7}\,\mathrm{m}^2/(\mathrm{V \cdot s})$, which did not contradict the electro-hydrodynamic nature of charge carriers.

Collision ionization threshold

Nowadays it is assumed that the field strength required for the inception of collision ionization in nonpolar liquids is several megavolts per centimeter, for example, it is equal to $7\,\mathrm{MV/cm}$ for pentane, decane, and cyclohexane, $4\,\mathrm{MV/cm}$ for argon, and $11\,\mathrm{MV/cm}$ for liquid nitrogen [64–67]. This conclusion was made based on the measured dependence of the current on the voltage for the tip-plane electrode system with the tip radius changing in the interval 0.5–$10\,\mu\mathrm{m}$. The experiment demonstrated the following:

– short current pulses ($\leq 4\,\mathrm{ns}$) were observed under the above-indicated field strength,
– the charge injected per pulse is determined only by the radius of curvature and is independent of the applied voltage and pressure,
– time interval between pulses decreases with increasing voltage and demonstrates high stability,
– each pulse generates a bubble near the tip; the size and lifetime of this bubble depend on the external pressure.

1.4 Phenomena at the Electrodes

The electric conduction of liquids and pressure in the liquid depend on the properties of the electrode-liquid interface. The electrode processes play the important role in the liquid conduction, especially in strong electric fields. In any case, whatever current runs through the gap, the same current will run through the contact by virtue of the current continuity. Strictly speaking, Ohm's law holds true only in the differential form [6]. This is the case not only for liquids but also for semiconductors [69]. To a lesser extent, this refers to solid dielectrics because of a smal number of free charges in them. These substances with radically different properties can be joined together because all they have a contact metal electrode – medium interface.

Processes in contacts are most extensively studied for semiconductors. The contact between two semiconductors or a semiconductor and metal gives rise to processes of charge transfer connected with equalizing chemical potentials of charge carriers in different media. Equalizing the chemical potentials of charge carriers on both sides of the contact leads to the formation of a potential jump at the interface. A current running through the contact can have different character, and the contact itself can be a) injecting when charge carriers of

only one sign penetrate into the medium, b) ohmic when carriers of both signs have equal opportunities to run through the contact, and c) blocking when charge carriers do not run through the medium-electrode interface.

In the first case, a space charge whose sign coincides with the electrode charge, the so-called homocharge, is formed near the electrode under voltage application. In the case of the ohmic contact, no space charge is formed, and a charge of the opposite sign, the so-called heterocharge, is formed near the blocking contact. From here it can be easily understood that integral Ohm's law is valid only in the case of ohmic contact between the electrodes. In other cases, the space charge breaks the field uniformity thereby leading to nonlinearity of the current-voltage characteristic.

It is well known that Ohm's law in liquids is valid under low voltages $U < 1\,\mathrm{V}$. It seems likely that the contacts under low voltage are always ohmic. The metal-solid and metal-liquid contacts differ not only by the medium into which charge carriers run but also by the charge carrier type. According to studies performed at the LEMD [45, 46, 50, 63], in all cases of electric conduction of liquid dielectrics in which it was possible to identify charge carriers, they appeared to be *ions.* In metal electrodes and semiconductors, electrons and holes take part in electric conduction. The continuity of current in contacts *in all cases* is provided by electron transfer. In this case, the material balance must be obeyed for any type of charge carriers. The contact is blocking for non-discharging ions, injecting for ionizable neutrals, and ohmic for ions transferring charge.

1.4.1 Double electric layer

Let us consider first the reasons for the violation of Ohm's law. We are based primarily on [45, 63, 70]. First of all, we must elucidate where do the charge carriers come from? And where do they escape? A certain number of ions is always present in liquid owing to dissociation of molecules of the basic substance and impurity. The ions reorganize the surrounding medium forming solvation sheaths that prevent their recombination. The ion interaction in weakly polar liquids results in the formation of weakly bound complexes of ion pairs, and the ion interaction with electrodes results in the formation of double electric layers (DEL). There are different methods of DEL formation depending on the type of ion interaction with the electrode surface. In this case, the potential jump at the interface is primarily determined by the presence of the so-called potential-determining ions chemically adsorbed on the surface.

The double electric layer consists of two parts. The dense part (the Helmholtz layer) is formed by the adsorbed desolvated ions, polar molecules adjacent to the electrode, and solvated ions. The diffusion part (the Gouy–Chapman layer) extends deep into the gap approximately to depths $x_{d.l} = (2 \cdot D_i \cdot \tau_{\mathrm{M}})^{0.5}$, where D_i is the average ion diffusion coefficient and τ_{M} is the Maxwell dielectric relaxation period. The double electric layer controls the electric liquid conduction due to electrochemical reactions in the contact

region. It can generate ions from neutral molecules or neutralize ions transforming them into neutral molecules or atoms. These reactions occur in the Helmholtz layer, and the reaction products or adducts exchange with the volume by means of diffusion. The reaction type is determined by the relationship between occupied and unoccupied energy levels of the electrode and each reacting particle. In this case, the electrode plays the role of one very large reacting particle [70].

Under electric field, ions are accumulated near the electrodes of the corresponding sign, changing the contact potential difference (the double-layer potential). Only particles whose electron state energy levels are close to the Fermi energy level in metal react with the electrode. With increasing voltage, the interphase potential also increases due to undischarged ions, and new components with other electron energy levels enter the reaction with the electrode. An increase in the number of charges in the medium, naturally, leads to a disproportionate current increase and hence, violation of Ohm's law. When the system is returned to a lower voltage, the initial conduction is not restored; as a rule, the electric conduction increases. With further voltage increase, the rate of growth of the electric conduction increases.

The electrode reactions can be both reversible and irreversible. In reversible reactions, the ion generated on one electrode is discharged on the second electrode, diffuses to the first electrode in the neutral form, and then turns again into the ion. The total charge does not change, and no chemical transformations are observed. In the second case, a chemical transformation of reaction component takes place. If the reaction product interacts with the electrodes or liquid molecules with the formation of ions, a catastrophic increase of electric conduction of the liquid may occur.

The characteristic feature is that the rate of growth of the electric conduction increases with further increase in the voltage. As pointed out in [47, 71], the exponential growth of the electric conduction was previously attributed to the processes of shock ionization of liquid molecules.

Ion generation near the metal electrode under strong electric field is controlled by changes of the double-layer potential ΔV:

$$J = 2J_0 \sinh\left[\Delta V \cdot e/\left(kT\right)\right] , \qquad (1.48)$$

where J_0 is the exchange current of the electrode reaction that depends on the concentration of reactive particles, reaction rate, and its energy barrier. The ΔV value changes both due to direct exposure to the electric field: $\Delta V_1 = X_a E$, where X_a is the distance from the electrode to the point of electron exchange, and due to undischarged ions: $\Delta V_2 = X_a \cdot q/\varepsilon_0\varepsilon$, where q is the surface density of charges of undischarged ions. Estimates of ΔV for $E = 150\,\mathrm{kV/cm}$, $X_a = 10\text{–}20\,\text{Å}$, $q = \sigma_E Et$, $\sigma_E = 10\text{–}14\,\mathrm{S/cm}$, $t \approx t_{\max}$ give $\Delta V_1 \approx \Delta V_2 = (1.5\text{–}3) \cdot 10^{-2}\,\mathrm{V}$. Of course, this value influences significantly the current through the gap, because the injection current is comparable with the exchange current. In this case, the current remains proportional to the initial liquid conduction.

In nonpolar liquids, there exists an additional potential barrier for injected ions connected with the action of image forces [45, 50]. The ion can become free only when it is detached by means of diffusion from the electrode at the distance $d_D = (e/4\pi\varepsilon_0\varepsilon E)^{0.5}$.

Since the distance d_D decreases with increasing E, the theory predicts a sharp dependence of the injection current on the field strength. This was confirmed in [45] where it was found that the current in a nonpolar liquid (cyclohexane) increased approximately 2000 times in the field with a strength of 150 kV/cm compared to the value observed for the electric conduction under low voltage. Qualitatively the same results were obtained in [72] in the study of the electric conduction of perfluorethyleneamine, where the increase of the electric conduction approximately by three orders of magnitude was registered in the field with strength up to 250–300 kV/cm in comparison with the low-voltage electric conduction.

Thus, the electrochemical injection of charge carriers can cause a significant increase in current which should be manifested in the current-voltage characteristic.

1.4.2 Near-surface charge generation

Let us consider the most probable mechanisms of forming the double electric layer. In electrochemistry [70, 73], the mechanisms of polar molecule adsorption and electron donor and acceptor impurities are usually considered. These impurities are specific for each electrode - basic liquid - impurity system. However, a nonspecific mechanism determined by different permittivities of liquid and another medium can be suggested.

It is well known [24] that the image force caused by the polarization of dielectrics:

$$F = \frac{e^2 \cdot (\varepsilon_1 - \varepsilon_2)}{4\pi \cdot \varepsilon_1 \cdot \varepsilon_0 \cdot (2h)^2 \cdot (\varepsilon_1 + \varepsilon_2)} \tag{1.49}$$

acts on the charge at the interface between two different phases with permittivities ε_1 and ε_2. Here h is the distance between the charge and interface.

Transforming (1.49) for the charge in liquid with permittivity ε_1 near the surface of the electrode with the formal permittivity equal to infinity, we obtain

$$F = -\frac{e^2}{4\pi \cdot \varepsilon_1 \cdot \varepsilon_0 \cdot (2h)^2} \cdot \tag{1.50}$$

It can be seen that the interaction force is negative, that is, it characterizes the attraction of charges from the dielectric liquid to the contact metal surface. The thickness of the layer with increased ion content is estimated by the method accepted in electrochemistry. To this end, we equate the charge energy in the field of image forces to thermal energy image forces:

$$\frac{e^2}{4\pi \cdot \varepsilon \cdot \varepsilon_0 \cdot 4h} = kT \, . \tag{1.51}$$

Numerical values for the nonpolar liquid with $\varepsilon = 2$ yield $h \sim 60\,\text{Å}$, and for the polar liquid with $\varepsilon = 80$ (water), $h = 2\,\text{Å}$. It is clear that for the polar liquid, this effect exists only for the first layer of molecules adjacent to the electrode, and for nonpolar dielectrics it is essential at greater depths. This mechanism of ion attraction from the gap to the electrodes can be one of the reasons of forming double electric layers near the electrode.

The image forces are responsible for one more mechanism of forming the double electric layers and surface conduction.

The presence of the neighboring phase with high permittivity promotes the dissociation of molecules. Let us examine this process in detail. Let the dissociation occur in the near-surface layer and the formed charges do not leave the surface (Fig. 1.11). The dissociation energy can be found by integration the charge interaction force over the coordinate from a certain value a equal to the ion spacing to ∞. Then after integration we obtain for dissociation in the liquid volume

$$W_i = \frac{e^2}{4\pi \cdot \varepsilon \cdot \varepsilon_0 \cdot a}. \tag{1.52}$$

For dissociation near the surface, we must take into account the force acting on the electron (or ion) running away from the opposite image charge of the second ion. With allowance for this, the ionization energy near the surface decreases, and for the case illustrated by Fig. 1.11, it will be $W_{is} = W_i/3$. For the case of ions with unequal sizes in an ionic pair, this force will be even smaller. It is obvious that the decrease of dissociation energy is a strong factor. The matter is that according to (1.46), the concentration of charge carriers is an exponential function of the ionization (dissociation) energy. Therefore,
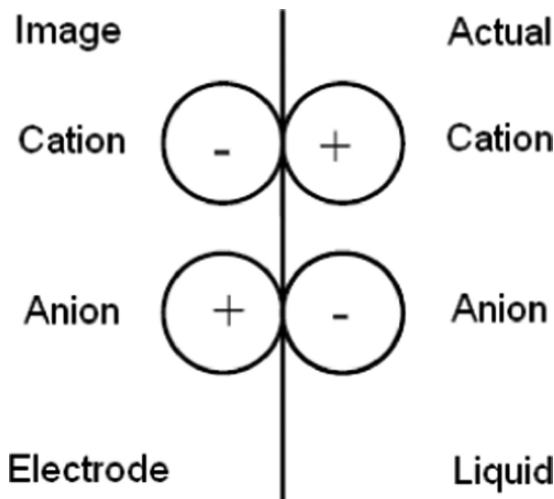
Fig. 1.11. Ionization scheme at the interface between the media with different permittivity values

a 3–4 fold decrease of the dissociation energy can lead to an increase in the concentration by several orders of magnitude. This means that ionization near the surface is much easier, and the concentration of charge carriers is greater here and the surface electric conduction is higher. This provides additional mechanism of forming the double electric layer and explains the presence of the near-surface layer with increased electric conduction.

Let us consider the importance of the effect on the concrete example of water molecules near the electrode. Our estimates are based on (1.46) with the recombination coefficient $k_{\mathrm{r}} \sim 10^{-15} \, \mathrm{m^3/s}$. Then calculating the concentration from the electric conduction $n_i \approx 10^{14} \, \mathrm{cm^3}$, we obtain the dissociation energy of water molecules in water $W \approx 1 \, \mathrm{eV}$. For a comparison, the dissociation energy of water molecules in the gas phase is $494 \, \mathrm{kJ/mol}$ [74], which is approximately equal to $5 \, \mathrm{eV}$. The difference is mainly due to the energy of ion interaction with the medium.

The inverse operation with $W_{is} \approx 0.33 \, \mathrm{eV}$ demonstrates that the charge concentration near the electrode will increase approximately by six-seven orders of magnitude and will be equal to $n_s \approx 10^{20} \, \mathrm{cm^{-3}}$. Is it high or low? If we consider that the layer with increased electric conduction in polar liquids occupies $2 \, \text{Å}$ [see (1.50)], the change of the concentration per unit area (of the surface charge density)

$$\Delta q \approx 3 \cdot 10^{-7} \mathrm{C/cm^2} \tag{1.53}$$

should be considered small in comparison with the surface charge density. For example, in the field with a strength of $100 \, \mathrm{kV/cm}$,

$$\Delta q \approx 10^{-6} \mathrm{C/cm^2} \ . \tag{1.53a}$$

However, this factor can play an essential role in the electric conduction. This conclusion is based on the fact that the rate of ion formation is rather high, as can be seen from (1.44). Indeed, substituting the numerical data, we obtain $dn_i/dt \approx 10^{28} \, \mathrm{cm^{-3} \cdot s}$. After removal of ions of one sign from the region adjacent to the electrode, the electric field equilibrium between the formation of ions and their recombination is shifted, thereby causing the formation of additional ions. Estimates demonstrate that the equilibrium is restored in approximately $10 \, \mathrm{ns}$. From here it follows that regions adjacent to the electrodes can be a source of rather high currents in weak electric fields $\leq 20 \, \mathrm{kV/cm}$. In strong fields, the final rate of ion generation should have an effect, and the current density caused by it will be as great as $1 \, \mathrm{A/cm^2}$ disregarding the strong field effects.

The Schottky effect that reduces the potential barrier also intensifies significantly the dissociation in a strong electric field, but only for nonpolar liquids:

$$W\left(E\right) = W\left(0\right) - \left(\frac{e^3 E}{4\pi\varepsilon_0\varepsilon}\right)^{1/2} \ . \tag{1.54}$$

For example, the ionization energy of n-hexane with allowance for this effect decreases by $0.2 \, \mathrm{eV}$ in the field with a strength of $1 \, \mathrm{MV/cm}$.

Dissociation-recombination equilibrium at the interface between dielectrics

The problem of forming near-surface layers with increased electric conduction is important for several fields of science and technology. Nonpolar dielectric liquids together with more polar solid dielectrics (for example, transformer oil - paper) are widely used in electrical engineering. The formation and accumulation of charge on the surface presents a severe problem for liquid fuel transportation through pipe lines and in tankers. The double electric layers are also formed near the electrodes in electric devices and near the microparticles in various disperse and colloid systems.

The kinetics of generation and loss of ions at the interface can be considered in more detail by means of calculating reaction constants [75].

From (1.49) it follows that the ion behavior in the liquid with ε_1 near a body with small ε_2 (for example, a bubble with $\varepsilon_2 = 1$) or near the solid dielectric surface with $\varepsilon_2 > \varepsilon_l$ is different. The positive force sign in the case of the bubble wall means that the charge repels from the boundary. It is interesting that if the ion approaches the boundary on the side of the gas phase, the image force attracts the ion to the surface. Near the surface of dielectric with high permittivity, charges will move from the volume toward the surface under the action of this force. An analogous effect should be observed near the metal-liquid interface. The force is negative, which corresponds to the charge motion from the volume of the liquid toward the surface of the conductor; as a result, a layer with increased ion concentration will be formed. Ions will be trapped near the surface. Analogous behavior of ions near the electrode surface was suggested in [46, 76]. It was assumed that ions formed near the electrode as a result of electrode reaction are in a potential well, and to be injected into the liquid volume, they must overcome an additional potential barrier by means of diffusion.

The image forces are responsible for one more mechanism of forming the double electric layer and surface electric conduction. Ionization and dissociation are facilitated in dielectric liquids in comparison with gases due to the increased permittivity of liquids since the ionization energy decreases ε_1 times [see (1.52)]. Moreover, the presence of the neighboring phase with high permittivity ε_2 intensifies the dissociation of molecules, because the dissociation energy decreases near the surface due to the effect of phase polarization [77].

Energy estimates

We consider that a dissociating additive whose molecules can form ion pairs or free ions is dissolved in a nonpolar liquid. The dissociation energy for the ion pair W can be calculated by integration of the Coulomb force over the distance from $R_1 + R_2$ equal to ion spacing in the ion pair to ∞. We assume that dissociation occurs in the near-surface layer. Integration is simplified if we consider that dissociating ions do not leave the surface (Fig. 1.11). In addition,

we assume that the permittivity of the solid dielectric is much greater than the permittivity of the liquid. Integrating the Coulomb force with allowance for the image charge, we obtain

$$W_{is} = W_i \left(1 - \frac{R_1 + R_2}{\sqrt{(R_1 + R_2)^2 + 4R_1 R_2}} \right) . \qquad (1.55)$$

Here W_i refers to dissociation in the liquid volume, and W_{is} refers to dissociation at the surface. As demonstrated above, when the ion radii are equal $R_1 = R_2$, the dissociation energy near the surface should be approximately 3 times less than the volume energy, that is, $W_{is} \sim 0.3W_i$. In the case of unequal radii, for example, for $R_1 = 2R_2$, $W_{is} \sim 0.27W_i$; and for $R_1 = 3R_2$, $W_{is} \sim 0.24W_i$. A decrease in energy is a strong factor that increases the degree of molecule dissociation. To estimate the importance of the effect, we can accept that the number of free ions is an exponential function of the dissociation energy. If, for example, the degree of dissociation in the volume is equal to 10^{-4}, at the interface it will be approximately equal to 10^{-1}. The lower the dissociation degree in the volume, the greater the relative difference between the dissociation degrees. An increase in the number of surface charge carriers will cause the surface electric conduction to increase. The exact estimate of the number of charge carriers should include a consideration of dissociation-recombination processes in the region near the boundary. From the mathematical viewpoint, this is a difficult two-dimensional problem with complex boundary conditions, but for physical estimate, it can be subdivided into two simpler problems. When calculating near-surface dissociation and recombination, we assume that the force depends only on the distance between the surface ion and the detaching ion, that is, we will neglect eccentric forces. When estimating the number of surface charge carriers, we will consider that individual charges are attached and detached, that is, we will neglect the interaction between ions.

Dissociation-recombination processes

According to the ordinary dissociation and recombination model for nonpolar liquids (detailed consideration can be found in [48, 49]), the expression for the charge carrier density has the form

$$n_i = \sqrt{\frac{n_0 \cdot k_D}{k_r}} , \qquad (1.56)$$

where n_0 is the ion pair density, k_D is the dissociation constant, and k_r is the recombination constant. In the context of the Onsager theory, k_D can be estimated from the expression

$$k_D = [(D_1 + D_2)L_B^2/R_{12}^4] \, e^{-L_B/R_{12}} , \qquad (1.57)$$

where D_1 and D_2 are the diffusion coefficients for ions 1 and 2, respectively; R_{12} is the sum of their radii, and L_B is the so-called doubled Bjerrum radius:

$$L_B = \frac{e^2}{8\pi\varepsilon_0\varepsilon \cdot kT} \tag{1.58}$$

equal to the ion spacing for which the thermal energy is equal to the electrostatic energy of their interaction. The Bjerrum radius for the nonpolar liquid with $\varepsilon = 2.3$ is equal to $125\,\text{Å}$ at room temperature. The problem of estimating the ion radii is more difficult. Organic salts are commonly present in nonpolar liquids like transformer oil. Let us consider that their sizes differ. For definiteness of estimations, in calculations below we set $R_2 = 1\,\text{Å}$ and $R_2 = 5\,\text{Å}$. For the recombination constant, the equation

$$k_r = 4\pi(D_1 + D_2)L_B \tag{1.59}$$

can be derived from which the well-known Langevin formula is obtained

$$k_r = \frac{e(\mu_- + \mu_+)}{\varepsilon_0 \cdot \varepsilon}, \tag{1.60}$$

where μ_+ and μ_- are the mobility values of positive and negative ions, respectively. According to (1.60), $k_r \sim 1.6 \cdot 10^{-10}\,\text{cm}^3/\text{s}$ for $\mu_+ \sim \mu_- \sim 10^{-4}\,\text{cm}^2/(\text{V}\cdot\text{s})$.

The dissociation constant estimated from (1.57) is $k_D \sim 1.4 \cdot 10^{-7}\,\text{s}^{-1}$. If we substitute these values into (1.56), we obtain that the charge carrier density in the liquid must be approximately $n_i \sim 2 \cdot 10^{10}\,\text{cm}^{-3}$ for the ionic pair concentration $n_0 \sim 10^{-4}\,\text{mol/l}$. This is a very small value which yields the additional electric conduction no more than $3 \cdot 10^{-14}\,\text{S/cm}$.

Omitting detailed calculations for the ion distribution function near any reference ion, in our case the surface ion (the calculation procedure was presented in [48, 49]), we present the final expressions suitable for estimation in the near-surface region

$$k_{Ds} = \frac{(D_1 + D_2)}{\int_{R_{12}}^{R_B} e^{L_B/r - L_B/(r^2 + R_{12}^2)^{1/2}} r^2 dr \cdot \left(\int_{R_{12}}^{R_B} e^{-L_B/r + L_B/(r^2 + R_{12}^2)^{1/2}}/r^2 dr\right)}, \tag{1.61}$$

$$k_{rs} = 4\pi(D_1 + D_2)L_{Bs}, \tag{1.62}$$

where $L_{Bs} = \left(L_B R_{12}^2/2\right)^{1/3}$ is an analog of the Bjerrum radius for the two-dimensional near-surface region.

This procedure repeated for the ion located at greater distances from the surface yields values close to solutions (1.57) and (1.59).

According to (1.61) and (1.62), k_{rs} is by about an order of magnitude smaller than the corresponding volume coefficient, and k_{Ds} is by about seven orders of magnitude greater than k_D.

As to the ion concentration near the surface, (1.56) remains valid despite the fact that the ion density is comparable with the ionic pair concentration. In this case, the diffusion flux of ion pairs makes the concentrations in the volume and near-surface region equal. The volume can be considered as an infinite reservoir; therefore, the near-surface concentration of ion pairs $n = n_0$ should be independent of the number of newly formed ions.

Ion attachment to the interface

An ion + ion image complex can be considered as an ionic pair. In this case, ion separation from the surface is equivalent to dissociation of the ion pair, and ion attachment to the boundary is equivalent to recombination of the ion pair. Forces in this complex are very similar to forces in the actual ion pair. However, it is necessary to specify that the rate of force decrease with increasing ion distance from the boundary is smaller when the direction of ion motion is not perpendicular to the surface. Therefore, the ion bond with the image must be stronger than in the ion pair. The dissociation constant of the complex should be smaller than the dissociation constant of the ion pair, whereas the situation with the recombination constant is opposite. These constants differ for positive and negative ions simply due to different ion sizes:

$$k_{r_i} = 8\pi D_i L_B \, , \tag{1.63}$$

$$k_{D_i} = D_i R_B^2 / (2 r_i^4) e^{-L_B / 2R_i} \, . \tag{1.64}$$

As follows from (1.63) and (1.64), the dependence of the recombination constant on the ion size should be very weak (through the dependence of D_I on the ion size), and the dependence of the dissociation constant on the ion radius should be very strong.

For equal ion radii, ion attachment to the interface is the key process. In the first approximation, the dissociation degree of the complex should be the same as the dissociation degree of the typical ion pair in the liquid volume. An additional difference is that the attached ions can be considered free when they move along the boundary. They are not free in attempts to detach from it. We now try to estimate their concentration n_s considering that they are localized in the near-surface layer:

$$\frac{dn_s}{dt} = k_{D_i} n_s - k_{r_i} n_i^2 \, . \tag{1.65}$$

In equilibrium $dn_s / dt = 0$; as to n_I, its value is determined by the dissociation-recombination processes in the liquid volume according to (1.56). After substitution, we obtain

$$n_s = n_0 \frac{k_D k_{r_i}}{k_{D_i} k_r} \, . \tag{1.66}$$

Since $k_{r_i} \approx k_r$ and $k_{D_i} = k_D$ in the case of equal ion radii, $n_s \approx n_0$. This means that the near-surface ion concentration is equal to the volume concentration of neutral ion pairs in the liquid.

In the case of unequal ion radii, the concentration of small ions should be much greater than the concentration of large ions. If the radii differ several times, the concentrations will differ by many orders of magnitude. For example, if the negative ion radius is $1\,\text{Å}$ and the positive ion radius is $5\,\text{Å}$, the near-surface concentration of negative ions will exceed the concentration of positive ions by 80 orders of magnitude. Hence, the surface (in the absence of specific adsorption) should be covered by a layer of negative ions. Because of the total electroneutrality, a positive charge should exist near the surface in the liquid volume. This is the well-known pattern in electrochemistry of the double electric layer. Ions of smaller size form a dense part of the double layer, and larger ions prevail in the diffusion part of the double layer.

Both dense and diffusion parts of the double layer should take part in the surface electric conduction if the electric field is applied along the surface. The estimated value of the resistance does not exceed $10^{13}\Omega$. When the field is perpendicular to the surface, we can expect the injection of charge carriers from the diffusion part of the double layer if the direction of field application promotes the displacement of ions forming the diffusion sheath of the double layer from the interface. In the opposite case, no additional electric conduction is expected, since the electric field will keep ions of the diffusion parts of the double layer close to the interface. Only under application of strong fields when ions are separated from the surface, injection of charge carriers into the volume is possible.

Influence of the electric field on ion dissociation and recombination in the near-surface layer

If the field is perpendicular to the phase interface, dissociation increases with increasing electric field. The behavior of the coefficient k_D is very close to that described by the standard Onsager effect in weak electrolytes $k_{DE} = k_D F(p)$,

$$F(p) = \frac{I_1(4p)}{2p} \,,$$

where

$$p = \frac{e^2}{2\,kT} \left(\frac{E}{4\,\pi\varepsilon_0\varepsilon} \right)^{1/2} , \qquad (1.67)$$

and $I_1(p)$ is the first-order modified Bessel function. The characteristic field at which dissociation sharply increases is observed at $4p \sim 1$, which corresponds to the field strength of approximately $3\,\text{kV/cm}$.

If the electric field is parallel to the surface, the characteristic field strength can be estimated through a decrease of the potential barrier by analogy with the Schottky effect. In this case, a simple procedure gives

$$E^* \sim \frac{3kT}{2eL_{Bs}}, \qquad (1.68)$$

which corresponds approximately to $200\,\mathrm{kV/cm}$. As to the form of the dependence, it must be stronger than the standard Onsager law:

$$k_{\mathrm{D}E} \sim k_{\mathrm{D}} \exp(E/E^*)^{3/4} . \qquad (1.69)$$

Thus, as a result of physical considerations of the dissociation and recombination processes in the near-surface region, the novel mechanism of forming surface charge carriers and surface electric conduction can be suggested in the case of contact between a nonpolar liquid and a polar solid dielectric. It is based on intensification of dissociation of ionic pairs under the action of the image forces during polarization of the dielectric.

1.4.3 Emission of charge carriers and electrode reactions

The double electric layer cannot be formed in well purified nonpolar liquids simply because of insufficient number of charge carriers and dissociating impurities. In principle, this state of the electrode-liquid system should be considered nonequilibrium. Nevertheless, a number of experiments (for example, see [78,79]) with pure liquids were carried out in the absence of double layers.

It was demonstrated that the dependence of current on voltage $I(U)$ in nonpolar liquids like hexane, tetramethylsilane, cyclohehane, etc. had three characteristic sections for the electrodes creating a sharply inhomogeneous field: a linear dependence at low voltage, a sharp increase by two-three orders of magnitude after achievement of a certain critical voltage, and then transition to a relatively weak dependence $I \sim U^2$. The first section is described by Ohm's law, the second section is characterized by field emission of charge carriers from the electrode, and the third section is characterized by the space-charge limited current. Estimates of the field strength at which transition to the regime of space-charge limited current occurs demonstrate that in nonpolar liquids like hexane, the transition occurs at comparatively low local field strengths $E < 10^7\,\mathrm{V/cm}$. The characteristic feature of the regime of space-charge limited current is a weak dependence of the field strength near the electrode on the potential difference.

Practically the same results were obtained for transformer oil. The current-voltage characteristics and schlieren photographs of electrihydrodynamic flows in a sharply nonuniform dc field created by needle-plane and blade-plane electrode systems in transformer oil were presented in [80]. Currents depended only weakly on the tip polarity; three sections were identified in the curve: the ohmic section up to 3–5 kV, the section of a sharp field growth approximately to 8 kV, and the section of space-charge limited current. The effect of polarity was significant: the breakdown voltage for the positive tip was approximately halved compared to that for the negative tip. Dotoku et al. [79] pointed out that for positive polarity, the space charge reached the flat electrode, thereby leading to field amplification near it with subsequent injection followed by field amplification near the tip electrode. The

calculated data confirmed the correctness of the model; however, no data on the difference between the processes at different polarities were presented, which casts some doubt upon the correctness of interpretation of the results obtained.

As already pointed out above, the electrode reactions can be reversible and irreversible. In the course of reversible reactions, the ion formed on one electrode is discharged on the other, diffuses as a neutral formation to the first electrode, and then turns again into the ion. The total charge does not change, and chemical transformations are not observed. In the course of irreversible reactions, a chemical transformation of reaction components occurs. If the reaction product interacts with the electrodes or liquid molecules with the formation of ions, a catastrophic increase in the electric conduction can occur under the action of the field. This case was described in [46] on the example of acetonitrile. The initial high resistance $\rho > 10^{13} \Omega \cdot$ cm in a cell with metal electrodes fast decreased with increasing field strength at the expense of the formation of reactive protons in the process of oxidation of the basic substance or water impurity.

If the product of electrode reaction remains uncharged and sufficiently inert, the total charge of the system can decrease. In some cases, a decrease in the electric conduction was observed in moderate electric fields due to irreversible reactions. In [81], the electrical conduction of freshly refined transformer oil was compared with the electric conduction of oil removed from service. Experiments demonstrated that the electric conduction of the aged oil in uniform field $E \sim 180 \, \text{kV/cm}$ exceeded by a factor of ~ 1.5 the electric conduction of the fresh oil. One more distinctive feature was the time behavior of the electric conduction. In the fresh oil, electrorefinement was observed, and the electric conduction decreased by about 3 times in $10 \, \text{min}$, whereas in the aged oil it remained unchanged. In the context of electrochemistry, this result is noncontradictory: in the aged oil the impurity reduced the interphase potential to values at which no irreversible reactions of electrorefinement were observed.

The electric conduction can be influenced by both impurities in the liquid and electrodes. In [52] it was demonstrated that addition of some substances to liquid result in intensive injection of charge carriers from the electrode. Thus, for example, iodine added to nonpolar liquids causes injection of negative charges from the cathode. Here it should be noted that the dominant injection of negative charge under natural conditions without additives was reported in many works. Among the advantages of [82,83], the clarity of problem formulation should be mentioned. To establish what electrode is ignitor one, the electrodes were alternately coated by a dielectric layer, and the arising gap potential was measured [82] or a meniscus of liquid near the vertical electrode (cathode or anode) [83]. By these methods it was proved that the cathode injects carriers of negative charge into the liquid, whereas injection from the anode is much weaker.

Injection of charge carriers of different signs was obtained in experiments [84] by adjusting the proper electrode pairs, for example, copper-stainless steel or brass-aluminum electrode pairs. Injection was detected by measuring the electric field distribution with the use of the Kerr effect technique. In the presence of injection, the field near the electrodes was attenuated at most by 20–40% for properly adjusted ignitor electrode pairs.

As applied to the problem of liquid insulation, we note the following. The intensity of charge generation depends on the initial degree of purity of the liquid and its permittivity. The ion charge density is as great as 10^{-9} C/cm^3 for the liquid having the electric conduction $\sigma \approx 10^{-13} \Omega^{-1} \cdot \text{cm}^{-1}$, and the mobility of charge carriers $\mu = 10^{-4}$ cm^2/(V $\cdot$ s). If undischarged ions are deposited on the electrodes and no thermal autoionization occurs in the volume, the potential of the dense part of the double electric layer with a thickness of 10 Å will not exceed a few millivolts. From here it follows that ionogenic impurity must be eliminated from the liquid that must have the least possible permittivity (except liquid insulation application in intermediate capacitive energy storages). Fluorocarbon liquids whose chemical inertness prevents their interaction with possible products of electrochemical reactions are best suited.

1.4.4 Field distribution at the electrodes

To control the electrode processes to eliminate or amplify injection by the method, for example, of adjustment of proper electrodes, the corresponding electrooptical method can be used based on a study of the electric conduction distribution over the electrode surface [85] or the electric field distribution over the gap with the help of the Kerr effect technique.

Nowadays the Kerr effect is most often used to investigate the field distribution. Its essence is that a medium in an electric field acquires the optical properties of a uniaxial crystal with the optical axis oriented along the field. Transmitting light through the medium and analyzing the light polarization state at the exit from the medium, the spatial and temporal distribution of the electric field can be reconstructed. The space charge distribution, injection, and so on can be judged from the character of electric field distribution and its dynamics.

Experiments with nitrobenzene [60–62] and water mixtures [84,86] on registration of strong electric fields with the help of the Kerr effect technique gave unique information on pre-breakdown processes in polar liquids.

One of the initial processes registered under exposure to strong electric fields is injection of charge carriers from the electrode. Figures 1.12–1.15 show the experimental data on the distribution of pre-breakdown electric fields, behavior of charge carriers, and pre-breakdown bubbles in nitrobenzene at the cathode and anode. The experimental setup (Fig. 1.12) comprised a pulsed ruby laser operating in quasi-continuous wave regime for slit scanning and in giant pulse regime to record a frame series, a cell with a tip–plane electrode system placed between crossed polarizers, and a ultrahigh-speed photoregister.
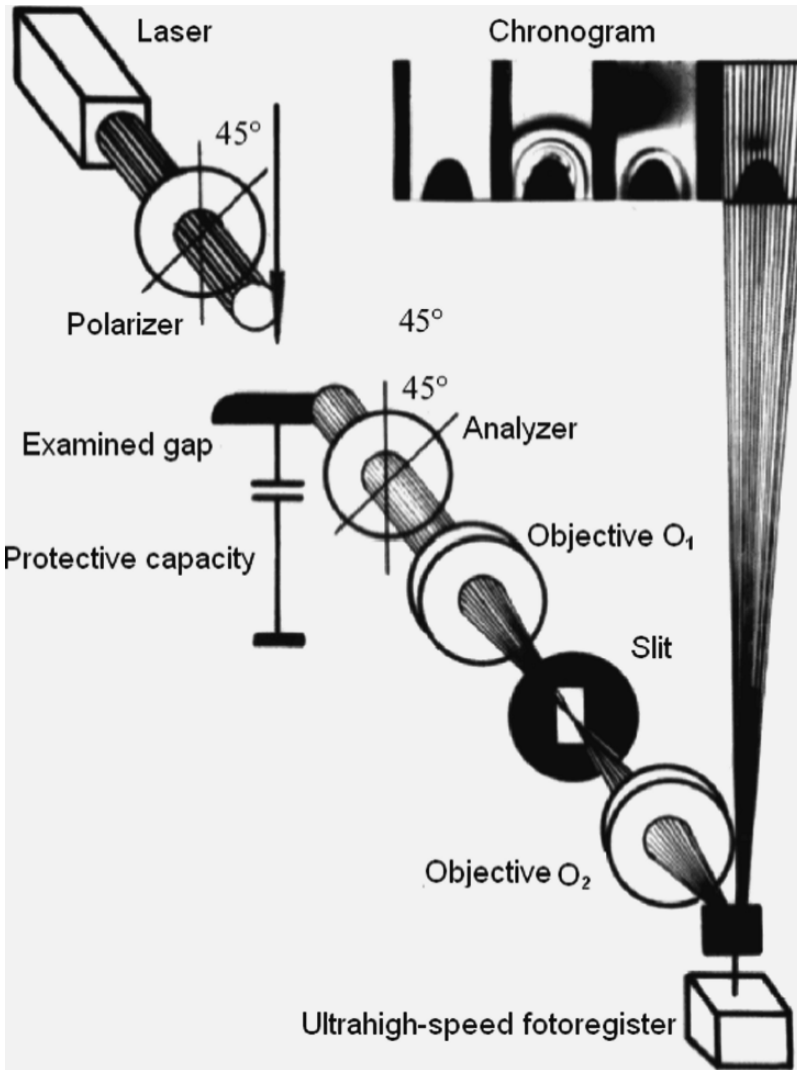
Fig. 1.12. Experimental setup for measuring pre-breakdown electric fields in nitrobenzene with the help of the Kerr effect

Nitrobenzene with an electric conduction of $10^{-7}\Omega \cdot$ cm was placed in a glass tube. An ignitor electrode was a needle with a radius of $300\,\mu$m. The second electrode – the plane – was placed at a distance of $3\,$cm. The voltage pulse with 1–$3\,\mu$s front duration and $50\,\mu$s duration at half maximum had amplitudes up to $200\,$kV.

It was revealed that the charge carriers were emitted from the electrodes when the field strength reached $0.5\,$MV/cm at the cathode and $1\,$MV/cm at
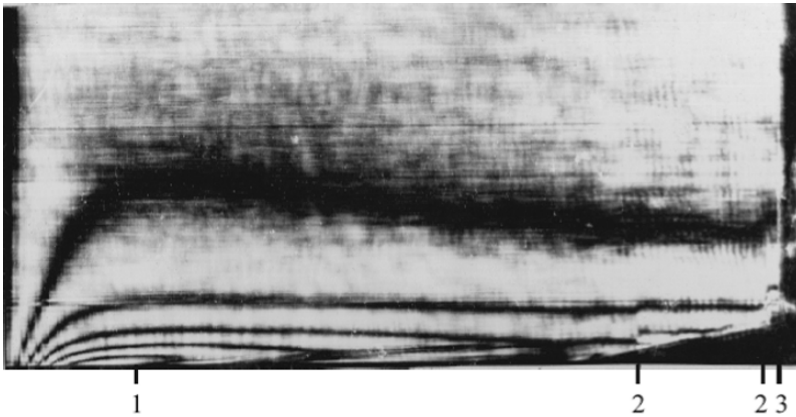
Fig. 1.13. A fragment of the chronographic scanning of the optical image near the cathode. Tracks show moving bubbles (**1**). Bands whose shapes are close to the voltage pulse waveform show the Kerr bands. Bending of the bands illustrates the motion of injected charges. Instants of ionization in the bubble region (**2**) and gap breakdown (**3**) are also indicated

the anode. The field at the emitting electrode decreased. Figure 1.13 shows slit scanning pattern of the field near the cathode to the instant of breakdown initiation. In the absence of injection of charge carriers from the electrodes, the Kerr bands must repeat the waveform of the voltage pulse. The specific feature of the bands (the presence of "a claw") allows us to conclude that the charge carriers emitted from the cathode move with a velocity of a few tens of meters per second. The mobility of charge carriers determined from here is $(5 \pm 2) \cdot 10^{-3}\,\mathrm{cm}^2 \cdot \mathrm{V}^{-1} \cdot \mathrm{s}^{-1}$, which approximately corresponds to the hydrodynamic mobility [45, 63]. The tracks crossing the Kerr bands display, as mentioned above, moving bubbles. Jumps of the Kerr bands are caused by ionization processes in the zone occupied with bubbles. The discharge is initiated exactly in this zone. Electric field distortions, bubbles, and breakdown initiation are clearly seen from the sequence of frames shown in Fig. 1.14.

The anode processes differ from the cathode ones (Fig. 1.15). The charge carriers are also emitted, but the emission threshold ($\sim$1 MV/cm) is higher;
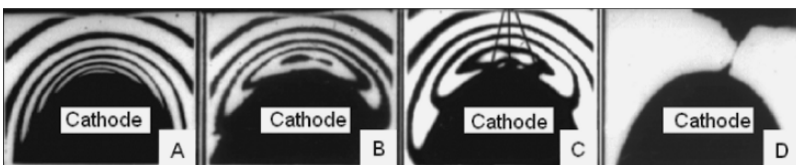
Fig. 1.14. Experiment on detection of the space charge, bubbles, and breakdown initiation at the tip cathode in nitrobenzene. Photographs were taken at time moments 1.2 (**A**), 2.6 (**B**), 4.5 (**C**), and 10 (**D**) μs after the voltage application
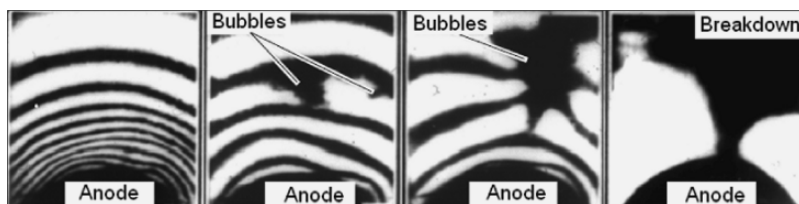
Fig. 1.15. Experiment on detection of the space charge, bubbles, and breakdown initiation at the tip anode in nitrobenzene. Photographs were taken at time moments 1.2, 6.7, 11.5, and 15 μs after the voltage application

in addition, bubbles and charge carriers are more localized. The velocities of charge carriers and bubbles are slightly higher than for the cathode by virtue of higher values of the electric field strength; however, the mobility of charge carriers remains approximately the same, that is, it corresponds to the electrohydrodynamic mobility. The discharge channel is initiated in the region of bubble localization where the strongest electric field distortion is registered.

Electrooptical registration of the electric field in water and water mixtures with ethyleneglycol performed in [84, 86] revealed conditions at which electric fields near the electrodes are attenuated under the action of voltage pulses. By adjusting the ignitor electrodes, the pulsed electric strength was increased by 40%. In [87], *vice versa*, the breakdown field strength in the Kerr cells under dc voltage was increased by adjusting electrode coatings *to eliminate* the injection processes. The two last examples demonstrate that the Kerr effect technique can be used to control the field distribution to increase the working field strength.

As to nonpolar liquids and gases with the Kerr constants being by 3–4 orders of magnitude smaller, it is difficult to measure fields in them. Experiments [84,87,88] on the study of field distribution in weakly birefringent media are worthy of notice. Measurements in transformer oil, SF_6, and silicone oil were carried out in [84]. The sensitivity was increased by using photomultipliers to scan the gap with a narrow laser beam.

The novel scheme of electrooptical measurements was suggested in [88]. It was based on the use of elliptically polarized light and high-frequency modulation of the measurable electric field. It was demonstrated that the sensitivity of measurements of dc fields in oil can be made as great as 100 V/cm. We note that the nonuniformity of electric field distribution was established by means of direct measurements there; moreover, it increased with time. This demonstrates that irreversible reactions run in the electrochemical system transformer oil - electrode system in which charges are generated. It is not clear what components of the system interact. The electric field nonuniformity causes the field strength to increase, as a rule, at one of the electrodes. Obviously, this reduces the electric strength of the gap under dc voltage. The matter is not only that the field nonuniformity is indicative of the electrochemical

processes accompanied by possible contamination of liquid by reaction products. This situation promotes the formation of bubbles at the igniter electrode under the action of the Coulomb forces on the liquid. Their transfer to the regions of stronger field with EHD flows can cause the discharge ignition in them and the subsequent breakdown.

The control of uniformity of the electric field distribution allows one to estimate the suitability of electrode systems for use at dc voltage, to estimate the efficiency of measures for an increase in the electric strength. The presence of space charges in nonpolar liquids under application of dc voltages was demonstrated in [53]. The space charge has a complex structure. The homocharge layer formed at the electrode is followed by the heterocharge layer. In the first layer, the Coulomb forces repeal the liquid from an electrode, and in the second layer, they press it. Naturally, this situation is unstable, and electrohydrodynamic flows arise with increasing voltage applied to the liquid.

1.5 Pressure Distribution during Charge Carrier Emission

1.5.1 Uniform field

The space charge generated near the electrodes upon injection from the electrode or, more precisely, from the double layer at the electrode will change the electric field distribution. We now consider the one-dimensional variant which can be used to describe experiments in uniform or weakly nonuniform electric fields. This variant is also applicable to experiments in sharply nonuniform fields when the extension of the space charge region is less than the tip curvature radius.

The additional Coulomb force with volume density $f = \rho_{s.c} \cdot E$ acts on the liquid in the region of the space charge having density $\rho_{s.c}$. Under the action of this force, the liquid is displaced from the electrode. Since the liquid layer adjacent to the electrode is fixed and is not displaced from the electrode, a pressure gradient arises. The pressure gradient increases as the liquid moves, and in equilibrium $\nabla P = \rho_{s.c} \cdot E$. Since in the one-dimensional case $\nabla P = dP/dx$ and $\rho_{s.c} = \varepsilon_0 \varepsilon dE/dx$, we obtain

$$P = P_0 - \varepsilon_0 \varepsilon \left(E_b^2 - E^2 \left(x \right) \right) /2, \qquad (1.70)$$

where P_0 is the liquid pressure outside of the space charge region, and E_b is the field strength on the space charge boundary. Usually P_0 is set to be equal to the external pressure P_{out}; then from (1.70) it follows that in the space charge region, the pressure is always reduced. Moreover, the larger the degree of electrode screening, the lower the pressure.

Figure 1.16 shows the electric field distribution near the electrode in the presence of the uniformly distributed homocharge. It is assumed that the charge is strong enough to decrease the field strength near the electrode to
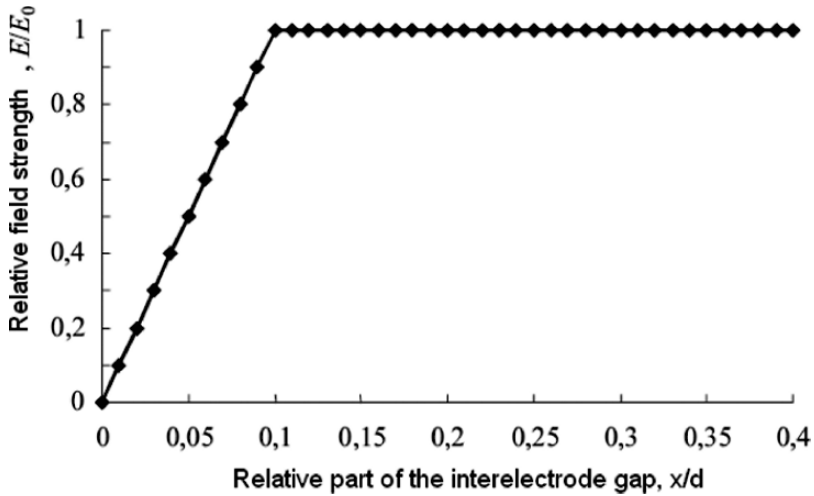
Fig. 1.16. Field distribution in the space charge zone for complete electrode screening

zero. Figure 1.17 shows the pressure distribution for the indicated relationship between P_{out} and $\varepsilon_0\varepsilon E^2/2$ and field distribution illustrated by Fig. 1.16. It can be seen that the pressure at the electrode can reach large negative values $P = P_{\text{out}} - \varepsilon_0\varepsilon E^2/2$. For pre-breakdown fields in polar liquids, the estimated
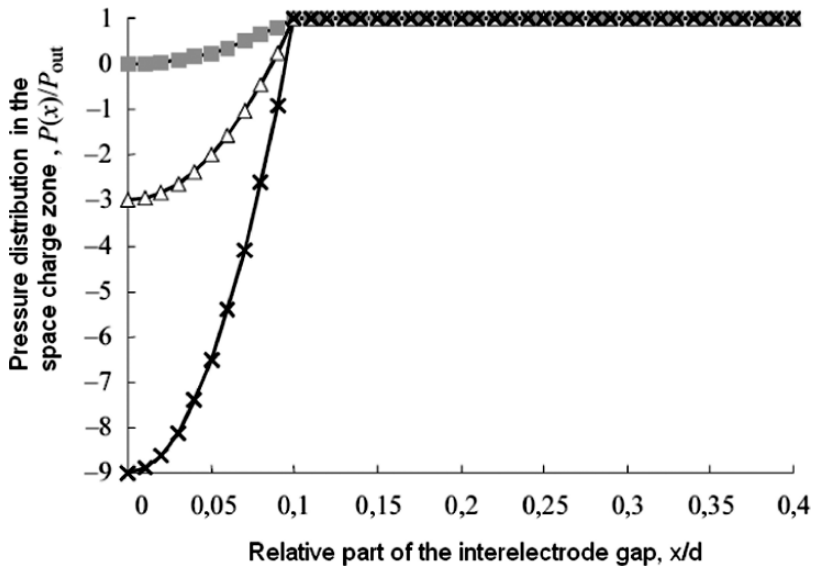
Fig. 1.17. Pressure distribution near the electrode where the uniformly distributed homocharge is localized. The upper curve is for $\varepsilon_0\varepsilon E^2/2 = P_{\text{out}}$, the intermediate curve is for $\varepsilon_0\varepsilon E^2/2 = 4 \cdot P_{\text{out}}$, and the lower curve is for $\varepsilon_0\varepsilon E^2/2 = 10 \cdot P_{\text{out}}$

negative pressure changes from a few fractions to units of MPa. For nonpolar liquids, the negative pressure is smaller, and under pre-breakdown conditions it usually does not exceed a few fractions of MPa.

Here it is necessary to compare the effects of energy release for the screened electrode and of the negative pressure formed at its surface on the formation of bubbles in the liquid and on the bubbles that already exist. For example, we now estimate the temperature change for the lower curve in Fig. 1.17 at $P_{out} = 1$ atm:

$$\Delta T = \frac{\varepsilon_0 \cdot \varepsilon \cdot E^2}{2 \cdot c \cdot \rho} \sim \frac{10^6}{10^3 \cdot 10^3} \sim 1^\circ C. \qquad (1.71)$$

It can be seen that upon strong injection into the uniform macrofield, the negative pressure in the space charge region has the determining effect in comparison with the temperature change. When the space charge is insufficient for complete screening of the electrode, the field strength at the electrode is less than the external field strength. The hydrostatic pressure distribution over the gap is similar to the pressure distribution in the previous case described by (1.70).

1.5.2 Sharply nonuniform field

Simple distributions of the field strength and pressure shown in Figs. 1.16 and 1.17 are inapplicable to sharply nonuniform fields created by the tip-plane electrode system. To determine the injected charge, a system of electrodynamics equations with the corresponding initial and boundary conditions must be solved. The problem on the injection current was solved in a number of works devoted to the study of charge transfer in semiconductor and dielectric materials (for example, see [69, 89]).

The general solution of the problem is difficult because of the nonlinearity of the equations; therefore, the problem is solved for particular cases of non-stationary space-charge limited currents injected from flat [69] or spherical electrodes [89] connected to a source of dc voltage. Two cases are analyzed, namely, when the space charge is created at the electrode at the initial instant by photoinjection, or when the electrode is a reservoir. In the case of charge emission from the electrode into the liquid under the action of an electric field, these assumptions are unsuitable. As indicated above, the field strength at the electrode increases with voltage in the ohmic regime and changes only slightly after transition to the regime of space-charge limited current. In the intermediate regime, the current is described by the Fowler–Nordheim formula. Attempts to solve the problem on the emission current in a liquid dielectric under pre-breakdown electric fields were repeatedly undertaken. Simplifications used not always had clear physical meaning.

We have developed a method for solving equations for an arbitrary emission law and a symmetric electrode system [59, 90]. Here we restrict ourselves to an examination of the most important practical case of a spherical electrode with a simplified emission law. Since in calculations of space charges,

pressure, and energy release we can neglect the contribution of the first two sections of the current-voltage characteristic, we assume that emission starts when the field strength exceeds a certain threshold value E_i and after that the electrode will become a reservoir [69]. To solve the problem, we need the data on the mobility of charge carriers. Here we consider it to be equal to the hydrodynamic mobility [69] and neglect its dependence on time and field strength.

We now write down the initial dimensionless system of equations including the continuity, Poisson, total current, and total voltage equations:

$$\frac{1}{r^2}\frac{\partial}{\partial r}\left(r^2 E\rho\right) + \frac{\partial \rho}{\partial t} = 0,$$

$$\frac{1}{r^2}\frac{\partial}{\partial r}\left(r^2 E\right) = \rho,$$

$$\frac{\partial E}{\partial t} + \rho E = J, \tag{1.72}$$

$$\int_1^\infty E\left(r,t\right)dr = U\left(t\right).$$

In the dimensional form, we have

$$J_{\mathrm{d}} = \frac{\varepsilon_0 \varepsilon U^2 \mu}{r_0^3} J,$$

$$t_{\mathrm{d}} = \frac{r_0^2}{\mu U} t, \tag{1.73}$$

$$\rho_{\mathrm{d}} = \frac{\varepsilon_0 \varepsilon U}{r_0^2} \rho.$$

Here J is the current density and U is the voltage pulse amplitude. Hyperbolic system of equations (1.5.2) is solved by the method of characteristics [27]. To this end, we substitute the second equation into the first one. We obtain

$$\frac{\partial \rho}{\partial t} + \frac{\partial \rho}{\partial r} \cdot E + \rho^2 = 0. \tag{1.74}$$

The characteristics of this equation are the curves $\frac{dr}{dt}\left(r\left(t,t_0\right)\right) = E$, where t_0 is the moment at which the characteristic leaves the electrode (emission of each portion of the charge). From the conditions satisfied on the characteristic, we obtain that

$$\frac{d\rho}{dt}\left(r\left(t,t_0\right)\right) = -\rho^2,$$

$$\frac{d\left(E\cdot r^2\right)}{dt}r\left(t,t_0\right) = J\cdot r^2, \tag{1.75}$$

or after integration,

$$r\left(t, t_0\right) = 1 + 3\left(l\left(t\right) - l\left(t_0\right) - Q\left(t_0\right)\left(t - t_0\right)\right)^{1/3},$$
$$\rho\left(r\left(t, t_0\right)\right) = \rho_0 / \left(1 + \left(t - t_0\right)\rho_0\right), \qquad (1.76)$$
$$E\left(r\left(t, t_0\right)\right) = \left(E_i + Q\left(t\right) - Q\left(t_0\right)\right) / r^2 .$$

Here ρ_0 is the space charge density on the electrode at the moment t_0 at which the characteristic leaves the electrode, $Q\left(t\right) = \int J\left(t\right) dt$, and $l\left(t\right) = \int Q\left(t\right) dt$. Substituting (1.76) into the total voltage equation and regrouping terms, we obtain the equation

$$Q\left(t\right) = U\left(t\right) - E_i + \int\limits_0^t \frac{Q\left(t\right)\left[E_i + \frac{dQ}{dt_0}\left(t - t_0\right)\right] dt_0}{\left\{1 + 3\left[l\left(t\right) - l\left(t_0\right) - Q\left(t_0\right)\left(t - t_0\right)\right]\right\}^{4/3}}, \qquad (1.77)$$

suitable for numerical calculations. For quite short voltage pulses, (1.77) can be solved by the method of successive approximations. For the zero approximation, it is convenient to take $Q_0 = U\left(t\right) - E_i$. The physical meaning of the zero approximation is obvious: it is a charge of geometrical capacity. In this case, the change of the capacity due to the space charge is neglected. Substituting Q_0 into the right-hand side of (1.77), we obtain Q_1, and so on. The physical meaning of Q_1 and successive approximations is an increase in the capacity due to space charge emission. Choosing a convergence criterion of the iterative process $\left(Q_n - Q_{n-1}\right) / Q_n < \delta$, where δ is a preset small number, we obtain the solution $Q(t)$. Using this solution and the foregoing expressions, we obtain distributions of interest to us. Figure 1.18 shows the calculated field strength distribution at the spherical igniter electrode for the indicated moments of time and emission intensities. It can be seen that the field at the electrode is not always minimum throughout the gap as in the case of the flat electrodes. Moreover, for large time, the space charge is so smeared over the gap that the field strength maximum is restored at the electrode.

The heating of the liquid near the electrode, pressure drop, and maximum possible radius of the electrolytic bubble generated in the course of irreversible electrode reaction can be estimated from the dimensionless quantity $Q(t)$.

The heating of the liquid is described by the expression

$$\Delta T = \frac{\varepsilon_0\varepsilon \cdot E_0^2}{c_p} Q\left(t\right) E_{\mathrm{em}}.$$

The pressure drop is

$$\Delta P = \varepsilon_0\varepsilon \cdot E_0^2 \frac{d}{dt}\left(Q - U\right).$$

The maximum possible size of the electrolytic bubble is

$$R_0 = \sqrt[3]{\frac{3\varepsilon_0\varepsilon \cdot Q\left(t\right) \cdot D \cdot t}{en}}.$$
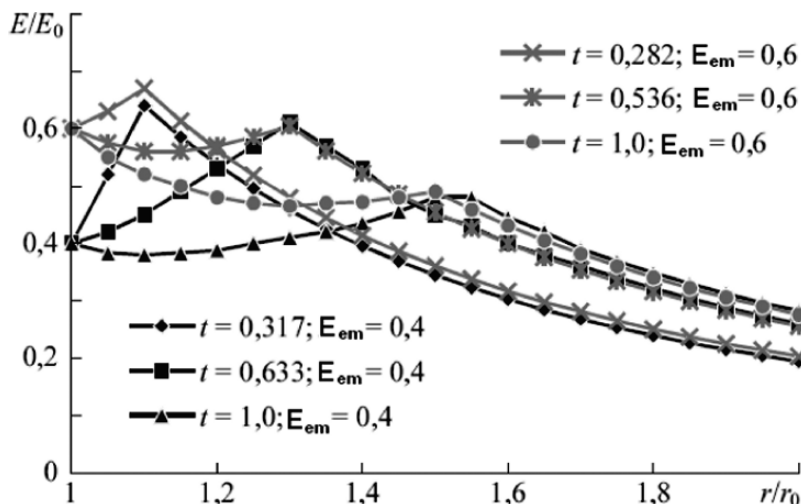
Fig. 1.18. Calculated dynamics of the electric field distribution at two emission levels of charge carriers

Estimates based on these expressions demonstrate that under conditions of experiments on pre-breakdown processes in nitrobenzene, the temperature change was negligibly small ($<1\,\mathrm{K}$), the possible electrolytic bubble radius did not exceed $10^{-5}\,\mathrm{cm}$, and the determining factor of bubble occurrence was the negative pressure.

References

1. K. C. Kao and J. B. Higham, The effect of hydrostatic pressure, temperature and voltage duration on the electric strength of hydrocarbon liquids, J. Electrochem. Soc., **108**, 252–258 (1961).
2. I. Kalyatskii and V. V. Krivko, Investigation of impulse electric breakdown of water at elevated pressures and temperatures, in: Breakdown of Dielectrics and Semiconductors [in Russian], Tomsk (1964), pp. 29–39.
3. V. M. Lagunov, Investigation of Electric Breakdown of Water Insulation, Candidate's Dissertation in Technical Sciences, Institute of Nuclear Physics of the Siberian Branch of the Russian Academy of Sciences, Novosibirsk (1969).
4. K. Yoshino, Dependence of dielectric breakdown of liquids on molecular structure, IEEE Trans. El. Insul., **15**, 386 (1980).
5. J. S. Mirza, C. W. Smith, and J. H. Calderwood, Liquid motion and internal pressure in electrically stressed insulating liquids, J. Phys., **D3**, 580–585 (1970).
6. G. A. Ostroumov, Interaction of Electric and Hydrodynamic Fields [in Russian], Nauka, Moscow (1979).
7. I. E. Balygin, Electric Strength of Liquid Dielectrics [in Russian], Energiya, Moscow-Leningrad (1964).

8. K. S. Kao, Some electromechanical effects on liquid dielectrics, Br. J. Appl. Phys., **12**, 141–148 (1961).

9. J. B. Higham, Investigations of electrical breakdown in liquids, Proc. IEE, **3**, No. 4, 623 (1964).

10. S. S. Hakim and J. B. Higham, Mechanical forces in dielectrics, Proc. IEE, **109**, No. 15, 158–161 (1962).

11. C. G. Garton and Z. Krasucki, Bubbles in insulating liquids: stability in an electric field, Proc. R. Soc. London, **A280**, 211–226 (1964).

12. B. M. Smolyak, Influence of an electric field on surface tension of liquid dielectrics, in: Thermal-Physical Properties of Liquids and Explosive Boiling up [in Russian], Publishing House of Ural Scientific Center of the USSR Academy of Sciences (1976), pp. 79–84.

13. R. S. Allan and S. G. Mason, Particle behavior in shear and electric fields. I. Deformation and burst of liquid drops, Proc. R. Soc. London, **A267**, 45–47 (1962).

14. S. Torza, R.G. Cox, S.G. Mason, Elektrohydrodynamic deformation and bursts liquid of drops, Phil. Trans. R. Soc. London. 2694 (1971) pp.295–319

15. K. S. Kao, Some electromechanical effects on liquid dielectrics, Br. J. Appl. Phys., **12**, 141–148 (1961).

16. J. B. Higham, Investigations of electrical breakdown in liquids, Proc. IEE, **3**, No. 4, 623 (1964).

17. E. V. Yanshin, I. T. Ovchinnikov, and Yu. N. Vershinin, Optical investigations of the pre-breakdown phenomena in water in nanosecond range, Zh. Tekh. Fiz., **43**, No. 10, 1067–1071 (1973).

18. H. Lamb, Hydrodynamics, 6 th Edition. Series: Cambridge Mathematical Library, Trinity college, Cambridge (1994).

19. Ya. Yu. Akhadov, Dielectric Properties of Pure Liquids [in Russian], Publishing House of Standards, Moscow (1972).

20. M. I. Shakhparonov, Methods of investigation of thermal motion of molecules and composition of liquids [in Russian], Publishing House of Moscow State University, Moscow (1963).

21. M. Valisko, D. Boda, J. Lisci, and I. Szalai, Relative permittivity of dipolar liquids and their mixtures. Comparison of theory and experiment, Phys. Chem. **3**, 2995–3000 (2001).

22. S. M. Korobeinikov, Bubble model of ignition of the impulse electric discharge in liquids, Author's Abstract of Doct. Phys.-Math. Sci. Dissert., Tomsk (1998).

23. J. S. Jakobs and A. W. Lawson, An analysis of the pressure dependence of the dielectric constant of polar liquids, J. Chem. Phys., **20**, No. 7, 1161–1164 (1952).

24. L. D. Landau and E. M. Lifshits, Electrodynamics of Continuous Media [in Russian], State Physical and Mathematical Press (1958).

25. S. M. Korobeinikov, Elektrostrictional waves in nonuniform fields, Deposited in Informelektro, No. 6-d79, Moscow (1979).

26. S. M. Korobeinikov and E. V. Yanshin, Dynamics of electrostrictional pressure at a spherical electrode, Zh. Tekh. Fiz., **53**, No. 10, 5 (1983).

27. S. K. Godunov, Equations of Mathematical Physics [in Russian], Nauka, Moscow (1979).

28. M. I. Abramowitzch and I. M. Stegun, eds., Handbook of Special Functions with Formulas, Plots, and Mathematical Tables [in Russian], Nauka, Moscow (1979).

29. D. Sette, Study of simple liquids by ultrasonic methods, in: Physics of Simple Liquids, Ed. By H. N.V. Temperly, 7. Rowlinson, G.S. Rushbrooke, North Holland, (1968).

30. A. A. Vorobjev, G. A. Vorobjev, E. K. Zavadovskaya, et al., Impulse Breakdown and Destruction of Dielectrics and Rocks [in Russian], Publishing House of Tomsk State University, Tomsk (1971).

31. K. S. Kao and J. B. Higham, The effect of hydrostatic pressure, temperature and voltage duration on the electric strength of hydrocarbon liquids, J. Electrochem. Soc., **108**, 252–258 (1961).

32. K. C. Kao and McMath, Time dependent pressure effect in liquid dielectrics, IEEE Trans. El. Insul., **5**, 64–68 (1970).

33. I. T. Ovchinnikov, K. V. Yanshin, and E. V. Yanshin, Experimental investigations of pulsed electric fields in water near the tip electrode with the help of the Kerr effect, J. Tekh. Fiz., **748**, No. 12, 2595–2698 (1978).

34. V. V. Lopatin, V. Y. Ushakov, and V. P. Chernenko, Ignition and propagation of nanosecond discharge in liquids, Izv. Vyssh. Uchebn. Zaved., Fiz., No. 3, 100–105 (1975).

35. J. C. M. Bokris and B. E. Conway, Modern Aspects of Electrochemistry, London Bitterwortts, (1964).

36. I. T. Ovchinnikov, K. V. Yanshin, and E. V. Yanshin, Investigations of pre-breakdown electric field distribution in water with the help of the Kerr effect, Zh. Tekh. Fiz., **44**, No. 2, 452–454 (1974).

37. E. V. Yanshin, Optical investigations of nanosecond pre-breakdown phenomena in water, Author's Abstract of Cand. Tech. Sci. Dissert., Novosibirsk (1977).

38. E. Hart and M. Unbar, Hydrated Electron, Atomizdat, Moscow (1973).

39. D. E. Anderson, J. B. Green, S. C. Glidden and M. Richter, 1,2 MV, 800 kA, 150 ns Pulsed Power Generator for Powering Field Reversed Ion Ring Experiments, 10 th IEEE Intern Rulsed Power Conf., Albuquerque, New Mexico, (1995).

40. Yu. Ya. Iossel, Calculation of potential fields in power engineering [in Russian], Energiya, Leningrad (1978).

41. G. A. Mesyats, A. S. Nasibov, and V. V. Kremnev, Shaping of Nanosecond High-Voltage Pulses [in Russian], Energiya, Moscow (1970).

42. E. A. Morozov, Interference technique of registration of electric fields in liquid dielectrics with the help of the Kerr effect, in: Abstracts of Reports at the All-Union Conf. on Physics of Dielectrics, Baku (1982).

43. E. A. Morozov and G. S. Kuchinskii, Investigation of the physical phenomena in water in pre-discharge electric fields, in: Abstracts of Reports at the All-Union Conf. on Physics of Dielectrics, Baku (1982).

44. S. M. Korobeynikov, S. I. Kosyrikhina, K. V. Yanshin, and E. V. Yanshin, The Kerr effect in nitrobenzene in strong electric fields, Deposited at VINITI, No. 4176–82, Moscow (1982).

45. N. J. Felici, B. Gosse, and J. P. Gosse J.P. Aspects electrochimique et electrohydrodynamiques de la conduction des liquides isolants, RGE, **85**, 861–864 (1986).

46. J. P. Gosse, Electric conduction in dielectric liquids, IEEE Trans. El. Insul., **21**, 503–517 (1986).

47. I. Adamchevskii, Electric Conduction of Liquid Dielectrics [in Russian], Energiya, Leningrad (1972).

48. A. I. Zhakin, Magn. Elektrodin., No. 1, 63–70 (1991).

49. A. I. Zhakin, F. F. Niyazi, A. E. Kuzko, and S. A. Lunev, Trudy Kursk. Gostekhuniv., **7**, 58–85 (2001).

50. N. J. Felici, Conduction mechanisms in liquid dielectrics. Modern aspects, in: Proc. World Electrotechnical Congress, Moscow (1977), p. 19.

51. Yu. K. Stishkov and A. A. Ostapenko, Electrohydrodynamic flows of direct current and low-voltage conduction, in: Abstracts of Reports at the All-Union Conf. on Physics of Dielectrics and New Fields of Their Application, Karaganda (1978).

52. Yu. K. Stishkov, Phenoma of nonlinear interaction between the field and liquid low-conductive medium, Author's Abstract of Doct. Phys.-Math. Sci. Dissert., Leningrad State University, Leningrad (1985).

53. Yu. M. Rychkov and Yu. K. Stishkov, Electric field strength and space charge in technical liquid dielectrics, Kolloidn. Zh., **40**, No. 6 (1978).

54. Yu. K. Stishkov and A. A. Ostapenko, Electrohydrodynamic flows in liquid Dielectrics [in Russian], Publishing House of Leningrad State University, Leningrad (1989).

55. G. Theodossiou et al. The influence of electrodynamic motion on the breakdown of dielectric liquids, Appl. Phys., **21**, No. 1 (1988).

56. V. Ya. Ushakov, Insulation of High-Voltage Equipment, Springer-Verlag Berlin Heidelberg (2004).

57. S. M. Korobeynikov, E. V. Yanshin, and K. V. Yanshin, Optical investigation of prebreakdown processes in insulating liquids, in: Proc. 4th Int. Symp. on High Voltage Engineering, Athenes (1983).

58. S. M. Korobeynikov, E. V. Yanshin, and K. V. Yanshin, Space charge and prebreakdown bubbles formation near point electrodes under pulse voltage, in: Rec. 8th Int. Conf. on Conduction and Breakdown in Dielectric Liquids, Pavia (1984).

59. S. M. Korobeynikov, K. V. Yanshin, and E. V. Yanshin, Prebreakdown processes in liquid insulation under pulse voltage, in: Pulse Discharge in Dielectrics, G. A. Mesyats, ed. [in Russian], Nauka, Novosibirsk (1985), pp. 99–114.

60. S. M. Korobeynikov, K. V. Yanshin, and E. V. Yanshin, Electrooptical investigations of emission of charge carriers in sharply nonuniform fields in nitrobenzene, Deposited at VINITI, No. 5407–82, Moscow (1982).

61. S. M. Korobeynikov, K. V. Yanshin, and E. V. Yanshin, Investigation of pulsed prebreakdown fields in nitrobenzene with the help of the Kerr effect, in: Abstracts of Reports at the All-Union Conf. on Physics of Dielectrics and New Fileds of their Application (1978), pp. 20–22.

62. S. M. Korobeynikov, E. V. Yanshin, and K. V. Yanshin, Experimental evidence of bubble model of discharge initiation, in: Proc. of the 1998 Int. Conf. on Electrical Insulation and Dielectric Phenomena, Atlanta (1998), pp. 436–438.

63. N. J. Felici, Electrostatics and hydrodynamics, J. Electrostat., **4**, 119–139 (1977–1978).

64. R. Kattan, A. Denat, and O. Lesaint, Generation, growth, and collapse of vapor bubbles in hydrocarbon liquids under a high divergent electric field, J. Appl. Phys., **66**, No. 9, 4062–4066 (1989).

65. N. Bonifaci and A. Denat, Transport phenomena in point-plane geometry in liquid argon, in: Proc. 12th Int. Conf. on Dielectric Liquids, IEEE Publ. No. 96CH35981, Roma (1996), pp. 37–40.

66. A. Denat, F. Jomni, F. Aitken, and N. Bonifaci, Generation of bubbles in liquid argon and nitrogen in divergent electric fields, in: Proc. 13th Int. Conf. on Dielectric Liquids, Nara (1999), pp. 384–387.

67. A. Denat, F. Aitken, and N. Bonifaci, High-field conduction phenomena in nonpolar liquids, in: Proc. 6th Int. Conf. on Modern Problems of Electrophysics and Electrohydrodynamics of Liquids, Saint Petersburg (2000), pp. 38–42.

68. Record of the 10th International Conference on Conduction and Breakdown in Dielectric Liquids, Sec. 8, Electrohydrodynamic Phenomenon, Grenoble (1990), pp. 275–333.

69. M. Lampert and P. Mark, Current Injection in Solids, Academic Press, New York, (1970).

70. A. Adamson, Physical Chemistry of Surfaces, 6 th Edition by Arthur W. Adamson, Alice P. Gast (1976).

71. A. H. Sharbaugh, J. C. Devins, and S. J. Rzad, Progress in the field of electric breakdown in dielectric liquids, IEE Trans. El. Insul., **13**, No. 4, 249–276 (1978).

72. S. M. Korobeynikov, S. G. Sarin, and G. G. Furin, Electric conduction of perfluotriethylamine under dc voltage, Zh. Prikl. Khim., **69**, No. 2, 321–326 (1996).

73. E. D. Shchukin, A. V. Pertsov, and E. A. Amelina, Colloid Chemistry [in Russian], Publishing House of Moscow State University, Moscow (1982).

74. K. P. Mishchenko and A. A. Ravdel', eds., Brief Handbook of Physical and Chemical Quantities [in Russian], Khimiya, Moscow–Leningrad (1965).

75. S. M. Korobeynikov, A. V. Melekhov, G. G. Furin, V. P. Charalambakos, and D. P. Agoris, Mechanism of surface charge creation due to image forces, J. Phys., **D35**, No. 11, 1193–1196 (2002).

76. A. Denat, B. Cosse, and J. P. Gosse, Ion injection in hydrocarbons, J. Electrostat., **7**, 205–225 (1979).

77. S. M. Korobeynikov and Yu. N. Sinikh, Bubbles and breakdown of liquid dielectrics, in: Proc. 1998 IEEE Int. Symp. on Electrical Insulation, IEEE No. 98CH36239, Arlington (1998), p. 603.

78. W. F. Schmidt and W. Shnabel, Electron injection into dielectric liquids by fields emission, Z. Naturforsch., **A26**, 169–170 (1971).

79. K. Dotoku, H. Yamada, S. Sakamoto, S. Noda, and H. Voshida, Field emission into nonpolar organic liquids, J. Chem. Phys., **69**, 1121–1126 (1978).

80. R. Hanaoka, R. Ishibashi, T. Aoyagi, Y. Asada, and T. Nishi, Effect of liquid motion on breakdown voltage under divergent electric fields in transformer oil, in: Rec. 10th Int. Conf. on Dielectric Liquids (1990), pp. 301–305.

81. A. A. El-Sulaiman, A. S. Ahmed, and M. E. Qureshi, High field DC conduction current and spectroscopy of aged transformer oil, IEEE Trans. PAS, **101**, No. 11, 4358–4360 (1982).

82. Zein-Eldin, M. E. Zaky, A. A. Hawley, and M. S. Gullingford, Influence of electrode coating on space charge distributions in transformer oil, Nature, **201**, No. 4926, 1309 (1964).

83. A. Watanabe, Investigations of some electric force effect in dielectric liquids, Jpn. J. Appl. Phys., **12**, No. 4, 593 (1973).

84. M. Zahn et al., Electrooptic field and space charge mapping measurements in gaseous, liquid, and solid dielectrics, in: Proc. Interdisciplinary Conf. on Dielectrics: Properties, Characterization, Applications, Antibes (1992), pp. 130–139.

85. V. M. Kopylov, I. T. Ovchinnikov, S. G. Sarin, and E. V. Yanshin, Spatial distribution of pulse high-voltage conduction of n-hexane, in: Insulation of High-Voltage Electrical Equipment Systems [in Russian], Publishing House of Tomsk Polytechnic Institute, Tomsk (1988), pp. 19–24.

86. M. Zahn, Y. Ohki, D. B. Fenneman, R. J. Gripshover, and V. H. Gehman, Dielectrical properties of water and water/glycol mixtures for power systems, Proc. IEEE, **74**, 1182 (1986).

87. J. C. Filippini, Recent progress in Kerr cells technique, J. Phys., **D8**, 201–213 (1975).

88. T. Maeno and T. Takada, Dependence of an applied DC voltage on electric field distribution in insulating oil using the Kerr effect technique, in: Proc. 2nd Symp. Elec. Insul. Mater., Tokyo (1988), pp. 123–126.

89. A. I. Rudenko, Nonstationary currents limited by the spatial charge in spherical geometry, Fiz. Tekh. Poluprovodn., **8**, No. 10, 1928–1935 (1974).

90. S. M. Korobeynikov, Injection current and formation of bubbles in strong sharply nonuniform electric fields, Prikl. Mekh. Tekh. Fiz., **41**, No. 5, 75–80 (2000).

2

Behaviour of the Gas Phase in Liquids in Strong Electric Fields

An interest in the occurrence of the gas phase in liquid and its behavior is primarily caused by the circumstance that the electric strength of gas is much less than that of liquid. Therefore, if gas is presented in liquid, the problem of a mechanism of liquid breakdown initiation can be reduced, at least on the level of general considerations, to a simpler and better understood problem of gas breakdown. In fact, it is considered that the breakdown of a gas bubble somehow leads to liquid breakdown.

In view of the important role of the gas (in more general case, vapor-gas) phase in discharge ignition, some problems concerning the formation and existence of vapor-gas bubbles and their evolution in an electric field should be primarily considered.

The gas phase in liquid consists of air and other gases arising in the process of liquid manufacture, storage, and use. In addition, both gas and vapor bubbles can arise in the liquid volume under the effect of the electric field. The conditions of liquid equilibrium in the electric field considered in Chap. 1 enable us to calculate the influence of the field on thermodynamic bubble equilibrium in liquid. In this case, the main problem is whether the electric field promotes or interferes with bubble formation. The practical importance of this question follows from the fact that when the electric field promotes the bubble formation, achievement of a certain critical field will inevitably lead to bubble occurrence, and hence will limit the opportunity of obtaining higher fields because of bubble ionization and subsequent breakdown. When the electric field interferes with bubble growth, a lever of additional control over the electric breakdown arises due to its possible influence on the factors determining the breakdown occurrence.

2.1 Nature and State of the Gas Phase (Bubbles) in Liquids

2.1.1 Bubbles in Liquid before the Electric Field Application

The question on the mechanism of bubble existence is of principal importance for physics of boiling and cavitation of liquids. The matter is that the assumption about the nucleation of bubbles directly at the moment of experiment calls for substantial superheating during liquid boiling and tensile forces during cavitation. Actually, it is very difficult to realize these states of liquid in experiments on liquid boiling up and cavitation. Bubbles are mainly formed under pressure close to that of saturated vapor [1, 2]. Therefore, we can state that micronuclei (most likely microbubbles) permanently exist in liquid. Even in the experiments in which especially pure conditions were obtained using special methods (degassing or filtering), the bubbles were apparently formed from nuclei.

Theoretical models do not substantiate the stationary existence of gas bubbles in liquid. The gas must leave the bubble and dissolve in liquid, because it experiences the effect of increased pressure due to capillary forces. The dissolution time τ_{dis} depends on the bubble size r, coefficient of gas diffusion in liquid D, solubility C_s, and gas content C in the liquid [3]:

$$\tau_{\mathrm{sol}} = \frac{r^2}{2D\,(C_s - C)}\ .\tag{2.1}$$

It can be seen that the bubble can be *kinetically stable* in liquids with either small coefficient D (high viscosity) or low gas solubility or when the dissolved gas concentration C is close to the limiting gas content C_s.

There are several models of bubble *static stability*. According to one of these models [1], the bubble surface adsorbs surfactants which form a framework on the surface. The framework structure is such that it precludes the compression of the bubble without inhibiting its expansion. In this case, mechanical and molecular-kinetic equilibria are uncorrelated. The bubble size determined by establishing its mechanical equilibrium is maintained by the framework, and the gas pressure depending on molecular-kinetic equilibrium is set equal to that for a flat surface.

A more obvious variant of the existence of gas bubbles is connected with the presence of a microrelief on the solid surface in contact with the liquid, namely, pores and bulges. In this case, depending on the wetting angle of the surface by liquid and the pore geometry, there is a set of pores in which a stable existence of bubbles is possible. Thus, in bottle-shaped pores having a narrow exit to the surface and expanding deeper into the pore, bubbles can exist for any wettability. In pores of conical or cylindrical shape, stationary bubbles can exist only in the case of incomplete wettability [2, 4]. When the preliminary applied pressure exceeds that produced by capillary forces, a part of pores collapses, that is, gas is dissolved in the liquid.

Optical observations of the behavior of bubbles in water revealed the stationary existence of micron-size bubbles in distilled filtered water in a significant amount of 10^3–10^4 cm^{-3} [5,6]. This was demonstrated with the help of registration of the normalized light scattering phase function. The angles at which maxima of the scattered signal amplitudes were registered corresponded to inclusion sizes of 2–3 μm. To clearly distinguish between the scattering on bubbles and microparticles, additional experiment was performed under application of a pressure pulse. As the pressure increased, bubbles were compressed, and the maxima of the normalized scattering phase function were registered at angles corresponding to reduced bubble sizes. This unambiguously indicates the presence of exactly bubbles!

To explain their insolubility, it was suggested to treat the mechanism of interaction between gas and liquid with allowance for the physical adsorption of gas molecules on the surface. According to [6,7], equilibrium of the dissolved gas can be established with gas above a flat surface and inside the bubble. Thus, the micron-sized gaseous bubbles can stationary exist in the liquid.

In the overwhelming majority of cases, the main gas in the bubble must be air. In the process of preparation, the surface of the liquid is typically in contact with air. In some cases, for example, when preparing transformer oil, air is used in the production technology: in one of the last stages of oil preparation, air is blown through oil to dehumidify it [8]. Clearly, the gas concentration is close to saturation after this operation. According to the available data, 0.086 cm^3 of nitrogen, 0.16 cm^3 of oxygen, and 1.2 cm^3 of carbonic acid are dissolved in 1 cm^3 of transformer oil at room temperature. Bubbles in pure oil should consist of these main gases. If oil was in service, it must contain dissociation products of oil molecules: hydrogen, ethylene, acetylene, and other gases.

Other liquids, as a rule, contain bubbles consisting mainly of air. In addition, low-boiling liquids quite often used in experiments must contain vapors of these liquids.

However, even in experiments with pure degassed liquids, they may contain gas bubbles. The matter is that metal electrodes comprise sufficiently large amount of gas. For example, the approximate level of dissolved gas concentration in stainless steel is (1–10) (mm^3·atm)/g [9]. This means that 1 g of substance contains $\sim$1 mm^3 of gas at atmospheric pressure. In addition to gas in metal volume, there can be a large amount of gas on its surface. In contact with a degassed liquid, the gas from the surface and volume slowly diffuses into the liquid. The characteristic value of gas inflow even from carefully processed metal calcinated in vacuum is $\sim$1 cm^3/(s·cm^2) at a pressure of 10^{-3} Torr [9]. This means that 10^{-6} cm^3, that is, a gas bubble with a diameter of about 100 μm, intersects every second an area of 1 cm^2 moving into the degassed liquid given that the hydrostatic liquid pressure is equal to the atmospheric one.

Therefore, gas is always present in subsurface regions, and the most probable regions of gas localization are nonwettable surface areas of the electrodes, mostly pores. These areas are the nucleation centers for macroscopic bubbles.

2.1.2 Deformation in an Electric Field

It is experimentally established [10–13] that bubbles and drops suspended in a dielectric liquid are elongated along the electric field. In a theoretical description of this phenomenon, the following contradiction arises. According to [10, 11], from the equation of the interphase boundary

$$\frac{1}{R_1} + \frac{1}{R_2} = \frac{P_1 - P_2}{\sigma} - \frac{\varepsilon_0(\varepsilon_2 - \varepsilon_1)}{2 \cdot \sigma}(E_{t1}^2 + \frac{E_{n1}^2}{\varepsilon}) + \rho_2\frac{\partial\varepsilon_2}{\partial\rho_2}\frac{\varepsilon_0 E_2^2}{2 \cdot \sigma} - \rho_1\frac{\partial\varepsilon_1}{\partial\rho_1}\frac{\varepsilon_0 E_1^2}{2 \cdot \sigma}$$
$$(2.2)$$

it follows that bubbles should flatten along the field rather than elongate. Here R_1 and R_2 are the main radii of surface curvature, σ is the surface tension, P_1, ε_1, E_{n1}, E_{t1}, and E_1 are the pressure, permittivity, and normal and tangential components and total electric field strength in the bubble, respectively. The same quantities in liquid have subscript 2. If we exclude from (2.2) the last two terms and consider that P_1 and P_2 are constant for the entire bubble surface, the solution of the equation gives the result which does not contradict the experiment. Based on this, in [10] it was concluded that the electrostriction pressure in liquid was fictitious in character and hence can be disregarded. The incorrectness of this conclusion was pointed out in [11]. To obtain the agreement between the experiment and theory, in [11] it was suggested that the surface tension coefficient depends strongly on the field vector even in rather weak fields $E \sim 10\,\text{kV/cm}$. According to [11], the agreement with the experiment can be obtained by fitting the dependence for the given liquid.

However, inclusion of the dependence $\sigma(E)$ allows one to explain only the fact of bubble elongation along the electric field but not the deformation magnitude. The predicted deformation magnitudes are independent of the initial bubble size, whereas numerous experimental data [10,12,15] demonstrate that deformation of both bubbles and drops is proportional to the initial size of inclusions. Calculations performed in [14] were used to determine a criterion for bubble breakdown [16]. The assumption [17] that the bubble volume remains unchanged during deformation in an electric field was replaced with a more strict account of changes in the bubble volume and pressure. In the derivation of the bubble breakdown criterion it was assumed that the voltage drop on the bubble corresponds to a minimum of Paschen's curve $U = f(pd)$, where p and d are the pressure in the bubble and its size, respectively. Among disadvantages of this work are the incorrect account of the electrostriction pressure and hence the pressure in the bubble. In addition, it was considered that the field is electrostatic, and it remained unclear what factors led to the formation of bubbles. From the viewpoint of discharge ignition in the liquid, it is incorrect to identify the discharge initiated in the bubble with the discharge initiation in liquid. We believe that the discharge initiation in the bubble is necessary but insufficient condition for the discharge ignition in liquid.

In [18], the bubble stability was examined in the sense of occurrence and growth of waists and grooves on its surface. In so doing, it was assumed that $\varepsilon_0\varepsilon E^2/2 \gg 2\sigma/r$, and hence the bubble was elongated transforming into a long cylinder. A wavy cylindrically symmetric surface perturbation was considered; in this case, the pressure exerted by the electric field on the bubble decreased in the concave region and increased in the convex region of the bubble. The electric field in this case is the stabilizing factor, because it prevents the instability increase. However, there are a number of contradictions in this work. On the one hand, it is considered that the electric field flattens the bubble; on the other hand, the bubble volume is set constant in calculations. The fields for which $\varepsilon_0\varepsilon E^2/2 \sim 2\sigma/r$ were not examined in the work; probably, the bubble stability could be violated for these fields. In addition, for the ionized bubble, the instability only in the sense of infinite distance was considered. Though in this case the electric field is perpendicular to the surface, it has the opposite effects on concave and convex regions in comparison with the effect on the dielectric bubble. One more interesting result of this work is an analysis of electron losses in the elongated bubble caused by diffusion of hot electrons toward the bubble walls.

These works explain qualitatively the dependence of the electric strength of liquids on the temperature and pressure $E(T, p)$. However, they disregarded the factors that caused the bubble nucleation and maintained its existence. With allowance for these factors, the pressure, temperature, bubble size, and electric field in its vicinity can considerably differ from those used in [16, 17], and hence the significance of these criteria is reduced. These criteria should take into account concrete thermodynamic states of liquid and bubbles.

Thus, to solve the main problem whether the electric field promotes or precludes the formation of pre-breakdown bubbles, it is necessary to consider:

a) bubble deformation with allowance for the electrostriction pressure,
b) bubble stability,
c) shift of thermodynamic equilibrium of the bubble-liquid system under the effect of electric field.

2.1.3 Deformation and Stability

To elucidate the conditions of forming pre-breakdown bubbles, it should be taken into account that charge carriers are emitted from the electrodes when the field strength exceeds a certain threshold value (see Chap. 7). In nitrobenzene, the threshold field strength at the cathode is $500\,\mathrm{kV/cm}$. It is much higher at the anode ($1\,\mathrm{MV/cm}$) [19, 20]. The bubble formation near the cathode in liquid pentane and decane was observed at threshold field strength of $7\,\mathrm{MV/cm}$ [21]. It is believed that approximately the same or greater values are characteristic of intensive emission from the electrodes for other liquids as well. Therefore, the bubbles already existing on the electrode surface or formed at the electrodes are affected by strong electric fields; their influence on the shape and stability of bubbles must be taken into account.

Since the bubble in liquid is deformed in the electric field, it can lose its mechanical stability at the critical field strength depending on the properties of liquid and bubble sizes. As a result, it breaks into smaller bubbles as in the case of drops. This limits a maximum pre-breakdown bubble size, and as a consequence, increases their electric strength, especially under dc voltage. Therefore, to describe the pre-breakdown processes in liquids, it is necessary to analyze the conditions of violation of the mechanical stability of the bubble under the effect of the external electric field and to derive expressions for a maximum bubble size in pre-breakdown electric fields with allowance for the electrostriction of liquids.

2.1.4 Deformation in the Linear Approximation

Let us now analyze the initial premises used in [10,11]. They consider that the pressure in liquid $P = $ const, that is, is independent of the field strength and distribution. Vorobjev and Malyshenko [22] are also inclined to this viewpoint. This assumption is physically unjustified, because it ignores the dependence of the chemical potential of the liquid on the electric field strength. With allowance for this dependence, the liquid pressure distribution, including the region adjacent to the bubble surface, must be described by (1.5). In this case, the liquid overflows from weak to strong field regions, that is, from the bubble poles to its equator due to the nonuniformity of the electric field near the bubble theirby increasing the pressure near the equator and reducing it at the poles. The characteristic times of liquid overflow are determined by the bubble size and sound velocity. For micron-size bubbles, we have $d/c \sim 10^{-9}$ s. This means that local equilibrium is always established under pre-breakdown conditions.

According to [23], we now consider the bubble deformation with allowance for equilibrium condition (1.5). Substituting (1.5) into (2.2), neglecting electrostriction in the gas, and setting the gas permittivity $\varepsilon = 1$, we obtain the equation of equilibrium for the interphase boundary in the form:

$$\frac{1}{R_1} + \frac{1}{R_2} = \frac{P_1(\rho) - P_0}{\sigma} - \frac{\varepsilon_0(\varepsilon - 1)}{2 \cdot \sigma \cdot \varepsilon} E_1^2 - \frac{\varepsilon_0(\varepsilon - 1)^2}{2 \cdot \sigma \cdot \varepsilon} E_1^2 \cdot \sin^2(\theta), \quad (2.3)$$

where θ is the angle between the normal to the surface and the field direction, and R_1 and R_2 are the main radii of the surface curvature. We now demonstrate that under small deformations, (2.3) describes an ellipsoid. For the ellipsoid of rotation,

$$\frac{1}{R_1} + \frac{1}{R_2} = \frac{b}{a^2}(\sin^2(\theta) + \frac{a^2}{b^2}\cos^2(\theta))^{3/2} + \frac{1}{b}(\sin^2(\theta) + \frac{a^2}{b^2}\cos^2(\theta))^{1/2}, \quad (2.4)$$

where a and b are the lengths of the ellipsoid semiaxes. Expanding in a series and condidering terms of the first order, we obtain equation analogous to (2.3). Equating the corresponding terms, we determine the ellipsoid parameters $\Delta_1 = (a - R_0)/R_0$ (which describes the relative elongation along

the field) and $\Delta_2 = (R_0 - b)/R_0$ (which describes the relative compression along the equator). The gas inside the bubble is considered ideal:

$$\Delta_1 = \left[\frac{P_{\text{out}} \cdot R_0 \varepsilon_0 (\varepsilon - 1)}{4 \cdot \sigma \cdot \varepsilon} E_1^2 - \frac{\varepsilon_0 (\varepsilon - 1)}{2 \cdot \varepsilon} E_1^2 \cdot + P_{\text{out}} - P_0 \right] \cdot \left(3 \cdot P_{\text{out}} + \frac{4 \cdot \sigma}{R_0} \right)^{-1}$$

$$\Delta_2 = \left[\frac{P_{\text{out}} \cdot R_0 \varepsilon_0 (\varepsilon - 1)}{8 \cdot \sigma \cdot \varepsilon} E_1^2 + \frac{\varepsilon_0 (\varepsilon - 1)}{2} E_1^2 \cdot - P_{\text{out}} + P_0 \right] \cdot \left(3 \cdot P_{\text{out}} + \frac{4 \cdot \sigma}{R_0} \right)^{-1}$$

$$(2.5)$$

For the ellipsoid eccentricity $\Delta = (a - b)/R_0 = \Delta_1 + \Delta_2$, we obtain

$$\Delta = \frac{R_0 \varepsilon_0 (\varepsilon - 1)^2}{8 \cdot \sigma \cdot \varepsilon} E_1^2 = \frac{9 \cdot R_0 \varepsilon \varepsilon_0 (\varepsilon - 1)^2}{8 \cdot \sigma \cdot (2\varepsilon + 1)^2} E. \qquad (2.6)$$

From here it follows that $\Delta > 0$ irrespective of P_0, that is, the electric field acting on the bubble placed in a dielectric liquid transforms the bubble into an elongated ellipsoid of rotation with the major axis oriented along the field, as observed in experiments [10, 11]. Since in the linear approximation employed the electrostriction is not included into the expression for deformation, analogous expression for the deformation is obtained when the electrostriction is formally dropped as in [10] and as implicitly assumed in works [12, 15] devoted to the deformation of drops. However, to calculate the absolute values of elongation across the field (Δ_1) and along the field (Δ_2) and of changes in the bubble volume $\Delta V/V = (\Delta_1 - 2\Delta_2)$ that play the important role in bubble formation and discharge propagation in them, the electrostriction pressure should be taken into account.

A special case should be mentioned when the field on the bubble boundary is redistributed due to the electrical conduction of the liquid. This occurs if the applied voltage pulse duration exceeds the Maxwell time of dielectric relaxation. In this case, we find the bubble deformation based on calculations of the electrohydrodynamic deformations of drops presented in [12]. Simplifying the tension tensor obtained in [12] for the nonviscous gaseous phase with permittivity $\varepsilon = 1$ and taking into account the electrostriction by analogy with derivation of (1.5), we obtain the expression for bubble deformation under constant voltage:

$$\Delta = \frac{9 \cdot R \cdot \varepsilon_0 \cdot \varepsilon \cdot E_0^2}{8 \cdot \sigma} \cdot \frac{\rho_{\text{rat}}^2 \cdot (1 - 3.2q) + 1.2 \cdot \rho_{\text{rat}} + 1}{(2 \cdot \rho_{\text{rat}} + 1)^2}, \qquad (2.7)$$

where ρ_{rat} is the ratio of the specific resistance of the bubble to that of the liquid $q = 1/\varepsilon$. In the absence of ionization phenomena, there are virtually no charge carriers in the bubble. From here is follows that $\rho_{\text{rat}} \gg 1$, and the deformation is

$$\Delta = \frac{9 \cdot r_0 \cdot \varepsilon_0 \cdot E_0^2}{32 \sigma} \cdot (\varepsilon - 3.2). \qquad (2.8)$$

The characteristic feature of this case is that the deformation sign depends on the liquid permittivity value. For nonpolar liquids with $\varepsilon < 3.2$, $\Delta < 0$, that is, the bubble is flattened, whereas for polar liquids, $\Delta > 0$, and the bubble is always elongated along the electric field.

Thus, for small deformation of the bubble placed in the dielectric liquid, consideration of the electrostriction pressure has allowed us to derive expressions for deformation without invoking additional hypotheses.

2.1.5 Stability

The condition of small deformation can be violated for pre-breakdown bubbles in a strong electric field, and more complex calculations are required to determine the deformation. To this end, we now take advantage of the equations describing bubble deformation without assumption of its smallness; the main assumption here is that the bubble shape does not differ from an ellipsoid. Strictly speaking, this assumption is not fulfilled as well. However, it seems likely that under strong deformations for which $a/b \sim 2$, the bubble still remains stable, and the bubble shape differs from ellipsoidal one only insignificantly. We derive expressions for bubble deformation by analogy with [10] with the only difference that we will use the equilibrium pressure P_0 rather than the constant pressure P_2. We now introduce the quantity r_0 specified by the formula

$$\frac{2 \cdot \sigma}{r_0} \cdot r_0{}^3 = \left(P_{\text{out}} + \frac{2 \cdot \sigma}{R_0} \right) \cdot R_0{}^3 = P_1 \cdot b^3 \gamma, \tag{2.9}$$

which relates the pressure and volume for the ideal gas. This quantity is equal to the bubble radius at zero external pressure. The equilibrium conditions on the bubble pole and equator have the form

$$P_0 + \varepsilon \cdot P_{\text{eq}} + \frac{2 \cdot \sigma \cdot \gamma}{b} - P_1 = 0, \tag{2.10}$$

$$P_0 + P_{\text{eq}} + \frac{\sigma \cdot \left(\gamma^2 + 1 \right)}{b \cdot \gamma^2} - P_1 = 0.$$

The pressure exerted by the electric field on the bubble surface near the equator is

$$P_{\text{eq}} = \frac{\varepsilon_0 \cdot (\varepsilon - 1)}{2} \cdot \left(\frac{\varepsilon \cdot E}{\varepsilon - (\varepsilon - 1) \cdot G} \right)^2, \tag{2.11}$$

where G is the depolarization coefficient:

$$G = \frac{1}{\gamma^2 - 1} \left(\frac{\gamma \cdot \arccos \gamma}{\left(\gamma^2 - 1 \right)^{1/2}} - 1 \right). \tag{2.12}$$

From (2.10)–(2.12) we obtain a cubic equation for P_{eq}:

$$\left(\frac{P_{eq}}{P_{out}}\right)^3 - \frac{B \cdot \sigma^2 \cdot \varepsilon^2 \cdot A^2}{2 \cdot (\varepsilon - 1)^3 \cdot \gamma \cdot r_0{}^2 \cdot P_{out}{}^2} \cdot \left(\frac{P_{eq}}{P_{out}}\right) - \frac{\sigma^2 \cdot \varepsilon^2 \cdot A^3 \cdot \gamma}{2 \cdot r_0{}^2 \cdot (\varepsilon - 1)^3} \cdot \frac{P_0}{P_{out}{}^3} = 0,$$

(2.13)

where $A = 2\gamma - 1 - 1/\gamma^2$ and $B = 2\varepsilon\gamma^3 - 1 - \gamma^2$.

Let us rewrite it in the canonical form for the third-order equations:

$$y^3 + 3py + 2q = 0.$$

(2.14)

The form of the solution depends on the sign of the quantity $Q = p^3 + q^3$. For $Q > 0$, the solution is unique and real:

$$P_{eq} = \frac{\sigma\varepsilon A}{r_0}\left[\frac{2B}{3\gamma(\varepsilon - 1)^3}\right]^{\frac{1}{2}}\cosh\theta,$$

$$\theta = \frac{1}{3}\operatorname{arccosh}(y_0),$$

(2.15)

$$y_0 = \frac{P_0 r_0}{\sigma}\left[\frac{27\gamma^5(\varepsilon - 1)^3}{2B^3}\right]^{\frac{1}{2}}.$$

For $Q < 0$, there are three real roots of (2.14); moreover, two of them are negative for $q < 0$. Since P_{eq} by definition (2.11) is positive, these solutions are physically meaningless and must be rejected. For $q > 0$, there are two positive roots:

$$P_{eq} = \frac{\sigma\varepsilon A}{r_0}\left(\frac{2B}{3\gamma(\varepsilon - 1)^3}\right)^{\frac{1}{2}}\cos(\theta),$$

$$P_{eq} = \frac{\sigma\varepsilon A}{r_0}\left(\frac{2B}{3\gamma(\varepsilon - 1)^3}\right)^{\frac{1}{2}}\cos\left(\theta - \frac{\pi}{3}\right),$$

(2.16)

where θ is determined from the formula:

$$\theta = \frac{1}{3}\arccos(y_0).$$

(2.17)

This case corresponds to a negative liquid pressure. For $y_0 < -1$, the real solution is unique and negative; therefore, there is no solution in principle in this interval of negative pressures.

Substituting P_{eq} into (2.11), we express E through γ. In particular, for $y_0 > 1$,

$$E = \left(\frac{\sigma}{4\varepsilon_0\varepsilon r_0}\right)^{1/2} \cdot \left(\frac{\varepsilon}{\varepsilon - 1} - G\right) \cdot \left(\frac{8A^2 B}{3\gamma(\varepsilon - 1)}\right)^{1/4}\cosh^{1/2}\Theta,$$

(2.18)

and for $0 < y_0 < 1$,

$$E = \left(\frac{\sigma}{4\varepsilon_0 \left(\varepsilon r_0 \right)} \right)^{1/2} \left(\frac{\varepsilon}{\varepsilon - 1} - G \right) \left(\frac{8A^2 B}{3\gamma(\varepsilon - 1)} \right)^{1/4} \cos^{1/2} \Theta. \qquad (2.19)$$

In a sharply nonuniform field, $P_0 = P_{\text{out}}$ and $y_0 > 0$ in the absence of charge emission. For this case, formulas (2.18), (2.19), and (2.5) describing small deformations were used in calculations. A bubble with a radius of $1\,\mu$m in n-hexane with $\sigma = 18.42 \cdot 10^3$N/m and $\varepsilon = 1.883$ was considered. Figure 2.1 shows the dependences of the bubble deformation on the field strength described by these formulas.

It can be seen that the curves almost completely coincide for the weak electric field, and for the strong field, the maximum difference is as great as 15%, that is, in this case the linear approximation is sufficiently accurate. However, the linear approximation does not predict the dependence of the deformation on the pressure if the pressure changes in an electric field. When P_0 decreases because of the electrostriction:
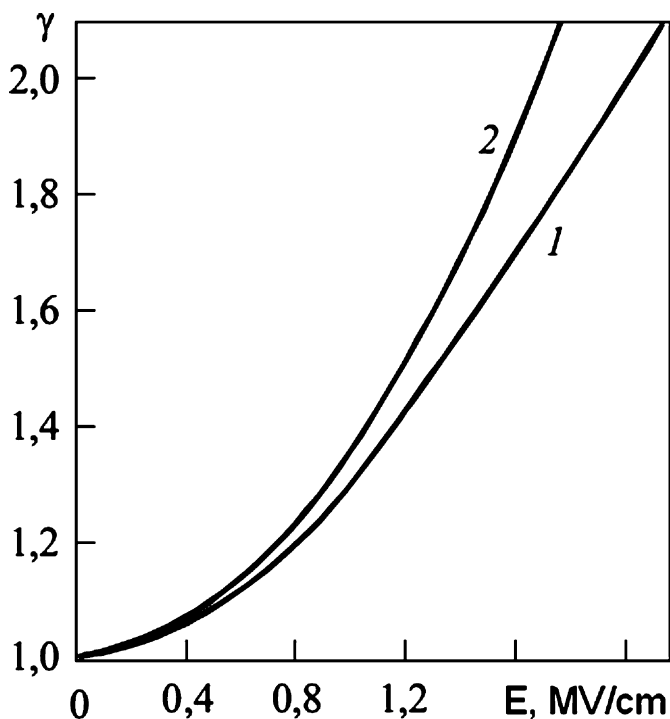
Fig. 2.1. Deformation of the bubble with $R_0 = 1\,\mu$m in hexane under the effect of the electric field. *Curve 1* shows the results calculated from (2.18) and (2.19), and *curve 2* shows the results calculated in the linear approximation

$$P_0 = P_{\text{out}} - \varepsilon_0 \rho \frac{\partial \varepsilon}{\partial \rho} \cdot \frac{E^2}{2}, \tag{2.20}$$

calculations were carried out for a bubble with a radius of $1\,\mu$m in n-hexane. Figure 2.2 shows the calculated results. The deformation for $P_0 = P_b$ and the dependence of the pressure in the bubble on the field strength for these two cases are also shown in the figure. It is important that for $E_{\text{cr}} > 2.25\,$MV/cm, the bubble of this size cannot exist if the pressure in the liquid decreases because of electrostriction. This problem was investigated in more detail. To this end, a special program of calculating E_{cr} from (2.18) for $y_0 = 1$ was developed. Calculations were carried out for typical polar and nonpolar liquids hexane and water. Figure 2.3 shows the dependences of γ_{cr} and E_{cr} on R_0 for the bubble radius increasing from 10^{-8} to $2 \cdot 10^{-6}\,$m. From Fig. 2.3 it can be seen that the region of solution existence is bounded from above by the curve $E_{\text{cr}}(r)$, and the minimum field strength at which this effect is observed is $2\,$MV/cm. For water (Fig. 2.4), the critical field strength is approximately
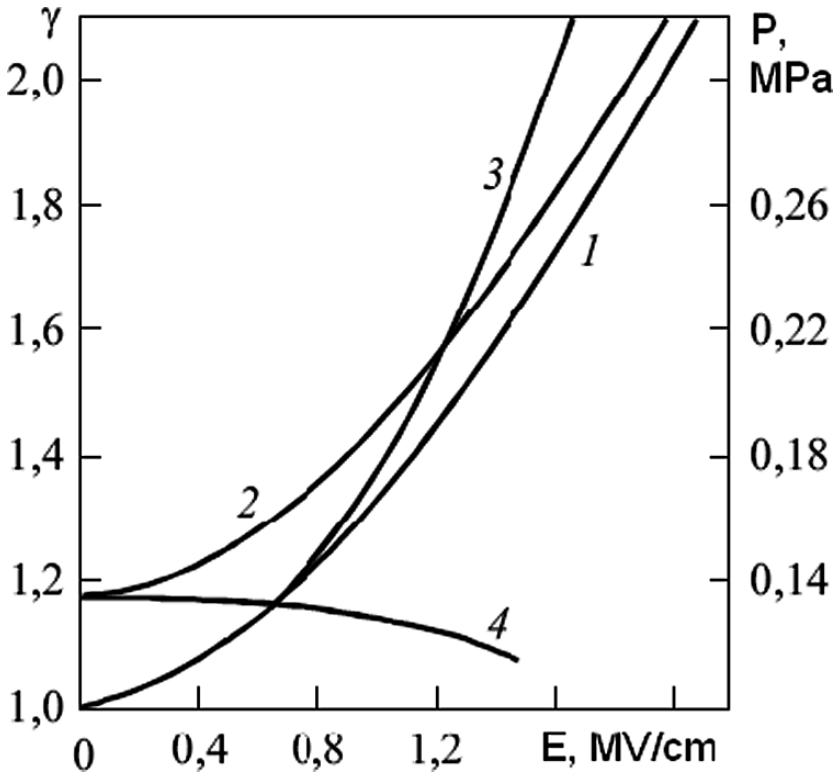
Fig. 2.2. Dependences of the bubble deformation (*curves 1* and *1'*) and pressure (*curves 2* and *2'*) on the electric field strength with (*curves 1* and *2*) and without consideration of the electrostriction (*curves 1'* and *2'*) for $R_0 = 1\,\mu$m in hexane
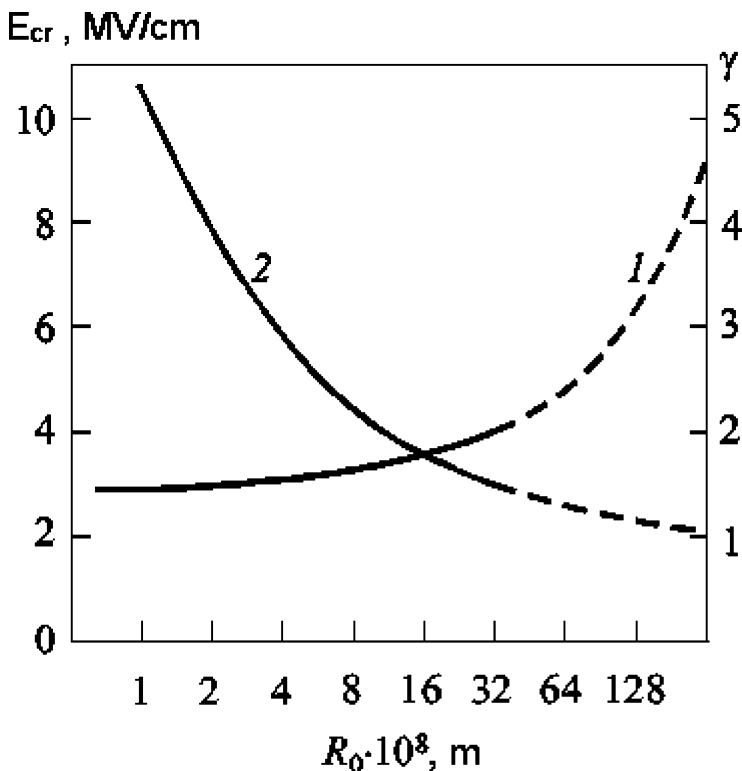
Fig. 2.3. Dependences of the critical deformation (*curve 1*) and electric field strength (*curve 2*) on the bubble radius in hexane

equal to $0.4\,\mathrm{MV/cm}$ for a 1-μm bubble; it is equal to $4\,\mathrm{MV/cm}$ for a 10^{-8}-m bubble. The physical nature of the absence of solution for $E > E_{\mathrm{cr}}$ is the impossibility of bubble equilibrium under significant negative pressure values created because of electrostriction according to (2.20). It is not clear how equilibrium will be established, but it is obvious that the electric field tends to break off the bubble, because, as can be seen from Figs. 2.3 and 2.4, the bubble remains stable under the same field when its sizes are reduced.

Let us consider the second solution for $-1 \leq y_0 < 0$. For $y_0 = -1$, this solution for the critical field coincides with the first one, and for all other y_0 values, it describes higher deformation intensities than the first solution.

The solutions examined above only demonstrate that under certain conditions the bubble is in mechanical equilibrium with the liquid. However, it is not clear whether equilibrium is stable. Since the surface energy of the bubble increases as the bubble grows, under certain deformation degree it becomes energetically favourable to divide the bubble into two or more fragments. Disregarding changes in the electrostatic energy, the surface energy of the bubble can be determined from the expression:
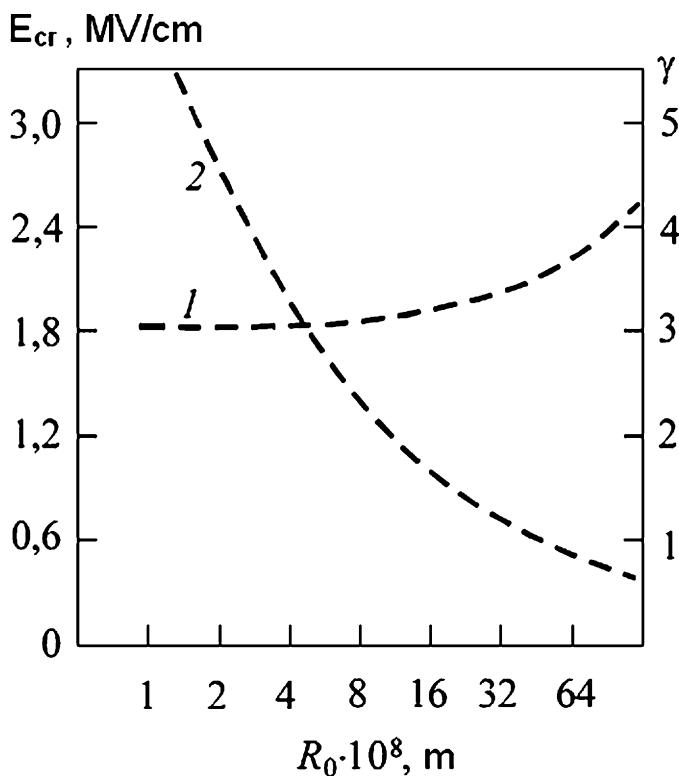
Fig. 2.4. Dependences of the critical deformation (*curve 1*) and electric field strength (*curve 2*) on the bubble radius in water

$$\sigma S = \frac{2\pi\sigma R_0{}^2 \cdot \gamma^{4/3}}{\sqrt{\gamma^2 - 1}} \left[\frac{\sqrt{\gamma^2 - 1}}{\gamma^2} + \arcsin\frac{\sqrt{\gamma^2 - 1}}{\gamma} \right]. \qquad (2.20a)$$

After division into two bubbles whose deformation we neglect, their total surface energy $\sigma S = 8\pi R_0{}^2 \sigma 2^{-2/3}$ will not exceed the surface energy of the initial ellipsoid for $\gamma \geq 4$. From here we conclude that bubbles with deformation $\gamma \approx 4$ are unstable and cannot stationary exist. Since the deformation depends on the radius and in the linear approximation is proportional to it, the critical deformation for large bubbles is observed for weaker fields. Strictly speaking, the estimate $\gamma \approx 4$ is rather approximate, since a correct consideration of stability must involve small deviations of the waist shapes and analysis of the accompanying changes of the total energy of the system.

A rigorous solution of the problem on the bubble stability faces significant difficulties; at the same time, there are no detailed experimental studies of the bubble stability under the effect of electric field. The results of drop collapse in a flow or an electric field [12, 15] demonstrate that the drop is divided into
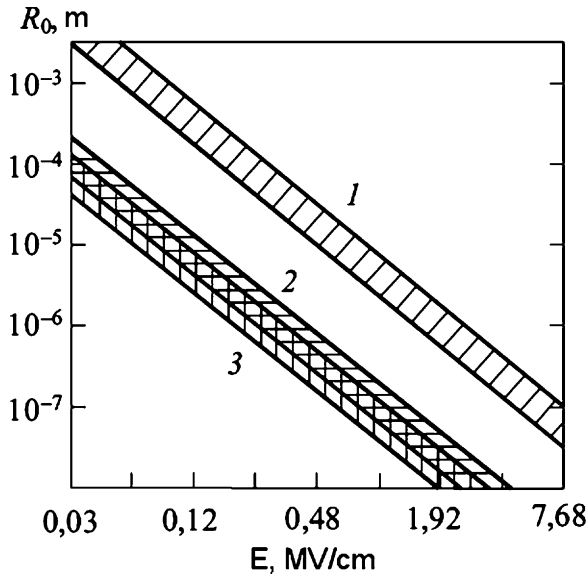
Fig. 2.5. Dependence of the maximum bubble radius on the electric field strength. The stability region boundaries are $2 < \gamma < 4$. Here *curve 1* is for hexane, *curve 2* is for nitrobenzene, and *curve 3* is for water

two or more drops already for $\gamma \approx 2$. Apparently, for bubbles we can consider that they are unstable for $\gamma \approx 2 - 4$. Figure 2.5 shows instability regions for the bubble in water, nitrobenzene, and hexane.

As to the experimental data on the bubble stability in an electric field, there are only occasional data on the bubble behavior in exotic enough dielectric (liquid six-fluoric sulfur) [24,25]. Optical measurements [24] demonstrated that vapor bubbles with low mobility are divided into fragments when the field strength achieved the critical value. The fixed bubble size was characteristic of each field strength value, namely, 0.3 mm for 350 kV/cm and 0.1 mm for 630 kV/cm. It can be seen that the dependence of maximum bubble radius on the field strength is square-law, as it follows from (2.5) given that Δ is fixed. Formally, substituting the physical parameter values, including the permittivity, surface tension coefficient, bubble radius, and field strength into (2.5), we obtain that the deformation in linear approximation must be approximately $\Delta \sim 3$. This means that $\gamma \approx 4$ corresponds to division of bubbles in liquid SF_6.

These results are confirmed by experimental investigations of the prebreakdown bubbles in hexane [26]. The normalized optical scattering phase function was measured under application of voltage at which partial discharges were formed. The analysis of the results demonstrated that the average bubble radius at the tip anode was $1\,\mu m$, and at the tip cathode it was $0.7\,\mu m$. Considering that the boundary of the stability region corresponds to $\gamma = 2$, from

Figs. 2.1 and 2.5 we conclude that the electric field strength near the anode in experiment [26] was 2 MV/cm, which was apparently close to the experiment. For the tip cathode, two variants of explanation are possible, namely, either the electric field strength exceeded by a factor of 1.1–1.2 the field strength near the anode due to an increase in the breakdown voltage with allowance for the polarity effect [27], or charge carriers were emitted near the anode thereby decreasing the pressure near the electrodes and reducing the bubble stability by analogy with the electrostriction effect considered above.

2.2 Influence of the Electric Field on the Bubble Formation

2.2.1 Electrostatic Mechanism of Bubble Formation

The feasibility of implementation of this mechanism was discussed in a number of works [27–31]. The important role in the construction of the model of bubble breakdown mechanism was played by Kao [30] who put forward several hypotheses explaining the bubble formation in the gap and the bubble role in electric breakdown. One of the reasons for bubble occurrence is extraction of the gas from cracks and pores on the electrode surface. It is considered that the bubble formed under the action of electrostatic forces tends to be elongated, while its volume remains constant. The breakdown occurs when the voltage on the bubble reaches a minimum in Paschen's curve. These assumptions allowed Kao [30] to explain on the qualitative level the dependence of the electric strength on pressure and temperature for long and microsecond voltage pulses [32]. However, within the framework of this model it is impossible to explain the absence of the dependence of the electric strength on the above-enumerated factors for nanosecond voltage pulses [33, 34]. Some unjustified assumptions, in particular, about the constancy of the bubble volume were indicated by the Grenoble team [18, 35].

An attempt to explain the bubble formation by stretching of thermofluctuation holes was made in [36] where it was assumed that the liquid has a special quasicrystal structure. However, according to the hole theory of liquids [37], the size of thermofluctuation holes does not exceed 10^{-7} cm. Hence, significant drag (tension) forces should be applied to the hole to stretch it. These forces can be estimated from the equality of capillary pressure and tension from which it follows that tension must be as great as several tens and hundreds of MPa. Moreover, a mechanism of tension in liquid under the effect of the electric field remained unclear in [36]. In [38–41] it was considered that the free energy of a dielectric in an electric field decreases by $\varepsilon_0 \varepsilon E^2 V_{cr}/2$ with bubble formation, where V_{cr} is the volume of the critical bubble. This bubble can be the reason for breakdown.

The change in the free energy of dielectrics with incorporated substances having reduced permittivity was studied in [42] where it was demonstrated

that in this case, the free energy increased. In addition, the increase in the free energy was testified by the experimental fact of forcing out bubbles from the region of a strong electric field [43–45]. However, boundaries of the liquid were not taken into account in [42]; meanwhile, as follows from (1.5)–(1.8), the conditions on the boundaries can promote tension in liquid. It seems likely that with occurrence of the bubble, the total free energy in some cases will decrease. Therefore, the problem of electrostatic cavitation remains unsolved.

The breakdown of hexachlordiphenyl was experimentally and theoretically investigated in [31] where an attempt was made to use these results to analyze the pre-breakdown phenomena in other liquids. The main mechanism of bubble formation was detachment of liquids from the electrode surface. It was assumed that the detachment occured in the region of field amplification caused by an impurity particle lying on the electrode. The particle was considered spherical, the electric field on its surface was nonuniform, and the maximum field strength was amplified by a factor of 4.2 in comparison with the external field. The detachment mechanism implies that the electric charge at the particle-liquid interface repels the liquid exerting the pressure $p_\sigma = \varepsilon_0 \varepsilon E^2/2$ to the liquid surface. It is considered that when p_σ becomes equal to the external pressure, a cavity arises. When it is separated at a sufficiently large distance, evaporation occurs from its walls due to energy liberation and dissociation in the process of bubble wall bombardment by electrons. However, from the results of this work it is not clear whether the charge remains on the metal surface or leaves the metal to be incorporated into the liquid. If the charge remains on the metal surface, only electrostatic forces will act on the liquid. In order that the charge acted directly on the liquid and could transfer a momentum, it must escape the range of attraction of the image forces, that is, must be *emitted* into the liquid. In this case, the mechanism of charge carrier emission should be considered (for example, as was made in Chaps. 1 and 7) together with charge carrier motion in liquid. Then it is already impossible to consider the electrostatic mechanism of bubble formation.

The idea of Krasucki [31] about liquid detachment from the microparticle was used in [14] to study the probability of liquid detachment from the tip electrode. In this case, the value of the local amplified field strength near the tip E_{tip} was used in the expression for the pressure instead of $4.2 \cdot E_0$. It was considered that the bubble was shaped as a semicylinder resting on a metal surface. Based on the conditions of equilibrium at the bubble pole and equator, it was concluded that the bubble with radius smaller than $1\,\mu$m was flattened, while the bubble with radius greater than $1\,\mu$m was elongated along the field force lines. However, this work has a number of disadvantages and unreasonable assumptions. First, by analogy with [31], the liquid discontinuity was considered incorrectly. Second, the assumption about the semicylindrical bubble shape on the surface was not tested; this test would be made based on an analysis of equilibrium conditions not only on the pole and equator but also on the entire gas-liquid interface. Third, it was assumed that the liquid pressure remained constant, and the electrostriction pressure was not

taken into account. The common disadvantage of works analyzed above is the assumption that bubbles are inevitably formed when the critical field strength is achieved.

Among recent works devoted to this subject, works [46,47] should be mentioned in which the electromechanical forces were examined promoting the occurrence of microcavities and their transformation into a streamer. Without going into details, it should be noted that great forces can be realized only at microtips with significant field amplification. However, in an attempt to create high field strengths $E \sim 10^8$ V/cm, the near-electrode processes of charge carrier emission must be observed at much lower field strengths $E \sim (3–7)$ $\cdot 10^5$ V/cm; they make obtaining higher field strengths impossible.

Based on an analysis of works devoted to the formation of pre-breakdown bubbles under the effect of electric field, a conclusion can be made that this question remains unclear, and in order that to answer it, the dynamics of bubble nucleation and growth should be considered with allowance for all forces acting on the bubble surface. Rigorous consideration of bubble growth faces significant difficulties even in rather simple cases of bubble nucleation in superheated or stressed liquids [1, 2, 48, 49]. The complexity of calculations is caused by the necessity of inclusion of a number of factors: viscosity, inertia, evaporation dynamics, thermal fluxes, etc. When bubbles grow in an electric field, the influence of the electric field on bubble deformation and change of the bubble pressure are added to the above-enumerated factors. Therefore, a rigorous solution to the problem on the dynamics of growth of pre-breakdown bubbles is a very complicated problem, and its solution is hardly possible now. To solve this problem qualitatively, that is, to answer the main question wether the electric field promotes or precludes the bubble formation, there is no need to solve the dynamic problem. It is suffice to consider changes in the conditions of static equilibrium for the bubble under the effect of the electric field.

2.2.2 Influence of Pressure Variations Inside the Bubble on Phase Equilibrium

Based on the results of calculations of bubble deformation and conditions of electrohydrostatic equilibrium (Chap. 1), we now consider the problem of displacement of thermodynamic equilibrium for a liquid-vapor system under the effect of electric field [50].

As is well known, conditions of phase equilibrium for the liquid-bubble system are fulfilled when the temperatures, chemical potentials, and pressures of the coexisting phases are equal. In our case, the equality of temperatures is a trivial condition; therefore, joint changes in the chemical potentials and pressures of the bubble and liquid should be analyzed. We now consider that before voltage application, the liquid and vapor chemical potentials were equal: $\xi_1 = \xi_2$. Their change under the effect of the electric field can be described by expressions [42]

$$\xi_1 (P, T, E) = \xi_1 (P, T) - \varepsilon_0 \frac{\partial \varepsilon_1}{\partial \rho_1} \cdot \frac{E_1^2}{2},$$

$$\xi_2 (P, T, E) = \xi_2 (P, T) - \varepsilon_0 \frac{\partial \varepsilon_2}{\partial \rho_2} \cdot \frac{E_2^2}{2}. \tag{2.21}$$

Since for gas $\rho \dfrac{\partial \varepsilon}{\partial \rho} \approx \varepsilon - 1 \ll 1$, we neglect the change in the chemical potential of vapor under the effect of the electric field and consider only its change caused by pressure changes in the bubble which can be expressed as

$$\xi_1 (P, T) = \frac{kT}{m} \ln \frac{P_s}{P_{so}} + \xi_1 (T, P_{so}), \tag{2.22}$$

where P_s is the saturated vapor pressure and P_{so} is the saturated vapor pressure in the absence of field. Under conditions of liquid equilibrium, $\xi_1 = \text{const}$ and we obtain

$$\xi_1 (P, T, E) = \xi_2 (P_0, T) \approx \xi_1 (T, P_0) + \frac{P_{\text{out}} - P_0}{\rho}, \tag{2.23}$$

where P_0 is determined from condition (2.5). Equating (2.22) and (2.23), we obtain

$$\frac{kT}{m} \ln \frac{P_s}{P_{so}} = \frac{P_{\text{out}} - P_0}{\rho}. \tag{2.24}$$

If we take into account only changes of the chemical potentials and ignore mechanical equilibrium, from (2.24) we obtain that the change in the saturated vapor pressure $\dfrac{P_s}{P_{so}}$ necessary for compensation of the change in the chemical potential is usually insignificant. From here it follows that the displacement of the curve of phase equilibrium is insignificant, as demonstrated in [51].

Let us consider the change in the bubble pressure. Since the saturated vapor pressure in the electric field remains virtually unchanged, its change in the bubble in the process of establishing mechanical equilibrium causes the chemical potential of vapor to change. The latter is much less sensitive to the field than to the pressure. This is explained by the fact that, as demonstrated above, the change in the chemical potential of liquid can be compensated by a small change in the pressure inside the bubble. From (2.24) it follows that

$$\Delta P_s \sim \frac{P_{so}}{nkT} (P_{\text{out}} - P_0),$$

where n is the number of liquid molecules in unit volume. Since nkT has the dimensionality of pressure and its value is a few hundred MPa, the change in the saturated vapor pressure caused by the change in the chemical potential of liquid under the effect of the electric field is small and can be neglected. Therefore, if the pressure in the bubble has increased, the chemical potential of vapor exceeds the chemical potential of liquid, and vapor condensation on

the bubble walls will be observed thereby decreasing the pressure inside the bubble. Since the pressure of the electric field on the bubble and hence the pressure inside the bubble are kept constant, the bubble volume will decrease and after a while, the bubble will be dissolved in the liquid.

Hence, when the external electric field causes the pressure inside the bubble to increase $\Delta P > 0$, the thermodynamic vapor stability decreases; on the contrary, when $\Delta P < 0$, the electric field promotes the formation and growth of bubbles. The electric field influences analogously the gas bubbles in the saturated liquid with the only difference that the rate of bubble dissolution will be determined by the difference between the pressure inside the bubble and the partial pressure in the liquid.

To calculate the displacement of the curve of phase equilibrium under the effect of electric field, we must elucidate the degree of similarity of this situation to the case when phase equilibrium is displaced as a result of changes in the external pressure. It is well known that the external pressure causes virtually equal changes in pressures inside the liquid and bubble. In our case, the pressure inside the bubble changes, whereas the pressure in the liquid can remain constant.

However, from the viewpoint of the phase transition, this difference is insignificant, since the change in the chemical potential of the liquid with pressure can be neglected. Therefore, we can consider that the phase equilibrium curve is displaced under the effect of electric field as if the external pressure has been changed by ΔP determined from the conditions of bubble deformation with allowance for electrohydrostatic equilibrium.

2.2.3 Calculations of the Pressure Inside the Bubble upon Small Deformations

Let us consider a change in the pressure inside the bubble under the effect of electric field. This problem is most simply and vividly solved within the framework of the linear approximation. Based on (2.5), we write down the relative change in the bubble volume:

$$\frac{\Delta V}{V} = \left(P_{\text{out}} - P_0 - \frac{3\varepsilon_0 \varepsilon \left(\varepsilon - 1 \right) E_0^2}{2 \left(2\varepsilon + 1 \right)} \right) \left(P_{\text{out}} + \frac{4\sigma}{3R_0} \right)^{-1} . \qquad (2.25)$$

From here the change in the pressure is

$$\Delta P = \frac{P_{\text{out}} + \dfrac{2\sigma}{R_0}}{P_{\text{out}} + \dfrac{4\sigma}{3R_0}} \left[\frac{3\varepsilon_0 \varepsilon \left(\varepsilon - 1 \right) E_0^2}{2 \left(2\varepsilon + 1 \right)} - \left(P_{\text{out}} - P_0 \right) \right] . \qquad (2.26)$$

To simplify the subsequent expressions, we designate the quantity before the square brackets by A. Let us analyze the above expression with allowance for conditions (1.1)–(1.9). When $P_0 = P_{\text{out}}$, the liquid is drawn in the region

of electric field, and the conditions on the volume boundary do not influence the pressure value inside the bubble:

$$\Delta P = A\frac{3\varepsilon_0\varepsilon\,(\varepsilon-1)\,E_0^2}{2\,(2\varepsilon+1)}. \tag{2.27}$$

The electric field increases the pressure inside the bubble, that is, precludes its formation and growth. If the liquid is in contact with the atmosphere and values of the normal and tangential components are equal: $E_{\mathrm{n.b}} = E_{\mathrm{t.b}}$, with allowance for (1.8) we obtain

$$\Delta P = A\frac{\varepsilon_0\,(\varepsilon-1)\,E_0^2}{2}\left[\frac{3\varepsilon}{2\varepsilon+1}-\frac{\varepsilon E_{\mathrm{n.b}}^2}{E_0^2}-\frac{E_{\mathrm{t.b}}^2}{E_0^2}\right]. \tag{2.28}$$

From here it follows that $\Delta P > 0$ if the field on the boundary is small in comparison with E_0. If the field on the boundary has only the tangential component $E_{\mathrm{t.b}} = E_0$,

$$\Delta P = A\frac{\varepsilon_0\,(\varepsilon-1)^2\,E_0^2}{2\,(2\varepsilon+1)}. \tag{2.29}$$

If the field has only the normal component $E_{\mathrm{n.b}} = E_0$,

$$\Delta P = -A\frac{\varepsilon_0\,(\varepsilon-1)^2\,\varepsilon E_0^2}{2\varepsilon+1}. \tag{2.30}$$

For a uniform field when the liquid inflow is impossible or has no time to occur, taking into account (2.5), we obtain that

$$\Delta P = A\left[\frac{3\varepsilon_0\varepsilon\,(\varepsilon-1)\,E_0^2}{2\,(2\varepsilon+1)}-\varepsilon_0\rho\frac{\partial\varepsilon}{\partial\rho}\frac{E_0^2}{2}\right], \tag{2.31}$$

that is, both value and sign of pressure change depend on the dielectric polarity. For nonpolar dielectrics, from (2.31) and (1.2) we obtain that

$$\Delta P = -A\frac{\varepsilon_0\,(\varepsilon-1)^3\,E_0^2}{2\,(2\varepsilon+1)}<0. \tag{2.32}$$

For polar liquids, the result depends on the expression employed for $\frac{\partial\varepsilon}{\partial\rho}$. If theoretical expression (1.3): $\rho\dfrac{\partial\varepsilon}{\partial\rho}=\varepsilon-\varepsilon_\infty$ is used,

$$\Delta P = A\frac{\varepsilon_0\,\left(\varepsilon^2+(2\varepsilon_\infty-4)\,\varepsilon+\varepsilon_\infty\right)E_0^2}{2\,(2\varepsilon+1)}, \tag{2.33}$$

and the use of empirical expression (1.4): $\rho\dfrac{\partial\varepsilon}{\partial\rho}\sim k\varepsilon$ yields not so unambiguous result

$$\Delta P = A \frac{\varepsilon \varepsilon_0 \left[\varepsilon\left(3 - 2\kappa\right) - \kappa - 3\right]}{2\left(2\varepsilon + 1\right)} E_0^2. \tag{2.34}$$

Taking into account that for the majority of technical liquids $\kappa < 1.5$, we obtain that $\Delta P > 0$ as in the case described by (2.34). For conducting liquids, the expression for the change in the pressure inside the bubble is derived from formula (2.7):

$$\Delta P = A \left(\frac{3\varepsilon_0 \left(2\varepsilon - 1\right)}{8} E_0^2 + P_0 - P_b\right). \tag{2.35}$$

A comparison of this expression with (2.25) demonstrates that in non-polar liquids with other conditions remaining unchanged, the change in the pressure inside conducting liquids is approximately doubled compared to dielectric liquids. With increase in the permittivity, this difference decreases and, for example, for water these expressions yield virtually identical results.

Thus, the linear theory allows simple expressions to be obtained that consider the influence of the electric field on the phase transition and cases to be revealed when the electric field precludes or promotes boiling up of the liquid.

2.2.4 Influence of the Bubble Shape Instability on Boiling of Liquids

The main laws established with the help of the linear theory are also observed under large deformations. We note the salient feature following from the bubble stability in an electric field. In the theory of phase transitions it is assumed that the condition of equilibrium between the liquid and bubble of infinite radius is fulfilled on the phase transition curve (binode) [1, 48].

For superheated liquids when thermodynamic liquid parameters are enclosed between the spinode and binode, the liquid is in equilibrium with the bubble of finite radius R. And in the case of maximum superheating (the attainment of the spinode), the liquid is in equilibrium with the bubble of zero size. Thus equilibrium is unstable; an excess of the equilibrium size leads to infinite bubble growth.

However, in our case stationary equilibrium with a large bubble placed in an electric field is impossible. This circumstance should influence the mechanism of bubble formation. We consider two cases: when the radius of the critical nucleus r_{cr} is less than the radius R_{cr} of the bubble whose deformation is critical $\gamma(R_{cr}) = \gamma_{cr} \cong 2 - 4$ and the formation of bubbles for the opposite relationship between the radii. If $r_{cr} < R_{cr}$, the potential barrier for the bubble growth is determined by the r_{cr} value and the pressure produced by the electric field. When the bubble size exceeds r_{cr} due to thermal fluctuations, it will grow and will be deformed until its size reaches R_{cr}; then it will be divided into two or more bubbles with sizes that will grow until R_{cr}, and so on. If $r_{cr} > R_{cr}$, boiling is impossible. The bubbles with sizes $r_{cr} > R_{cr}$ formed due to thermal fluctuations are unstable; they are divided into bubbles of smaller sizes, and since the pressure inside them is higher than

the saturated vapor pressure, they are dissolved in the liquid. It seems likely that instability of boiling in the electric field will cause nonstationarity of the boiling process. We note that nonstationarities of boiling should be promoted also by electrohydrodynamic flows.

Nonstationarity of the boiling process and conditions determining boiling up in electric field follows directly from the results presented in [52]. Our results demonstrate that for the onset of stationary boiling, additional super-heating should be provided at which the radius of the critical nucleus will be smaller than R_{cr}. Therefore, to determine the displacement of the phase transition point, the additional pressure

$$\Delta P_{\mathrm{cr}} = \frac{2\sigma}{R_{\mathrm{cr}}} \tag{2.36}$$

caused by the surface tension should be taken into account.

Assuming that R_{cr} is determined by the stability condition $\gamma \sim 2$, ΔP_{cr} can be estimated simply in the context of the linear theory. Setting $\Delta = 1$ in (2.5) and determining $2\sigma/R_{\mathrm{cr}}$ from this equation, we obtain

$$\Delta P_{\mathrm{cr}} = \frac{9}{4} \frac{\varepsilon_0 \varepsilon (\varepsilon - 1)^2}{(2\varepsilon + 1)^2} E_0^2. \tag{2.37}$$

Therefore, the phase transition point will be displaced toward higher temperatures or lower pressures. Analytically, this influence should be taken into account by addition ΔP_{cr} to ΔP values determined by (2.25)–(2.35):

$$\Delta P_{\mathrm{bubble}} = \Delta P + \Delta P_{\mathrm{cr}}. \tag{2.38}$$

From here we can conclude that the binode in its classical understanding is absent in the electric field.

2.2.5 Influence of the Electric Field on the Boiling Point of Liquids

Let us consider experiments [53–55] devoted to the influence of electric field on the boiling point of alcohol under the effect of ac fields with strengths $\leq 10\,\mathrm{kV/cm}$. In [53] the electric field influenced only on the gas phase, and no displacement of the boiling point (to within $0.1\,\mathrm{K}$) was detected. According to our considerations, the boiling point in these experiments should remain unchanged, since the electric field was absent in the region of bubble nucle-ation, and the change in the chemical potential of vapor directly under the effect of the electric field was negligibly small.

In [54, 55], the electric field influenced not only liquid and vapor but also the interphase surface. No changes in the boiling point were registered to within $0.2\,\mathrm{K}$.

The liquid-atmosphere interface was acted upon by a tangential field, that is, $E_{\mathrm{n.b}} = 0$ and $E_{\mathrm{t.b}} = E_0$. Then according to (2.29) and (2.37) $\Delta P_{\mathrm{bubble}} > 0$

and hence, the liquid should boil at an elevated temperature. Let us estimate a possible change in the boiling temperature T_b from the expression $\Delta T \sim \Delta P \dfrac{\partial T_{cr}}{\partial P}$ in which $\dfrac{\partial T_{cr}}{\partial P}$ is determined from the data tabulated in [56] for the phase transition. For methanol with $\dfrac{\partial T_{cr}}{\partial P} \sim 250\,\mathrm{K/MPa}$ and $\varepsilon \sim 20$, using (2.29) and (2.37), we obtain that the the boiling temperature must change in the field with strength of $25\,\mathrm{kV/cm}$ by $10^{-1}\,\mathrm{K}$. It seems likely that its deviation from the experimentally measured value is caused by the fact that the field strength was nonuniform at the liquid-vapor interface, and the average field strength value $E_{t.b}$ exceeded E_0. Then according to (2.28), the change in the bubble pressure is weaker and ΔT is smaller than $10^{-1}\,\mathrm{K}$ and apparently, should be within the limits of the experimental error $2 \cdot 10^{-2}\,\mathrm{K}$.

2.2.6 Influence of the Electric Field on Metastable Liquids

In experiments on investigation of metastable liquids in strong electric fields [39–41], cells were used in which a sharply nonuniform electric field was created, and the volume of the liquid in which this field acted was negligibly small in comparison with the remaining volume of the liquid. When the voltage was applied to the electrodes, the liquid freely flew into the strong field region and hence, the condition $P_0 = P_u$ was fulfilled. Then, as can be seen from (2.27), the electric field should increase the pressure inside the bubbles irrespective of the liquid polarity and, with allowance for (2.35), of the electrical conduction, and thus to prevent boiling up of the liquid. According to [39], the calculated value of the field strength was $5 \cdot 10^8\,\mathrm{V/m}$. Substituting this value into (2.27), we find that the influence of this field, for example, on n-hexane is equivalent to an increase in the external pressure by $1.2 \cdot 10^6\,\mathrm{N/m}$. Hence, the concept of Parmar and Jalabyddin [39] about stimulation of liquid vaporization by the electric field at the expence of a decrease in the free energy of the system under conditions of these experiments was erroneous.

Apparently, the decrease in the delay time of the phase transition observed in these experiments was caused by the emission of charge carriers from the electrode. In this case, as considered in Chap. 1, additional factors which promote boiling up of the liquid came into being. In addition to conventionally considered Joule heating, the excess pressure ΔP decreases because of the field attenuation at the electrodes due to space charge emission and the pressure gradient arising in the region of this charge [57]. In addition, as follows from the results presented in Chap. 1, the field strength is sufficient for the ionization processes in micronuclei and their subsequent growth.

2.2.7 Analysis of the Feasibility of Forming Pre-breakdown Bubbles Under the Effect of Electric Field

Of principal importance for the problem of electric breakdown of liquid dielectrics is a question about the reasons for the occurrence of pre-breakdown

bubbles near the electrodes, because ionization processes in these bubbles initiate the discharge in liquids. These initial vapor-gas bubbles were registered in experiments under long-term and pulsed (up to nanosecond) voltages [20, 31, 58–60].

In the explanation of experimental results it is frequently assumed that pre-breakdown bubbles can arise without charge carriers directly under the effect of electric field due to the factors considered above:

a) gas and vapor extraction from nonwettable pores on the electrode surface [17],
b) electrostatic forces acting on charges [16] or particles located on the electrode surface [31],
c) stretching of thermofluctuation holes in liquid [36, 46, 47].

These hypotheses are qualitative in character; therefore, it is of interest to determine the conditions of their implementation.

In the study of electric breakdown of liquid dielectrics, cells are commonly used in which the interelectrode gap volume is small in comparison with the remaining passive liquid volume. Gas cavities are often left in the weak field region of the cell to prevent cell destruction by hydraulic impact accompanying electric breakdown. Therefore, we can consider that the equilibrium hydrostatic pressure in liquid is $P_0 = P_{\text{out}}$.

The time of establishing the equilibrium pressure τ, as demonstrated in Chap. 1, is determined by the electrode geometry and sound velocity in liquid. For tip electrodes with curvature radius r_0, this time is $\tau \sim r_0/c$. For flat electrodes $\tau \approx l_{\text{min}}/c$, where l_{min} is the minimum distance from the observation point in the interelectrode gap to the electrode surface. In experiments, electrodes with sizes $r_0 \sim 10^{-5}$ m and $l_{\text{min}} \sim 10^{-2}$ were commonly used. The characteristic times of establishing the equilibrium pressure for such electrodes are 10^{-8} and 10^{-5} s for the sound velocity $c \sim 1.5 \cdot 10^5$ cm/s. From the moment of voltage application during time τ the pressure in the interelectrode gap is reduced. To simplify our analysis, disregarding the pressure dynamics during the transient period, we consider that the pressure inside the bubble is determined by (2.31) during time τ. According to (2.32), the change in the pressure inside the bubble in nonpolar liquid is $\Delta P < 0$, and in polar liquids it is $\Delta P > 0$, but the total pressure ΔP_{tot} is positive in both cases.

Thus, under exposure to voltage pulses whose duration is longer than τ, the electric field prevents the bubble formation, and their occurrence cannot be explained by expansion of thermofluctuation holes and gas extraction from pores.

As to the hypothesis about cavitation under the effect of the electric field on the surface charge [16,31], it remains not clear where this charge is located. If the charge remains on the surface of the solid body, the situation does not differ from the above-considered case, and cavitation is impossible. If the charge is in the liquid, its motion relative to the liquid must be taken into account. Therefore, the question on the feasibility of cavitation is reduced,

in essence, to a solution of the problem on the influence of the space charge in the liquid on its mechanical stability that has already been considered in Chap. 1.

The critical tension amplitude at which the liquid thermofluctuation holes start to grow to sizes of microscopic bubbles depends on the size of these holes. The average radius of the thermofluctuation holes is independent of the size of molecules and is determined by the expression [37]

$$r \approx \frac{1}{2\pi} \sqrt{\frac{kT}{\sigma}} \approx 10^{-10} \, \text{m}. \tag{2.39}$$

Therefore, a very high tension exceeding $10^8 \, \text{N/m}^2$ is required for their burst. Experimental data on the maximum tensile strength of the liquid give $2 \cdot 10^7 \, \text{N/m}^2$. If we consider that such reduction of the liquid tensile strength is due to thermofluctuation holes of relatively large size, it can be estimated from the expression

$$r \leq \frac{2\sigma}{P_{\text{cr}}} \approx 10^{-9} \text{m}. \tag{2.40}$$

The condition of burst of these holes in nonpolar liquid dielectrics under the effect of electric field can be written as follows:

$$1.5 \frac{\varepsilon_0 (\varepsilon - 1)}{2(2\varepsilon + 1)} E^2 = m_{\text{cr}} > 2 \cdot 10^7 \text{N/m}^2, \tag{2.41}$$

where the coefficient $A = 1.5$ considers that bubbles have submicron sizes. For $\varepsilon = 2$, the critical field must be $E_{\text{cr}} > 2.7 \cdot 10^9 \, \text{V/m}$. These estimates demonstrate that because of small sizes of thermofluctuation holes, they do not influence the electric strength of liquids, and too strong fields are required for their expansion.

Analyzing the hypothesis about bubble occurrence due to vapor or gas extraction from pores on the electrode surface, it is pertinent to note the following. In a nonuniform electric field when the field is maximum on the electrode, the pressure exerted on its surfaces starts to rise from the moment of field application due to liquid inflow from the surrounding region. Therefore, $\Delta P > 0$ on the electrode surface during the entire period of voltage exposure. The pressure on the electrode surface decreases only for the flat electrodes forming a uniform field in the gap, especially near the electrode rounding off, where the pressure can be reduced directly on the electrode surface. However, the changes in the pressure are relatively small, and this factor is not determining, but can promote the bubble formation and must be taken into account in the design of high-voltage equipment with liquid insulation.

Figure 2.6 shows the most probable variants of gas and vapor existence in pores on the electrode surface. These models are widely used in physics of boiling, and the bubble occurrence from pores during boiling of liquid was proved by direct experimental observations [61]. As the pressure in the liquid decreases at the expence of electrostriction, the meniscus is displaced toward
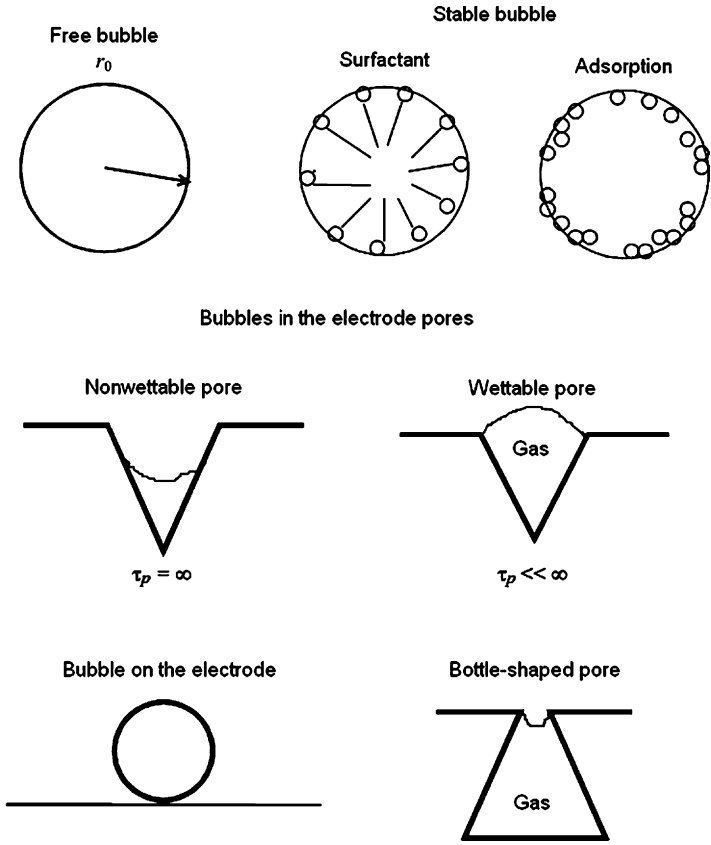
Fig. 2.6. Variants of bubbles

the pore mouth. Let us assume that the volume of the expanding vapor-gas phase can exceed the pore volume. In this case, the gas phase will form a bubble resting on the pore edges (see Fig. 2.6), and all above-calculated results will be applicable to this bubble. Then the change in the pressure inside the bubble $\Delta P_{\text{bubble}} > 0$, and hence, the electric field should compress the bubble precluding its growth and formation. Therefore, the assumption that the vapor-gas phase volume is greater than the pore volume is incorrect, and the electric field precludes the gas extraction from the pores.

2.3 Analysis of Pre-breakdown Bubbles

The experiments in which pre-breakdown bubbles were registered in nitroben-zene and water under microsecond voltage pulses demonstrate the follow-ing [59, 60]. The charge carriers and bubbles move in pre-breakdown fields approximately with the same velocities 20–50 m/s in fields up to 1 MV/cm.

The mobility value equal to $(5 \pm 2) \cdot 10^{-7}\,\mathrm{m^2/(V \cdot s)}$ does not contradict the electrohydrodynamic origin. This means that electrohydrodynamic flows arose in liquid under exposure to microsecond voltage pulses.

Consideration of the relaxation times of pre-breakdown bubbles, in particular, the gas bubble dissolution time, bubble and liquid cooling times, and time of cavitation bubble collapse demonstrates that under conditions of experiments with water and nitrobenzene under exposure to microsecond voltage pulses, the registered bubbles have non-electrolysis origin.

2.3.1 Deformation of a Moving Bubble in an Electric Field

If we assume that a spherical bubble moves with velocity V relative to the liquid, the pressure distribution in the vicinity of the bubble surface is determined by the expression [62]

$$P_1 = P_0 + \frac{\rho_{\mathrm{liq}} \cdot V^2}{8}(9\cos^2\theta - 5), \qquad (2.42)$$

where P_0 is the equilibrium hydrostatic pressure (see Chap. 1), θ is the angle between the normal to the surface and the direction of bubble motion. We note that the pressure is positive at the bubble poles and negative at the equator, that is, it causes the bubble to flatten. We now calculate the average pressure on the bubble surface due to motion

$$P_1 = \frac{\iint\limits_{S} P_1 dS}{S} = -\frac{\rho_{\mathrm{liq}} V^2}{4}. \qquad (2.43)$$

For the bubble moving in the field direction, we find the additional pressure caused by the field using the results of Sect. 2.2:

$$P_2 = \frac{9\varepsilon_0\varepsilon(\varepsilon - 1)E^2}{2(2\varepsilon + 1)^2}[\varepsilon - (\varepsilon - 1)\cos^2\theta]. \qquad (2.44)$$

The condition at which the bubble will not deform can be obtained from the requirement of independence of $P_1 + P_2$ on θ:

$$\frac{\rho_{\mathrm{liq}} \cdot V^2}{2} = \frac{\varepsilon_0\varepsilon \cdot E^2}{2}. \qquad (2.45)$$

In this case, the average pressure on the bubble will be positive if the liquid has time to flow into the strong field region (see Sect. 1.1, for example, for a nonuniform field) and equal to

$$P_{\mathrm{av}} = \frac{\varepsilon_0\varepsilon \cdot E_0^2}{2}\left[\frac{4\varepsilon + 5}{4\varepsilon + 4}\right]. \qquad (2.46)$$

When the liquid has no time to flow into the strong field region (which is the case, for example, for the flat electrodes and micro- and submicrosecond

voltage pulse duration), by analogy with (2.32) and (2.33), for nonpolar liquids we obtain

$$P_{\mathrm{av}} = -A\frac{\varepsilon_0 \left(\varepsilon - 1\right)^3 E_0^2}{2\left(2\varepsilon + 1\right)} - \frac{\varepsilon_0 \varepsilon \cdot E_0^2}{4} < 0, \tag{2.47}$$

and for polar liquids we have

$$P_{\mathrm{av}} \approx \frac{\varepsilon_0 \left(\varepsilon^2 + \left(2\varepsilon_\infty - 4\right)\varepsilon + \varepsilon_\infty\right) E_0^2}{2\left(2\varepsilon + 1\right)} - \frac{\varepsilon_0 \varepsilon \cdot E^2}{4}. \tag{2.48}$$

It can be seen that the pressure for nonpolar liquids is negative, while for polar liquids with $\varepsilon \gg 1$ it is close to zero. This means that if the bubble moves relative to the liquid with the velocity determined by the hydrodynamic ion mobility, it can exist both in nonpolar and polar liquids.

2.3.2 Influence of Electrohydrodynamic Flows

Since from experiments it is not clear whether the bubbles move in the motionless liquid or are entrained by the moving liquid, is of interest to analyze an opportunity of liquid motion under exposure to pulsed voltage.

Watson in [63] described a rather exotic theory of high field conduction in liquid with ramped voltage application based on the formation of quasi-particles in the process of injection. These quasi-particles are electrons entrained by rotating microflows – the so-called Beltrami flows. This conclusion was drawn by a comparison of experimental current dependences on the pulse slope with the equations describing electromagnetic transformations and electrohydrodynamic flows.

It is well known that an electrohydrodynamic flow arise in liquid under ac voltage application [64–67]. It is considered that the reason for liquid motion can be heating of regions adjacent to the electrodes [64] or violation of the electroneutrality condition in the liquid volume due to an excess ion charge [65]. There are qualitative considerations that liquid should move under application of pulsed voltage. In [35, 68] the liquid motion was attributed to charge carrier injection. It is considered that the liquid motion develops in the space charge region when the voltage drop in this region exceeds the critical value

$$V_{\mathrm{cr}} = T_e \frac{\eta \cdot \mu}{\varepsilon_0 \varepsilon}, \tag{2.49}$$

where T_e is the dimensionless number less than 161.

The V_{cr} value for polar liquids is typically equal to a few ten volts, and for nonpolar liquids it is equal to a few hundred volts. The time of developing the electrohydrodynamic instability that causes flows to develop is described by the expression

$$\tau_R \approx 100 \frac{\eta}{4\pi \cdot \varepsilon_0 \varepsilon \cdot E^2}. \tag{2.50}$$

This expression was theoretically derived by the Grenoble team in [35, 68, 69]. A somewhat different variant was suggested by Wang and Cross [70] who derived the following expression for the instability of a two-layer liquid with conducting and dielectric layers:

$$\tau_{R2} = \frac{3.11 \cdot \ln \alpha_s \cdot \rho_{\text{liq}}^{1/6} \cdot \eta^{2/3} \cdot d^2}{(\varepsilon_0 \varepsilon)^{5/6} \cdot C_i^{1/3} \cdot U^{5/3}} \ , \tag{2.51}$$

where α_s is the relative displacement caused by the instability, $C_i = \sigma_{\text{el}} d^2 / (\varepsilon_0 \cdot \varepsilon \cdot \mu \cdot U)$ is the parameter characterizing the intensity of charge carrier emission from the electrode, and σ_{el} is the electrical conduction in the space charge zone.

Times calculated from these expressions differ significantly. We have made an attempt of direct experimental determination of the instability development time. To this end, by the optical interferometric method we registered the initiation of flows with voltage application to a heated wire placed in glycerin [71]. According to [72], a zone with increased electrical conduction

$$\ln \sigma_{\text{el}} = -7.92 + 4553/T - 1.132 \cdot 10^6/T^2 \tag{2.52}$$

arises in the liquid on pulsed heating. This is equivalent to strong emission for which the parameter C_i is in the range 10^3–10^4.

A space charge was generated near the heated electrode under voltage application and hence, the occurrence of the electrohydrodynamic instability. Figure 2.7 shows interferograms illustrating the electrohydrodynamic flows in liquid under application of microsecond voltage pulses. The voltage amplitude was $10\,\text{kV}$, the field strength on the space charge boundary was 150–$200\,\text{kV/cm}$, and the voltage pulse duration was $40\,\mu\text{s}$ in the first case (Fig. 2.7a) and $100\,\mu\text{s}$ in the second case (Fig. 2.7b). It can be seen that in the first case, the instability only starts to develop, more precisely, the flow dimensions slightly exceed the dimensions of the heated region. In the second case, we see the developed instability in the entire near-electrode layer. It is difficult to obtain unambiguous estimates from (2.51) and (2.52). The matter is that all parameters in the near-electrode layer, beginning with the viscosity and ending with the field strength, are changed. The maximum-likelihood estimate can be obtained if we consider the viscosity and field strength on the interface. Then (2.58) gives about $40\,\mu\text{s}$, and (2.52) gives $1.5\,\text{ms}$. Thus, our experimental data are in agreement with the Felici model.

Based on [35, 39, 68], we now consider the results of experiments [20, 73]. In these experiments, the emission of charge carriers from the electrodes, formation of visible pre-breakdown bubbles in the same places where emission was observed, and pre-breakdown bubble motion were registered. The bubble velocity was independent of their size and was in the range 20–$100\,\text{m/s}$. This is approximately equal to the velocity of charge carriers. The velocity of bubbles near the electrode was typically higher than that of distant bubbles. The first bubbles moved more slowly than the subsequent ones, the bubbles during the
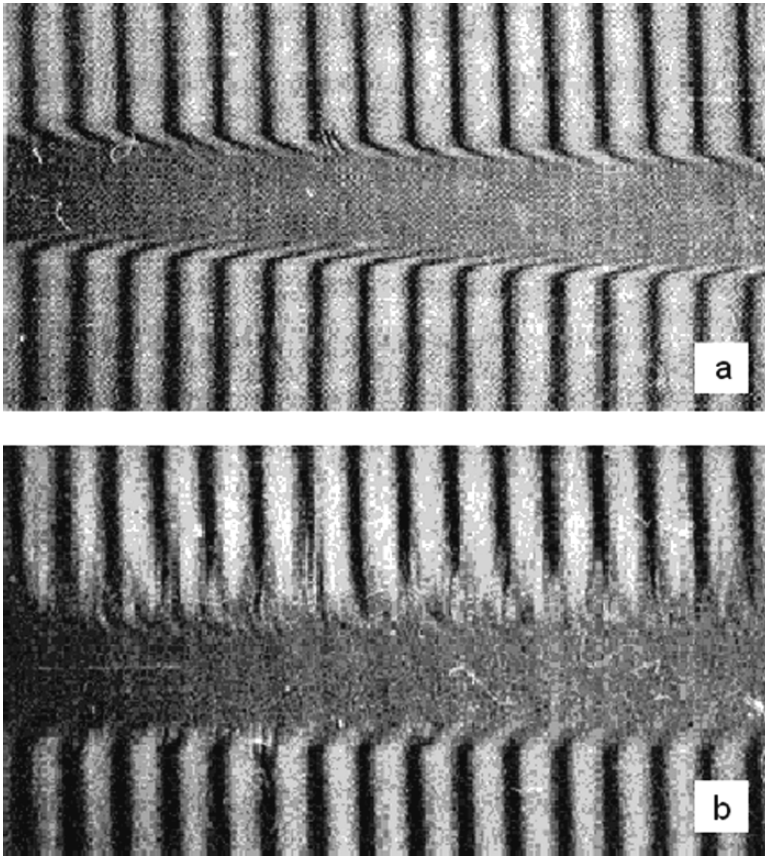
Fig. 2.7. Electrohydrodynamic instability near the heated wire electrode. The electrode diameter was $400\,\mu$m. The upper photograph (**a**) is for volage pulse duration of $40\,\mu$s, and (**b**) the lower photograph is for voltage pulse duration of $100\,\mu$s

flat-topped part of the voltage pulse did not cross the front of charge carriers. Bubbles started with a delay relative to the onset of emission; as a rule, they overtake the front of moving charge carriers. On the pulse decay, the moving bubbles could intersect the front of moving charge carriers; then they were dissolved for less than $20\,\mu$s. When the emission of charge carriers causes the formation of a field maximum outside of the tip electrode surface, the bubbles remained in the space charge region, except the rare cases when they emerge virtually simultaneously with the space charge. They moved with the space charge front, and on the pulse decay could move ahead of the space charge front.

From the experiments it is not clear whether the bubbles move relative to the liquid or are entrained by the liquid and move with it. Though from estimates (2.50)–(2.52) it follows that the liquid motion must be synchronous

with the emission of charge carriers; nevertheless, the assumption that liquids move with velocities up to 10^4 cm/s under application of microsecond pulses seems unrealistic.

Let us analyse the contribution of various forces to bubble motion. What forces act on them in motionless liquid? First, this is the well-known force caused by the difference between the permittivities of liquid and vapor-gas content of the bubble, the so-called dielectrophoretic force [43]

$$F_{\mathrm{d}} = 4\pi\varepsilon_0\varepsilon(D_{\mathrm{d}}\nabla)E, \tag{2.53}$$

where D_{d} is the dipole moment of the bubble which according to [42] is expressed for an ellipsoid of rotation through semiaxes a and b and the field amplification coefficient K_E as follows:

$$D_{\mathrm{d}} = a \cdot b^2 \cdot K_E \cdot E \left(\varepsilon - 1\right)/3. \tag{2.54}$$

Second, the force pushing the bubble in the direction opposite to charge motion must act on the uncharged bubble in the space charge region. At first sight, it is difficult to comprehend the origin of this force; however, the action of this force on the bubble can be imaged as an action of the Archimedes force on the bubble. In both cases the force acts on the liquid, and this is equivalent to the action of the oppositely directed force on the bubble:

$$F_{\mathrm{s.c}} = -\rho_{\mathrm{s.c}} \cdot E \cdot V_{\mathrm{bubble}}, \tag{2.55}$$

where V_{bubble} is the bubble volume. If forces F_{d} and $F_{\mathrm{s.c}}$ determine the bubble motion in the space charge region, the bubble will move toward the electrode when the field maximum is located in the gap or is slightly displaced to this or that side depending on the space charge density. When the bubble intersects the boundary of the space charge region, its velocity should discontinuously increase. In the electrostatic field zone where $F_{\mathrm{s.c}} = 0$, the bubble velocity should depend on the distance from the tip electrode center as $1/r^5$. In addition, the bubble velocity must strongly depend on the bubble size R, approximately as R^2.

In experiments these laws are disobeyed. The bubbles move with practically constant velocities in the space charge region, their trajectories undergo fluctuations of both signs, and outside of the space charge region they most likely move by inertia.

All these facts are a convincing proof that bubbles are entrained by liquid flows; moreover, these flows are turbulent. That fact that the bubble velocity near the electrode is higher than the velocity of space charge region boundary can be caused by additional action of the electrophoretic force. As can be seen from Fig. 1.14, the field in the space charge region has two local maxima: near the electrode and near the front of charge carriers. Therefore, the dielectrophoretic force will promote bubble pushing out near the electrode. The other factor influencing the bubble motion is the time of flow onset. Since a

flow at each point of the gap originates when the space charge region reaches it, the degree of flow development will be maximum near the electrode and hence, and bubble velocity will also be maximum near the electrode.

Thus, we conclude that electrohydrodynamic liquid flows were observed in experiments [20, 73]. This experimentally confirms the results obtained in [35, 68, 69].

In our experiments on the study of pre-breakdown processes in water with microsecond voltage pulse application [74], we also observed moving bubbles (see Fig. 2.8). A pulsed voltage was applied to a gap with distilled water in a uniform field. Photographs were produced in multiframe regime with frame exposure time of $100\,\mathrm{ns}$ and time interval between successive frames of $7\text{–}10\,\mu\mathrm{s}$. Three successive frames illustrate that the bubble formed on anode moves toward cathode. The average bubble velocity was $10\,\mathrm{m/s}$ for a field strength of $300\,\mathrm{kV/cm}$. Considering that the bubble is entrained by the electrohydrodynamic liquid flow, we obtain that the mobility of charges that maintain the flow is sufficiently close to the corresponding electrohydrodynamic mobility $\mu_{EHD} \approx 3 \cdot 10^{-3}\,\mathrm{cm}^2/(\mathrm{V}\cdot\mathrm{s})$.

Let us consider the influence of flows on the formation and existence of bubbles. Considering that the characteristic flow velocities are $V \approx 20\text{–}100\,\mathrm{m/s}$ and the transverse flow dimensions are $\Delta x \approx 10\,\mu\mathrm{m}$, we obtain that the Reynolds number in low-viscosity liquids with $\eta \approx 1\,\mathrm{mPa}\cdot\mathrm{s}$ will be $Re = \rho_{\mathrm{liq}} \cdot \Delta x \cdot V/\eta \approx 1000$. The turbulence in liquid flows arises approximately at these values of the Reynolds number. The bubble in the turbulent flow should experience the effect of large-scale density and pressure fluctuations. According to [104], the pressure fluctuations can be estimated from the expression

$$\Delta P_{\mathrm{fl}} \approx \frac{\rho_{\mathrm{liq}} \cdot \Delta V^2}{2}, \tag{2.56}$$
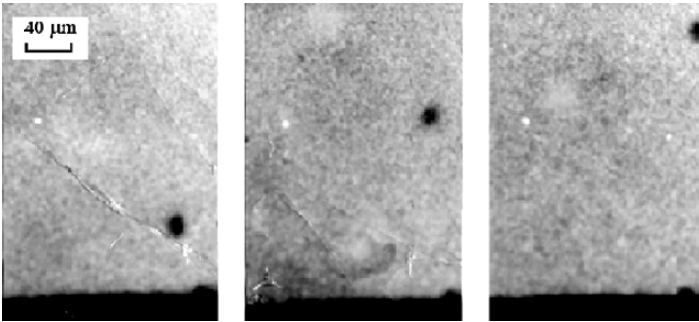
Fig. 2.8. Dynamics of bubble motion in water in a uniform field with application of a microsecond voltage pulse. The anode is below, the second electrode is not seen $40\,\mu\mathrm{m}$

where ΔV denotes the velocity fluctuations. For estimates, we can take $\Delta V \sim V$. The sign of the change in the pressure can be both positive and negative; therefore, the pressure fluctuations can both promote and preclude bubble formation. The fluctuation lifetime can be estimated as a ratio of the transverse dimension to the velocity: $\Delta x/V \sim 10^{-7} - 10^{-6}$s.

The other mechanism of pressure decrease both in laminar and turbulent flows is the Bernoulli decrease in the pressure in the flow:

$$\Delta P_{\mathrm{B}} \approx -\frac{\rho_{\mathrm{liq}} \cdot V^2}{2}. \tag{2.57}$$

It is pertinent to present numerical estimates of the pressure from (2.56) and (2.57). The pressure decreases approximately by $2\,\mathrm{MPa}$ given that the velocity is $20\,\mathrm{m/s}$; it decreases by $50\,\mathrm{MPa}$ for a velocity of $100\,\mathrm{m/s}$. This means that the micronuclei that always present in the liquid can stretch in these flows; this can cause their growth, fragmentation by flows and electric field, and so on, that is, the formation of a microbubble cloud near the electrode.

2.4 Experimental Investigations of Gas Bubble Behavior in an Electric Field

An attempt of experimental study of the behavior of artificially created microbubbles under the action of a strong electric field is undertaken in this Section.

2.4.1 Methods and Procedures

Microbubbles 20–$100\,\mu\mathrm{m}$ in size were created near the electrode, then their photographs were produced with large magnification with the help of a pulsed nanosecond laser using a single- or multiframe system. In this case, time moments of photography should be obligatory referenced to the moment of pulse voltage application. The sequence of frames, including frames from different series with the same bubble sizes and field strengths, has allowed the bubble dynamics to be followed from the very instant of pulsed voltage application [49, 50].

The bubbles from a few units to a few tens of microns in size should be created on the electrode in a strong field zone; moreover, the optical system should be adjusted exactly to this zone. The requirements on the optical magnification ($\sim$100 times) and total image size on the photographic film ($\sim$30 mm) yield a detector field of view of about $0.3\,\mathrm{mm}$. This means that a microbubble must be formed exactly in this region. To increase the probability of bubble occurrence and discharge ignition in this region, it is expedient to fabricate the electrode whose size is comparable with the above-indicated one,

that is, 0.3–0.5 mm. This can be hemispherical or tip electrode of this radius. The variant intermediate between extended and tip electrodes is also possible: a wire electrode less than 0.3 mm in diameter bent as a loop of minimum radius.

It is difficult to create bubbles with preset sizes, since they always will be nonequilibrium. The time of bubble collapse depends on the nonequilibrium degree and type. Vapor bubbles collapse in microseconds. Gas bubbles, according to (2.1), have the dissolution time τ_d proportional to the squared radius r and inversely proportional to the coefficient of gas diffusion to the liquid D, solubility C_s, and gas content C in the liquid. Clearly, the bubble can exist for a long time in liquids with small coefficient D (high viscosity), low gas solubility, or concentration of the dissolved gas C close to the saturation gas content C_s. For a nonsaturated liquid, the estimated lifetime of the bubble 10 μm in radius is 5 s given that the solubility is $C_s \sim 10^{-2}\,\mathrm{cm^3/cm^3}$ and the diffusion coefficient is $D \sim 10^{-5}\,\mathrm{cm^2/s}$.

The liquid can be preliminary oversaturated. By this method, the bubble dissolution time can be increased. However, in this case many bubbles will be formed in the entire liquid volume, and small bubbles will be dissolved faster in the ensemble than large bubbles that can even grow during some time. In addition, bubbles will inevitably be formed on the walls, including the optical windows of the chamber, which will complicate optical registration.

Heating of the liquid to the temperature close to the boiling point can provide a sufficiently simple method of bubble generation, since the gas solubility is low near the boiling point.

The microbubbles can be most simply generated by local heating of the wire electrode. In this case, local boiling of liquid, gas diffusion into the vapor bubble, and cooling of the electrode and bubble will be observed accompanied with vapor condensation and reduction of the bubble size. Then the slower stage of diffusion dissolution of the gas microbubble follows. The lifetime of bubbles with sizes of 30–50 μm in the liquid saturated with gas should exceed 100 s; therefore, having generated a bubble of a certain size, we can wait while it decreases to the required size. The bubble size can be increased by successive application of current pulses.

The most realistic method is the determination of the size of the bubble obtained in the field-of-view of the detector and its registration with the subsequent field application and registration of bubble changes.

2.4.2 Setup

The block diagram of the experimental facility shown in Fig. 2.9 comprises a cell with four coaxial optical windows (*1*), pulsed voltage generators (*6*), semiconductor laser (*4*), pulsed ruby laser with a telescope (*7*) or (in experiments with pre-breakdown fields) CdS laser with electron pumping, photoattachment with a set of filters (*5*), delayed-pulse generator (*8*), dc current source (*2*) with a time relay (*3*), photocell (*9*), and oscillograph (*10*).
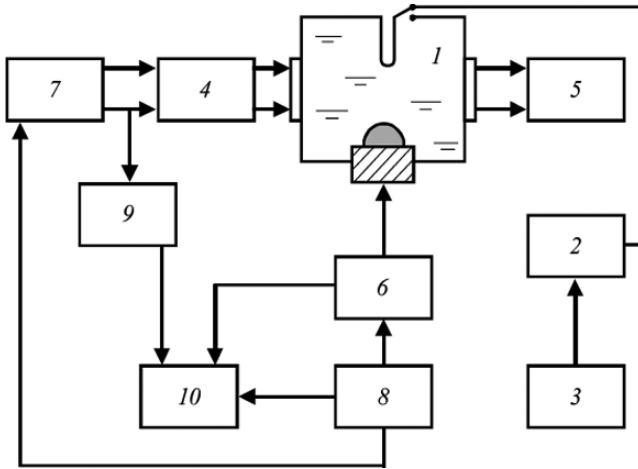
Fig. 2.9. Block diagram of the experimental facility comprising electrode chamber (*1*), B5-47 dc source (*2*), time relay (*3*), stationary laser diod (*4*), MBS-2 microscope (*5*), voltage-pulse generator (*6*), OGM-40 pulsed ruby laser (*7*), delayed-pulse generator (*8*), photomultiplier and photodiode (*9*), and S8-14 oscillograph (*10*)

The four-stage Marx - generator with a peaker is capable of generating voltage pulses with amplitudes up to 100 kV, front duration 0.2 μs, and tail duration of 50 μs. The pulsed light source is the OGM-40 laser capable of producing pulses with duration of 30–40 ns.

The bubbles are generated as a result of pulsed heating of a quasi-tip electrode in the form of a U-shaped Nichrome wire 0.2 mm in diameter with a bend radius of 0.5 mm grounded upon termination of the current pulse. The flat cell electrode served as a high-voltage electrode. The duration of current pulses with amplitudes up to 3 A was varied with the time relay in the range from 0.1 to 5 s. After relaxation to temperature equilibrium in the vicinity of the wire (∼1 s), a voltage pulse was applied to the high-voltage electrode. The current pulse was considered to be rectangular, and the contribution made by its fronts to the energy absorbed in the load gave the correction no more than 10% for pulse durations exceeding 300 ms.

The electric field strength in the vicinity of wire must be specially calculated, because no analytical solutions exist for the employed electrode system. To solve this problem, the ELSTAC subroutine of the TELMA computer codes intended for solving three-dimensional electrostatics problems by the finite element method (FEM) was used. Figure 2.10 shows the field strength calculated in the vicinity of wire in the sectional plane of its bend. It can be seen that at a voltage of 100 kV, the field strength at the center is 900 kV/cm; as the distance from the electrode surface increases, the field strength varies approximately as $1/r$. As to the field distribution in the perpendicular plane, without presenting the calculated results, we only stress that in the vicinity of
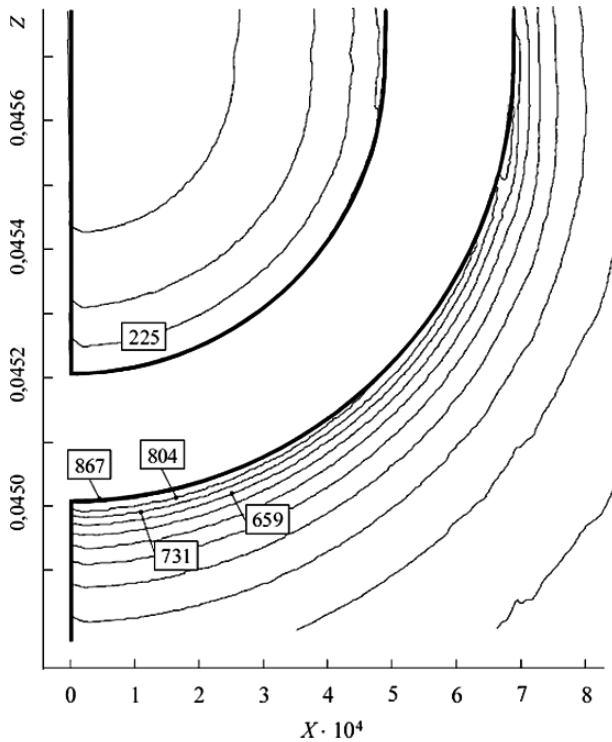
Fig. 2.10. Field strength calculated near the electrode. The numbers adjacent to the curves indicate the field strength (in kV/cm) at a voltage of $100 \, \text{kV}$

the surface it decreases approximately by 10% as the distance from the center is equal to the radius, that is, the field is fairly uniform in this direction.

When a bubble is generated on the electrode surface, the field nonuniformity with respect to the size of the most dangerous bubble does not exceed 10%, and the region of optical recording coincides with that of the maximum field, thereby enabling one to observe and register bubbles with a high magnification.

The experiments on discharge ignition with the help of artificially produced bubbles are performed as follows. A bubble of a certain radius r is generated on the electrode in the region of strong field; then bubble is photographed and a voltage pulse is applied with the amplitude at which the field strength is sufficient for the onset of the ionization processes in the bubble. Then, after a fixed time delay, the bubble is photographed using a laser pulse and a camera with an open stop aperture. Then another bubble is generated of approximately the same size and the same operations are repeated but with a different time of delay between the voltage pulse application and the instant of photographing. When a series of frames has been produced, the process is repeated for different bubble sizes and field strengths. The results of each

series are processed, the variation of the bubble shape under the effect of the electric field is estimated, and a comparison is made with the model. In the case of failure of generating a single bubble, experiments are performed with several bubbles (the main thing is that the distance between the bubbles must be much greater than their sizes).

Based on the results of analysis of different schemes of microobject registration, optical recording with the use of a microscope and a semiconductor laser was chosen. This scheme provides the most qualitative image with adequate magnification. The use of this scheme provided a spatial resolution of at least 25 lines per mm.

2.4.3 Formation of Long-living Bubbles and their Behavior in Pre-breakdown Fields

Formation of Long-living Bubbles

It was established that the formation of bubbles in both distilled and tap water has a threshold character and depends on the current pulse amplitude and duration.

Figure 2.11 illustrates the emergence of the first bubbles 10–50 µm in size in distilled, tap, and settled tap water depending on the current pulse amplitude and duration. It can be seen that in fresh tap water, the first bubbles emerge at a much lower current than in distilled water, and in settled water the first bubbles arise under conditions close to those of emergence of the first bubbles in distilled water. In this case, distilled water was kept for a long time in an air medium.

In freshly prepared distilled water, as well as in settled water subject to boiling for 5–10 min, with the wire carefully washed out and wiped in water, no microbubbles were observed at a current of 3 A until the maximal duration of
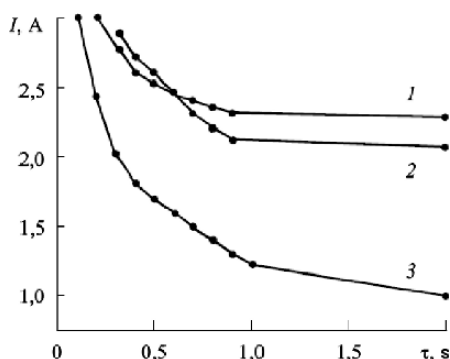
Fig. 2.11. Emergence of the first bubbles 10–50 µm in size in settled tap water (*1*), distilled water (*2*), and tap water (*3*) depending on the current pulse amplitude and duration

current pulse. Using the same water but with the wire blown intensively with compressed air before measurements, we succeeded in obtaining the bubble generation at currents smaller than 3 A. In this case, the I–t characteristics were comparable with the results obtained in settled tap water (curves *1* and *2* in Fig. 2.11.). Hence, we can conclude that the emergence of bubbles is mainly affected by the gas dissolved in water and adsorbed on the electrode surface.

As regards the bubble dynamics, we note the following. Visually, the maximum bubble size is attained immediately after the termination of the current pulse. After this, the bubble size sharply decreases approximately by 20%, which is followed by the stage of slower decrease in size. Figure 2.12 illustrates the time dependence of the bubble diameter starting from the maximum size until the bubble collapse. Experiments were carried out in distilled settled water at $I = 2.6$ A and $t = 0.4$ s. As can be seen from the figure, the bubble lifetime ranges approximately from 2 to 10 min, that is, in this time the bubble is completely dissolved in water. This time is quite sufficient for photographing the bubble and performing the necessary investigations.

Behavior of Bubbles

Figure 2.13*a* shows a photograph of microbubbles of different radii ranging from 20 to 40 µm (7 microbubbles) on the cathode surface before voltage application, and Fig. 2.13*b* shows the same microbubbles 4 µs after voltage application. The voltage was 30 kV, and the field strength in the vicinity of the electrode (where the bubbles were located) was 300 kV/cm. Figure 2.14*b* shows one more series of photographs of bubbles on the electrode surface at a voltage of 30 kV produced 1.6 µs after pulse application. The following regularities were established from the photographs.
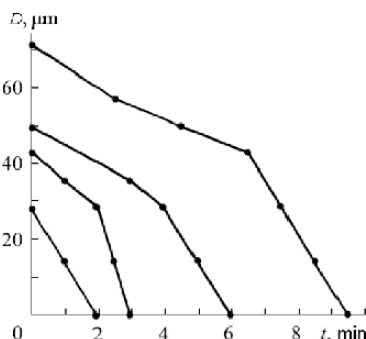
Fig. 2.12. Time dependence of variation of the bubble diameter starting from the maximum bubble size to its complete collapse
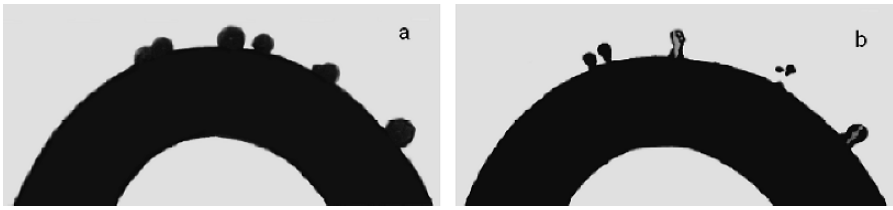
Fig. 2.13. Configuration of bubbles on the cathode surface before (**a**) and 4 µs after the effect of the field (**b**). The maximum field strength was 300 kV/cm. The bubble elongation, perturbations arising on the surface, waists, and the bubble detachment are seen

1. The bubbles elongate in the direction of the electric field. They lengthen by a factor of 1.5–2 relative to the initial size.
2. The bubbles flatten in the transverse direction. The compression can be insignificant and can reach a factor of 1.5–2 relative to the initial size. The bubbles have different shapes. More frequently observed is the close-to-cylindrical shape with a hemispherical top. The droplet shape is less frequently observed. On one occasion, a bubble shaped as a cone with a hemispherical top having a radius of 5 µm was registered (Fig. 2.14*a* and *b*). In this case, initial bubble radius was 20 µm. The field strength was approximately 250 kV/cm.
3. The bubbles are divided in two parts or are detached from the electrode surface. A transverse waist usually arises in 5–8 µs; in so doing, no explicit dependence on the field strength was detected. The bubbles are detached from the electrode surface in 15–20 µs.
4. The bubble velocity (in late stages) corresponds to the electrohydrodynamic mobility of charge carriers. This conclusion can be made from several pairs of photographs, for example, from the bubble that passed a distance of 200 µm for 50 µs. In this case, the field strength in the vicinity
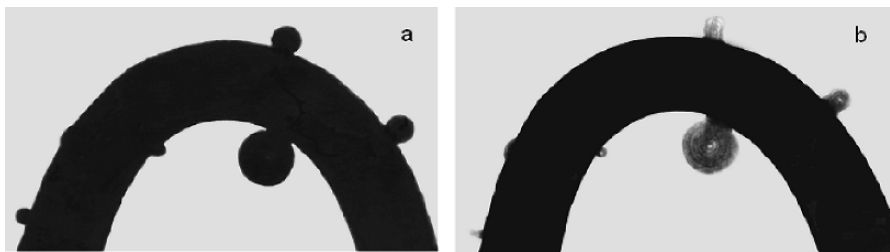
Fig. 2.14. Shape of bubbles on the cathode before (**a**) and 1.6 µs after the effect of the electric field (**b**). The maximum field strength was 200 kV/cm, and the field strength in the inner band was 50 kV/cm. The most deformed bubble is seen on the left, and the bubble with clearly expressed perturbations of the surface is seen at the top

of the bubble at the first exposure moment was 200 kV/cm; it decreased to approximately 40 kV/cm in 50 μs. The estimated average velocity was 4 m/s, and the estimated mobility was $\sim 4 \cdot 10^{-3}$ cm^2/(V·c). The shape of moving bubbles varies: both oblate and prolate bubbles were recorded.

5. The smaller the bubble size, the greater its deformation. This conclusion is most brightly illustrated by Fig. 2.14, where large bubbles (60–80 μm) are weakly deformed (the longitudinal-to-transverse size ratio is 1.3–1.5), whereas smaller bubbles (40 μm) are more deformed, and this ratio can reach 2–3. The exception is provided by small bubbles in a weak field on the concave part of the electrode. From Fig. 2.14 it can be seen that in the region of weak field ($E \sim 60$ kV/cm), the bubble with diameter $D \sim 30$ μm remains almost undeformed.

6. At the early stages, the bubble surface experiences small-scale perturbations. For example, perturbations with a wavelength of 25–30 μm were recorded on the surface of the bubble with radius of 60 μm located on the concave part of the electrode for a field strength of about 50 kV/cm (Fig. 2.14b). Shown in the same figure is a bubble located on the convex part of the electrode. Both longitudinal and transverse perturbations with a characteristic size of 10–15 μm can be seen on its surface.

The bubbles on the anode surface behave mainly as cathode bubbles. However, their behaviour is characterized by at least one noticeable difference. Anode bubbles in the region adjoining the electrode expand along the electrode (bubbles 1, 2, and 3 in Fig. 2.15a). The width of this formation can exceed by a factor of 1.5–2 the initial bubble diameter.

2.4.4 Discussion of Experimental Results

Formation and Dynamics of Bubbles

Clearly, the long-living bubbles must be filled with gas, because the vapor bubbles should disappear during microseconds at temperatures below the boiling point. Experimental data on bubble dissolution were approximated
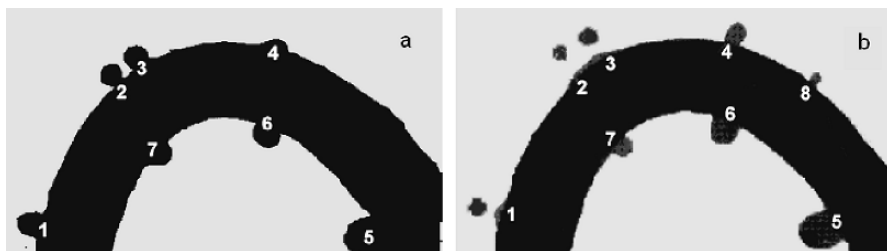
Fig. 2.15. Shape of bubbles on the cathode before (**a**) and 8 μs after the effect of the electric field (**b**). The maximum field strength was 200 kV/cm. The characteristic conical shape of bubbles *1–3* that remained on the electrode can be seen
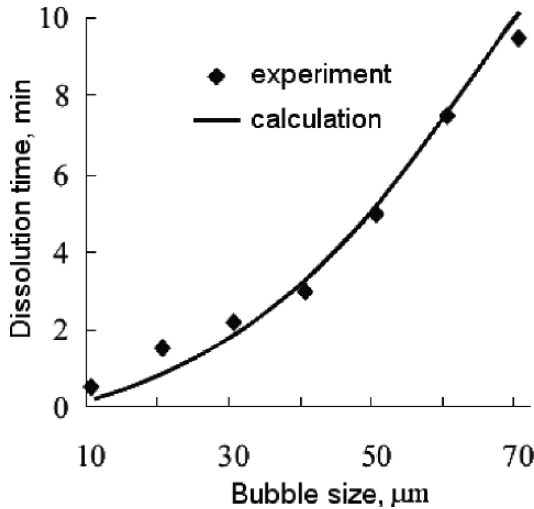
Fig. 2.16. Approximation of the experimental data on dissolution of microbubbles in settled distilled water

by expression (2.1). Figure 2.16 shows the experimental results (symbols) and the calculated data (the solid curve). Quite satisfactory agreement between the experimental and calculated results can be seen. If we set the diffusion coefficient $D \approx 2 \cdot 10^{-5}\,\mathrm{cm^2/s}$ [77], we obtain the best agreement for $C_s - C \approx 4 \cdot 10^{-3}\,\mathrm{cm^3/cm^3}$. For the solubility of air under standard conditions $C_s \approx 2 \cdot 10^{-2}\,\mathrm{cm^3/cm^3}$ [77], this means that water was saturated slightly greater than by 80% of the maximum content, that is, bubbles were under conditions close to the equilibrium ones.

To elucidate a mechanism of bubble formation, nonstationary thermal fields were calculated in liquids with pulsed heating of the wire. Calculations were carried out using the Teplo subroutine of the TELMA computer code. Figure 2.17 shows the time dependence of the temperature at different points in the vicinity of the wire under application of a current pulse with threshold values of pulse amplitude and duration ($I = 2.6\,\mathrm{A}$ and $\tau = 0.4\,\mathrm{s}$). It can be seen that the temperature near the surface insignificantly exceeds the boiling point of water. Calculations of temperatures under other threshold conditions demonstrated that the boiling point is achieved in all cases. On boiling, vapor bubbles are formed on the surface. It is clear that the gas dissolved in liquid in the supersaturated state at elevated temperatures must diffuse into the bubbles. Estimates of gas diffusion into a vapor bubble of radius r_0 during characteristic time $t \sim 0.1\,\mathrm{s}$ (see Fig. 2.17) yield the diffusate volume

$$V \sim 4\pi \cdot r_0^2 \cdot (D \cdot t)^{1/2} \cdot C. \qquad (2.58)$$

On cooling of the bubble, vapor is condensed, and the vapor-gas bubble is transformed into a purely gas bubble whose size, according to estimate (2.58),
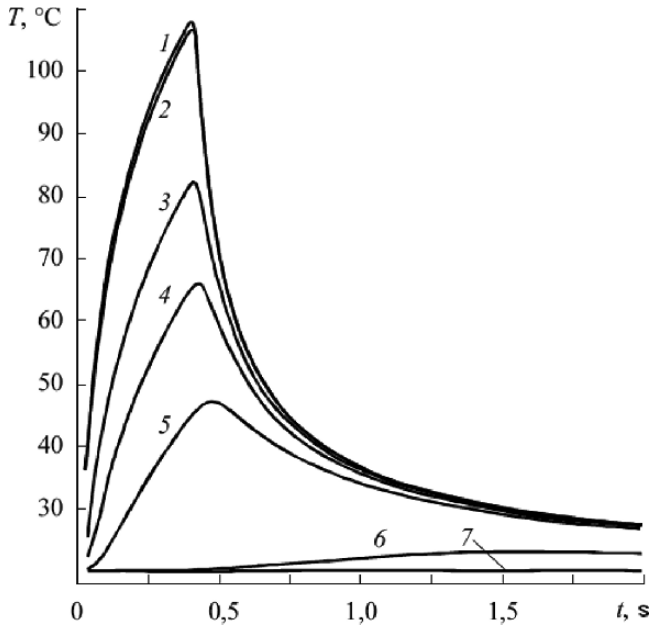
Fig. 2.17. Time dependences of the temperature at different points: at the center and on the surface of the wire (*curves 1 and 2* virtually merge) and at distances of 50 (*curve 3*), 100 (*curve 4*), and 200 μm (*curve 5*) and 1 (*curve 6*) and 2 mm from the electrode surface (*curve 7*)

will be 3–4 times smaller than the maximum size of the initial vapor bubble. The fact that no bubbles are formed in degassed water can be easily explained based on (2.58).

Thus, the mechanism of forming the long-living bubbles is the following: local boiling up of the liquid, gas diffusion into the vapor bubble, and cooling of the electrode and bubble accompanied by vapor condensation and decrease of the bubble size. Then the slower stage of diffusion dissolution of the gas microbubble follows.

Forces Influencing the Bubble Behavior

Let us analyse the contribution of various forces to motion and deformation of bubbles in motionless liquid under the effect of the electric field.

First, this is the force caused by different permittivities of liquid and bubble which leads to bubble elongation in the field direction and a more significant bubble compression in the transverse direction. According to (2.6), the deformation is proportional to the bubble radius r and the squared field strength E^2. We will calculate a relative decrease in the bubble volume under the action of this force from (2.27).

The second force caused by the difference in the permittivities and the field gradient acts on the bubble in a nonuniform electric field. This is the so-called dielectrophoretic force determined by (2.53), where D_d is the induced dipole bubble moment. For a spherical bubble, it is described by the relation

$$D_d = \frac{4\pi \cdot \varepsilon_0 \cdot \varepsilon \cdot (\varepsilon - 1) \cdot r^3 \cdot E}{(2\varepsilon + 1)}. \tag{2.59}$$

If we neglect the curvature of the wire electrode, that is, consider that the field distribution in the vicinity of the wire is cylindrically symmetrical, we can express F_d through the distance R from the wire axis:

$$F_d = \frac{4\pi \cdot \varepsilon_0 \cdot \varepsilon \cdot (\varepsilon - 1) \cdot r^3 \cdot E^2}{(2\varepsilon + 1) \cdot R}. \tag{2.60}$$

The third factor is formed by partial discharges (PD) in the bubbles. In this case, the bubble elongation can be calculated for the bubble model of discharge initiation [78–80]. The occurrence of surface and space charges near the bubble poles due to PD results in the bubble deformation due to the Coulomb forces. The equivalent pressure in the direction of field can be estimated from the expression

$$P = 3\varepsilon_0 \varepsilon E^2 \left(\mu E\tau/r + 1\right)/2, \tag{2.61}$$

where μ is the charge carrier mobility in the liquid, and τ is the time duration of electric stress.

The fourth factor is the most debatable one. It has already been mentioned in Sect. 2.3.3. The force directed opposite to the Coulomb force must act on an uncharged bubble located in the space charge region. The additional condition is establishing of mechanical equilibrium in the liquid. We calculate this force from (2.55). In the case of a space homocharge at the electrode surface, the force $F_{s.c}$ must attach the bubble to the electrode. In the case of a heterocharge, the force $F_{s.c}$ must detach the bubble from the electrode.

The last factor to be considered is the bubble instability. It is assumed that bubbles should have instability of several types. The types of bubble instability in the electric field were considered in [10,18,81]. It was demonstrated that the unionized bubble is stable in the electric field, while the ionized conducting bubble should have the sausage-like instability with the wavelength [18]

$$\lambda \sim \frac{2\pi \cdot \sigma}{\varepsilon_0 \cdot \varepsilon \cdot E^2} \cdot \frac{b^4}{a^4}, \tag{2.62}$$

where a and b are bubble sizes along and transverse to the field, respectively. The instability arises when a/b attains 1.85 and is manifested as a series of small bubbles formed near the bubble pole. The factor $(b/a)^2$ in expression (2.62) obtained for the isolated bubble characterizes the field near the poles of the ionized bubble [18]. For the bubble located on the electrode surface, the field amplification near the pole remoted from the bubble surface will exceed

this value, and this additional increase can reach 3–4 times. Correspondingly, the wavelength of the sausage-like instability must be approximately by an order of magnitude less than that described by (2.62).

The effect of the field and Coulomb forces must generate the oscillation mode corresponding to elongation and division of the bubble into two or several bubbles. Without electric field, the lowest frequency of bubble oscillation is

$$\omega^2_{\min} = \frac{8 \cdot \sigma}{\rho \cdot r^3}. \tag{2.63}$$

All the above-mentioned factors increase the oscillation frequency.

Another instability type is small-scale perturbations of the surface caused by the instability of the charged surface in an electric field. The instability wavelength, according to [81], is

$$\lambda = \frac{4\pi \cdot \varepsilon_0 \cdot \varepsilon \cdot \sigma}{\sigma_s^2}. \tag{2.64}$$

Here σ_s is the surface charge density. For the completely charged surface of the bubble located on the electrode surface (this means that the bubble is completely discharged as suggested in the bubble model [78–80]),

$$\sigma_s \approx 4 \cdot \varepsilon_0 \cdot \varepsilon \cdot E. \tag{2.65}$$

Substituting, we obtain

$$\lambda = \frac{\pi \cdot \sigma}{4 \cdot \varepsilon_0 \cdot \varepsilon \cdot E^2}. \tag{2.66}$$

Comparison with Experiment

A comparison of different factors and estimation of their applicability to the conditions of experiments [76] based on a study of the behavior of artificial bubbles in water have demonstrated the following [82]. The voltage drop across the bubble 30–60 μm in diameter will exceed the breakdown voltage according to Paschen's law ($U_{\min} \sim 300$–$500\,\mathrm{V}$) for the field strength exceeding $100\,\mathrm{kV/cm}$. Hence, discharges should arise virtually in all registered bubbles. According to (2.6), the Coulomb force acting on the charged bubble wall [it can be recalculated using (2.61)] should exceed at least ε times ($\varepsilon = 80$) the force that elongates the uncharged bubble. Moreover, according to (2.6), the deformation is proportional to r; therefore, this should result in stronger deformation of large bubbles. This contradicts the experimental data. Dielectrophoretic force (2.60) is less than the Coulomb force by a factor of R/r, which in our case gives $R/r \sim 4$–8. As to the force acting on the bubble in the space charge region, it seems likely that it was not realized under conditions of the experiments. Here the liquid is not motionless, and there is no continuous zone occupied with the space charge.
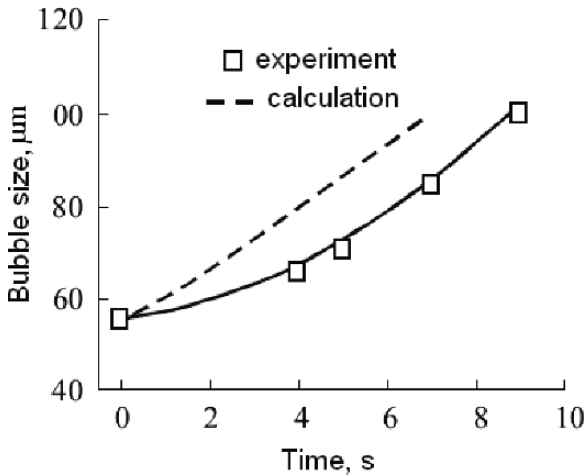
Fig. 2.18. A comparison between the calculated and experimentally measured elongation of the bubble with a size of $55\,\mu$m under the effect of the electric field with strength of $100\,$kv/cm

Hence, the Coulomb force is most suitable as a source of bubble motion. Figure 2.18 compares the calculated and experimentally measured bubble elongations. Experimental points were obtained for different series, the cathode bubbles with radius $r = 27 \pm 5\,\mu$m were chosen for a field strength of $100 \pm 10\,$kV/cm. Experimental points are shown in Fig. 2.18 by small rectangles. Curve *1* shows the results calculated for the bubble model. It can be seen that the agreement between the curve and symbols is not satisfactory. It is clear that a certain factor is absent in the model. Here it should be noted once again that the bubble in the model is considered to be completely discharged, that is, the field inside it is set equal to zero. Actually, the residual field strength should be observed in the bubble. If we consider that a discharge burns continuously in the bubble, this implies that the field strength inside the bubble is no less than the breakdown value. If periodic discharges arise in the bubble, all the same, the field strength cannot be much lower than the breakdown one. In both variants, the surface charge after the discharge in the bubble must decrease approximately by 1.5–3 times in comparison with the completely discharged bubble. The exact value depends on the bubble size and the field strength. The larger the bubble and the field strength, the higher the surface charge, and the closer we are to the case of the completely discharged bubble.

Correct expressions can be derived with allowance for this circumstance. The surface charge in (2.65) will decrease:

$$\sigma_s \approx 4 \cdot \varepsilon_0 \cdot \varepsilon \cdot \left(E - \frac{U_{\mathrm{br}}}{2r} \cdot \frac{2\varepsilon + 1}{3\varepsilon} \right), \tag{2.67}$$

where $U_{\mathrm{br}} \sim 300\,\mathrm{V}$ is Paschen's breakdown voltage. The equivalent pressure that causes the bubble wall to move in the field direction will also decrease:

$$P \approx \frac{3 \cdot \varepsilon_0 \cdot \varepsilon \cdot \left(E - \dfrac{U_{\mathrm{br}}}{2r} \cdot \dfrac{2\varepsilon + 1}{3\varepsilon} \right)^2}{2} \left(\frac{\mu \cdot E \cdot \tau}{r} + 1 \right). \qquad (2.68)$$

Results of computer calculations of bubble elongation for the refined model are shown by curve *2* in Fig. 2.18. It can be seen that the model describes well the experimental data.

As to the bubble instability, several moments can be pointed out. The bubbles are divided into two fragments in 5–10 μs. This does not contradict (2.63), since according to this expression, the characteristic time is 5–10 μs for bubbles with sizes of 30–50 μm. The observed small-scale surface perturbations have a wavelength of approximately 4–5 μm, and they are not necessarily on the bubble pole. This does not correspond to the sausage-like instability. Against the sausage-like instability is the fact that the characteristic length estimated by (2.62) for $a/b \sim 2$–3 and $E = 200\,\mathrm{kV/cm}$ is approximately 0.1 μm. With allowance for the additional field amplification, the wavelength will be even smaller. Estimates from (2.66) give approximately 0.2 μm. If the surface charge is changed in accordance with (2.67), the instability wavelength will increase to 1–5 μm depending on the electric field and the bubble size. Thus, the small-scale perturbations of the bubble surface can be caused by the action of the Coulomb forces. In this case, the bubble should not be considered conducting; it is more correct to consider that on its surface there is a charge that partly decreases the field inside the bubble.

The nontrivial behaviour of the anode microbubbles similar to the instantaneous deterioration of the electrode surface wettability by the liquid admits several hypothetical explanations.

The most simple is the following. As is well known, the electrode surface from Nichrom actually consists of oxides NiO and Cr_2O_3 [83]. Good wetting of the electrode with water is apparently due to hydrogen bonds of water molecules with partially ionized oxygen atoms of oxides. Under the effect of the electric field, water molecule dipoles are oriented with their oxygen atoms (more likely ions) toward the anode surface. The arising mutual repulsion means the instantaneous occurrence of the electrode nonwettability with water.

Another variant of explanation can be based on the presence of double electric layers at the electrode-water interface. In this case, the mobile part of the double layer located in water can consist not only of positive but also of negative ions, depending on the electrode surface and the electrolytic water impurity type. At the electrode surface with oxide layers, a double layer should arise and positive ions should be most probably accumulated at the electrode surface in water. Under the effect of the electric field, ions move into the liquid volume. The arising Coulomb force detaches the liquid from the electrode, and

in the region of contact with the bubble the liquid can be detached from the electrode.

If any of these hypotheses is true, this effect will not be observed in a nonpolar liquid.

2.4.5 Discharge Ignition in Water with the Help of Bubbles

Experimental setup and high-voltage experimental procedure. The experimental setup was identical to that described above, but instead of an OGM-40 ruby laser, a CdS semiconductor laser with electron pumping by a PLEN-1 system was used. Due to this replacement, a shorter light pulse of $\sim 3\,\mathrm{ns}$ was generated. In addition, the laser generated single light pulses with a delay between pulses equal to a few seconds. Experiments were carried out under the voltage corresponding to maximum field strength in the cell of $800\,\mathrm{kV/cm}$. Breakdown and light exposure moments were recorded together with the image of the region in the vicinity of the electrode with bubbles on which the image of the luminous discharge channel was superimposed, because photographs were produced using a camera with an open stop aperture. To suppress the excess brightness of the discharge channel, a special interference filter was inserted into the optical channel. This enabled us to compare the location of bubbles and discharge channel.

For the anode discharge in the presence of bubbles, the discharge formation time was $1.1\,\mu\mathrm{s}$, and the statistical delay time was approximately $0.5\,\mu\mathrm{s}$. Without visible microbubbles, both components of the pre-breakdown time considerably increased: $t_{\mathrm{st}} \approx 2.4\,\mu\mathrm{s}$ and $t_{\mathrm{f}} = 1.8\,\mu\mathrm{s}$. The cathode discharge in the presence of bubbles took much longer time: $t_{\mathrm{st}} = 22\,\mu\mathrm{s}$ and $t_{\mathrm{f}} = 21\,\mu\mathrm{s}$. Without bubbles, no discharge was initiated.

The terms *statistical discharge time lag* and *discharge formation time* used above require some comments.

For a long time in studies devoted to physics of liquid breakdown it was assumed that the discharge in liquid under a uniform field propagates from the cathode, and the basic mechanism of its initiation, as in gases, is the *effective* electron capable of generating an electron avalanche. Owing to exaggeration of analogies in the mechanisms of discharge initiation and propagation in liquids and gases, the main time parameters like the *statistical time lag* (t_{st}) and *discharge formation time* (t_{f}) were generalized to liquid breakdowns. More recently, in connection with the establishment of anode, cathode, and mixed liquid discharge initiation under a uniform field and of the determining role of the first-order phase transitions rather than of the electron avalanche processes in the discharge initiation in liquid it became obvious that the term statistical time lag is inapplicable to liquid breakdown if it is understood as the time interval from the moment when the voltage reaches the static breakdown vaue to the moment of generation of the first effective electron (as accepted in the gas discharge). For this reason, the term *the discharge ignition time lag* was introduced in [27]. It is understood as a time interval from the beginning of

voltage rise to the first registered disruptions of continuity of the medium in the vicinity of the initiating electrode. It is applicable for any discharge ignition mechanism.

For convenience of material presentation, especially of the material borrowed from other publications, alongside with the *ignition time lag*, we use the term *statistical time lag*, but with the physical meaning of the term *the time lag of the discharge ignition*.

The discharge formation time considered in the gas discharge as the time interval from the moment of the discharge channel formation to the moment the discharge intersects the entire interelectrode gap can be applied to the liquid breakdown.

The optical patterns of the pre-breakdown processes near the cathode and anode also differ significantly both with and without the artificially created bubbles at the electrodes.

The typical processes near the anode in the presence of the artificial bubbles are illustrated by a sequence of frames shown in Fig. 2.19. Frames *a* and
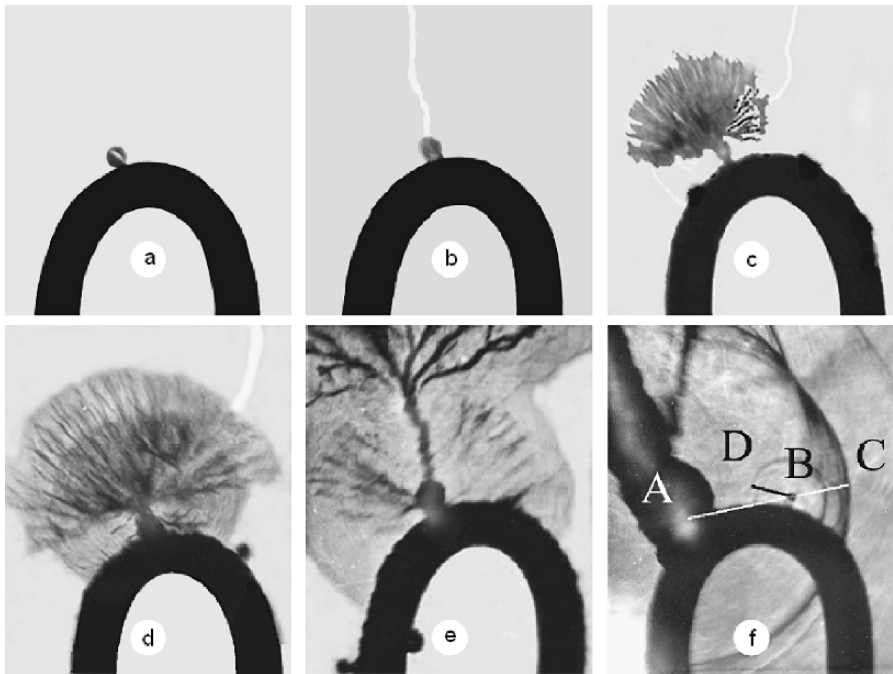
Fig. 2.19. Successive events of the anode breakdown: **a)** initial bubble, **b)** deformed bubble photographed at $\tau_1 = 0.45\,\mu$s after voltage application for the discharge initiation time $\tau_b = 1.2\,\mu$s after voltage application; **c)** strimer fan (brush) from the bubble top for $\tau_1 = 1.0\,\mu$s and $\tau_b = 1.3\,\mu$s; **d)** strimer fan before its termination for $\tau_1 = 1.2\,\mu$s and $\tau_b = 1.4\,\mu$s; **e)** disappearance of the first strimer fan and appearance of the next fan for $\tau_1 = \tau_b = 1.5\,\mu$s; **f)** post-breakdown hydrodynamics for $\tau_1 = 1.7\,\mu$s and $\tau_b = 1.2\,$ms

b are from one series, and the remaining frames are from different series. From the photographs, we can conclude the the following:

- the discharge ignition is connected with bubbles,
- in the initial stage (in the first 0.4–0.5 μs), the bubbles are elongated along the field, decreasing in the transverse direction. The deformation degree reaches 2–2.5 times. The bubble increases in all directions 1 μs after the voltage application. The bubble compression means that the compressing dielectrophoretic forces act near the bubble equator, that is, the bubble behaves like a dielectric, and the field inside the bubble is not disturbed et all or is disturbed only slightly. Significant further deformation in all directions means that not only the Coulomb forces but also the increased pressure inside the bubble (caused probably by the ionization processes) act on the bubble surface.

The first supersonic channels ∼5–10 μm in diameter propagate from the top of one of the bubbles ($v \sim 2$ km/s). The channels form a hemisphere with a radius of about 600 μm. The distance between channel ends is 40–60 μm, and their number apparently exceeds 100. The channel formation is accompanied by generation of shock waves whose center coincides with the channel base, that is, with the bubble top.

Approximately in 100–150 ns, when the shock waves reach the end of the discharge figure, primary channels disappear except one channel, and a new fan of channels arises from the site where this channel stops. These channels have a length of ∼1.5 mm, their diameter is ∼20–30 μm, and their number is less than 30. The rate of elongation of the secondary figure, estimated from the difference between the moments of occurrence of shock waves produced by these channels and of the main discharge, is ∼5 km/s. The main discharge develops along one of the channels and is accompanied by the most intensive shock wave.

From the fact that the anode discharge can be registered from the moment of its glow (the luminous strip in Fig. 2.19b, c, and d) it follows that either all discharge figures are optically transparent or they disappear by the moment the channel closes the gap.

The physical pattern of the cathode processes is illustrated by a sequence of frames shown in Fig. 2.20. From these photographs we conclude the following:

1. As in the case of the anode, the bubbles on the cathode promote the discharge ignition significantly reducing the discharge ignition time.
2. In the initial stage that lasts 0.4–0.5 μs, the bubbles are elongated along the field and decrease in the transverse direction. In 0.7–1.0 μs, the bubble acquires the characteristic mushroom-like shape. Large bubbles ($D \geq 100$ μm) do not acquire this form.
3. A bush-like discharge figure with the characteristic inhomogeneity scale less than 10 μm starts to grow from the bubble top. The moment the growth starts is random, and the minimum discharge time lag is less than 0.2 μs. The channels propagate with subsonic velocities 400 m/s > $V > 100$ m/s.
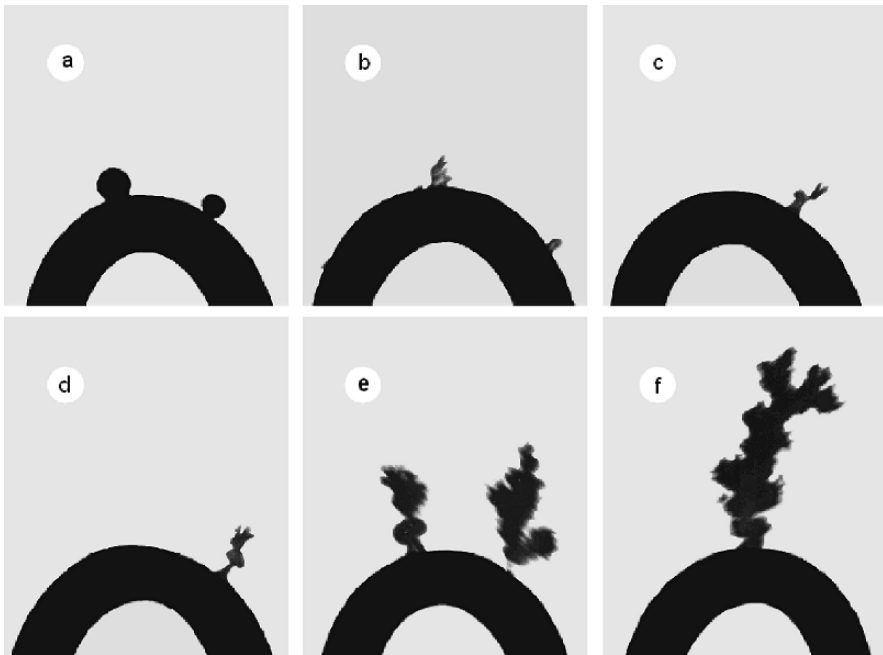
Fig. 2.20. Successive events of the cathode breakdown: **a)** initial bubbles, **b)** deformed bubbles with the elongated smaller bubble and bush-like formation that starts to grow from the surface of the larger bubble for $\tau_1 = 0.25\,\mu s$; **c)** bubble acquires a mushroom-like shape with an elongated thin stem and a cap for $\tau_1 = 0.65\,\mu s$; **d)** the bubble is shaped like a mashroom with a bush-like formation that grows on the bubble surface for $\tau_1 = 0.65\,\mu s$; **e)** several bubbles on the surface with a bush growing from a smaller bubble for $\tau_1 = 1.0\,\mu s$; **f)** bush of maximum size for $\tau_1 = 1.5\,\mu s$

4. The bush-like region is opaque, it is expanded not only in the field but also in the transverse direction.
5. When several bubbles are generated, the channels grow virtually from all bubbles. In some cases, when the bubble is detached from the electrode, it takes no part in the formation of the discharge channel.
6. The bush structure is optically dense, since no glow was registered in the gap breakdown.

The pre-breakdown processes *without artificially created bubbles* are illustrated by Fig. 2.21. On the anode (Fig. 2.21a), dark formations with the nonuniformly growing surface are seen. Sometimes they have regular enough structure. The most elongated formation initiates a discharge. The formations on the cathode (Fig. 2.21b and c) in the initial stage of growth are shaped as bubbles elongated in the electric field direction. Then perturbations whose shape is similar to the shape of channels arising in the process of discharge ignition with the help of artificial bubbles are seen on the surface of these
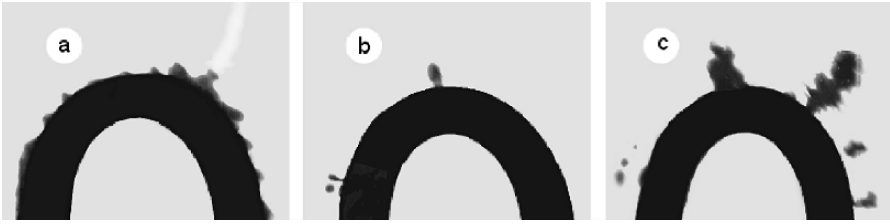
Fig. 2.21. Characteristic frames illustrating the pre-breakdown phenomena (bubbles are invisible): **a)** anode; growth of a dark inhomogeneous region from the electrode surface for $\tau_1 = 4.0\,\mu s$ and $\tau_b = 6\,\mu s$; **b)** cathode; emergence and growth of bubbles for $\tau_1 = 1.1\,\mu s$; **c)** cathode; a bush-like formation on the surface for $\tau_1 = 1.1\,\mu s$

formations. These processes are described in more detail in Chaps. 3, 4, 7, and 8.

The main results of consideration of the gas phase behaviour in liquids under the effect of strong electric field can be reduced to the following.

- Under the pre-breakdown conditions, the electric field precludes the bubble formation in the liquid, and the effect of the electric field is equivalent to an increase in the external pressure which makes the electrostatic cavitation impossible.
- The contradiction between the theory and experiment in the explanation of bubble elongation along the electric field direction has been eliminated through the correct consideration of the electrostriction pressure.
- In pre-breakdown electric fields, the bubble growth is limited by mechanical instability, and the pre-breakdown bubble size in dielectric liquids cannot exceed 10^{-5}–$10^{-6}\,m$.
- Electrostriction tension in the liquid promotes the development of bubble instability and causes an additional decrease in their sizes.
- Unlike the conventional boiling liquid, the liquid in an electric field has no binode.
- The pre-breakdown bubbles in liquids (at least, in nitrobenzene and water) have nonelectrolysis origin. Flows of electrohydrodynamic origin are developed in these liquids under application of microsecond voltage pulses.
- The microbubbles 40–100 μm in size artificially created on the electrode surface considerably reduce the pre-breakdown time under the effect of the field with strength of 800 kV/cm. The cathode discharge ignition is caused by the formation of bush-like channels on the bubble surface and their subsequent growth. The anode discharge ignition is accompanied by generation of the shock wave whose center is on the bubble surface, and formation of a supersonic channel fan from this place.

References

1. R. T. Knapp, J. W. Daily, F. G. Hammit, Cavitation, Mc Grow Hill Book Company New York (1970), 687 P.
2. E. I. Nesis, Boiling of Liquids, Nauka, Moscow (1973).
3. C. Lieberman, Air bubbles in water, J. Appl. Phys., **28**, 205–208 (1957).
4. E. I. Nesis, I I. Markov and T. S. Chigareva "Mechanism of bubble separation from cylindrical pores after buildup during the boiling of a liquid" Journal of Engineering Physics and Thermophysics. Volume 23, Number 3/ September, 1144–1145 (1972)
5. A. S. Besov and V. K. Kedrinskii, J. de-Vries, M. Kloosterman. Cavitation thresholds, free surfaces and cavity cluster dynamics in liquid at shock wave reflections. In Book. Liquid under negative pressure. NATO. Sciences Series (eds: A. R. Imre, H.J. Maris, P.A. Villiams) Kluwer Dordretch, (2002), pp. 255–265.
6. A. S. Besov, A mechanism of gas microbubble stabilization in water, in: Explosive and Nonstationary Processes in Continuous Media, Publishing House of Hydrodynamics Institute, Novosibirsk (1990).
7. A. S. Besov, Microinhomogeneities in actual liquids and cavitation effects, Author's Abstract Cand. Phys.-Math. Sci. Dissert., Hydrodynamics Institute, Novosibirsk (1994).
8. Methodical Service Instructions on Transformer Oil, RD.34.43-105-89 SPO, ORGRES, Moscow (1995).
9. B. S. Danilin and V. E. Minaichev, Principles of Vacuum System Design, R. A. Nilender, ed., Energiya, Moscow (1971).
10. C. G. Garton and Z. Krasucki, Bubbles in insulating liquids: stability in electric fields, Proc. R. Soc. London, **A280**, 211–226 (1964).
11. B. M. Smolyak, Influence of an electric field on surface tension of liquid dielectrics, in: Thermal Physics Properties of Liquids and Explosive Boiling, Ural Scientific Center of the USSR Academy of Scientces, Sverdlovsk (1976), pp. 79–84.
12. S. Torza, R. Cox, and S. G. Meison, Electrohydrodynamic deformation and burst of liquid drops, in: Rhil. Trans. R. Soc. Lond. 269 A, 295–319 (1971).
13. S. M. Korobeynikov, A. V. Melekhov, V. G. Posukh, et al., Experimental Investigation of Bubble Behavior in Water, Teplofiz. Vys. Temp., **39**, No. 2, 163–168 (2001).
14. J. S. Mirza, C. W. Smith, and J. H. Calderwood, Liquid motion and internal pressure in electrically stressed insulating liquids, J. Phys., **D3**, 580–585 (1970).
15. R. S. Allan and S. G. Mason, Particle behavior in shear and electric fields. I. Deformation and burst of liquid drops, Proc. R. Soc. London, **A267**, 45–47 (1962).
16. J. S. Mirza, C. W. Smith, and J. N. Calderwood, The elongation of small bubbles in electrically stressed dielectric liquids and the breakdown criterion, IEE Conf. Publ., **67**, 228–232 (1970).
17. K. C. Kao, Breakdown of liquid dielectrics, in: Conf. Report AIEE Winter Meeting (1960), pp. 60–84.
18. N. J. Felici, Bubbles, partial discharges and liquid breakdown, in: Electrostatics Phenom. Conf, Oxford (1979), pp. 181–190.
19. S. M. Korobeynikov, K. V. Yanshin, and E. V. Yanshin, Optical investigation of pre-breakdown processes in insulating liquids, in: Proc. 4th ISH, Athens (1983), paper 24.09.

20. S. M. Korobeynikov, K. V. Yanshin, and E. V. Yanshin, Pre-breakdown processes in liquid insulation under pulsed voltage, in: Pulsed Discharge in Dielectrics, G. A. Mesyats, ed., Nauka, Novosibirsk (1985), pp. 99–114.

21. R. Kattan, A. Denat, and O. Lesaint, Generation, growth, and collapse of vapor bubbles in hydrocarbon liquids under a high divergent electric field, J. Appl. Phys., **66**(9), 4062–4066 (1989).

22. S. M. Korobeynikov and S. P. Malyshenko, Nucleation of new phase in electric fields, Zh. Eksp. Teor. Fiz., **120**, No. 3(9), 863–870 (2001).

23. S. M. Korobeynikov, Bubble deformation in an electric field, Inzh. Fiz. Zh., **36**, No. 5, 882–884 (1979).

24. A. V. Antonov, E. P. Zimin, and A. G. Lyapin, Deformation and fragmentation of vapor bubbles of six-fluoric sulfur in a strong electric field, in: Abstracts of Reports at the 5th All-Union School-Seminar on Physics of Pulsed Discharges in Condensed Media, Nikolaev (1991), p. 60.

25. A. V. Antonov, Investigations of SF_6 electric strengthin a two-phase state, Author's Abstract of Cand. Phys.-Math. Sci. Dissert., Institute of Power Engineering, Moscow (1987).

26. B. Singh, C. W. Smith, and J. H. Calderwood, Light sattering from electrically stressed insulating liquids, in: Proc. 4th Int. Conf. on Conduction and Breakdown in Dielectric Liquids, Dublin (1972), pp. 202–205.

27. V. Y. Ushakov, Pulsed Electric Breakdown of Liquids, Publishing House of Tomsk State University (1975).

28. G. I. Skanavi, The Physics of Dielectrics: Region of High Fields, Fizmatgiz (1958).

29. I. Adamczewski, Ionization, Conductivity and Breakdown in Dielectric Liquids, Taylor and Francis, (1969).

30. K. C. Kao, Breakdown of liquid dielectrics, in: Conf. Rep. AIEE Winter Meeting (1960), pp. 60–84.

31. Z. Krasucki, Breakdown of liquid dielectrics, Proc. R. Soc. London, **A294**, 393–404 (1966).

32. A. H. Sharbaugh, J. S. Devins, and S. J. Rzad, Progress in the field of electric breakdown in dielectric liquids, IEE Trans. Elec. Insul., **13**, No. 4, 249–276 (1978).

33. V. V. Lopatin, V. Y. Ushakov, and V. P. Chernenko, Ignition and propagation of a nanosecond discharge in liquids, Izv. Vyssh. Uchebn. Zaved., Fiz., No. 3, 100–105 (1975).

34. A. P. Alkhimov, V. V. Vorobjev, V. F. Klimkin, et al., Electric charge propagation in water, Dokl. Akad. Nauk SSSR, **194**, 1052–1056 (1970).

35. N. J. Felici, Electrostatics and hydrodynamics, J. Electrostatics, **4**, 119–139 (1977-1978).

36. P. Ignacz, Explanation of bubble creation in high electric fields by a new consideration on the structure of a liquid, J. Electrostatics, **7**, 309–326 (1979).

37. Ya. I. Frenkel, The Kinetic Theory of Liquids, Academic Press, Moscow (1945).

38. D. Kaschiev, On the influence of the electric fields on nucleation kinetics, Philos. Mag., **25**, No. 2, 459–470 (1972).

39. D. S. Parmar and A. K. Jalaluddin, Nucleation in superheated liquids on the influence of electric fields, J. Phys., **D6**, No. 10, 1287 (1973).

40. D. S. Parmar and A. K. Jalaluddin, Pre-nucleation relaxation phenomenon in electric field induced nucleation in superheated liquids, Phys. Lett., **A61**, 43–44 (1977).

41. D. S. Parmar and A. K. Jalaluddin, Pre-nucleation relaxation phenomenon in electric field induced liquid-vapour phase transition in superheated liquids, in: Proc. Symp. Phase Transform and Phase Equilibria, Bangalore (1977), pp. 140–157.
42. L. D. Landau and E. M. Lifshits, Electrodynamics of Continuous Media, Chief Editorial Board of Physical and Mathematical Literature, Moscow (1992).
43. T. B. Jones and G. W. Bliss, Bubble dielectrophoresis, J. Appl. Phys., **48**, No. 4, 1412–1417 (1977).
44. M. Hara, Z.-C. Wang, and H. Saito, Thermal bubble breakdown in cryogenic liquids under non-uniform fields, in: Proc. of the 11th Int. Conf. on Conduction and Breakdown in Dielectric Liquids, IEEE No. 93CH3204-6, Baden-Dattwill (1993), pp. 249–253.
45. Y. Suda, K. Mutoh, and Y. Sakai, Bubble motion in liquid nitrogen between electrodes in a microgravity environment, in: Proc. 12th Int. Conf on Conduction and Breakdown in Dielectric Liquids, Roma (1996), pp. 144–147.
46. T. J. Lewis, A new model for the primary process of electrical breakdown of liquids, IEEE Trans. Dielectrics and Electrical Insulation, (1998) pp. 306–315.
47. T. J. Lewis, The electrode-liquid interface under high fields, in: Proc. Int. Conf. on Dielectric Liquids, IEEE Catalog No. 02CH37319 (2002), pp. 91–95.
48. V. P. Skripov, A Metastable Liquid, Nauka, Moscow (1972).
49. Yu. L. Levkovskii, Structure of Cavitation Flows, Sudostroenie, Leningrad (1978).
50. S. M. Korobeynikov, Influence of an electric field on the boiling point of liquids, Inzh. Fiz. Zh., **41**, No. 6, 1131–1134 (1981).
51. S. M. Korobeynikov, Yu. N. Sinikh, V. M. Posukh, et al., Bubbles behavior at strong electric field, in. Proc. 2nd Int. Workshop on Conduction and Convection in Liquids, Grenoble (2000), pp. 99–102.
52. S. M. Korobeynikov, A. V. Melekhov, V. G. Posukh, et al., Experimental investigations of bubble behavior in water, Teplofiz. Vys. Temp., **39**, No. 2, 163–168 (2001).
53. P. K. Katti, P. K. Pillai, and V. Ramahrisha, Effect of strong electric field on boiling point of alcohol, Nature, **198**, 181–182 (1963).
54. R. A. Anderson and S. S. Infirri, Effect of electric and magnetic fields on the boiling points of alcohols, Nature, **196**, No. 4851, 267 (1963).
55. R. S. Sharma, Effects of electric fields on the boiling point of liquids, J. Appl. Phys., **42**, No. 3, 1234–1235 (1971).
56. N. B. Vargaftik, Handbook on Thermal Physical Properties of Gases and Liquids, State Physical and Mathematical Press, Moscow (1963).
57. O. M. Stuezer, Ion drag pressure generation, J. Appl. Phys., **30**, 984 (1959).
58. I. T. Ovchinnikov, K. V. Yanshin, and E. V. Yanshin, Experimental investigations of pulsed electric fields in water near the tip electrode with the help of the Kerr effect technique, Zh. Tekh. Fiz., **748**, No. 12, 2595–2698 (1978).
59. E. V. Yanshin, I. T. Ovchinnikov, and Yu. N. Vershinin, Optical investigations of the pre-breakdown phenomena in water in the nanosecond range, Zh. Tekh. Fiz., **43**, No. 10, 1067–1071 (1973).
60. S. M. Korobeynikov, E. V. Yanshin, and K. V. Yanshin, Experimental evidence of bubble model of discharge initiation, in: Proc. of the 1998 Int. Conference on Electrical Insulation and Dielectric Phenomena, Atlanta (1998), pp. 436–438.
61. H. B. Clark, P. S. Strenge, and J. W. Westwater, Active Sites for Nucleate Boiling,. Chem. Eng. Prog. Symp., Vol. 55, 103–110 (1959).

62. L. D. Landau and E. M. Lifshits, Hydrodynamics, State Physical and Mathematical Press, Moscow (1986).

63. A. Watson, High field conduction in dielectric liquid with ramped voltage application: A theory of the mechanism, in: Conference Record of the 10th Int. Conf. on Conduction and Breakdown in Dielectric Liquids, Grenoble (1990), pp. 156–160.

64. G. A. Ostroumov, Interaction of Electric and Hydrodynamic Fields, Nauka, Moscow (1979).

65. Yu. K. Stishkov, Phenomen of nonlinear field interaction with a liquid low-conducting medium, Doctoral Thesis in Technical Sciences, Leningrad State University, Leningrad (1985).

66. Yu. M. Rychkov and Yu. K. Stishkov, Electric field strength and space charge in technical liquid dielectrics, Kolloidn. Zh., **40**, No. 6, (1978)

67. Yu. K. Stishkov and A. A. Ostapenko, Electrohydrodynamic Flows in Liquid Dielectrics, Publishing House of Leningrad State University, Leningrad (1989).

68. N. J. Felici, La conduction dans les liquids dielectriques. Idees modernes et progress recents. Aspects electrochimiques et electrohydrodynamiques, J. Phys. (Paris), **37**, No. 1, 61–117 (1976).

69. N. J. Felici, B. Gosse, J. P. Gosse, Aspects electrochimique et electrohydrodynamiques de la conduction des liquides isolants, RGL, **8,** 861–864 (1986).

70. J. D. Cross and H. T. Wang, Interfacial instability as an explanation of EHD umc delays, in: Conf. Record of the 10th Int. Conf. on Conduction and Breakdown in Liquid Dielectrics, Grenoble (1990), pp. 281–285.

71. S. G. Sarin, E. V. Yanshin, and S. M. Korobeynikov, EHD Instabilities Registration in Liquids, in: Proc. of the 3rd Inter. Conf. on Properties and Application of Dielectric Materials, Tokyo (1991), pp. 898–900.

72. G. Noyel, Properties dielectriques du glycerol et de l'eau sous refroidie jusqu a la transition vitreuse, Doctorat These Nb 10, Saint-Etienne (1987).

73. S. M. Korobeynikov, E. V. Yanshin, and K. V. Yanshin, Space charge and pre-breakdown bubbles formation near point electrodes under pulse voltage, in: Conf. Record of the 8th Int. Conf. on Conduction Breakdown in Dielectric Liquids, Pavia (1984), p. 5.

74. S. M. Korobeynikov, E. V. Yanshin, and K. V. Yanshin, Occurrence of electrohydrodynamic flows in liquid insulation under pulsed voltage, in: Abstracts of Reports at the All-Union Conf. on Electric Discharge in Liquid, Nikolaev (1984), p. 2.

75. S. M. Korobeynikov, A.V. Melekhov, V. G. Posukh, V. M. Antonov, Yu. N. Sinikh, "Deformation and motion of bubbles at action of strong fields", Int. Conf. "Modern Problems of Electrophysics and Electrohydrodynamics of Liquids", Sankt Petersburg, SpBU, 2000, pp. 187–191.

76. S. M. Korobeynikov and A. V. Melekhov, Microbubbles and breakdown initiation in water, in: Proc. 14th Int. Conf. on Dielectric Liquids, Graz (2002), pp. 127–130.

77. K. P. Mishchenko and A. A. Ravdelya, Brief Handbook on Physical and Chemical Quantities, Khimiya, Moscow-Leningrad (1965).

78. S. M. Korobeynikov, A bubble model of ignition of the pulsed electric discharge in liquids, Author's Abstract of Doct. Phys.-Math. Sci. Thesis, Tomsk (1998).

79. S. M. Korobeynikov, On the role of bubbles in electric breakdown of liquids. 1. Pre-breakdown processes, Teplofiz. Vys. Temp., No. 3, 362–367 (1998).

80. S. M. Korobeynikov, On the role of bubbles in electric breakdown of liquids. 2. Comparison with experiment, Teplofiz. Vys. Temp., No. 4, 541–547 (1998).

81. I. Alexeff, M. O. Pace, T. V. Blaock, and A. I. Winterberg, Possible models for the earliest pre-breakdown events in dc stressed hexane, in: Conf. Record of the 10th Int. Conf. on Conduction and Breakdown in Dielectric Liquids, Grenoble (1990), pp. 387–391.

82. S. M. Korobeynikov, A. V. Melekhov, Yu. N. Sinikh, and Yu. G. Soloveichik, Influence of strong electric fields on the behavior of bubbles in water, Teplofiz. Vys. Temp., **39**, No. 3, 395–399 (2001).

83. Yu. V. Koritskii, ed., Handbook on Electrical Engineering Materials, Vol. 3, 3rd edition, Energoatomizdat, Moscow (1988).

84. S. M. Korobeynikov, A. V. Melekhov, and A. S. Besov, Discharge ignition in water with the help of bubbles, Teplofiz. Vys. Temp., No. 5, 706–713 (2002).

85. Yu. D. Korolev and G. A. Mesyats, Physics of Pulsed Gas Breakdown, Nauka, Chief Editorial Board of Physical and Mathematical Literature, Moscow (1991).

86. P. K. Watson, T. Sufian, W. G. Chadband, and H. Yamashita, The growth and collapse of streamer channels in insulating liquids, in: Proc. Int. Conf. on Conduction and Breakdown, IEEE No. 93CH3204-6, Baden-Dattwill (1993), pp. 234–237.

87. Yu. P. Raizer, Physics of a Gas Discharge, Nauka, Chief Editorial Board of Physical and Mathematical Literature, Moscow (1987).

88. P. K. Watson, T. Sufian, and W. G. Chadband, A thermal model of positive pre-breakdown streamers in insulating liquids, in: Proc. Int. Conf. on Conduction and Breakdown, IEEE No. 93CH3204-6, Baden-Dattwill (1993), pp. 229–233.

89. P. Gournay and O. Lesaint, On the gaseous nature of positive filamentary streamers in hydrocarbon liquids. II: Propagation, growth and collapse of gaseous filaments in pentane, J. Phys., **D27**, 2117–2127 (1994).

90. V. V. Rozhdestvenskii, Cavitation, Sudostroenie, Leningrad (1977).

3

Discharge Propagation in Short Gaps with a Quasiuniform Field

Significant and often principal differences in the nature and mechanisms of discharge ignition and propagation in liquids pointed out in works published from the beginning of the last century to the 60-70s were caused largely by the lack of equipment for direct observations of these phenomena.

The data presented in Chaps. 3 and 4 were obtained by recording space-time patterns of natural discharge luminescence using image-converter cameras in chronograph and single- or multiframe regimes, shadowgraphic technique in the frame regime with additional laser illumination, light emission from photomultipliers or light-emitting diodes, current, and charge, and static photographing with cameras with open shutter. Registration of natural luminescence of discharge channels together with current recording provides valuable information on ionization and excitation of molecules and atoms in the process of discharge propagation and on the discharge kinetics. The shadowgraphic technique provides information on phase inhomogeneities in liquid (discharge channels, gas-vapor bubbles, cavitation voids, etc.). Equipment and experimental techniques have already been briefly described in the Introduction; more detailed information can be found in the references.

Especially heavy demands are imposed on the temporal and spatial resolution of recording equipment intended for experimental investigation of electric discharges in short (millimeter or submillimeter) gaps with a uniform field. Therefore, experimental data on electric discharge propagation under these conditions are few in number in the literature, especially for nanosecond voltage exposures.

The term *streamers* is most frequently used for self-luminescent plasma channels propagating through the interelectrode gap and initiating breakdown. However, as demonstrated in the next chapters, these channels differ significantly by their characteristics and nature from the *classical streamers* of gas discharges. For this reason, generalization of this term to the discharge in liquids may cause confusion. Therefore, it is expedient to use neutral terms like *discharge channel*, *discharge figure*, and *discharge formation* when there is no necessity or opportunity to assign physical meaning to the terms.

In the literature, first of all English one, other terms are also widely used, namely, terms *slow* and *fast* classify discharges by their velocity, and *tree-like*, *bush-like*, *filamentary*, *umbrella-like*, *pagoda-like*, *coniferous tree-like*, etc. classify the discharges by their external appearance. The discharge figures (processes) propagating with subsonic velocities are called *slow*, and those propagating with supersonic velocities are called *fast*. All other terms comprise the basic characteristic of the parameter of interest and require no additional explanation. In some cases (mainly in Chaps. 4 and 8), we will use these terms when needed. The variety of terms is caused primarily by a wide variety of the discharge phenomena in liquids.

This Chapter describes the results of investigations of electric discharge propagation in liquids under conditions of a uniform field for different field strengths (voltage exposure times), interelectrode distances, and external pressures.

3.1 Discharge Propagation from Anode

Figure 3.1 shows single-frame photographs of natural luminescence of discharge channels propagating in water [1] for a field strength of $\sim 0.4\,\mathrm{MV/cm}$ with a breakdown lag time of $\sim 300\,\mathrm{ns}$.

It can be seen that the electric discharge is initiated on the positive electrode, and the average velocity of its propagation in the gap is $\sim 1.5 \cdot 10^7\,\mathrm{cm/s}$, increasing as the cathode is approached. It should be noted that luminescence in the discharge gap was not observed 200–250 ns after voltage application, even when a light amplifier with amplification coefficient up to 10^7 was used. The electric discharge formation time and the average channel propagation velocity $\overline{V}_{\mathrm{ch}}$ depend on the field strength E. For field strengths of $\sim 0.3 - 0.45\,\mathrm{MV/cm}$ and interelectrode distances of 5 mm, $\overline{V}_{\mathrm{ch}} \sim E^\alpha$, where $\alpha \sim 2 - 3$. The gap breakdown (the sharp voltage drop) occurs when the channel has touched the negative electrode.

Interesting results were obtained using the schlieren-photograph method. With the help of a ZIM-2 ICC, photographs of natural channel radiation were
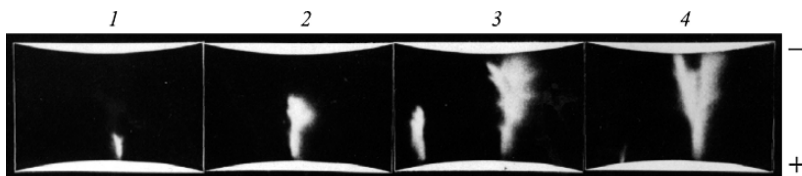
Fig. 3.1. Photograph of natural luminescence of the discharge channel in distilled water. The specific resistance of water was $\rho \sim 3 \cdot 10^6\,\Omega \cdot \mathrm{cm}$, the frame exposure time was 3 ns, and the interelectrode distance was 5 mm. Frames 1 and 2 were produced 35 and 18 ns before the breakdown, and frames 3 and 4 were produced directly before and after the gap breakdown
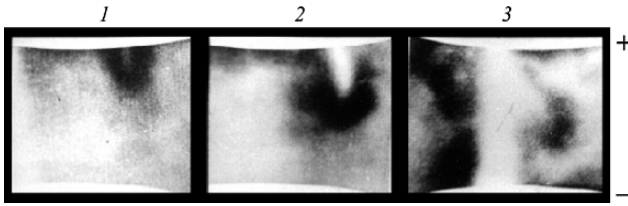
Fig. 3.2. Combined photographs of electric discharge propagation in distilled water 30 (**1**) and 20 ns before the breakdown (**2**) and at the breakdown moment (**3**)

produced simultaneously with shadowgraphs of the surrounding region (with the use of a ruby laser – ICC complex) [1]. Figure 3.2 shows several frames with an exposure time of 5 ns (with other conditions remaining the same) from which it is clearly seen that a parallel light beam of laser illumination is intensively scattered on the shell formed around the plasma channel.

Measurement of the channel radius at the moment of channel initiation seems important. To this end, streak photographs of transverse expansion of the discharge channel were produced. The typical streak photograph synchronized with the voltage pulse is shown in Fig. 3.3. Cross section views of the channel at different moments of time recorded with an MF microphotometer are shown below. The analysis of the results obtained has demonstrated
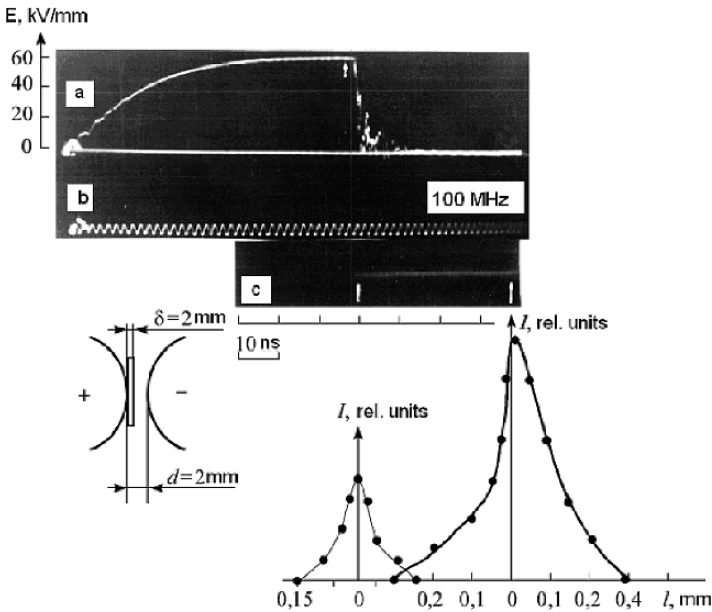
Fig. 3.3. Streak photograph of transverse expansion of the discharge channel in distilled water

that the initial diameter of the discharge channel registered by this method is $\sim 80\,\mu$m, and its average expansion velocity is $\sim 9 \cdot 10^4$ cm/s.

The method of Schlieren-photography on the ICC screen does not allow one to obtain sufficiently high spatial resolution and to reveal the processes before the discharge channel formation in liquid that determine the discharge initiation and propagation. Therefore, Schlieren-photography was performed separately on a KN-4 negative film. Its resolving power is ~ 100 lines/mm, which significantly exceeds that of the ICC. The ICC was used in these experiments only to record the natural luminescence of the discharge.

Figure 3.4 shows a sequence of photographs synchronized with the voltage pulse. From the photographs it can be seen that an optical inhomogeneity with a high density gradient is formed on microinhomogeneities of the positive electrode surface before the luminescence. The optical inhomogeneity has a fine structure. It has a bush-like form with transverse dimensions of channel base $\sim 10 - 20\,\mu$m and channel lengths of $\sim 50\,\mu$m. The time interval between the termination of the stage of development of the optical inhomogeneity and the electric discharge initiation inside it can be determined by this method. A correlation between the ICC images and laser Schlieren-photographs has allowed us to establish that the ionization processes start when the optical inhomogeneity has reached a critical size of $\sim 100\,\mu$m developing toward the cathode [2, 3].

The laser Schlieren-photographs reveal a thin structure of the electric discharge in the stage of intensive development of the ionization processes.

A photomultiplier with maximum spectral sensitivity in the range $3000 - 6500\,$Å and time resolution of $\sim 5\,$ns was used for more accurate registration of luminescence in the discharge gap and measurement of the average velocity of the ionization processes. Figure 3.5 shows a set of synchronously recorded signals from a photomultiplier and a voltage pickup. From these time histories it can be seen that the time interval between the onset of luminescence and the sharp voltage drop is approximately equal to $25\,$ns for a field strength of $0.6\,$MV/cm. The average velocity of discharge channel propagation was estimated from these data. It was $\sim 8 \cdot 10^6$ cm/s, which is smaller than the velocity measured with the ICC ($\sim 1.5 \cdot 10^7$ cm/s). This is caused by the fact that the ICC records only a faster (more intensive) process, whereas the photomultiplier is capable of recording also the initial slower stage of processes. At the same time, this velocity is higher than the average velocity of the discharge formation $\overline{V}_f$ found from the statistical analysis ($\sim 5 \cdot 10^6$ cm/s). This indicates that the initial stage of the discharge formation (the increase of the optical inhomogeneity size to the critical value) is a much slower process.

Let us now estimate the average velocity of the discharge formation $\overline{V}_{f1}$ in this stage using the data of statistical analysis and the average velocity of channel propagation through the gap measured with the ICC. We designate by l_{cr} the critical size of the optical inhomogeneity at which the channel is formed. Then we obtain $\overline{t}_f \sim d/\overline{V_{ch}} + l_{cr}/V_{f1}$. For a field strength of $0.6\,$MV/cm and interelectrode distance $d = 2\,$mm, $\overline{t}_f = 42\,$ns ($N_0 = 510$ was the num-
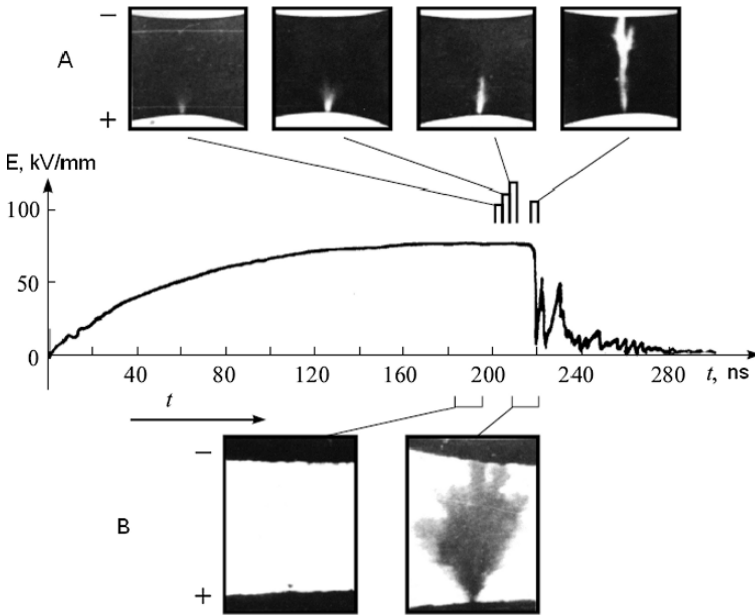
Fig. 3.4. Pre-breakdown phenomena in distilled water with specific resistance $\rho \sim 10^7\,\Omega \cdot cm$: natural luminescence of the channel with a frame exposure time of 3 ns (**A**) and laser Schlieren-photographs of the optical inhomogeneity with an exposure time of ~ 10 ns (**B**). The interelectrode distance was 2 mm
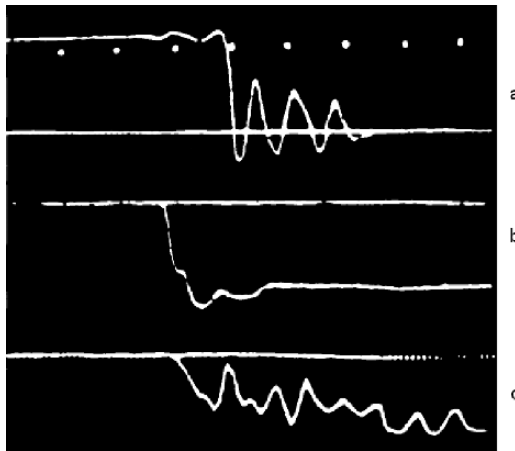
Fig. 3.5. Oscilloscope traces of voltage decay at the moment of gap breakdown (**a**) and of photomultiplier signals (**b** and **c**) for an interelectrode distance of 2 mm. Time marks are spaced at 20 ns

ber of successive measurements, and the average breakdown lag time was $\overline{t}_{\text{lag}} = 58\,\text{ns}$), the average velocity of channel propagation $\overline{V}_{\text{ch}} \sim 2.0 \cdot 10^7\,\text{cm/s}$, and $l_{\text{cr}} \sim 100\,\mu\text{m}$, $\overline{V}_{\text{fl}} \sim 3 \cdot 10^5\,\text{cm/s}$, which is close to the sound velocity in liquid.

To elucidate a nature of the initial optical inhomogeneities, experiments were carried out to estimate the influence of the external pressure on the inhomogeneities and on the breakdown as a whole. A strong dependence of the electric strength on the external pressure was established in [1, 2]. For example, distilled water at a pressure of $1.5 \cdot 10^7\,\text{Pa}$ withstood a field strength of $0.7\,\text{MV/cm}$ for 10–15 μs. Strong influence of the external pressure confirms the important role of gas formations in the initial stage of electric discharge propagation.

Thus, the results of optical measurements allow us to describe qualitatively the pattern of the electric discharge propagation from anode in a uniform field as follows. After the voltage application, the process depending on the electric field starts in the gap, which gives rise to an optical ingomogeneity having a complex structure. The ionization processes start later on, and the moment of their onset is determined by the time the optical inhomogeneity reaches a critical size of $\sim 100\,\mu\text{m}$ developing toward the cathode. At the beginning of this stage, slow ionization processes are observed inside the optical inhomogeneity that are terminated with the formation of the discharge channel base. Then the ionization processes develop with much higher velocities.

The discharge formation time is a period of time during which the size of the optical inhomogeneity increases to the critical one (the first slower stage) and a channel is initiated and propagated in the gap (the second faster stage).

Superfast laser Schlieren-photographs of the electric discharge in distilled water produced with a three-frame Schlieren system [4], have allowed us to follow the dynamics of the electric discharge propagation from anode and to establish some details of the optical inhomogeneity formation. The first frame in Fig. 3.6 was produced approximately 15 ns before the gap breakdown. It corresponds to the termination of the first stage of the electric discharge. The size of optical inhomogeneities near the electrode surface was $\sim 85\,\mu\text{m}$.
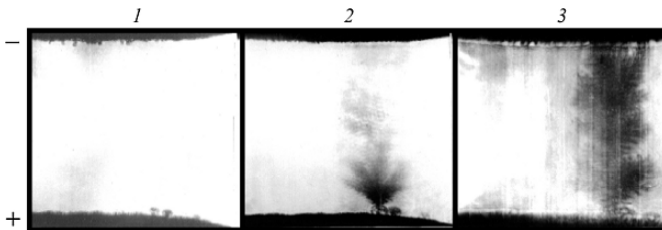
Fig. 3.6. Laser Schlieren-photographs of the electric discharge in distilled water for a field strength of $0.6\,\text{MV/cm}$, an interelectrode distance of $2\,\text{mm}$, a breakdown lag time of about 60 ns, a frame exposure time of $\sim 5\,\text{ns}$, and time interval between two successive frames of 6 ns

In the second frame produced in 6 ns, the transition to the faster stage of the electric discharge is seen when the size of the optical inhomogeneity has reached $\sim 100\,\mu$m. The intensively developing ionization processes reach the cathode in 6 more ns (the third frame).

Detailed investigations into the structure and dynamics of optical inhomogeneities have demonstrated that the first stage is characterized by a local energy release near the electrode surface, formation of shock waves, and generation of microbubbles with characteristic sizes of $\sim 10\,\mu$m behind their front. Ionization processes developing in microbubbles cause the formation of the base of the plasma channel.

It should be noted that in the nanosecond range, another mechanism of breakdown from anode is observed. It is characterized by the absence of the first slower stage. The electric discharge from the very beginning propagates with a high velocity approximately equal to that of the plasma channel propagation in the first mechanism [5,6]. Figure 3.7 shows superfast laser Schlieren-photographs that illustrate a competition between two different mechanisms of breakdown from anode in distilled water [5]. The exposure time of the first frame was approximately $10 - 12$ ns before the gap breakdown. The optical inhomogeneities (a) and (c) in the figure correspond to the first slower stage, and (b) corresponds to generation of an intensive discharge without this stage. The second frame illustrates the intensive discharge propagation (b) and transition from the first stage to the fast-propagating electric discharge (a). According to frames 1 and 2, the velocity of discharge propagation in the first stage $(a$ and $c)$ is $\sim 2\cdot 10^5$ cm/s, and that of the intensive discharge is $\sim 10^7$ cm/s. The third frame was produced $2 - 3$ ns after the gap breakdown. According to frames 2 and 3, the discharge propagation velocity increases and is $\sim 2\cdot 10^7$ cm/s near the cathode.

Figure 3.8 illustrates superfast laser Schlieren-photographs of the fine structure of the electric discharge in distilled water. They were produced with
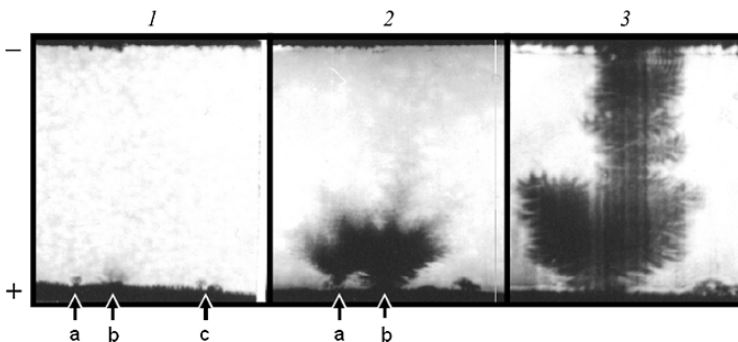
Fig. 3.7. Laser Schlieren-photographs of the electric discharge in distilled water for a field strength of 0.6 MV/cm, interelectrode distance of 2 mm, frame exposure time of ~ 5 ns, and a 6-ns time interval between the subsequent frames
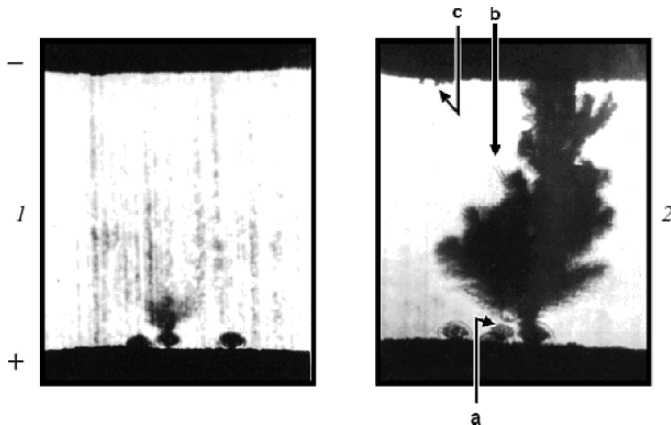
Fig. 3.8. Laser Schlieren-photographs of the electric discharge in distilled water for a field strength of 0.6 MV/cm, interelectrode distance of 2 mm, and frame exposure time of ∼5 ns produced 10 ns before the breakdown (**1**) and directly after the gap breakdown (**2**)

a single-frame Schlieren-system having higher spatial resolution. The configuration of shock waves is clearly seen in the first frame. The second frame illustrates the structure of the ionization processes behind the shock wave front (*a*). The transverse channel diameter in the stage of intensively developing ionization processes is ≤ 5 mm (*b*). Weaker shock waves and bubble structures behind their front are also observed near the cathode, but these processes do not initiate gap breakdown (*c*).

For a comparison, experiments were carried out with other liquids having radically different structure. Their main parameters of the liquids are presented in Table 3.1. The first three liquids are typical polar, and others have weak polar properties.

In liquids with low permittivity and conductivity, weaker shock waves are observed, and single microbubbles are formed behind the shock wave front. Figure 3.9 shows single-frame laser Schlieren-photographs of the pre-breakdown phenomena in *n*- hexane [5].

In the first frame, the onset of the ionization processes from a single microbubble ∼30 μm in size is seen in the liquid. The second frame shows the origin of the fast-propagating electric discharge on the front the primary channel. The primary channel has a length of ∼150 μm and a transverse size of ∼10 μm. The rough estimate of its propagation velocity yields ≥ 10^5 cm/s.

According to the second frame, the average velocity of the intensive discharge propagation is ∼1.7·10^7 cm/s. The third frame shows the fine structure of the fast electric discharge.

A sequence of single-frame superfast laser Schlieren-photographs of the electric discharge in *n*-hexane and water is shown in Fig. 3.10. They were produced a few tens of nanoseconds (∼30 − 100 ns) after the gap breakdown.

Table 3.1. Physical properties of the investigated liquids

Liquid	Specific resistance ρ, $\Omega\cdot$cm	Permittivity ε	Boiling temperature, T°C	Critical parameters	
				T, $^\circ$C	P, atm
Distilled water, H_2O	$10^5 - 10^6$	80	100	374	225.6
Ethanol, C_2H_6O	10^6	25	78.4	243	63
Acetone, C_3H_6O	10^7	21	56.5	235.5	46.6
Hexane, C_6H_{14}	10^{12}	1.8	68.7	234.7	29.9
Carbon tetra-chloride, CCl_4	10^{12}	2.2	76.7	283.2	45
Ether, $C_4H_{10}O$	10^{10}	4.3	34.6	194	35.6

Of interest is the fact that the discharge channel propagation in liquids is accompanied by shock wave generation and bubble formation behind the shock wave front. This is clearly seen on the example of primary (frame 1) and secondary undeveloped discharge channels (frame 2) or after the gap breakdown (frame 3).

The methods of superfast interferometry [7] allow one to improve the quality of recording of the shock waves and microstructure of strong hydrodynamic perturbations behind the shock wave front.

Figures 3.11 and 3.12 show typical single-frame superfast laser interferograms of the electric discharge in different liquids.

Spherical shock waves with a radius of $\sim 100 - 150$ mm (for example, a) propagating in distilled water from a site of local energy release near the positive electrode surface are clearly seen in Fig. 3.11 (*1*). The interference bands on the shock wave front are shifted toward the cathode. This is indicative of
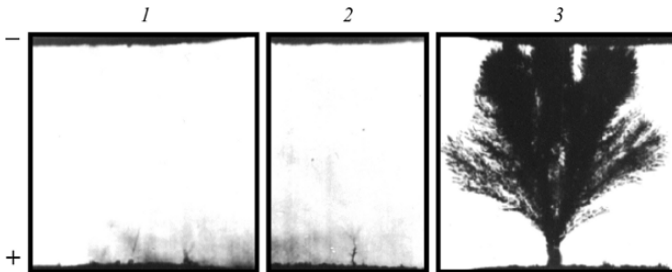
Fig. 3.9. Laser Schlieren-photographs of the electric discharge in n-hexane for a field strength of 0.7 MV/cm, interelectrode distance of 2 mm, breakdown lag time of ~ 150 ns, and frame exposure time of ~ 5 ns produced 40 (**1**) and 10 ns before the breakdown (**2**) and directly after the gap breakdown (**3**)
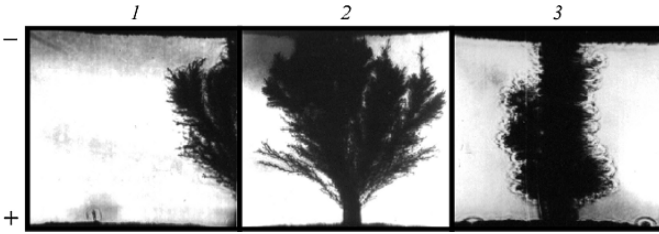
Fig. 3.10. Laser Schlieren-photographs of the electric discharge in *n*-hexane (**1** and **2**) and distilled water (**3**) for an interelectrode distance of 2 mm and a frame exposure time of ~ 5 ns
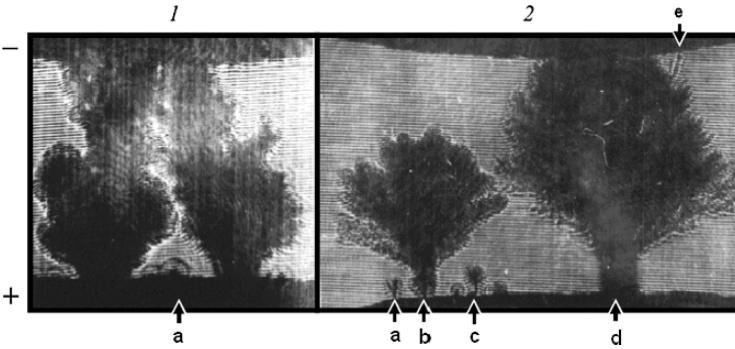
Fig. 3.11. Laser interferograms of the electric discharge in distilled water (**1**) and ether (**2**) for a field strength of 0.6 MV/cm, interelectrode distance of 2 mm, breakdown lag time of ~ 50 ns, and frame exposure time of ~ 5 ns produced 70 (**1**) and 25 ns after the gap breakdown (**2**)
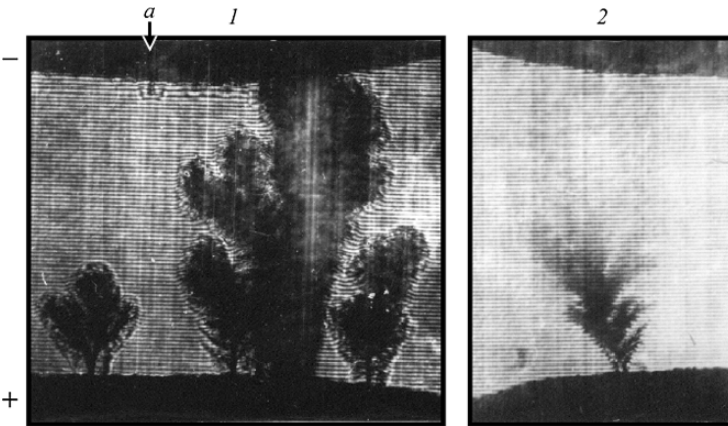
Fig. 3.12. Laser interferograms of the electric discharge in ethanol for a field strength of 0.6 MV/cm, interelectrode distance of 2 mm, breakdown lag time of ~ 60 ns, and frame exposure time of ~ 5 ns produced 45 ns after (**1**) and 7 ns before the gap breakdown (**2**)

an increase in the refractive index in comparison with the environment, that is, $\Delta n > 0$. Behind the shock wave front, the interference bands regain their position or are shifted toward the anode (that is, $\Delta n < 0$) toward the site of local energy release.

The structure of the initial perturbation in ether typical of liquid dielectrics with low permittivity is clearly seen in Fig. 3.11 (*2*). The common feature of the liquid dielectrics is the formation of a single channel accompanied by the formation of microbubble and cylindrical shock waves (*a* and *c*). Then the initial perturbation acquires a treelike shape and when its length has reached ~ 200 mm, a fast-propagating electric discharge is initiated (*b*), which leads to the gap breakdown (*d*).

As indicated above, shock waves and complex bubble structures behind their front are observed not only on the anode but also near the cathode. Figure 3.12 (*1*) more vividly illustrates the structure of an optical inhomogeneity near the cathode in ethanol (*a*).

An analysis of a large number of interferograms has allowed us to establish some important peculiarities of the electric discharge propagation. The discharge propagates from the positive electrode irrespective of the structure of the examined liquids for field strengths in the range $\sim 0.3 - 1$ MV/cm. In this case, the discharge propagation pattern remains approximately unchanged, though the initial optical perturbation shapes somewhat differ. As a rule, in liquids with high permittivity and conductivity (water, alcohol, and acetone), stronger shock waves are observed with vividly pronounced bubble structure behind their front. The structure of the secondary channels is seen after passage of the ionization channel as a chain of microbubbles with characteristic sizes of ~ 10 μm and shock waves separated from them (for example, see Fig. 3.11 (*2e*).

Figure 3.12 (*2*) shows the typical interferogram produced in the period of intensively developing ionization processes in the discharge gap. As established in numerous experiments, in the stage of formation of the main discharge channel propagating with velocity $\geq 10^7$ cm/s and shaped as a complex treelike structure, neither significant shear of the interference bands nor microbubble generation were observed. This suggests that the second stage of the discharge propagation characterized by the local electric field amplification is determined by the ionization processes developing in the liquid itself. The characteristic transverse size of discharge channels in this case is ≤ 5 μm and cannot be precisely measured with the employed optical system.

We can assume that the discharge is initiated by the ionization process that starts near the anode surface in sites with local electric field amplification [7]. A sharp increase in the conductivity in this site results in the strong energy absorption and generation of the shock wave whose intensity is controlled by the growth of the primary ionization channel. In the first hydrodynamic stage, the base of the future discharge channel is formed that can be considered already as a macrotip on the anode surface. The sizes of the amplified field region reach $\sim 100 - 200$ μm, and conditions for the origin of fast-propagating

electric discharge are created. When one of the growing branches has touched the opposite electrode, the discharge propagation is terminated by the complete gap breakdown. A decrease in the breakdown lag time in n-hexane after incorporation of additives with low ionization energy and weak influence (or absence of the influence) of additives trapping electrons indicate the important role of the self-ionization processes in the electric discharge propagation from anode [8].

Thus, the explosive process of energy deposition into a certain liquid volume near the electrode surface required for microbubble generation must be included in the mechanism of electric discharge formation.

The important role of electrode microgeometry in the discharge initiation is confirmed by experiments with the so-called diffusion electrodes. In [9] it was suggested to form a transitive diffusion layer near the electrode surface. The electrical conductivity in this layer smoothly decreased with increasing liquid depth. The effective thickness of the conducting layer part should significantly exceed microinhomogeneity heights but should be much smaller than the distance between the electrodes. Under voltage application, the electric field is forced out from the region of high conductivity near the electrode surface, and the influence of microinhomogeneities is shielded by the diffusion electrode.

Results of investigations into the pulsed electrical breakdown of distilled water ($\rho \sim 10^6 - 10^7 \, \Omega \cdot \text{cm}$) in a uniform field with electrodes shielded by the diffusion layers are presented in [10, 11]. It was established that the electric discharge is not initiated from anode in the presence of the diffusion layer near the anode. The gap breakdown is initiated by the discharge from cathode. In this case, the water breakdown field strength is approximately doubled (for breakdown lag times $\overline{t}_{\text{lag}} \leq 2 \, \text{ms}$). It should be noted that no significant changes in the breakdown character are observed in the presence of the diffusion layer near the cathode. This demonstrates that the cathode processes do not influence the electric discharge initiation from anode in a homogeneous field. Studying the pre-breakdown electric field distribution in water for a field strength of $1.3 \, \text{MV/cm}$ (pulse duration $\sim 200 \, \text{ns}$) with the help of the Kerr effect technique also demonstrates that the discharge initiation from anode cannot be caused by the field amplification in its vicinity at the expense of the space charge generated in the gap due to electron emission from cathode [12]. When both electrodes are shielded by the diffusion layers, the electric discharge is initiated in the liquid volume near the layer boundary. In this case, the pulsed electric strength of water increases approximately 4 times (for the voltage pulse front duration $t_{\text{fr}} \sim 0.3 - 1 \, \mu\text{s}$).

It should be noted that Alkhimov *et al.* [1] and Abramyan *et al.* [2] first investigated the pre-breakdown phenomena in liquids with the use of a ruby laser as an illumination source for high-speed Schlieren-photographing. They established that the electric discharge from anode in a uniform field has complex character and involves some consecutive stages that differ by mechanisms and propagation velocities. Simultaneously and independently of [1,2] the fact of discharge initiation in a uniform field on the anode rather than on the

cathode was established in [13, 40] by single-frame photographing with the ICC. The results obtained are fundamental, since they demonstrate the need for revision of the conventional role of electron emission from cathode in the electric discharge initiation in a uniform field.

The discharge propagation from anode was also observed under conditions of a quasi-uniform electric field in water solutions of sodium chloride [14], white mineral oil [15], and transformer oil [16]. In [17] the direction of side branches of discharge channels in hydrocarbon liquids indicated that the electric discharge propagated from anode. However, insufficient time resolution of the equipment employed by Wong and Forster in [17] and [18–20] did not allow them to trace the dynamics of channel initiation and propagation.

3.2 Discharge Phenomena in Submillimeter Distilled-Water Gaps

The well-known fact of the increase in the dielectric strength with decreasing interelectrode distance calls for detailed investigations of mechanisms of electrical breakdown of liquids for a wide range of discharge gap lengths. Results of electrical breakdown of water in submillimeter gaps are presented below.

Experiments were carried out with distilled water (specific resistance $\rho \sim 10^5 \, \Omega \cdot \mathrm{cm}$) for field strengths $E \sim 0.6 - 0.9 \, \mathrm{MV/cm}$ (duration of the discharge phenomena $\bar{t}_\mathrm{d} \sim 300 - 700 \, \mathrm{ns}$). The experimental data obtained can be summarized as follows [21]. The gap breakdown probability due to discharge initiation and propagation from cathode increases as the interelectrode gap length and voltage exposure time decrease. For water, the threshold values are $d \approx 400 \, \mu\mathrm{m}$ and $E = 0.6 \, \mathrm{MV/cm}$. For smaller d and larger E, the electric discharge propagates from cathode. Figure 3.13 shows the typical laser Schlieren-photograph produced before the gap breakdown and showing details of its propagation. Cone-shaped optical inhomogeneities with a high refractive index gradient and having characteristic size of $\sim 10 \, \mu\mathrm{m}$ are first formed on the cathode surface. The average rate of their growth is $\sim 10^4 - 10^5 \, \mathrm{cm/s}$, and depends on the electric field strength. As the inhomogeneity size increases and the primary channel with a length of $\sim 20 - 25 \, \mu\mathrm{m}$ is formed (Fig. 3.13a), a region of weak perturbation is formed ahead of it. Then it is transformed into an optical inhomogeneity with a high refractive index gradient which further takes a complex shape. The study of its structure with more intensive laser illumination has demonstrated that it consists of microinhomogeneities with sizes of $\sim 15 \, \mu\mathrm{m}$ which are reminiscent of vapor-gas microbubbles. The motion of the optical inhomogeneity with a strong refractive index gradient in the gap is accompanied by preliminary formation of weaker perturbations (for example, see Fig. 3.13b).

The number of channels is $\sim 1 - 3$, and the velocity of their propagation is $\sim (1 - 2) \cdot 10^5 \, \mathrm{cm/s}$. These parameters depend on the electric field strength. The breakdown terminates when one of the channels touches the opposite
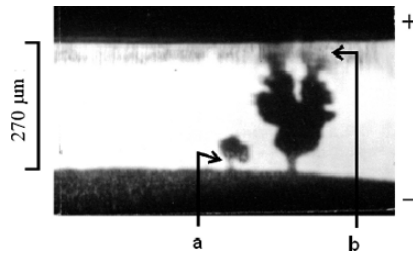
Fig. 3.13. Laser Schlieren-photograph of the electric discharge from cathode in distilled water for a field strength of 0.6 MV/cm, breakdown lag time of ~ 700 ns, and frame exposure time of ~ 5 ns. The frame was produced 10 ns before the gap breakdown

electrode. In general, the pattern of the discharge propagation from cathode is described by the bubble breakdown mechanism, and the discharge itself can be referred to slow, that is, subsonic (see Chap. 4 and 8). In the intermediate region, the electric discharge propagates either from cathode or from anode. In this region, two different breakdown mechanisms coexist and compete. The pattern of discharge propagation from anode as a whole corresponds to that described above. The optical inhomogeneities on the cathode at the initial time moment are similar to perturbations on the anode, but are slightly smaller in size. The average velocity of discharge propagation from anode in this stage is $\sim 10^4 - 10^5$ cm/s. When the optical inhomogeneity reaches a critical size of $\sim 40 - 50$ μm, the second stage begins characterized by the initiation of the intensive electric discharge propagating toward the cathode with an average velocity of $\sim 10^6$ cm/s. The critical size of the optical inhomogeneity and the characteristic velocity of discharge propagation are smaller than in millimeter gaps.

The typical laser Schlieren-photograph illustrating simultaneous discharge propagation from cathode and anode is shown in Fig. 3.14. The characteristic size of electric discharge channels from cathode is $\sim 40 - 50$ μm (*a*). A faster discharge process (*b*) is initiated on the front of the primary channel propagating from anode. The velocity of its propagation higher than from the cathode leads to the gap breakdown by the discharge from anode.

As follows from the foregoing, the structure of pre-breakdown processes, their mechanisms, and velocities of the discharge propagation from cathode and anode differ in principle.

It should be noted that velocities of electric discharge propagation from cathode of the order of $\sim 10^5$ cm/s were also obtained in millimeter gaps with distilled water [22, 23]. The characteristic velocities of discharge propagation from cathode were $\sim 10^4$–10^5 cm/s under conditions of quasi-uniform fields in hydrocarbon liquids [15, 16, 24]. Thus, the velocities of discharge channel propagation from cathode are by one-two orders of magnitude smaller than from anode under conditions of quasi-uniform fields as well.
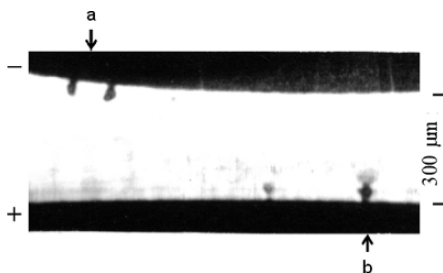
Fig. 3.14. Laser Schlieren-photographs of pre-breakdown processes in distilled water for a field strength of 0.6 MV/cm, breakdown lag time of ~ 680 ns, and frame exposure time of ~ 5 ns. The frame was produced 20 ns before the gap breakdown

3.3 Time Boundaries of Anode and Cathode Discharges in n-Hexane

The most complete experimental results on the boundaries of the cathode and anode mechanisms of electrical breakdown were obtained for n-hexane in a quasi-uniform field for different discharge gap lengths [25, 27]. Experiments were carried out with chemically pure n-hexane (specific resistance $\rho = 10^{12}\,\Omega\,\cdot\,$ cm).

Figure 3.15 shows the dependences of the breakdown lag time in n-hexane on the field strength for two discharge gap lengths. Each point was averaged over 100–150 measurements. Horizontal bars show standard deviations of the results. The horizontal dashed straight lines indicate quasi-static breakdown field strengths. The analysis of a large number of Schlieren-photographs has allowed us to establish the time boundaries of different mechanisms of electrical breakdown of n-hexane. In Fig. 3.15 they are indicated by vertical solid and dashed straight lines for discharge gap lengths of 150 and 100 μm, respectively.

In region *1*, the dependence of the electric strength on the pulse duration ($t_{\mathrm{lag}} \leq 1\,\mu$s) has the form $E_- = 1/t^{0.3}$, and the breakdown is initiated by the electric discharge from cathode.

Qualitative and quantitative characteristics of the phenomena observed in the gap are similar to those described in Sect. 3.2 for the discharge from cathode in water.

In region *3* (see Fig. 3.15), the breakdown is initiated by the discharge from anode. The dependence of the electric strength on the pulse duration ($t_{\mathrm{lag}} \leq 0.5\,\mu$s) has the form $E_+ = 1/t^{0.14}$. The pattern of discharge propagation as a whole corresponds to that for water described above. As a rule, a single cone-shaped optical inhomogeneity with reduced density is formed on the anode surface. The average velocity of discharge propagation in this stage is $\sim 10^4 - 10^5$ cm/s. When the size of the optical inhomogeneity achieves a critical value of $\sim 15 - 20\,\mu$m, the second stage begins. It is characterized by the formation of a bright luminous channel propagating to the cathode with an
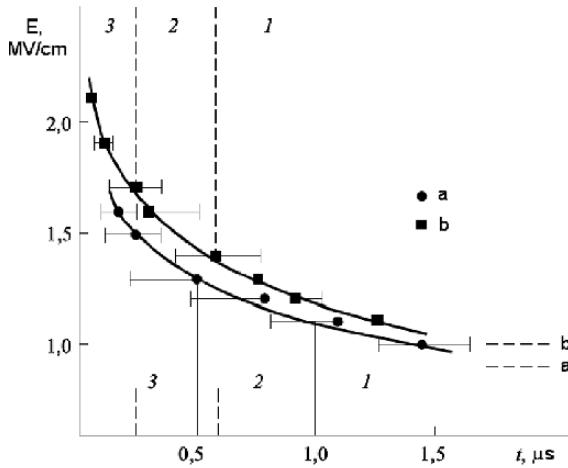
Fig. 3.15. Dependence of the breakdown lag time in n-hexane on the field strength for interelectrode distances of 150 (**a**) and 100 μm (**b**)

average velocity of $\sim 10^6$ cm/s. The critical size of the optical inhomogeneity and the characteristic velocities of discharge propagation are smaller than those for millimeter gaps. It should be noted that optical inhomogeneities are formed near the anode surface under higher electric field strengths, but exactly higher velocities of the channel propagation provide the breakdown completion with the discharge from anode.

For field strengths of $\sim 1.9 - 2.1$ MV/cm and interelectrode distance of 100 μm, another mechanism of breakdown from anode is realized simultaneously with above-described mechanism. It has the form of a uniform (by the structure) electric discharge. It is characteristic that no bubble stage is observed during the discharge initiation. The electric discharge propagates from the very beginning with a high velocity approximately equal to the velocity of the intensive discharge ($\sim 10^6$ cm/s).

Region 2 (see Fig. 3.15) is transitive. In this region, breakdown is initiated by discharges from both cathode and anode. The duration of the transitive region (on the time scale) decreases with decreasing of the interelectrode distance.

From a comparison of data shown in Fig. 3.15 it follows that as the interelectrode distance increases, the field strengths at the boundaries of different mechanisms of n-hexane electrical breakdown decrease, that is, the boundaries themselves are displaced toward longer voltage exposure times. For example, for a field strength of ~ 1.3 MV/cm, the critical distance between the electrodes at which the breakdown mechanism changes is equal to about 150 μm. With increase in the field strength, the critical distance decreases.

Thus, three n-hexane breakdown mechanisms are realized under conditions of quasi-uniform electric field depending on the field strength. One mechanism

describes the electric discharge from cathode, and two more describe the discharge from anode.

The results obtained are important because they explain in more details and more convincingly the fast increase in the electric strength of liquids at times smaller than a certain critical value ($\leq 1\,\mu$s) depending on the inter-electrode distance (see Sect. 6.6.3) established many decades ago. To explain this fact, the breakdown mechanism based on electron emission from cathode and subsequent electron multiplication at the expense of collision ionization and formation of electron avalanches in the liquid itself was usually invoked. The analysis of the results presented here indicates that this phenomenon is caused by transition from the mechanism of breakdown from cathode (the bubble mechanism) to the electric discharge from anode involving both bubble and ionization breakdown mechanisms. The last mechanism requires higher field strengths and has higher propagation velocities. For even higher field strengths, conditions for direct ionization discharge initiation (homogeneous discharge) are created. The discharge formation time decreases due to the absence of the bubble stage. It seems likely that this mechanism of breakdown from anode will be dominant for voltage pulse exposure times $\leq 10\,$ns. From the data obtained it follows that the discharge from anode is initiated in a quasi-uniform field under higher voltages applied to the gap in comparison with the cathode discharge.

The critical time is of great importance in the theory of electrical breakdown because it is used in calculations of charge carrier mobility in strong fields [28, 29]. Taking into account the complex character of the electric discharge from anode, it should be noted that such estimates of the mobility of charge carriers should be used with care.

In [30] it was assumed in the context of the ionization breakdown mechanism that the critical distance is determined by the condition of generation of the critical space charge in the avalanche, necessary for the transformation of the avalanche into the streamer. As follows from the results presented here, when the interelectrode distance exceeds the critical value, the electric discharge propagates from anode. Exactly high velocities of intense discharge propagation cause the weak dependence of the breakdown lag time on the discharge gap length for interelectrode distances larger than critical ones.

3.4 Influence of the Pressure on the Electric Discharge Mechanisms

An increase in the external pressure is one of the methods of increasing the electric strength of liquid dielectrics (Sect. 6.3). Elucidation of physical principles underlying this method is of great practical interest. Scientific interest is caused by the important but not always clear role of gas and its formation for discharge ignition and propagation in liquid.

The influence of pressure on electrical breakdown of liquids of various types was investigated in [31]. A special discharge chamber with optical windows was used in experiments; the pressure in the chamber was produced with the help of a manual hydraulic press of piston type.

Figure 3.16 shows the dependences of n-hexane breakdown lag time on the pressure for the indicated field strengths and an interelectrode distance of 100 μm. Each point was averaged over 100–150 measurements. The dashed curves interpolate the experimental data to pressures at which the breakdown probabilities are $\leq 40\%$.

The strong influence of pressure on the electric discharge was revealed under conditions of breakdown from cathode for field strength of ~ 1.3 MV/cm (see curve 1 in Fig. 3.16). No breakdown was observed during 50 μs (time constant of voltage pulse decay) already under a comparatively low pressure of ~ 0.4 MPa.

Under conditions of competitive coexistence of the discharge from both cathode and anode ($E = 1.6$ MV/cm and $d = 100$ μm), the external pressure influences primarily the electric discharge from anode.

For example, the breakdown propagated from cathode as a single channel at a pressure of ~ 0.7 MPa. The pressure affects the velocity of channel propagation which is equal to $\sim 7 \cdot 10^4$ cm/s. As can be seen from curve 2 in Fig. 3.16, the breakdown is no longer initiated at a pressure of ~ 1 MPa.
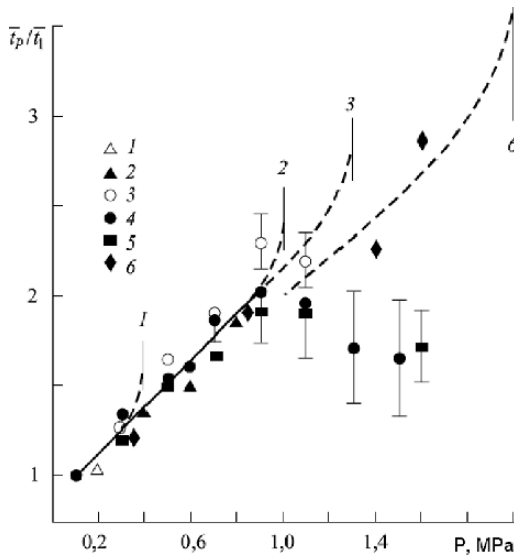
Fig. 3.16. Dependence of the relative breakdown lag time $\bar{t}_P/\bar{t}_1$ for n-hexane (1–5) and distilled water (6) on the external pressure. Here $\bar{t}_1$ is the average breakdown lag time at atmospheric pressure. The electric field strengths were 1.3 (1), 1.6 (2), 1.7 (3), 1.9 (4), 2.1 (5), and 0.9 MV/cm (6); $\bar{t}_d = 750$ (1), 290 (2), 230 (3 and 6), 100 (4), and 50 ns (5)

Under conditions of the breakdown terminated by the discharge from anode for a field strength of $\sim 1.7\,\mathrm{MV/cm}$, the pressure mainly influences the electric discharge from anode hindering its propagation. At elevated pressure, the breakdown is also initiated from the cathode. The electric discharge from anode, unlike the conventional one, is shaped as a homogeneous zone $\sim 30-40\,\mu\mathrm{m}$ wide with smeared boundaries. The velocity of discharge propagation is the same as of the intensive discharge; it is equal to $\sim 2\cdot 10^6\,\mathrm{cm/s}$ for $E = 1.7\,\mathrm{MV/cm}$. In this case, no cone-shaped perturbations corresponding to the initial bubble stage were observed near the electrode surface. Channels of the electric discharge from cathode differ by their rectilinearity; they had transverse sizes of $\sim 10-15\,\mu\mathrm{m}$. Separate optical inhomogeneities with characteristic sizes of $\sim 10-15\,\mu\mathrm{m}$ spaced at the same distance were also observed near the cathode surface. The breakdown started mainly from the cathode as the pressure increases, and no breakdown was observed at a pressure of $\sim 1.3\,\mathrm{MPa}$.

Thus, for field strengths of $\sim 1.3-1.7\,\mathrm{MV/cm}$, the electric discharge from both cathode and anode can be suppressed with the help of external pressure. The breakdown field strength increases with pressure according to the law $E_{\mathrm{br}} = p^{1/5}$.

The character of pressure influence on the breakdown lag time changes significantly for field strengths $\geq 1.9\,\mathrm{MV/cm}$ (for nanosecond voltage pulses). From curves *4* and *5* in Fig. 3.16 it can be seen that the breakdown lag time increases with pressure up to 1 MPa. However, with further increase of pressure, this dependence saturates or the breakdown lag time even slightly decreases. Carbon liberated in the discharge region and changes in the *n*-hexane composition at elevated pressures can somewhat decrease the breakdown lag time. A comparison with the results of optical investigations demonstrates that at elevated pressures, the homogeneous discharge propagates mainly from the anode. The external pressure does not influence the velocity of the discharge propagation equal to $\sim 2\cdot 10^6\,\mathrm{cm/s}$. Thus, exactly the coexistence and competition of two different mechanisms of breakdown from anode determine the complex character of the influence of the external pressure on the average discharge lag time in the nanosecond range.

For a comparison, curve *6* in Fig. 3.16 shows the dependence of the breakdown lag time on the pressure in distilled water under conditions of breakdown from cathode in the nanosecond range (the interelectrode distance equal to $200\,\mu\mathrm{m}$ was smaller that the critical one). The qualitative character of the dependence remains unchanged. The strong influence of the pressure on the electric discharge from cathode is confirmed. For a field strength of $\sim 0.9\,\mathrm{MV/cm}$, no breakdown is initiated at a pressure of $\sim 2\,\mathrm{MPa}$.

The external pressure influences the origin and development of optical inhomogeneities near the electrode surface. The decreased influence of the external pressure on the liquid breakdown field strength under conditions of a uniform electric field (the tendency toward saturation) is due to the transition

from the bubble mechanism of breakdown from cathode at low pressures to the ionization mechanism of breakdown from anode at elevated pressures.

3.5 On the Nature of Electric Hardening of Liquids in Micron Gaps

Competitive coexistence of three discharge forms in submillimeter gaps allows us to suggest a new approach to the explanation of fast increase in the electric strength of liquids with decrease in d. To this end, the condition of avalanche-streamer transition borrowed from the gas discharge is conventionally used.

In addition to the material presented in Sects. 3.3–3.4, the results of comparison of optical and statistical investigations of pulsed electrical breakdown of n-hexane in gaps $25-150\,\mu m$ long [33] are presented below. The experimental setup, measurement procedure, and experimental conditions were similar to those described in [27].

Figure 3.17 shows the dependences of the n-hexane breakdown lag time on the field strength for the indicated interelectrode distances. Each point was averaged over 100–150 measurements. Horizontal bars indicate the sampling standard deviation. Horizontal dashed straight lines on the right indicate the quasi-static breakdown field strength. An analysis of the results demonstrates that the character of the volt-second characteristics is determined by the competition of different breakdown types. Change of their boundaries as a
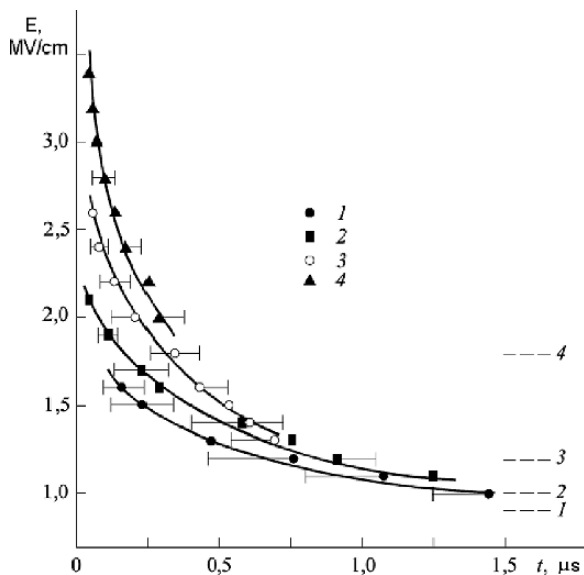
Fig. 3.17. Dependence of the n-hexane breakdown lag time on the field strength for interelectrode distances of 150 (*1*), 100 (*2*), 50 (*3*), and 25 μm (*4*)

Table 3.2. Boundaries of different mechanisms of *n*-hexane breakdown depending on the interelectrode distance *d*

D, µm	β	Breakdown from cathode		Breakdown from anode		Transition region, MV/cm
		E, MV/cm	$E_{cr} \cdot 10^{-2}$, MV/cm	E, MV/cm	$E_{cr} \cdot 10^{-2}$, MV/cm	
25	65	1.8	1.17	2.1	1.4	2.1–3.0
50	90	1.2	1.08	1.7	1.5	1.7–2.3
100	110	1.0	1.1	1.4	1.5	1.4–1.7
150	135	0.9	1.2	1.1	1.5	1.1–1.3

function of the interelectrode distance is illustrated by Table 3.2. In the transition region, the breakdown is initiated by discharges from both cathode and anode. At lower field strengths, the breakdown is initiated by the discharge from cathode, and at high field strengths it is initiated by the discharge from anode.

The increase of the (quasi-static) breakdown field strength with decreasing interelectrode distance occurs for the bubble mechanism of breakdown from cathode. In this case, the main ionization processes resulting in the electric discharge propagation proceed in the vapor-gas phase. Thus, the collision ionization in the liquid itself cannot explain this fact. The dependence of the breakdown field strength on the interelectrode distance can be described by the function $E_{br} \approx 1/d^{0.25}$.

The displacement of the boundaries of breakdown mechanisms toward higher field strengths (shorter pulse duration) with decreasing interelectrode distance leads to different effects of the external pressure on the electric discharge in the nanosecond range.

As demonstrated in Chaps. 1 and 2, the important role in the initiation of the electric discharge is played by the fine physical and chemical processes at the electrode-liquid interface. The important role is played by such factors as the electrode surface microrelief and its changes under the action of previous discharges, adsorbed gas, dielectric or semiconductor microinclusions and films, etc. [34]. For the conditioned electrodes, microbulges on the electrode surface can play the dominant role. They cause the local increase of the field strength.

Using the data on the dependence of the field amplification coefficient β (the ratio of the electric field strength at the top of the bulge to the average electric field strength) on the interelectrode distance in vacuum [35,36], we can roughly estimate the critical field strengths corresponding to different breakdown mechanisms under our conditions. These data are also given in Table 3.2. Here $E_{cr} = \beta(d) \cdot E$, where E is the average field strength. The critical field strengths (microscopic) are independent of the interelectrode distance and are $(1.1 - 1.2) \cdot 10^2 \, \mathrm{MV/cm}$ and $(1.4 - 1.5) \cdot 10^2 \, \mathrm{MV/cm}$ for discharges from cath-

ode and anode, respectively. At such field strengths, the processes of electron emission from cathode to liquid [37] and of ionization of atoms near the anode (electron emission from the liquid) [38] proceed due to a tunnel transition. Exactly these processes can be determining for electric discharge initiation. For cold electron emission in n-hexane, field strengths $\geq 10\,\mathrm{MV/cm}$ [39] are required, and even higher field strengths are required for ionization.

Thus, the increase in the pulsed electric strength of n-hexane with decreasing interelectrode distance can be caused by a decrease in the local electric field strength near the electrode surface that affects the electric discharge initiation.

In conclusion, it should be noted that the results obtained explain the nature of many tendencies characterizing the electric strength of liquids in short gaps with quasi-uniform electric fields. Together with the materials of other sections of the monograph, they will be used to construct models of pulsed discharge in liquids.

References

1. A. P. Alkhimov, V. V. Vorobjev, V. F. Klimkin, et al., On the electric discharge propagation in water, Dokl. Akad. Nauk SSSR, **194**, No. 5, 1052–1054 (1970).
2. E. A. Abramyan, V. A. Kornilov, V. M. Lagunov, *et al.*, Megavolt energy concentrator, Dokl. Akad. Nauk SSSR, **201**, No. 1, 56–59 (1971).
3. V. F. Klimkin and A. G. Ponomarenko, Optical investigations of the electric discharge in water, in: Electrophysical Processes in Liquid Dielectrics and Scientific Problems of Insulating Liquid Application in Electric Power Engineering, Publishing House of Tomsk State University, Tomsk (1976), pp. 196–198.
4. V. F. Klimkin and A. G. Ponomarenko, Investigation of the initial discharge stage in liquid dielectrics by optical methods, in: Proc. XIV Int. Congress on High-Speed Photography and Photonics, Moscow (1980), pp. 385–389.
5. V. F. Klimkin, Super high-speed anode pre-breakdown phenomena in liquid dielectrics with uniform fields, in: Proc. 11th Int. Conf. on Conduction and Breakdown in Dielectric Liquids, Baden-Dättwil (1993), pp. 299–303.
6. V. F. Klimkin, Mechanisms of nanosecond electrical breakdown of water from tip anode, Pis'ma Zh. Tekh. Fiz., **16**, No. 4, 54–58 (1990).
7. V. F. Klimkin and A. G. Ponomarenko, Investigations of pulsed electrical breakdown of liquids by the methods of optical interferometry, Zh. Tekh. Fiz., **49**, No. 9, 1896–1904 (1979); Preprint No. 4, Institute of Theoretical and Applied Mechanics of the Siberian Branch of the USSR Academy of Sciences, Novosibirsk (1978).
8. J. L. Maksiejewski, The effect of additives on the time characteristics of a liquid trigatron, IEEE Trans. Electr. Insul., **EI22**, No. 3, 237–239 (1987).
9. D. D. Ryutov, Diffusion electrodes for investigations of liquid dielectrics breakdown, J. Appl. Mech. Tech. Phys., No. 4, 186–187 (1972).
10. V. V. Vorobjev, V. A. Kapitonov, and É. P. Kruglyakov, Increase in the electric strength of water in a system with diffusion electrodes, Pis'ma Zh. Tekh. Fiz., **19**, No. 2, 95–98 (1974).

11. V. V. Vorobjev, V. A. Kapitonov, É. P. Kruglyakov, and Yu. A. Tsidulko, Investigation of water breakdown in a system with diffuse electrodes, Zh. Tekh. Fiz., **50**, No. 5, 993–999 (1980).

12. I. T. Ovchinnikov, K. V. Yanshin, and E. V. Yanshin, Investigation of pre-breakdown electric field distribution in water with the help of the Kerr effect technique, Zh. Tekh. Fiz., **44**, No. 2, 472–474 (1974).

13. V. V. Lopatin, V. J. Ushakov, and V. P. Chernenko, Ignition and propagation of a nanosecond discharge in liquids, Izv. Vyssh. Uchebn. Zaved., Fiz., No. 3, 100–106 (1975).

14. V. Y. Ushakov, O. P. Semkina, V. V. Ryumin, and B. B. Lopatin, On a nature of pulsed electrical breakdown of water electrolytes, Electronn. Obrab. Mater., No. 2, 48–54 (1972).

15. J. C. Devins, S. J. Rzad, and R. J. Schwabe, Pre-breakdown phenomena in sphere-sphere electrode configurations in dielectric liquids, Appl. Phys. Lett., **31**, No. 5, 313–314 (1977).

16. E. F. Kelley and R. E. Hebner, Pre-breakdown phenomena in sphere-sphere electrodes in transformer oil, Appl. Phys. Lett., **38**, No. 4, 231–233 (1981).

17. E. O. Forster and P. P. Wong, High speed laser schlieren studies of electrical breakdown in liquid hydrocarbons, IEEE Trans. Electr. Insul., **EI12**, No. 6, 435–441 (1977).

18. P. P. Wong and E. O. Forster, High-speed schlieren studies of electrical breakdown in liquid hydrocarbons, Can. J. Chem., **55**, 1890–1898 (1977).

19. P. P. Wong and E. O. Forster, The dynamics of electrical breakdown in liquid hydrocarbons. I, // J. Electrostat. **5**, 157–168 (1978).

20. R. E. Hebner, E. F. Kelley, E. O. Forster, and G. J. Fitzpatrick, Observation of pre-breakdown and breakdown phenomena in liquid hydrocarbons, J. Electrostat., **12**, 265–283 (1982).

21. V. F. Klimkin, Special features of electrical breakdown in water in submillimeter gaps, Zh. Tekh. Fiz., **57**, No. 4, 805–807 (1987).

22. A. P. Avrorov and V. V. Vorobjev, Statistical investigations of the mechanism of microsecond water breakdown, Preprint No. 83–69, Nuclear Physics Institute of the Siberian Branch of the USSR Academy of Sciences, Novosibirsk (1983).

23. S. N. Komin, G. S. Kuchinskii, and E. A. Morozov, A mechanism of disruption of the electric strength of water in the microsecond range, Zh. Tekh. Fiz., 54, No. 9, 1826–1829 (1984).

24. J. L. Maksiejewski, Time-lags of triggered spark gaps in liquid hydrocarbons, IEEE Trans. Electr. Insul., **EI20**, No. 2, 339–342 (1985).

25. V. F. Klimkin, Special features of the development of a micronanosecond electrical breakdown in n-hexane, Zh. Tekh. Fiz., **56**, No. 10, 2041–2043 (1986).

26. V. F. Klimkin, A pulsed electrical breakdown in n-hexane under a uniform field, in: Conf. Record of the 10th Int. Conf. on Conduction and Breakdown in Dielectric Liquids, Grenoble (1990), pp. 574–578.

27. V. F. Klimkin, Boundaries of mechanisms of electrical breakdown in n-hexane with quasi-uniform field, Zh. Tekh. Fiz., **61**, No. 8, 80–83 (1991).

28. P. Felsenthal, Nanosecond breakdown in liquid dielectrics, J. Appl. Phys., **37**, No. 10, 3713–3715 (1966).

29. K. D. Metzmacher and J. T. Brignell, Apparent charge mobility from breakdown times in a dielectric liquid, J. Phys., **D3**, No. 2, 103–104 (1970).

30. V. F. Klimkin and V. V. Pikalov, Opportunities of microinterferometry for a study of nonstationary processes, Zh. Prikl. Mekh. Teor. Fiz., No. 3, 14–26 (1979).
31. I. K. Kikoin, ed., Tables of Physical Quantities, Atomizdat, Moscow (1976).
32. N. M. Baron, É. I. Kvyat, E. A. Podgornaya, *et al.*, Handbook of physical and chemical quantities, Khimiya, Lenengrad (1972).
33. V. F. Klimkin, V. V. Pikalov, and R. I. Soloukhin, Optical interferometry of spherical shock waves, in: Shock Waves, Explosions and Detonations, J. R. Bowen, N. Manson, A. K. Oppenheim, and R. I. Soloukhin, eds.; AIAA J., **87**, 196–204 (1983).
34. D. W. Swan and T. J. Lewis, Influence of electrode surface conditions on the electrical strength of liquified gases, J. Electrochem. Soc., **107**, No. 3, 38–43 (1960).
35. K. Tsuruta, Impulse electrical breakdown fields of short vacuum gaps, IEEE Trans. Electr. Insul., **EI22**, No. 1, 77–79 (1987).
36. G. A. Mesyats and D. I. Proskurovskii, Pulsed Electric Discharge in Vacuum, Nauka, Novosibirsk (1984).
37. B. Halpern and R. Gomer, Field emission in liquids, J. Chem. Phys., **51**, No. 3, 1031–1047 (1969).
38. B. Halpern and R. Gomer, Field ionization in liquids, J. Chem. Phys., **51**, No. 3, 1048–1056 (1969).
39. K. Dotoku, H. Yamada, S. Sakamoto, *et al.*, Field emission into nonpolar organic liquids, J. Chem. Phys., **69**, No. 3, 1121–1125 (1978).
40. V. V. Lopatin, Candidate's Dissertation in Physical and Mathematical Sciences, Tomsk Polytechnic Institute, Tomsk (1972).

Discharge Propagation in Gaps
with a Non-Uniform Field

Many phenomena observed in discharge gaps under a uniform electric field at the stage of ionization process propagation from the initiating electrode (Chap. 3) are also observed in gaps under a sharply non-uniform field, primarily at the initial stages of discharge propagation. This is quite explicable, because in the first case, the initial plasma formations (in the incipient channel) convert the uniform field into a non-uniform one. In the second case, the incipient processes develop in the region adjacent to the electrodes, that is, in the region of strong field whose magnitude is close to the electric strength of liquids in short gaps with uniform fields. This as though levels the difference between the conditions of discharge propagation in gaps with uniform and non-uniform fields.

The discharge propagation in gaps with a non-uniform field, in particular, for long interelectrode distances (in the so-called long gaps) is the stage of the breakdown more important than the stage of discharge ignition; it determines largely the impulse electric strength of liquids. In addition, the parameters of the propagation channel predetermine the properties of the spark channel used in practice as a source of various impulse disturbances.

As already indicated in the Preface, investigations of spatial and temporal laws of discharge propagation in dielectric liquids with the help of cameras with mechanical scanning [1–4] and high-speed chronographs built around image converter cameras [5–7] have demonstrated that the discharge in long liquid gaps with non-uniform field under application of impulses whose duration changes from a few microseconds to a few hundred microseconds is very similar to the discharge in long gaseous gaps. Using terminology most commonly used in the literature on the gas discharge, Komelkov [1, 2] called *a leader process* the discharge propagation in a liquid under such conditions.

In [6, 7] it was demonstrated that the leader process with typical stepwise lengthening of the high-conduction channel includes propagation and successive transformation of the *initial channel*. In [7], this term was used for a thin (with a thickness of a few microns) low-conduction channel that propagates continuously (or quasi-continuously) and is accompanied by a weak

luminescence and low current that remain unchanged with time. In more recent studies, these channels were referred to as monochannels [8,9] or weakly luminous filaments [10–13]. In some specific cases, for example, in liquids with low electrical conduction, when the voltage applied to the discharge gap is close to or less than the minimum breakdown voltage, the discharge propagates on the impulse tail or on the oblique impulse with a mild slope, and the initial channel can propagate at long distances without conversion into a leader channel.

After the leader bridges the electrodes, *the main* or *back discharge* is propagated. When the power capacity of the high-voltage source is sufficient, the main discharge is followed by *an arc*.

When the low-conduction initial channel is not converted into a leader or the leader channel loses its electrical conduction in the propagation process, *a secondary ionization* process will propagate from the plane to the tip electrode through the channel that has already been formed. Only after that the main discharge and arc are propagated.

In the literature, opinions on the use of the term *leader* differ. Some authors (for example, see [10–12, 14–16]) prefer to use the term *streamer* based on the fact that the leader process in liquids differs significantly from that in gases. Other authors (for example, see [8, 9, 17–19]), on the contrary, use the term *leader* placing strong emphasis on the similarity (at least, external) rather than on the difference. Moreover, they considered that streamers in gases and liquids differ even greater than leaders. To describe the discharge processes in long interelectrode gaps, we adhere to the terminology already used in [7], avoiding, as in the previous chapter, the use of the term *streamer*. When we need not pay attention to fine mechanisms of discharge channel propagation, as in preceding chapters, we will use neutral terms: *a discharge channel*, *discharge figure*, and *discharge structure*.

4.1 Spatial Structure of a Discharge

The shape of discharge figures is one of the sources of information on the liquid breakdown mechanism. Moreover, since discharge channels have high enough electrical conduction, the discharge figure parameters (the shape and dimensions of the figure and the density of channels forming the figure) determine the shape and strength of a macroscopic (average) field at the head of the propagating channel and thereby influence its propagation velocity and finally the electric strength of liquids.

The shape of the discharge figures and their evolution in space and time are extremely sensitive to changes in the applied voltage parameters (in particular, in the impulse amplitude and polarity), discharge gap geometry, and properties and state of the liquid. In this regard, it is expedient to describe the discharge under certain reference conditions and then to demonstrate its changes depending on the factors listed above.

   With allowance for the available data volume and their practical importance, we have chosen the following reference conditions:

– transformer oil (in separate cases, distilled water) under normal conditions (atmospheric pressure, room temperature, and technical purity grade) as a liquid under study,
– standard (lightning) or close to rectangular voltage impulse.

4.1.1 Appearance of Discharge Figures

Numerous thin channels are propagated on the voltage impulse front (less often on the voltage impulse peak) from the tip electrode. They comprise spherical formations that reproduce well the electric force lines in the gap [10, 20, 21]. Successive conversion of this figure includes lengthening of channels, their branching, origin of new channels at the electrode surface, and decay of the majority of them. These channels are converted into microbubble chains that generate weak shock waves.

   According to the classification suggested by the researchers from the LEMD laboratory [10, 11, 14], this figure is the *1st mode** discharge. It is characterized by a subsonic propagation velocity ($\leq 10^5$ cm/s) and low current ($\sim 10^{-4}$ A).

   Within a few (2–5) microseconds from the inception, a small number of channels (typically 2–6) continue to propagate toward the opposite electrode. Their radii increase from several units to several tens of microns.

   As can be seen from Fig. 4.1, the velocity of channel propagation remains essentially unchanged ($\sim(1.5$–$2)\cdot10^5$ cm/s) in the entire interelectrode gap;
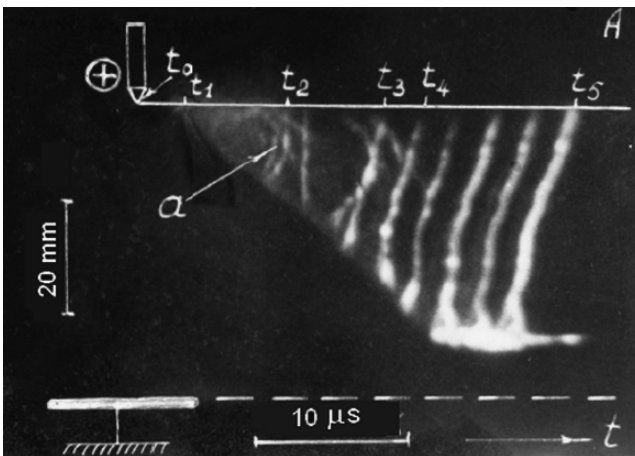
Fig. 4.1. Streak photograph of a partial discharge in transformer oil for the $+$T $-$P gap, $d = 5$ cm, and $U = U_{50\%} = 145$ kV [7]

it exceeds the sound velocity in transformer oil ($1.4 \cdot 10^5$ cm/s) [7]. The figure formed by these channels is called the *2nd mode discharge figure*.

The 2nd mode discharge figures are recorded for a sufficiently wide range of applied voltage impulse amplitudes (Figs. 4.2 and 4.3 [10,11]). Roughly, the external contours of the 2nd mode discharge figure are considered cylindrical in [10, 11] with the cylinder diameter equal to 0.3–0.6 of the interelectrode distance. The dependence of the length of the 2nd mode partial discharge channels on the applied voltage was close to a linear one, that is, their propagation velocity was independent of the applied voltage for a certain range of voltages (see Fig. 4.4 [22]). The critical length of partial discharge channels was $(0.75$–$0.8)d$. Its increase caused the breakdown to terminate (except cases described in Sect. 4.6).

*Below these figures will be juxtaposed with the figures described in the literature under other names.

With further increase in U above the limiting value U_1 close to $U_{50\%}$, the number of channels propagating simultaneously from the tip increases, and at $U \approx U_\mathrm{a}$ (see Fig. 4.3), they form a quasi-sphere whose diameter is comparable with the interelectrode distance. Sometimes the width of the figure formed by the channels exceeds its length. As demonstrated below, exactly the formation and propagation of this discharge figure determines the constant rate of increase of the channel length in the voltage range U_1–U_a. Two stages of discharge channel propagation, namely, the fast stage with $v \approx (1$–$5) \cdot 10^6$ cm/s that lasts 1–3 µs and the slow stage analogous to the 2nd mode discharge
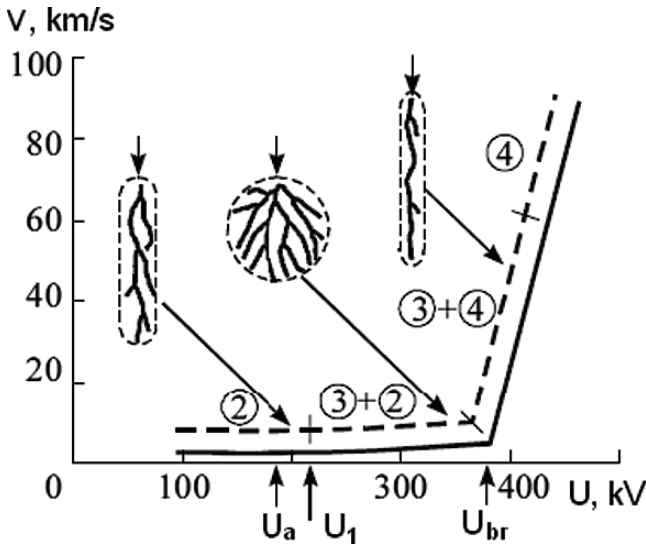
Fig. 4.2. Dependences of the average propagation velocity and shape of discharge figures in transformer oil on the applied voltage for the +T −P gap, $d = 10$ cm, $r_0 = 100$ µm under a 0.4/1400 µs impulse [10]
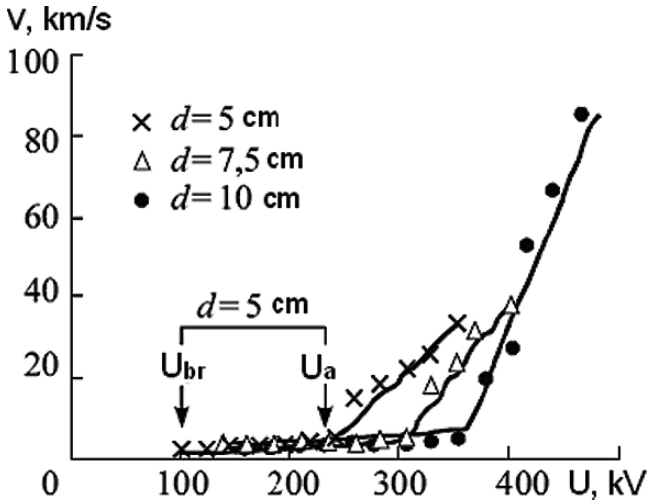
Fig. 4.3. The same as in Fig. 4.2 but for the indicated d values [11]

propagation with $v \approx (1.5\text{–}2) \cdot 10^5$ cm/s are clearly seen in streak photographs taken for the voltage range U_1–U_a. In [3], the fast discharge stage was considered as a separate one called the *initiating streamer*. In [7], high-speed streak photographs were used to demonstrate that this process is a conventional discretely luminescent leader arising on the impulse front under high dU/dt values. An increase in the discharge propagation velocity with dU/dt was established in special-purpose experiments with breakdowns initiated under
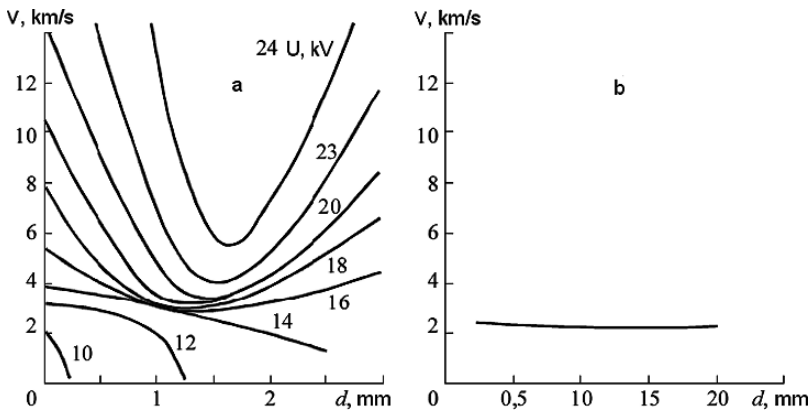
Fig. 4.4. Dependence of the propagation velocity of partial discharges in transformer oil on the $0.4/1400\,\mu$s voltage impulse amplitude for three d values (**a**) and on the position of the channel head in the gap (**b**) for the $+\mathrm{T}\ -\mathrm{P}$ electrode system [22]

application of oblique voltage impulses [23]. In [10, 11, 24], the fast discharge phase was called the *3rd mode discharge*.

When the clearly pronounced threshold U_a is exceeded, the average discharge velocity starts to increase very fast with U (Fig. 4.3). This is due to the fact that at $U > U_a$, the discharge channel (usually one, less often two) is propagated from the spherical discharge figure whose propagation velocity remains essentially unchanged and almost independent of U. This discharge channel is propagated with the velocity exceeding 10^7 cm/s, and closes the remaining part of the gap [5, 7, 24, 25]. In [24, 25], this fast discharge stage was called the *4th mode discharge*.

Because of high discharge velocity in this region and the discharge time close to that of the very bright main discharge, it was impossible to investigate its detailed characteristics except for the rise rate of the accompanying current and luminescence. They increased fast as the channel approached the plane.

Ushakov [23] and Linhjell et al. [24] took several streak photographs and concluded that bright luminosity at this stage was propagated both toward the tip electrode and plane. We failed to find any additional data on this phenomenon in the literature.

The voltage in the 4th mode discharge channel U_a was close to $2U_{br}$ for $d \geq 10$ cm.

Results of measurements of U_{br} of very long (up to 100 cm) rod-plane gaps under 600/3600 μs switching impulses fit well the dependence $U_{br} = f(d)$ obtained for smaller d and shorter (0.4/1400 μs) impulses (Fig. 4.5) [10]. In this case, the discharge time corresponded to a velocity of $\sim 2 \cdot 10^5$ cm/s typical of the 2nd mode discharge. It seems likely that for 1/40 μs short (lightning) impulses in long gaps (>15 cm), breakdown is initiated only by fast dis-
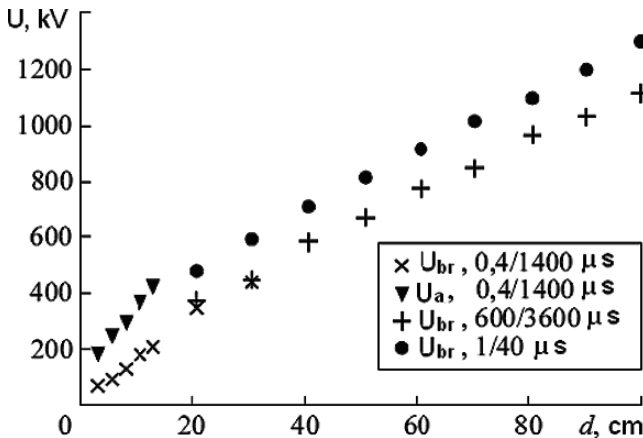
Fig. 4.5. Dependence of U_{br} and U_a on d for oil gaps formed by the tip (or *rod*) – plane electrodes for positive polarity of voltage impulses with different parameters [10]

charges, that is, by the 3rd and 4th mode discharges when the voltage is close to U_{a}. Moreover, U_{a} is much less than U_{br} measured under switching impulses. Lesaint [10] concluded that breakdown of high-voltage oil insulation under overvoltages (for example, in tests with ac voltage and lightning and switching impulses) was initiated by the 3rd and 4th mode discharges.

The terms used above (the 1st, 2nd, 3rd, and 4th mode discharges) are convenient enough for a detailed description of discharge figure conversion accompanying changes in the main influencing factors – applied voltage or voltage rise time (when a breakdown occurs on the voltage impulse front). In this case, changes of the two parameters, namely, of the discharge figure shape and velocity of its propagation to the opposite electrode, are traced.

4.1.2 Electrostatic Properties of Discharge Figures

Considering that discharge channels in liquids are well conductive plasma filaments, it was indicated in [26] based on photographic studies of the discharge figures that "...with increase in the overvoltage, branching of the discharge was considerably intensified. This was the case for both branch density and branching zone diameter, which caused the field to level in the pre-breakdown gap region. Thus, an increase in the voltage applied to the gap was compensated by intense leveling action of the branched discharge region". In [5] this assumption was confirmed by the results of comprehensive study of the discharge with synchronous registration of streak photographs using image converter cameras, still photographs, and current and voltage waveforms. It was established that the number of channels propagating from the tip electrode increased considerably with the rate of voltage increase $A \approx dU/dt$ (a breakdown was initiated on the exponential front of impulses having different slopes). Already for $A > 8$–$10\,\text{kV/µs}$ (in distilled water), channels formed a spherical figure. Events occurring in the discharge gap are well illustrated by Fig. 4.6 [7]. In the still photograph shown in Fig. 4.6B we can see the spherical figure formed by partial discharge channels and the monochannel closing the electrodes.

From the streak photograph it can be seen that relatively slow propagation of the spherical figure is followed by fast propagation of the monochannel. Lesaint [10] succeeded in fixing the inception of this fast channel – the head of one of the streamer channels forming the spherical figure. In [7] it was established that a part of the gap closed with the fast channel increased with U (or A). It was assumed that "the formation of this spherical figure causes mutual deceleration of discharge channels that influences the behavior of the volt-second characteristic of discharge water gaps under a non-uniform field". In this regard, a nature of the very strong dependence of the average discharge velocity on the voltage for $U > U_{\text{a}}$ (Fig. 4.3) becomes evident.

Under voltages significantly exceeding U_{a}, the discharge is formed by 1–2 brightly luminous growing channels that form a cylinder together with branches. In this case, the dependence of charge Q injected into the gap by the
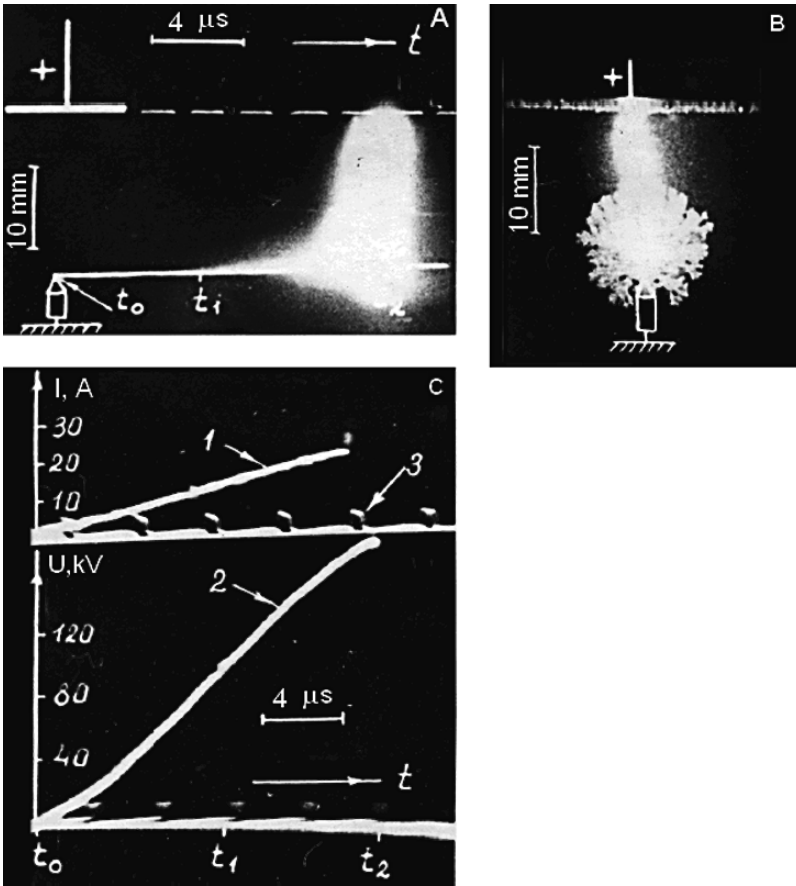
Fig. 4.6. Discharge pattern in distilled water for the –T +P gap, $d = 2\,\text{cm}$, and $A = 11\,\text{kV/μs}$ [7]

discharge channels on the applied voltage changes noticeably (Fig. 4.7) [11]. Whereas Q almost linearly increases for $U_{\text{br}} < U < U_{\text{a}}$ due to an increased number of simultaneously propagating channels, a sharp decrease in Q is observed at $U \approx U_{\text{a}}$ followed by its slow increase as U exceeds the threshold value U_{a}.

Thus, the foregoing indicates the existence of functional relationships among the discharge figure shape, propagation velocity, and charge injected into the insulation gap.

To establish a quantitative relationship among these parameters, calculations of the charge and electric field strength on the external surface of figures formed by channels, including spherical figures for $U_{\text{br}} < U < U_{\text{a}}$ and cylindrical figures for $U = U_{\text{br}}$ and $U > U_{\text{a}}$, were performed in [11].
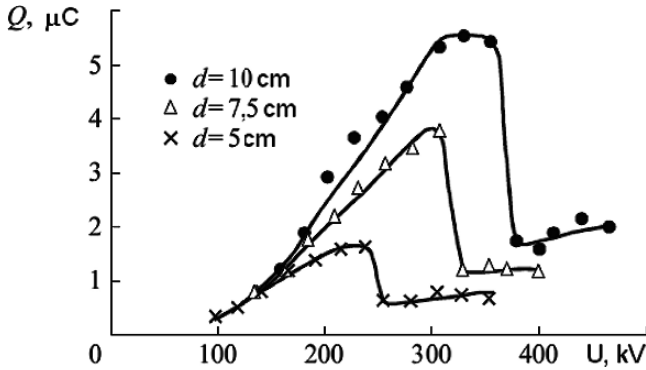
Fig. 4.7. Dependence of the maximum charge induced into the discharge gap on the applied voltage for the $+T-P$ electrode system and a $0.4/1400\,\mu s$ impulse [11]

In the first case, calculations were done for a spherical conducting figure whose potential was equal to that of the high-voltage electrode. The figure diameter increased with the growth of the true figure formed by the channels. Figure 4.8 shows dependences of the calculated and measured injected charges on the ratio of the figure diameter d_{sp} to the interelectrode gap length d. Good agreement between the calculated results and measurements demonstrates that the electrical conduction of the channel is fairly high and that the voltage drop across the channels can be neglected in these calculations.

For the cylindrical discharge figures, the fitting parameter – the cylinder diameter d_{cyl} – was introduced. Good agreement between the results of calculations and measurements can also be seen from Fig. 4.9 for $d_{cyl} = 1\,cm$, $U = U_a = 376\,kV$ $(d = 10\,cm)$ and $d_{cyl} = 3.8\,cm$, $U = U_a = 184\,kV$. These
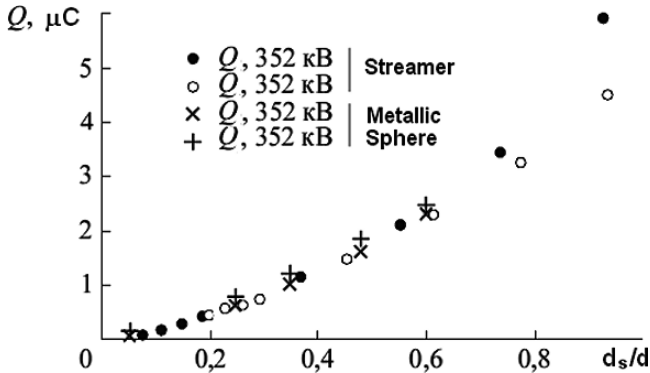
Fig. 4.8. Dependence of the calculated and measured space charge on the ratio of the diameter of the spherical figure (or *spherical electrode*) d_s to the interelectrode distance d $(d = 10\,cm)$ [11]
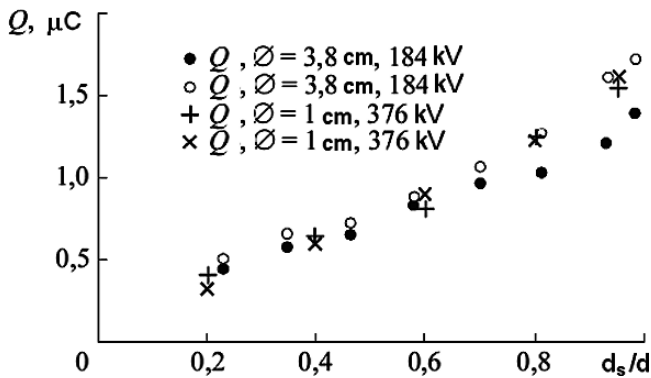
Fig. 4.9. The same as in Fig. 4.8, but for the cylindrical figure

values of d_{cyl} correspond to diameters of figures formed by branched channels with allowance for weak glow surrounding them.

The results obtained allowed Massala and Lesaint [11] to calculate the electric field strength E_f on the surface of the figure formed by discharge channels and to elucidate a reason of changes in the discharge figure shape with U. Figure 4.10 shows changes in the calculated E_f values in the process of discharge figure propagation to the plane for three cases: cylindrical figure at $U = U_{br}$, spherical figure at $U \leq U_a$, and cylindrical figure at $U > U_a$. From Fig. 4.10 it can be seen that the discharge propagates with a low velocity ($\sim 2 \cdot 10^5$ cm/s) when E_f is close to 200 kV/cm; it propagates with a high velocity ($>10^6$ cm/s) when $E_f > 200$ kV/cm. At $U = U_{br}$, E_f slowly increases as the discharge figure grows, but remains less than 200 kV/cm. The discharge then propagates with a low velocity.
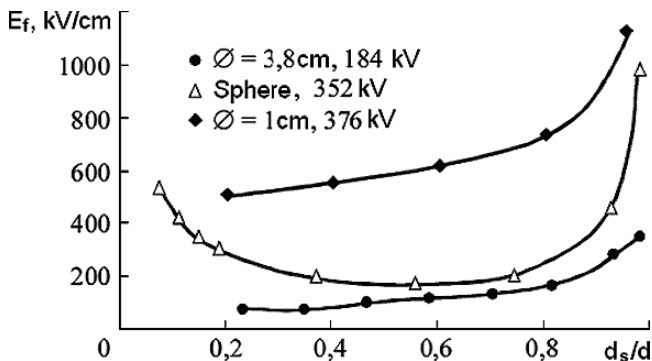
Fig. 4.10. Electric field strength variation on the discharge figure surface E_f during its propagation to the plane ($d = 10$ cm) [11]

The discharge figure shape becomes more and more similar to a sphere with U increasing in the range $U_{br} < U < U_a$. Calculations at $U = U_a$ demonstrated that E_f first decreases, passes through an almost flat minimum ($E_f \approx \text{const}$ for $0.3 < d_f/d < 0.8$), and then increases near the plane electrode. The shape of the curve $E_f = f(d_f/d)$ follows the behavior of the discharge propagation velocity as the discharge propagates from the tip to plane electrode.

Thus, under voltages changing in the range $U_{br} - U_a$, an increase in the number of simultaneously propagating channels and their branching act as a regulating mechanism that compensates for the increase in U and provides essentially unchanged E_f and, as a result, a constant discharge propagation velocity. When the discharge figure assumes a quasi-spherical shape ($U = U_a$), the process of "geometrical field regulation" is terminated. Under large U, the field between the "sphere" and plane approaches a uniform one, and its value is sufficient for initiation of the discharge channel propagating with a high velocity from the head of one of the numerous channels because of high average and local field strengths (the upper curve in Fig. 4.10). This suggests that U_a is the threshold voltage; when the threshold voltage is exceeded, E_f never decreases below $\sim 200\,\text{kV/cm}$. This is also confirmed by the results of calculations shown in Fig. 4.11 [5]. For three U_a values typical of the three inter-electrode distances, the minimum E_f value is kept at a level of $\sim 200\,\text{kV/cm}$. The foregoing demonstrates that the shape of discharge figures determines the macroscopic field strength E_f, which in its turn determines the discharge mode and the main characteristics describing the impulse electric strength of liquids.

Lopatin et al. [21] tried to explain on the qualitative level intensive channel branching for the positive discharge and complex (with a minimum) character of changing the discharge figure propagation velocity toward the plane considering interactions between the Coulomb and Laplace fields. The position of the minimum in curves $v = f(d)$ allows a relationship between these two fields to be estimated which, under assumption that the space charge is localized
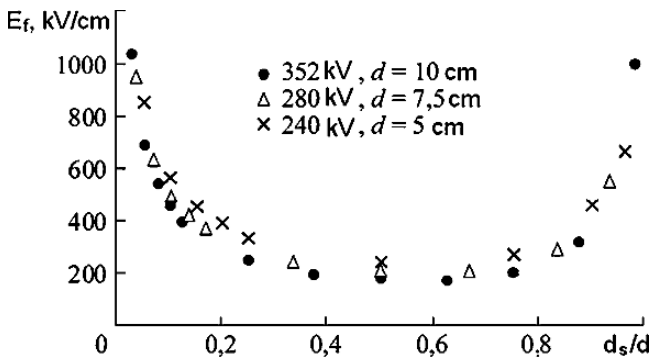
Fig. 4.11. The same as in Fig. 4.10, but for $U \approx U_a$ for the indicated d values and the spherical discharge figure [11]

at the discharge channel head, gives an estimate of the charge of a few tens of picacoulombs. For the discharge channel growth, the field strength at the head E and hence the charge should exceed certain values. When the head is splitted into two heads, the charge is also divided between them. The increase of charge necessary for further growth of both branches is provided by good conduction of the branch.

Depending on the local conditions in the immediate proximity of the channel head, the probability of creation of favorable conditions for branch propagation in alternative directions arises from time to time. Further growth of both branches depends on the head charge. If it exceeds more than twice the charge necessary for branch propagation, it is expected that both branches will grow. If this condition is not satisfied, one of the branches fast decays, which is observed in optical studies of the discharge. Investigations of the branching degree of the discharge channel can give information to estimate roughly the charge (current) that should run through the channel to support branching. This estimate gave a current of $1\,\mathrm{mA}$ [27]. This is in good agreement with measurements of pre-breakdown currents (for example, in [28]).

4.1.3 Dependence of the Spatial Structure of Discharge Figures on the Main Influencing Factors

Polarity of the Initiating Electrode

Breakdown in aliphatic and aromatic hydrocarbons is characterized by the normal polarity effect, that is, the breakdown voltage for negative polarity of the electrode specifying the field non-uniformity is higher than for positive polarity. Quantitatively, for the same liquid it depends on the discharge gap geometry (primarily on d and r_0).

In chlorinated and fluorinated hydrocarbons, the polarity effect is either absent [29] or reverse in character [30] (see below). The discharge figure velocity and shape differ significantly. It is well illustrated by Tables 4.1 and 4.2 borrowed from [24].

In [24], an attempt was undertaken to establish more definite mechanisms of influence of the electrode polarity on the discharge figure shape. It was found that shapes of negative discharge figures change with the voltage more unpredictably than of positive discharge figures. It is pertinent to describe these changes using terms preferably, mainly, and roughly.

Table 4.1. Propagation velocity of positive and negative discharge figures

Positive polarity	Negative polarity	Reference
Supersonic, $\leq 10^6$ cm/s	Subsonic	[31, 32]
Supersonic, $\leq 10^6$ cm/s	Subsonic and supersonic	[18]
Subsonic and supersonic, $\sim 10^6$ cm/s		[33]

Table 4.2. Shape and velocity of positive and negative figures

Positive		Negative		Reference
Shape	Velocity	Shape	Velocity	
Bush-like	Slow	Bush-like	Slow	[34]
Weakly pronounced bush-like	Fast	Weakly pronounced bush-like	Fast	[18]
Bush-like		Branchy		[35]
Filamentary or bush-like		Bush-like		[36]
Bush-like		Bush-like		[32]
Bush-like, treelike	Depends on the pressure and sort of liquid	Bush-like, treelike	Depends on the pressure and sort of liquid	[37, 38]

At low voltages, the negative discharge figure most often resembles the positive bush-like figure, but with a rough structure. It has no very thin peripheral branches. This shape can be kept unchanged as U increases up to $2U_{50\%}$.

The dependence of discharge figure shapes on the voltage polarity was investigated in [39] under impulse breakdown of n-hexane (pure and with different additives). The positive discharge propagated with an average velocity of $2.6 \cdot 10^5$ cm/s, which exceeded the velocity of shock waves propagating from channels in radial directions ($1.09 \cdot 10^5$ cm/s). The discharge figure was bush-like at the initial stage, but converted into filamentary as the process developed further.

Discharge Gap Geometry

The influence of the discharge gap geometry, primarily of the curvature radius of the initiating electrode r_0 and interelectrode distance d, on the breakdown voltage and electric strength is analyzed in Sect. 6.6. This problem has already been discussed in detail in [40,41,119]. To explain this influence, it is of interest to study the behaviour of spatial and temporal discharge characteristics versus the geometrical factors.

In a number of works (for example, see [38,42–46]), it was established that the curvature radius of the tip electrode (in the region of its small values) affects both the discharge structure (its appearance) and propagation velocity.

Figure 4.12 shows dependences of the discharge ignition voltage (the appearance of slow discharge figures) U_{sl} and of the appearance of fast filamental figures U_{fast} on the tip electrode radius and interelectrode distance obtained in [42] for cyclohexane. In [43], these dependences were presented for cyclohexane and pentane.
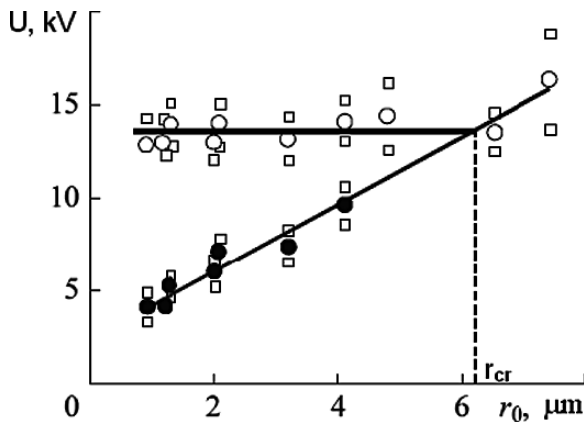
Fig. 4.12. Dependence of the voltage of occurrence of slow (•) and fast (○) channels on the electrode curvature radius (□, 10 and 90% probability of occurrence of channels of both types) in cyclohexane for $d = 2.5\,\mathrm{mm}$ and $t_\mathrm{d} \leq 15\,\mathrm{ns}$ [42]

A certain critical tip electrode radius was established. For $r_0 < r_\mathrm{cr}$ ($\approx 6\,\mu\mathrm{m}$), U_sl increased with r_0, while U_fast remained unchanged. For $r_0 > r_\mathrm{cr}$, slow discharge figures were not observed, and U_fast started to increase with r_0. (According to Gourny and Lesaint [43], $r_\mathrm{cr} \approx 3\,\mu\mathrm{m}$ in pentane.) The field strength E_sl (calculated for an electrostatic field) corresponding to U_sl slowly decreased from 10 to $6\,\mathrm{MV/cm}$ as r_0 increased from 0.9 to $6\,\mu\mathrm{m}$; moreover, it was independent of d. The voltage U_fast depended only on d.

In [45] it was established that at negative polarity and very small r_0 ($\sim 0.5\,\mu\mathrm{m}$), the first observable discharge processes in cyclohexane were thin ($\sim 4\,\mu\mathrm{m}$) filamental channels $\sim 13\,\mu\mathrm{m}$ long, which within 40 ns from the inception were converted into a sphere $\sim 19\,\mu\mathrm{m}$ in diameter [45]. Further evolution of the discharge figures propagating in cyclohexane from the tip ($r_0 = 0.5\text{–}15\,\mu\mathrm{m}$) with positive and negative polarity was investigated in [44]. A $0.2/540\,\mu\mathrm{s}$ voltage impulse was applied, and the interelectrode distance was $5\,\mathrm{mm}$.

Under a low voltage ($6.18\,\mathrm{kV}$), the sphere generates a gas bubble expanding with a rate of $\sim 10^3\,\mathrm{cm/s}$. When the voltage increases to $7.95\,\mathrm{kV}$, the sphere is converted into a hemisphere previously observed in n-hexane [47] and organosilicone oil [48]. In [48], this was explained by the action of electrohydrodynamic forces. With further voltage increase, the discharge forms a figure reminiscent of a pagoda (a pagoda-like figure). From the top of this figure, a channel is propagated which engenders a new pagoda-like figure (as though the second floor). The figures following one after another occupy approximately $50\text{–}70\,\mu\mathrm{m}$ of the gap and then are separated into groups of bubbles oscillating with attenuation.

Under even higher voltage ($29.14\,\mathrm{kV}$ at $r_0 = 15\,\mu\mathrm{m}$), bush-like figures are observed for r_0 lying in the range $0.5\text{–}15\,\mu\mathrm{m}$. Their propagation velocity increases from $1.8 \cdot 10^3\,\mathrm{cm/s}$ to $6 \cdot 10^3\,\mathrm{cm/s}$ as r_0 increases in this range. For

$3 < r_0 < 5\,\mu$m, the bush-like figure grows from the head of a thin monochannel located at a distance of several microns ($<10\,\mu$m) from the electrode rather than from the electrode itself. If the diameter of this channel is greater than $2r_0$, the charge is injected directly from the electrode; if it is smaller than $2r_0$, the charge is injected from the channel head. Figure 4.13 shows the diagram of various discharge figures in the coordinates applied voltage – tip electrode radius.

For positive polarity of the tip having a small radius ($r_0 < 3\mu$m), the discharge under low voltage is bush-like and propagates with the velocity $(1.2$–$2.7) \cdot 10^4$ cm/s. For large r_0 ($> 5\,\mu$m), as for negative polarity, a thin monochannel is initiated under low U. If the voltage increases above a certain limit, the discharge acquires a filamental shape; it propagates with a velocity of $(1.1$–$2) \cdot 10^4$ cm/s. Figure 4.14 illustrates the diagram of positive discharge shapes versus r_0 and U. As in [42, 43], Fig. 4.14 demonstrates the presence of several threshold U and r_0 values for filamental channels.

Significant influence of the voltage not only on the shape but also on the sequence of events and parameters of discharge channels was pointed out in [7] for long discharge gaps. It was found that under low U ($U < U_{50\%}$), the discharge in transformer oil is shaped as the initial poorly conducting channel without its conversion into a high-conduction channel, while under high U, the initial channel is converted into a leader channel after passage of a distance of 1–2 mm (for $d = 2$–10 cm) (for more details, see Sect. 4.2).

The main results obtained in [7] were confirmed in [9, 49], and the strong influence of the tip electrode curvature radius (the degree of field non-uniformity) on the conversion of the initial channel (the monochannel according to the terminology used in [9, 49]) into a leader channel was reported.
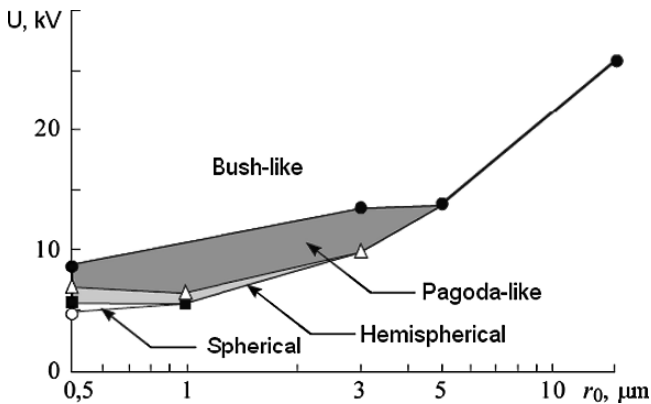
Fig. 4.13. Change of the shape of discharge figure propagating from the negative tip attendant to changes in its radius and voltage impulse amplitude [44]
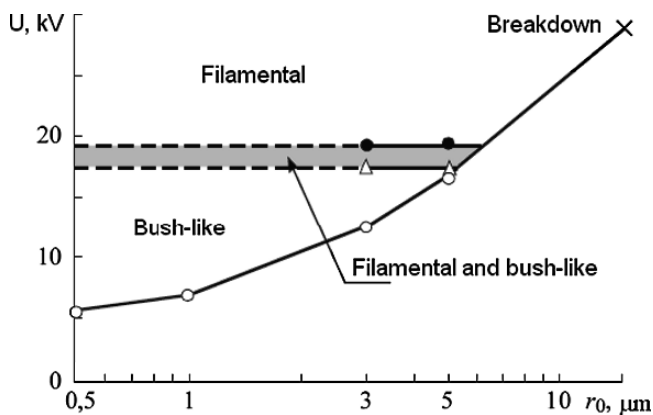
Fig. 4.14. The same as in Fig. 4.13, but for positive tip polarity [44]

Liquid Properties and State

Since the discharge in transformer oil has been studied in most details, we often compare (where it is possible and expedient) the influence of properties and state of liquids on the discharge propagation mechanism with transformer oil.

Attempts of studying the influence of *viscosity* on the breakdown characteristics of liquids with radically different viscosity values, as a rule, did not provide unambiguous results. This is explained by the fact that in these studies it was not possible to separate the viscosity effects from the effects caused by the difference of the entire set of liquid characteristics. Experiments with one liquid whose viscosity is adjusted by changing the temperature are more correct.

In [50], the spatial characteristics of the discharge in transformer oil were investigated at 6 fixed temperatures from the interval $-40 - +25°$C at which the viscosity changed from 3114 to 15 cSt (cantiStokes).

For positive tip electrode polarity, the discharge ignition voltage (when the first visible changes in the optical density of the liquid are observed) U_{ign} increases from 91 kV at $\eta = 15$ cSt to 130 kV at $\eta = 1518$ cSt. For small η, the discharge propagates as a hemispherical (umbrella-like) figure with an angle wider than 180°; it consists of many straight filamants. Down to $\eta = 270$ cSt, this shape remains unchanged, but the angle decreases and several thicker and brightly luminous channels arise near the tip anode. A breakdown of the gap is initiated by one-two dominant channels propagating from the initial umbrella-like structure and growing with a velocity of $(1.1–1.6)\cdot10^6$ cm/s. At $\eta = 3114$ cSt, only 1–2 channels propagate from the tip. The independence of the initial structure propagation velocity $((2–3)\cdot10^5$ cm/s$)$ of the viscosity turned out to be unexpected. However, the discharge time t_d decreased

with increase in η, since the fast channel bridges all the larger part of the interelectrode gap.

For negative tip electrode polarity, U_{ign} and the channel propagation velocity are essentially independent of η and make ~ 68 kV and $(1–3) \cdot 10^6$ cm/s, respectively. As η increases, the discharge shape is converted from the bush-like into a fan-shaped.

Important data on the liquid breakdown mechanism were obtained in the study of changes in the discharge processes after incorporation of *additives* that influence generation and further behavior of charge carriers into the liquid.

In [36] it was established that after incorporation of additives – electron acceptors – into the liquid, the rate of growth and length of channels of partial discharges propagating from the tip with negative polarity increase. These additives reduce the free path of electrons injected from the channel head. The latter, in turn, reduces the volume of the liquid where the energy of these electrons is liberated. This promotes heating and boiling of the liquid. If the excess electrons penetrate deeper into the liquid and do not cause boiling, their influence on the channel propagation is reduced to shielding of the channel head field.

For the discharge from the tip with positive polarity, a decrease in U_{fast} was established in [51], and an increase in the velocity was established in [36] after incorporation of additives with low ionization potential. According to [52], such additives facilitate the development of avalanches warming the liquid. Shielding of the positive channel head field is less significant compared with negative channel head field or is not observed at all. The additives influence also the number of channels propagating from the tip electrode, their branching, and propagation velocity.

The positive discharge propagation velocity increases after incorporation of easily ionized additives into *n*-hexane, and the negative discharge propagation velocity increases after incorporation of additives with large electron interaction (capture) cross section. In this case, the positive figure is shaped as a spheroid or is treelike, and the negative figure is bush-like or filamental [39].

The data on the influence of the additive sort and concentration on the average propagation velocities of positive and negative discharges in *n*-hexane are tabulated in Tables 4.3 and 4.4. Figure 4.15 shows the dependence of the positive discharge propagation velocity on the applied voltage for pure *n*-hexane and *n*-hexane with addition of dimethylaniline (DMA).

The data presented in Tables 4.3 and 4.4 were obtained for the tip-plane (T–P) gap with $d = 10$ mm under $U = \pm 45$ kV. The average values are indicated in parentheses.

A purposeful study of the polarity effect in two Galden–XAD and Galden–D40 fluorinated polyethers with molecular weights of 800 and 2000 e.w., Fluorinert–FC–77 chlorinated hydrocarbon, Baysilon M50 organosilicon, and AGIP–ITE 360 transformer oil was carried out in [53]. Generalizing the results of measuring the breakdown voltage and discharge time and comparing

Table 4.3. Influence of additives on the positive discharge propagation velocity in *n*-hexane

Additives	Concentration, M	Velocity $\bar{v}_d \cdot 10^{-5}$, cm/s
Pure		2.60
DMA	0.008	2.62
	0.016	2.63
	0.040	2.70
	0.079	2.78
	0.158	2.86
	0.395	2.78
	0.007	2.58
$SH_3C_{10}H_7$	0.072	2.96
	0.145	3.22
	0.362	3.19

them with the results presented in [54, 55] for other liquids, Forster et al. [53] concluded that the affinity of liquid molecules to electrons and the negative ion mobility in a strong field are important characteristics of the liquid influencing the discharge processes.

Murooka et al. [56] generalized the data on the propagation velocity and discharge figure shapes in $+T -P$ and $-T +P$ electrode systems for 13 liquids presented in [37, 38, 57] and in a number of other studies (see Table 4.5).

The voltage U_{sl} of appearance of slow channels (of the 1st mode with $v = (1-2) \cdot 10^4$ cm/s) and the voltage U_{fast} of appearance of fast filamental

Table 4.4. Influence of additives on the negative discharge propagation velocity in *n*-hexane

Additives	Concentration, M	Velocity, $\bar{v}_d \cdot 10^{-4}$, cm/s
Pure		0.6∼0.9(0.8)
	0.010	1.0∼2.3(1.8)
	0.052	1.9∼4.3(2.9)
CCl_4	0.104	3.3∼6.9(4.7)
	0.208	3.3∼7.5(4.8)
	0.520	4.4∼7.3(5.9)
	0.005	1.4∼2.2(1.9)
	0.050	1.8∼2.8(2.3)
$CF_3(CF_2)CF_3$	0.100	3.0∼4.0(2.8)
	0.250	3.2∼6.2(4.1)
	0.007	1.3∼2.1(1.6)
$SH_3C_{10}H_7$	0.072	1.9∼2.2(2.1)
	0.145	1.6∼2.2(1.9)
	0.362	1.7∼2.2(2.0)
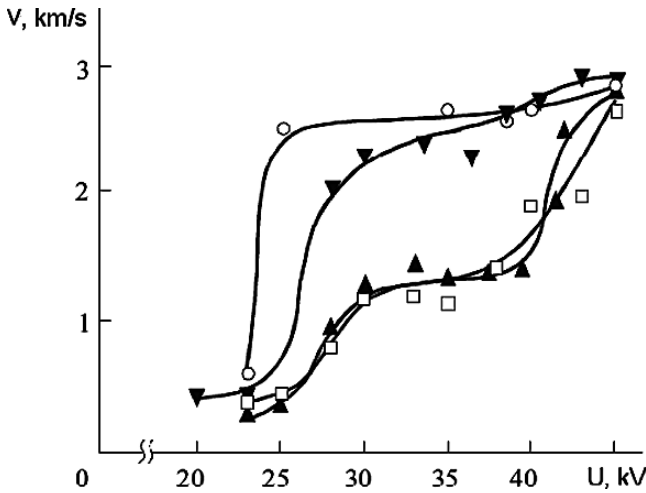
Fig. 4.15. Dependence of the positive discharge propagation velocity on the applied voltage for n-hexane without additives ($\square$) and with addition of DMA with concentration of 0.040 ($\blacktriangle$), 0.158 ($\blacktriangledown$), and 0.395 M ($\circ$) [39]

channels (of the 2$^{\text{nd}}$ mode with $v = (1\text{--}2) \cdot 10^5$ cm/s) measured in [42] for 10 different liquids and 2 mixtures with fixed gap geometry ($r_0 = 1.2\,\mu$m and $d = 1.6$ mm) and impulse parameters (breakdown on the impulse front $\tau_{\text{fr}} = 10$ ns) are tabulated in Table 4.6.

The tip field strength corresponding to U_{sl} was also calculated. Other parameters presented in Table 4.6 (relative permittivity ε, electric strength E_{br}, and ionization potential I_{ion}) were borrowed by Lesaint and Gournay [42] from the literature.

Based on an analysis of the results obtained, Lesaint and Gournay [42] concluded the following.

The field strength near the tip necessary for the discharge ignition (appearance of a slow figure) E_{sl} is between 10 and 11 MV/cm for most liquids. Much lower E_{sl} values were obtained for cyclopentane characterized by the lowest ionization potential, in transformer oil containing 17% of easily ionized aromatic molecules, and in cyclohexane. This is in agreement with the auto-ionization mechanism of charge carrier generation near the tip anode.

The field strength E_{fast} correlates with the electric strength of liquids measured in very short gaps with a sharply non-uniform field; at the same time, E_{sl} and E_{fast} are uncorrelated. These special features demonstrate that under such experimental conditions, breakdown is determined by discharge propagation (the filamental channel) rather than by the discharge ignition (appearance of a slow figure). This is paradoxical enough if we take into account very high average field strengths (1–2 MV/cm). This paradox can be avoided if we take into account that E_{br} were measured in very short gaps ($\sim$50 μm) under U_{br} as low as 6.6–9.6 kV. These values are close to the threshold U_{fast} value at

Table 4.5. Propagation velocity and discharge figure shape (Here B denotes bush-like and T denotes treelike shapes)

Liquid	Inter-electrode distance, mm	Impulse shape	Impulse amplitude, kV		Propagation velocity, km/s		Discharge shape	
			+	−	+	−	+	−
N-pentane	4	2.3/1500	30.9	45.9	0.52	0.18	B	B
			40.4		6.97		T	
N-hexane	4	2.3/1500	32.7	48.1	0.48	0.63	B	B
			45.1		7.61		T	
N-heptane	4	2.3/1500	12.8	48.1	6.32	0.20	T	B
N-octane	4	2.3/1500	30.9	48.1	6.2	0.23	T	B
N-nonane	4	2.3/1500	47.5	48.1	6.67	0.28	T	B
N-decane	4	2.3/1500	52.3	50.4	7.48	0.22	T	B
Cyclohexane	4	2.3/1500	45.1	52.7	3.22	0.35	T	B
2-methylpentane	4	2.3/1500	45.1	48.1	9.33	0.48	T	B
2,3-dimethylbutane	4	2.3/1500	45.1	48.1	5.59	0.24	T	B
H_2O	4	2.3/1500	28.5	37.9	2.73	0.48	B	B
			33.2		45.28		T	B
Liquid N_2	4	1/1600	39.6	43.1	0.31	0.23	B	B
			41.5		29.61	0.23	T	B
Transformer oil	4	2.3/1500	43.3	35.7	5.00	2.3	T	B
						3.38		T
Naphthene oil	67	1/180	327	343	17.8	17.8	B	T

which the fast filamental channel can propagate. If we consider U_{fast} for a uniform field, a breakdown in it at small d is determined by the discharge propagation rather then by its ignition.

Addition of polyaromatic molecules (pyrene) to cyclohexane causes U_{fast} to decrease from the maximum value observed in experiments (14.5 kV) to the minimum value (5.8 kV). *Vice versa*, addition of a large amount of an electron absorber (carbon tetrachloride) does not change U_{fast}. This can be regarded as a confirmation of the fact that ionization of molecules is the main process determining the discharge propagation.

The relationship between the spatial and temporal discharge characteristics, that is, the strong influence of the electrostatic properties of the discharge figure on the electric strength of liquids was illustrated in [58] for benzyltoluene better than for the reference liquids – transformer oil and water.

For positive tip polarity ($r_0 = 2\,\mu\text{m}$ and $d = 6\,\text{mm}$), discharge figures of two types were observed. Under low voltages near the tip, slow channels were recorded that form a spherical figure whose diameter did not exceed 100 μm. Under voltages higher than a certain threshold value ($\sim$12 kV), the discharge continued as a monochannel that propagated with a velocity of

Table 4.6. Voltages of appearance of slow, U_{sl}, and fast channels, U_{fast}, in the indicated liquids and mixtures

Liquids	U_{fast}, kV	U_{sl}, kV	E_{sl}, MV/cm	ε	$I_{ion}(204°C)$, eV	E_{br}, MV/cm
2,2-dimethylbutane	6.2	5.2	9.96	1.87	8.73	1.33
2,3-dimethylbutane	7.3	5.7	10.92	1.89		1.38
Isooctane (2,2,4-trimethylenepentane)	7.4	5.6	10.72	1.94	8.3	1.4
Nytro TOG transformer oil	7.6	4.4	8.43	2.2		
Marcol 52 white oil	8.8	5.3	10.15			
Cyclooctane	9.2	5.3	10.15			
N-pentane	10.3	5.4	10.35	1.84	9.15	1.44
Cyclopentane	10.3	3.4	6.51		7.4	
Π-decane	11.3	4.9	9.39	1.99		1.92
Cyclohexane	14.5	4.4	8.43	2.02	8.75	
Mixtures						
Cyclohexane + pyrene (saturation at 20°C)	5.8	4.4				
Cyclohexane +10% carbon tetrachloride	13.2	4.1				

$(0.8–1.0)\cdot10^5$ cm/s. An increase in U in the range $\sim(12–30)$ kV caused a gradual increase in the number of simultaneously propagating channels that formed a hemispherical figure whose center coincided with the tip electrode point. Further increase in U caused the occurrence of figures that were not observed in other liquids (Fig. 4.16). A hemispherical secondary discharge figure similar to that propagating from the tip electrode was propagated from the head of the dominant channel. This process repeated several times until the entire gap between the tip and plate fabricated from polytetrafluoroethylene coating the plane electrode was covered. (Something similar was observed only when the discharge propagated in transformer oil along the pressboard surface (see Fig. 4.17 borrowed from [52]). Unlike the discharge channels in other liquids, their continuous and repeated branching was not observed.

The kinetic characteristics, for example, the dependence of the channel stopping lengths (Fig. 4.18 [58]) and of the probability that the channel achieves the substrate (Ψ, %) on the voltage impulse amplitude were also anomalous. Both dependences were similar. An almost linear increase in L for $U = 11–17$ kV was followed by a fast increase in L for $U \approx 17–25$ kV and its successive smooth increase. (Under analogous conditions, L and Ψ, in %, smoothly increased with U in transformer oil and alcohol.) The number of channels N forming hemispherical figures smoothly increased for the entire range of U variations ($N \approx 14$ for $U = 30$ kV), and the figure size reached maximum ($L \approx 3.3$ mm at $U \approx 16$ kV) and then decreased down
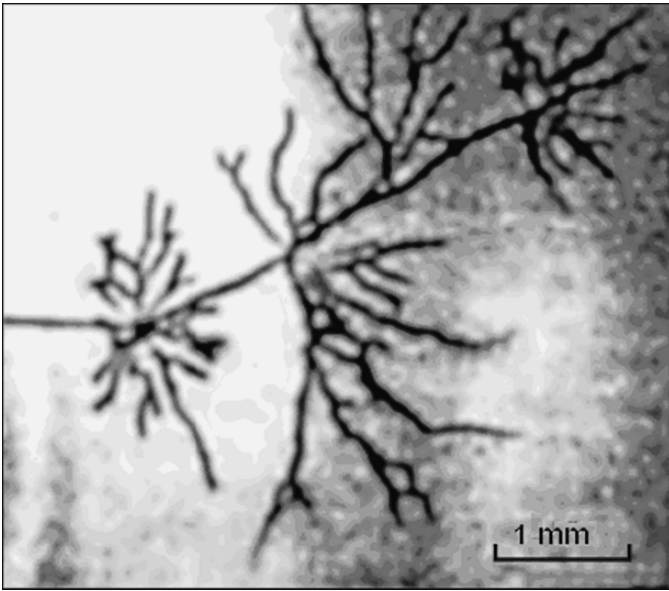
Fig. 4.16. A discharge figure in benzyltolyene from the tip electrode ($r_0 = 2\,\mu m$) of positive polarity $2\,\mu s$ after the beginning of propagation. The distance between the electrodes was $6\,mm$ [58]

Fig. 4.17. Schematic image of the discharge in transformer oil propagating over the pressboard surface [52]
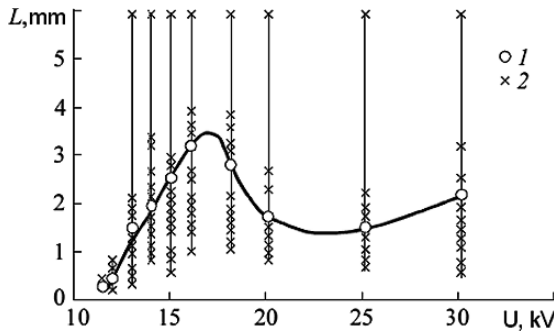
Fig. 4.18. Dependence of the maximum channel length L on the positive impulse amplitude. Here *curve 1* shows average values, and *curve 2* is for the current measurements [58]

to 0.5–0.7 mm under $U = 30\,\text{kV}$. The velocity of discharge channel propagation increased from $\sim 0.7 \cdot 10^5\,\text{cm/s}$ under $U \approx 12\,\text{kV}$ to $1.0 \cdot 10^5\,\text{cm/s}$ under $U \approx 17\,\text{kV}$ and remained constant with further increase in U. Many of the above-indicated special features were observed in breakdowns of benzyltoluene in long discharge gaps [59]. In particular, it was found that the partial discharge channel length L in this liquid remained essentially unchanged as the voltage in the gap increased in the range $(0.5–0.7)U_{50\%}$ (Fig. 4.19), while in transformer oil under the same conditions L approximately linearly increased with U (Fig. 4.20 [60]).
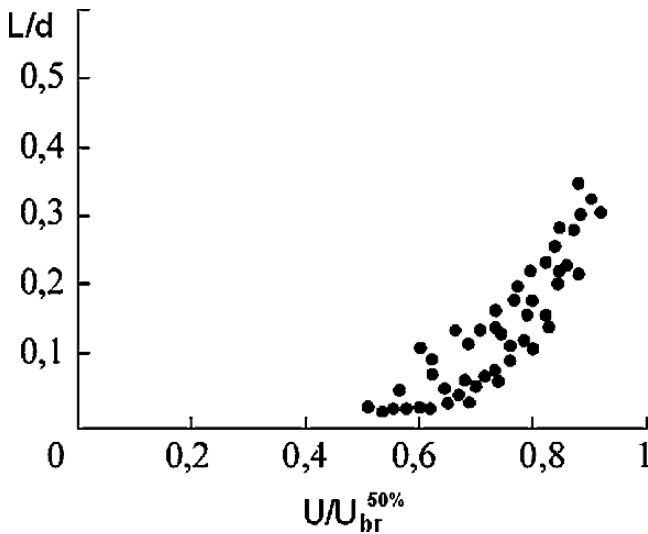
Fig. 4.19. Dependence of the relative length of partial discharge channels in benzyltoluene on the impulse amplitude normalized by $U_{\text{br}}^{50\%}$ ($U/U_{\text{br}}^{50\%}$) [59]
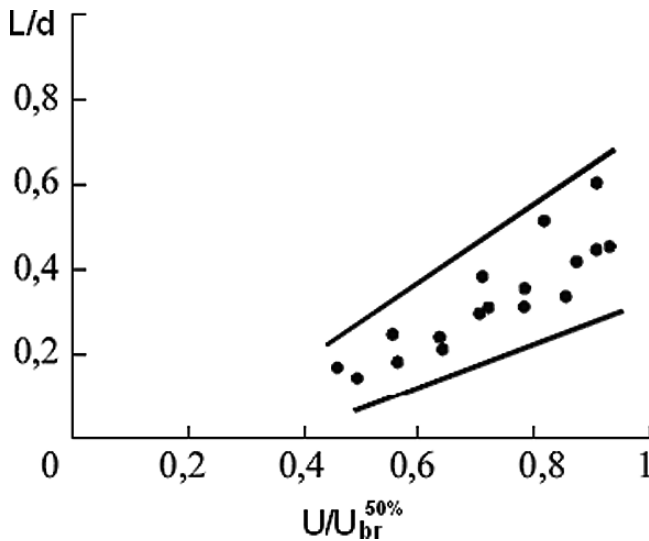
Fig. 4.20. The same as in Fig. 4.19, but for transformer oil [60]

Numerous attempts were undertaken to establish a relationship of the spatial and temporal characteristics with the *molecular structure* of liquids. Cyclic and linear hydrocarbons with double and triple bonds were investigated (for example, see [61, 62]).

In all studies, a weak dependence of the spatial structure, propagation velocity, and current accompanying the discharge structure propagation on the molecular structure of liquids was pointed out.

Thus, for example, according to [62] the discharge propagation velocity for n-hexane, n-heptane, n-octane, and n-decane as well as for the same liquids but having double and triple bonds in molecules changed in the limits $(2.01–2.65){\cdot}10^5$ cm/s, the average number of channels in the discharge figure was within the limits 1.4–3.2, the total current impulse duration was between 4.3 and 7.0 μs, and the figure shapes were treelike or filamental. Investigations were carried out for the T–P discharge gap having $d = 10$ mm under application of 1.1/225 μs impulses with positive and negative polarities.

As demonstrated in Sect. 6.5.1, the impulse electric strength of liquids is also poorly correlated with the molecular structure of liquids.

4.2 Discharge Kinetics under Microsecond Impulse Voltage

The discharge figure shapes and modes distinguished by their appearance (spherical, bush-like, treelike, etc.) or propagation velocity (slow, fast, and very fast) and their interconversion were described in Sect. 4.1 without

consideration of their time history and interdependence. In our opinion, this is quite justified to clarify a wide variety of the phenomena caused by high sensitivity of the discharge processes in a liquid to the experimental conditions.

To understand a nature of the liquid breakdown, the time history of the discharge processes and temporal variations of their parameters are of principal importance. As in Sect. 4.1, we first consider the discharge phenomena under the reference conditions: a) transformer oil, b) the voltage impulse close to lightning or rectangular one, c) tip (or rod) – plane electrode system, and d) positive initiating electrode polarity. After that, the special features of the phenomena for other experimental conditions will be considered.

4.2.1 Highly Non-uniform Fields (Small r_0)

The discharge gaps with highly non-uniform field are meant discharge gaps whose non-uniformity coefficient μ ($\mu = E_{max}/E_{av}$) increases from a few tens to a few thousands, which for centimeter scale interelectrode distances is provided by tip electrodes with micron sizes r_0 (from a few tenth of a micron to a hundred microns).

Low Breakdown Probabilities ($U \leq U_{10\%}$)

In [7] it was found that the discharge phenomena near the electrode with small r_0 start with a weak spherical luminous figure accompanied by low currents ($\sim 10^{-3}$–10^{-1} A) that after propagation from the electrode at a distance of a few tens of microns with a velocity of $(1.3$–$1.6)\cdot 10^5$ cm/s gradually decays when $U << U_{br}$. In [9, 21], using higher spatial resolution it was established that luminescence is formed by several thin channels (microchannels). Their number increased from several units to several tens within 4–5 ns from the channel inception, and the discharge figure was converted into a hemisphere. Shock waves were formed on the front of the figure. Within 0.5–3 μs from the inception of the first microchannels (the discharge ignition), a dominant monochannel (less often 2–4 channels) was propagated with a constant velocity from the hemispherical discharge figure to the opposite electrode (Fig. 4.21). We called this channel initial [7], and in [9] it was called the monochannel.

Other channels stopped and gradually decayed leaving chains of microbubbles with shock waves registered on the periphery.

The initial channel diameter increased from 1–5 μm at the head to 30–50 μm at the tip electrode. The average velocity of the initial channel under these conditions was estimated to be $\sim 10^2$ cm/s.

When the initial channel came in contact with the opposite electrode, no breakdown occurred in the gap. One more process propagating from the plane through the initial channel to the opposite (tip) electrode is required to initiate the breakdown. (For more details, see Sect. 4.6.) This phenomenon first described in [6, 7] was subsequently observed in [9, 49, 60, 120].
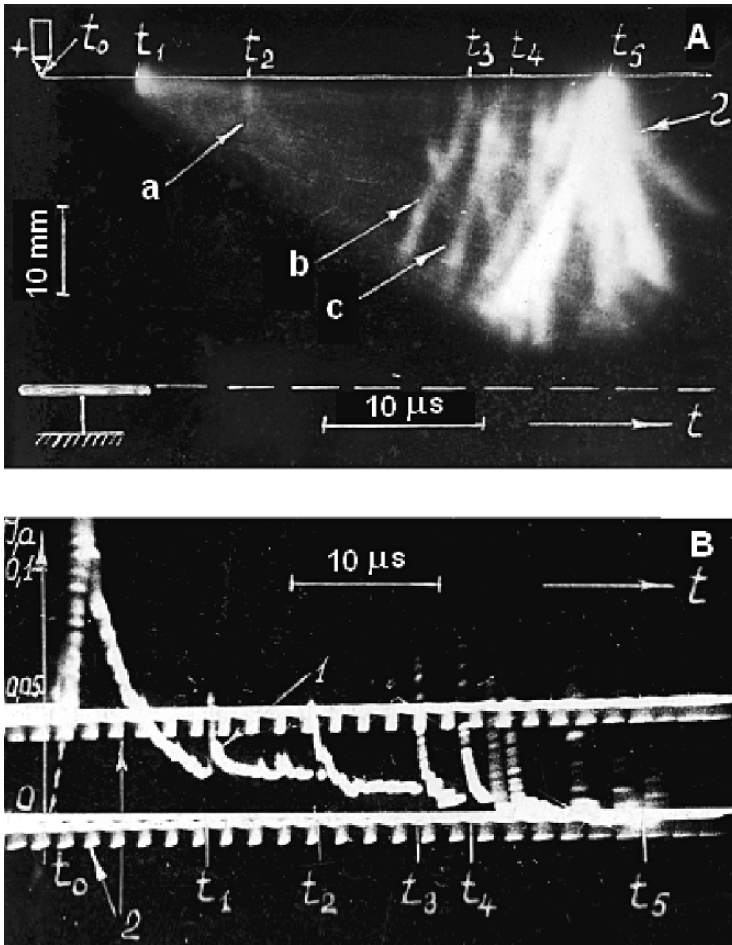
Fig. 4.21. Discharge in transformer oil for the $+$T $-$P system, $d = 5$ cm, $U = 1.4U_{50\%}$, and a 1.2/70 μs impulse. Here **A** is the streak photograph and **B** is the oscillograph record of the current (*curve 1*) and calibration marks (*2*) [7]

Intermediate Breakdown Probabilities ($U \approx U_{50\%}$–$U_{100\%}$)

When the voltage increases, the discharge shape changes as described in Sect. 4.1. Even greater changes are observed in the spatial and temporal structure of the discharge.

For $U \approx U_{50\%}$, spherical luminescence of microchannels (at time t_1 in Fig. 4.21) and sufficiently uniform glow produced by the continuously propagating initial channel ($t_1 - t_2$) is followed by bright light flashes arising in the channel (a). As the channel propagates, the light flashes become periodical (b and c) with 2–4 μs time delays. We call this mode of channel propagation stepwise and the channel itself the leader channel.

In the process of propagation, the discharge channel repeatedly branches, which is especially pronounced when it has already covered about half the gap. From streak photographs it is clearly seen that newly formed sections of the leader channel are much brighter than its remaining sections.

Short (10–30 ns) current impulses whose amplitude increased from 0.05 to 0.2 A as the leader penetrates deeper into the gap are accompanied by light flashes in the channel. During time intervals between successive light flashes in the leader channel, it uniformly and weakly luminances, and a current of 0.001–0.005 A, nearly the same as in the stage of the initial flashless channel propagation, runs through it. Whereas several leader channels propagate simultaneously, lignt flashes are not simultaneous, though in some uncontrollable cases they can be synchronous [24].

In the case shown in Fig. 4.21, the leader channel did not reach the plane because the voltage was chopped at time t_5 due to a parallel gap. The voltage chopping was accompanied by an intense light flash of the leader channel (d) caused by the ionization processes in the electric field created by the space sharge concentrated mostly at the gas/liquid interface as well as by the running capacitive current. This phenomenon is observed whether the voltage is chopped during time interval between successive flashes or simultaneously with the light flash. The flash brightness at the instant of voltage chopping is much higher than the brightness of the leader channel at the instant of step. In the still photograph of the interrupted discharge, the luminescence of a large channel that veils the fine structure of the discharge figure growing to the moment of voltage chopping is observed. As demonstrated in [63], this phenomenon is the main source of errors in the study of spatial discharge structure based on still photographs and Lichtenberg figures with the use of discharge interruption when the voltage is chopped. A similar phenomenon was observed in [36].

In [64] it was demonstrated that the main role in propagation of the partial discharge channel head after its detachment from the electrode is played by the field created by the excess space charge concentrated on the gas/liquid interface (on the gas bubble surface).

High Breakdown Probabilities ($U > 2U_{50\%}$)

The initial stages of the discharge propagation under high overvoltages were described in ample detail in [9, 19, 49].

The discharge ignition (initiation) is the inception of 2–3 local zones with low-illuminating channels 200–250 μm long arising from the point of the tip electrode (Fig. 4.22) [9]. Then microchannels 10–12 μm in diameter with 2–3 branches are observed whose brightness and diameter (3–6 μm) are identical to those of the the initial channel for $U < U_{10\%}$. The number of microchannels increases, which results in the formation of a spherical figure consisting of 2–3 "large" complexes at the tip. Each complex consists of a fairly bright channel and several side branches with brush-like figures at the end. By their
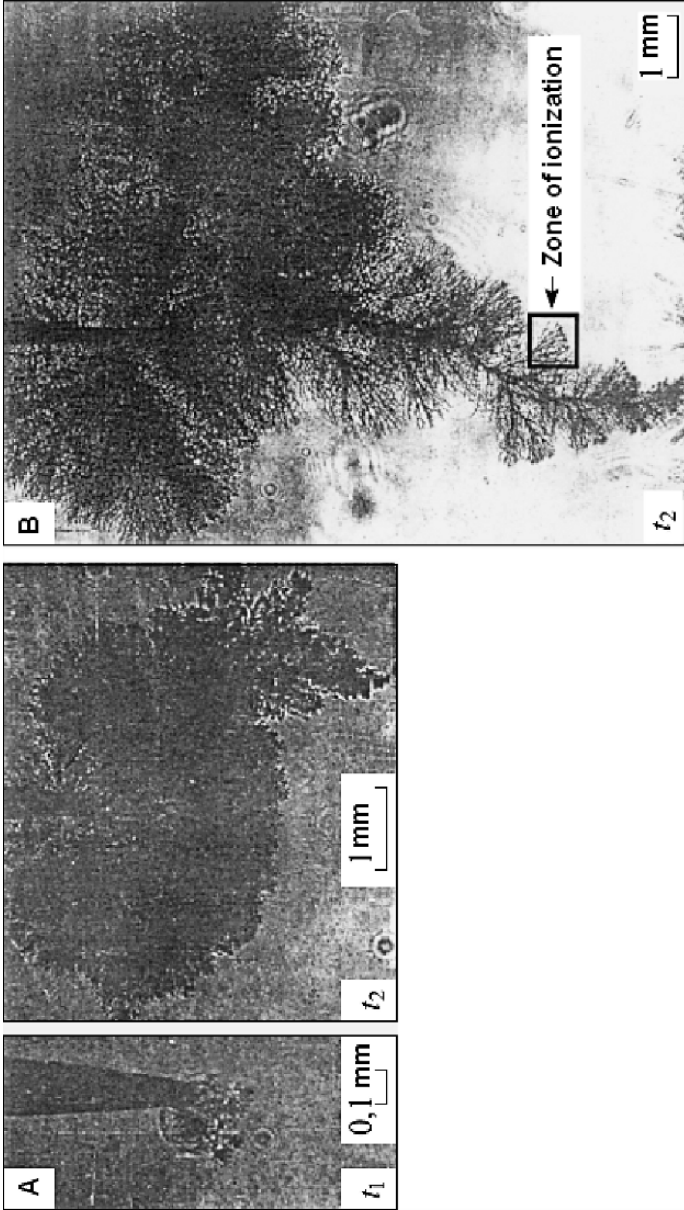
Fig. 4.22. Initial stages of discharge formation in transformer oil for the $+\mathrm{T}\ -\mathrm{P}$ gap, $d = 2.75\,\mathrm{cm}$, and $U = 180\,\mathrm{kV}$. **A** and **B** are Schlieren photographs of the discharge propagation at different moments of time (for frame exposure of $10^{-8}\,\mathrm{s}$) [9]

appearance, these complexes remind branches of a coniferous tree. In early propagation stages, these processes are accompanied by continuous glow, and in final stages they are accompanied by light flashes (it is difficult to identify their source) and current impulses with amplitudes up to 0.05 A. These phenomena were recorded in [9] with the use of a Schlieren system. Simultaneous registration with an image converter camera demonstrated that the spatial resolution was insufficient for recording of these fine structures. Exactly for this reason, these structures were not detected in our previous investigations [7].

Further evolution of the discharge phenomena involves stepwise propagation of the initial channel that is transformed into a leader channel, thereby causing its stepwise lengthening deeper into the gap. The stepwise leader propagates from the spherical figure when its diameter reaches 0.3–0.4 mm.

For $U \approx 3U_{50\%}$, the stepwise leader propagation is started at the impulse front with a velocity of $(1–5) \cdot 10^6$ cm/s during 1.5–2 μs (Fig. 4.23). In this case, the light flashes of the channel are observed every 0.2–0.3 μs. Then the effective velocity of channel propagation decreases approximately by an order of magnitude, and time intervals between successive light flashes increase to 1–2 μs.

An increase in the voltage (overvoltage) in this range is accompanied by a fast increase in the average velocity and a decrease of time intervals between the successive light flashes of the channel and hence time intervals between successive current impulses. In this case, no noticeable increase in the current amplitude was observed [24].

The leader channel has bright glowing side branches and bush-like figures 1.4–2.4 mm in diameter consisting of a few tens of weakly glowing channels
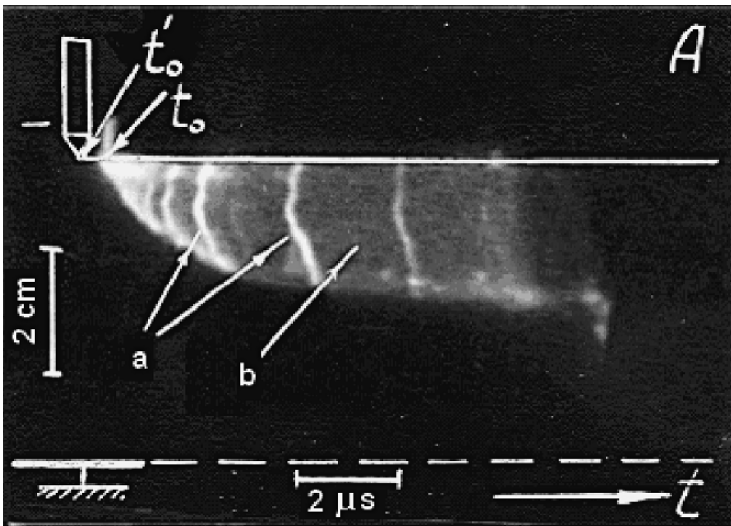
Fig. 4.23. Initial stages of stepwise leader propagation in transformer oil [7]

6–12 μm in diameter. Shock waves are formed on their fronts (Fig. 4.22c). Lengthening of the leader channel during a single step (light flash), estimated in [7] to be no more than 3–6 mm, well coincides with sizes of bush-like figures.

In the immediate proximity of the plane, the channel propagation velocity sharply increases. By analogy with the phenomenon in the leader process in air gaps, we called it a final jump [6] (see Sect. 4.6); in [65] it was called the superfast discharge.

4.2.2 Weakly Non-uniform Fields (Large r_0)

In [9, 49, 120] it was demonstrated that the degree of field non-uniformity affects substantially the transition from the initial channel discharge to a two-stage leader process.

Figure 4.24 shows Schlieren photographs of discharges in the gap 2.75 cm long with a curvature radius of the rod electrode of 0.5 mm and a field non-uniformity factor of 40 [9]. The minimum discharge ignition voltage and U_{br} for this gap coincided and were 108 kV. This value was by a factor of 2.6 higher than for the same d but for $r_0 = 30$ μm. Within 2 μs from the discharge ignition, the stepwise leader was observed with structure and sizes of elements similar to those observed for gaps with a sharply non-uniform overvoltage field. During further discharge propagation, numerous weakly luminous channels were observed that arose continuously to the contact with the plane electrode without transformation into the leader channel.

When the overvoltage increased to 2.2 and the average field intensity in the gap was $\sim 9{\cdot}10^4$ V/cm, the initial stage of discharge propagation was formed by a short bunch comprising several weakly luminous channels propagating from one point and generating shock waves, by analogy with a sharply non-uniform field (but for an overvoltage of ~ 3.3 and $E = 6.5 \cdot 10^4$ V/cm) (Fig. 4.24). The channels propagated with a velocity of $\sim 2{\cdot}10^5$ cm/s and continuously glowed. When they passed 0.5–0.6 mm, one of the channels brightly flashed, and a short filamental channel that appeared at the bundle origin propagated further stepwise and, as a matter of fact, formed the first leader step. The fact that the leader process is realized at a very short distance from the electrode (about 1 mm) under the given field intensity confirms the assumption [2] that the leader in liquids can be used for modeling of processes in a lightning. It is also important that this allows the discharge in moderately short gaps to be considered as a propagation of primary channels that under certain conditions are transformed into a two-stage leader process. With further decrease of the field nonuniformity down to 10 (for $r_0 = 1.5$ mm and $d = 2$ cm), the initial phases of discharge propagation as a whole were analogous to those described above; however, the stepped leader was observed without preliminary formation of a spherical figure near the electrode. The velocity of leader propagation decreased from $\sim 4.5 \cdot 10^6$ to $(1.5–2){\cdot}10^6$ cm/s, and the transverse dimensions of the discharge figure increased due to repeated channel branching as the plane was approached. Leader steps were recorded at ~ 30 ns time intervals.
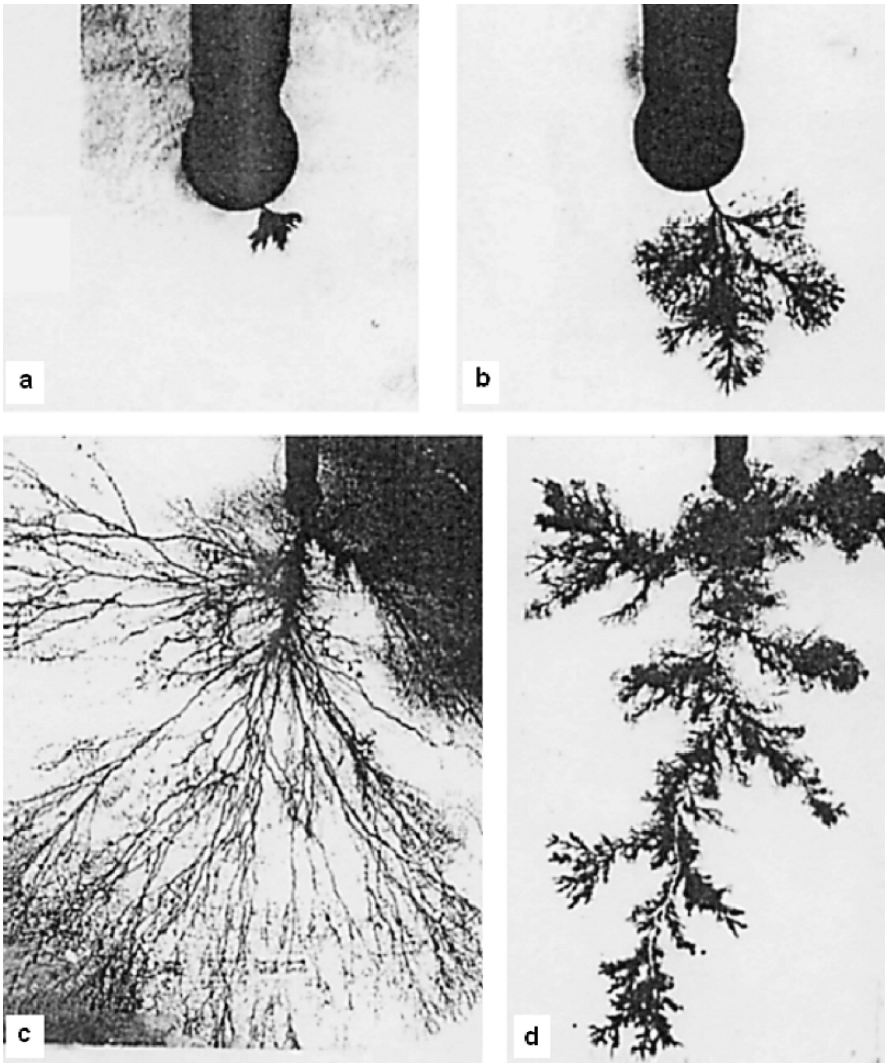
Fig. 4.24. Schlieren photographs of the characteristic stages of leader propagation for the rod-plane gap ($r_0 = 0.5$ mm, $d = 2.75$ cm, and frame exposure of 10^{-8} s) under different overvoltages $U = 2.2U_{50\%} = 245$ kV (**a** and **d**) and $U \approx U_{50\%}$ (**b** and **c**) [9]

The important feature of gaps with a slightly non-uniform field is that the leader process is observed under the voltage approximately equal to $U_{10\%}$, that is, without overvoltage. However, it should be born in mind that the average field strength in this case is much higher than in the previous cases and is about $1.2 \cdot 10^5$ V/cm.

The above-described discharge phenomena are also observed when the field nonuniformity decreases to 1.8–4 (for example, at $r_0 = 7.9\,\text{mm}$ and $d = 8.2\,\text{mm}$). The leader process is observed at $E_{\text{av}} = 4.2 \cdot 10^5\,\text{V/cm}$, which corresponds to a breakdown probability of 1%.

4.2.3 Discharge in Purified Water and Ethyl Alcohol

Most investigations of the discharge propagation in long water gaps with a non-uniform field were carried out at Tomsk Polytechnic University, Nuclear Physics Institute of the Siberian Branch of the Russian Academy of Sciences, and Siberian Scientific-Research Power Engineering Institute and at Novosibirsk State University. This Section is based on the results of these investigations and also includes recent data obtained in laboratories of some other countries.

Two main stages of water breakdown – the discharge ignition and propagation of discharge channels toward the opposite electrode in water – are especially sensitive to the experimental conditions. Even when they change insignificantly, the sequence, intensity, and contributions of charge carrier injection and hydrodynamical, electrostriction, and thermal disturbances to the discharge ignition significantly change, which in turn causes the gap field non-uniformity and phase non-uniformity of the medium. In the stage of discharge propagation in water, as in other liquids, the number, appearance, and velocity of channels and their spatiotemporal and electric characteristics [66–69] depend on the experimental conditions.

In this regard, it is expedient to describe first the experimental data on water breakdown under long voltage impulses (from a few microseconds to a few hundreds of microseconds) when the energy and time are optimal for all complex of the above-listed processes.

The results of investigations of the processes occurring in deionized water with $\rho = 2 \cdot 10^6\,\Omega\cdot\text{cm}$ in the tip anode – plane cathode electrode system were presented in [66–69]. The tip curvature radius was $200\,\mu\text{m}$, and the discharge gap was $6\,\text{cm}$ long. The voltage impulse with an amplitude of 17–50 kV, a front rise time of $10^{-7}\,\text{s}$, and a decay time down to half amplitude of $\sim 10^{-3}\,\text{s}$ was applied to the tip. The discharge phenomena were registered by the shadowgraphic technique with the help of lasers and a VFU-1 high-speed camera using the procedure described in [70]. This equipment allowed Kukhta et al. [70] to record chronograms with time resolution of $10^{-8}\,\text{s}$, a series of frames with an exposition of 10^{-7}–$10^{-6}\,\text{s}$, and single frames with an exposition of $10^{-9}\,\text{s}$.

Depending on the electric field strength at the tip surface, the discharge in water was super- or subsonic, and under voltage impulses with an amplitude of 20–25 kV, the discharge channels of both types propagated in the gap. Point-like optical inhomogeneities delayed by $(1$–$10)\,\mu\text{s}$ arise in the initial stage of discharge formation near the tip surface. They scatter intensively external illumination.

For large r_0 and (or) low voltages, the most probable discharge channels are slow, and they formed a bush-like figure. For $r_0 \leq 100\,\mu m$ under $U = 15$–$18\,kV$, slow channels and figures formed by them were similar to those formed in hydrocarbon liquids. Their velocity depended on E_{av} and increased within the limits 10^3–$10^4\,cm/s$. In the case of partial discharge, slow channels were unstable and were subdivided into separate fragments within 10–$50\,\mu s$, starting from the tip electrode surface (Fig. 4.25). Small fragments (10–$100\,\mu m$) collapsed for 1–$10\,\mu s$, and large fragments collapsed for 50–$100\,\mu s$. Gas bubbles $\sim 10\,\mu m$ in diameter were formed at the sites of distorted channels. Slow channels never caused the complete breakdown of the gap.

With decrease in r_0 and (or) increase in U, the probability of forming fast luminous channels increases. They can propagate from the tip electrode in the form of a bush-like figure whose sizes grow to 100–$800\,\mu m$; then the rate of their growth decreases. Under $U \leq 20\,kV$, the breakdown does not occur. The discharge is completed if the fast tree-like figures reminiscent of leader channels are formed.

For $r_0 \approx 100$–$600\,\mu m$, different ways of discharge figure initiation are possible. In one case, hemispherical formations with reduced density, sizes of 5–$10\,\mu m$, and base diameter of 20–$70\,\mu m$ are first observed. Then they are deformed and assume elliptic or conical shape with unstable tip shape. These formations are ether electrically conductive or carry a charge on their surface, since they are stretched by the field but do not separate from the electrode. Their propagation velocity is $(5$–$10)\cdot10^2\,cm/s$ and only weakly depends on U. For $E_{max} = (0.4$–$0.6)\,MV/cm$, the tip surface is covered by these formations within 1–$10\,\mu s$. Simultaneously, the velocity of their growth increases to $(0.5$–$2)\cdot10^4\,cm/s$, and luminous treelike channels start to propagate from their surface. This process is accompanied by shock wave generation and increase in the current up to $1\,A$.

Relaxation products in the zone of shock wave formation, compressed at the moment of discharge ignition, are subsequently expanded with a rate of $\sim 10^3$–$10^4\,cm/s$. Moreover, these shock waves do not cause any deformation of the subsonic discharge formations generated before, as it would be the case for a vapor-gas complex. With increase in the voltage, the discharge processes are intensified: the number of simultaneously propagating supersonic channels and shock waves formed by them increases, the time delay of subsonic formations somewhat decreases, the size of subsonic perturbations at which the supersonic channel starts to propagate decreases, and time interval between the formation of two successive channels decreases.

For impulse amplitudes higher than $25\,kV$, supersonic channels from the electrode are delayed by $(0.3$–$2.5)\cdot10^{-6}\,s$. Their initial diameter is on the limit of the spatial resolution (1–$3\,\mu m$). The rate of growth of separate branches in the stage of their propagation reaches $\sim 10^7\,cm/s$. The channels are registered as semitransparent, their optical density increases, and a diffusion region and a shock wave are recorded around them. The initial shock wave velocity is in
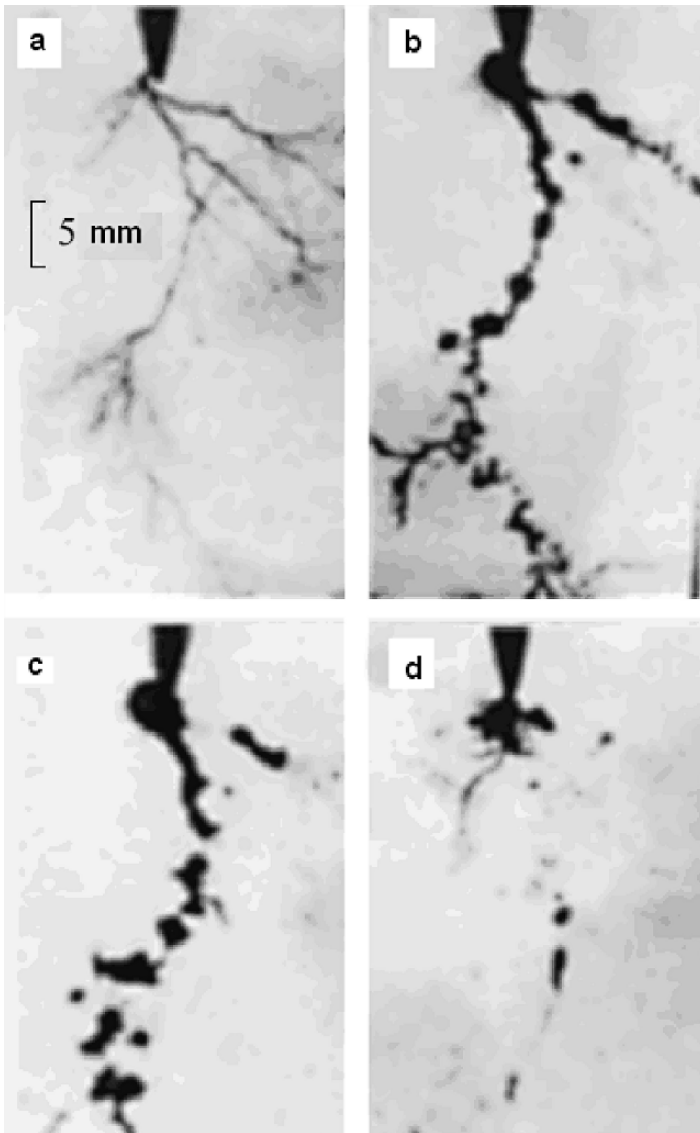
Fig. 4.25. Evolution of anode channels in water for an impulse amplitude of $30\,\mathrm{kV}$, impulse duration of $10^{-3}\,\mathrm{s}$, $d = 8\,\mathrm{cm}$, and $r_0 = 250\,\mu\mathrm{m}$ 2 (**a**), 52 (**b**), 78 (**c**), and $190\,\mu\mathrm{s}$ (**d**) after the voltage application for frame exposure of $60\,\mathrm{ns}$ [68]

the limits $(1.8\text{--}3)\cdot10^5\,\mathrm{cm/s}$. The instantaneous velocity of channel propagation is $\nu \sim 10^7\,\mathrm{cm/s}$, and the average velocity, because of stepwise propagation, is only $\nu \sim 10^4\text{--}10^5\,\mathrm{cm/s}$. Discharges formed at low field intensity when time interval between two successive impulses exceeds $\sim\!10\,\mu\mathrm{s}$ are the least stable

ones. It is important to note that the trajectory of channels newly formed at the tip does not coincide with previous trajectories.

Partial channels are mainly formed under voltages in the range 17–22 kV. The channels can be as long as a few millimeters. The characteristic feature of this stage is the cyclicity of the process: slow propagation with a velocity of 10^2–10^4 cm/s during 0.1–2 µs, fragmentation into regions generating light flashes with a period of (40–100) µs, and generation and growth from the tip of new subsonic discharge formations. In regions occupied with relaxation products, microbubbles were observed drifting with a velocity of $\sim 10^2$ cm/s. They did not influence the successive discharge processes.

To understand the mechanism of water electric breakdown, it is important to establish a nature of the optical inhomogeneity formed near the initiating electrode and the feasibility of predischarge phase transitions in water (see Chap. 7). In the above-described experiments, no phenomena preceding the formation of channels, which could be identified with hydrodynamical processes, were detected. The field strength near the electrode (without taking into account microgeometry) did not exceed 10^6 V/cm. The calculated dissipated energy density for such values of E gives the temperature rise no more than a few degrees during the delay time of the first channels. An analysis of optical images of the discharge revealed no phenomena which can be identified with thermal processes. In a number of current studies, the optical inhomogeneity was associated with hydrodynamic processes. Moreover, not only origin, but also propagation of the discharge channel was considered to be a consequence of ionization of the two-phase liquid-gas system. At present, optical data confirming this point of view are lacking. In [66–69] experiments, authors recorded no hydrodynamic phenomena in the stage preceding the formation of the optical inhomogeneity in front of the channel head.

In the phase of motion, discharge channels have filamental structure with filament (channel) diameter of ~ 1 µm, and their motion is not preceded by bubbles and shock waves. Shock waves and cavitation bubbles arise at a later stage of channel propagation. Careful analysis of instantaneous (with a frame exposure of ~ 1 ns) images of discharge channels in the stage of their relaxation in partial discharge mode demonstrated that cavitation zones arising behind the shock wave fronts do not facilitate the formation of new channels. The cavitation influences the stability of secondary structures, but does not influence the propagation of the channel itself.

Under shorter voltage impulses (1.2/70 µs) with amplitudes of 40–70 kV, the optical phenomena in distilled water registered with an image converter camera [6, 66], as a whole, were similar to those in transformer oil. For the discharge in water, three basic features can be indicated:

– essential difference between the discharge characteristics at positive and negative polarities of the tip electrode (the effect of polarity),
– higher brightness of channel luminescence and larger currents running through the channels,

–   a greater difference between the brightness of channel luminescence during
    steps (flashes) and time interval between two successive impulses.

In the $+$T $-$P gap under 1.5/70 μs impulses with amplitudes close to $U_{50\%}$,
the discharge is accompanied by regular light flashes of the channel from the
instant of its origin to the instant of contact with the plane (Fig. 4.26) [71].
The time history in Fig. 4.26 is delayed from the inception of the discharge
processes, and static patterns developed by the moment t_0 in discharge chan-
nels are seen on the photographs taken with a streak gated camera in addi-
tion to spatiotemporal patterns. The discharge process involves propagation
from the tip of numerous leader channels reilluminating every 0.2–0.4 μs. The
leader consists of channel a and a bright spherical head. High-speed ICC
records (Fig. 4.26b) show that during each successive flash, the leader channel
head penetrates deeper into the gap with a velocity of $(0.8–2) \cdot 10^7$ cm/s dur-
ing 0.01–0.03 μs; then the delay between two successive impulses is recorded
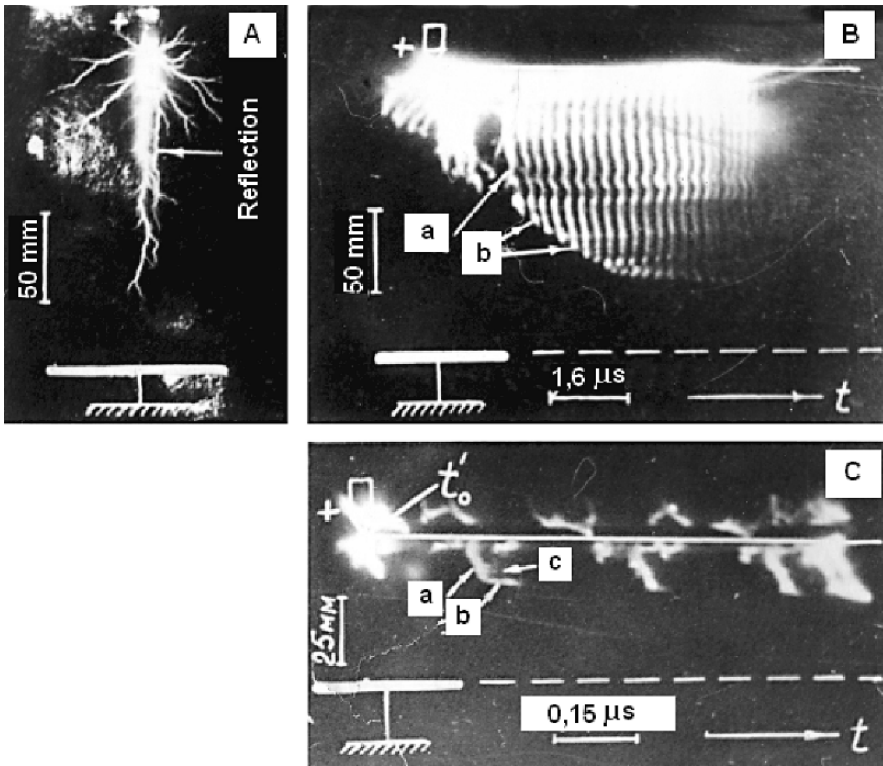
Fig. 4.26. Propagation of a partial leader in clear water for the $+$T $-$P gap under
$U = U_{50\%}$. Here **A** is a still photograph, **B** is a streak photograph, and **C** is a
high-speed streak photograph for $d = 16.5$ cm and $U = 70$ kV (**A** and **B**); $d = 5$ cm
and $U = 40$ kV (**C**) [6]

during which the channel glow weakens significantly. In the next step, the leader channel head starts to move from the point at which the motion of the channel head was stopped during the preceding step. During a light flash, the leader channel has sharp left boundary a that is smoothly transformed into diffusion glow c with decreasing brightness. The velocity of luminescence propagation through the channel exceeds 10^8 cm/s and is outside the limits of ICC resolution; for this reason, it was impossible to determine experimentally the direction of its propagation. The effective rate of lengthening of the leader channel was $(1.5–2) \cdot 10^6$ cm/s. In [62] in the wire (75 μm in diameter) – plane gap with interelectrode distance $d = 2.2$–3.6 cm, the velocity of positive discharge channel propagation was established to be $3.2 \cdot 10^6$ cm/s. The velocities obtained are in good agreement with allowance for the fact that the voltage impulse in [72] was much shorter ($\sim$500 ns) and that the created the field strength in the gap was higher than in our experiments [6, 7].

For the discharge in water from the negative tip, a low velocity of the leader propagation is typical, which for $U \approx U_{50\%}$ makes $6 \cdot 10^4$ cm/s. In the process of negative leader propagation, light flashes were observed in the channel every 0.1–0.15 μs. On low-speerd oscillograph records, the discharge is shaped as a uniformly luminous triangle, and on still photograpns it is a branch-like formation with specific bubbly (hoarfrost-like) structure. Because of the low propagation velocity of the negative leader, the strength of the $+$P $-$T gap is 3–4 times greater than of the $+$T $-$P gap. The discharge from the negative tip was investigated in the reversed electrode system when an impulse of positive polarity was applied to the plane electrode, and the tip electrode, placed at the bottom of the discharge chamber fabricated from an organic glass, was grounded. This allowed the experimenters to avoid creepage discharges over the cable insulation surface with removed braid whose copper conductor was given 3–4 mm exposure and tapered down with a tip radius of $\sim$100 μm to serve as a tip electrode. In [72] the polarity effect was manifested as follows: for a wire with negative polarity, only weak luminescence near its surface was observed under $U = 120$ kV, whereas for a wire with positive polarity, discharge channels propagated at distances exceeding 1.5 cm.

For both tip electrode polarities, the discharge propagation in distilled water was accompanied by an increase in current from 10–15 A at the moment of discharge ignition to 30–50 A by the moment of leader contact with the plane. Current impulses during flashes (steps) of the channel make only an insignificant fraction of the total conduction current closing on numerous channels of the discharge figure. For this reason and owing to asynchronous steps, current impulses accompanying them were weak oscillations superimposed on the total current impulse.

When the leader reached the opposite electrode, a complete breakdown occurred in all cases.

It was impossible to reveal a more detailed structure of the discharge with negative polarity in water using image converter cameras. Only a

shadowgraphic technique allowed Kukhta et al. [70] to establish that the growing negative slow discharge figure was similar to the 1st mode positive figure, but it could be transformed into a treelike figure similar to the 2nd mode positive figure.

The first slow figures that appeared near the tip propagated with a velocity of $(2–4) \cdot 10^3$ cm/s during 80–200 μs. The instability arising on the figure surface did not cause the formation of fast channels.

For $E_{max} \geq (0.4–0.5)$ MV/cm, weak shock waves were formed near the channel surfaces followed by fast luminous channels surrounded with slow discharge figures. The fast channels propagate deeper into the gap with acceleration, acquiring treelike shapes. If the shock waves were absent, the sizes and velocities of fast channels decreased. No regions with decreased density similar to those observed near the tip anode were recorded.

A discharge in *ethyl alcohol* that takes an intermediate position between transformer oil and distilled water by its physical and chemical properties (in particular, ε and γ) has special features of discharges in both these liquids. The polarity effect in breakdown of alcohol is weakly expressed, as in oil. The structure of the discharge process as a whole and its separate elements in alcohol in +T −P and −T +P systems were similar to those in water in the +T −P system. The characteristic pattern of the discharge phenomena in alcohol is illustrated by Fig. 4.27. (The right part of the figure is distorted by the nonlinear bias voltage applied to the ICC plates.) During each step, the channel head moved deeper into the gap with a velocity of $3 \cdot 10^7$ cm/s during 0.04–0.06 μs, and the leader channel glowed over the entire length. Time intervals between two successive impulses in the leader were 1.1–1.3 μs. A current impulse with amplitude of 4–8 A corresponded to each step of the leader propagation. Under $U = U_{50\%}$, the leader passed the greater section of the interelectrode gap with an effective velocity of $(2–2.5) \cdot 10^5$ cm/s.
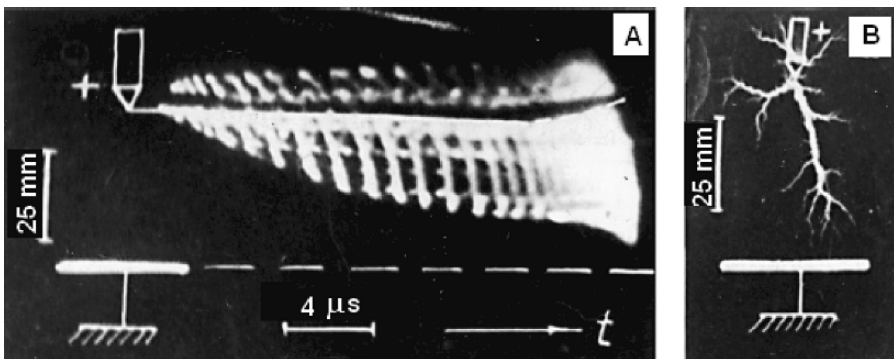
Fig. 4.27. Discharge in ethyl alcohol for the +T −P gap, $d = 5$ cm, and $U = U_{50\%} = 80$ kV. Here **A** is a streak photograph, and **B** is a still photograph [6]

4.2.4 Discharge in Liquids with Increased Electrical Conduction

Investigations of the discharge phenomena in liquids with increased conductivity can provide additional information useful for understanding of the liquid breakdown mechanism. This information is also of practical interest in connection with technological applications of the electric discharge in liquids, including liquids with increased conductivity [73–77]. Tap water ($\gamma \approx 10^{-3}$–$10^{-4}\,\Omega^{-1}\cdot\text{cm}^{-1}$) and aqueous solutions of NaCl and other salts with electrical conductivity up to $\sim 10^{-2}\,\Omega^{-1}\cdot\text{cm}^{-1}$ were investigated in [78]. It was established that for $\gamma > 10^{-4}\,\Omega^{-1}\cdot\text{cm}^{-1}$, the stepwise leader process was replaced by continuous propagation of the discharge channel whose conductivity, luminescence brightness, and appearance were similar to the leader channel. In liquids with increased conductivity, the effect of polarity has its own peculiarities. The velocity of the positive discharge propagation remains virtually unchanged with increasing γ; it decreases for $\gamma > 10^{-3}\,\Omega^{-1}\cdot\text{cm}^{-1}$. For the negative discharge, on the contrary, it increases (Fig. 4.28). The constant average propagation velocity of the positive discharge when going from distilled ($\gamma \approx 1.5\cdot 10^{-4}\,\Omega^{-1}\cdot\text{cm}^{-1}$) to tap water ($\gamma \approx 1.5\cdot 10^{-4}\,\Omega^{-1}\cdot\text{cm}^{-1}$) was also indicated in [72]. The appearances of positive and negative discharges also differ significantly. Channels of the negative partial discharge have original coral-like or bubbly structure (Fig. 4.29). The positive discharge figure was reminiscent of the figure in transformer oil, but differed from it by a much greater number of channels and their higher brightness.

A number of authors [79–84] investigated the discharge kinetics in water and water electrolits and long gaps with non-uniform field using a high-speed photocameras with mechanical scanning. Despite low spatial and temporal resolutions and low optical sensitivity of this equipment, materials supplementing the discharge pattern in water and water electrolits in long discharge
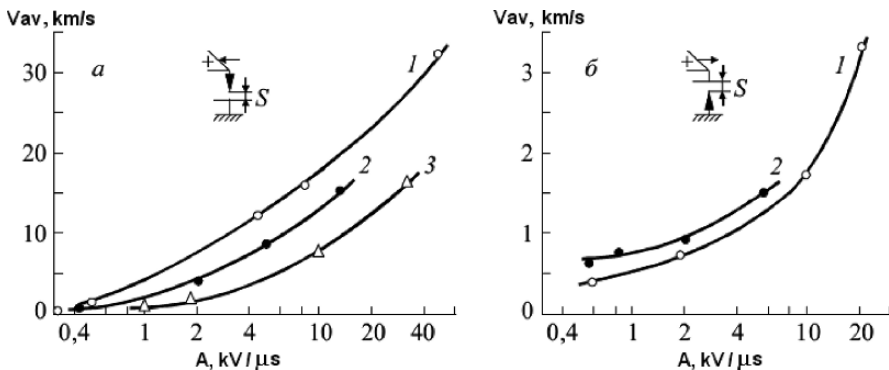
Fig. 4.28. Dependence of the average discharge propagation velocity on the voltage slope for positive (**a**) and negative tip polarities (**b**) in distilled water with $\gamma = 7\cdot 10^{-6}\,\Omega^{-1}\cdot\text{cm}^{-1}$ (*curve 1*), NaCl aqueous solution with $\gamma = 10^{-4}\,\Omega^{-1}\cdot\text{cm}^{-1}$ (*curve 2*), and NaCl aqueous solution with $\gamma = 10^{-3}\,\Omega^{-1}\cdot\text{cm}^{-1}$ [78]
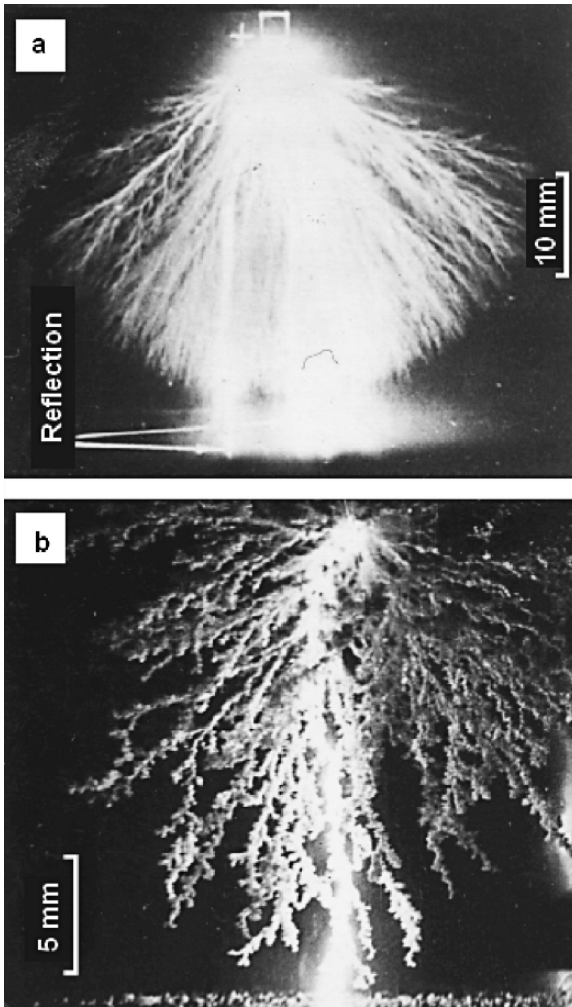
Fig. 4.29. Still photographs of the discharge in NaCl aqueous solution with $\gamma = 1.4 \cdot 10^{-2} \, \Omega^{-1} \cdot cm^{-1}$ for the +T −P (**a**) and +P −T gaps (**b**) [78]

gaps under microsecond voltage impulses were obtained. Of greatest interest, in our opinion, are the following results.

1. Breakdown of conducting nondegassed liquids ($\gamma = 2 \cdot 10^{-5}$–$2 \cdot 10^{-3} \, \Omega^{-1} \cdot cm^{-1}$) in long gaps ($d = 3.5$–$13 \, cm$) with non-uniform field is not connected with preliminary formation of the continuous gas bridge even at times of a few tens of microseconds. Gas bubbles are formed near the electrode or the discharge channel head. Ionization of these bubbles promotes the discharge channel propagation [89].

2. In [82–84] it was demonstrated that for duration of applied voltage of a few tens of microseconds, the discharge channel (called a brush) propagation velocity decreases with increasing solution concentration. A breakdown occurs in the gas contained in branches of the grown brush. It was assumed that the gas liberation processes play a key role in the formation of gas bubbles at low solution concentrations, and the vaporization processes play a main role at intermediate and high concentrations.

3. According to [80], gas bubbles are formed near the tip electrodes in water with $\gamma = 2.5 \cdot 10^{-4}\,\Omega^{-1} \cdot cm^{-1}$ under field strengths lying in the range 8–36 kV/cm. Within a few hundreds – a few thousands of microseconds from the moment of voltage application, luminescence arises near the tip, whose expansion to the opposite electrode results in the gap breakdown. This breakdown mechanism is treated as electrothermal. For $E = 36$–180 kV/cm, the leader discharge occurs; moreover, the leader formation is preceded by high-voltage electrode luminescence. For $E > 180$ kV/cm, no luminescence is observed before the leader formation. For low E, the leaders propagate stepwise, and for high E, they propagate continuously.

4.2.5 Special Features of the Discharge on the Voltage Impulse Front

Specifics of the discharge processes in *transformer oil* developing on the voltage impulse front, that is, under the high-voltage electrode potential continuously increasing with rate A, are manifested primarily through an increase in the instantaneous velocity of the leader as its head approaches the plane. Variations of the leader channel length L_l with time t are well described by the equation

$$L_l = \alpha \left[\exp\left(\beta \cdot t\right) - 1\right],$$

where α and β are constants depending on the slope and polarity of the voltage impulse and the properties of the liquid.

For $A = 4$ kV/µs, the instantaneous positive leader velocity increases along the gap from $(1.5$–$1.6)\cdot 10^5$ cm/s near the tip to $(4.5$–$5)\cdot 10^5$ cm/s near the plane. The discharge kinetics at mild front slope as a whole is analogous to that described for lightning impulses at low breakdown probabilities. For $A \approx 4$ kV/µs, continuous luminescence of the channel in the initial phases of discharge propagation is further accompanied by light flashes every 1.5 µs (Fig. 4.30). With increase in A, the average leader velocity increases according to the law shown in Fig. 4.31 (curves *1* and *1'*). The leader channel luminescence is discrete in character from the very beginning, and delays between two successive flashes of the leader channel gradually decrease. For $A = 400$ kV/µs, the delay between two successive light flashes is 0.05–0.06 µs for positive leader, while it is indistinguishable for the negative leader and $A = 400$ kV/µs. Under all examined experimental conditions, the characteristics of positive and negative leaders in transformer oil differ insignificantly. For
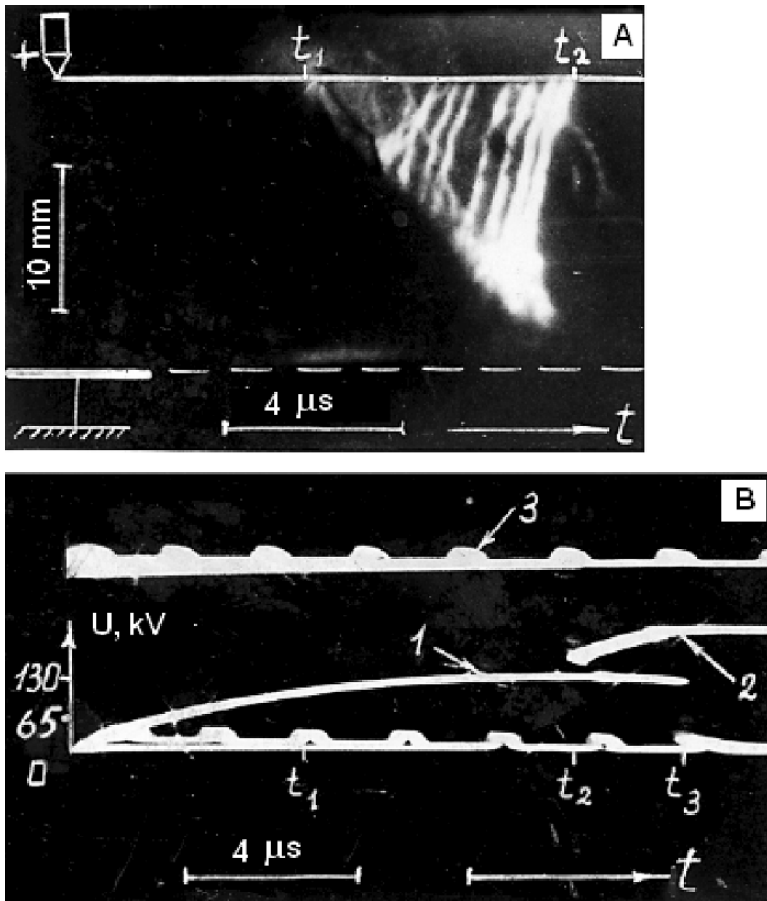
Fig. 4.30. Discharge in transformer oil for the $+$T $-$P gap and $d = 3$ cm under oblique-angled impulse with $A = 4$ kV/µs. Here **A** shows the streak photograph and **B** shows the signal waveform (*curve 1*), ICC gate impulse (*curve 2*), and calibration marks (*curve 3*) [78]

the negative leader, the propagation velocity is smaller, the channel branching is less pronounced, and the delay between two successive flashes are shorter.

The discharge propagation in *distilled water and alcohol* on the voltage impulse front depends stronger on the front slope than in oil. For $A \leq 10$–15 kV/µs, the leader develops as on the 1.5/70 µs impulse for $U \leq U_{50\%}$. For the same voltage impulse parameters, the leader velocity in ethyl alcohol is less than in water (curves *2*, *2′*, *3*, and *3′* in Fig. 4.31), and the delay between the successive steps is 4–5 times longer. With increase in A, the delay between steps decreases.

In water at $A = 6$–8 kV/µs and in alcohol at $A = 10$–15 kV/µs, steps of the leader are indistinguishable in streak photographs. Probably, this is due
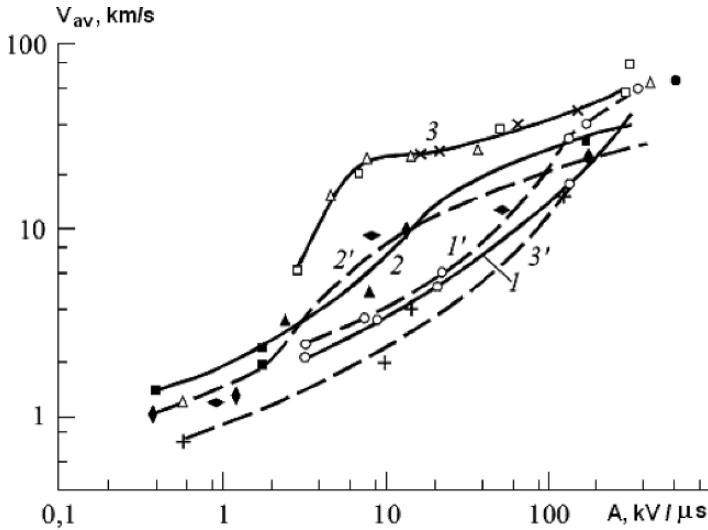
Fig. 4.31. Dependence of the average velocity of leader propagation on the voltage rise rate for transformer oil (*curves 1* and *1'*), ethyl alcohol (*curves 2* and *2'*), and distilled water (*curves 3* and *3'*) under positive and negative (*dashed curves*) voltage polarities [7]

to a superposition of luminescence of numerous simultaneously propagating channels (see Sect. 4.1). For the given slopes, bending is observed on curves $\nu_1 = f(A)$, that is, the rate of ν_1 growth slows down with further increase in A (curves *2*, *3*, and *3'* in Fig. 4.31).

4.2.6 Summary and Discussion of Results

In connection with a wide variety of appearances and characteristics of discharge figures formed in sharply non-uniform fields and with their high sensitivity to the field parameters, it is expedient to summariese the preliminary results of optical investigations of this phenomenon presented in Sects. 4.1 and 4.2. We put emphasize on the discharge from the positive tip electrode in liquid hydrocarbons and purified water for which the greatest number of experimental results have been obtained.

Unlike the phenomena in submillimeter gaps under high overvoltages, the phenomena which could be attributed to thermal or hydrodynamic processes were not registered in long gaps in the stages preceding the formation of optical inhomogeneity and initial discharge figure. In the phase of channel penetration deeper into the gap, neither bubbles no shock waves were registered in front of the channel heads. They arose in successive stages of channel propagation. The initial discharge figure (IDF) consists of many low-conduction channels having small diameters. The channels propagate with subsonic velocities, occupy a small region near the point of the tip electrode, and can decrease $E_{\max}$ near the

tip. The delay time of this structure is determined by $E_{\max}$ and is essentially independent of E_{av}. The region in which only IDFs are observed and the probability of complete breakdown is equal to zero lies under straight line *1* in Fig. 4.32 [21]. For small ($<50\%$) but nonzero breakdown probabilities (for example, under conditions illustrated by Fig. 4.32 with $E_{\mathrm{av}} = 7 \cdot 10^4$ V/cm at $d = 1$ cm and $E_{\mathrm{av}} = 2.2 \cdot 10^4$ V/cm at $d = 7$ cm), several channels from the initial structure continue to penetrate deeper into the gap. Moreover, by their shape and diameter, these channels are similar to the filamentary channels observed in short discharge gaps and can be identified with the initial channels in the first stage of the two-stage stepwise leader [7]. These channels form a rare bush-like figure and seldom close the entire gap because of their rather low electrical conduction (10–$50\,\Omega^{-1}{\cdot}\mathrm{cm}^{-1}$ according to [7] and $1.3\,\Omega^{-1}{\cdot}\mathrm{cm}^{-1}$ according to [8]) and hence large voltage drop across them as well as because of voltage decrease in the case of discharge propagation on the impulse tail. The region of realization of this discharge mode is enclosed between straight lines *1* and *3* in Fig. 4.32. With increase in E_{av}, the number of channels increases by one-two orders of magnitude, and they form a dense bush-like figure. The region of transition from rare to dense bush-like figures is rather narrow; it is enclosed between straight lines *1* and *2* in Fig. 4.32.

Further increase in E_{av} causes transformation of the bush-like figures into treelike ones. One channel (less often 2–3 channels) of bush-like figure increases the electrical conduction, the field strength at its head increases, and it moves with a higher velocity toward the opposite electrode. The transformation of the low- conduction – initial channel – into a high-conduction – leader channel – is discrete in character and characterizes the propagation of
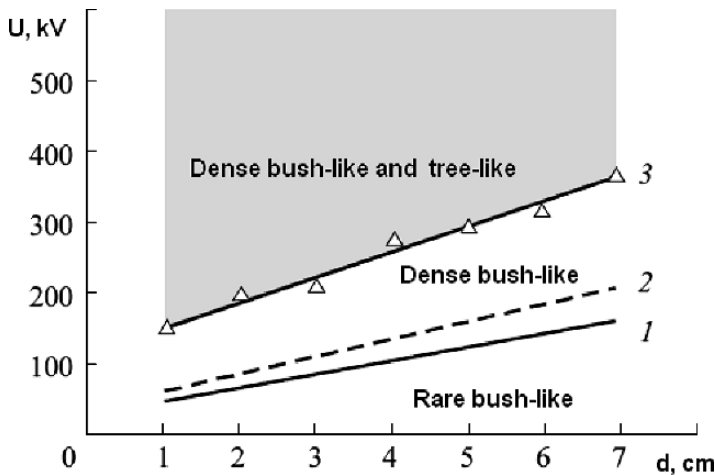
Fig. 4.32. Regions of existence of the indicated discharge shapes in water for voltage – gap length coordinates [21]

the stepwise leader. According to [7], the electrical conductivity of the leader channel is $(2\text{--}10)\cdot10^2\,\Omega^{-1}\cdot\text{cm}^{-1}$; according to [8], it is $1\,\Omega^{-1}\cdot\text{cm}^{-1}$.

For all examined gaps with sharply non-uniform field, the anomalous dependence of the discharge time t_d on the applied voltage is observed (Fig. 4.33) [21]. The discharge time smoothly decreases with increasing U to a certain limit, at which t_d changes abruptly. Such behavior of t_d can be explained by a decrease in the discharge time (the occurrence of the initial discharge figure) and earlier transformation of the bush-like figure into the treelike one. This transformation is accompanied by a sharp increase in the discharge velocity (Figs. 4.1 and 4.3). When the voltage is less than the critical one, a decrease in the time of discharge ignition is a key factor for the decrease in the discharge time. Under the critical voltage, the time of occurrence of a treelike structure undergoes strong fluctuations.

In [21] it was assumed that the transformation of the bush-like figure into a treelike one is caused by the current instability in discharge channels. In turn, the current instability can be caused by the S-shaped volt-current characteristic due to, for example, thermal instability. In early stages of the bush-like figure propagation, the channels have low electrical conduction and grow mainly along the force lines of the external electrostatic field. Their electric conductivity gradually increases, and the slightest current fluctuations can cause instability. Charges of high-conduction channel heads shield other channels and suppress their propagation. Under low voltages, the current instability develops slowly, and the bush-like figure has enough time to bridge almost all interelectrode gap. Under high voltages, the instability develops very fast, and the size of the bush-like figure before its transformation
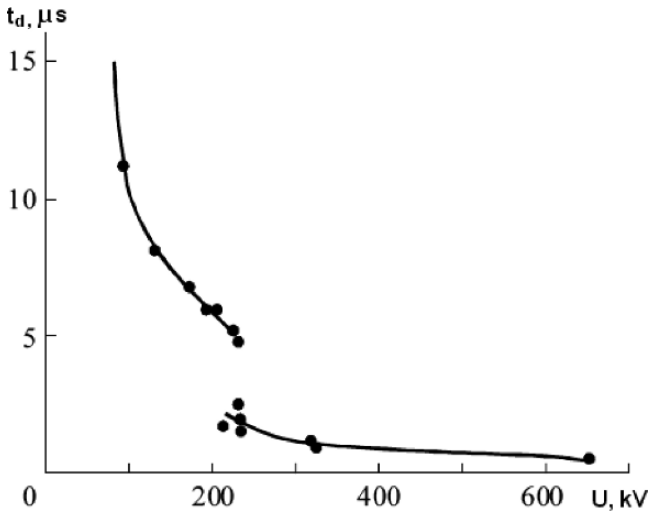
Fig. 4.33. Dependence of the discharge time on the voltage impulse amplitude for $d = 2\,\text{cm}$ [21]

into a treelike one is very small. There is a certain critical potential difference between the electrodes under which the greatest spread of times required for the transformation of the bush-like figure into a treelike one and of the total discharge time is observed. Under this voltage, according to [21], the rates of growth of the discharge figure and instability appear most close in values.

It is interesting to note that in [7,85] it was demonstrated that the anomalous – ladle-like – volt-second breakdown characteristic of gaps with a sharply non-uniform field under oblique impulses is caused by the anomalous dependence of the time required for the transformation of the bush-like figure into a tree-like one and hence of the voltage under which such transformation occurs on the impulse slope dU/dt. (Due to low spatial resolution of the ICC, the initial bush-like figure was registered as a uniform luminous sphere called torch). The initial channels in the stage of bush-like figure propagation and after its transformation into a tree-like figure propagate continuously and are accompanied by a continuous luminescence of the entire channel. After transformation of the channels forming a bush-like or tree-like figure into a leader channel, it periodically luminesces brightly; newly formed segments of the channel (near the head) luminesces most brightly. A nature and mechanism of such transformations are discussed in Chap. 8. It should be noted that in spite some nuances, the structure and the main mechanisms of the discharge in deionized water and mineral oils are similar.

4.3 Kinetics of Nanosecond Discharges

The strong dependence of the electric strength (see Sect. 6.1) and the liquid discharge characteristics (see Sect. 4.2) on the acting voltage impulse duration and practical interest to the behavior of liquids under nanosecond voltage impulses stimulated investigations of liquid breakdown under such extreme conditions [86, 87]. The experimental setup comprised a discharge chamber, a voltage impulse generator, and a superfast multiframe laser Schlieren imaging system. A discharge gap was formed by the tip and hemispherical electrodes from stainless steel. The curvature radius of the tip point was ∼50–100 μm, and the curvature radius of the hemispherical electrode was ∼5 mm. The distance between the electrodes was ∼1–2 mm. A voltage impulse with amplitudes up to 40 kV was applied to the electrodes. The impulse front duration was ∼10 ns, and the duration of discharge processes was ∼100–800 ns (depending on the impulse amplitude). The Schlieren imaging system allowed up to six frames to be recorded with time intervals between them in the range ∼5–50 ns. A ruby laser with output pulse duration of ∼5 ns was used as an illumination source.

4.3.1 Discharge in Distilled Water

Distilled water had specific resistivity $\rho \sim 10^5\,\Omega \cdot$ cm; electrodes and liquid were nondegassed.

For voltage impulse duration equal to or greater than 500 ns, as time passes after voltage application to the discharge gap (depending on its length), initial channels with a weak density gradient arise near the tip electrode (in contact with it or directly in the liquid). The discharge channel propagation is accompanied by a phase transition, occurrence of microbubbles, and their hydrodynamic expansion. The transverse channel dimensions increase up to ~10–20 μm, the density gradient significantly increases, and channels are clearly seen in Schlieren photographs. These processes are intensified near the electrode surface, which results in the occurrence of cone-shaped optical inhomogeneities with sizes of ~20–40 μm at the electrode/liquid interface. The discharge channels propagate along radial directions; therefore, the initial disturbance has approximately spherical shape. Figure 4.34 shows typical Schlieren photographs of the electric discharge in water from the anode under a voltage of 27 kV (field strength of 1.3 MV/cm near the tip electrode). The exposition of the first frame was ~60 ns before the gap breakdown. The characteristic size of the initial inhomogeneity was ~250 μm, and the velocity
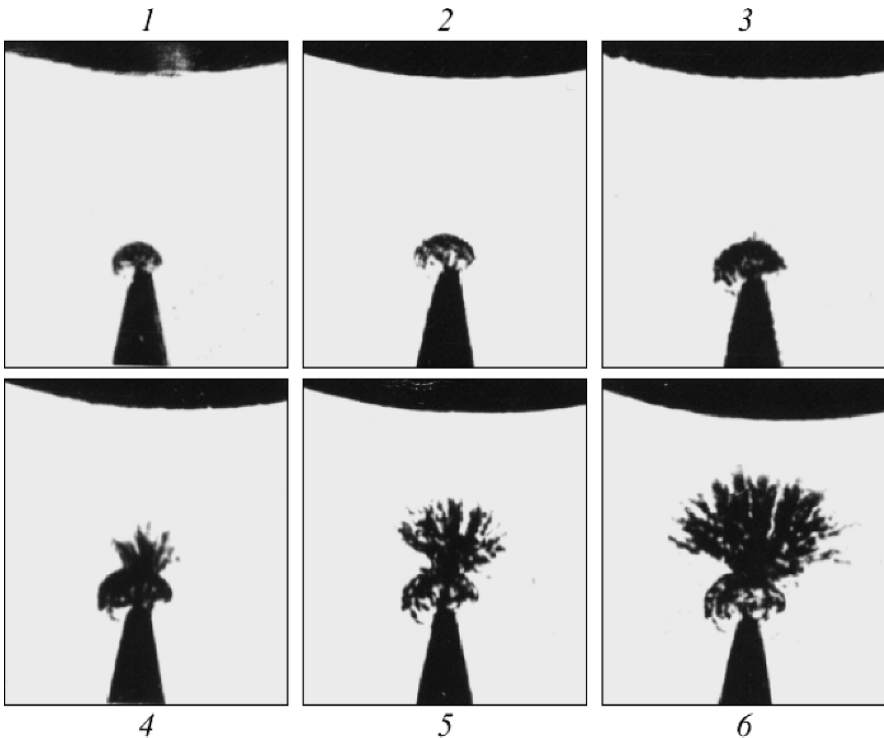
Fig. 4.34. Superfast laser Schlieren photographs of the electric discharge from the anode in distilled water. The distance between the electrodes was 2 mm, the breakdown delay time was 750 ns, and the frame exposure was ~5 ns. The time interval between the first and second frames was 25 ns, and between other frames it was 10 ns

of its propagation toward the cathode was $\sim 3 \cdot 10^5$ cm/s. It seems likely that the pattern is complicated a little by shock wave generation as a result of intensive energy absorption in the discharge channels. The successive frames in Fig. 4.34 show the occurrence and propagation of a faster stage of the electric discharge. It originates on the front of the initial inhomogeneity corresponding to the boundary of the initial channels (the 3$^{\text{rd}}$ frame). The velocity of discharge channel propagation considerably increases. Intense channel branching is observed, the electric discharge is brush-like and strongly scatters external light (dark regions in the photographs). According to frames 3–6, the velocity of intensive discharge propagation is $(3–4) \cdot 10^6$ cm/s and decreases a little as the discharge penetrates deeper into the gap. On the boundary of the dark region or sometimes slightly ahead of it, new ionized channels with slight changes in the refractive index develop in the liquid. The discharge channels near the tip electrode are collapsed. The similar pattern of the electric discharge was observed in a uniform field under voltages ≤ 1 MV/cm (see Chap. 3). It was suggested that the stage of intensive discharge proceeds at the expense of propagation of ionization processes in the liquid as a result of local amplification of the electric field. Since it arises only after phase transformations in the initial channels, the process of electric discharge propagation as a whole is complex and includes both bubble and ionization breakdown mechanisms.

With increase in the voltage applied to the gap, the pattern of electric discharge propagation is kept unchanged. The size of the initial inhomogeneity decreases several times (by a factor of 1.4–2), and the structure of intensive discharge becomes more dense. As an illustration, Fig. 4.35 shows typical Schlieren photographs of the electric discharge from the anode in distilled water under a voltage of 32 kV (the field strength near the tip electrode was ~ 1.9 MV/cm). It can be seen that within a characteristic time of ≤ 100 ns, it is possible to trace the origin and propagation of the electric discharge in the gap. High speed of registration of the Schlieren system (up to 100 mln frames/s) has allowed transition to a faster stage of the electric discharge and its propagation to be traced.

However, it appeared that simultaneously with the above-described breakdown mechanism, another mechanism exists and competes under voltage impulse duration of $\sim 50–200$ ns. The difference between them is vividly pronounced from a comparison of Figs. 4.35 and 4.36.

The last figure was recorded under a voltage of 30 kV (the field strength near the tip electrode was 1.8 MV/cm). It can be seen that the stage of intensive discharge (frame *2* in Fig. 4.36) was not preceded the by formation of inhomogeneities near the tip surface (frame *1* in Fig. 4.36). The electric discharge propagated from the very beginning with a high velocity $\geq 5 \cdot 10^6$ cm/s, which then decreased to $\sim 3 \cdot 10^6$ cm/s. A set of thin channels that weakly scatter light can be seen in front of the strong inhomogeneity (dark region) in frame 3; some of these channels reach the cathode. Exactly different velocities allow one to determine the time delay between the two processes, namely, between the discharge channel propagation and the formation of the dark
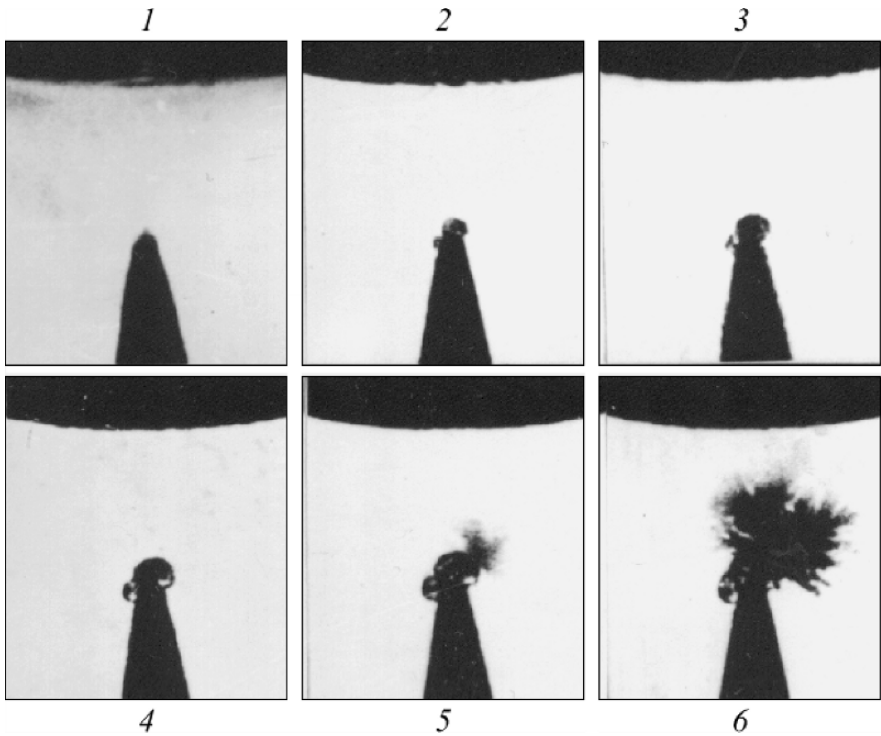
Fig. 4.35. Superfast laser Schlieren photographs of an electric discharge from the anode in distilled water. The distance between the electrodes was 1 mm, the breakdown delay time was 90 ns, and the frame exposition was ∼5 ns. The time interval between the first and second frames was 25 ns, and between other frames it was 10 ns
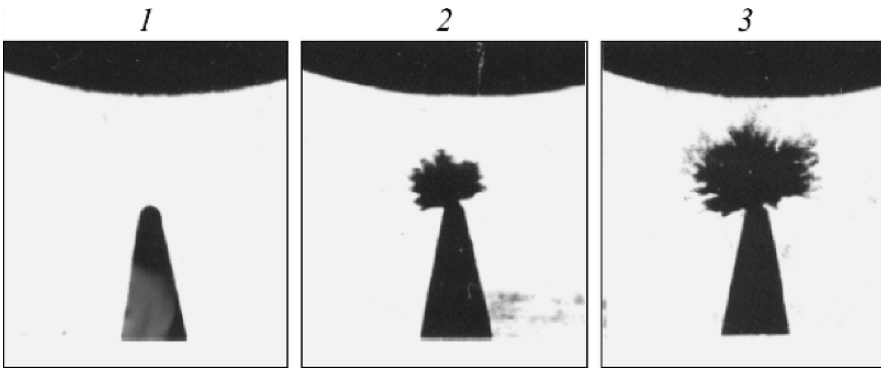
Fig. 4.36. Superfast laser Schlieren photographs of the electric discharge from the anode in distilled water. The distance between the electrodes was 1 mm, the breakdown delay time was 110 ns, and the frame exposition was ∼5 ns. The time interval between successive frames was 10 ns

region consisting of microbubbles and opaque to external light. The third frame in Fig. 4.36 was obtained approximately 2–4 ns before the gap breakdown. The propagation of ionization with a high velocity of $(0.8–2)\cdot10^7$ cm/s during the successive time period terminates the initial stage of the electric discharge formation. An analysis of the results obtained indicates that this breakdown mechanism is connected with the propagation of ionization processes in the liquid. During propagation of the electric discharge through the gap, the ionization processes develop as well in the newly formed microbubbles; however, they are not initial and basic ones. In Chap. 3 it is demonstrated that the electric discharge propagation from the anode in distilled water with a high initial velocity (without first slower stage) under nanosecond impulses is also observed in a uniform field.

With further increase in the voltage applied to the gap, when the voltage impulse duration is ≤50 ns, the second mechanism of breakdown from the anode (Fig. 4.36) is dominant.

The results obtained demonstrate a variety and complexity of the phenomena observed during the electric discharge formation from the anode in water under nanosecond impulses. They allow one to understand qualitatively the mechanisms established previously and to reveal a reason of arising contradictions. Insignificant changes in the liquid density connected with the thin discharge channel propagation can hardly be recorded with image converter cameras because of image distortions for nanosecond expositions. Therefore, only the successive stages of generation and fast expansion of microbubbles were recorded in [88]. Exactly this fact leads to the absence of a dependence of the transparency of the dark region (the fast propagating discharge) on the external illumination wavelength. Secondary elementary processes that develop in these microbubbles cause the emission of narrow lines of the Balmer series [89]. A weaker dependence of the impulse electric strength of water on the pressure with decreasing voltage impulse duration (see Sect. 6.3) can be explained by the dominant second (ionization) breakdown mechanism from the anode.

4.3.2 Discharge in Transformer Oil

Figure 4.37 shows typical Schlieren photographs of the electric discharge in well refined transformer oil for a field strength near the tip electrode of ~2.8 MV/cm [87]. An analysis of a large number of Schlieren photographs has allowed Klimkin [87] to elucidate in detail the breakdown mechanism under these conditions. The initial channels arise near the tip electrode within $30 - 50$ ns from the moment of voltage application to the discharge gap. New discharge channels arise in the liquid on the boundary of the initial inhomogeneity and in front of it. Their occurrence is mostly random in character. The channel length is $\sim20 - 200\,\mu$m. The discharge channels decay near the tip electrode and in the gap. The electric discharge has a fine structure with corresponding weak variations of the refractive index. According to frames shown
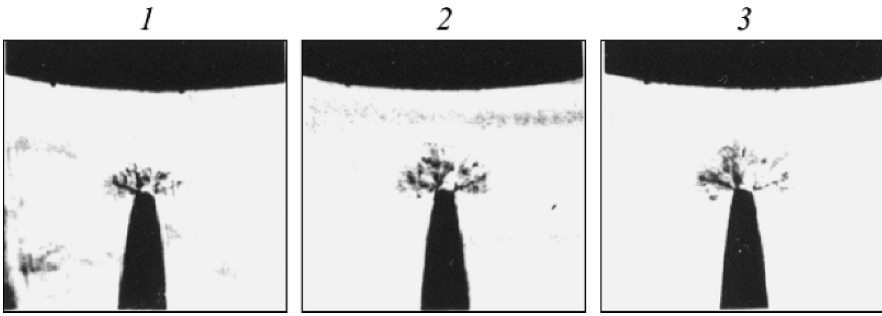
Fig. 4.37. Superfast laser Schlieren photographs of the electric discharge from the anode in transformer oil. The distance between the electrodes was 1 mm, the breakdown delay time was 280 ns, and the frame exposition was ∼5 ns. The time interval between the first and second frames was 30 ns and between the second and third frames it was 60 ns

in Fig. 4.37, the average velocity of discharge propagation is ∼$3 \cdot 10^5$ cm/s. It should be noted that for field strengths near the tip electrode up to 3 MV/cm in transformer oil, intensive discharges with a velocity of 10^6–10^7 cm/s are not observed. Exactly this determines a higher impulse electric strength of oil in comparison with distilled water.

For a comparison, Fig. 4.38 shows Schlieren photographs of the electric discharge propagating from the cathode in distilled water (frames *1* and *2*) and transformer oil (frames *3* and *4*) [87]. They correspond to field strengths near the tip electrode of ∼2.2 and ∼2.4 MV/cm and breakdown delay times of ∼0.5 and 1 µs, respectively. It can be seen that the prebreakdown processes are approximately identical. This indicates that the main ionization processes leading to the electric discharge propagation occur in the vapor-gas phase. The average velocity of cathod channel propagation in distilled water was ∼10^5 cm/s, and their propagation was accompanied by generation of shock waves. In transformer oil, it is slightly less than ∼$5 \cdot 10^4$ cm/s. Of interest are the details of the electric discharge. The propagation of electrohydrodynamic instability (dark cone-like peaks at the vapor/liquid interface in frames *2* and *3*) and the origin of discharge channels on the instability boundary (frames *3* and *4*) can be seen.

The results obtained support the hypothesis on the ionization and bubble breakdown mechanisms from the anode and cathode, respectively.

4.4 Discharge in a Liquid with a Solid Dielectric Interface

The results described in Sects. 4.1 and 4.2 demonstrate that one of the methods of control over the spatial structure and kinetics of the discharge, and through them over the electric strength of insulation gaps with liquid
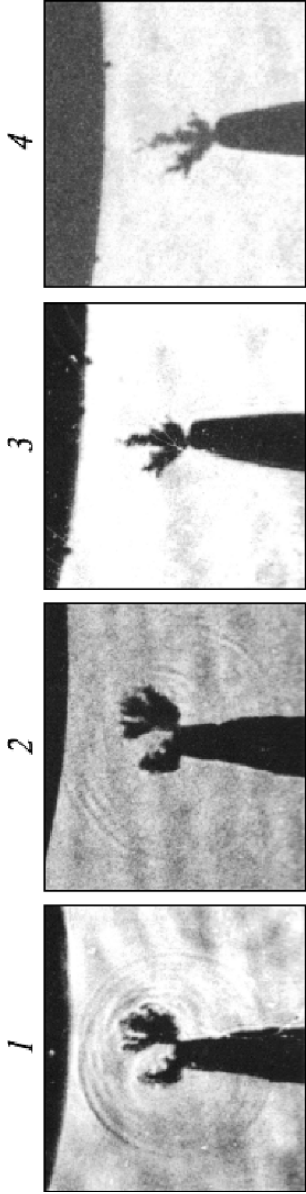
Fig. 4.38. Superfast laser Schlieren photographs of an electric discharge from the cathode in distilled water (*1* and *2*) and transformer oil (*3* and *4*). The distance between the electrodes was 0.9 (*1* and *2*) and 0.7 mm (*3* and *4*), and the frame exposition was ∼5 ns. The time interval between successive frames was 90 ns

dielectrics, is changing the field distribution on the front of the discharge figure. This can be made by introduction of solid dielectrics whose surface is perpendicular or parallel to the main electric field line. Of great interest for designing high-voltage equipment and understanding mechanisms of the electric discharge in liquids is a breakdown of such systems.

4.4.1 Barrier Effect

The barrier effect, as is well known, is taken to mean an increase in the breakdown voltage of an insulation gap with a non-uniform field by placing of a solid dielectric barrier perpendicular to the electric field force lines. Despite long-term application of barriers in the design of high-voltage equipment to increase the reliability of operation and to reduce dimensions, the nature of the barrier effect has been investigated insufficiently. The authors of the majority of works devoted to the barrier effect in insulation gaps with liquid dielectrics are limited, as a rule, by its quantitative characteristics under different experimental conditions. Generalizing the material of these investigations, the following main results can be formulated:

– the barrier effect under impulse voltages is weaker than under ac or dc voltages,
– the barrier effect is intensified with increasing field non-uniformity in the insulation gap; in gaps with uniform fields, the barrier can even reduce the impulse breakdown voltage U_{br},
– the effect is maximum when the barrier is placed near the electrode determining the field non-uniformity (the initiating electrode) at distances of 0–25% of the gap length,
– for positive polarity of the initiating electrode, the effect is stronger than for negative polarity.

The first attempts of studying spatiotemporal discharge patterns in +T −P and −T +P gaps with transformer oil and distilled water under $1.2/70\,\mu s$ impulses [90] demonstrated that the discharge in the tip-barrier gap under application of the first impulse differed only insignificantly from the discharge in the tip-plane gap of equivalent length. When the applied voltage is much less than the breakdown one, the leader channel propagates along the trajectory typical of such gaps to the barrier. Only at a distance of 3–5 mm from the barrier (for total distances from the tip to the barrier of a few tens of millimeters), the channel bends almost at a right angle, comes close to the barrier, and further propagates as a creepage discharge.

With increase in the voltage amplitude, a part of impulses causes a breakdown of the barrier at points located at certain distances from the projection of the initial leader trajectory onto the barrier. Further increase in the voltage impulse amplitude results to the fact that the breakdown of the barrier and the projection of the initial leader trajectory coincide. The barrier breakdown

by the leader is always accompanied by the complete breakdown of the interelectrode gap. The discharge pattern does not virtually change versus the barrier position. Figure 4.39 shows the dependence of the relative increase in U_{br}, in percent, for a 50% breakdown probability of T–P gaps in transformer oil on the barrier position. A celluloid sheet (395 mm $\times$ 295 mm) 0.13 mm thick clamped rigidly in a textolite frame was used as a barrier.

From Fig. 4.39 it can be seen that the maximum increase in the gap strength (by 30%) due to the barrier was recorded for the +T –P electrode system with the barrier placed in the immediate proximity of the tip electrode. The barrier effect in the –T +P gap is weaker.

An increase in U_{br} of the gap in distilled water due to the presence of a barrier is insignificant, and for positive tip polarity its value changes from 13% (the barrier is near the tip) to 7% (the barrier near the plane) (Fig. 4.40). For negative tip polarity, U_{br} increases only by 8.5% when the barrier is placed at a distance of $\sim$0.20d from the tip electrode. When the barrier is placed at distances $> 0.6d$ from the tip, the barrier effect is within the limits of experimental error.

Analogous quantitative laws were reported for the barrier effect in [91]. The dependences of the breakdown voltage of an insulation gap in transformer oil on the position of a bakelite barrier 1 mm thick were investigated. The gap 600 mm long was formed by a rod with a small sphere ($d = 0.5$ mm) at the end and a plane. Measurements were performed under both positive and negative lightning impulse voltages by the up-and-down method under application of 10 impulses with a 60 s time delay between two successive impulses.

Results of measurements are shown in Fig. 4.41. As in [90], the effect is maximum when the barrier is near the initiating electrode under application of a positive impulse voltage.
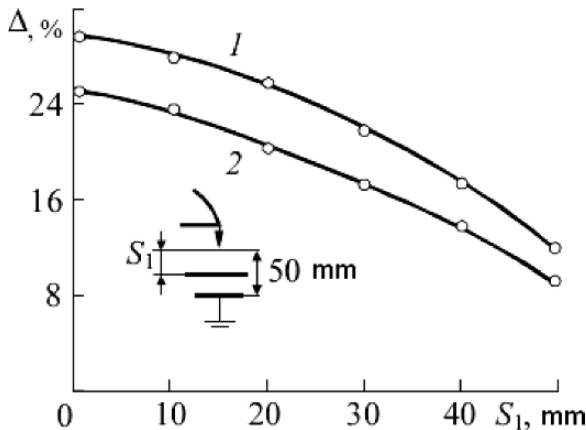
Fig. 4.39. Dependence of the relative increase in U_{br} for the +T −P (*curve 1*) and −T +P gaps (*curve 2*) in transformer oil on the position of the celluloid barrier ($\delta = 0.13$ mm) for $d = 50$ mm [90]
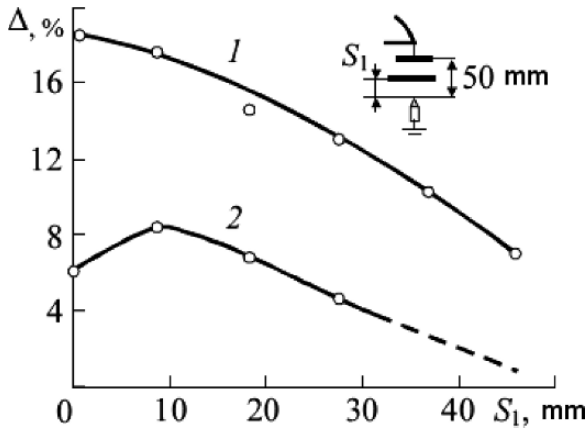
Fig. 4.40. The same as in Fig. 4.39, but for distilled water [90]

An attempt was undertaken to calculate the optimal position of the barrier based on the simplest electrostatic model. The model considered redistribution of the electric field in the gap with the barrier with allowance for the geometrical parameters of the system and the main dielectric characteristics (ε, γ) of the barrier material and the liquid. Beroual et al. [91] pointed out that
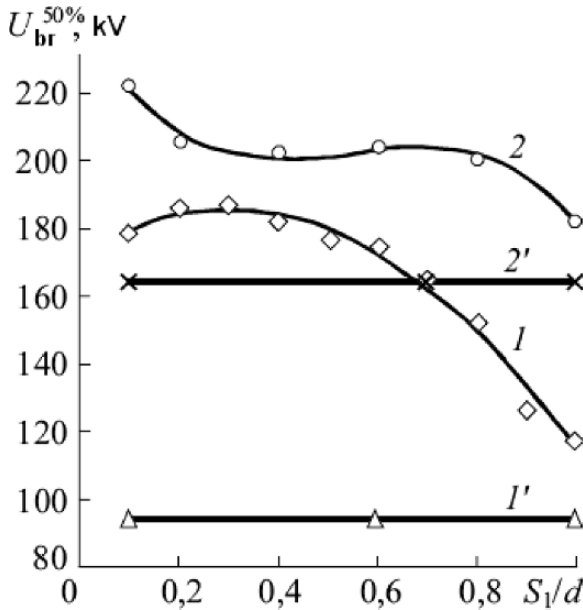
Fig. 4.41. Dependence of $U_{br}^{50\%}$ for the gap in transformer oil on the position of the barrier (S_1/d) for positive (*curves 1* and *1′*) and negative impulse polarities (*curves 2* and *2′*). Here curves *1′* and *2′* show U_{br} for the gap without barrier [91]

the data on a charge in the gap with and without the barrier are required for a more correct estimation of the barrier efficiency.

The data on spatiotemporal laws of discharge propagation in a gap with a barrier presented in [44, 92, 93] are in agreement with the data presented in [90], and the data on quantitative characteristics of the barrier effect are in agreement with materials presented in [90, 91]. However, in [44, 92] the data were presented on the parameters of the discharge channel in the tip-barrier gap that testified to the influence of effects of barrier charging on the discharge phenomena when the channel reached the barrier and on the discharge propagation under successive voltage application.

The barrier effect in an oil gap with slightly non-uniform and quasiuniform fields with $\mu \leq 1.8$–2.0 was investigated in [44] for a breakdown initiated by 0.85/100 μs positive impulses. The discharge gap was a laboratory model of the oil-barrier insulation for high-power transformers. Two barriers were placed simultaneously in the gap, and the first and second gap lengths were $S_1 = 1$ mm (2 mm) and $S_2 = 2$ mm (4 mm), respectively. Similar investigations with a single barrier, positive and negative impulse polarities, and the field nonuniformity coefficient lying in the range $\mu = 1.8$–1500 were carried out in [92]. In both studies, barriers were made from a commercial pressboard with thickness $\delta = 0.55$ and 1.0 mm, respectively.

In particular, in [92] it was established for gaps with sharply non-uniform field that the leader channel trajectory in a tip-barrier gap under voltages much less than the breakdown voltage did not change when the channel approached at distances of 0.5–1 mm to the barrier. At small overvoltages roughly corresponding to those used in [90], after the leader approached the barrier, the delay between steps (flashes) increased from ∼0.1 μs to 1–1.5 μs, and the brightness of each flash increased approximately by an order of magnitude. The channel trajectory during each successive flash was bent, and the channel extended and deviated from the barrier. At very large overvoltages after the first contact of the channel with the barrier, the channel deviated during successive flashes already when it was at distances of 10 mm from the barrier.

According to estimates presented in [92], during the first contact of the leader and barrier, a charge of ∼30 pC with surface charge density of ∼600 pC/cm^2 capable of forming a potential well at a distance of 4 mm from the electrode and causing deviation of the leader channel during successive steps was transferred to the barrier. After contact between the leader and barrier, shock waves propagated to the electrode with a velocity of (1.4–1.5)·10^5 cm/s. According to [92], these shock waves promote the extinguishing (collapse) of the channel during next steps.

In gaps with a slightly non-uniform field at impulse amplitudes of 1–10% of the breakdown value, the average breakdown field intensity was 150 kV/cm, the velocity of leader propagation in the tip-barrier gap was (2–3)·10^6 cm/s, and the time interval between two successive flashes of the channel was ∼20–30 ns. The characteristics of the leader channel after contact with the barrier

were close to those of a stationary arc in transformer oil (the current density in the channel was 3–$10\,\mathrm{kA/cm^2}$ and the particle concentration was $2{\cdot}10^{16}\,\mathrm{cm^{-3}}$), and the channel was capable to transfer the high-voltage electrode potential to the barrier. In this case, the insulation gap length decreased by the distance between the tip and barrier S_1. The average field strength E_{av} necessary for a breakdown of the gap S_1 is less than the field strength necessary for a breakdown of the barrier E_{b}. The smaller S_1, the lower E_{b}, and the higher the breakdown voltage. Values of E_{av} and E_{b} are much greater than E_{br} of the oil gap. Their ratio k characterizes the magnitude of the barrier effect. The dependence on the degree of field non-uniformity μ is characterized by the following figures:

a) $k = 4$–4.5 for $\mu = 36$,
b) $k = 1.35$–1.45 for $\mu = 13$,
c) $k = 1.2$ for $\mu = 5.4$,
d) $k = 1$ for $\mu = 1.2$.

For a short length of the first oil channel $S_1 \approx 1.0\,\mathrm{mm}$ in the oil-barrier insulation model [94] and a small voltage amplitude, the results are similar [90, 92]. Repeated discharges on the barrier are displaced from the hemispherical electrode tip ($r_0 = 3.25\,\mathrm{mm}$) approximately by $1.5\,\mathrm{mm}$ (Fig. 4.42). The number of current impulses before the complete termination of the discharge processes in the first oil channel decreases with increasing U, and the impulse amplitude increases up to a few amperes – a few tens of amperes. A single current impulse with an amplitude of $30\,\mathrm{A}$ is observed at $U = U_{\mathrm{br70\%}}$ approximately 10–$15\,\mathrm{\mu s}$ before the complete breakdown.

The damage of the barrier in the form of carbonized traces (tracks) is localized at distances of 5–$6\,\mathrm{mm}$ from the gap axis. Further deepening of tracks and increase in their length cause the breakdown of the first barrier. The region of the second barrier breakdown is usually localized under the region of breakdown of the first barrier (the distance between the electrodes $d = S_1 + S_2 + 2\delta = 4.6\,\mathrm{mm}$).

No current impulse train was observed for a larger-scale model ($r_0 = 7.9\,\mathrm{mm}$, $d = 8.2\,\mathrm{mm}$, $S_1 = 2\,\mathrm{mm}$, and $S_2 = 4\,\mathrm{mm}$). The complete breakdown of the model was observed 10–$15\,\mathrm{\mu s}$ after the occurrence of a 30-A single current impulse.

Barriers in the gap reduce the average value $U_{\mathrm{br10\%}}$ from 322 (for the gap without barrier) to $192\,\mathrm{kV}$. Lobanov et al. [94] connect this effect with the influence of fibers on the barrier surface.

The average velocity of discharge propagation in complete breakdown of the model was $(0.3$–$1){\cdot}10^5\,\mathrm{cm/s}$, the channel diameter at the instant of breakdown of the the first gap S_1 was 160–$200\,\mathrm{\mu m}$, and the velocity of discharge propagation was $2\cdot10^5\,\mathrm{cm/s}$. The charge transferred to the first barrier in the model breakdown was 0.5–$1\,\mathrm{\mu C}$, the average field strength was $300\,\mathrm{kV/cm}$, the current density in the channel was $\sim150\,\mathrm{kA/cm^2}$, and the temperature in the channel at the instant of contact with the barrier was $3600°\mathrm{C}$.
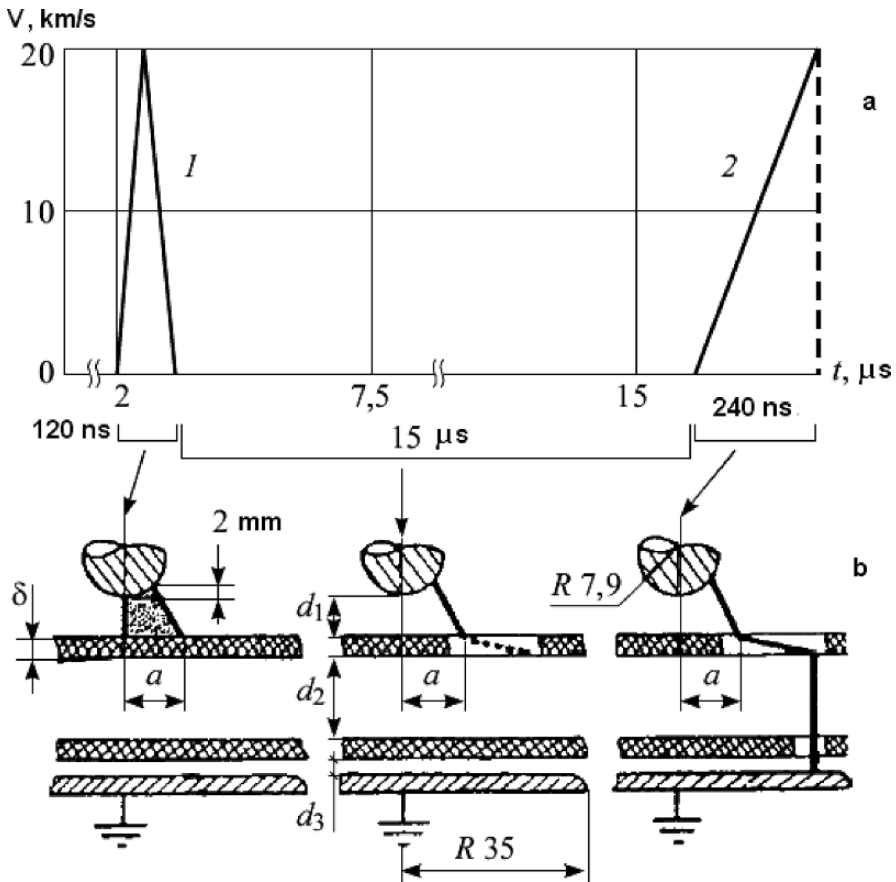
Fig. 4.42. Discharge in the first oil channel and complete breakdown of the oil-barrier insulation model: **a**) time variations of the discharge propagation velocity and **b**) breakdown channel formation with the breakdown current impulse of the first oil channel (*curve 1*) and the current impulse at the moment of complete breakdown (*curve 2*) [94]

In [93] investigations were focused on studying a role in the barrier break-down of three processes:

– accumulation or redistribution of charges,
– local barrier heating,
– accumulation of mechanical damages.

The effects can be distinguished due to a large difference in their characteristic times.

The polyethene, paper, and novaflex (a glass fiber weave impregnated with a silicone resin) barriers in transformer oil or organosilicone liquids were investigated. The most part of investigations was performed with a liquid having

a viscosity of 10 cSt. The discharge gap 2–3 mm long was formed by a tip and a sphere, and the barrier was placed in the middle of the gap. A negative impulse was applied to the tip electrode. The first process – accumulation and redistribution over the barrier of charges from the preceding discharges – was estimated based on the two possible effects, namely, on the discharge blocking in the tip-barrier gap and change of the external shape of the discharge figure (changes in the deviation angle of partial channels of the discharge figure and deviation of the breakdown channel from the gap axis). The blocking barrier effect was not established.

Investigations of the second effect are impeded by a wide scatter of the results due to the random nature of discharge processes (Fig. 4.43). Nevertheless, certain laws governing the phenomenon were revealed. For the polyethene barrier, well expressed cyclicity of changes in the deviation angle of partial discharge channels from the axis was observed (Fig. 4.44). The angle increased for the the first 3–4 discharges and then sharply decreased to the initial value. After several cycles, the regularity was broken, and a tendency toward an increase in the deviation angle was clearly manifested.

This tendency was kept unchanged when the time interval between two successive voltage impulses increased to 1 min. But it was broken when the time interval was longer than 1–5 min. When the discharge or neutralization time of the charge changes due to an increase in the barrier surface conductivity, the surface discharge occurs at the barrier support system or the critical time constant remains at a level of a few minutes.

Weak light flashes were also observed in the tip-barrier gap (the back-flash effect) whose periodicity was equal to the periodicity of changes in the angle of channel deviation from the gap axis.
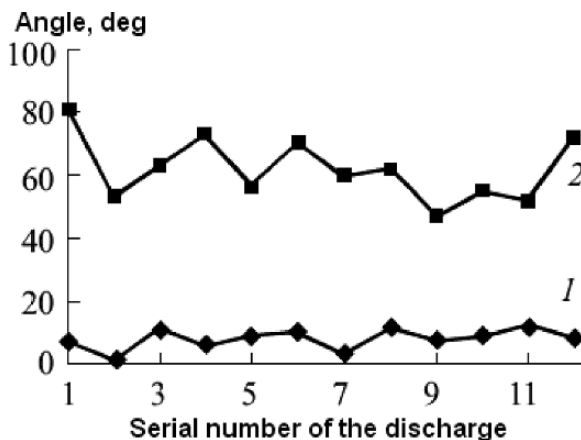
Fig. 4.43. Angles of deviation of the discharge channel that causes a complete breakdown from the gap axis (*curve 1*) and angles of maximum deviation of partial channels (*curve 2*) for the T-Sp gap without barrier in an organosilicon liquid [93]
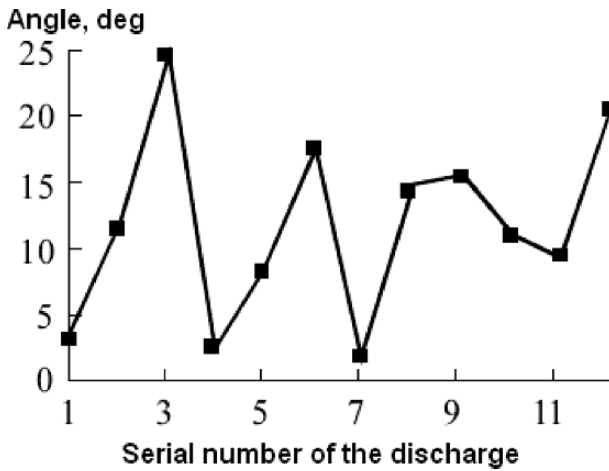
Fig. 4.44. The same as in Fig. 4.48 (*curve 2*), but for the gap with a polythene barrier, impulse amplitude of 75 kV, and delay between successive impulses of 10 s

It was suggested that the charge transferred to the barrier from the preceding discharges was deposited irregular, namely, it formed spots. Channels of successive discharges were aimed at non-charged barrier regions. For large number of impulses and hence discharges at the barrier, its surface was charged more uniformly, and the cyclicity of changes in channel deviation angles was broken.

A maximum impulse amplitude and design parameters of the experimental chamber were such that no leaks to grounded structures and no breakdowns of new (non-aged) barriers were observed. Under repeated voltage application, only the paper barrier was damaged due to its mechanical (physical) degradation. In this case, the breakdown voltage of the gap with the paper barrier decreased from 75 kV under application of the first 15–20 voltage impulses to 65 kV under application of 60–80 impulses.

The results of studies considered above allow us to conclude that the determining factors of the barrier effect are:

– its action as a mechanical barrier to the discharge channel (for free motion of charge carriers) at the instant of its first contact with the barrier,
– change in conditions for repeated components of this discharge due to changes in the field geometry caused by charges deposited on the barrier,
– changes in conditions of the discharge propagation when voltage impulses are applied in series with time intervals between two sucessive impulses no longer than a certain value due to charge accumulation on the barrier.

4.4.2 Creepage Discharge(Frashover).

High electric strength of liquids often cannot be realized in full measure to produce compact insulation systems and devices, because it can be reduced

significantly through the introduction of dielectric spacers, standoff and through insulators, etc. whose surface is parallel (or nearly parallel) to the electric field lines.

At present, a lower electric strength of the interface is explained by the action of primarily three factors, including field distortions due to different dielectric characteristics (ε, γ) of the medium and the solid body, influence of sorbates contained in the dielectric medium and atmosphere (before immersion into a hermetic system), and also by additional charging of the propagating discharge channel through the insulator capacity. The greatest inhomogeneity (amplification) of the electric field is observed at the triple point where the electrode, solid insulation, and dielectric medium are in contact.

Due to the manifestation of the above-described effects, the creepage discharge voltage along the insulator surface U_{fl} is determined by a combination of many factors, including the character of the electrode contact with the insulator, insulator size and surface shape, orientation of the insulator surface relative to the electric field lines, properties of the solid dielectric and medium, parameters of the applied voltage, etc.

Since U_{cr} of insulators determines the short-term electric strength of devices, the electric strengths of the dielectric medium and solid insulation should be matched, insulator design should be optimized, and the solid insulation material should be chosen with allowance for the electric and mechanical strengths. The additional requirement can be stability to some adverse factors.

It is convenient to reduce a variety of positions of the surface solid dielectric with respect to the electric field lines in the study of the creepage discharge to three characteristic insulation systems (Fig. 4.45). The least field distortion due to the dielectric inserted in the field is typical of the design shown in Fig. 4.45a, and the greatest one is typical of the design shown in Fig. 4.45c.

The material of the preceding sections demonstrate that the electric strength of liquids depends very strongly on the electrical conduction of the discharge channel and hence on the current running through it. In the case of surface discharge, a change in the specific surface capacity of the substrate and the relationship between the normal and tangential field components for
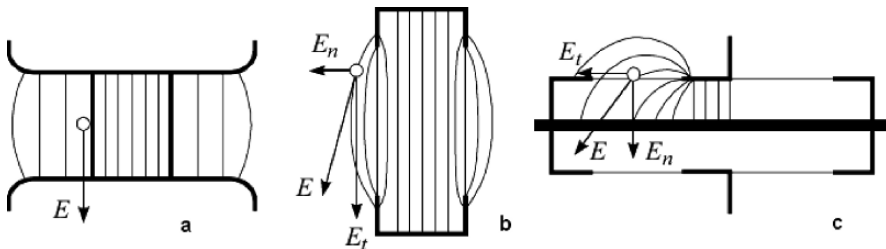
Fig. 4.45. Typical insulation systems used for investigation of surface breakdown with a unifom (**a**) and non-uniform fields with dominant tangential E_t and normal E_n components of the electric field vector (with respect to the solid dielectric surface)

the same liquid and impulses whose paramaters are kept unchanged allows the current in the discharge channel to be varied over wide limits.

The total current consists of ionization and capacitive currents (the ion conduction current in this case can be neglected for the majority of dielectric liquids). The capacitive current consists of the capacitive charge current formed by the discharge channel and the opposite electrode closed through the liquid (I_{C2}) and the current closed through the solid dielectric on the grounded electrode (I_{C1}) (Fig. 4.46) [7].

For the electrode systems used in experiments [7,85], the component I_{C2} was much less than I_{C1}. To estimate the contribution of I_{C1} to the total current, it was assumed that the capacity C_1 is formed by two parallel cylindrical conductors with radii a_1 and a_2 placed at distance δ equal to the thickness of the dielectric substrate (here a_1 is the radius of the guiding electrode, and a_2 is the radius of the leader channel). One of the cylinders is extended with the velocity equal to the propagation velocity of the leader channel $\nu(t)$, and the length of the second cylinder modeling the grounded guiding electrode is equal to the creepage discharge length l_1 (in this case, we consider the system with dominant normal component).

It then follows that I_{C1} is expressed as

$$I_{C1} = C_1 \frac{dU}{dt} + U \frac{dC_1}{dt},$$
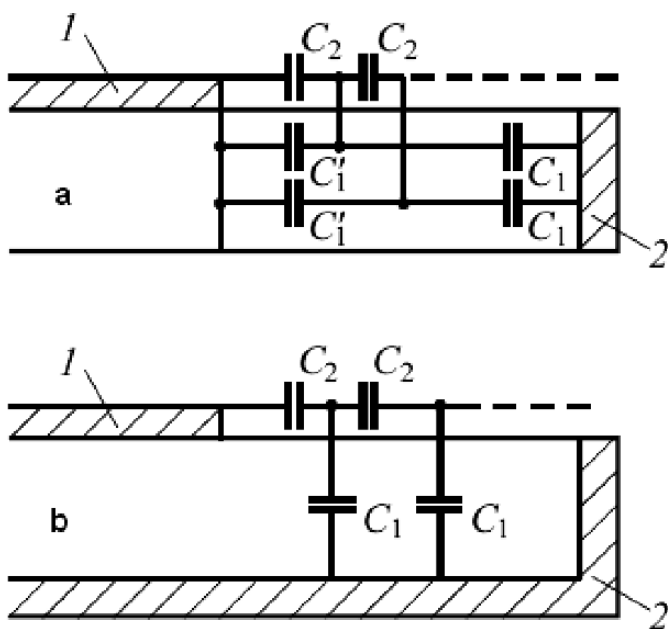
Fig. 4.46. Equivalent circuit for calculation of capacitive currents for the electrode system with dominant tangential (**a**) and normal (**b**) components of the field $\bar{E}_0$ [7]

and $\dfrac{dC_1}{dt}$ is expressed as follows:

$$\frac{dC_1}{dt} = \frac{dl}{dt} \cdot \frac{dC_1}{dl} = \nu\,(t)\,\frac{dC_1}{dl}.$$

Having solved these equations for realistic values of the parameters $l_1 = 7\,\text{cm}$, $a_1 = 0.3\,\text{cm}$, $a_2 = 0.005\,\text{cm}$, $\delta = 1\,\text{cm}$, $\varepsilon = 3.5$, $U = 120\,\text{kV}$, $dU/dt \approx A \approx 35\,\text{kV/μs}$, and $\nu = 2\,\text{cm/μs}$ in the stage of the discharge with the leader 4 cm long, we obtain

$$C_1\frac{dU}{dt} = 0.27A, \quad U\nu\frac{dC}{dl} = 1.45A.$$

Measurements of the current under analogous conditions yield the total current $I \approx 2.8\,\text{A}$. It can be seen that the current closed through the solid dielectric and depending on C_{sp} makes a significant fraction ($\sim$60%) of the total leader current. Therefore, changing it, one can change the total current in the developing discharge channel and study its influence on the spatiotemporal characteristics. A series of works [95–98] carried out in the LEMD in the 90s confirmed the conclusion about the capacitive nature of a significant fraction of the current running through the creepage discharge channel.

In comparison with the space discharge, many special features of the creepage discharge can be explained by higher currents running through the discharge channel and hence by larger values of energy liberated in it. For example, these special features involve the following experimental facts established in [7, 52, 85]:

– stepwise propagation of the channel from the moment of its inception,
– more regular character of leader steps (periodic flashes of the channel and current impulses corresponding to them) during discharge propagation in transformer oil over the pressboard surface parallel to the discharge gap axis,
– brighter light flashes in the channel and larger current impulse amplitudes. In addition, in [52] it was established that
– the fast phase of channel propagation over the dielectric surface was observed already under voltages slightly exceeding the minimum breakdown voltage; in this connection, a fast decrease in the creepage discharge time was observed under the voltage approximately half that of the volume discharge;
– the velocity of fast creepage discharge approximately doubled in comparison with the volume discharge and reached $8 \cdot 10^7\,\text{m/s}$ given that all other conditions remained the same;
– fast discharge can propagate from the tip of one of the branches of the discharge figure propagating from the tip anode.

Lundgaard et al. [52] pointed out that a significant contribution to the manifestation of these special features of the creepage discharge comes from

breaking of the axial symmetry of the discharge figure due to the presence of the solid dielectric that changes the electrostatic properties of this figure.

Spatial Structure of the Creepage Discharge

A system comprising a tip electrode placed on the solid dielectric surface (or in the immediate proximity of this surface) and a plane electrode deposited on the opposite dielectric surface by sputtering or formed by a massive plate closely adjacent to this dielectric surface is most frequently used to study the spatial structure and kinetics of the creepage discharge. Without guiding electrode (discussed in more detail below), the discharge figure is roughly axisymmetric (Fig. 4.47a) [99]. Numerous branches propagate in radial directions with approximately constant rates. Their quantity and branching increase with increasing the specific surface capacity by means of reduction of the solid dielectric substrate thickness or owing to use the substrate from materials with high permittivity [121].

The photograph of a partial creepage discharge in transformer oil recorded with a videocamera (Fig. 4.47) and the ICC photograph of a complete discharge taken in the single-frame mode through a slit in an opaque screen (Fig. 4.47b) [7] vividly show two regions of each branch of discharge figure, namely, thick and thin, that is, the leader and initial channels. Two clear distinguishable parts of the creepage channel – thin and thick – you can see in the photos in [122].

The influence of the substrate material caused the length of branch of the partial discharge on the hard silicate glass surface to double compared to that over the pressboard surface. Nakao et al. [99] concluded that discharge chan-
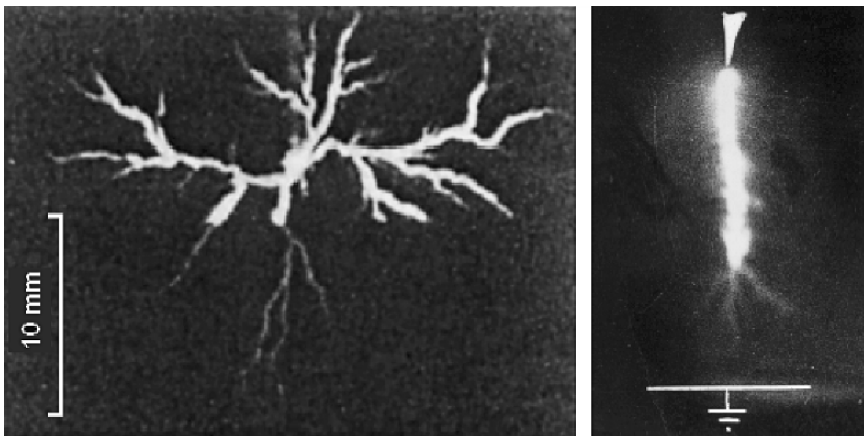
Fig. 4.47. Photograph of a positive discharge figure in transformer oil for the discharge propagating (**a**) over the hard-glass surface and (**b**) over the organic glass surface [7]

nels propagate easier in the direction of smaller difference in height between peaks and troughs, that is, over a smoother surface.

The polarity effect observed in [99] was manifested as follows:

– the positive discharge velocity $[(1.3–1.7)\cdot10^5\,\mathrm{cm/s}]$ was higher than the negative discharge velocity $[(0.6–0.8)10^5\,\mathrm{cm/s}]$,
– positive channels propagated stepwise from peak to peak over the press-board surface, and the direction of propagation of negative channels was determined by a smooth substrate surface.

In [100] propagation of the creepage discharge in transformer oil on the hard glass and soda-lime glass plate surfaces placed perpendicularly or in parallel with the T–P gap axis was investigated. It was established that in the second case, the channel was much longer, though the velocities of channel propagation were approximately identical given that all other factors remained unchanged. In the second case, the discharge figures and shock waves generated by them on the soda-lime glass surface had less regular (axisymmetric) shape.

The influence of dielectric and surface properties of the substrate material, potential, its charges by previous discharges, and impulse ($1.2/50\,\mu\mathrm{s}$) voltage polarity on the kinetics of the creepage discharge in transformer oil was investigated in [101]. An original experimental setup (Fig. 4.48) was used. It comprised the third electrode – grounded plane 4 – in addition to two electrodes – high-voltage 1 and grounded 2 – placed on the opposite surfaces of substrate 3. By changing distance l, the initial substrate potential U_{in}, calculated in the electrostatic approximation from the system geometry and dielectric characteristics of transformer oil and dielectric substrate, was changed. The field strength E_{in} created by U_{in} increased exponentially with decreasing l. In this case, U_{in} decreased with l for the given substrate material with relative permittivity ε_{T}, and at fixed l, U_{in} increased with ε_{T}. The Coulomb force acting on charge carriers that take part in the formation of the discharge channel increased with E_{in}. It is accepted that this force hinders the discharge propagation, since the vector E_{in} is perpendicular to the solid dielectric surface. The potential U_{in} depending on l also influenced the discharge propagation. The potential of the substrate charged by a unit creepage discharge (U_{ch}) was measured by the contactless method with a vibrating capacitance potentiometer. The influence of U_{ch} on the creepage discharge propagation was investigated only for the negative polarity of rod electrode 1, that is, for the positive polarity of initiating (tip) electrode 2. It is natural that the polarity of U_{ch} was opposite to the polarity of U.

The measurable discharge parameters were the length of partial discharge channels, time of their propagation, and longitudinal potential gradients in the discharge channel.

The substrate characteristics are tabulated in Table 4.7.

Some of the results illustrating the discharge kinetics are shown in Figs. 4.49–4.51. It was established that the length of discharge channels of
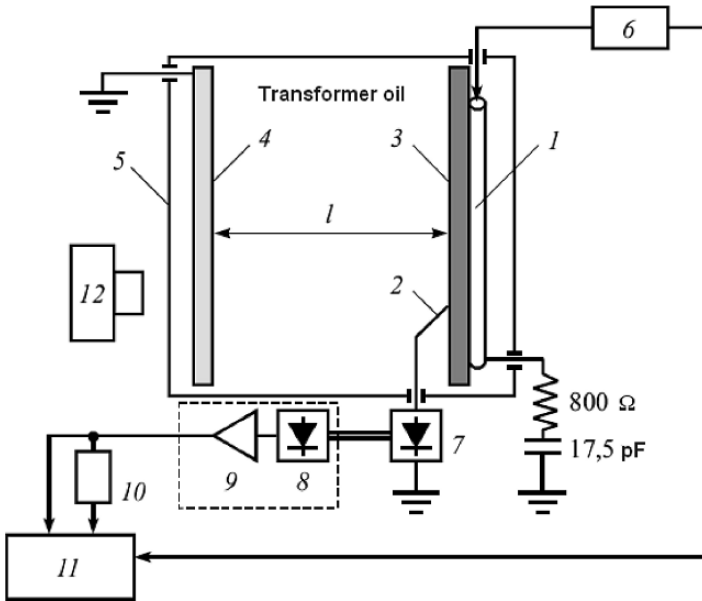
Fig. 4.48. Experimental setup comprising high-voltage electrode *1* (a copper rod with $d = 4\,\mathrm{mm}$), grounded tip electrode $2(r_0 \approx 10\,\mu\mathrm{m})$, solid dielectric substrate *3* ($\delta = 3\,\mathrm{mm}$), grounded semitransparent plate *4* (150 mm × 150 mm), test cell *5*, impulse voltage generator *6*, light-emitting diode *7*, photodiode *8*, amplifier *9*, *C-R* integrator *10*, oscillograph *11*, and image amplifier *12* [101]

both polarities linearly increased with applied voltage U and substrate potential U_{in}. Moreover, $L = f(U_{\mathrm{in}})$ for positive channels was insensitive to l and to the substrate material. For negative channels, $L = f(U_{\mathrm{in}})$ was also independent of l, but depended on the substrate material. Hanaoka et al. [101] suggested that this difference in the behavior of positive and negative discharges was caused by the fact that negative channels during their propagation, unlike positive ones, were close to the substrate and hence sensitive to the state (in particular, to the roughness) of its surface.

The influence of the charge deposited on the substrate from the previous discharge, can be understood from Fig. 4.51. For negative polarity U_{ch}, the channel is longer, and for positive polarity it is shorter than in the case of uncharged surface. It is assumed that when the positive discharge propagates

Table 4.7.

Substrate material	δ,mm	ε_{T}	ρ_{v}, $\Omega{\cdot}\mathrm{cm}$
High-density polythene (HDPE)	3.0	2.3	10^{16}
Organic glass (PMMA)	3.0	2.5	10
Glass fiber weave impregnated with an epoxy resin	3.0	6.0	10^{13}–10^{15}
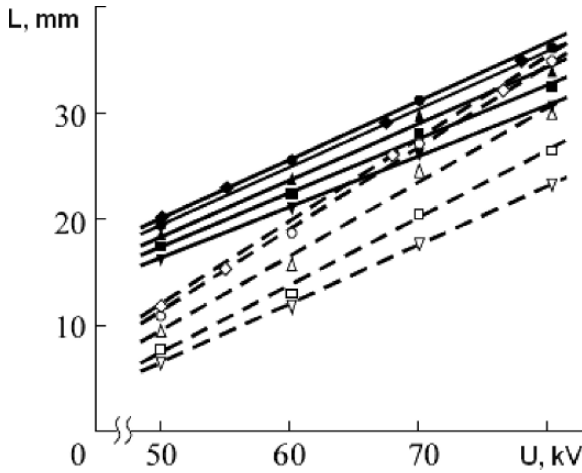
Fig. 4.49. Relationships among the partial discharge channel length L, voltage impulse amplitude and polarity, and distance to the grounded plate l. Dashed curves are for positive impulse polarity and negative polarity of the initiating electrode: ♦, without grounded plate; •, $l = 150$ mm; ▲, $l = 70$ mm; ■, $l = 40$ mm; ▼, $l = 20$ mm. The substrate was fabricated from HDPE [101]

over the negatively charged surface, the potential field component is greater than U, and this increases the energy supplied to the channel head and hence increases L. On the contrary, the amount of supplied energy decreases in the presence of positive charges on the surface.
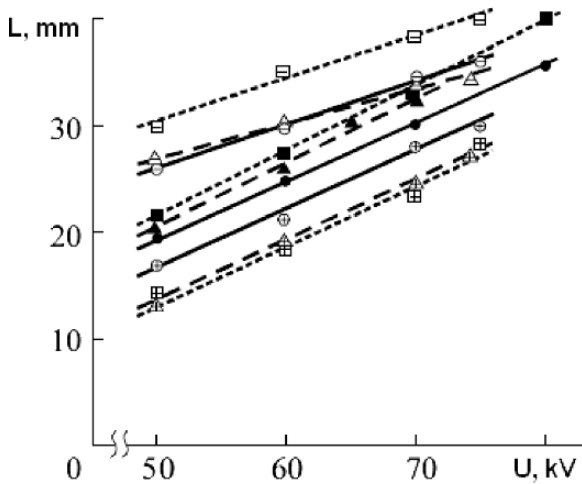
Fig. 4.50. Dependence of L of positive discharges on the voltage impulse amplitude for the substrate with uncharged (filled symbols) and positively or negatively charged surfaces (empty symbols with plus or minus signs, respectively) at $l = 150$ mm: ○, HDPE, 10 kV; Δ, PMMA, 15 kV; □, GFWIER, 19 kV [101]
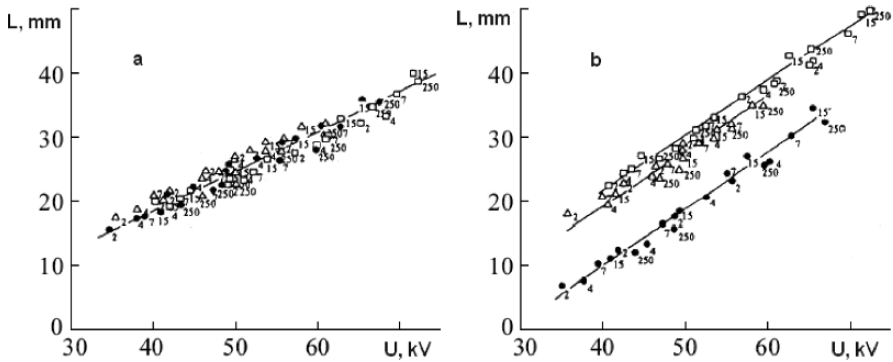
Fig. 4.51. Dependence of L on the substrate potential U_p for positive (**a**) and negative (**b**) creepage discharge and substrate materials: ●, HDPE; △, PMMA; □, GFWIER. Figures near the symbols indicate l values, in cm [101]

The potential of the charged substrate surface U' is a sum $U' = -U_\mathrm{in} + U_\mathrm{ch}$. The dependence of L on U' is also displayed by a straight line whose slope to the abscissa is smaller for negative creepage discharge polarity. This suggests that the positive discharge propagation is limited by the region of the initial surface charging.

The velocity ν of positive creepadge discharge is within the limits $(2\text{--}2.5)\cdot10^5\,\mathrm{cm/s}$, and that of negative one is $(1.27\text{--}1.43)\cdot10^5\,\mathrm{cm/s}$. In this case, the substrate charging influences v only weakly.

Kinetics of the Creepage Discharge

The spatiotemporal pattern of the creepage discharge in transformer oil is in many respects similar to that for the discharge in the ethyl alcohol volume and somewhat differs from the pattern of the discharge in the transformer oil volume [7, 102]. For $U \geq U_{50\%}$, the discharge from the moment of occurrence of the first light phenomena to the breakdown termination is a leader process (Fig. 4.52a). The discharge is observed on the impulse front with the formation of a brightly luminous channel 2–4 cm long near the tip. The channel is formed by a series of leader steps with progressively increasing delays (from 0.1–0.2 to 0.25–0.5 μs). The effective rate of channel lengthening in this region is $(0.8\text{--}1.5)\cdot10^7\,\mathrm{cm/s}$. When the discharge propagates on the tail of the 1.2/70 μs voltage impulse, the time delay between successive light flashes are 3–5 μs, and the effective rate of channel lengthening is $(0.4\text{--}1)\cdot10^6\,\mathrm{cm/s}$. The leader consists of the channel and the brightly luminous head extended along the gap axis. The head length corresponds approximately to the increment of the brightly luminous channel for the next step. Weak continuous glow similar to that observed for the discharge in transformer oil volume is observed between light flashes of the channel.
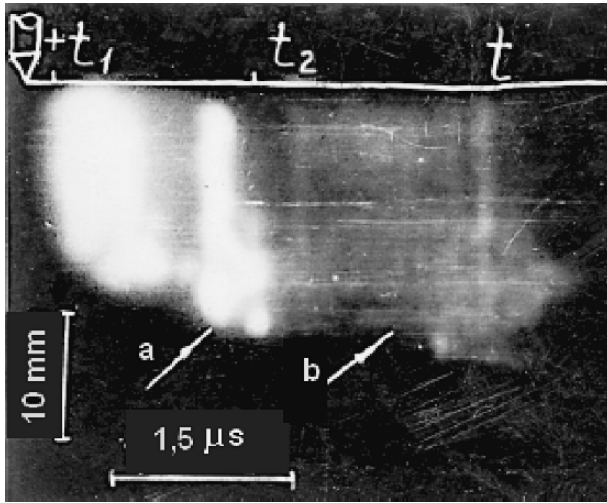
Fig. 4.52. ICC image of the discharge in transformer oil over the organic glass surface in a field with dominant tangential component for leader (**a**) and initial channels (**b**) [7, 102]

Under voltage insufficient for bridging, the spatial and temporal structures of the leader channel change at a certain moment of time t_2 (Fig. 4.52), namely, a) the luminescence of the propagating channel is virtually continuous, though periodic brightness amplifications are also observed, b) the luminescence intensity is much less than the intensity of light flashes in the leader channel, and c) no head is observed at the channel end. Analogous phenomena were observed in [122] for the discharge initiated in the purified water volume.

The weakly glowing channel can propagate to the opposite electrode without its complete flashover, that is, it has characteristics of the initial channel (see Sect. 4.7).

In the field with dominant normal component, this phenomenon can be observed at much lower voltages which decrease with increase in the specific surface capacity. An increase in C_{sp} causes the average impulse amplitude of the leader step current and the effective leader velocity to increase given that the impulse amplitude remains unchanged (Fig. 4.53). For constant C_{sp}, the creepage discharge kinetics and the discharge characteristics are essentially independent of the substrate material.

An increase in the overvoltage in all cases leads to an increase in the section of the discharge gap occupied by the fast process, to a decrease in the delay between successive leader steps, and to an increase in the current pulse amplitude and effective leader velocity (Fig. 4.54).

For *oblique-angle impulses*, the dynamics of the creepage discharge is analogous to the dynamics of the discharge depending on the front slope, namely, in strongly polar liquids (high slopes) or transformer oil (low slopes). With
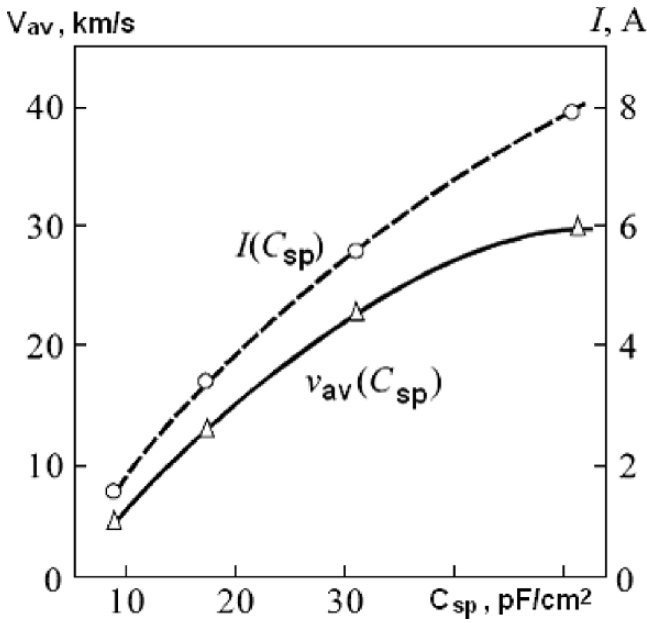
Fig. 4.53. Dependence of the velocity and current of the discharge over the organic glass surface on the specific surface capacity for the $-T +P$ system at $d = 10\,\text{cm}$ [7]
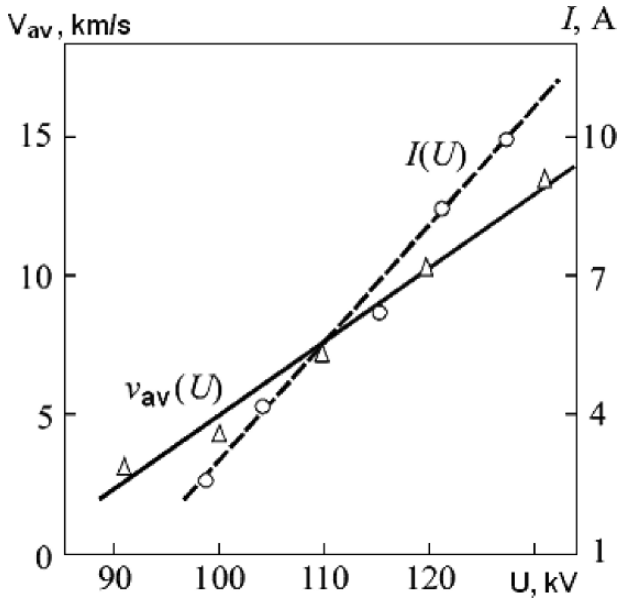
Fig. 4.54. The same as in Fig. 4.48, but on the voltage impulse amplitude [7]
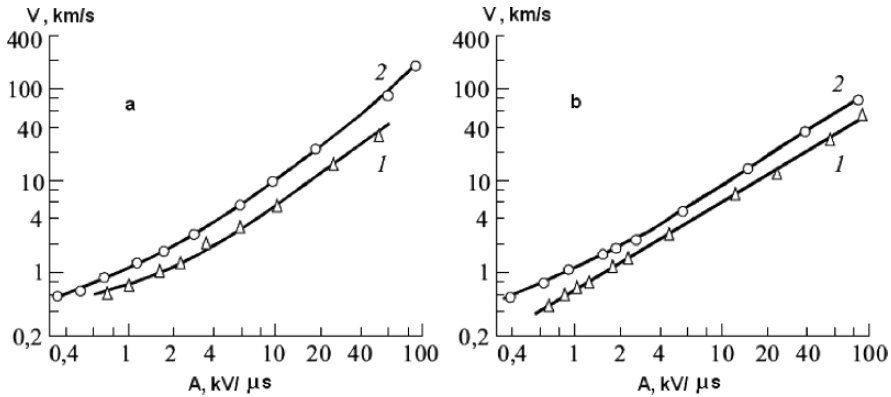
Fig. 4.55. Dependence of the average velocity of creepage discharge propagation for positive (**a**) and negative polarities (**b**) on the impulse front slope in the field with dominant tangential (*curve 1*) and normal (*curve 2*) components [85]

decrease in A, the region occupied by the channel with weak glow increases, and the average discharge velocity decreases (Fig. 4.55). In the field with dominant tangential component, transition to this discharge shape occurs at high slopes of the impulse front. Creepage discharges from positive and negative electrodes are similar as a whole.

A correlation of the creepage discharge dynamics (velocity, delay between light flashes of the channel, laws of the initial channel transformation into a leader one, and luminescence brightness) with the current running through the discharge channel confirms the assumption that the current is the key parameter for the propagation dyamics attendant to changes in the properties of the medium and the parameters of voltage impulse.

Comparing the laws of propagation and the discharge parameters in the volume of the liquid and at the liquid/solid dielectric interface, we can conclude that the creepage discharge has the same nature as the volume one. Differences in the spatial and temporal characteristics (the external discharge shape and the velocity of discharge propagation, the channel diameter, etc.) and in the electric discharge parameters[1] (the current and the current density, longitudinal gradients of the potential, and the electrical conduction and temperature of the plasma in the channel) are caused primarily by much higher capacitive current in the creepage discharge channel. Breaking of symmetry of the discharge figure by the solid dielectric surface and adsorption of impurities (foreign liquids, gas, and solid particles) by this surface also give significant contributions.

---

[1] For convenience, the channel parameters are described in a separate section (see Sect. 4.5).

4.5 Ionization Region and its Parameters

According to [103], ionization processes in front of the head should generate sufficient number of charged particles, and the voltage on the electrodes should be sufficient to provide the required rate of removal of this charge from the gap in order that the high-conduction leader channel propagated in air. This is required to restore the field in front of the leader channel head and the rate of energy liberation in it. In this case, the role of the charged particle source is played by the impulse corona and leader coronas (the streamer zone), having two characteristic regions, namely, a highly ionized stalk propagating with a velocity of about 10^8 cm/s and branches penetrating deeper into the gap at distances of a few ten and hundred centimeters from the leader head with velocities of $(5$–$10)\cdot10^8$ cm/s.

The data on the discharge kinetics in a liquid demonstrate that the leader channel is the secondary phenomenon preceded by preliminary ionization of the liquid volume. However, if the term impulse corona is applicable only to the phenomenon having a complex of properties, including high propagation velocity (10^8–10^9 cm/s), large number (a few tens or hundreds) of simultaneously propagating branches capable of propagating in fields with average strength of several kilovolts per centimeter, etc. [104, 105], we must accept that the impulse corona (the streamer zone) is absent from the discharge in liquid.

The term *corona* used in a number of works for the discharge in liquid describes radically different physical phenomena. For example, in [106] corona is a branched structure formed by numerous leader channels; in [107] it is used for branches of the leader channel.

Neither our works nor other works reported the discharge stage similar to the leader corona in air. The assumption that it cannot be registered because of the imperfection of optical devices and measurement techniques appears groundless if we take into account other indirect but rather convincing experimental facts.

1. The effective velocity of the leader channel head in a liquid remains essentially unchanged along the entire gap, except the region occupied by the leader channel propagating on the front of the voltage wave. The leader channel velocity also increases in the final stage when the sphere formed by numerous channels occupies the greater fraction of the gap, thereby leveling the field in the part of the gap without breakdown. At the same time, in long air gaps where the ionization zone is comparable with the interelectrode distance, the contact of this ionization zone with the plane is accompanied by a fast increase in the leader current and leader head velocity.
2. A dielectric barrier placed in the path of leader propagation in a liquid does not change the structure and velocity of the leader until it approaches the barrier at distances of 2–5 mm. The position of the barrier in the

discharge gap does not influence the discharge propagation from the tip to the barrier, but determines the electric strength of the gap (see Sect. 4.3).

In air in discharge gaps with a barrier, the discharge is decelerated and its trajectory changes under the action of the excess space charge induced from the ionization zone and deposited on the barrier long before the leader arrival to the barrier.

3. Synchronous time recording of the leader and voltage waveforms on the probe located in the path of the leader head demonstrated that the probe potential grows significantly only when the head of the leader channel approaches at distances no longer than 2–5 mm (see Sect. 4.6).

Thus, this suggests that the sole process providing preliminary ionization of the liquid before the stepwise lengthening of the leader channel is the process of penetration of thin weakly glowing filaments – *initial channels* – one of which under certain conditions is transformed into the leader channel.

Under conditions of leader propagation, initial channels propagate at distances no more than 2–5 mm before transformation into a leader (for an inter-electrode distance of a few centimeters). Only under some specific conditions, the initial channels can penetrate deeper into the gap at distances of a few centimeters without transformation into a leader channel (see Sect. 4.2).

The spatial structure of the ionization zone was elucidated in [7] by means of a comparison of streak images of partial discharges with still photographs taken with a still-gated camera and by the contact method (from the Lichtenberg figures) and in [8, 49] with the help of a Schlieren system. It was established that the region in front of the leader channel is shaped as a bush comprising several thin channels, one of which is then transformed into a leader channel. Other channels stop to propagate and collapse. The part of the initial channel transformed into the leader brightly luminesces. This light flash is registered as a spherical or ellipsoid head at the end of the leader channel because of the background illumination of the ICC screen. The luminescence of the discharge channel head brighter than the column one was recorded in [72] and in some other works (see Sect. 4.2).

When the initial channel approaches the opposite electrode under the voltage less or close to $U_{50\%}$, a breakdown of the gap or a flashover with voltage chopping occurs only after transformation of the initial channel into a leader under the action of the process developing from the plane (Sect. 4.7). In this case, the average longitudinal gradients of the potential E_{av} can be calculated in the initial channel. The true value of E_{av} lies in the range between the values

$$E_{\mathrm{av\,max}} = \frac{U_{\mathrm{res}} - \Delta U}{k \cdot d - l_l} \text{ and } E_{\mathrm{av\,min}} = \frac{U_{\mathrm{res}}}{k \cdot d}.$$

Here U_{res} is the voltage across the gap at the moment of contact of the initial channel with the plane, ΔU is the voltage drop across the leader channel of length l_l measured with a probe (see Sect. 4.6), d is the gap length, and $k = 1.2$–1.3 is the coefficient taking into account the channel bending.

For a $1.5/70\,\mu s$ impulse and $U \approx U_{50\%}$, calculations yield a) for a discharge in the oil volume $E_{min} \approx 15\,kV/cm$ and $E_{max} \approx 17\,kV/cm$ and b) for a creepage discharge in oil in the field with dominant tangential component $E_{min} \approx 10\,kV/cm$ and $E_{max} \approx 16\,kV/cm$. As demonstrated in Sect. 4.6, measurements of the longitudinal potential gradients in the initial channel with a probe are impossible, since the discharge through the initial channel of the probe capacitance transforms it into a leader having gradients of 2–$8\,kV/cm$ under similar conditions.

The diameter of initial channels measured from the Lichtenberg figures, photographs with a still-gated camera, and streak photographs was about $5\,\mu m$. The current density in the initial channel was $(2$–$10)\cdot10^3\,A/cm^2$.

In calculations of the current density in the initial channel, the current registered in the gap before transformation of the initial channel into a leader or between two leader steps ($\sim 10^{-2}$–$10^{-3}\,A$) is shared by simultaneously propagating initial channels (~ 6).

The electrical conduction of the substance in the initial channel averaged over its cross section and determined as

$$\gamma = \frac{4I}{\pi D^2 \cdot E_{av}},$$

was 0.1–$0.8\,\Omega^{-1} \cdot cm^{-1}$.

Table 4.8 summarizes the data on the main parameters of the initial channel in transformer oil measured by three research groups from Tomsk Polytechnic University [7], All-Russian Electrotechnical Institute (AEI) [9], and LEMD [10, 35, 95]. Irrespective of the terms used for the discharge channel, the data presented in the table most probably belong to the first stage of the two-stage leader process (propagation of the initial channel) or to the initial channel that was not transformed into a leader due to the experimental conditions.

Table 4.8 demonstrates good agreement of the main parameters of the initial channel (the monochannel or filamental channel) measured directly despite different measuring equipment and conditions of experiments as well as quite natural difference in transformer oil composition.

Table 4.8. Main parameters of the positive initial channel in transformer oil

Parameters	References		
	[7]	[9, 49]	[5, 10, 35, 123]
The most probable velocity, cm/s, for $U_{10\%} \leq U \leq U_{50\%}$	$1.3\cdot10^5$	$(1.45$–$1.5)\cdot10^5$	$2 \cdot 10^5$
Diameter, μm	1–5	6–12	5–10
Current, A	10^{-3}–10^{-4}	$(0.5$–$5)\cdot10^{-3}$	10^{-3}
Average longitudinal gradients of the potential in the channel, kV/cm	15–17	15–22	20–30

As demonstrated below (Chap. 7), a noticeable difference in the initial channel diameters measured in [7] and [9, 49, 92] caused the difference of the calculated parameters: current density, electrical conductivity of substance in the initial channel, etc.

As a whole, these measurements provide the reliable basis for the construction of a physical model of the first and most important stage of the discharge process. The channel propagation velocity, current running through it, and the average longitudinal gradients of the potential are among the most reliable parameters. For example, in addition to the data on the channel propagation velocity presented in Table 4.8, these data were reported by researchers from Norway [24, 52, 65, 108], Germany [50, 109], Japan [37, 99, 110], Canada [17], Great Britain [22, 111], Sweden [112], and other countries.

According to these studies, the velocity of discharge propagation in transformer oil at $U_{10\%} \leq U \leq U_{50\%}$ is changed in the narrow interval (1.3–3)$\cdot 10^5$ cm/s for gaps with sharply non-uniform field.

4.6 Parameters of the Leader Channel

To elucidate a nature of the processes causing the transformation of the initial channel into a leader and the role of the leader channel in creating conditions for discharge propagation at low field strength averaged over the interelectrode space, the data on the main parameters of the leader channel are required, in particular, longitudinal gradients of the potential, current density, rate of changing the longitudinal and radial channel dimensions, electron concentration, etc. Measurements of these parameters in the stage of transition from the initial channel to a leader, that is, during a single leader step are most difficult. These processes develop for a few nanoseconds and, being a fragment of the discharge that lasts several microseconds, undergo high spatial and temporal instability.

4.6.1 Channel Parameters in the Stage of Conversion into a Leader

To measure the rate of expansion of the initial channel during its transformation into a leader, the method of slit streak photograph was used. Photographs were taken with high-speed ICC (60 ns on the screen).

Difficulties of exact determination of the discharge channel diameter by the optical methods are well known. They are caused by 1) possible disagreement between the glow and plasma formation dimensions and 2) disagreement between the dimensions of the object and its image owing to imperfections of actual optical systems. Main sources of errors in optical measurements of sizes of plasma formations are the processes that develop with the shock wave velocity. These processes develop beyond the registered plasma formations and can

be accompanied by fluorescence. However, for dense liquid media, the thickness of the transition layer from the plasma to the weakly perturbed liquid does not exceed a few tenth of a micron for process duration of $\sim 10^{-7}$ s [106]. The sizes of the channel image recorded with the ICC were recalculated to determine the true dimensions of the discharge channel. In individual experiments, the initial and final discharge channel diameters were estimated from photographs taken with a still-gated camera and from the Lichtenberg figures recorded simultaneously with the photographs. Results of measurements by different methods differed by no more than 20–25%.

To estimate time variations of the main channel parameters, slit streak photography was accompanied by synchronous recording of current and voltage. An example of a slit streak photograph and discharge current waveform in oil is shown in Fig. 4.56. Because of low luminescence brightness of the initial channel, it is not seen on the superhigh-speed slit streak photograph. On the oscillograph record shown in Fig. 4.56 the current accompanying the initial channel propagation was also not recorded, because it was by three orders of magnitude less than the leader step current, and a higher sensitivity of the registration scheme is required to record it. The transformation of the initial channel into a leader started when the channel expanded approximately from 3 to $\sim 50\,\mu$m. The maximum leader current was by ~ 8–12 ns ahead of
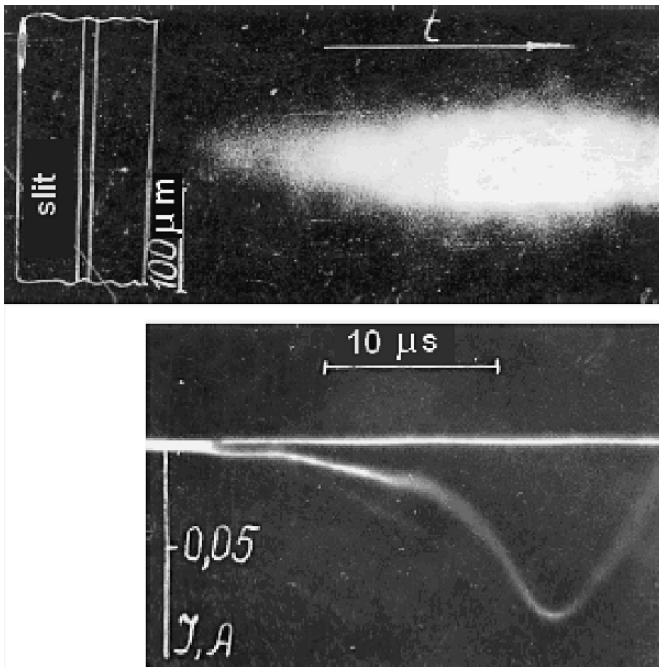
Fig. 4.56. Slit streak photograph and oscillograph record of the leader step current in transformer oil under a positive oblique-angled impulse with $A = 6\,\text{kV}/\mu$s [7, 102]

the channel expansion to the maximum (more precisely, of the moment of sharp reduction of the channel expansion rate). As the current decreased, the brightness of the leader channel also decreased, which was seen on the streak photographs as a decrease of its diameter. In principle, it is possible that the decrease of the current density in the channel and its cooling are accompanied by a decrease in the channel diameter (collapse). However, this assumption has not yet been tested experimentally because of the low intensity of the channel luminescence between two successive steps insufficient for recording with the superhigh-speed slit streak photographs.

Figure 4.57 shows results of processing of fifteen slit streak photographs and oscillograph records of the discharge current in the $+T$ $-P$ system in oil (a) and of the creepage discharge in oil in the field with dominant normal component ($C_{sp} = 3.1 \cdot 10^{-13} \, F/cm^2$) ($b$). The gap length was $7 \, cm$, and the voltage impulse was oblique-angled with slope $A = 40 \, kV/\mu s$. The zero time was set at the moment of fast current increase. The data were processed before the maximum channel expansion. As can be seen from Table 4.9, the duration of these processes is approximately equal to the duration of the step leader current impulse, and according to different authors, is 10–30 ns. It is characteristic that the current density in the channel during its transformation for the first 5–10 ns increases from $(7–10) \cdot 10^3$ to $(1–5) \cdot 10^5 \, A/cm^2$, passes through a maximum, and then decreases. (Here and below, larger values of the parameters are for the creepage discharge.)

Three sections are clearly pronounced in the decreasing branch of the curve $j = f(t)$. The first and third sections are characterized by a fast decrease in the current density, whereas the second section between 3 and 8 ns
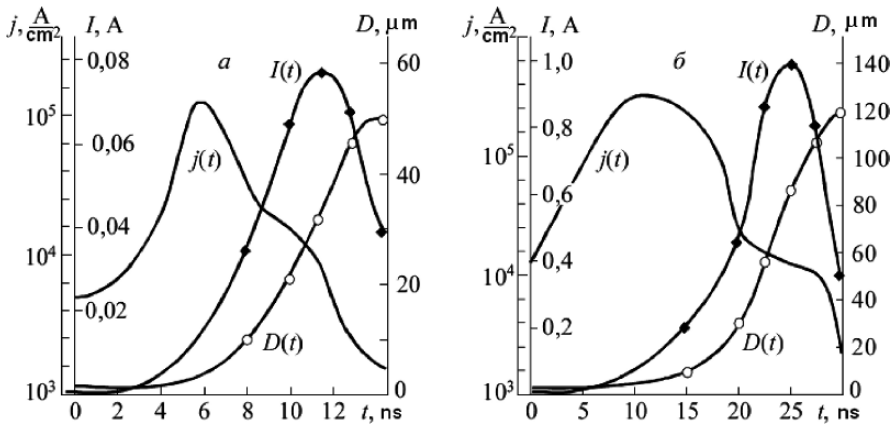
Fig. 4.57. Variations of the channel diameter D, current I, and current density j during transformation of the initial channel into a leader: **a)** discharge in the transformer oil volume for the $+T$ $-P$ electrode system and **b)** creepage discharge in oil in the field with dominant normal component for $C_{sp} = 3.1 \cdot 10^{-13} \, F/cm^2$ ($d = 7 \, cm$ and $A = 40 \, kV/cm$) [7, 102]

Table 4.9. Main parameters of the positive leader channel in transformer oil

Parameters	References			
	[7]	[21, 48, 97]	[3, 22, 23, 68]	[15, 70]
Average velocity, cm/s, for $U_{10\%} < U < U_{50\%}$	$(1.3–1.5) \cdot 10^5$	$(1.45–1.5) \cdot 10^5$	$(1.5–2) \cdot 10^5$	$2 \cdot 10^5$
Diameter, μm	50–120	60–65	60–80	
Current impulse amplitude, A	0.08–0.2	0.05	1–10	0.3–4
Current impulse duration, ns	10–20		< 20	15
Delay between successive impulses (leader steps), μs	2–4	1–3	1–10	2–6
Average longitudinal potential gradients, kV/cm	2–8	1.5–8	5–11	

has much smaller rate of current density change. The boundary between the second and third sections approximately corresponds to the current maximum $dI/dt = 0$. The minimum current density in the leader channel can be determined if we accept that the cross section of the leader channel between successive steps remains approximately equal to the cross section of the newly formed leader section, and the current through the leader channel is created by initial channel propagation and makes $\approx 10^{-2}$–10^{-3} A (as follows from the available experimental data). In this case, $j_{\min} = 30$–$80\,\text{A/cm}^2$. The average rate of channel expansion during transformation is $(3–5) \cdot 10^5$ cm/s. Hence, the channel expansion in the stage of transformation into a leader has a shock character and is accompanied by the formation of shock waves experimentally registered in many studies (see above).

The data on the current density and average longitudinal gradients in the leader channel allow the electrical conduction of the leader channel plasma to be estimated during the step formation. Under various experimental conditions, its value for the leader in transformer oil was in the limits 2–$10\,\Omega^{-1}\text{cm}^{-1}$, which is by an order of magnitude higher than the electrical conduction of substance in the initial channel.

Valuable information on the behavior of the discharge channel in a liquid in different stages of channel propagation for different distances from the tip electrode can be obtained from [112].

Based on spectroscopic investigations of radiation of the discharge channel in transformer oil, the electron density averaged over the channel cross section was estimated. The method of Stark broadening of hydrogen emission lines was used. The main results are shown in Figs. 4.58 and 4.59.

It was established that N_e was less than $10^{16}\,\text{cm}^{-3}$ during the entire channel propagation time, except the stage immediately before the breakdown termination that lasted for about $1\,\mu\text{s}$. In this stage, the radiation corresponding to both low electron density $N_e < 10^{16}\,\text{cm}^{-3}$ and high electron density $N_e > 10^{18}\,\text{cm}^{-3}$ was registered. For radiation corresponding to
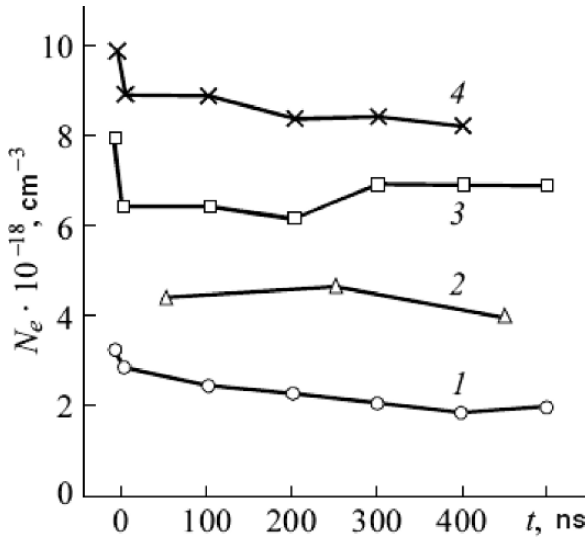
Fig. 4.58. Dependence of the electron density N_e in the discharge channel in transformer oil on the time before breakdown termination for four distances from the tip to the probe point: 0 (*curve 1*), 3 (*curve 2*), 5 (*curve 3*), and 8 mm (*curve 4*), $d = 10$ mm, and $r_0 = 30\,\mu$m [112]
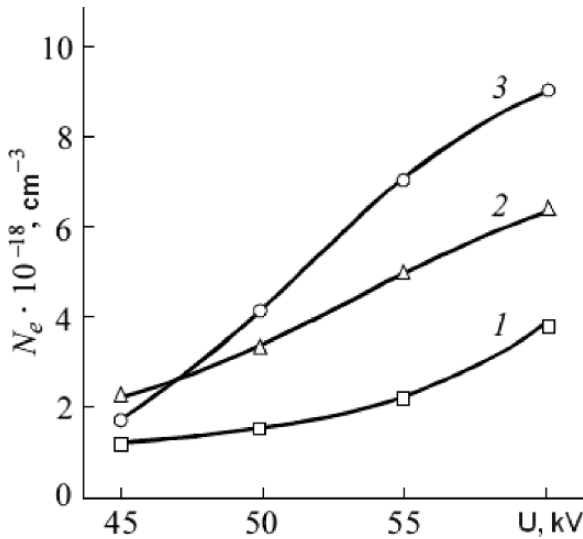
Fig. 4.59. The same as in Fig. 4.53, but for the dependence of N_e on the applied voltage; the distance to the probe point was 0 (*curve 1*), 2.5 (*curve 2*), and 4 mm (*curve 3*), $d = 7$ mm, and $r_0 = 30\,\mu$m [112]

$N_e > 10^{18}\,\mathrm{cm}^{-3}$ (that is, during the last microsecond of discharge propagation), the following laws have been established:

- N_e increases in the direction from the tip to the channel head. The difference between N_e values can reach four times.
- N_e does not change with time for a fixed distance from the tip to the sensing point.
- N_e increases with the applied voltage.
- The radiation intensity increases by several orders of magnitude during the last microsecond before the breakdown.

These results complete significantly the results obtained by the authors previously. In previous investigations, the authors indicated extremely high electron density lying in the range 10^{18}–$10^{19}\,\mathrm{cm}^{-3}$, which did not agree with the ionization energy and charge density in the channel estimated in [18].

It has been suggested that the channel had a radial structure in the final propagation stage. The dense plasma can be concentrated either in the center (on the axis) or on the periphery of the channel. The positive ions formed in the process of channel propagation can be considered as immovable in comparison with electrons providing running of a current through the channel. Positive ions are accumulated in branches (initial channels), more exactly, on the boundary with the liquid due to the action of electrostatic forces. Layers of positive ions, attracting electrons, can form dense plasma on the periphery of the channel. It is also assumed that fast growth of N_e in the last stages of channel propagation is a consequence (or reason) of phase changes in the channel, which mean the transition from the initial channel to a leader or from the streamer to a leader (according to the terminology used in [112]). The main difficulty in interpretation of these results is impossibility of referencing of measured N_e values to a concrete stage of discharge propagation, including the initial channel propagation, its transformation into a leader (formation of a single leader step) or to the existence of the channel leader (trunk) in time intervals between successive steps. We can carefully assume that radically different values of N_e ($10^{16}\,\mathrm{cm}^{-3}$ and $10^{18}\,\mathrm{cm}^{-3}$) are caused by temporal rather than spatial channel non-uniformity (its radial structure), that is, they refer to different stages of the leader process.

4.6.2 Steady-state Values of the Leader Channel Parameters

One of the main electric characteristics of the discharge channel in a liquid that can be measured is the voltage drop. The field strength at the head of the developing channel substantially depends on the voltage drop. In its turn, it determines the space and time characteristics of the discharge, including the degree of branching, propagation velocity, channel length (for a partial discharge), etc.

In this case, the creepage discharge appears more convenient for measuring the electric channel characteristics, because an individual channel can be

separated and stabilized in space by special methods, and measurements of the channel potential can be performed without disturbing its natural propagation. This can be done, for example, with the use of a guiding electrode (a bar, a narrow conducting strip, etc.) placed on the back substrate surface [85, 101, 102]. In this case, the creepage discharge develops mostly above the guiding electrode. Another method was used in [95–98]. A thick sheet of a dielectric material with a narrow gap was put on the surface of the substrate over which the discharge propagated. The initiating tip electrode was placed at the bottom of this gap, and the discharge was propagated through the gap bottom as a guided channel with small lateral branching. It was demonstrated that the characteristics of this discharge did not differ from the characteristics of a free creepage discharge propagating from the initiating electrode in the form of radially diverging branches.

Since the main laws of discharge propagation in the volume of a liquid and over the solid dielectric surface are very similar [7, 95–98], the data on the parameters of one of them can be generalized to the other.

Discharge Propagation in an Electrode System with a Probe

The developing discharge channel is galvanically coupled only with one electrode and hence its gradients can be estimated only by an indirect method. The experience in application of various methods of determining gradients in the study of the gas discharge accumulated by the 70s in [7, 85, 102] suggested that the method based on the application of a probe inserted into the channel is the most promising one.

The probe used in [7, 85, 102] comprised a thin metal prod inserted into the channel and a capacitive voltage divider. The probe structure was as follows (Fig. 4.60). Three separate ring silver strips were brazed on hollow ceramic cylinder *1* 2.4 cm in diameter. Central strip *2* served as a low-voltage electrode of the high-voltage arm of the divider. Lateral strips *3* were used as
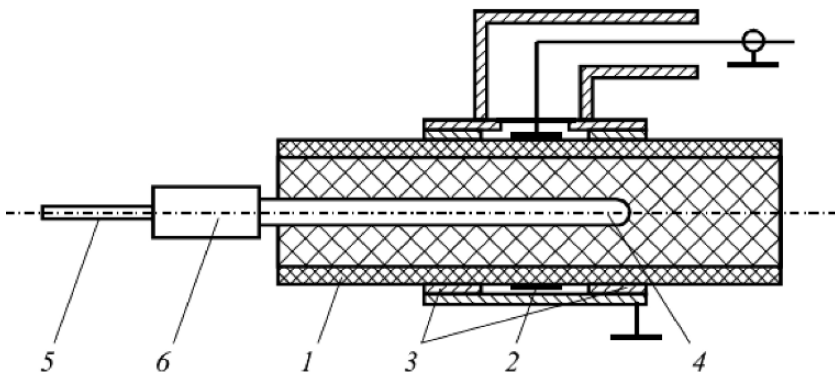
Fig. 4.60. Sketch of the probe

screens. Coaxial bar *4* 0.25 cm in diameter served as a high-voltage electrode. Cylinder *1* was filled with polythene to fix the position of the high-voltage electrode. The low-voltage arm of the divider was formed by the capacity of strip *1* relative to the screening elements, the capacity of the connecting cable section, and the capacity of oscillograph plates. The capacity of high-voltage arm of the divider was 0.9 pF, and that of the low-voltage arm was 75 pF. Prod *5* of the probe was made from a copper wire 0.08 cm in diameter and was connected to the internal probe electrode through low-inductive resistor *6* (100 kΩ). The time constant of the high-voltage circuit of the divider was 90 ns. An analysis of the electric equivalent circuit for the electrode system with the probe demonstrated that the current through the probe can be 9–16% of the leader current in transformer oil, and the current of the capacity discharge through the channel can reach 12–20%. In experiments, the probe prod was put in the most probable path of discharge channel propagation at different distances from the tip. The voltage drop in the channel was determined by subtraction of the probe potential from the high-voltage electrode potential. The potential gradient was determined as average one for the path section from the tip to the probe.

Before measurements, it was necessary to estimate the distortion of the natural discharge process caused by the probe. It was established that the influence of the probe on the discharge propagation was largely caused by its grounding through a small but finite capacity as well as by the discharge of the probe capacity through the channel. For the reverse registration circuit, when the plane was under a high potential and the tip electrode was grounded – the first factor was manifested through the fact that the discharge can propagate to the plane from the probe prod rather than from the tip electrode. The probability of this situation is the higher, the closer the probe to the plane. Because of this, the reverse circuit was not used in these measurements. In the direct circuit, the discharge in all cases propagated from the high-voltage tip electrode. The influence of the probe caused the discharge in the tip-probe gap to propagate with an increased velocity, that is, the probe in this case increased the field strength in the tip-probe gap (Fig. 4.61). The probe influence decreased as it moves away from the tip. For $U \approx U_{50\%}$ and the probe placed at a distance of about half the interelectrode distance and longer, the probe did not virtually influence the discharge propagation until it approached the initial channel. At the moment of contact with the probe, the channel luminescence was observed caused by the discharge of the probe capacity through it and by the source discharge through the channel-probe-ground circuit. With further discharge penetration deeper into the gap, the brightness of luminescence of the channel section between the probe and tip was approximately the same as of the leader channel newly formed by transformation of the initial channel. These results and the estimated currents closing through the probe demonstrated that the error in measuring the potential gradients in the leader channel were within the allowable limits, though a certain underestimation of gradients was observed. The influence of the probe on
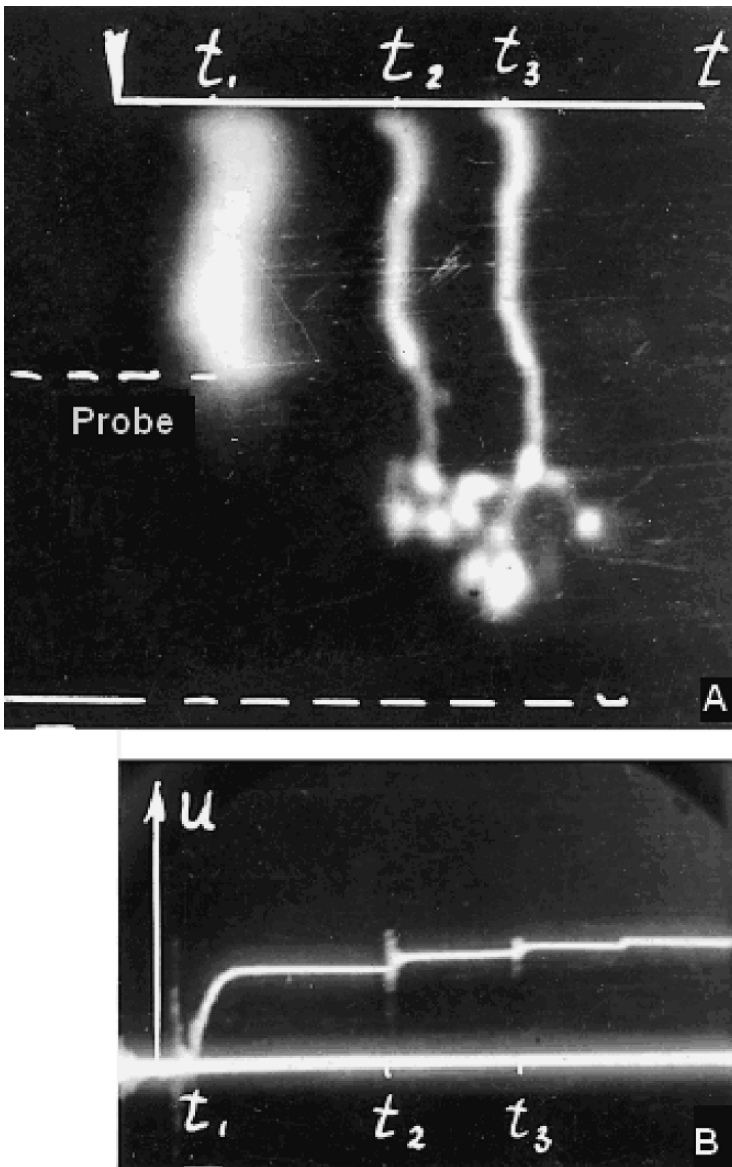
Fig. 4.61. Streak photograph (**A**) and oscillograph record of the leader channel potential (**B**) for the creepage discharge in transformer oil in the field with dominant normal component [7, 102]

the initial channel propagation was stronger. If in the gap without probe the discharge begins with the initial channel that is not transformed into a leader, placement of the probe accelerates the channel transformation. If conditions are created at which the initial channel is propagated in the tip-probe gap, its

transformation into a leader channel will occur at the moment of its contact with the probe. Moreover, the probe capacity discharge current considerably exceeds the initial channel current. To measure gradients in the gap with the probe, its capacity should be so small that it seems impossible to construct it. Therefore, the potential gradients in the initial channel were estimated by the method used in [103] to estimate gradients in the leader channel of a long spark in air (Sect. 4.4).

Spatiotemporal and Electric Parameters of the Leader Channel

Dependences of gradients on the polarity, leader channel lengths, voltage impulse shape (a 1.8/80 µs oblique-angled impulse with slope $A = 1.5$–20 kV/µs), leader propagation time, and field shape (the discharge in oil, the creapage discharge in oil in the field with dominant tangential or normal component) were investigated in [7, 85, 102].

It was established that the difference in longitudinal gradients for positive and negative discharge channels was within the limits of errors in measurements by the probe method.

Figure 4.62 shows variations of the average longitudinal gradients E_{av} of the creepage discharge propagating on the 1.8/80 µs impulse tail for $U \approx U_{50\%}$ with the channel length. (The gap length was 10 cm, the tip polarity was negative, the field had dominant normal component, and $C_{sp} = 3.1 \cdot 10^{-13}$ F/cm^2.) It can be seen that E_{av} increases from 4.5 to 6.5 kV/cm when the distance
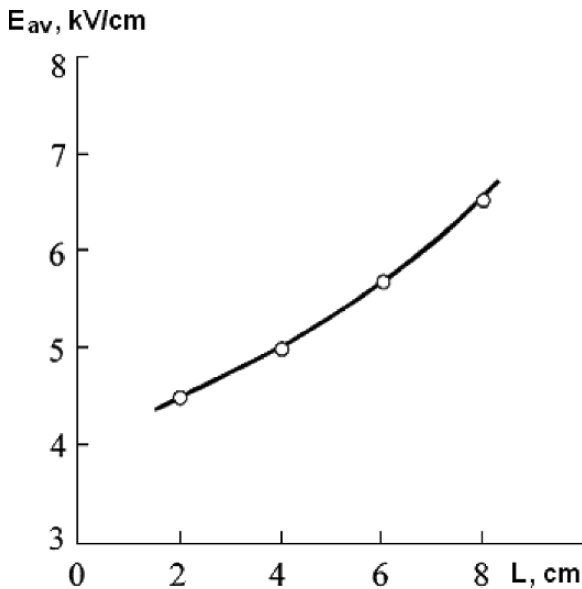
Fig. 4.62. Variations of the average longitudinal gradients of the potential E_{av} versus the creepage discharge channel length in transformer oil [7, 102]

from the tip to the probe increases in the range 2–8 cm. The same character of the dependence of E_{av} on the distance to the tip electrode was reported in [97] for creepage discharge propagation in oil on the tail of an aperiodic impulse with $\tau_{fr} < 2\,\mu s$. Figure 4.63 borrowed from [95] shows variations of the potential of a local channel region with its length. The character of the behavior of nonlinear curve $U_{ch} = f(l^*)$ demonstrates an increase in the potential gradient in the channel with increasing distance from the tip electrode. On the contrary, gradients in the discharge channel at the front of the oblique-angled impulse decrease with increasing distance from the tip to the probe (Fig. 4.64). Moreover, the gradients decrease with increasing impulse slope given that all other conditions remain the same (Fig. 4.65). For the given section of the channel, gradients decrease during progressive leader propagation on the oblique-angled impulse. Thus, from the data shown in Figs. 4.62–4.68 it follows that the potential gradients in the leader channel are determined by the age of the channel, that is, the time interval from its inception to gradient measurements, and on the amplitude and rate of voltage variations across the gap. A correlation between the E_{av} value and the leader current and hence the degree of nonlinearity of the channel resistance can be judged if we compare E_{av} (Fig. 4.61) for the discharge in water (curve *1* in Fig. 4.66), creepage discharge in oil in fields with dominant normal (curve *2*) and tangential components (curve *3*), and discharge in oil volume (curve *4*). Higher
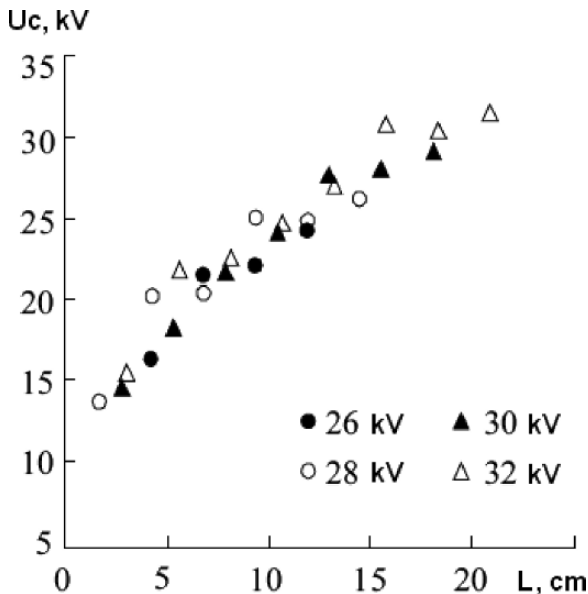
Fig. 4.63. Local channel potential as a function of the distance from its head to the probe point under a negative impulse with an amplitude of 31 kV for $C_m \approx 1\,nF$ and thickness of the glass substrate of 3 mm [95]
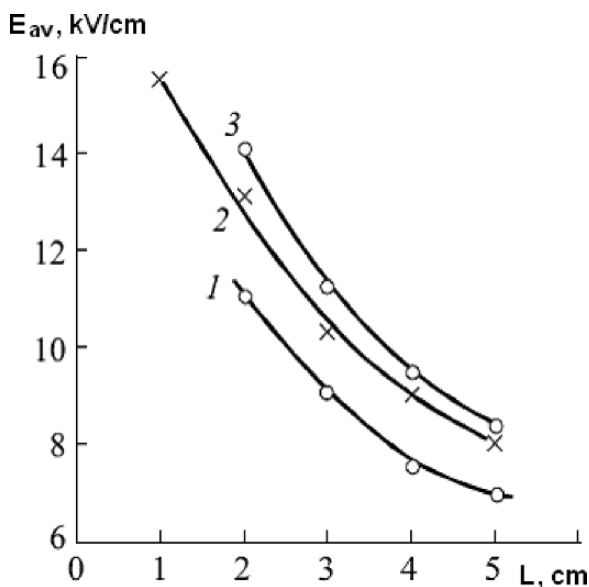
Fig. 4.64. Variations of E_{av} with length l of the creepage discharge leader in oil in the field with dominant normal (*curve 1*) and tangential components (*2*) and of the discharge in oil volume (*3*) under a positive oblique-angled impulse with $A = 6\,\text{kV/cm}$ ($d = 7\,\text{cm}$) [7,92]

leader currents correspond to smaller gradients, higher discharge propagation velocities, and lower impulse breakdown voltages.

In [95,98] and other studies of these authors, the potential gradients were measured using capacitive sondes (probes) and optical fiber sensors at the moment of channel approach to the point on the substrate surface lying above the corresponding probe. The experimental setup and measurement procedure are described in detail in [96,97]. Here we only describe important details of the procedure. The measurement scheme is shown in Fig. 4.67, and the registered signals are shown in Fig. 4.68 [95].

The discharge channels propagated over the surface of circular glass sheet *1* 3 mm thick in radial direction from high-voltage tip electrode *2*. Channel *3* under study was artificially oriented and stabilized in space by gap walls as described above. The grounded electrode was formed by copper rings *4* with probes *5* placed in the gaps between them. The area of a single probe shaped as a circular plate was ~1 mm². Probes *5* were connected to oscillograph *6* through capacities C_m. These capacities together with equivalent capacities formed by the channel and probe C_s, represented capacitive voltage dividers. The current position of the propagating channel head was determined with the help of optical fiber sensors *7* whose axes coincided with the axes of the corresponding probe (it was projected onto it). To provide registration of the
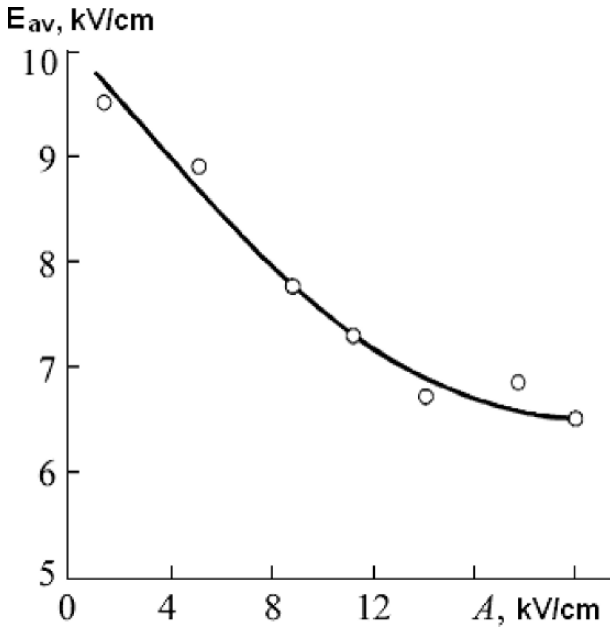
Fig. 4.65. Dependence of E_{av} in the positive creepage discharge channel in oil in the field with dominant normal component ($C_{sp} = 3.1 \cdot 10^{-13}$ F/cm^2) on the slope of the voltage impulse front [7, 102]

head luminescence only at the moment of its approach to the sensor-probe axis, opaque sheath *8* was 1 cm longer than the fiber.

The probes were calibrated by substituting the discharge channel with a copper wire whose diameter was equal to the channel diameter under application of a rectangular impulse with amplitude of 10 kV. The dependence of the probe response on the distance between the end of the wire modeling the channel and the probe axis was also investigated.

This procedure provides higher accuracy of measuring the potential gradients in the channel in comparison with the procedure used by us in [7, 102]. However, unfortunately, it also has a number of disadvantages. First, it does not allow one to measure potential gradients in the discharge channel in the liquid volume. In addition, as indicated in [95], "this procedure does not allow one to measure with satisfactory accuracy spatial and temporal variations of the channel potential. The potential distribution along the channel length can be measured very reliably immediately when the propagation stops".

All measurements were performed only with negative polarity of impulses with amplitude $\leq$40 kV. In this case, the channel propagated with approximately constant velocity of $0.8 \cdot 10^5$ cm/s.
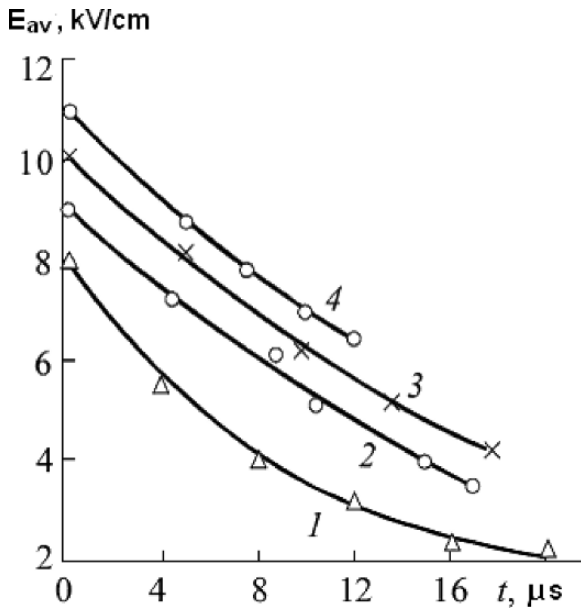
Fig. 4.66. Time variations of E_{av} in the creepage discharge channel in water (*curve 1*) and oil (*curves 2* and *3*) in the field with dominant tangential (*curves 1* and *3*) and normal (*curve 2*) components and in the leader channel propagating in oil volume under positive oblique-angled impulse with $A = 5\,kV/\mu s$ ($d = 7\,cm$ and $l = 3\,cm$) [7, 102]

The distribution of the potential along the channel length $U(x)$ was measured versus the impulse amplitude U, that is, versus the channel length before the propagation stopped. Results are shown in Fig. 4.63.

It can be seen that it is independent of U. From the data shown in Fig. 4.63 it follows that the channel propagation stops when the potential of his head has been reduced to $\approx 10\,kV$, which is much less than the potential of the tip electrode at which the discharge starts ($\sim 17\,kV$).

According to [96,97], the potential gradient along the channel propagating over the glass substrate surface depends mainly on the substrate thickness and changes within the limits 5–$11\,kV/cm$, which is in very good agreement with our data [7, 102]. In [95, 98], the data of [110, 113] were generalized, and the dependence of E_{av} on the specific channel capacitance per unit length relative to the opposite electrode were obtained (Fig. 4.69). Saker and Atten [95, 98] plotted the potential gradients in the positive discharge channel obtained in [35, 114] in the transformer oil volume.

In [101], the voltage drop ΔU was measured in the creepage discharge channel. The procedure of measuring ΔU was similar to our measurement procedure [7, 85, 102]. The probe in the form of a copper wire $0.1\,mm$ in diameter connected to an oscillograph through a capacitor divider was inserted
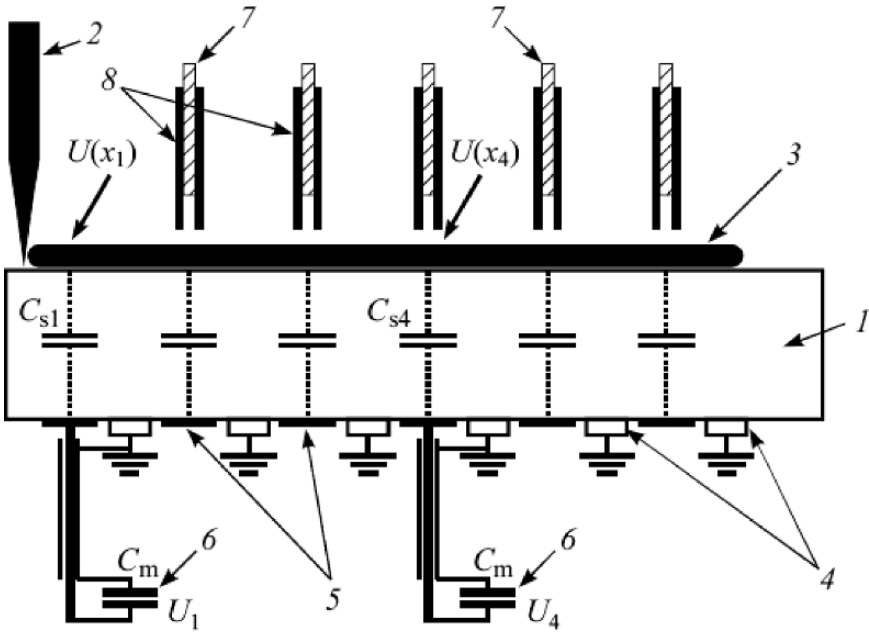
Fig. 4.67. Schematic diagram of measuring the creepage discharge channel parameters comprising glass substrate *1*, high-voltage electrode *2*, discharge channel *3*, grounded electrode *4*, capacitive probes *5*, oscillograph deflection plates *6*, optical fiber probes *7*, and opaque sheath *7* [95]

into the channel. The voltage drop in the channel was calculated by subtraction from the source voltage at the given time $U(t)$ of the channel potential at the same moment of time at fixed distance from the tip electrode $U_{\mathrm{fix}}(x)$, that is, $\Delta U(x) = U(t) - U_{\mathrm{fix}}(x)$.

Fig. 4.68. Signals from probes 3, 4, 5, and 6 under a voltage of 31 kV for $C_{\mathrm{m}} \approx 1\,\mathrm{nF}$ and glass substrate thickness of 3 mm [95]
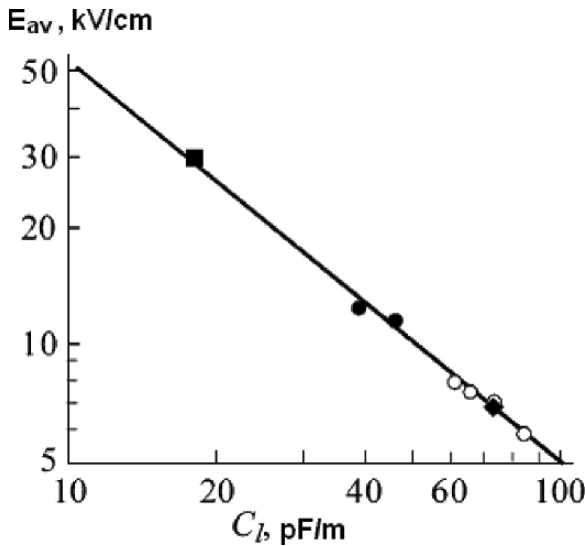
Fig. 4.69. Dependence of the potential gradient in the positive channel on its specific capacity per unit length [95]: ○, according to [96,97]; ■, according to [35,114]; ●, according to [113]

From Fig. 4.70 it can be seen that ΔU is essentially independent of the voltage impulse amplitude, potential of the substrate surface U_s, and substrate material. The maximum ΔU values were observed near the channel head. The creepage discharge propagation stopped when the threshold value ΔU exceeded (≥ 12–$15\,\text{kV}$).

Space and Time and Electric Parameters of the Leader Channel

Table 4.9 generalizes the data on the key parameters of the discharge channel. It presents only a small part of experimental materials.

This is primary the case for the data on the propagation velocity, current in the channel, and channel diameter.

Since the *average* rate of channel lengthening is presented as one of the parameters of the leader channel disregarding the stepwise character of this process, it coincides with the velocity of the initial channel penetration deeper into the gap.

As well as for the initial channel (Table 4.8), the parameters of the leader channel obtained by different authors either coincide or differ only insignificantly.

The parameters of substance in initial and leader channels are estimated (and estimates of other authors are presented) in Chap. 7 when a physical model of the leader process is examined. Here it makes sense to present
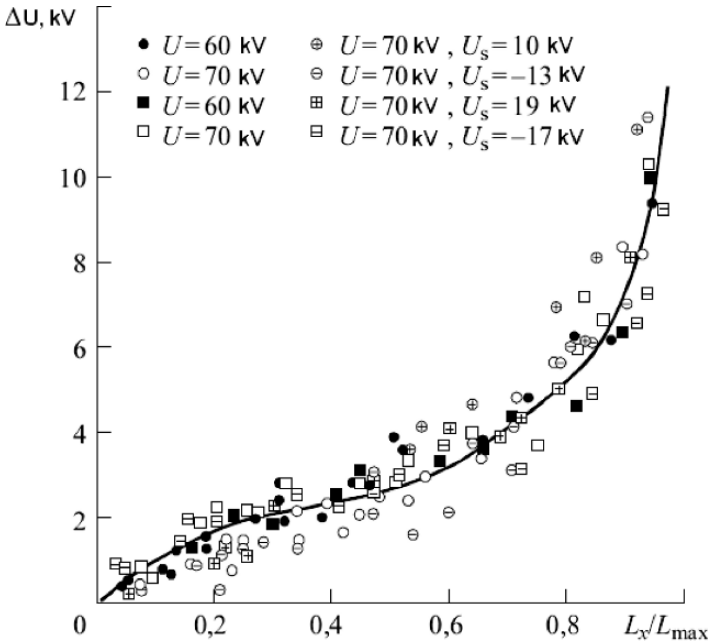
Fig. 4.70. Dependence of the voltage drop in the positive creepage discharge channel on the ratio of the distance between the probe and tip electrode L_x to the maximum channel length $L_{\max}$ [95]

measured and calculated electrostatic properties of the discharge channels developing in the volume of transformer oil and on the surface of a dielectric substrate in oil in addition to the data generalized in Table 4.9. In particular, the radial E_r and axial E_z fields of the discharge channel were estimated in [95] based on experimental data on the channel and fundamental principles of electrostatics.

It was accepted that the channel is a cylinder of radius a with a hemispherical head. Variation of the potential (and charge) along the channel axis were neglected. Using the classical expression for the distribution of charge $Q \approx C_l U(z)$, for $E_r(r)$ we obtain

$$E_r(a) = \frac{Q}{2\pi\varepsilon_0 \cdot \varepsilon_L \cdot a},\tag{4.1}$$

where ε_L is the oil permittivity.

The field strength near the hemispherical channel E_z can be calculated by the specula reflection method. The increment of the channel length by δL causes an increase in the capacitance and electrostatic energy of the system. Equating this energy increment to the corresponding increment of the work against forces of electrostatic pressure acting on the channel head, we obtain

$$\frac{1}{2}\delta C U^2 = F \delta L,$$
$$\frac{1}{2}C_l U^2 = F \tag{4.2}$$

where U is the potential of the channel head.

The force F directed along the Z axis can be expressed in terms of $E_n(\Theta)$ – the field strength component normal to the hemispherical head surface:

$$E_n^2(\Theta) = E_r^2 + \left(E_z^2 - E_r^2\right) \cdot \cos\Theta, \tag{4.3}$$

where Θ is the angle between the Z axis and the normal to the hemispherical surface, as follows:

$$F = \int_0^{\pi/2} (f \cdot \cos\Theta) \cdot 2\pi a^2 \cdot \sin\Theta \cdot d\Theta = \frac{\pi a^2 \cdot \varepsilon_0 \cdot \varepsilon_L}{3} \left[E_z^2 + \frac{1}{2}E_r^2\right], \tag{4.4}$$

where $f = \dfrac{\varepsilon_0 \cdot \varepsilon_L \cdot E_n^2(\Theta)}{2}$.

From (4.2) and (4.4), we have

$$E_z = \left[\frac{1}{2}\left(\frac{3U^2}{\pi a^2 \cdot \varepsilon_0 \cdot \varepsilon_L} \cdot C_l - E_r^2\right)\right]^{1/2}. \tag{4.5}$$

The charge distribution on the channel periphery is not known, and hence, it is impossible to determine the field strength. (The fact of excess charge concentration on the channel periphery – on its interface with the liquid – can be considered proved, see Chap. 7.)

Nevertheless, two estimates are possible:

– the thickness of the layer in which the charge is concentrated is negligibly small in comparison with the channel radius, and hence we can consider the surface charge density to be localized at distance $r = a$ from the channel axis;

– the thickness of the layer in which the charge is concentrated is greater than or equal to a, and the external radius of this layer can be connected with the "electric" channel radius.

Both estimates give the same expressions, but with different a values.

For the creepage discharge and the wire-plane model of the channel capacity [86], it was derived

$$E_r(r = a) \approx \frac{\varepsilon_g}{\varepsilon_L} \cdot \frac{U}{a \cdot \ln\left(2d/a\right)}, \tag{4.6}$$

where ε_g is the relative glass permittivity, d is the thickness of the glass substrate, and U is the local potential of the channel.

From (4.6) it follows that

$$E_z = E_r \left[\frac{3\varepsilon_L}{\varepsilon_g} \ln \left(\frac{2d}{a} \right) - \frac{1}{2} \right]^{1/2}. \tag{4.7}$$

For the channel propagating in oil volume, the expression for the capacitance of the channel of length L and radius a normal to the plane electrode

$$C_l = 2\pi\varepsilon_0\varepsilon_L \frac{\ln \left(\frac{L}{a} \right) - 1}{\left[\ln \left(\frac{L}{a} \right) \right]^2} \tag{4.8}$$

was used.

From (4.1), (4.5), and (4.8) we derive

$$E_z \approx E_r \left[3 \ln \left(\frac{L}{a} \right) + \frac{5}{2} \right]^{1/2}. \tag{4.9}$$

Figure 4.71 shows dependences of E_r on a for the creepage (curve *1*) and volume discharges (curve *2*). Setting $a = 5$–$10\,\mu$m for the volume discharge, we obtain $E_r \approx 2.5$–$4.5\,$MV/cm; for the creepage discharge at $a = 30$–$40\,\mu$m, E_r increases from 3.3 to 4.1 MV/cm. It can be seen that these values are close enough.
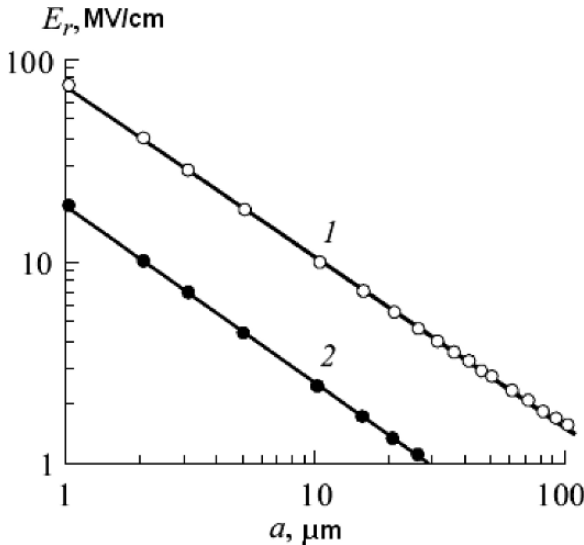
Fig. 4.71. Radial field distribution for creepage (*1*) and volume discharge channels (*2*) in transformer oil under $U = 20\,$kV for the volume discharge channel length $L = 1\,$cm, glass substrate thickness $d = 3\,$mm, and oil and glass permittivities $\varepsilon_{\text{oil}} = 2.1$ and $\varepsilon_{\text{g}} = 7$, respectively [95]
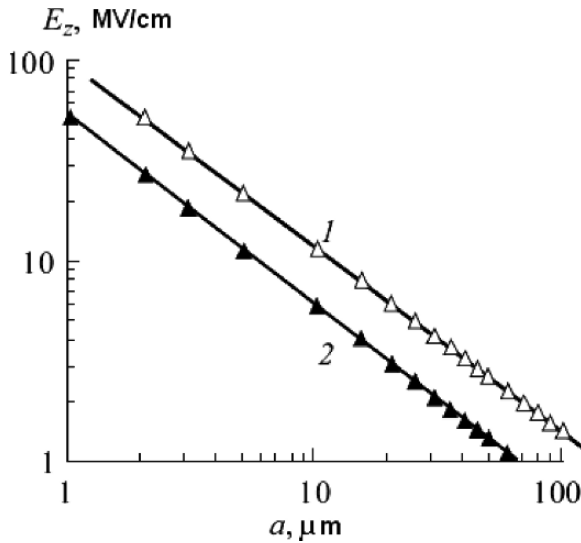
Fig. 4.72. Distribution of the axial field E_z before the head of the creepage (*curve 1*) and volume discharge channels (*curve 2*) in oil under $U = 10\,\mathrm{kV}$. The remaining parameters are the same as in Fig. 4.71 [95]

For a set equal to the "electric" channel radius a', we naturally obtain smaller E_r values for creepage and volume discharges. This decrease in E_r cannot be significant, since according to calculations [95], a' cannot exceed a significantly.

Figure 4.72 shows rough estimate of the E_z value at the head of creepage (curve *1*) and volume (curve *2*) discharge channels in oil versus the channel radius. For positive volume discharge channel, E_z changes within the limits 6–11 MV/cm, and for the creepage discharge channel, it is within the limits 3–4 MV/cm.

It is important to note that these values agree well with the data on the critical field strength ($E_{\mathrm{cr}} \approx 5\,\mathrm{MV/cm}$ [8, 115]) necessary for the occurrence of prebreakdown processes in a liquid. According to other data (for example, see [42, 49, 116, 117]), this quantity changes within the limits 4–20 MV/cm depending on the radius of the initiating electrode and the sort of the liquid.

4.7 Processes in the Stage of Transition from the Leader to an Arc

At the moment of contact of the leader channel with the plane or of meeting two counterpropagating leader channels (in the tip-tip gaps), the qualitatively new main stage of the discharge starts. For voltages exceeding $U_{50\%}$, the main discharge stage in all investigated liquids does not differ in principle from the corresponding stage of a long spark in air and is characterized by a high intensity of channel luminescence and fast variations of the current in the circuit.

The maximum current in the main stage exceeds the current in the circuit with a metal closing the discharge gap. This excess is caused by the two processes:

– neutralization of the excess charge injected into the interelectrode gap by the leader and by the charge of the opposite sign induced on the plane electrode surface or carried out by the leader channel propagating from the opposite electrode;
– the discharge through the channel of the capacitance formed by the electrodes of the gap.

The optical phenomena in the gap characteristic of this discharge stage are shown in Fig. 4.73. After the final step (a), a bright flash of the leader channel is recorded at time moment t_1 (b), the voltage across the gap is chopped, and an arc (b) is observed. (The final step was also registered in [24].) On streak images recorded with a rate of $5 \cdot 10^7$ cm/s, the left boundary of the bright luminescence region in the main discharge stage b is parallel to the still photograph of the leader d causing a gap breakdown. This means that the velocity of luminescence propagation over the channel exceeds 10^9 cm/s in the main stage. Taking into account close values of the leader channel parameters in the liquid and air, we can assume that the velocity of luminescence region propagation in the liquid in the main stage is close to that of a long spark in air and in a lightning, that is, $\approx$0.2–0.5 of the velocity of light.
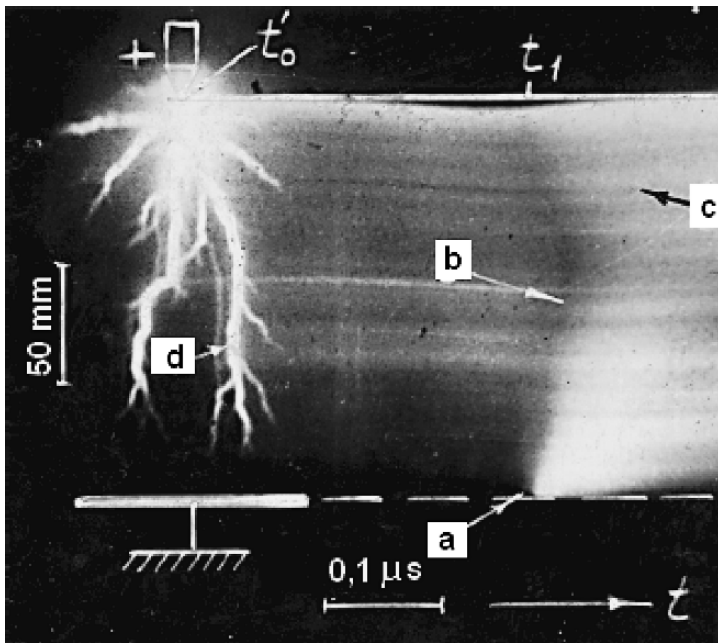
Fig. 4.73. Streak photograph of the final stage of leader propagation in distilled water under $U = U_{50\%}$ [7]

In transformer oil for low breakdown probabilities, when the initial channel can propagate to the opposite electrode without transformation into a leader or its transformation into a leader can stop at a certain time moment, its contact with the plane is not accompanied by a breakdown of the gap, that is, by complete breaking of its insulation properties. One more process which transforms the initial channel into a highly conducting channel [6, 7] is necessary for breakdown initiation.

The phenomena accompanying this discharge phase are illustrated by Fig. 4.74. In the case shown in Fig. 4.74, two channels, a and b, whose luminesce intensively only near their heads, move to the plane. At time moment t_2, the channel a reached the plane, thereby causing a rather bright light flash b and a series of current impulses with amplitudes of 0.1–0.2 A. The bright
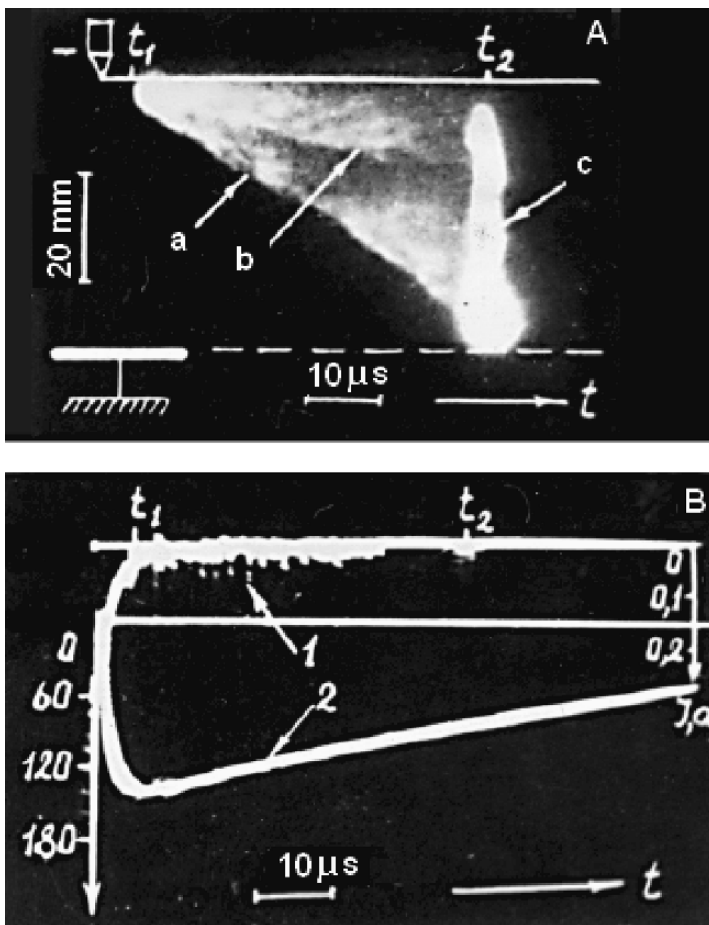
Fig. 4.74. Partial discharge in transformer oil under $U \approx U_{10\%}$: streak photograph (**A**) and oscillograph records of current (*1*) and voltage (*2*) [7]

luminescence occupies ~90–95% of the channel length; the voltage on the gap is not chopped, and the discharge phenomena in the gap are not terminated. At higher streak rates (Fig. 4.75), the channel luminescence at the moment of contact with the plane is separated into a series of light flashes propagating one after another (every 1.2–5 µs) from the plane. The flash brightness decreased, but flashes occupied increasingly larger fraction of the channel. Flashes repeat from 3 to 6 times. The breakdown of the gap occurs only when flashes reach the tip or the section of the leader channel propagating from the tip and having not enough time to cool. Figure 4.75 shows that after four flashes (a–d) with 1.4 µs delays, a time delay of 8.7 µs was observed followed with a breakdown and voltage chopping on the gap. Probably, one more flash that occupied all or the most part of the channel was observed at time moment
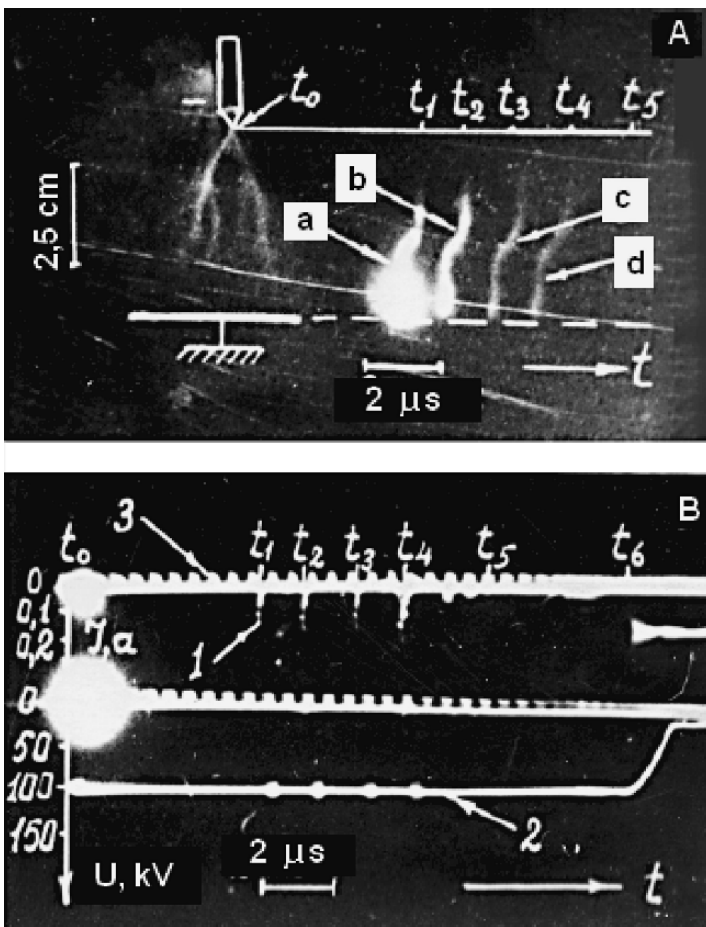
Fig. 4.75. Completed discharge in transformer oil under $U = U_{50\%}$: streak photograph (**A**) and oscillograph record (**B**) of current (*1*) and voltage (*2*) [7]

t_6. It caused the discharge to terminate. (The ICC shutter was closed at time moment t_5.)

For positive tip polarity, the phenomenon as a whole is similar to that described for negative polarity, but the number of repeated light flashes of the channel is typically 1–2. The total time of termination of this process was 5–15 μs for negative polarity and 1.5–5 μs for positive polarity. The similar phenomenon was more recently described in [9, 49]. The transformer oil of two types that differ by structural composition and a 0.5/85 μs 60 kV voltage impulse approximately corresponding to a 1% probability of breakdown of the gap 2.75 cm long were used in the experiments. The maximum time interval between the contact of the initial channel with the plane and the breakdown termination was ∼3 μs.

In [60] this phenomenon was observed in transformer oil under the following experimental conditions: the +T –P gap 5 cm long, a 1.2/700 μs impulse of positive polarity with amplitude of 82 kV, and the tip electrode with a radius of 3 μm.

The described phenomena as a whole are similar to the phenomena observed in the process of transformation of the initial channel into a leader: the discrete character of luminescence and current, close values of delays between successive light flashes (steps), current impulse amplitudes, and luminescence brightness. There are grounds to assume the common nature of these processes.

These phenomena should not be identified with the process of alternative arc breaking and ignition in liquid dielectrics in the presence of large limiting resistances in the circuit pointed out in [1, 2, 118]. In this case, electrodes are closed by the conducting channel, and the insulation properties of the gap are broken. However, because of artificial current limitation, it is insufficient for maintenance of the arc. Under certain conditions, the channel is cooled and collapsed. Its repeated ignition occurs when the voltage on the gap has been restored.

New materials about discharge propagation in a liquid upon exposure to microsecond voltage for long discharge gaps demonstrate that the leader process in liquids and gases differs significantly only in the first stage. Subsequent phases of the leader process and the stage of the main discharge in liquids and gases are qualitatively similar. Differences in the quantitative characteristics are caused mainly by different rates of hydrodynamic expansion of the discharge channels in these media.

References

1. V. S. Komelkov, The mechanism of impulse breakdown of liquids, Dokl. Akad. Nauk SSSR, **47**, 269–272 (1945).
2. V. S. Komelkov, Propagation of an impulse discharge in a liquid, Zh. Tekh. Fiz., **31**, No. 8, 948–960 (1961).

3. T. W. Liao and I. G. Anderson, Propagation mechanism of impulse corona and breakdown in oil, AIEE Trans. Part 1, **72**, 641–648 (1953).

4. I. G. Anderson and T. W. Liao, The propagation mechanism of impulse creepage discharges over oil immersed surface, AIEE Trans. Part 1, **74**, 218–226 (1955).

5. V. Y. Ushakov, Investigation of breakdown of distilled water by oblique waves of positive polarity, in: Breakdown of Dielectrics and Semiconductors [in Russian], Energiya, Moscow (1964), pp. 207–211.

6. I. S. Stekolnikov and V. Y. Ushakov, Investigation of discharge phenomena in liquids, Zh. Tekh. Fiz., **35**, No. 9, 1692–1700 (1965).

7. V. Y. Ushakov, Pulsed Breakdown of Liquids, Publishing House of Tomsk State University, Tomsk (1975).

8. Yu. V. Torshin, On the existence of leader discharges in mineral oil, IEEE Trans. Disch. El. Insul., **2**, No. 1, 167–179 (1995).

9. Yu. V. Torshin, To a problem of existence of a leader process in impulse electric breakdown of transformer oil, Elektrichestvo, No. 5, 4–16 (1993).

10. O. Lesaint, Propagation of positive discharges in long liquid gaps, in: Proc. 12th Int. Conf. on Conduction and Breakdown in Dielectric Liquids, Roma (1996), pp. 161–166.

11. G. Massala and O. Lesaint, On the correlation between propagation mode, charge and shape of streamers in mineral oil, in: Proc. 12th Int. Conf. on Conduction and Breakdown in Dielectric Liquids, Roma (1996), pp. 255–258.

12. P. Rain and O. Lesaint, Pre-breakdown phenomena in mineral oil under step and AC voltages in large gap divergent fields, IEEE Trans. Disch. El. Insul., **1**, No. 4, 692–701 (1994).

13. O. Lesaint, P. Gournay, and R. Tobazeon, Investigation on transient current associated with streamer propagation in dielectric liquids, IEEE Trans. El. Insul., **26**, No. 4, 699–707 (1991).

14. O. Lesaint, P. Gournay, A. Saker, R. Tobazeon, J. Aubin, and M. Mailhot, Streamer propagation and breakdown under AC in mineral oil for gaps up to 80 cm, in: Proc. 12th Int. Conf. on Conduction and Breakdown in Dielectric Liquids, Roma (1996), pp. 251–254.

15. A. Saker, O. Lesaint, and R. Tobazeon, Ann. Rep. CEIDP, IEEE Publ. 94CH3456-1 (1994), pp. 889–894.

16. J. Aubin, A. Saker, O. Lesaint, R. Tobazeon, and C. Boisdon, Discharge propagation in large oil volumes: Influence of particles, in: CIGRE paper WG 12–301, Paris (1996).

17. N. G. Trinh and A. Saker, Interpretation of the physical mechanisms in the breakdown of long gaps in transformer oil, in: Proc. 12th Int. Conf. on Conduction and Breakdown in Dielectric Liquids, Roma (1996), pp. 287–291.

18. N. J. Felici, Blazing a fury trail with the hounds, IEEE Trans. El. Insul., **23**, No. 4, 497–503 (1988).

19. Yu. Torshin, The Universal Mechanism in Mineral Oil and Possible Estimation of Its Breakdown Voltage, in: Proc. 14th Int. Conf. on Dielectric Liquids, Graz (2002), pp. 107–110.

20. R. E. Hebner, in: Measurements of Electrical Breakdown in Liquids, in the Liquid State and its Electrical Properties, E. E. Kunhard, L. G. Christophoreau, and L. H. Luessen, Eds., Plenum Press, New York (1988), pp. 519–537.

21. V. V. Lopatin, M. D. Noskov, R. Badent, K. Kist, and A. J. Schwab, Positive discharge propagation in insulating oil. Optical observation and simulation, IEEE Trans. Disch. El. Insul., **5**, No. 2, 250–255 (1998).
22. W. G. Chadband, From Bubbles to Breakdown, or vice-versa, in: Proc. 11th Int. Conf. on Dielectric Liquids, Baden-Dättwil (1993), pp 184–193.
23. V. Y. Ushakov, Propagation of the discharge in liquid dielectrics under oblique voltage waves, Zh. Tekh. Fiz., **35**, No. 10, 1844–1847 (1965).
24. D. Linhjell, L. Lundgaard, and G. Berg, Streamer propagation under impulse voltage in long point-plane oil gaps, IEEE Trans. Disch. El. Insul., **1**, No. 3, 447–458 (1994).
25. G. Massala, A. Saker, and O. Lesaint, Study of streamer propagation in mineral oil in overvoltage gap under impulse, Ann. Rep. CEITDP, 592–595 (1995).
26. V. Y. Ushakov and N. M. Torbin, Study of discharge propagation in liquid dielectrics, in: Breakdown of dielectrics and semiconductors [in Russian], Energiya, Moscow (1964), pp. 227–231.
27. W. G. Chadband, The ubiquitous positive streamer, IEEE Trans. El. Insul., **23**, 697–706 (1988).
28. O. Lesaint et al., Transient current associated with streamer propagation in dielectric liquids, IEEE Trans. El. Insul., **26**, 699–707 (1991).
29. C. Fenimore et al., The inception and structure of pre-breakdown streamers in perfluoro polyethers, in: Record 10th Int. Conf. on Conduction and Breakdown in Dielectric Liquids, IEEE # 90CH2812-6 (1990), pp. 430–435.
30. E. O. Forster et al., The effect of molecular structure on the properties of dielectric fields, IEEE Trans. El. Insul., **26**, 749–754 (1991).
31. E. O. Forster, Progress in the field of electric properties of dielectric liquids, IEEE Trans. El. Insul., **25**, 45–53 (1990).
32. E. F. Kelley, R. Hebner, G. J. Fitzpatrick, et al., The Effect of pressure on streamer initiation in n-hexane, in: Proc. EEE Int. Symp. on Electric Insulation, Washington (1986), pp. 66–68.
33. H. Yamada, T. Murakami, K. Kusano, et al., Positive streamer in cyclohexane under microsecond impulse voltage, IEEE Trans. El. Insul., **26**, 708–714 (1991).
34. A. Beroual and R. Tobazeon, Pre-breakdown Phenomena in Liquid Dielectrics, IEEE Trans. El. Insul., **21**, 613–627 (1986).
35. O. Lesaint and R. Tobazeon, Streamer generation and propagation under AC Divergent Field Conditions, IEEE Trans. El. Insul., **23**, 941–954 (1988).
36. J. C. Devis, S. J. Rzad, and R. J. Schwabe, Breakdown and pre-breakdown phenomena in liquids, J. Appl. Phys., **52**, 4531–4545 (1980).
37. H. Yamashita and H. Amano, Pre-breakdown and light emission in transformer oil, IEEE Trans. El. Insul., **20**, 247–255 (1985).
38. H. Yamashita and H. Amano, Pre-breakdown phenomena in hydrocarbon liquids, IEEE Trans. El. Insul., **23**, 739–750 (1988).
39. Y. Nakao, H. Itoh, and S. Hoshino, Effect of additives on pre-breakdown phenomena in n-hexane, IEEE Trans. Disch. El. Insul., **1**, No. 3, 383–390 (1994).
40. G. I. Skanavi, Physics of Dielectrics (Region of Strong Fields) [in Russian], Physical and Mathematical Literature Press, Moscow (1958).
41. V. Y. Ushakov, Insulation of High-Voltage Equipment [in Russian], Energoatomizdat, Moscow (1994).

42. O. Lesaint and P. A. Gournay, A study of the initiation of positive pre-breakdown phenomena in liquid hydrocarbons, in: Proc. 11th Int. Conf. on Dielectric Liquids, Baden-Dättwil (1993), pp. 284–288.

43. P. Gourny and O. Lesaint, Study of the dynamics of gaseous positive streamer filament in pentane, in: Proc. 11th Int. Conf. on Dielectric Liquids, Baden-Dättwil (1993), pp. 289–293.

44. H. Yamashita, K. Yamazawa, W. Machidori, and Y. S. Wang, The Effect of tip curvature on the pre-breakdown density charge streamer in cyclohexane, in: Proc. 12th Int. Conf. on Dielectric Liquids, Roma (1996), pp. 226–229.

45. K. Yamazawa, M. Okumura, M. Uemura, et al., Observation of cathode streamer initiation in dielectric liquids under high magnification, IEEE CEIDP, 93 CH 3269–8, 324–329 (1993).

46. K. Yamazawa, F. O. Forster, M. Uemura, et al., The measurements of streamer initiation in cyclohexane under high magnification, IEEE ISEI, Pittsburgh, USA, 94 CH 3445, 398–401 (1994).

47. K. L. Stricklett, C. Fenimore, E. F. Kelley, et al., Observation of partial discharge in hexane under high magnification, IEEE Trans. El. Insul., **26**, No. 4, 692–698 (1991).

48. P. K. Watson, W. G. Chadband, and M. Sadeghzden-Araghi, The role of electrostatic and hydrodynamic forces in the negative-point breakdown of liquid dielectrics, IEEE Trans. El. Insul., **26**, 543–559 (1991).

49. Yu. V. Torshin, Monochannel propagation mechanism in transformer oil at low breakdown probabilities, in: Proc. 12th Int. Conf. on Dielectric Liquids, Roma (1996), pp. 230–233.

50. R. Badent, K. Kist, and A. J. Schwab, The effect of viscosity on streamer propagation in insulating oil under impulse condition, in: Proc. 12th Int. Conf. on Dielectric Liquids, Roma (1996), pp. 181–184.

51. O. Lesaint and P. Gourny, Initiation and propagation thresholds of positive pre-breakdown phenomena in hydrocarbon liquids, IEEE Trans. Disch. El. Insul., **1**, No. 4, 702–708 (1994).

52. L. Lundgaard, D. Linhjell, G. Berg, and S. Sigmond, Positive and negative streamers in oil gaps with and without pressboard interfaces, in: Proc. 12th Int. Conf. on Conduction and Breakdown in Dielectric Liquids, Roma (1996), pp. 175–180.

53. E. O. Forster, H. Yamashita, C. Mazzetti, M. Pompili, L. Carol, and S. Patrissi, The effect of the electrode gap on the breakdown process in liquid dielectrics, in: Proc. 11th Int. Conf. on Dielectric Liquids, Baden-Dättwil (1993), pp. 383–389.

54. C. Fenimore et al., The inception and structure of prebreakdown streamers in perfluoro polyethers, in: Record 10th Int. Conf. on Conduction and Breakdown in Dielectric Liquids, IEEE # 90CH2812-6 (1990), pp. 430–435.

55. E. O. Forster et al., The effect of molecular structure on the properties of dielectric fluids, IEEE Trans. El. Insul., **26**, 749–754 (1991).

56. Y. Murooka, T. Nakano, and H. Yamashita, On a definition of positive and negative streamers observed optically in liquids, in: Proc. 12th Int. Conf. on Dielectric Liquids, Roma (1996), pp. 193–196.

57. R. E. Herber, E. F. Kelly, G. J. Fitz Patrick, and E. O. Forster, Pre-breakdown cathode processes in liquid hydrocarbons, IEEE Trans. El. Insul., **22**, No 4, 453–458 (1987).

58. O. Lesaint and F. Roldan, On the correlation between positive streamer shape and propagation in benzyltoluene, in: Proc. 13th Int. Conf. on Dielectric Liquids, Nara (1999), pp. 167–170.

59. F. M. J. Mc Cluskey, O. Lesaint, and A. Denat, Breakdown and pre-breakdown phenomena in insulating liquids at large distance, in: Proc. 11th Int. Conf. on Dielectric Liquids, Baden-Dättwil (1993), pp. 274–278.

60. P. Rain and O. Lesaint, A comparison of pre-breakdown phenomena in mineral oil under step and AC voltages in divergent fields at large distances, in: Proc. 11th Int. Conf. on Dielectric Liquids, Baden-Dättwil (1993), pp. 259–263.

61. Y. Nakao, T. Yamazaki, K. Miyagi, Y. Sakai, and H. Tagashira, The effect of molecular structure on prebreakdown phenomena in dielectric liquids under nonuniform field, IEE Trans. Jpn., **A121**, No. 4, 307–313 (2001).

62. N. Hamano, Y. Nakao, T. Naito, Y. Nakagami, et al. Influence of molecular structure on propagation of streamer discharge in hydrocarbon liquids, in: Proc. 14th Int. Conf. on Dielectric Liquids, Graz (2002), pp. 119–122.

63. V. Y. Ushakov, On the problem of photographic methods of investigation into a mechanism of criping discharges in liquids, Izv. Vyssh. Uchebn. Zaved., Fiz., No. 4, 96–100 (1966).

64. L. Costeanu and O. Lesaint, On mechanisms involved in the propagation of subsonic positive streamers in cyclohexane, in: Proc. 14th Int. Conf. on Dielectric Liquids, Graz (2002), pp. 143–146.

65. D. Linhjell, G. Berg, and L. Lundgaard, Streamer propagation in long point-Plane oil gaps, in: Proc. 11th Int. Conf. on Dielectric Liquids, Baden-Dättwil (1993), pp. 268–273.

66. P. G. Petrov, V. R Kukhta, and V. V. Lopatin, On the nature of anode streamers in water, Zh. Tekh. Fiz., **58**, No. 6, 1185–1188 (1988).

67. I. M. Gavrilov, V. R. Kukhta, V. V. Lopatin, P. G. Petrov, V. Y. Ushakov, Formation of the impulse discharge in water, Izv. Vyssh. Uchebn. Zaved., Fiz., No. 1, 88–92 (1989).

68. V. R. Kukhta and V. V. Lopatin, Discharge propagation in water in non-uniform field, in: Proc. 12th Int. Conf. on Conduction and Breakdown in Dielectric Liquids, Roma (1996), pp. 259–262.

69. V. R. Kukhta and V. V. Lopatin, Inception and propagation of pre-breakdown cavities in water, in: Proc. 13th Int. Conf. on Conduction and Breakdown in Dielectric Liquids, Nara (1999), pp. 116–119.

70. V. R. Kuhta, V. V. Lopatin, and P. G. Petrov, Installation for investigation of the initial stage of the electric discharge in dielectrics, Electr. Obrab. Met., No. 3, 66–68 (1986).

71. V. Y. Ushakov, Optical and oscillographic investigations of the impulse discharge in liquids, Candidate's Dissertation in Technical Sciences, Tomsk Polytechnic Institute, Tomsk (1965).

72. S. Katsuki, H. Akiyawa, A. Abou-Ghazala, and K. H. Schoenbach, Parallel streamer discharge between wire and plane electrodes in water, IEEE Trans. Disch. El. Insul., **9**, No. 4, 498–506 (2002).

73. L. A. Yutkin, Electrohydraulic Effect [in Russian], Machgiz, Moscow (1955).

74. A. A. Vorobjev, Destruction of Rocks by Electric Impulse Discharges [in Russian], Publishing House of Tomsk State University, Tomsk (1961).

75. B. V. Semkin, A. F. Usov, and V. I. Kurets, Principles of Electropulse Destruction of Materials [in Russian], Nauka, Saint Petersburg (1993).

76. A. A. Dulson and V. Y. Ushakov, State and development perspective of technological applications of high-voltage high-powered impulses, in: Proc. Int. Conf. on Impulsed Power Application, Gelsenkirchen (2001), pp. A.02/1-A.02/6.

77. V. I. Kurets, A. F. Usov, and V. A. Tsukerman, Electropulse Disintegration of Materials. Izv. Kolsk. Nauchn. Tsentra Ross. Akad. Nauk (2002).

78. V. Y. Ushakov, O. P. Semkina, V. V. Ryumin, et al., On the nature of impulse electric breakdown of aqueous electrolits, Elektr. Obrab. Mater., No. 2 (44), 48–54 (1972).

79. N. B. Trofimova, Study of Breakdown of Conducting Nondegassed Liquids. In Breakdown of Dielectrics and Conductors [in Russian], Energiya, Moscow (1964), pp. 219–224.

80. I. P. Kuzhekin, A study of breakdown of a liquid in a non-uniform field under rectangular voltage waves, Zh. Tekh. Fiz., **36**, No. 12, 2125–2130 (1966).

81. B. Brodskaya, R. Eiscop, and A. Payu, Special features of propagation of impulsed discharges in highly conducting liquids, Izv. Akad. Nauk Est. SSR. Khim., Geol., **17**, No. 3, 251–257 (1968).

82. N. P. Melnikov, G. A. Ostroumov, and M. Y. Stoyak, Formation of electric breakdown in aqueous solutions of sodium chloride, Zh Tekh. Fiz., **34**, No. 5, 949–951 (1964).

83. N. P. Melnikov, G. A. Ostroumov, and A. A. Shteinberg, Some special features of electric breakdown of electrolits, Dokl. Akad. Nauk SSSR, **147**, No. 4, 822–825 (1962).

84. M. Y. Stoyak, Experimental investigation of the process of electric discharge propagation in electrolits, Elektronn. Obrab. Mater., No. 4, 6–13 (1966).

85. V. A. Butenko and V. Y. Ushakov, Creepage discharge in transformer oil under oblique voltage impulses, Izv. Vyssh. Uchebn. Zaved., Energ., No. 1, 31–35 (1973).

86. V. F. Klimkin, Mechanisms of electric breakdown of water from the tip anode in the nanosecond range, Pis'ma Zh. Tekh. Fiz., **16**, No. 4, 54–58 (1990).

87. V. F. Klimkin, High-speed optical and statistical investigation of prebreakdown phenomena in liquid dielectrics in the nanosecond region, in: Proc. 13th Int. Conf. on Dielectric Liquids, Nara (1999), pp. 152–155.

88. E. V. Yanshin, I. T. Ovchinnikov, and Y. N. Vershinin, Optical investigations of the pre-breakdown phenomena in water in the nanosecond range, Zh. Tekh. Fiz., **43**, No. 10, 2067–2074 (1973).

89. J. S. Clements, M. Sato, and R. N. Davis, Preliminary investigation of pre-breakdown phenomena and chemical reaction using a impulse high-voltage discharge in water, IEEE Trans. Industry Appl., **23**, No. 2, 224–234 (1987).

90. V. Y. Ushakov, On the mechanism of the barrier effect in impulse breakdown of liquids, Izv. Tomsk. Politekhn. Inst., **180**, 57–61 (1971).

91. A. Beroual and A. Zoughi, Barrier effect on the pre-breakdown and breakdown phenomena in long oil gaps, in: Proc. 12th Int. Conf. on Dielectric Liquids, Roma (1996), pp. 300–303.

92. Yu. V. Torshin, Pre-discharge optical, light, and electrical phenomena under impulse breakdown of various oil gaps, in: Proc. 11th Int. Conf. on Dielectric Liquids, Baden-Dättwil (1993), pp. 304–308.

93. I. Argirakis, T. Zinoulis, W. G. Chadband, and D. W. Auckland, A study of the interaction of the negative liquid discharge with a solid insulating sheet, in: Proc. 12th Int. Conf. on Dielectric Liquids, Roma (1996), pp. 292–295.

94. A. Lobanov, Yu. Torshin, and C. Mazzetti, Physical characteristics of pre-breakdown channels under positive impulse breakdown of oil gaps with barriers, in: Proc. 13th Int. Conf. on Dielectric Liquids, Nara (1999), pp. 195–198.

95. A. Saker and P. Atten, Properties of streamers in transformer oil, IEEE Trans. Disch. El. Insul., **3**, No. 6, 784–791 (1996).

96. P. Atten and A. Saker, Streamer propagation over a liquid-solid interface, IEEE Trans. El. Insul., **28**, 230–242 (1993).

97. A. Saker and P. Atten, Potential distribution along a single negative creeping streamer in transformer oil, IEE Proc, **A140**, No. 5, 375–381 (1993).

98. A. Saker and P. Atten, Electrical characterization of a single creeping streamer in transformer oil, in: Proc. 11th Int. Conf. on Dielectric Liquids, Baden-Dättwil (1993), pp. 279–283.

99. Y. Nakao, A. Mouri, T. Itooka, et al., Propagation of creepage discharge on solid insulator in insulating oil, in: Proc. 13th Int. Conf. on Dielectric Liquids, Nara (1999), pp. 257–260.

100. Y. Nakao, M. Naruse, Y. Suzuki, et al., Influence of sort and thickness of insulating barriers on the positive impulse creepage discharge in transformer oil, in: Proc. 12th Int. Conf. on Dielectric Liquids, Roma (1996), pp. 316–319.

101. R. Hanaoka, T. Kohrin, T. Miyagawa, and T. Nishi, Creepage discharge characteristics over solid-liquid interfaces with grounded side electrode, in: Proc. 12th Int. Conf. on Dielectric Liquids, Roma (1996), pp. 201–205.

102. V. A. Butenko, Impulse creepage discharge in transformer oil, Candidate's Dissert. in Technical Sciences, Tomsk Polytechnic Institute, Tomsk (1972).

103. V. S. Komelkov, Structure and parameters of a leader discharge, Izv. Akad. Nauk SSSR, No. 6, 851–865 (1950).

104. I. S. Stekolnikov, Nature of a Long Spark [in Russian], Academic Press (1960).

105. E. M. Bazelyan and Y. P. Raizer, Spark Discharge, 4th Edition, CRC Press, Boca, Raton (1997).

106. K. A. Naugolnykh and N. A. Roy, Electric Discharges in Water (Hydrodynamical Description) [in Russian], Nauka, Moscow (1971).

107. N. Zessoules, I. Brinkerhoft, and A. Thomas, Recombination and mobility of nuclear radiation induced ionization in liquid hydrogen, J. Appl. Phys., **34**, 2010–2014 (1963).

108. D. Linhjell, G. Berg, L. Lungaard, and R. S. Sigmond, Light emission from a long point-plane oil gap under impulse stress, in: Record of the Nordic Insulation Symposium (1999), pp. 7.3:1–7.3:14.

109. J. C. Devins, S. J. Rzad, and R. S. Schwabe, Streamer propagation in liquids and over liquid-solid interfaces, IEEE Trans. El. Insul., **17**, No. 6, 512–516 (1982).

110. H. Okubo, M. Ikeda, M. Honda, and S. Yanabu, Creepage discharge propagation in transformer oil with impulse voltage, in: Proc. 4th Int. Symp. on High-Voltage Engineering, Athens (1983), Paper 24–04.

111. P. K. Watson, T. Sufian, and W. G. Chadband, A thermal model of positive pre-breakdown streamers in insulating liquids, in: Proc. 11th Int. Conf. on Dielectric Liquids, Baden-Dättwil (1993), pp. 229–233.

112. P. Brämann and A. Sunesson, *In-situ* spectroscopic measurements of streamer properties (electron density and temperature) in dielectric liquids, in: Proc. 12th Int. Conf. on Dielectric Liquids, Roma (1996), pp. 197–200.

113. P. N. Nikolopoulos and G. C. Sakkas, Discharge propagation on the surface and in the volume of a pressboard - mineral oil combination under impulse voltages, in: Proc. 4th Int. Symp. on High-Voltage Engineering, Athens (1983), Paper 24–11.

114. P. Gournay, Génération et Propagation des Streamers Positifs dans Quelques Hydrocarbures, Doctoral Thesis I.N.P., Grenoble (1994).

115. A. Denat, J. P. Gosse, and B. Gosse, Electrical conduction of purified cyclohexane in a divergent electrical field, IEEE Trans. El. Insul., **23**, 545–553 (1988).

116. R. Tobazéon, Pre-breakdown phenomena in dielectric liquids, in: Proc. 11th Int. Conf. on Dielectric Liquids, Baden-Dättwil (1993), pp. 172–183.

117. A. Badent, K. Kist, A. J. Schwab, A. Beroual, W. G. Chadband, M. Danikas, A. B. Sierota, Y. Torshin, and M. Zahn, Preliminary report for the IEEE DEIS Liquid Dielectrics Committee International Study Group on "Streamer Propagation in Liquids," in: Proc. 12th Int. Conf. on Dielectric Liquids, Roma (1996), pp. 375–378.

118. I. E. Balygin, Electric Strength of Liquid Dielectrics [in Russian], Energiya, Leningrad (1964).

119. V. Y. Ushakov, Insulation of High-Voltage Equipment, Springer-Verlag, Berlin Heidelberg, New York (2004).

120. Yu. V. Torshin, Prediction of breakdown voltage of transformer oil from predischarge phenomena, IEEE Trans. Disch. El. Insul., **10**, No. 6, 933–940 (2003).

121. L. Kebbabi and A. Beroual, Optical and electrical investigations on creeping discharges over solid/liquid interfaces under impulse voltage, 2005 IEEE Interu. Conf. on Diel. Liquids, Portugal, Coimbra, June 26-July 1, 131–134 (2005).

122. J. Nieto-Salazar, N. Bonifaci, A. Denat, and O. Lesant, Characterization and spectroscopic study of rositive streamers in water, in: Proc. 2005 IEEE Int. Conf. on Dielectric Liquids, Coimbra (2005), pp. 91–94.

123. A. Denat, High field conduction and prebreakdown phenmena in dielectric liquids, in: Proc. 2005 IEEE Int. Conf. on Dielectric Liquids, Coimbra (2005), pp. 57–62.

5

Statistical Investigations
of the Electrical Breakdown

The statistical nature of the breakdown forces the researchers to use statistical methods of measuring its key parameters and processing measurement results.

The statistical approach not only increases the reliability of the data used in practice but also provides a method of investigating a breakdown nature. This is especially valuable when direct methods of observation of the discharge processes in space and time cannot be employed. In the study of the pulsed breakdown, the most important time characteristics are *the statistical discharge time lag*, *discharge formation time*, and *discharge (or breakdown) time lag*. (A description of the special features of the application of the term *statistical discharge time lag* applied to the discharge in liquids see in Sect. 2.4.4).

5.1 Possibilities and Methods of Statistical Investigations

5.1.1 Relationship between the Statistical Characteristics and Nature of the Discharge Processes

The statistical theory of liquid dielectric breakdown, first formulated in [1, 2], was further developed by other authors (for example, see [3]), and statistical approaches to calculations of high-voltage insulation, including liquid one, were generalized in [4].

A character of distribution of the discharge formation time t_f can be elucidated experimentally if the average statistical time lag is $\bar{t}_{st} \approx t_f$. Measurements of the breakdown time lag for n-hexane at high field strengths (in the nanosecond range) have demonstrated that the t_f distribution is close to a normal one [5]. With allowance for this, the distribution of the total breakdown time lag is determined as a superposition of the exponential (t_{st}) and normal distributions (t_f) [6]. Exponential distributions of the breakdown time lag were obtained in [7] for the nanosecond breakdown of the transformer oil and distilled and tap water in gaps 31 and $36\,\mu m$ long with uniform fields.

Results of statistical investigations of the time breakdown characteristics including t_f were used in [8, 9] to estimate the mobility of charge carriers in strong electric fields. In connection with the contradictory conclusions about the character of the t_{lag} distribution and in connection with the fact that very short (a few tens of microns) interelectrod gaps were used in these studies, the time lag distributions for the nanosecond liquid breakdown of long (0.75 and 1.5 mm) gaps with a uniform field were investigated in [10]. As in [5, 6], a normal t_{lag} distribution was obtained, and it was concluded that the relative contribution of t_{st} to the total breakdown time lag t_{lag} is small for nanosecond breakdowns of liquids in comparison with the relative contribution of t_f.

Investigations of the electric discharge propagation from anode in distilled water (with a quasi-uniform field) performed in [11] demonstrated that t_{st} strongly decreased with increase in the field strength. Statistical measurements of t_f demonstrated that the average discharge propagation velocity amounted to $\sim 10^6$–10^7 cm/s as a function of the field strength.

Important information on the pre-breakdown processes can be obtained from an analysis of probability distributions of some characteristic quantities, for example, the duration of pre-breakdown luminescence, breakdown field strength, breakdown time lag, etc.

Pre-breakdown light pulses were observed in hydrocarbon liquids at field strengths $E \sim 0.4 - 0.7$ MV/cm with the use of a photomultiplier [12]. It appeared that their occurrence is random in character. The statistical analysis of the time lag between the moment of voltage application and the first and second light pulses demonstrated that the average frequency of their occurrence depends on the field strength, electrode material, and liquid type. It was assumed that the light flashes were due to microscopic discharges near the electrodes caused by small charged particles and initiating the gap breakdown in strong electric fields. The time lag distribution for the first light pulse in n-hexane was investigated in [13]. It was found that the character of distribution changed at high field strength $E \sim 2.3$ MV/cm (in the nanosecond range), thereby indicating the change of the discharge initiation mechanism.

Results of statistical analysis of the breakdown field strength in liquid helium were presented in [14]. The two characteristic maxima caused by a superposition of two distributions were established. Different characters of the pressure influence on these distributions were revealed. The dependence of the position of the first distribution (characterized by a lower breakdown field strength) on the pressure was in agreement with the hypothesis about the bubble breakdown mechanism. The position of the second distribution was determined by the liquid density and was independent of the pressure. The different mechanisms of liquid helium breakdown were hypothesized.

The breakdown time lag distribution for n-hexane (in the Laue coordinates) versus the interelectrode distance was investigated in [15] for voltage pulse duration of ~ 100 ns. It was found that at a certain critical interelectrode distance (E was kept constant), the character of the distributions changed. The critical distance depended on the electric field strength and decreased

with increase in the field strength. For example, at $E = 3.5\,\mathrm{MV/cm}$, the critical distance was about $45\,\mu\mathrm{m}$. By analogy with the gas discharge, it was assumed that the critical distance between the electrodes was caused by the critical length of the avalanche-streamer transition. A strong dependence of t_{st} and t_{f} on the field strength was also reported in [16] when studying the pulsed electric breakdown of liquefied gases. The discharge formation time (at constant field strength) increased with the interelectrode distance. However, t_{st} was independent of the interelectrode distance. The estimated formation velocity (the drift velocity) under assumption of the single-avalanche breakdown mechanism of liquid argon demonstrated that it was in the range $\sim 10^5 - 10^6\,\mathrm{cm/s}$.

Avrorov and Vorobjev [17] analyzed the statistic breakdown time lag of distilled water as a function of the electric field strength. They revealed that in the microsecond range (for an interelectrode distance of $3\,\mathrm{mm}$), the breakdown time lag distribution had a characteristic break. A comparison with the results of optical investigations demonstrated that under these conditions, the discharge propagated not only from anode but also from cathode. A method of analyzing statistical distributions of the breakdown time lag was suggested that allowed the cathode discharge formation velocity to be estimated ($\sim 10^5\,\mathrm{cm/s}$).

The statistical analysis of the breakdown time lag was also carried out versus the electric field strength and liquid type [18], electrode material (for distilled water) [19], pressure and impurity type (for n-hexane) [20], geometry and gap length (for mineral oil) [21], cathode or anode discharge initiation (for hydrocarbon liquids) [22], and characteristics of additives incorporated into the liquid [23].

The statistical investigations have allowed a number of important and interesting results to be obtained. In particular, the opportunity of different liquid breakdown mechanisms was demonstrated. The common empirical laws to which the processes of electric discharge initiation and propagation in liquids obey were established. The velocity of the pre-breakdown processes was also estimated. At the same time, the analysis of publications allows us to conclude that they are small in number. Apparently, this is due to the fact that a detailed statistical analysis is labor-consuming and calls for application of automated systems of obtaining and processing experimental data.

5.1.2 Automated System for Statistical Investigations

As is well known, the accuracy of a statistical description increases with the number of successive measurements N_0 (the sample length). According to the central limiting theorem, if N_0 is large and values of a random variable are uncorrelated, the distribution of the sample average will obey a normal law with the variance σ^2/N_0, where σ^2 is the variance of the individual measurement. This result is valid for any distribution of the random variable (with limitations insignificant for practical cases), which gives reliable confidential

limits for the average value if $N_0 \geq 30$ and a distribution is not very asymmetric. As to estimates of the standard deviations, correlation coefficients, and statistical tests of hypotheses, in these cases N_0 must exceed 100 [24]. For example, for a Gauss distribution and $N_0 = 100$, the relative error in determining the sample average is 14%, and the standard deviation is halved. For oscilloscope recording of quantities with subsequent manual processing of the raw data, a statistical analysis calls for significant efforts and much time. Labor consumption of investigations can be considerably reduced and the measurement accuracy increased with the use of means for automated data acquisition, accumulation, and processing. A computer-controlled experimental setup provides an analysis of information directly in the process of measurements, thereby exercising control over the experiment. To develop automated systems, problems of the interface of the measuring equipment with a computer and of the system stability to external noise should be solved. Statistical investigations of pulsed electric breakdown of liquids with the help of an automated system have demonstrated high efficiency of this approach to the organization of experiment [25].

Figure 5.1 shows the block diagram of an automated system. Pulsed voltage with amplitudes up to $40\,\mathrm{kV}$ generated by pulsed voltage generator (1) is applied to discharge gap (2) filled with a liquid dielectric. The pulse front duration was $\sim 10\,\mathrm{ns}$, and the duration of its flat-topped part was $\sim 5\,\mathrm{\mu s}$. At the moment of gap breakdown, a sharp voltage drop occurs (during several nanoseconds), and a pulse of approximately rectangular shape is formed. To measure its duration (the breakdown time lag), device for measuring time
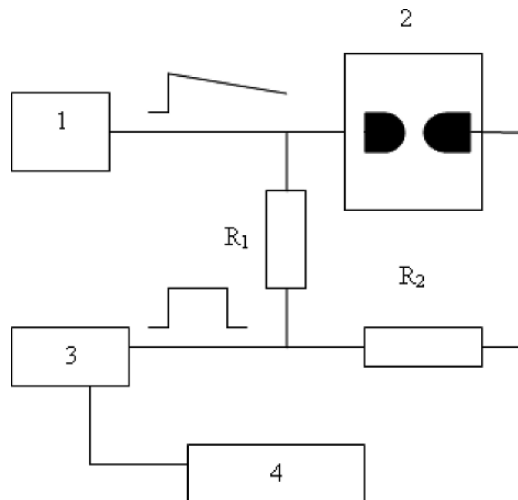
Fig. 5.1. Block diagram of the automated system for statistical analysis of the breakdown time lag comprising pulsed voltage generator 1, discharge chamber 2, device for measuring time intervals 3, and computer 4. Here $R_2 = 50$

intervals (*3*) is used. The input signal level is decreased by a low-inductive resistive divider (R_1, R_2) placed near the discharge chamber. The error in measuring time was 10 ns, and the resistance of the input channel was 50 Ω. The information on the measured quantity is then put in the computer. Specially developed software is employed for data acquisition, accumulation, and real-time processing, construction of histograms and Laue diffraction patterns, and calculations of the parameters of statistical distributions including the average breakdown time lag, standard deviation (empirical standard), root-mean-square error in calculating the average, drift of the parameters, etc. The opportunities of the software were tested in a computer experiment for a model of a random variable with a normal law of probability distribution. An actual experiment was modeled by addition of 3–10% noise level. Calibration of the automated measuring-computation system was carried out with the help of the pulsed voltage generator with durations of rectangular pulses of 10, 30 and 100 ns. As a whole, these results demonstrated a high degree of reliability of the method.

To carry out 150 measurements (one cycle) in the automated regime with a characteristic frequency of 0.1 Hz, 25 min are required. In the course of experiments, the state of the discharge gap was monitored by the optical method.

The application of the automated measuring-computer system has increased the rate of data acquisition and processing by more than an order of magnitude. This has allowed us to carry out regular statistical investigations of the pulsed electric breakdown of liquids versus the electric field strength, interelectrode distance, and external pressure.

5.1.3 Methods of Analyzing Statistical Distributions of the Discharge Time Lag

Analysis of the statistical discharge time lag. The distribution of events in a series of N independent successive tests or simultaneous observations of a set of N objects (if the event either occurs or does not occur) is described by a binomial or Bernoulli distribution [26].

We are interested in the probability of breakdown initiation during time interval t. The following conditions are met: the occurrence or absence of the event during time t is independent of the event prehistory (independence of events); the probability of the event occurrence during a small interval of time Δt is proportional to the duration of this interval, that is, $p = \mu \cdot \Delta t$, where μ is the probability of occurrence of a single event in unit time (depends on the field strength); the probability of two or more events during the interval of time Δt is considered small.

We now divide the time interval t into N small subintervals and assume that the probability of breakdown initiation in each subinterval is equal to p. The total probability for N intervals is

$$P(t) = N \cdot p (1-p)^{N-1}.$$

Going to the limit at $N \to \infty$, we obtain the probability distribution with the density

$$f(t_{st}) = \mu \exp(-\mu t_{st}). \qquad (5.1)$$

Thus, the statistical time lag obeys an exponential distribution law [2,3]. The average statistical time lag $\bar{t}_{st}$ (the mathematical expectation) is $\bar{t}_{st} = 1/\mu$. For the variance of the statistical time lag, we obtain $\sigma^2(t_{st}) = (\bar{t}_{st})^2$.

Analysis of the total discharge (breakdown) time lag. We now find the probability that the discharge will be initiated during time equal or greater than t_{st}:

$$P(t_{st}, \infty) = \int_{t_{st}}^{\infty} f(t_{st}) \, dt_{st} = \exp(-t_{st}/\bar{t}_{st}). \qquad (5.2)$$

The total time lag is conventionally measured in the experiment with fixed values of voltage, pressure, and interelectrode gap length. The frequency of the breakdown occurrence during time equal to or greater than t can be found from the experimental results:

$$F(t, \infty) = N_t/N_0,$$

where N_t is the number of pulses for which the breakdown time lag is equal or larger than t and N_0 is the number of breakdowns.

Based on the Bernoulli theorem [26], we can state that the frequency of event $F(t, \infty)$ approaches the event probability $P(t, \infty)$ for a large number of experiments (more precisely, it converges to it across the probability). If we assume that the discharge formation time t_f is approximately constant, (5.2) assumes the form

$$N_t = N_0 \exp\left[-(t - t_f)/\bar{t}_{st}\right]. \qquad (5.3)$$

Thus, the dependence between $-\ln(N_t/N_0)$ and t must be linear. The slope of the straight line specifies the average statistical time lag $\bar{t}_{st}$, and its intersection with the ordinate $-\ln(N_t/N_0) = 1$ gives the discharge formation time t_f. This provides the basis for the Laue method of analysis of the breakdown time lag distribution in gases.

Under conditions of actual experiment, the discharge formation time t_f undergoes fluctuations. The quantity Δt_f that specifies the spread of the discharge formation time can be expressed as the sum of a large number of independent (or weakly dependent) elementary deviations (caused by various factors), each influencing the sum comparatively small. According to the central limiting theorem, the law of distribution of the sum of a large number of independent random variables obeying any distribution laws (given that the above-indicated nonrigid restrictions are met) follows approximately a normal law [26]. Experimental investigations confirmed that the discharge formation time distribution is close to a normal distribution [5].

The normal distribution law is characterized by the probability density

$$f\left(t_{\mathrm{f}}\right) = \left(1/\sigma\sqrt{2\pi}\right) \exp\left[-\left(t_{\mathrm{f}} - \bar{t}_{\mathrm{f}}\right)^2 / 2\sigma^2\right],\qquad(5.4)$$

where $\bar{t}_{\mathrm{f}}$ and σ^2 are the average value (the mathematical expectation) and variance of the discharge formation time t_{f}.

In this case, the distribution of the total breakdown time lag can be described by a mathematical model based on a superposition of the exponential distribution of the statistical time lag and the normal distribution of the discharge formation time [6]. We now find the distribution of the breakdown time lag caused by two successive processes of the discharge initiation and propagation. We now assume that these processes are statistically independent. Let us assume that the first process with the average statistical time lag $\bar{t}_{\mathrm{st}}$ occurs during dt_{st}. The termination of this process leads to the occurrence and development of the second process with the average discharge formation time $\bar{t}_{\mathrm{f}}$. Let us also assume that the gap breakdown occurs during dt. The probability of breakdown occurrence during time interval $t, t + dt$ is determined by the product of probabilities of the two processes:

$$dP\left(t, t + dt\right) = \left(1/\bar{t}_{\mathrm{st}}\right)\exp\left[-t_{\mathrm{st}}/\bar{t}_{\mathrm{st}}\right] dt_{\mathrm{st}}$$
$$\times \left(1/\sigma\sqrt{2\pi}\right)\exp\left[-\left(t - t_{\mathrm{st}} - \bar{t}_{\mathrm{f}}\right)^2 / 2\sigma^2\right] dt.$$

For the probability of breakdown during time interval $[0, t]$, we obtain

$$P\left(0, t\right) = \left(1/\bar{t}_{\mathrm{st}}\right) \int_0^t \exp\left(-t_{\mathrm{st}}/\bar{t}_{\mathrm{st}}\right) \left\{ \left(1/\sigma\sqrt{2\pi}\right)\right.$$

$$\left.\times \int_{t_{\mathrm{st}}}^t \exp\left[-\left(t - t_{\mathrm{st}} - \bar{t}_{\mathrm{f}}\right)/2\sigma^2\right] dt\right\} dt_{\mathrm{st}}.\qquad(5.5)$$

Integrating numerically (5.5) and then proceeding to the opposite event, we obtain the probability $P\left(t, \infty\right)$ that the gap breakdown will take place during the time equal to or greater than t.

As an example, Fig. 5.2 shows the results of calculations in the Laue coordinates (in the semilogarithmic scale) with the following distribution parameters: $\bar{t}_{\mathrm{st}} = 100\,\mathrm{ns}$, $\bar{t}_{\mathrm{f}} = 150\,\mathrm{ns}$, and $\sigma = 25\,\mathrm{ns}$.

The dependence of the cumulative distribution (the right curve) differs from a linear one. However, it can be seen that the average statistical time lag $\bar{t}_{\mathrm{st}}$ and the average discharge formation time $\bar{t}_{\mathrm{f}}$ can be determined from the rectilinear section of the curve. Results of calculations for other characteristic relationships among the parameters of distributions demonstrated that if the average statistical time lag $\bar{t}_{\mathrm{st}}$ is much greater than the average discharge formation time $\bar{t}_{\mathrm{f}}$, the cumulative distribution differs only slightly
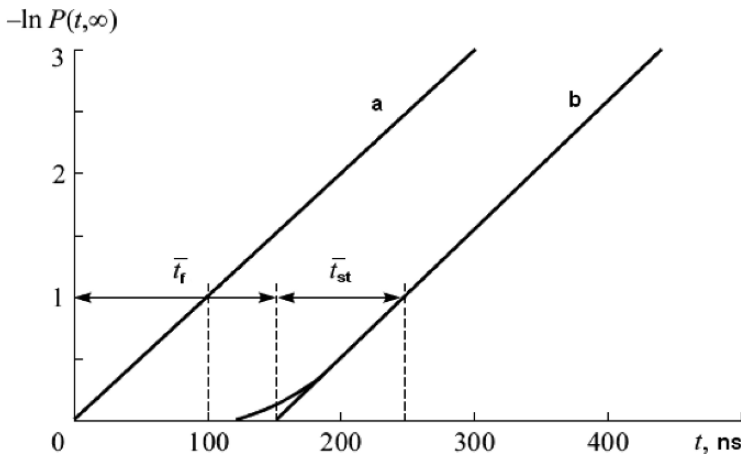
Fig. 5.2. Distribution of the statistical time lag (**a**) and total discharge time lag (**b**) caused by two successive processes

from an exponential one. Otherwise, the cumulative distribution is close to a normal one.

Parallel processes. The method of analysis of statistical breakdown time lag distributions for parallel processes was suggested in [17]. Taking into account the importance of the results obtained, we now consider the parallel processes in more detail.

Let us consider two competing statistically independent events, for example, a gap breakdown initiated by the discharge propagating from anode or cathode (or by other mechanisms developing from one electrode). For simplicity, we assume that the formation times for these processes are weakly fluctuating quantities. The probability that the first event occurs during time equal to or greater than t is given by the expression

$$P_1 (t, \infty) = \exp\left[-(t - t_{f1}) / \bar{t}_{st1}\right].$$

Analogously, for the second event we have

$$P_2 (t', \infty) = \exp\left[-(t' - t_{f2}) / \bar{t}_{st2}\right].$$

Let $t_{f2} > t_{f1}$. We note that

$$P_1 (t) = 0 \text{ for } t \le t_{f1} \text{ and } t' = \begin{cases} t_{f2}, & \text{for } t \le t_{f2}, \\ t, & \text{for } t > t_{f2}. \end{cases}$$

The probability of gap breakdown during time $\ge t$ is the probability of occurrence of both the first and second events. The cumulative probability of occurrence of two statistically independent events is equal to the product of the probabilities of these events (the theorem of multiplication of probabilities [26]):

$$P\left(t,\infty\right) = \exp\left[-\left(t - t_{\mathrm{f1}}\right)/\bar{t}_{\mathrm{st1}}\right]\exp\left[-\left(t' - t_{\mathrm{f2}}\right)/\bar{t}_{\mathrm{st2}}\right].\tag{5.6}$$

Taking the logarithm of (5.6), we obtain

$$-\ln P\left(t,\infty\right) = \left(t - t_{\mathrm{f1}}\right)/\bar{t}_{\mathrm{st1}} + \left(t' - t_{\mathrm{f2}}\right)/\bar{t}_{\mathrm{st2}}.\tag{5.7}$$

As an example, curve c in Fig. 5.3 shows the calculated cumulative probability distribution for the parameters $t_{\mathrm{f1}} = 100\,\mathrm{ns}$, $\bar{t}_{\mathrm{st1}} = 100\,\mathrm{ns}$, $t_{\mathrm{f2}} = 150\,\mathrm{ns}$, and $\bar{t}_{\mathrm{st2}} = 60\,\mathrm{ns}$ in the Laue coordinates. The probability distributions for the first (curve a) and second events (curve b) are also shown in the figure. It can be seen that the cumulative distribution has a break at $t = t_{\mathrm{f2}}$; the straight line segment for the interval $(t_{\mathrm{f1}}, t_{\mathrm{f2}})$ characterizes the first event, and at $t > t_{\mathrm{f2}}$, it characterizes the occurrence of simultaneously two events. From the slope of the first straight line, the average statistical time lag $\bar{t}_{\mathrm{st1}}$ can be determined. Knowing the slope of the second straight line, the average statistical time lag $\bar{t}_{\mathrm{st2}}$ can be found. Indeed, (5.7) for $t > t_{\mathrm{f2}}$ assumes the form

$$-\ln P\left(t,\infty\right) = \left[\left(\bar{t}_{\mathrm{st1}} + \bar{t}_{\mathrm{st2}}\right)/\bar{t}_{\mathrm{st1}}\bar{t}_{\mathrm{st2}}\right]t - \left(t_{\mathrm{f1}}\bar{t}_{\mathrm{st2}} + t_{\mathrm{f2}}\bar{t}_{\mathrm{st1}}\right)/\bar{t}_{\mathrm{st1}}\bar{t}_{\mathrm{st2}},$$

where

$$1/\tau = \left(\bar{t}_{\mathrm{st1}} + \bar{t}_{\mathrm{st2}}\right)/\bar{t}_{\mathrm{st1}}\bar{t}_{\mathrm{st2}} = 1/\bar{t}_{\mathrm{st1}} + 1/\bar{t}_{\mathrm{st2}}\tag{5.8}$$

is the coefficient that specifies the slope of the straight line.

From (5.8) we find that

$$\bar{t}_{\mathrm{st2}} = \tau\bar{t}_{\mathrm{st1}}/\left(\bar{t}_{\mathrm{st1}} - \tau\right).\tag{5.9}$$
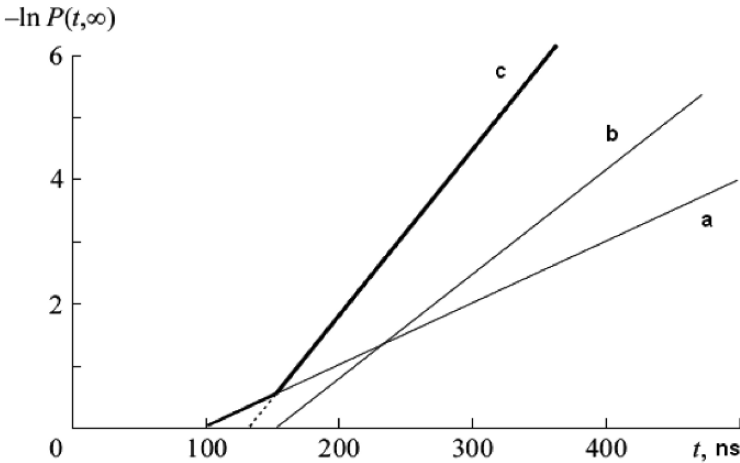
Fig. 5.3. Probability distributions for two individual events (*curves a* and *b*) and cumulative probability distribution for parallel processes (*curve c*)

Thus, the parameters of the processes involved in the breakdown mechanisms can be estimated from an analysis of the cumulative breakdown time lag distributions.

5.2 Dependence of the Statistical Characteristics on the Discharge Conditions

Experiments were carried out using an experimental setup comprising a voltage pulse generator, a discharge chamber, and a complex of superfast optical registration. The voltage pulse with amplitude of 150 kV had a front duration of 30 ns and a flat-topped part duration of 6 μs. The discharge gap was formed by two hemispherical electrodes (with radii in the range 0.5–1.5 cm) fabricated from stainless steel with interelectrode distance in the range 1.5–5 mm. The chamber was filled with distilled water, n-hexane, four-chloride carbon, or other liquids. The complex of experimental techniques included systems of superfast laser Schlieren-photography that allows the dynamics of pre-breakdown processes to be investigated with time resolution of ∼5 ns and spatial resolution of ∼15 μm, and photoregistration of the discharge luminescence with image converter cameras having time resolution of $\sim10^{-9}$ s. The electrodes and liquid were not degassed.

Figure 5.4 shows a histogram of the measured breakdown time lag in distilled water for a field strength of 0.6 MV/cm (a) and the breakdown time lag distribution in the Laue coordinates (b).

It can be seen that the distribution is not symmetric, and the Laue diffraction pattern differs from a straight line. The histogram and the Laue curve can be described by a mathematical model based on a superposition of an exponential distribution of the statistical time lag and a normal distribution of the discharge formation time (Sect. 5.1).

The average breakdown time lag was 55 ± 1 ns, and the standard deviation was 18 ns. From the rectilinear section of the curve we find that the average statistical time lag is 16 ns and the average discharge formation time is 42 ns. The average breakdown time lag $\bar{t}_{\text{lag}} = \bar{t}_{\text{st}} + \bar{t}_{\text{f}}$ is close to the sample average, which confirms the correctness of the statistical interpretation.

The voltage-time characteristic is important for practical application and understanding of the discharge mechanisms (see Sects. 4.2 and 6.1). In physical investigations, it is conventionally represented as $t_{\text{lag}} = f(E)$.

Figure 5.5 shows the dependences of the average breakdown time lag $\bar{t}_{\text{lag}}$ and average statistical time lag $\bar{t}_{\text{st}}$ on the electric field strength E for distilled water ($\rho \sim 10^5\,\Omega\cdot$ cm), n-hexane, and four-chloride carbon ($\rho = 10^{12}\,\Omega\cdot$ cm). Each point was averaged over $40-50$ measurements. The horizontal bars indicate the 0.95 confidence interval. The horizontal dashed straight lines indicate the quasi-statical breakdown field strength.

It appears that the dependence of the electric strength of the examined liquids on the pulse duration for a uniform field with strengths in the range $\sim0.3-1$ MV/cm can be approximated by the expression:

$$\bar{t}_{\text{lag}}\,(E - E_{\text{st}})^4 = K_i, \quad [K_i] = \left(\text{MV}^4\cdot\text{ns}\right)/\text{cm}^4,$$
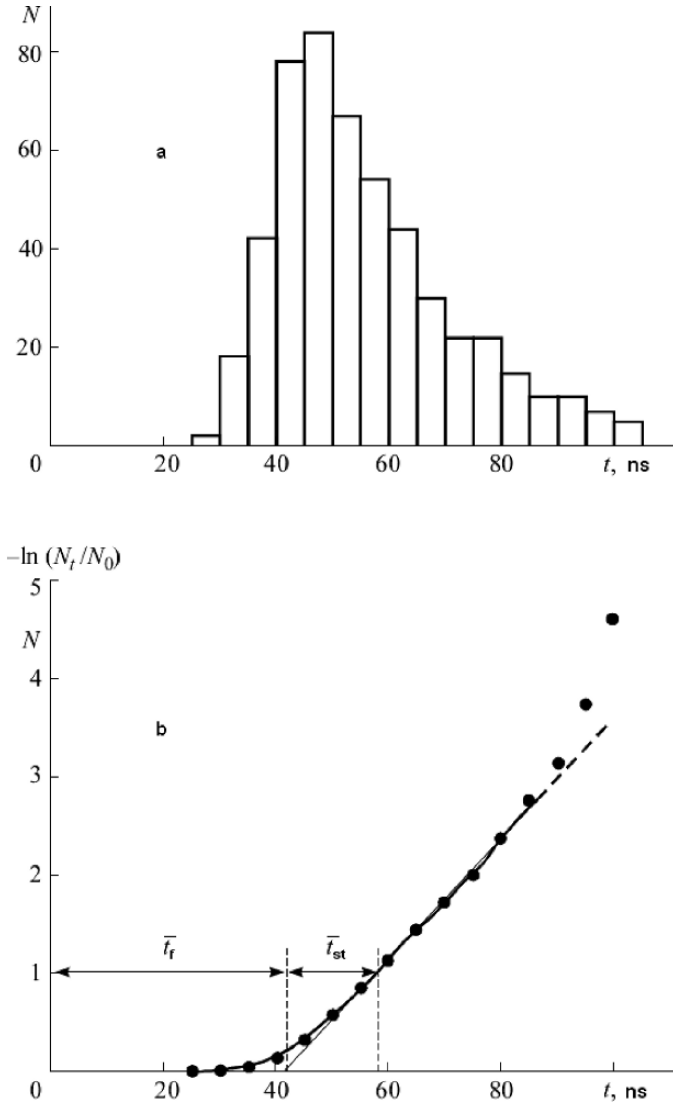
Fig. 5.4. The statistical analysis of breakdown time lag in distilled water: **a)** histogram of the measurements breakdown time lag ($N_0 = 510$) and **b)** breakdown time lag distribution in the Laue coordinates. The electric field strength was $0.6\,\mathrm{MV/cm}$, and the interelectrode distance was $0.2\,\mathrm{cm}$
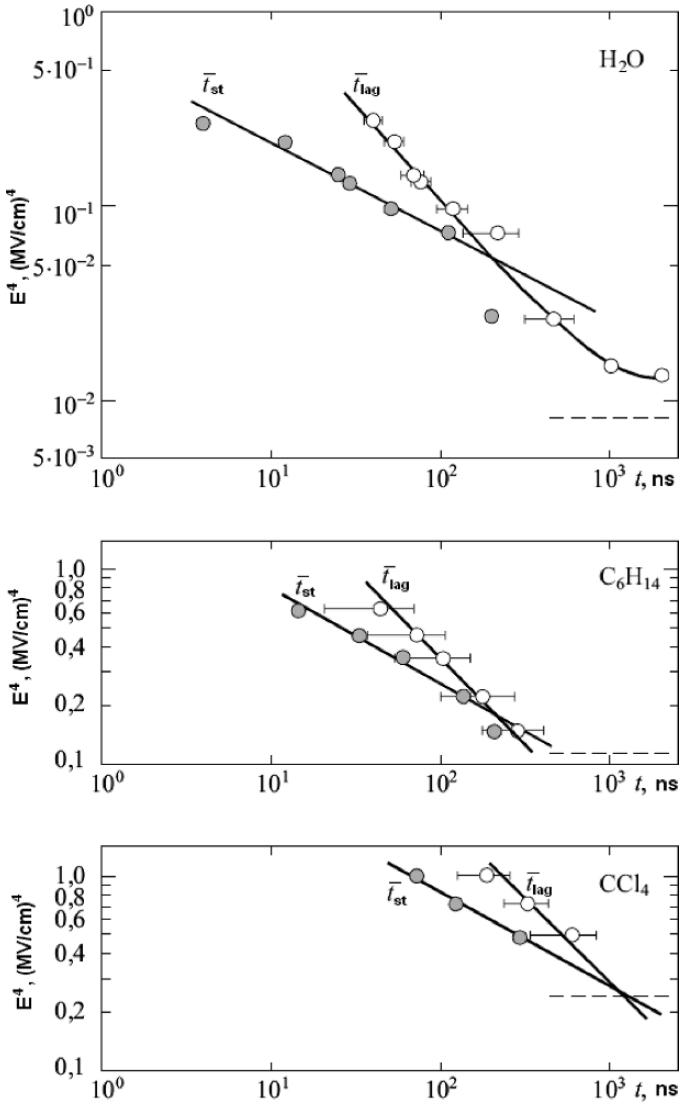
Fig. 5.5. Dependences of the average breakdown time lag $\bar{t}_{lag}$ and average statistical time lag $\bar{t}_{st}$ for distilled water, n-hexane (for an interelectrode distance of $0.2\,\mathrm{cm}$), and four-chloride carbon (for an interelectrode distance of $0.15\,\mathrm{cm}$) on the electric field strength

where $K_1 = 12.6$ for H_2O, $K_2 = 37.5$ for C_6H_{14}, and $K_3 = 200$ for CCl_4. Here E is the maximum field strength withstood by the liquid without breakdown during time $\bar{t}_{lag}$, and E_{st} is the quasi-static breakdown field strength.

Figure 5.5 allows us also to establish an approximate empirical dependence of the average discharge formation time $\bar{t}_f$ and average statistical discharge time lag $\bar{t}_{st}$ on the field strength E:

$$\bar{t}_{lag} = \bar{t}_{st} + \bar{t}_f \approx K_{st}/E^8 + K_f/E^3.$$

It can be seen that at high field strengths, the average statistical time lag is much less than $\bar{t}_f$. In this case, $\bar{t}_{lag} \approx \bar{t}_f \approx K_f/E^3$, which coincides with (6.5) suggested in [32] for high field strengths. For low field strengths, the average breakdown time lag is determined mainly by the statistical time lag, which explains the smooth dependence of t_{lag} on the field E.

By analogy with the average discharge formation velocity $\overline{V}_f$, the average velocity of the discharge ignition process $\overline{V}_{ign}$ can be introduced. (The velocity of the optical inhomogenety propagation, See Chap. 3). Obviously,

$$\overline{V}_{ign} \approx C_1E^3 \text{ and } \overline{V}_f = d/\bar{t}_f \approx C_2E^3,$$

where d is the interelectrode distance and C_1 and C_2 are constants.

Figure 5.6 shows the dependences of the average discharge ignition and formation velocities on the electric field strength for the indicated liquids.

Both dependences can be described approximately by empirical formula $\overline{V}_f \approx CE^3$. For example, the average discharge ignition velocity in distilled water is approximately $5 \cdot 10^6$ cm/s for $E \approx 0.6$ MV/cm ($d = 0.2$ cm). Values of the average velocity of the discharge channel propagation from positive
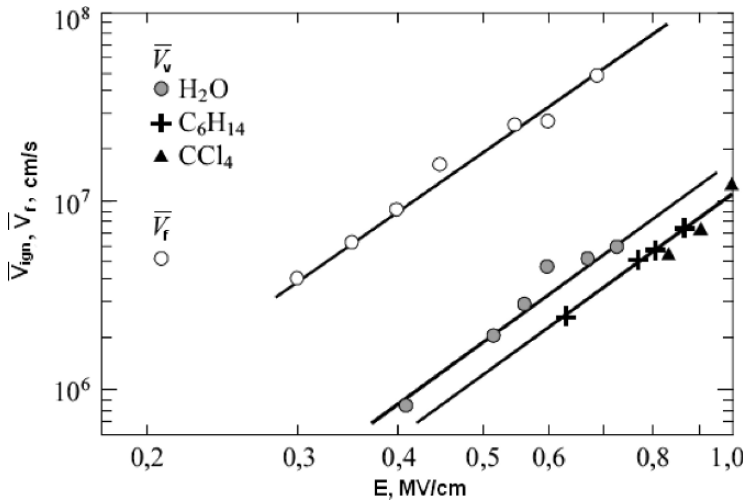
Fig. 5.6. Dependence of the average discharge ignition velocity $\overline{V}_{ign}$ and of the formation velocity on the electric field strength

electrode for purified distilled water with $\rho \sim 3 \cdot 10^6 \, \Omega \cdot cm$ and interelectrode distance of 0.5 cm measured directly with a PIM-3 ICC operating in the chronography mode are also shown in the figure. It can be seen that the average velocity of channel growth $\overline{V}_f$ is higher than the average discharge ignition velocity $\overline{V}_{st}$ found from the statistical analysis of the breakdown time lag. This confirms that there exists an initial stage of the discharge initiation which is not accompanied by optical radiation generation and cannot be registered with an ICC (Chap. 3).

Thus, preliminary results have demonstrated the efficiency of the statistical analysis of pulsed electric breakdown of liquids [11, 18].

5.3 Discharge Mechanisms in Liquids from the Data of Statistical Investigations

Since the discharge formation time decreases with the interelectrode distance, it is pertinent to carry out more detailed investigations of the processes responsible for the statistical delay in submillimeter gaps. In this case, the condition that the discharge formation time $\bar{t}_f$ is much less than the statistical time lag $\bar{t}_{st}$ can be easily met. It is of significant interest to study the influence on the statistical time lag and discharge formation time of the factors that can affect the physical mechanism of discharges in liquids.

In experiments *at increased pressures*, a special discharge chamber was used, the pressure in which could be increased up to several hundreds of atmospheres. The system of input of a grounded electrode allowed the gap length to be adjusted smoothly, keeping the pressure in the chamber unchanged. The discharge gap length was monitored during the experiment by the optical method based on the Fraunhofer diffraction pattern. The intensity distribution was determined with a photorecording system with the use of a computer to control over the experiment and to process the experimental data. The relative measurement error did not exceed 5%.

Figure 5.7 shows the results of statistical analysis of the breakdown time lag *n*-hexane. They were obtained in a quasi-uniform electric field with strength of $\sim$1.6 MV/cm for an interelectrode distance of 100 μm [25, 27]. The dependence (a) was obtained for five groups of successive measurements comprising 30 measurements in each group with the number of measurements equal to 150. For each group, the average breakdown time lag (filled circles) was calculated. Assuming that the average time lag and the number of breakdowns are linearly related, the experimental points were approximated by a straight line using the least square method. It can be seen that the average time lag is essentially independent of the number of breakdowns, which is indicative of the absence of aftereffect, that is, influence of the preceding breakdowns on the parameters of electric discharge.

Figure 5.7*b* shows the histogram of the measured breakdown time lag. Here the number of breakdowns per each time interval is plotted on the vertical axis.

Attention is drawn to the presence of two clearly pronounced peaks on the histogram. A comparison with the results of optical observations demonstrates that this is caused by the existence and competition of two different breakdown mechanisms. One of them corresponds to the electric discharge from cathode (C), and another corresponds to the discharge from anode (A) (see Chap. 3). From Fig. 5.7 it follows that the average breakdown time lag is 310 ± 13 ns, and the standard deviation is 160 ns.

The breakdown time lag distribution constructed by the Laue method is shown in Fig. 5.7c. Here N_t is the number of pulses at which the time lag is equal to or greater than t, and N_0 is the number of measurements. The solid broken curve illustrates the idealized limiting distribution. It can be seen that $\ln(N_t/N_0)$ varies with t approximately linearly, that is, the breakdown time lag obeys an exponential distribution law. The special feature of the curve is a break at the point with the ordinate approximately equal to 1. This behav-
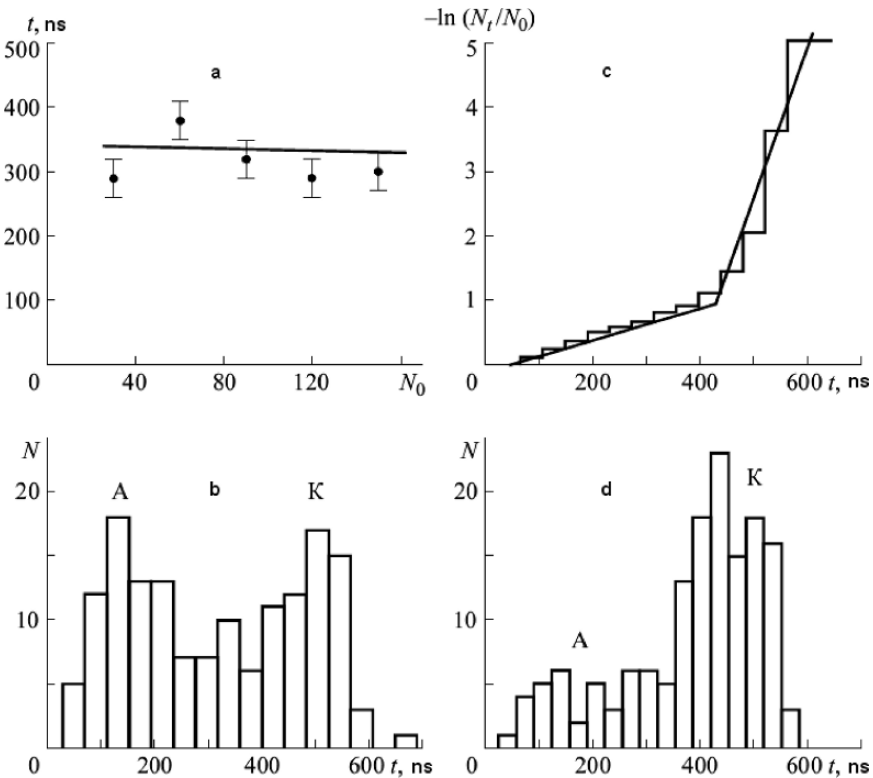
Fig. 5.7. Results of statistical analysis of the breakdown time lag for n-hexane: **a)** dependence of the average time lag on the number of breakdowns, **b)** histogram of the measured breakdown time lag at atmospheric pressure ($N_0 = 150$), **c)** breakdown time lag distribution in the Laue coordinates, and **d)** histogram of the measured breakdown time lag at an external pressure of 0.4 MPa ($N_0 = 150$)

ior of the Laue curve can be described by a mathematical model based on a superposition of two exponential distributions for competing statistically independent events with different characteristic times. Thus, the shape of the Laue curve with a break indicates the existence of two competing and independent breakdown mechanisms, which confirms the results of optical observations. From the analysis of the cumulative distributions, the parameters of the processes involved in the breakdown mechanisms can be estimated. For example, the average statistical time lag is about 40 ns for the breakdown from cathode, and the average discharge formation time is 430 ns. For the breakdown from anode, these parameters are equal to 380 and 50 ns, respectively. It should be noted that the average statistical time lag of the discharge from cathode is much smaller than that from anode. The average velocity of formation of the discharge from anode is $\sim 2 \cdot 10^5$ cm/s and is approximately by an order of magnitude greater than that from cathode. Figure 5.7d shows the histogram of the measured breakdown time lag under application of an external pressure of 0.4 MPa. It can be seen that the pressure influences significantly primary the discharge from anode.

Figure 5.8 shows the results of statistical analysis of the breakdown time lag for n-hexane at an electric field strength of ~ 1.3 MV/cm corresponding to the microsecond region. The histogram is shaped as a symmetric bell (a). Measurements are described by a normal distribution law. A comparison with the results of optical observations demonstrates that the breakdown is initiated by an electric discharge from cathode [28]. The average breakdown time lag is 750 ± 25 ns, and the standard deviation is 310 ns. From the Laue curve (b), we obtain that the average statistical time lag is about 100 ns, and the average discharge formation time is 670 ns.
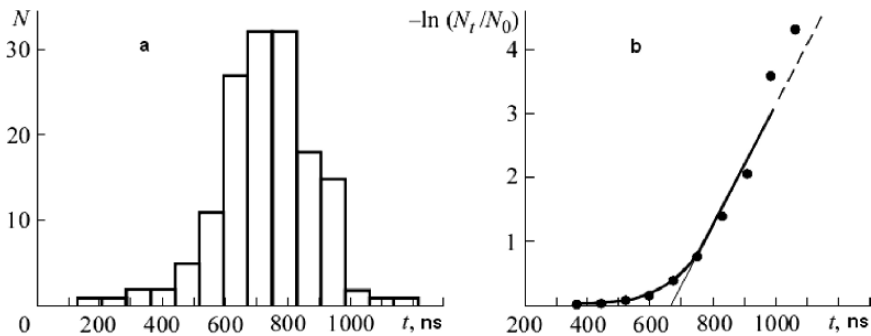
Fig. 5.8. Results of statistical analysis of the breakdown time lag for n-hexane: **a)** histogram of the measured breakdown time lag ($N_0 = 150$ and $P = 0.1$ MPa) and **b)** breakdown time lag distribution in the Laue coordinates. The field strength was 1.3 MV/cm, and the interelectrode distance was 100 μm. Here N_0 is the number of measurements

The average formation velocity for the discharge from cathode was $\sim$1.5 · 10^4 cm/s. The external pressure influences significantly primarily the average statistical time lag. At a pressure of 0.3 MPa, it increases by a factor of $\sim$2.5, and the average discharge formation velocity decreases to $\sim$1.3 · 10^4 cm/s.

For a comparison, Fig. 5.9 shows the results of statistical analysis of the time lag of the breakdown initiated in distilled water by an electric discharge from anode (the interelectrode distance was less that critical, see Sect. 3.3). The distribution at increased pressure is asymmetric (a). From the data of Fig. 5.9a, the average breakdown time lag amounts to 434 ± 28 ns, and the standard deviation amounts to 348 ns at an external pressure of 0.75 MPa. The dependence of the Laue diffraction patterns on the external pressure is shown in Fig. 5.9b. The influence of the pressure on the statistical time lag is significant. As follows from the analysis of the Laue curves, the average statistical time lag amounts to 75 ns at atmospheric pressure, and the average discharge formation time is 154 ns (the average breakdown time lag is in the nanosecond range). These parameters are equal to 235 ns and 180 ns, respectively, at the pressure $P = 0.75$ MPa. At the increased pressure, $\bar{t}_{st} > \bar{t}_f$, which determines the form of the distribution in Fig. 5.9a. The average discharge formation velocity for water is approximately by an order of magnitude greater than for n-hexane and amounts to $\sim$1.3$\cdot 10^5$ cm/s. It decreases to 1.1$\cdot 10^5$ cm/s with increasing pressure.

The analysis of the results of statistical investigations depending on the external pressure demonstrates that for a certain combination of the experimental conditions, the important role in the discharge ignition is played by the
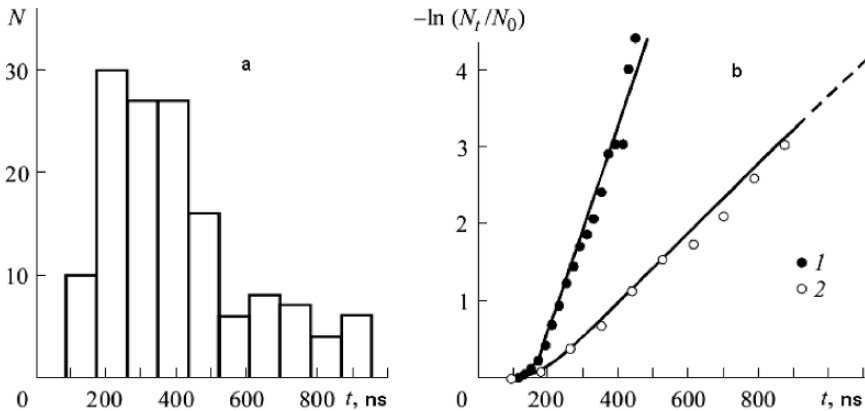
Fig. 5.9. Results of statistical analysis of the breakdown time lag in distilled water: **a)** histogram of the measured breakdown time lag (the number of measurements was $N_0 = 150$ and $P = 0.75$ MPa) and **b)** distribution of the breakdown time lag in the Laue coordinates (*curve 1* is for $N_0 = 150$ and $P = 0.1$ MPa and *curve 2* is for $P = 0.75$ MPa). The electric field strength was 0.9 MV/cm, the interelectrode distance was 200 μm

processes of bubble formation. The strong influence of the external pressure on the statistical delay indicates that the thermal mechanism of microbubble formation is dominant. Thus, the statistical delay of the electric discharge from anode includes the process resulting in fast local superheating of the liquid near the electrode surface and nucleation. Figure 5.10a–c shows histograms of the breakdown time lag distribution for n-hexane depending on the external pressure for field strength of $\sim$1.9 MV/cm [29]. It can be seen that the increase in pressure results in essential change of the distribution form. This is caused by the existence and competition of two breakdown mechanisms from anode (their structures are different, see Sect. 3.1). Attention is drawn to the occurrence of the second maximum in the distribution shown in Fig. 5.10b. A comparison with the results of optical observations demonstrates that the first maximum correlates with the uniform (in the structure) electric discharge, and the second maximum correlates with the complex discharge having the initial bubble stage.

Thus, the discharges from cathode and anode can be separated by their time characteristics with the help of the external pressure. This indicates different characters of the physical processes that lead to their occurrence. After determination of the most probable time lags for the corresponding breakdown mechanisms t_1 and t_2, it is of interest to follow their changes as functions of the external pressure. These results are shown in Fig. 5.10. Strong influence of pressure on the time lag t_1 confirms the important role of the bubble stage of complex electric discharge initiation. At the same time, the absence of a noticeable influence of pressure on the time lag t_2 indicates that the bubble stage is either absent or unimportant for the uniform electric discharge initiation. It should be noted that carbon liberated in the discharge zone and changes in the n-hexane structure influence the breakdown time lag at pressures $\geq$1 MPa. A certain decrease in the time lag t_2 at pressures in the range $\sim$1.1 − 1.5 MPa is most likely caused by this effect.

Figure 5.11 shows histograms of the breakdown time lag distribution for n-hexane at a field strength of $\sim$2.1 MV/cm corresponding to the nanosecond range for the indicated values of the external pressure [30, 31]. It can be seen that with increase in pressure, the distribution form changes from approximately symmetric (at atmospheric pressure) to noticeably asymmetric ($P = 0.9$ MPa). The average breakdown time lag $\bar{t}$ also increases with pressure.

The distributions of the breakdown time lag obtained constructed by the Laue method are shown in Fig. 5.12a for the indicated external pressures. The special feature of the curves is a kink observed in the curve with increasing pressure (see curves 3 and 4 in Fig. 5.12a). The kink in the Laue curves indicates the existence of two independent competing breakdown mechanisms. A comparison with the results of optical observations demonstrates that the breakdown is initiated by electric discharges from anode. The subsequent smooth transition to a straight line (see curve 5 in Fig. 5.12a) indi-
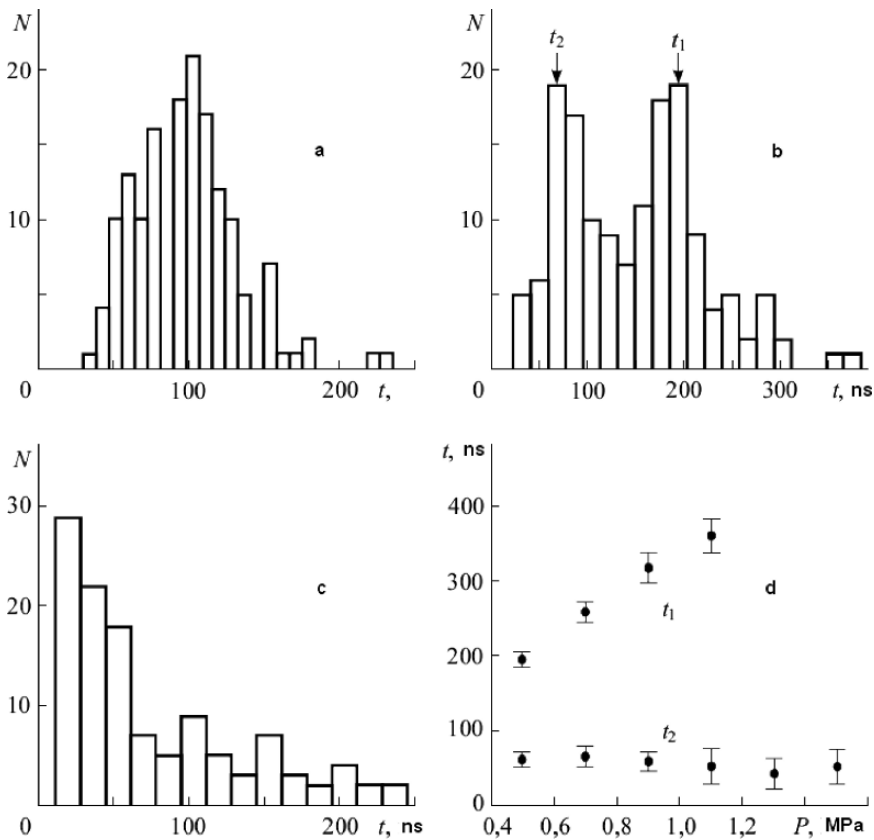
Fig. 5.10. Results of statistical analysis of the breakdown time lag for n-hexane with a field strength of $1.9\,\mathrm{MV/cm}$ and an interelectrode distance of $100\,\mu\mathrm{m}$. The histograms are drawn for: **a)** $\bar{t} = 98\,\mathrm{ns}$, the standard deviation of the individual measurement $\sigma = 34\,\mathrm{ns}$, atmospheric pressure, and the number of measurements $N_0 = 150$; **b)** $\bar{t} = 149\,\mathrm{ns}$, $\sigma = 72\,\mathrm{ns}$, $P = 0.5\,\mathrm{MPa}$, and $N_0 = 150$; **c)** $\bar{t} = 156\,\mathrm{ns}$, $\sigma = 133\,\mathrm{ns}$, $P = 1.3\,\mathrm{MPa}$, and $N_0 = 120$; **d)** dependences of the most probable breakdown time lag for two breakdown mechanisms on the external pressure

cates the change of the breakdown mechanism with increase in the external pressure.

Based on an analysis of cumulative breakdown time lag distributions (see Sect. 5.1), the average statistical time lag $\bar{t}_{\mathrm{st}}$ and the average discharge formation time $\bar{t}_{\mathrm{f}}$ can be estimated for each breakdown mechanisms together with their dependences on the external pressure. These data are shown in Fig. 5.12b. From the figure, the strong influence of the pressure on the first breakdown mechanism and the absence of influence of the pressure on the second breakdown mechanism are seen. The average electric discharge formation velocity increases and reaches $\sim 4 \cdot 10^5\,\mathrm{cm/s}$.
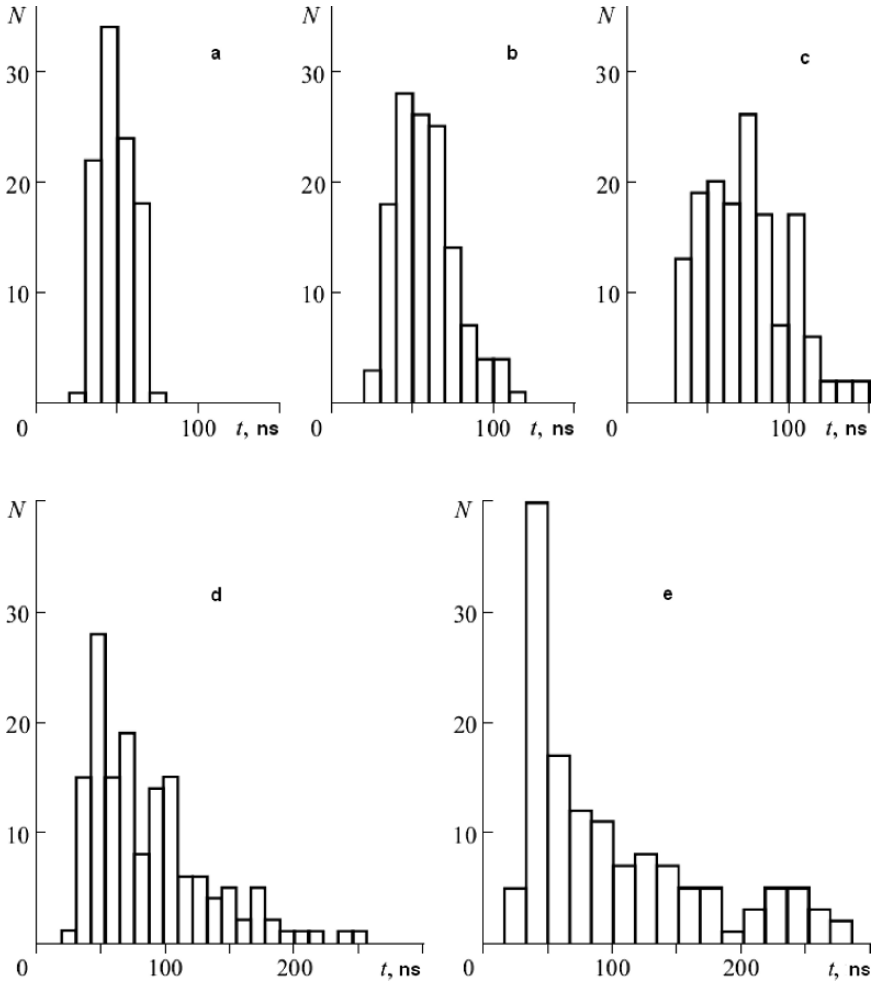
Fig. 5.11. Histograms of the breakdown time lag distribution for n-hexane versus the pressure P: **a)** $\bar{t} = 53$ ns, standard deviation of individual measurement $\sigma = 11$ ns, atmospheric pressure, and number of measurements $N_0 = 100$; **b)** $\bar{t} = 63$ ns, $\sigma = 19$ ns, $P = 0.3$ MPa, and $N_0 = 130$; **c)** $\bar{t} = 79$ ns, $\sigma = 28$ ns, $P = 0.5$ MPa, and $N_0 = 150$; **d)** $\bar{t} = 88$ ns, $\sigma = 45$ ns, $P = 0.7$ MPa, and $N_0 = 150$; and **e)** $\bar{t} = 101$ ns, $\sigma = 68$ ns, $P = 0.9$ MPa, and $N_0 = 136$. The field strength was 2.1 MV/cm, and the interelectrode distance was 100 μm
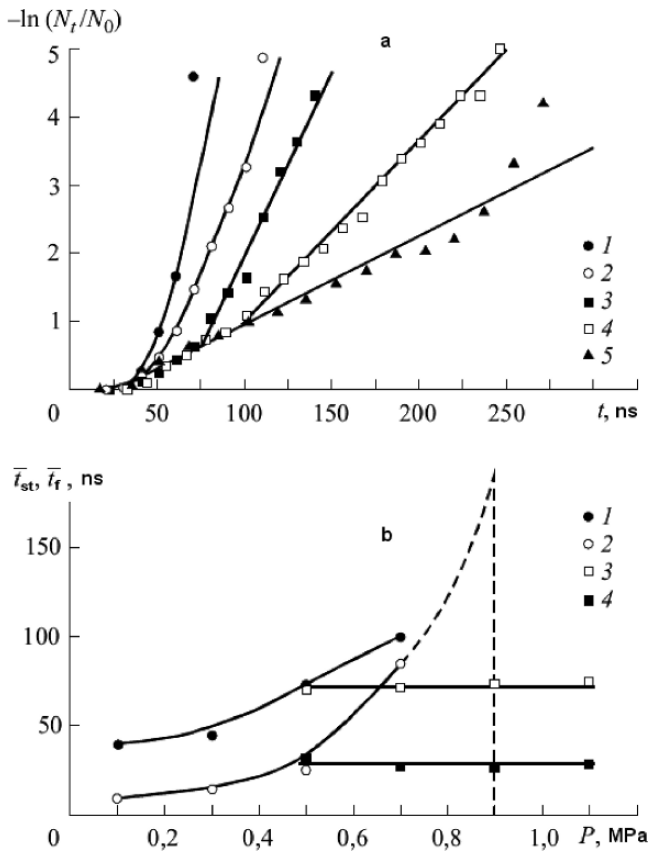
Fig. 5.12. Results of statistical analysis of the breakdown time lag for *n*-hexane at a field strength of 2.1 MV/cm: **a)** breakdown time lag distribution in the Laue coordinates for atmospheric pressure (*curve 1*) and $P = 0.3$ (*curve 2*), 0.5 (*curve 3*), 0.7 (*curve 4*), and 0.9 MPa (*curve 5*); **b)** dependences of the average statistical time lag and of the average discharge formation time for the first (*curves 1* and *2*) and second breakdown mechanisms (*curves 3* and *4*) on the external pressure

Figure 5.13 shows the dependences of the average breakdown time lag found from the analysis of statistical distributions ($\bar{t}_{lag} = \bar{t}_{st} + \bar{t}_{f}$) for the first (curve *1*) and second mechanisms (curve *2*) on the external pressure. The results of direct measurements of the breakdown time lag are also shown here (see curve *3*). Each point was averaged over 100–150 measurements. It can be seen that at atmospheric (or slightly higher) pressure, the first breakdown mechanism (with the complex discharge) is dominant. For it, $\bar{t}_{st}$ and the breakdown time lag obey a distribution law close to normal (Fig. 5.11*a*). With increase in pressure, the breakdown time lag caused by the first mechanism increases thereby leading to coexistence and competition of two breakdown
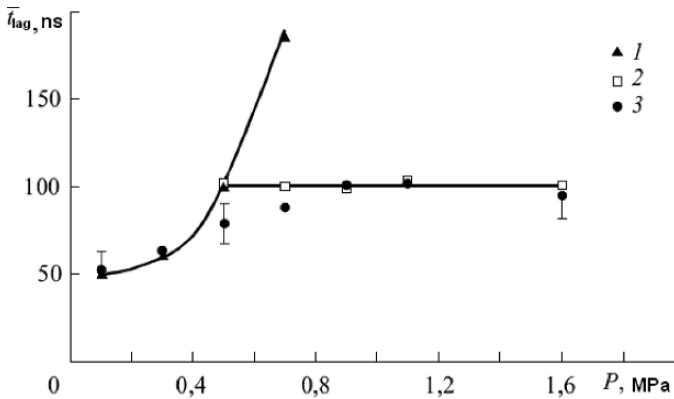
Fig. 5.13. Dependences of the average breakdown time lag for the first (*curve 1*) and second breakdown mechanisms (*curve 2*) on the external pressure. *Curve 3* shows direct measurements of the breakdown time lag

mechanisms. For pressure $P \geq 0.9\,\mathrm{MPa}$, the second mechanism (with the uniform discharge) is dominant. For this mechanism, $\overline{t}_\mathrm{f}$ and the breakdown time lag obey distribution laws close to exponential (see Fig. 5.11e). Thus, the weak influence of the external pressure on the average breakdown time lag is caused by the transition to the ionization mechanism of breakdown from anode (the uniform discharge) at increased pressure.

The vertical dashed straight line in Fig. 5.12b indicates the pressure at which the complex electric discharge has no time to be formed, and a transition occurs to the uniform electric discharge. The strong influence of the external pressure (comparatively low) on the statistical time lag for the complex electric discharge from anode indicates the thermal mechanism of the bubble stage. Hence, the statistical delay for the complex electric discharge involves the process leading to fast local heating of the liquid near the anode surface and formation of a vapor microbubble. The discharge formation time is connected with the bubble expansion, development of the ionization processes inside the bubble, and onset of the fast ionization processes in the liquid as a result of the electric field amplification at the pole of the deformed bubble (becoming conducting after the breakdown). The statistical time lag of the uniform (by the structure) electric discharge from anode is meant the time required for the onset of self-sustaining ionization processes in the liquid. The discharge formation time corresponds to the anode-to-cathode propagation of the ionization processes.

In conclusion it should be noted that the direct correlation of the prebreakdown phenomena with the character of statistical distributions of the breakdown time lag considerably increases the role of the statistical analysis and opens new opportunities for a study of the influence of various factors

(external pressure, temperature, impurity, etc.) on the discharge mechanism in the liquid.

References

1. B. W. Ward and T. J. Lewis, A new statistical theory for the breakdown of liquid hydrocarbons, J. Electrochem. Soc., **107**, No. 3, 191–195 (1960).
2. T. J. Lewis and B. W. Ward, A statistical interpretation of the electrical breakdown of liquid dielectrics, Proc. R. Soc. London, **A269**, No. 1337, 233–248 (1962).
3. I. Adamczewski, Ionization, Conductivity and Breakdown in Dielectric Liquids, Taylor and Francis Ltd., London (1969);
4. W. Hauschild, W. Mosch, Statistik fur Elektrotechniker. Eine Darstellung an Beispielen aus der Hochspannungtechnik. VEB Verlag Technik, Berlin, (1984)
5. A. J. Beddow and J. E. Brignell, Nanosecond breakdown time lags in a dielectric liquid, Electron. Lett., **2**, No. 4, 142–143 (1966).
6. A. J. Beddow and J. E. Brignell, Breakdown time lags in a dielectric liquid, Electron. Lett., **1**, No. 9, 253–254 (1965).
7. N. S. Rudenko and V. I. Tsvetkov, Investigations of the electric strength of liquid dielectrics under exposure to nanosecond voltage pulses, Zh. Tekh. Fiz., **35**, No. 10, 1840–1843 (1965).
8. P. Felsenthal, Nanosecond breakdown in liquid dielectrics, J. Appl. Phys., **37**, No. 10, 3713–3715 (1966).
9. K. D. Metzmacher and J. E. Brignell, Apparent charge mobility from breakdown times in a dielectric liquid, J. Phys., **D3**, No. 2, 103–104 (1970).
10. V. V. Bagin, A. A. Vorobjev, V. V. Lopatin, and V. Y. Ushakov, Distribution of discharge time lags in a nanosecond breakdown of liquid dielectrics under a uniform field, in: High-Power Electrical Equipment and Electrical Insulation, Energiya, Moscow (1970), pp. 343–349.
11. A. P. Alkhimov, V. V. Vorobjev, V. F. Klimkin, *et al.*, Electric discharge propagation in water, Dokl. Akad. Nauk SSSR, **194**, No. 5, 1052–1054 (1970).
12. O. A. Gzowski, R. Wlodarski, T. R. Hesketh, and T. J. Lewis, The luminescence of dielectric liquids under high electric stress, Br. J. Appl. Phys., **17**, No. 11, 1483–1489 (1966).
13. A. W. Palmer and H. House, A statistical analysis of the light pulses emitted before electrical breakdown of a liquid dielectric, J. Phys., **D5**, 1106–1110 (1972).
14. J. Gerhold, Helium breakdown near the critical state, IEEE Trans. Electr. Insul., **EI23**, No. 4, 765–768 (1988).
15. K. Arii, I. Kitani, and M. Kawamura, Avalanche breakdown in n-hexane, J. Phys., **D12**, 787–796 (1979).
16. K. Yoshino, Dependence of dielectric breakdown of liquids on molecular structure, IEEE Trans. Electr. Insul., **EI15**, No. 3, 186–200 (1980).
17. A. P. Avrorov and V. V. Vorobjev, Statistical investigations of the mechanism of water breakdown in the microsecond range, Preprint No. 83–69, Nuclear Physics Institute of the Siberian Branch of the USSR Academy of Sciences, Novosibirsk (1983).
18. V. F. Klimkin, Investigations of the initial stage of electric discharge propagation in liquids and dense gases by the methods of superfast optical registration, Author's Abstract of Cand. Phys.-Math. Sci. Dissert., Novosibirsk (1975).

19. D. V. Fenneman and R. J. Gripshover, Experiments on electrical breakdown in water in the microsecond regime, IEEE Trans. Plasma Sci., **PS8**, No. 3, 209–213 (1980).
20. K. Arii and I. Kitani, Effects of pressure and gaseous impurities on breakdown time lags of n-hexane, J. Phys., **D14**, No. 9, 1657–1659 (1981).
21. N. Hirai, A. Akumu, and K. Arii, The effect of electrode construction in breakdown time lag of impulse breakdown in mineral oil, Jpn. J. Appl. Phys., **37**, 4884–4886 (1998).
22. J. L. Maksiejewski, Time-lags of triggered spark gaps in liquid hydrocarbons, IEEE Trans. Electr. Insul., **EI20**, No. 2, 339–342 (1985).
23. J. L. Maksiejewski, The effect of additives on the time characteristics of a liquid trigatron, IEEE Trans. Electr. Insul., **EI22**, No. 3, 237–239 (1987).
24. D. Hudson, Statistics for Physicists, Mir, Moscow (1967).
25. V. F. Klimkin, Automated System for Statistical Investigations of the mechanism of electrical breakdown of liquids, Zh. Tekh. Fiz., **62**, No. 9, 160–164 (1992).
26. E. S. Ventsel, Probability Theory, Nauka, Moscow (1969).
27. V. F. Klimkin, A pulsed electrical breakdown of n-hexane under uniform field, in: Conf. Record of the 10th Int. Conf. on Conduction and Breakdown in Dielectric Liquids, Grenoble (1990), pp. 574–578.
28. V. F. Klimkin, Applicability limits of mechanisms of electrical breakdown of n-hexane under a quasi-uniform field, Zh. Tekh. Fiz., **61**, No. 8, 80–83 (1991).
29. V. F. Klimkin, Mechanisms of electrical breakdown of n-hexane in the nanosecond range, Zh. Tekh. Fiz., **60**, No. 6, 161–163 (1990).
30. V. F. Klimkin, High-speed optical and statistical investigation of prebreakdown phenomena in liquid dielectrics in the nanosecond region, in: Proc. of the 13th Int. Conf. on Dielectric Liquids, Nara (1999), pp. 152–155.
31. V. F. Klimkin, Statistical investigations of mechanisms of electrical breakdown of n-hexane in the nanosecond range, Zh. Tekh. Fiz., **72**, No. 9, 38–43 (2002).

Basic Laws Describing of the Impulse Electric Strength of Liquids

Before a description of the main physical models of discharge initiation and propagation, the authors have decided to present a chapter containing experimental data on the electric strength of liquids and its dependence on the nature (properties) of liquids and breakdown conditions.

This decision is dictated first, by the fact that the experimental data on the electric strength of liquids are additional material promoting elucidation of the nature (mechanisms) of liquid breakdowns. In some cases in which the discharge processes cannot be observed experimentally or convincingly described theoretically, the data on the electric strength are the only source of information on these processes. In this sense, they can be related to indirect methods of investigation of electric breakdowns.

Second, as already noted in the Preface, the development of pulsed power has significantly increased specifications for the liquid insulation. A square-law dependence of the energy density in capacitive energy storages on the field strength in the dielectric $W = \varepsilon E_{\mathrm{br}}^2/(8\pi)$ demonstrates that the electric strength E_{br} is the determining characteristic for the design of voltage pulse and current generators when especially stringent requirements are imposed on their parameters. In electrodischarge engineering, the electric strength of dielectric materials (insulation, working medium, and material being treated) in most cases is the parameter determining the production process, design, regime of treatment, etc.

Third, materials on physics of pre-discharge and discharge processes in liquids, presented in Chaps. 1–5, allow many laws describing their electric strength to be explained. This enables a more justified choice of working liquids and working gradients of insulation gaps to be performed.

6.1 Duration, Shape, and Frequency of Voltage Pulses

A characteristic feature of impulse liquid breakdown, in comparison with gas breakdown, is a dependence of the electric strength on the *voltage duration*

over a wider time interval. In the impulse breakdown of gases in a uniform field, the phenomenon of discharge delay starts to be manifested for pulse duration $\leq 10^{-6}$–10^{-7} s and is explained by the electron-avalanche processes and streamer propagation. In breakdown of liquids in a uniform field at times approximately by an order of magnitude greater than in gases, an increase in the electric strength is observed with decrease in the voltage pulse duration. Moreover, for longer t the dependence $E_{br} = f(t)$, though weaker, is also observed. By analogy with the gas discharge, the discharge delay in a liquid at $t \leq 10^{-5}$–10^{-6} s was previously explained by the electron-avalanche processes. The displacement of the bending point of the curve $E_{br}(t)$ toward larger t and a stronger dependence $E_{br} = f(t)$ for liquids remained inexplicable.

Since the drift of the electrode potential toward the head of the discharge channel and finally the velocity and discharge time lag in long gaps are mostly determined by the heating rate and hydrodynamic expansion of the initial channel and its transformation into a well-conducting leader channel, these rather slow processes should be involved in an analysis of special features of voltage-time characteristics of discharge gaps in a liquid. Owing to a high density of liquids, the velocity of the discharge channel expansion in liquids is much less than in gases for the same powers developed in the discharge channels. As a result, the limited velocity of channel expansion will preclude the formation of a well-conducting channel in liquids for pulse durations much longer than in gases and limit the discharge propagation into the gap depth. To obtain high velocities of primary channel propagation with high longitudinal potential gradients in these channels corresponding to short pulse durations, the voltage drop across the discharge gap must be significantly increased. In addition, a decrease in the duration of the applied voltage pulse decreases the role of gas formation in the discharge ignition and propagation.

In short gaps with a uniform field, this is manifested through changes in the discharge mechanisms for exposure times less than a certain critical one, namely, transition from the discharge from cathode (the bubble breakdown mechanism) to the discharge from anode (the ionization breakdown mechanisms or combined), see Sects. 3.3 and 3.4. In long gaps, changes in the voltage pulse duration (and, correspondingly, in the overvoltage magnitudes) are accompanied by changes in the external shape of the discharge figure and conditions of bush-like figure transformation into a treelike figure. This also influences significantly the voltage-time characteristics (see Sect. 4.1).

The voltage-time characteristics are especially steep under nanosecond voltage exposures (see Fig. 6.1).

For pulses with duration of several nanoseconds, the electric strength of even commercially pure liquids exceeds $1\,\mathrm{MV/cm}$; it reaches $4\,\mathrm{MV/cm}$ in a uniform field for $t \approx 4\,\mathrm{ns}$ and $d = 1.25\,\mathrm{mm}$. Moreover, liquids with radically different composition have electric strengths close in values. The data on the nanosecond electric strength of liquids for $t = 3$–$100\,\mathrm{ns}$ are well described by the equation of the form
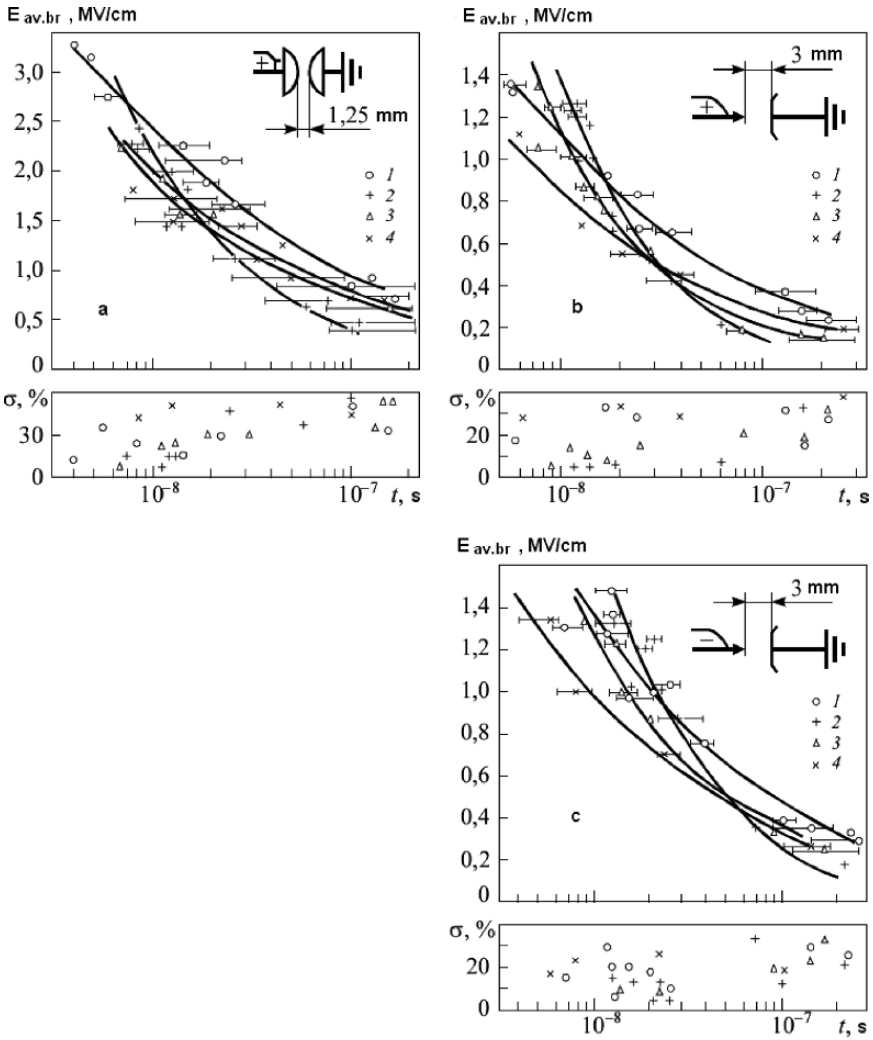
Fig. 6.1. Dependences of $E_{\mathrm{av.br}}$ and σ on t for a transformer oil (*1*), distilled water (+), glycerin (Δ), and castor oil ($\times$) in the hemisphere-hemisphere gaps for $d = 1.25\,\mathrm{mm}$ (**a**) and in $+\mathrm{T}-\mathrm{P}$ (**b**) and $-\mathrm{T}+\mathrm{P}$ (**c**) for $d = 3\,\mathrm{mm}$

$$\log E_{\mathrm{br}} = A - B \cdot \log t \,, \tag{6.1}$$

where A and B are coefficients specific for each liquid and insulation gap type, $E_{\mathrm{br}}(t)$ is measured in MV/cm, and t is in nanoseconds. Values of the coefficients for four examined liquids and three typical discharge gaps are presented in [1, 2].

In the case of electrothermal breakdown of well-conducting liquids (for example, tap water) in short gaps with a uniform field under exposure to

microsecond pulses when the discharge ignition voltage U_{ign} and the breakdown voltage U_{br} virtually coincide, the dependence of the electric strength on the pulse duration can be calculated from the condition of liquid boiling up.

The time of water boiling up and hence the breakdown time (according to the accepted assumption) can be determined from (6.2) which relates E_{br} and t:

$$t_{\mathrm{d}} = \frac{C \cdot \rho}{0.24 \cdot a \gamma_0 \cdot \cdot E^2} \ , \tag{6.2}$$

where C, ρ, and γ_0 are the specific heat capacity, density, and electrical conductivity of the liquid at the ambient temperature T_0 and a is the exponent:

$$\gamma = \gamma_0 \cdot e^{a(T-T_0)} \ . \tag{6.3}$$

Equation (6.2) is valid for the adiabatic case under assumption that the breakdown temperature tends to infinity. For example, for tap water, $T = 100°C$, $T_0 = 20°C$, $\gamma = 2 \cdot 10^{-4}\,\Omega^{-1} \cdot \mathrm{cm}^{-1}$, and $a = 0.011$, according to [3] we can write

$$E_{\mathrm{br}} = 10^3 \cdot t^{-1/2} \ . \tag{6.4}$$

The calculated and experimental data agree well when the voltage exposure exceeds $10\,\mu\mathrm{s}$ and the interelectrode distances range from several tenth to several units of millimeters.

For electrodes with large surface creating a weakly nonuniform field, the empirical equations suggested in [67] can be used to calculate E_{br} of treated water ($\gamma \approx 10^{-6}\,\Omega^{-1} \cdot \mathrm{cm}^{-1}$) for pulse exposure from a few tenth of microsecond and longer:

$$E_{\mathrm{br}}^{+} = \frac{0.3}{t^{1/3} S^{1/10}}, E_{\mathrm{br}}^{-} = \frac{0.6}{t^{1/3} S^{1/10}} \ , \tag{6.5}$$

where E_{br}^{+} and E_{br}^{-} are the breakdown field strengths for positive and negative pulse polarities, respectively, measured in MV/cm, t is the effective time during which the field strength exceeds $0.63 E_{\mathrm{br}}$, in $\mu\mathrm{s}$, S is the effective area, in cm^2, of the electrode the field strength of which exceeds $0.9 E_{\mathrm{br}}$. In publications devoted to high-power electron beam generation and thermonuclear fusion (for example, see [4]) it was pointed out that empirical equations (6.5) allow capacitive energy storages to be designed with high degree of reliability.

Obviously, (6.5) are applicable only when the interelectrode distance changes in small limits, because they ignore the influence of the interelectrode distance on E_{br} (see Sect. 6.6).

It is of interest to compare the results of calculations of E_{br} from (6.5) with the experimental data obtained in different laboratories. The results of comparison are illustrated by Fig. 6.2. Since in long gaps with uniform or weakly nonuniform field the discharge is ignited on anode, the first equation for E_{br}^{+} is used in calculations of E_{br} from (6.5). It can be seen that (6.5) yield a stronger dependence of E_{br} on the pulse duration than the experimentally observed one. The calculated and experimental curves agree satisfactory for
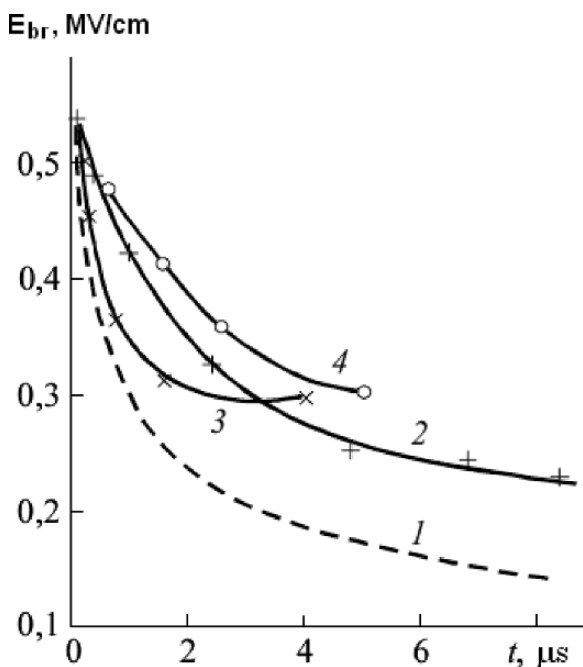
Fig. 6.2. Dependences of E_{br} on t for treated water ($\rho \approx 10^6\,\Omega \cdot$ cm) in a uniform field: calculations from (6.4) for $S_{eff} \approx 50\,\text{cm}^2$ (*1*), $S_{eff} \approx 45\,\text{cm}^2$ and $d = 1.5$см [2] (*2*), $S_{eff} \approx 14\,\text{cm}^2$ and $d = 0.5$ cm (*3*), and $S_{eff} \approx 70\text{cm}^2$ and $d = 1.5$–5 cm [66] (*4*)

$t = 0.1$–$1\,\mu$s. For nanosecond pulse exposures, the calculated E_{br} values were 2–5 times higher than experimentally measured ones described by (6.1).

Concerning the behavior of the voltage-time characteristics of insulating liquids under exposure to microsecond pulses, historically in practice of high-voltage engineering it was assumed that the electric strength of liquids asymptotically tends to the static breakdown electric strength. However, the fact that under exposure to voltage pulses of equal durations the electric strength of liquids differs for pulses of different shapes demonstrates that the pulse duration is the important but not unique parameter of the voltage pulse that determines the electric strength of liquids. This circumstance stimulated a search for voltage pulse parameters that influence the pre-breakdown processes in the liquid and, as a result, its electric strength. In addition, the increased role of internal overvoltages with transition of high-power systems to ultrahigh voltages calls for a search for test pulses reproducing the most dangerous influence of internal overvoltages on the insulation.

In [5] it was established that in long air gaps, the character of discharge processes and the breakdown voltage essentially depend on the slope of the oblique voltage pulses.

Investigations of the discharge in liquids under the effect of oblique waves [6–8] demonstrated a strong dependence of the discharge and breakdown voltage characteristics on the wave slope. A decrease in the slope (from 600 to $0.4 \, \mathrm{kV/\mu s}$) causes the discharge ignition voltage U_{ign} and the average leader propagation velocity V_{av} to decrease (Fig. 4.31).

For pulse duration of several tens or hundreds of microseconds, the dependences of the breakdown and flashover voltages in insulating liquids on the pulse slope (and hence the discharge time) have complex character [9–12]. Figure 6.3 shows the voltage-time characteristics of the $+\mathrm{T} -\mathrm{P}$ discharge gap in a transformer oil for interelectrode distances of 5 (*curve 1*), 15 (*curve 2*), and 25 cm (curve *3*) [9]. In Fig. 6.4, the dependences of flashover voltage (U_{fl}) of organic glass ($\delta = 1 \, \mathrm{cm}$) in a transformer oil for an asymmetric gap ($d = 7 \, \mathrm{cm}$) with predominant tangential (*I*) and normal field strength components (*II*) [2,12] are shown. Letters *a*, *b*, and *c* designate curves drawn for 90, 50, and 10% flashover probabilities, respectively. (The effective flashover voltages at the industrial frequency were 110 kV in case *I* and 72 kV in case *II*.) Each dependence was obtained by processing the data of 500–520 individual measurements.

As well as in the case of oil breakdown, the curve $U_{\mathrm{fl}} = f(t)$ has three typical sections. As t increases from 3 to 80–100 μs, U_{fl} decreases. Further increase in t to 160–200 μs is accompanied by an increase in U_{fl}. We may suggest that the increase in U_{br} and U_{fl} in the intermediate segment of the voltage-time characteristics results from the field attenuation due to the space charge created in the process of emission and primary ionization and concentrated near the initiating electrode. For mildly sloping pulse, the long-term ionization in
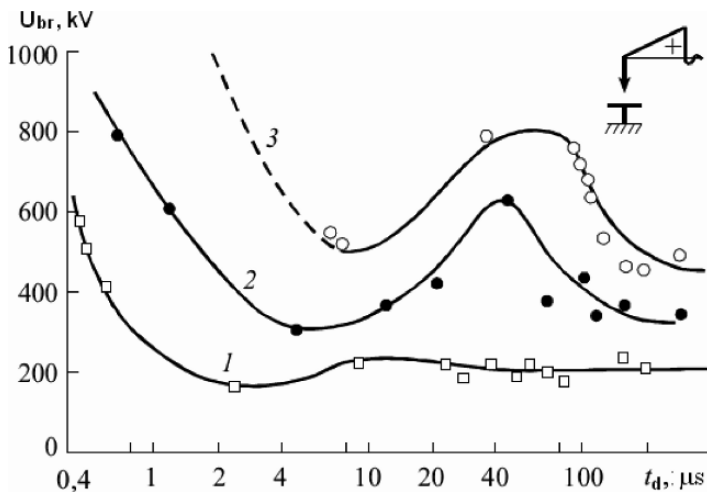
Fig. 6.3. Voltage-time characteristics of a transformer oil for $d = 5$ (*1*), 15 (*2*), and 25 cm (*3*) [9]
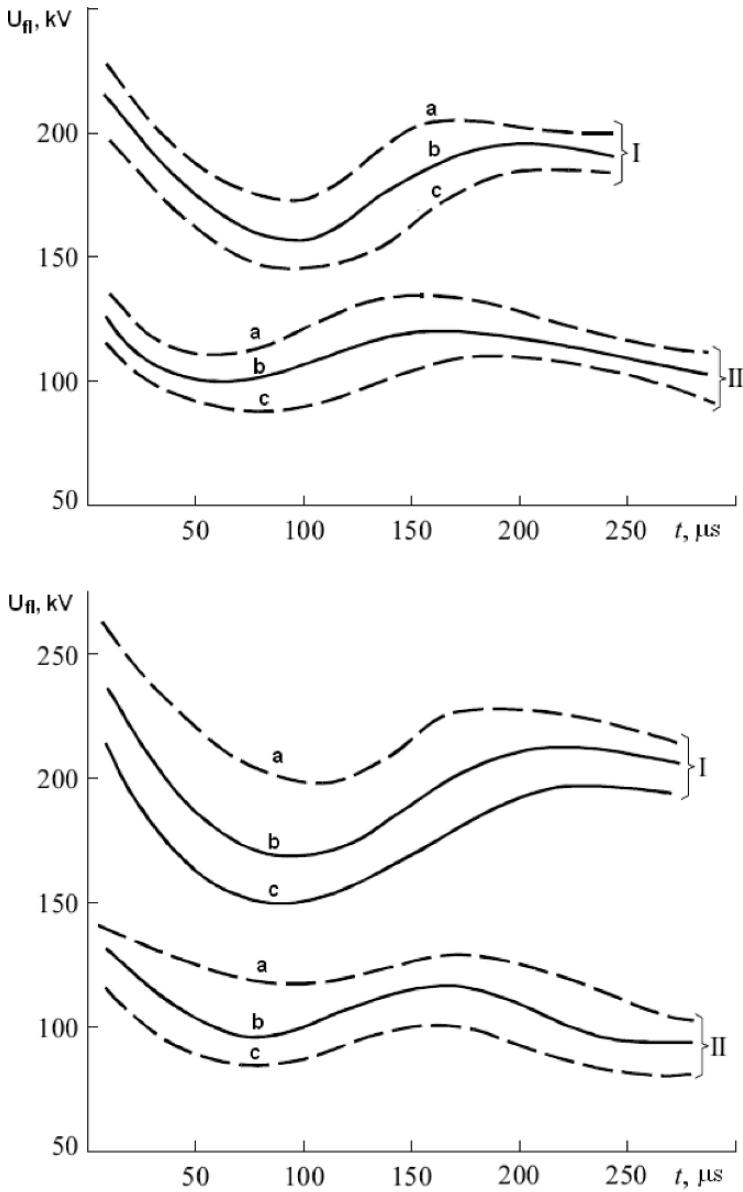
Fig. 6.4. Dependence of the flashover voltage of organic glass in transformer oil in fields with dominant tangential (*1*) and normal components (*II*) on the duration of positive (**a**) and negative oblique pulses (**b**) [12]

the vicinity of microinhomogeneities of the electrode surface creates a large space homocharge that shields the tip electrode and hinders the formation of the discharge channel. The greater the coefficient of field macroinhomogeneities, the stronger the decelerating effect of the space charge irrespective of the discharge ignition mechanism (bubble or ionization one).

For extremely small end radii of tip electrodes, the discharge ignition voltage and the voltage at which slow channels are transformed into fast ones increase as the pulse slope decreases (the pulse rise time - pulse front - increases) [13] (see Sect. 4.1). This confirms the shielding action of the space charge near the electrode. The smaller r_0, the more pronounced this effect. Further increase in t causes a smooth decrease in U_{fl}, which can be explained by the increased roles of relatively slow secondary processes of gas formation and impurity in the liquid.

When liquid breakdown occurs in the tail of the voltage pulse rather than in the front (small overvoltages, long gaps, and nonuniform fields), the breakdown voltage depends on the parameters of the pulse as a whole. The data in Table 6.1 demonstrate the influence of the rise time (front duration) and total duration of the aperiodic pulse on the 50% breakdown voltage of transformer oil in discharge gaps of different configurations [14]. The standard deviation σ for a 90% reliability level reached 25% for ac voltage with a frequency of

Table 6.1. Values of the pulse coefficient k^* for gaps insulated by a transformer oil

Configuration of the discharge gap	Interelectrode gap length, mm	Pulse coefficient for pulse width ratios, μs				
		11/2600	150/3000	430/4000	2700/4400	50 Hz
Tip–plane electrodes (with a rake angle of 10° and an end radius of 1 mm)	10	1.01	1.04	1.07	1.09	0.54
	30	1.04	1.08	1.09	1.12	0.51
	50	1.02	1.05	1.06	1.08	0.48
	70	1.02	1.04	1.06	1.06	0.44
Tip-tip electrodes	10	1.1	1.2	1.27	1.32	0.5
	20	1.12	1.24	1.29	1.38	0.48
	40	1.11	1.25	1.31	1.41	0.5
Faceted wires (20 × 20 mm) intersecting at an angle	10	0.825	0.78	0.78	0.78	0.48
	20	0.844	0.82	0.82	0.82	0.38
The same, but with round wires 20 mm in diameter	10	0.814	0.78	0.78	0.78	0.5

*Here k is a ratio of the 50% breakdown voltage of the given type to the 50% breakdown voltage for 1.2/50-μs pulses.

50 Hz and switching pulses. It is 15% for a pulse width ratio of $1.2/50\,\mu s$. From Table 6.1 it follows that for aperiodic pulses with $\tau_{fr} > 100\,\mu s$, U_{br} depends only weakly on the shape of pulse tail (the rate of voltage decay). The influence of high-frequency oscillations on U_{br}, superimposed on the aperiodic pulse component or dc voltage, is stronger. The increase in the high-frequency component from 0 to 100% reduces U_{br} by a factor of 1.5–2 and U_{fl} by a factor of 2.5–3. (By the percentage of oscillations we mean the ratio of the rms component of the ac voltage to the average value of the dc voltage.)

The voltage-time characteristics of the liquefied gases under exposure to micro- and nanosecond pulses do not differ both in their external view and absolute values of the electric strength from those of hydrocarbons and others liquids of complex structure and composition.

Under the joint influence of different voltage types applied in succession, the earlier voltage significantly affects the electric strength in the presence of the later. The electric strength increases if the polarity of previously applied voltage (pre-stressing) coincides with that of the applied voltage (for which the electric strength is measured). The maximum effect reaches tens of percent and depends primarily on the duration and magnitude of previously applied voltage, the time interval between the previously applied and applied voltages, and the type of voltage for which the electric strength is measured.

The electric strength of liquid dielectrics at low frequencies (up to several kilohertz) depends weakly on the *frequency*. Moreover, the effect of the frequency depends on the electrical conductivities (both intrinsic and impurity) and permittivities of liquids as well as on the geometry of the discharge gap. When dielectric losses in a liquid determined by the well-known expression

$$P = \frac{\varepsilon \cdot f \cdot \tan \delta}{1.8 \cdot \cdot 10^{12}} E^2 \; , \qquad (6.6)$$

are insufficient to heat the liquid to temperatures of electrothermal breakdown, the electric strength of the liquid in a uniform field is independent of the frequency or slightly increases with the frequency.

In formula (6.6), P denotes specific losses (the power dissipated in $1\,cm^3$ of the dielectric), in W/cm^3; f is the frequency, in s^{-1}; $\tan\delta$ is the tangent of the dielectric loss angle; and E is the field strength, in V/cm.

The increase in the breakdown field E_{br} is typically recorded for moderately pure liquids. The electric strength of commercially pure insulating liquids for the voltage at the industrial frequency is slightly (10–20%) higher than for dc voltages. The frequency dependence of U_{br} of gaps with a sharply nonuniform field with intense cavity processes, typically observed at relatively low ac electric fields, is U-shaped at frequencies of several hundred herz (Fig. 6.5) [15]. At high frequencies (10^3–10^6 Hz), the breakdown of even weakly polar liquids results from the intense heat release in the liquid and is characterized by a significant reduction in electric strength with increasing frequency. Thus, for
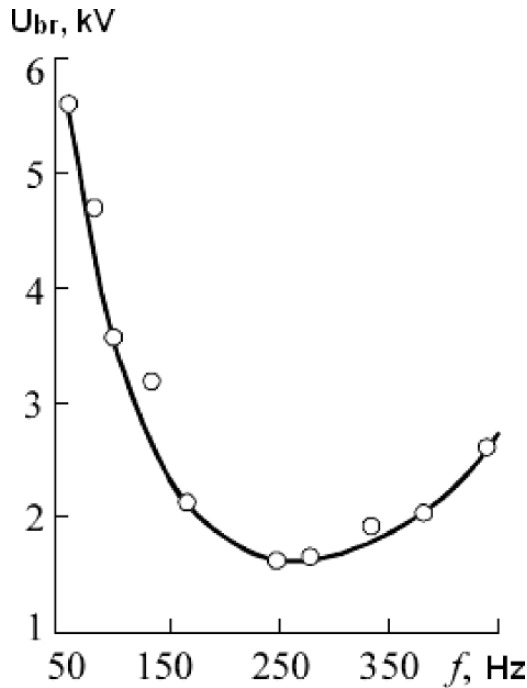
Fig. 6.5. Dependence of U_{br} of perfluorohaxane on the frequency in the tip-plane gap for an inter-electrode distance of 1.9 mm [15]

example, the breakdown voltage of a pure transformer oil in the gap with a uniform field amounts to 27 kV for $d = 0.5$ mm and $f = 50$ Hz, whereas at $f \approx 5 \cdot 10^5$ Hz it is equal only to 19.5 kV (its maximum values are given). Figure 6.6 shows the character of the frequency dependence of U_{br} at high frequencies.

The increase in voltage frequency alters a number of laws describing the electric strength of liquids. At high frequencies, the influence of impurities on E_{br} of liquids is much weaker than at low frequencies.

At positive temperatures, the maximum of $U_{br} = f(T)$ (see Sect. 6.4) shifts toward higher temperatures with increasing frequency. (This somewhat surprising result can be explained by the detailed behavior of the relaxation minimum of the loss angle tangent). With increasing frequency, the pressure exerts less of an influence on the electric strength of liquids, and likewise the degree of liquid degassing has less of an effect on the pressure dependence of the breakdown voltage.

As the repetition rate of microsecond pulses increases from 1 pulse per minute to 30 pulses per second, the electric strengths of a transformer oil and deionized water remain unchanged.
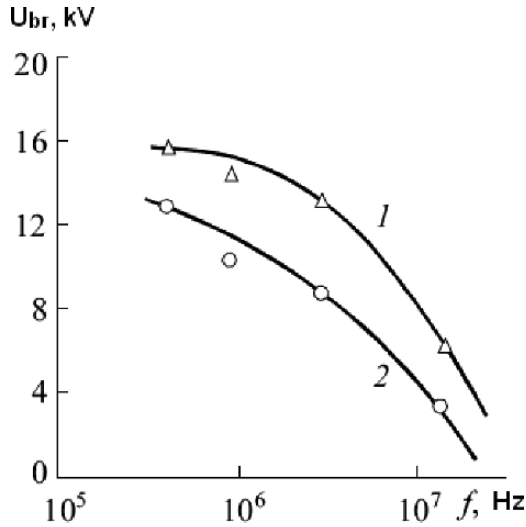
Fig. 6.6. Dependence of U_{br} of xylene (*1*) and a transformer oil (*2*) on the frequency in the gap formed by the spherical electrodes for $d = 1\,\mathrm{mm}$

6.2 Voltage Polarity

The overwhelming majority of studies of the breakdown mechanism and electric strength of liquids has been carried out for positive polarity of the initiating electrode. This is quite naturally explained by the fact that exactly this case corresponds to the minimum electric strength and hence is most dangerous to insulation of high-voltage equipment. This is also the case for the equipment operating at ac voltage, since its breakdown, as a rule, occurs during the positive voltage half-period. Only for interelectrode distances of several tens of microns, the breakdown voltage of the majority of liquids for positive polarity of the tip electrode is higher than for negative one.

Since pre-breakdown phenomena, their intensities, and even their sequence can change significantly when the breakdown conditions change, the quantitative polarity effect will also depend on these conditions. The difference between the breakdown voltages at positive and negative tip-electrode polarities ranges from several percent to several hundred percent. The properties of liquids have a prominent effect on the difference between U_{br}^{+} and U_{br}^{-}. As indicated in Sects. 4.1 and 4.2, the polarity effect is much more evident in liquids with high permittivity. For breakdown of liquids containing electronegative groups or molecules (for example, carbon tetrachloride, benzene chloride, etc.), the polarity effect is essentially nonexistent.

The effect of polarity on the breakdown of various liquids was studied in [16]. Hydrocarbon liquids with linear molecules (hexane, decane, etc.) and hydrocarbons with branched molecules (neopentane etc.), perfluorocarbons (perfluorohexane, perfluoropentane, etc.), and liquefied helium and nitrogen

were investigated. The breakdown voltage was measured under exposure to microsecond pulses with $\tau_{\text{fr}} < 0.1\,\mu\text{s}$ and nanosecond pulses with $\tau_{\text{fr}} < 0.2$ ns. The tip ($r_0 \sim 3\,\mu\text{m}$) - plane and sphere - plane electrode systems were investigated. Figure 6.7 shows the most typical results.

The behavior of curves for hexane and decane is approximately identical and demonstrates that $U_{\text{br}}^+ > U_{\text{br}}^-$ for small interelectrode distances (less than $\sim 400\,\mu\text{m}$ for hexane and $550\,\mu\text{m}$ for decane). For large d, the polarity effect becomes usual, that is, $U_{\text{br}}^+ < U_{\text{br}}^-$. For neopentane (Fig. 6.8), $U_{\text{br}}^+ < U_{\text{br}}^-$ for the entire range of d values. The polarity effect is essentially nonexistent for perfluorohexane and perfluoropentane. The polarity effect in liquefied nitrogen under exposure to microsecond voltage pulses is manifested as in hexane and decane, but is reversed at $d \approx 80\,\mu\text{m}$. Under exposure to nanosecond pulses, $U_{\text{br}}^+ < U_{\text{br}}^-$ even for small d values (to $d \sim 25\,\mu\text{m}$). The polarity effect is abnormal for liquefied helium: $U_{\text{br}}^+ > U_{\text{br}}^-$ for the entire range of d values (Fig. 6.9). This phenomenon was described in publications in the 50s.

The effect of polarity on the breakdown of liquids for long discharge gaps used in high-voltage equipment is illustrated by Table 6.2.

The addition of chlorinated hydrocarbons (the molecules of which possess considerable electron affinity) to transformer oil, whose breakdown is accompanied by a sizable polarity effect (Table 6.2), eliminates almost completely the polarity effect.
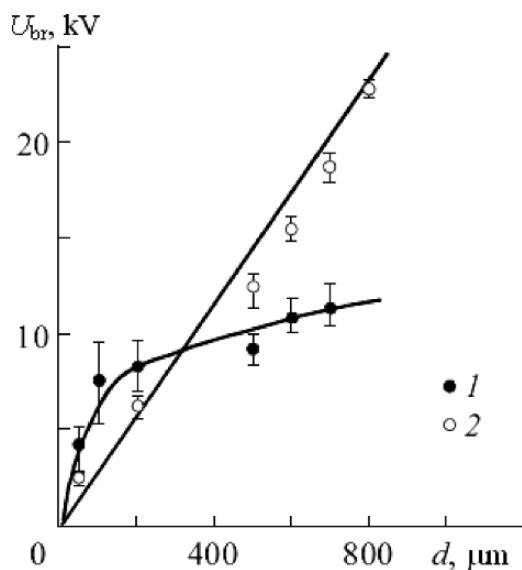
Fig. 6.7. Dependence of the breakdown voltage of hexane on the distance between the tip-plane electrodes for positive (*1*) and negative (*2*) polarities of the tip electrode, $r_0 = 3\,\mu\text{m}$, and $\tau_{\text{p}} = 6\,\mu\text{s}$ [16]
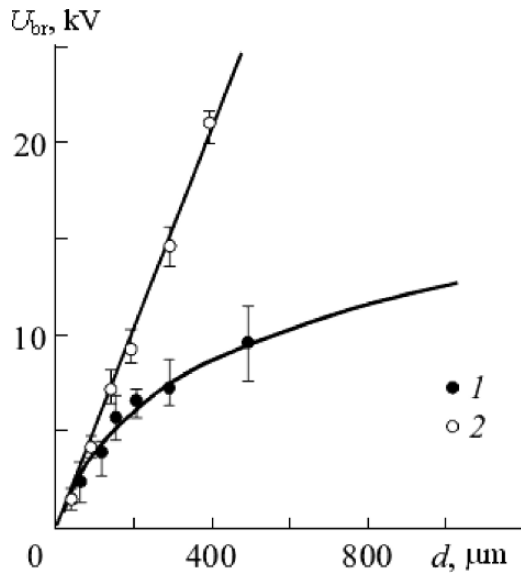
Fig. 6.8. The same as in Fig. 6.7, but for neopentane

In most studies on liquid breakdown, the polarity effect is explained similar to the analogous effect on breakdown of gases by different conditions of accumulation and influence of the space charge near the cathode and anode and hence near the head of the positive and negative discharge channels.

Based on an analysis of the field distribution near the tip electrode, it is demonstrated that under assumption of unipolar injection, the distortion
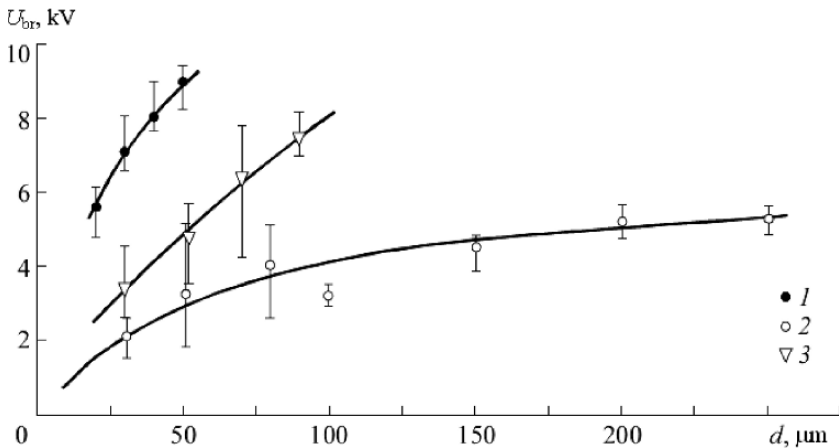
Fig. 6.9. The same as in Fig. 6.7, but for liquefied helium. *Curve 3* is for the sphere-plane discharge gap (a quasi-uniform field)

Table 6.2. Effect of polarity on breakdown initiated in various liquids for a tip-plane electrode system at $T = 293\,\mathrm{K}$

Liquid	Voltage	Negative polarity		Positive polarity	
		d, mm	U_{br}, kV	d, mm	U_{br}, kV
Toluene	$0.9/40\,\mu\mathrm{s}$	3	42.3	3	21.8
n-octane	$0.9/40\,\mu\mathrm{s}$	3	49.8	3	18.4
Chlorobenzene	$0.9/40\,\mu\mathrm{s}$	3	27.3	3	25.5
Carbon tetra-chloride	$0.9/40\,\mu\mathrm{s}$	3	21.8	3	21
Transformer oil	$1.5/40\,\mu\mathrm{s}$ dc voltage	12.7	86	25.4	60
		9.6	100	9.6	42
Dodecylbenzene	$1.5/40\,\mu\mathrm{s}$ dc voltage	12.7	175	25.4	122
		9.6	110	9.6	62

of the electrostatic field is proportional to the mobility of charge carriers injected from the tip. In many liquids the mobility of negative charge carriers is approximately 100 times higher than of positive ones. This is in agreement with the reduction (or even elimination) of the polarity effect when additives (electron acceptors promoting capture of injected electrons with the formation of ions possessing low mobility) are incorporated into the liquid.

The polarity effect in liquid dielectrics depends on the degree of electric field nonuniformity. For example, in transformer oil in highly nonuniform fields with nonuniformity coefficient $\mu > 25$–30, the pulsed breakdown voltage for negative polarity is 1.4–1.7 times U_{br} for positive polarity, while for $K < 16 U_{\mathrm{br}}^{+}$ it can even slightly exceed U_{br}^{-}.

Differences not only in U_{br} values but also in space-time laws of the discharge propagation from anode and cathode (see Chaps. 3, 4, and 7) allow a conclusion to be drawn on radical differences in their propagation mechanisms.

6.3 External Pressure

An increase in the hydrostatic pressure above a liquid to 150–200 atm, achievable in experiments on liquid breakdown and in high-voltage equipment and devices with liquid insulation, does not change the properties of liquids themselves owing to their virtual noncompressibility. Therefore, an increase in the electric strength of liquids with pressure, manifested to a certain extent depending on experimental conditions, should be attributed to the influence of three factors:

– presence of gas on the electrodes and in the liquid before field application,
– formation of gas (mainly on the electrodes) with voltage application due to boiling up, electrolysis, etc.,
– gas nature of the discharge channel in the liquid.

An increase in the pressure can change the conditions of gas formation, the equilibrium point between the molecular-dissolved gas and gas in the form of bubbles and affect the processes in the discharge channel that determine its electrophysical characteristics and primarily the longitudinal gradients of the potential. These gradients result in a dependence (though a weaker one) of the electric strength of liquids on pressure, even under conditions of electric (ionization) breakdown mechanism. Investigations of the space-time characteristics of the discharge in liquids with various properties attendant to changes of experimental conditions over a wide range [17–22] demonstrated that with increase in pressure:

– the discharge ignition voltage, that is, the occurrence of the first registered changes in the liquid, increases,
– discharge channel diameter decreases in all stages of discharge propagation (initial and leader channels),
– amplitudes of current pulses and luminescence, which accompany the discharge propagation, decrease,
– in gaps with a quasi-uniform field, the probability of transition from the discharge from cathode (the bubble breakdown mechanism) to the discharge from anode (the ionization breakdown mechanism) increases, see Chap. 7,
– slow discharge channels that propagate by the bubble mechanism are most sensitive to the pressure increase.

The effect of pressure on the electric strength of liquid dielectrics depends on the voltage duration, degree of liquid degassing, electrical conductivity, and electrode system configuration. For long-term applied voltage, the probability of gas formation due to thermal and electric processes increases. Newly formed gas bubbles in the liquid and on the electrode surface and gas bubbles existing before the voltage application are deformed by the field and leave the electrodes. Moving in the interelectrode gap, they form gas bridges initiating breakdown at low field strengths. In this case, the pressure dependence of the electric strength is linear or even power-law. After careful liquid degassing under laboratory conditions and with negligible volumes of liquid, the influence of pressure on E_{br} sharply decreases, because than only the gas produced under applied voltage on electrodes, in liquid volume, and in discharge channels affects it (Fig. 6.10) [23]. For polar and conducting liquids, this dependence is actively maintained, because in such liquids gases are actively produced as a result of conduction currents and dielectric losses (for ac voltage and high-frequency voltage pulses).

For voltage pulses, the dependence $E_{br} = f(p)$ saturates (Fig. 6.11) [24]. At pressures from 0.1 to 1.2 MPa, the p dependence of U_{br} for nanosecond pulses in water is

$$U_{br}(p) = U_{br}(p_0(p_0)(p - p_0)^n),$$
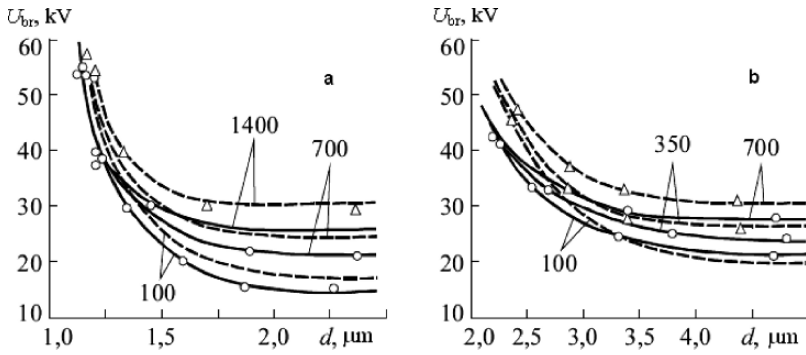
Fig. 6.10. Voltage-time characteristics of the $+$T$-$P (**a**) and $-$T$+$P gaps (**b**) in degassed (*dashed curves*) and nondegassed a transformer oil (*solid curves*) at hydrostatic pressure (*in Pa*) indicated by the figures adjacent to the curves. The interelectrode distance was 3 mm [23]

where $U_{br}(p_0)$ is the breakdown voltage at atmospheric pressure ($p_0 = 0.1$ MPa), and the exponent n depends on the pulse parameters. For a $1/100$-ns quasi-rectangular pulse, $n = 0.15$.

For a given pulse width, the effect of p on E_{br} is much stronger for a uniform field than for a nonuniform field (Figs. 6.11 and 6.12). An increase
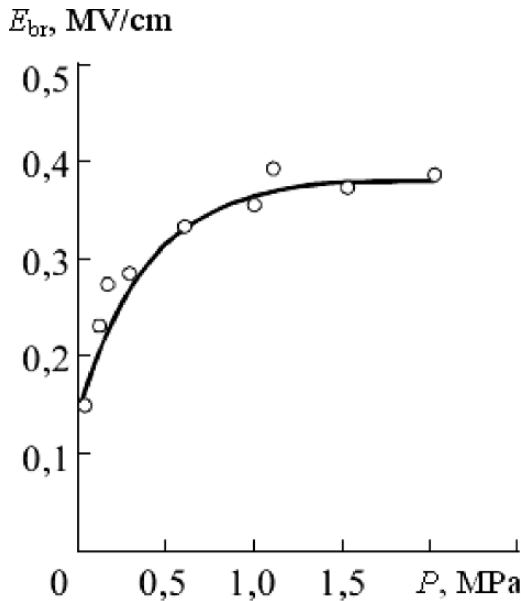
Fig. 6.11. Dependence of the electric strength of water ($\rho = 2 \cdot 10^6$ $\Omega\cdot$cm) on the pressure in a uniform field at $d = 0.8$–1.2 cm and $\tau_p = 0.2\,\mu$s [24]
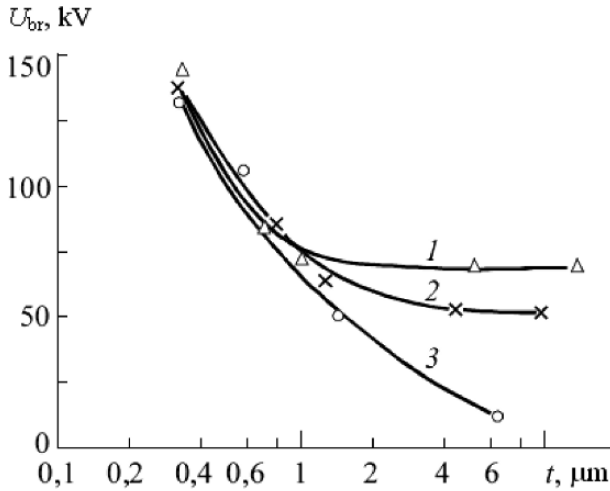
Fig. 6.12. Voltage-time characteristics of water ($\gamma = 1.67 \cdot 10^{-4}\,\Omega^{-1} \cdot cm^{-1}$) in the field of +T−P electrodes versus pressures and temperatures. Here *curve 1* is for $T = 200°C$ and $P = 50\,kg/cm^2$, *curve 2* is for $T = 200°C$ and atmospheric pressure, and *curve 3* is for $T = 1000°C$ and atmospheric pressure [71]

in the pressure above water to $150\,kg/cm^2$ for a nonuniform field causes the breakdown voltage to increase by 40–50% (Fig. 6.12), whereas for a uniform field, the breakdown voltage doubles (Fig. 6.11).

This can be explained by the fact that the breakdown field strength in a uniform field is largely determined by the breakdown initiation and evolution near the electrodes. Gas accumulated at the electrodes and subject to pressure has a major effect on breakdown initiation.

It is desirable to raise the hydrostatic pressure to increase the working gradient of insulation of high-voltage systems in the following cases: a) for liquids with high electrical conductivity, b) for large electrode areas, and c) for long voltage pulses ($>$0.5–1 μs).

6.4 Temperature

Under the breakdown conditions providing the greatest probability of the ionization liquid breakdown mechanism (short-term voltage exposure and high degree of clearing and degassing), the electric strength slowly decreases as the temperature increases from $273\,K$ to the temperature near the boiling point of the given liquid (curve *2* in Fig. 6.13) [25]. Moreover, the decrease in the voltage exposure weakens the influence of T on E_{br}. Good qualitative agreement of curves illustrating the dependence $E_{br} = f(T)$ and the density as a function of the temperature demonstrates that in this case, the main effect of T is due to the temperature-dependent density.
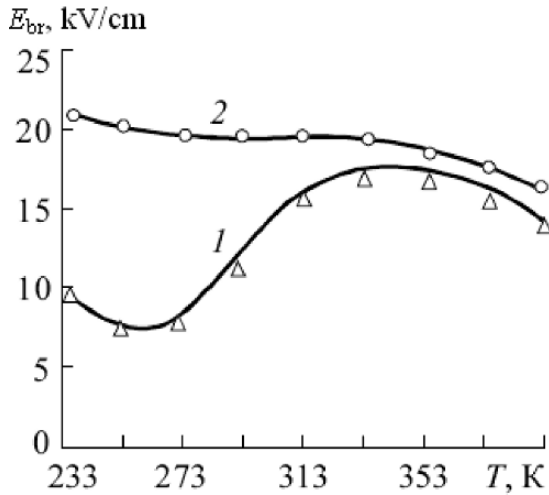
Fig. 6.13. Temperature dependence of the strength of a transformer oil under operating conditions (*1*) and dehumidified a transformer oil in a standard punch (*2*) [25]

For commercially pure liquids containing impurities of different types and long-term voltage exposure (regions *II* and *III* in the voltage-time characteristics, see Fig. 6.3), the temperature dependence of their electric strength is primarily due to the temperature dependence of moisture and gas content and their redistribution between the emulsified and molecular dissolved states. In addition, the thermal decomposition of liquids and changes in their viscosity, surface tension, density, and hence the rate of electroconvective processes and electrohydrodynamic flows must be taken into account. The rate of liquid flow influences the electric strength of the liquid, increasing it at the expense of breaking of bridges formed by impurity particles, liquid drops, and gas bubbles. However, the increase of the rate of liquid flow can also reduce the electric strength when bubbles are carried into the region of large E by this flow.

Bubbles will grow with increasing temperature and decreasing viscosity at the given energy, and the pressure inside them will decrease, thereby reducing their E_{br}. Large bubbles have high probability of being elongated along the electric field lines or coalescing with others bubbles. Bubbles $50\,\mu m$ in diameter or even larger with internal pressures up to $0.4\,MPa$ are typical of oil.

A great number of factors influence the temperature dependence of breakdown processes, resulting in a complex temperature dependence of the electric strength of actual liquid insulation (curve *1* in Fig. 6.13) [25]. When cold transformer oil is not in contact with ambient air, its electric strength has no local minimum at temperatures $\sim 273\,K$. For less pure liquids, the difference in E_{br} at $T \approx 273\,K$ and $535\,K$ can reach 200%. Qualitative behavior of the dependence $E_{br} = f(T)$ is maintained not only for liquids with different degrees of clearing, but also for composite insulation. For this insulation type

the influence of temperature on the electric strength also depends on the rate of gas release during decomposition of solid dielectric and moisture liberation, on the amount of moisture and gas the solid dielectric can absorb, and on the charge transfer mechanism in the composite insulation.

6.5 Chemical Nature and Composition of Liquids

The effect of liquid properties on space and time characteristics of the discharge in a liquid was considered in ample detail in Sects. 4.1 and 4.2. This section presents the dependences of the quantitative characteristics (E_{br} and U_{br}) on the properties and structure of liquids. In most cases, the reasons for these dependences become clear if we address the materials of previous sections of this book. In turn, these dependences provide additional information useful for understanding of the model of breakdown mechanisms.

The establishment of a relation between the liquid electric strength and the atomic-molecular structure would allow one to predict the dielectric properties of liquids from the known physical and chemical constants and to seek for and to synthesize the liquid insulation as well as to use additives improving the dielectric properties of liquids. However, no reliable relations have been derived by the present time because of the influence of impurities of different types that are always present in the liquid, a great variety of processes that affect the liquid breakdown, and the lack of a well-developed theory of the liquid phase of matter. Under pulsed voltages, the effect of impurity on the breakdown decreases due to inertia of the secondary processes, but the results obtained allow one to establish only tendencies of changes of the electric strength for liquids distinguished by those or other physical and chemical properties.

6.5.1 Chemical Nature of Liquids

Since the basic types of liquid insulation used in high-voltage engineering are mineral oils comprising paraffin, naphthene, and methane hydrocarbons in various proportions depending on their group, it is of interest to study a dependence of the electric strength on the molecular constants. In addition, these liquids are convenient objects for investigation, since some particular molecular constants can be changed by choosing liquids of the same series with other parameters remaining unchanged. An analysis of this problem [2] shows that for dc and ac voltage and microsecond voltage pulses, the influence of liquid properties (in particular, their density) on the electric strength is masked by a stronger influence of impurities and electrode state. For this reason, this influence was detected in some studies but not in others. For liquid paraffin hydrocarbons with a modest amount of clearing, a linear dependence of the discharge time (for $E = \text{const}$) on the density and other physicochemical parameters determining the intermolecular bond forces was established in [2] using nanosecond pulses and long discharge gaps, whereupon the role

of secondary effects engendered by impurities and electrode state decreased significantly. However, this dependence was only a special case, because it was detected only for normal hydrocarbons of the paraffin series. The density cannot be the key parameter governing the electric strength of hydrocarbons, because isomers possessing higher density possess lower electric strength than normal hydrocarbons. At the same time, electric strength of normal hydrocarbons and their isomers is directly proportional to the length of molecular chains. This dependence can be satisfactorily explained by the bubble and ionization mechanisms of liquid breakdown.

In [26] it was vividly demonstrated that rather inconsistent data on the influence of properties and structure of liquids on their electric strength were mostly due to difficulties in considering the influence of the electrode surface state.

Since in tests of liquids the electrode systems creating a uniform electric field are used, the situation is complicated simultaneously by two circumstances, namely, the electrodes have large surfaces difficult to monitor, and the discharge ignition time lag in a uniform field makes the most part of the total discharge time that depends primarily on the processes on the electrodes. A comparison of the measured electric strength of various liquids under conditions of self-breakdown (that is, typical ones) and laser-induced breakdown have shown that the series of liquids arranged in decreasing (or increasing) order of the electric strength differ radically for these breakdown types.

6.5.2 Electrical Conduction and Permittivity

Under long-term voltage exposure, the *electrical conductivity* of liquids affects significantly their electric strength. An increase in γ reduces the electric field strength necessary for the implementation of the electrothermal breakdown mechanism.

A study of the γ effect on the liquid electric strength is important for the determination of the applicability limits of various liquid breakdown mechanisms and estimation of the applicability of liquids with increased electrical conductivity for insulation of high-voltage pulsed systems.

For dielectric liquids whose chemical composition differ significantly, the discharge characteristics (the breakdown voltage, velocity of discharge propagation, etc.) are uncorrelated with the electrical conductivity when exposed to voltage pulses lasting tens of microseconds or less (Table 6.3).

(The data tabulated in Table 6.3 were obtained for the breakdown initiated in the $+T -P$ and $-T +P$ electrode systems with a 1.2/70-μs pulse for $t_d = 30\,\mu$s and $d = 5\,$cm). This result can be explained by the fact that conditions of pre-discharge gas formation are violated for the given γ and t values. For large γ and t, when the gas formation in the liquid during the pre-discharge period is quite probable, a γ dependence of the discharge characteristic is expected. The literature data on the γ influence on the electric

Table 6.3.

Liquids	Benzene alcohol	Distilled water	Ethanol	Glycerin	Transformer oil
$\gamma, \Omega^{-1}\,\mathrm{cm}^{-1}$	$1.8 \cdot 10^{-6}$	$4.3 \cdot 10^{-6}$	$1.5 \cdot 10^{-7}$	$6.4 \cdot 10^{-8}$	$1 \cdot 10^{-14}$
v_l^+, cm/s	$2 \cdot 10^5$	$1.4 \cdot 10^6$	$2.5 \cdot 10^5$	$8 \cdot 10^5$	$1.3 \cdot 10^5$
v_l^-, cm/s	$1.7 \cdot 10^5$	$6 \cdot 10^4$	$2 \cdot 10^5$	$3.3 \cdot 10^5$	$1 \cdot 10^5$

strength of liquids with increased conductivity (typically aqueous electrolytes) are contradictory [27, 28].

We established that these contradictions are mainly due to two reasons [30]. The first reason is a complex character of the E_{br} (or U_{br}) dependence on γ (it also depends on the field geometry and pulse polarity). The second reason is that the dependence of the electric strength of electrolytes on their electrical conductivity is determined not so much by the physical processes that occur in the discharge gap as by the pulse deformation (that depends on γ, the parameters Z_{w} and C of the discharge circuit, and the resistance of the examined object) due to the voltage drop in the discharge circuit because of high conduction currents running through the circuit. This statement is well illustrated by the results presented in [29]. In this regard, the incorrectness of experiments on breakdown of electrolytes in which significant deformation of the voltage pulse is not eliminated is obvious.

The use of voltage pulse generators with small Z_{w} in experiments allowed Ushakov et al. [30] to investigate a discharge gap with an electrolyte for a virtually undeformed rectangular pulse with $\tau_{\mathrm{p}} = 240\,\mathrm{ns}$ and $\tau_{\mathrm{fr}} = 7 - 10\,\mathrm{ns}$ and an oblique pulse with $\tau_{\mathrm{fr}} = 0.5 - 50\,\mu\mathrm{s}$.

Figure 6.14 shows the dependences of E_{br} and U_{br} of aqueous NaCl solution on γ for the nanosecond breakdown in a uniform (Fig. 6.14a) and nonuniform fields of the tip-plane electrodes (Fig. 6.14b). In the uniform field, the dependence $E = f(\gamma)$ has a well defined maximum at $\gamma \approx 10^{-3}\,\Omega^{-1}\cdot\mathrm{cm}^{-1}$ [2,30]. For the $-\mathrm{T} +\mathrm{P}$ gap, the dependence is described by the equation $U_{\mathrm{br}} = A + B \cdot \log \frac{1}{\gamma}$ presented in [31]. For positive tip polarity (curve 2 in Fig. 6.14b), U_{br} decreases as γ decreases from $10^{-2}\,\Omega^{-1} \cdot \mathrm{cm}^{-1}$ to $10^{-4}\,\Omega^{-1} \cdot \mathrm{cm}^{-1}$.

Analogous results were obtained for oblique pulses, but the maximum of the dependence $E_{\mathrm{br}} = f(\gamma)$ was observed at $\gamma = (3\text{--}5) \cdot 10^{-5}\,\Omega^{-1} \cdot \mathrm{cm}^{-1}$ (Fig. 6.15). The data for a highly nonuniform field ($d = 0.25\,\mathrm{cm}$), both polarities, and two slopes of the pulse front are given in Table 6.4.

The presence of the maximum in the dependence $E_{\mathrm{br}} = f(\gamma)$ in gaps with a quasi-uniform field and reverse dependences $U_{\mathrm{br}} = f(\gamma)$ for the $+\mathrm{T}$ $-\mathrm{P}$ and $-\mathrm{T} +\mathrm{P}$ electrode systems is in good agreement with the competitive coexistence of three discharge types described in Sect. 3.4. It seems likely that the ascending branch of the curve $E_{\mathrm{br}} = f(\gamma)$ in a uniform field corresponds to the discharge from anode, and the descending branch is for the discharge
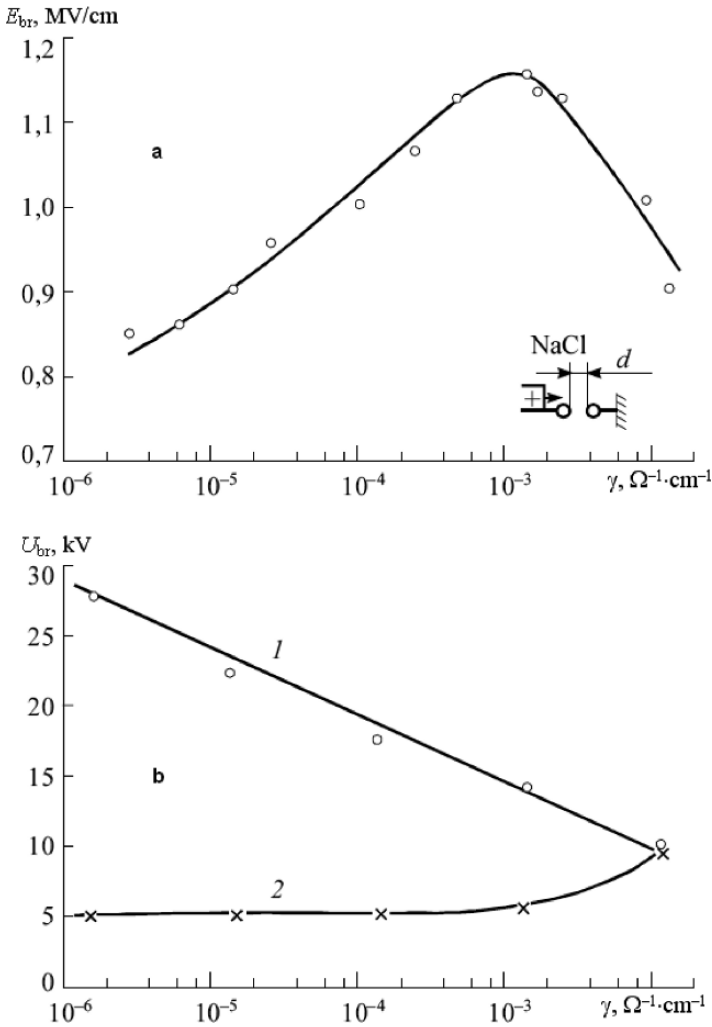
Fig. 6.14. Dependence of the electric strength of the NaCl aqueous solution on the electrical conduction in a uniform field at $t_d = 70$ ns and $d = 0.02$ cm (**a**) and in a non-uniform field at $t_d = 90$ ns and $d = 0.015$ cm for $-T + P$ (*curve 1*) and $+T - P$ electrodes (*curve 2*) [2, 30]

from cathode. (Optical observations of the discharge phenomena for the entire range of γ values were not carried out in [30]).

These results demonstrate that contrary to widespread belief, reducing the electrical conductivity of water by very careful clearing is an inefficient way to increase its electric strength for voltage pulses. The optimal value of γ for water must be selected taking into account the allowable resistance of
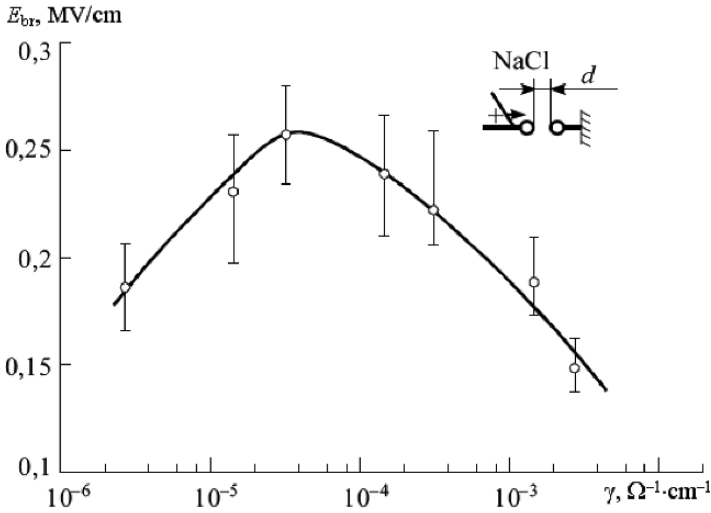
Fig. 6.15. The same as in Fig. 6.14a, but for $A = 1.47\,\text{kV}/\mu\text{s}$ and $d = 0.25\,\text{cm}$ [85]

a specific system with water insulation and the total cost of preparing and maintaining water with low γ.

For aqueous salt solutions, the dependence of their electric strength on the cation charge was also observed for nanosecond voltage exposures (40–220 ns). Salt solutions with smaller cation charges have greater electric strengths. No prominent dependence of E_{br} on the anion parameters was detected in experiments with salt solutions having identical cations, but different anions.

Liquids possessing high intrinsic conductivity, as a rule, have high permittivity ε. For long-term voltage exposure, high ε and hence high γ make gas formation easier due to effervescence and electrolysis, that is, they lead to the bubble breakdown mechanism with typically lower E_{br}. As demonstrated in [2], the elevated value of ε facilitates breakdown evolution and reduces E_{br} for purely ionization liquid breakdown. This dependence was first established experimentally in [32] for a set of liquids comprising xylene,

Table 6.4.

$\gamma, \Omega^{-1} \cdot \text{cm}^{-1}$	Tip polarity	$E_{\text{av br}}, \text{kV/cm}$	
		$A = 10\,\text{kV/cm}$	$A = 1\,\text{kV/cm}$
10^{-3}	$+$	200	130
	$-$	–	–
10^{-4}	$+$	108.5	76.5
	$-$	334	110
$7 \cdot 10^{-6}$	$+$	106	75
	$-$	676	304

toluene, transformer oil, threecresylphosphate, hitrobenzene, and glycerin. The strongest influence of ε on E_{br} was observed under long-term voltage exposure. More recently, the dependence of E_{br} (kV/cm) on ε in the form

$$E_{\mathrm{br}} = -0.0588\varepsilon + 3.026$$

was established in [33] based on test results for 22 well-purified liquids with ε in the range 1.88–15.06 for ac and dc voltages.

For gaps with highly nonuniform field (+T −P) and 1.2/70-μs pulses, the dependence of the average breakdown electric field strength ($E_{\mathrm{av.br}} = U_{\mathrm{br}}/d$), in kV/cm, on ε is [2]

$$\log E_{\mathrm{av.br}} = -0.092\varepsilon + 4.67.$$

For negative tip polarity, this dependence is complicated (it is described by a U-shaped curve).

With decreasing voltage duration, the difference between the electric strengths of polar and nonpolar liquids decreases, and for $t < 10^{-7}$ s, no well-defined ε-dependence of E_{br} is observed. For nanosecond voltage exposure, liquids whose physicochemical properties differ significantly have nearly the same strength. A consequence of the above discussion important for the design of high-voltage nanosecond pulsed systems is the fact that the electric strength of liquids cannot be the main criterion for choosing insulation of such devices. Depending on specific conditions, the choice is determined by electrical conductivity, permittivity, stability in an electric field and when exposed to a spark, nontoxicity, low cost, etc.

6.5.3 Soluble Additives

The working mechanism of various additives injected into liquid dielectrics to increase their electric strength is primary associated with the two effects: a) a decrease in the field nonuniformity in the insulation gap due to a local increase in the electrical conductivity, or to polarization processes at the interface between the solid and liquid phases (when solid particles are introduced into a liquid) and b) the effect of additives on the behavior of charge carriers produced by emission and ionization.

To reduce the influence on liquid dielectric breakdown of electrode microgeometry and processes adjacent to electrodes, it has been suggested [34] that surface conducting layers be created whose electrical conductivity decreases smoothly with depth, and whose effective thickness is significantly greater than the size of microinhomogeneities, but less than the interelectrode distance. The characteristic time required to displace the electric field from regions adjacent to the electrodes is approximately $\tau \approx \varepsilon/4\pi\gamma_0$, where γ_0 is the electrical conductivity of conducting layers of the liquid. To a first approximation [35], the temporal behavior of the electric field adjacent to the electrode surface (in the presence of a shielding layer) is given by

$$E_0(t) \approx \frac{U_0}{d} \frac{1}{\tau \left(\dfrac{4\pi\gamma_0}{\varepsilon} - \dfrac{1}{\tau_{\mathrm{rise}}} \right)} \left[\exp\left(-\frac{t}{\tau} \right) - \exp\left(\frac{4\pi\gamma_0}{\varepsilon} t \right) \right],$$

where U_0 is the voltage pulse amplitude, d is the interelectrode distance, τ_{rise} is the characteristic voltage rise time, and γ_0 is the electrical conductivity of the layer adjacent to the electrode surface.

If the voltage duration exceeds τ, the electric strength of the insulation gap is expected to increase due to the diminished effect of the near-electrode processes that initiate breakdown.

The electric strength of purified water ($\rho \approx 10^7\,\Omega \cdot \mathrm{cm}$) in which electrodes (such as Rogowski electrodes with plane parts $\sim 1\,\mathrm{cm}$ in diameter) are shielded by conducting layers has been investigated experimentally in [35]. Solid and porous (pore size $\sim 5\,\mu\mathrm{m}$) electrodes were used. The interelectrode distance ranged from 2.5 to 3 mm. The voltage pulse front varied over the range 0.1–1 μs and amplitude over the range ($U_0 = 60$–300 kV). Diffuse subsurface layers were formed by slow extrusion of conductive solutions through the porous electrodes. To prevent convective flows at the interface between media of differing density, an aqueous solution of $CuSO_4$ with density slightly exceeding that of water was incorporated into the lower electrode, while a solution of $FeCl_5$ in ethanol with density slightly less than that of water was incorporated into the upper electrode. The layer thickness was 0.3–0.4 mm. After each breakdown, the interelectrode gap was purged and the conductive layers were prepared.

Figure 6.16 shows the behavior of breakdown field strength of water. For unshielded electrodes, E_{br} was defined to be U_{br}/d, where d is the interelectrode distance. For shielded electrodes, $E_{\mathrm{br}} = U_{\mathrm{br}}/d_{\mathrm{eff}}$. Here $d_{\mathrm{eff}} = d - \Delta d$, where Δd is the thickness of the conducting layer (layers), and d_{eff} was determined by measuring the refractive index using the Toepler method with a cylindrical lens. In addition, E_{br} was determined using the Kerr effect technique as the electric field of water outside of the conducting layers. From Fig. 6.16 it follows that shielding of both electrodes quadruples the electric strength. In this case, the discharge channel is initiated at the external boundary of the conducting layer rather than near the electrode surface. The electric strength is doubled when only the anode is shielded and the pulse width is at least 3–4 μs (curve *2* in Fig. 6.16). In this case, the discharge is initiated at the cathode rather than the anode. When only the cathode is shielded, no effect is observed. The discharge is initiated at the anode, and the electric strength of the gap is the same as for conventional metal electrodes.

A novel method for increasing the pulsed electric strength of water by adding dipolar amino acid ions (zwitter ions) is described in [36]. The influence of glycine and β-alanine additives was studied in most detail when their concentration lay in the range 0.01–0.1 mol/L. The amino acids were injected into deionized water under sterile conditions and without contact with the atmosphere.
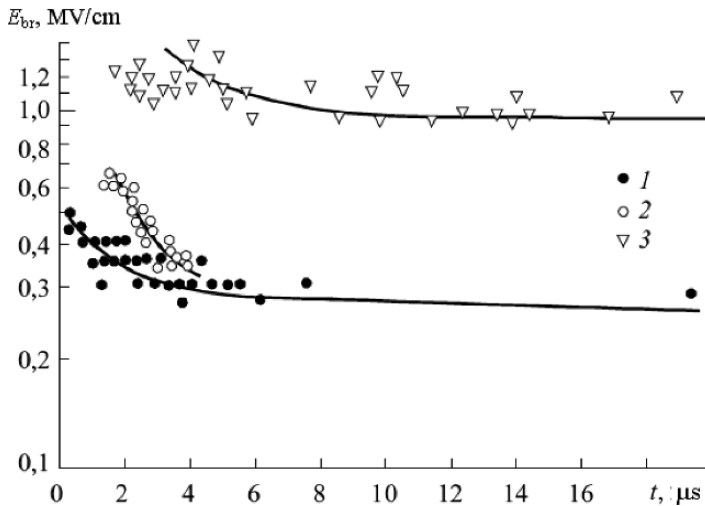
Fig. 6.16. Dependence of E_{br} of water on t for unshielded electrode and shielded cathode (*1*) or shielded anode (*2*) and for both shielded electrodes (*3*) [34]

Figure 6.17a shows the behavior of the normalized electric strength E/E_0 of water with β-alanine as a function of the additive concentration (E and E_0 denote the 50% breakdown strength of water with and without amino acid additives). The data were obtained for a high-voltage oblique-front pulse width of $5\,\mu s$, a distance between the plane electrodes of $1\,cm$, and areas of the stainless ferrite steel and aluminum electrodes of 30, 110, and $150\,cm^2$. From Fig. 6.17a it can be seen that E/E_0 is a complex function of amino acid concentration, with details determined by the electrode material. For the stainless ferrite steel electrodes, $E/E_0 = f(c)$ has a maximum at $c = 0.03\,mol/L$ equal to $E/E_0 = 1.33$. For $c \geq 0.06\,mol/L$, the electric strength of water with the additive is the same as that of pure water. For the system with austenitic steel electrodes, $E/E_0 = f(c)$ has two maxima at $c_1 = 0.03\,mol/L$ ($E/E_0 = 1.48$) and $c_2 = 0.055\,mol/L$ ($E/E_0 = 1.41$). For aluminum electrodes, the injection of amino acids into water reduces its electric strength over the entire range of concentrations examined.

An increase in the electric strength of water containing additives is accompanied by a decrease in the standard deviation of the breakdown field strength. Minimum values of σ correspond to maximal values of E_{br} (Fig. 6.17b). Tests with shorter high-voltage pulses ($\tau_p = 1.5\,\mu s$) and austenitic electrodes yield results qualitatively similar to those in Fig. 6.17. The only difference is that the minimum of $E/E_0 = f(c)$ shifts toward higher concentrations of the additives, and its amplitude increases to $E/E_0 = 1.38$. In this case, the maximum field strengths are also higher. For example, the normalized electric field strength is $E/E_0 = 1.52$ at concentration $c = 0.04\,mol/L$. Analogous results are obtained
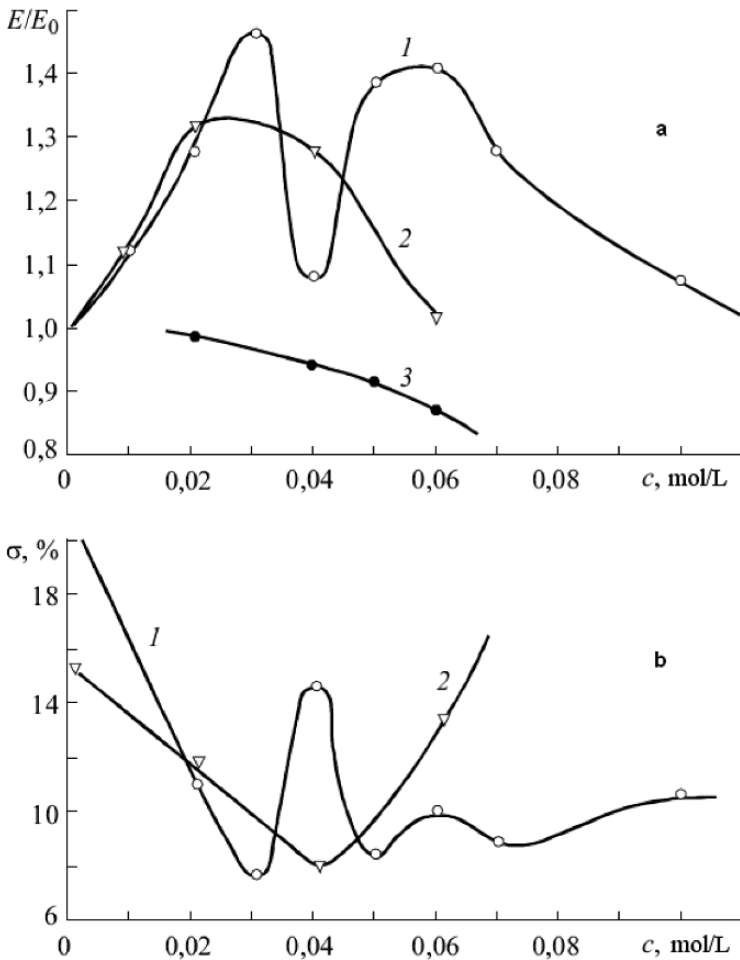
Fig. 6.17. Dependences of the relative electric field strength (**a**) and standard deviation of the water breakdown field strength (**b**) as function of the β-alanine concentration for electrodes from austenite (*curve 1*) and ferrite stainless steel (*curve 2*) and aluminum electrodes (*curve 3*) [36]

with titanium electrodes in this series of experiments. For electrodes manufactured from these materials, E/E_0 approaches unity for $c \geq 0.1$ mol/L.

It should be emphasized that the positive effect of the amino acid decreases with decreasing degree of water purification (with increasing γ). Thus, $E/E_0 = 1.26$ for $\gamma = 10^{-4} \Omega^{-1} \cdot m^{-1}$, while E/E_0 increases to 1.5 for $\gamma = 2 \cdot 10^{-5} \Omega^{-1} \cdot m^{-1}$.

The optimal choice of amino acid concentration and electrode material makes it possible to increase the operating field strength due to the 30–50% increase in E_{br} and its reduction in standard deviation by a factor of 2–3.

Komin et al. [36] suggest that because amino acids are surface-active substances, their presence in water significantly alters electric double layers at the electrode surface and the conditions of discharge initiation (see Chap. 1).

In [36] and more recent publications by the same authors, other materials besides amino acids were used as additives, including SF_6 dissolved in purified and degassed water at an excess pressure of 3 MPa, chloroform, and water-soluble polymers with strong structurization properties (polyacrylamide, polyvinyl alcohol, and polysaccaride).

It was established that SF_6 does not change the pulsed electric strength of water in a uniform field, but chloroform reduces it many folds. Both materials accept electrons, and their reaction rate with hydrated electrons is three orders of magnitude greater than that of amino acids.

Experiments with water-soluble polymers were conducted for an electrode system with a nonuniform field ($k_n = 3$), $d = 5$ mm, and test pulse width $\tau_p = 2.5\,\mu s$. Figure 6.18 shows the experimental results. The electric strength of the gap with the tip anode increases when polymers are added to water. For high concentration c, the electric strength of the gap becomes greater than for negative polarity.

Investigations performed in [37] were aimed at searching for mixtures of water with other liquids having good electrical characteristics and freezing temperature less than that of water. After a preliminary search, a mixture of water with ethylene glycile was chosen. For an ethylene glycol/waters ratio of 60/40, the freezing temperature of the mixture was 222 K. Figures 6.19 and
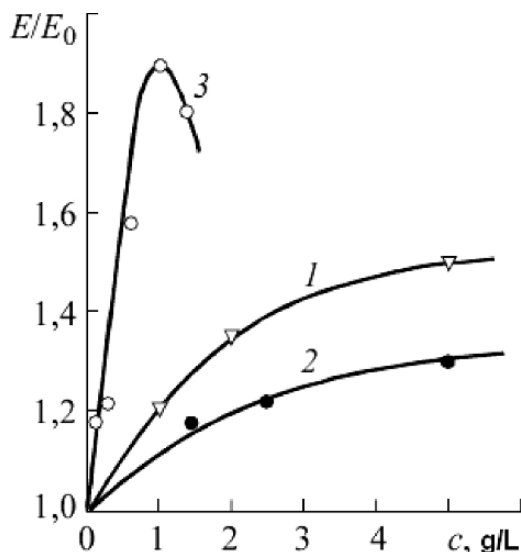
Fig. 6.18. Dependence of E/E_0 on the polymer concentration for polyvinyl alcohol (*curve 1*), polysaccharide (*curve 2*), and polyacrylamide (*curve 3*) [36]
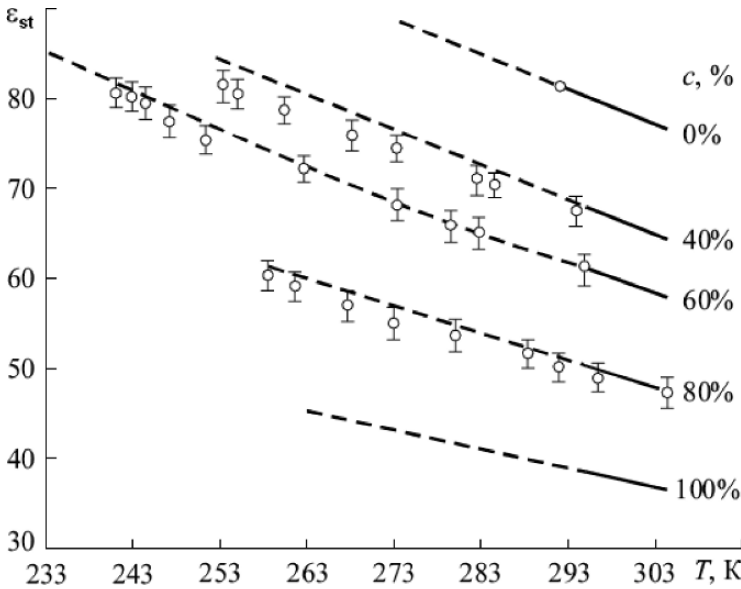
Fig. 6.19. Temperature dependences of the static permittivity of the mixture of ethylene glycol with water for the indicated mass contents c of ethylene glycol in water [37]

6.20 show the static permittivity ε_S and the Debye relaxation time τ_D. Each value of ε_S was averaged over measurements at 15 frequencies in the range 0.5–108 MHz. These values differed at most by 1%, that is, their difference was within the range of the measurement errors. The behavior of ε_S over the examined frequency range is described by the Debye model. The temperature dependence of ε_S of the mixture down to the freezing temperature can be described by the Akerlof empirical equation:

$$\varepsilon_S\,(T,c) = a\,(c)\exp\left[-b(c)T\right]\ ,\tag{6.7}$$

where T is the temperature, c is the mass content of ethylene glycol in the mixture, and $a(c)$ and $b(c)$ are constants tabulated for different c.

The values of τ_D shown in Fig. 6.20 were averaged over seven measurements taken at 50–108 MHz. They were in the range $\tau_D = 0.19$–0.30 ns, much less than the actual charging voltage pulse width.

Figure 6.21 shows the measured values of the mixture time constant τ_M. It can be seen that τ_M increases as the ethylene glycol concentration in water increases and the temperature of the solution decreases.

Of practical importance is the deformation of a charging voltage pulse due to energy dissipation in the insulation gap. It was found that the pulse decay time τ_{dec} correlates only weakly with τ_M. At standard temperature, τ_{dec} decreases with increasing temperature and field strength. This effect results from injection of the charge from the cathode and its flow toward
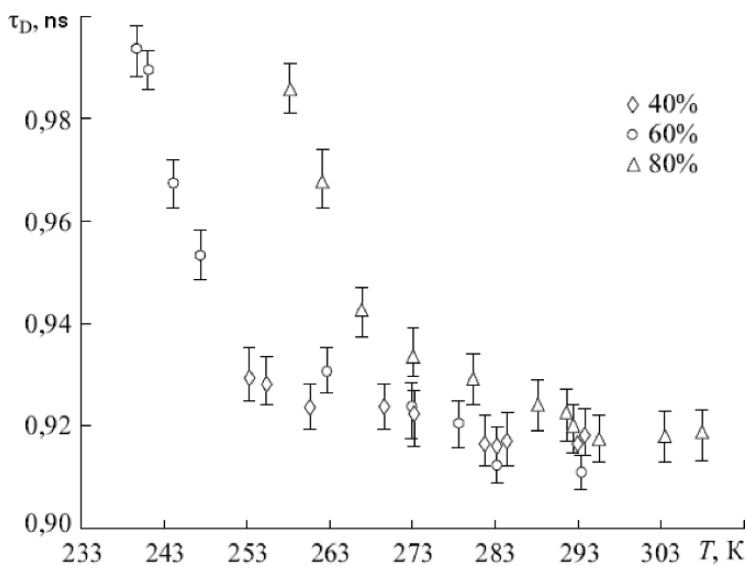
Fig. 6.20. Temperature dependences of the Debye relaxation time τ_D of ethylene glycol with water for the indicated mass contents c of ethylene glycol in water [37]
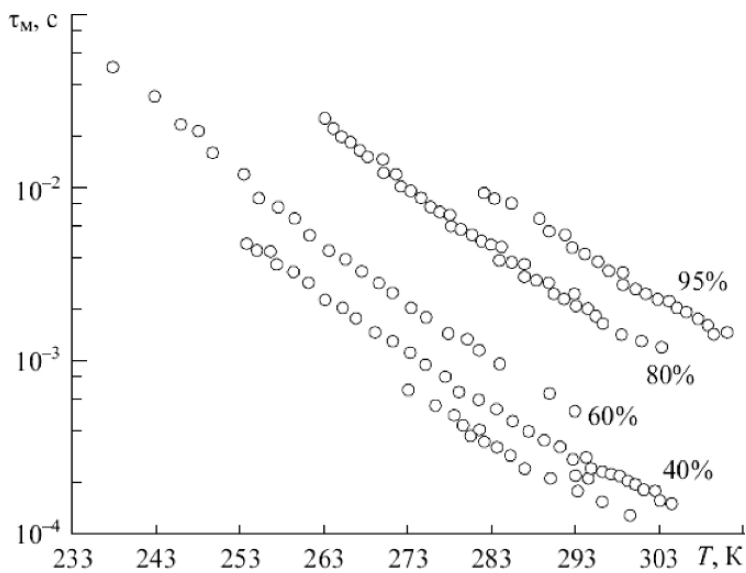
Fig. 6.21. Temperature dependences of the intrinsic time constant τ_M of ethylene glycol with water at the indicated mass content c of ethylene glycol in water [37]

the opposite electrode. This causes the effective conductivity of the liquid to increase when the transit time of the charge through the gap is at least equal to the charging voltage pulse width. Unlike the mixture decay time determined by the properties of the liquid, pulse attenuation during charge injection depends on the geometry of the electrode system and the electrode material.

Since the interelectrode distance varies between centimeters and tens of centimeters in high-voltage shaping lines, drift of the injected SC will not influence energy losses in the single-pulse mode. This problem is complicated for pulse periodic mode. In the first case, charges injected from the electrodes produce the positive effect due to the increased electric strength of the liquid and the increased energy density accumulated in energy storage devices.

When a storage device is commuted to a load and the voltage ranges from U_{ch} to U_0, a portion of its energy transferred to the load can be written as

$$\Delta W = W_{ch} - W_0 = \frac{1}{2} c \left(U_{ch}^2 - U_0^2 \right) , \tag{6.8}$$

given that the charge distribution remains unchanged.

This mode is typical of fast pulsed systems with commutation time (nanoseconds to tens of nanoseconds) much less than the relaxation and transit times of the charge through the gap (10^{-4}–10^{-3} s).

The stored energy density can be increased by increasing the electric strength of the dielectric medium through bipolar injection. The space charge in the dielectric causes the energy stored in the capacitor to increase without increasing the working field strength. This is due to the fact that effective separation of space charges is less than that of the electrode charges. As a consequence, the effective capacitance becomes greater than the geometrical value.

In this case, the energy stored in the capacitor is

$$W = \frac{1}{2} C \left\{ u^2 - \left[\int_0^l dx \int_0^x \frac{q\left(x'\right)}{\varepsilon} dx' \right]^2 + l \int_0^l dx \left[\int_0^x \frac{q\left(x'\right)}{\varepsilon} dx' \right]^2 \right\} , \tag{6.9}$$

where C is the geometrical capacitance, u is the instantaneous voltage, l is the interelectrode distance, q is the charge density, and ε is the permittivity of the medium.

Table 6.5 summarizes three main sought-after quantities:

$$E_{max}, W_{max} = 1/2 \varepsilon E^2, A = W_{max} t_{eff},$$

where t_{eff} is the effective time. As can be seen from Table 6.5, all three parameters increase as the ethylene glycol content in the mixture increases, whereas ε decreases. Cooling of the mixture increases A, but ε remains virtually unchanged and close to ε of pure water.

Table 6.5. Main parameters of the ethylene glycol and water mixture for indicated content of ethylene glycol

Content of ethylene glycol, %	T, °C	ε_S	τ_M, ms	τ_{ch}, ms	E_{max}, MV/m	W_{max}, kJ/m	A_{max}, J·s/m^3
0	0	80	0.67	0.25	13	66	16
40	25	67	0.2	0.1	16	16	8
	−11	79	2.7	0.4	16	90	36
60	30	58	0.3	0.18	16	66	20
	−23	77	15	0.97	14	67	65
80	25	49	1.4	0.45	21	96	43
	−10	60	23	1	17	77	77
95	28	40	2.5	–	27	129	26

One more advantage of such mixtures should be mentioned, namely, they enable the shaping line impedance and its electric length to be smoothly regulated without reconstructing the shaping line itself.

6.5.4 Insoluble Impurities

The electric strength of liquid dielectrics for dc and ac voltages is very sensitive to impurities, including insoluble solid ones. Any liquid poured into a system will contain impurities the specifics of which depend on production and clearing processes, delivery, and the nature of the liquid itself. When a liquid is poured into the system, it is additionally contaminated by system parts and the tank. Liquids used in switching devices or in electric strength tests will be heavily contaminated by decomposition products and electrode erosion debris produced by spark discharges unless they are flowed through the working gap at the specified rate. When liquids are used as working media in electrophysical technological systems that operate on the basis of spark discharge energy, they are contaminated by particles of the machined material and products of erosion and abrasion wear of the electrodes and parts of working chambers. Impurity particles can be arranged in order of decreasing effect on the electric strength of insulating liquids as follows: metals–metal oxides–wet dielectrics–dry dielectrics.

A contaminated liquid represents a complex multicomponent suspension. Suspended impurities differ, as a rule, in granulometry, properties of materials contained in them, and shapes of particles. In these suspensions, particles are clustered, colloid structures are formed, and particles are charged as a result of ion and electron adsorption. Salts, acids, and alkalis that enter into solid particles as impurities increase the charge carrier concentration. For long voltage duration, the polarized particles can form bridges that spark over the electrodes.

Solid products of hydrocarbon decomposition in discharge plasma not only reduce the electric strength of the liquid, but also influence the rate and character of its subsequent decomposition. The outgassing rate in electric discharges initiated in hydrocarbon-bearing liquids increases with carbon (soot) concentration especially quickly when the relative carbon concentration is 6–8% or more. For tip- plane electrodes, decomposition products from previous discharges reverse the polarity for dc voltage when the interelectrode distance exceeds a certain critical value (centimeters to tens of centimeters), that is, U_{br} for a +T −P gap exceeds that for a −T +P gap. Bridges of impurity particles as a reason for liquid breakdown for ac and dc voltages were examined in detail in [38].

Experimental investigations demonstrate that even for long voltage duration, very small impurity particles with concentrations typical of commercially pure insulating liquids exert essentially no influence on the electric strength. For example, a decrease in the filter pores from 5 to 1 μm has essentially no effect on E_{br} of transformer oil. This implies that there is no need to complicate the process and raise the cost by purging insulation liquids to remove impurity particles of submicron size.

The carbon and metal inclusions even at concentration of 0.0005–0.005% dramatically reduce U_{br} of oil for dc and ac voltages. At the same time, cellulose fibers (particles of cloth, electrocardboard, and paper), given that they are not very wet, have much less negative effect on U_{br}. Large impurity particles are effectively removed by the methods mastered in practice including centrifuging, repeated filtering through a system of filters under high pressure, and elutriation (introduction of finely dispersed clay) with subsequent filtering (Table 6.6) [25].

For voltage pulses, impurity particles in a liquid can be considered fixed. In this case, considering the particles as weak elements, one can take advantage of the solid insulation reliability equation to study the dependence of E_{br} on the impurity concentration c [39]:

$$P(E) = \exp\left[-\frac{dS}{0.482 v_0} Z \exp\left(-\frac{0.482 \ln \frac{0.65}{c^{5/3}}}{Z}\right)\right], \qquad (6.10)$$

Table 6.6. Electric strength of transformer oil for 50-Hz ac voltage versus clearing method

Clearing method	E_{br}, kV/cm
Unrefined oil	50
Centrifuging	130
Paper filter	160
Membrane filter	180
Sealed filter (single filtering)	230
Sealed filter (repeated filtering)	330

where

$$Z = \left[\ln \frac{1 - \dfrac{1}{v}}{\dfrac{AEe^{-BT} \ln ZW e^{BT+1} (ABE)^{-1}}{W - 2kT \ln (t/\tau_0)}} \right]^{0.82}$$

Here $P(E)$ is the probability that no breakdown is initiated for the average electric field E, S is the electrode area, d is the interelectrode distance, $v_0 = 2aS_0$ is the dielectric volume element (a is the impurity particle radius and S_0 is the cross-sectional area of the cylinder element), τ_0 is the relaxation time, W is the bond energy, A and B are constants depending on the dielectric structure,

$$v' = \frac{\gamma_1 + jW\varepsilon_1}{\gamma_2 + jW\varepsilon_2},$$

and γ_1, ε_1 and γ_2, ε_2 are electrical conductivities and permittivities of the inclusion and basic material, respectively. Equation (6.10) demonstrates that the decrease in E_{br} (for the given t) or in the discharge time (for $E = \text{const}$) with increase in c is described by a curve with saturation. The dependence of E_{br} (or U_{br}) on c predicted by (6.10) for nanosecond voltage exposures was confirmed in [2, 40]. However, the above approach to an analysis of the phenomenon of pulsed breakdown of suspensions is to a large extent formal, since it ignores a number of physical processes whose characteristic times are comparable to the voltage pulse width. Among them are the accumulation of free and bound charges at the solid body–liquid interface which specifies the relationship between the average electric field in a nonuniform dielectric and the local field, and the interaction of fields of suspended particles when their concentration exceeds a certain critical value and the particle spacing becomes comparable to the particle size.

The processes cited above should influence the relationship between the relaxation time τ and the pulse width τ_p. Analytical investigations and experiments show that for voltage exposure times comparable to the period needed to establish slow polarization (10^{-5}–10^{-6} s) and $c > 0.1\%$, the dependence $U_{br} = f(c)$ is complicated (Fig. 6.22) [2, 40]. As can be seen from Fig. 6.22, the breakdown voltage first decreases with increasing c and then increases and saturates when the concentration exceeds a certain critical value. The concentrations corresponding to the characteristic points in the curve depend on the suspension properties. Thus, in the region of the minimum $c = 0.35$–1.2%, while in the saturation region $c = 1.2$–2%.

When the particle material is conducting (soot), the dependence $U_{br} = f(c)$ exhibits a maximum. The most probable reason for the increase in U_{br} as c increases to 6–7% is that the conducting particles are charged in the electric field and make it less uniform in the region adjacent to the tip electrode. For $c > 6$–7%, the decrease in U_{br} can be explained by the fact that the increase in
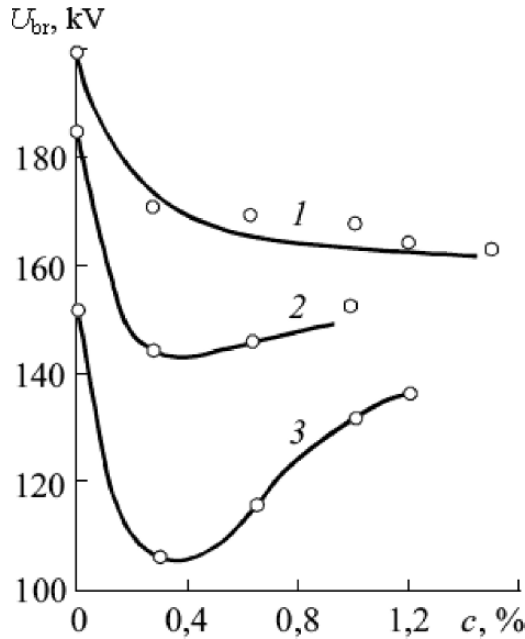
Fig. 6.22. Dependences of U_{br} of suspension on the solid phase concentration for the tip-tip electrode system, $d = 3\,cm$, and the pulse front slope $A = 1.15 \cdot 10^6$ (*curve 1*), $6.1 \cdot 10^4$ (*curve 2*), and $2.88 \cdot 10^4$ V/µs [72]. The liquid phase was glycerin, and the solid phase was formed by small glass spheres

the electrical conductivity of the medium dominates at these concentrations causing the probability of thermal breakdown of the suspension to increase.

Tests of transformer oil in an electrode system with a uniform field for $d = 0.5$–$2\,mm$ performed in [41] under pulses of standard shape yielded demonstrated that the discharge time t_d almost halved after injection of a 0.1% (by volume) copper powder. The average particle diameter was $100\,\mu m$ (Fig. 6.23). It is interesting to note that t_d reduced mainly due to the decrease in the discharge propagation time. The discharge ignition time is insensitive to the copper powder injected in oil. As expected, the effect of powder weakened with increasing overvoltage thereby resulting in a decrease of the voltage exposure time.

As to the nature of the observed effects, the authors drew the following conclusions:

– the discharge is initiated near microbulges on the electrode or on a copper particle settled on the electrode,
– the copper particles suspended in oil generate electrons that ionize molecules of the liquid
– the decrease of the discharge formation time is due to field amplification in oil interlayers between copper particles.
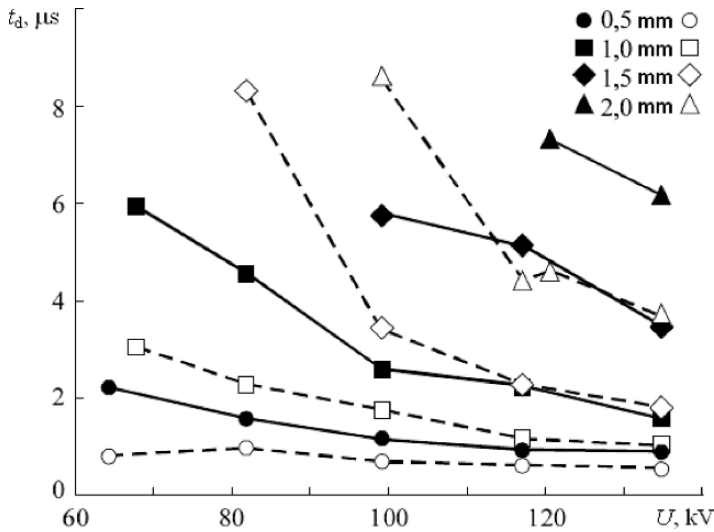
Fig. 6.23. Dependence of the discharge time on the 1.2/50 μs pulse amplitude for filtered a transformer oil (*filled symbols*) and a transformer oil containing 0.1% of a copper powder (*empty symbols*) [41]

One important practical problem is monitoring of impurity content in liquids. Based on the study of the influence of mechanical impurities on the electric strength of transformer oil and oil-barrier insulation for U with a frequency of 50 Hz, Kuchinskii and Kalentjev [42] demonstrated that the Russian Standard "Method for Determining Mechanical Impurity Content," which defines oil clarity in terms of content by weight of mechanical impurities, does not take account of a potentially significant decrease in the electric strength of oils containing impurities when their content by weight is below the critical (permissible) value.

For example, they demonstrated that for a number density $N = 200 \, \text{cm}^{-3}$ of particles with 50 μm average diameter in oil, their content by weight can increase from 10 to 40 g/t depending on the particle densities. According to the Standard, oil with these amounts of impurities is classified as pure. However, the electric strength of this oil can be half that for $N = 50 \, \text{cm}^{-3}$.

Kuchinskii and Kalentjev [42] drew the following conclusion important in the operation of oil-filled insulation equipment: the volume concentration N of mechanical impurity particles rather than their mass concentration primarily affects the electric breakdown of oil; the dependence of E_{br} on N in the range $5 \, \text{cm}^{-3} \leq N \leq 240 \, \text{cm}^{-3}$ is described by the equation $E_{\text{br}} = E_{01} - k \ln N$, where E_{01} and k are the parameters that depend on the impurity type and interelectrode distance (Table 6.7). For $N \leq 50 \, \text{cm}^{-3}$, $E_{\text{br}} = E_{01}$; for high-voltage oil-filled transformers, the maximum permissible

Table 6.7. Values of the parameters E_{01}, E_0, and k for different materials of impurity particles

Impurity type	Interelectrode distance, mm							
	4		6		8		10	
	E_{01}	k	E_{01}	K	E_{01}	k	E_{01}	K
Aluminum particles	31.5	4.7	29.4	4.4	27	4	21.6	3
Cellulose fiber, $W_{lw} = 7\%$	30.5	4.2	22.7	2.8	20.9	2.5	17.7	1.9
Silicon oxide particles	26.9	3.5	20.9	2.3	19	2.2	17.8	2
Cellulose fiber, $W_{lw} = 0.2\%$	25.2	3	20.6	2.2	19	2	13.8	1
	E_0=13.9kV/mm		E_0=11.5kV/mm		E_0=10.7kV/mm		E_0=10.0kV/mm	

concentration of mechanical impurities must be $\leq 50\,\text{cm}^{-3}$, and the liquid water content W_{lw} in solid cellulose must be $\leq 2.0\%$.

A method and device (developed by the Asthom Corporation) for monitoring and calculating the impurity particles in transformer oil was suggested in [43]. The method was approved by the Committee 10A of the International Electrotechnical Commission (IETC). The method enables particles with diameters from 1.5 to 90 μm to be calculated and classified into 9 different groups. A special breakdown tester with an interelectrode distance of 2.5 mm (like a conventional tester) but much greater oil volume in the range of field action was also developed. The results obtained with this special tester reflect the actual influence of impurity particles on the electric strength of oil-filled system insulation. The IETS Standard ASTMF-661 unifies measurements of the number and size of particles contained in a liquid.

A refined procedure of measuring the number of particles in oil-filled transformers is described in [44]. A system of classification of oils according to the degree of their purity was also suggested there.

6.5.5 Moisture

The low-voltage electric characteristics *of transformer oil* and its electric strength depend substantially on moisture content (Fig. 6.24), [45]. Therefore, determination of moisture content of the transformer oil and its effective drying are important for oil and oil-bearing insulation (including oil-paper and oil-barrier insulation types) [46]. Now it can be considered well established that in addition to molecular-dissolved water and emulsion water (according to [47], in the form of clusters) and water settled at the bottom of the system housing, the oil contains water bound to definite groups of hydrocarbons and surface-active impurities. When the oil is heated, water settled at
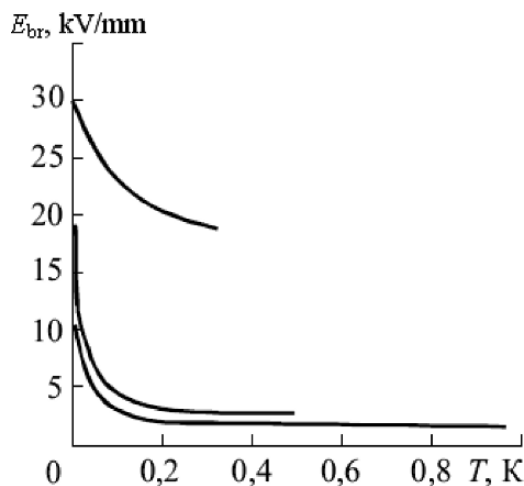
Fig. 6.24. Dependence of E_{br} of a transformer oil upon application of ac and dc voltage on the moisture concentration (generalization of studies of different authors)

the bottom can be transformed into emulsion or molecular-dissolved state. In turn, emulsion water can be transformed into dissolved state. Emulsion, dissolved, and bound waters cause the electric properties (γ and $\tan \delta$) of oil and other hydrocarbons to deteriorate markedly; however, the main contribution to the decrease in the electric strength with increase in moisture content comes from emulsion water. These effects cause E_{br} of liquids to increase as the temperature rises to a certain critical value; other factors come into play at higher temperatures, and E_{br} decreases with any other increase in the temperature (see Sect. 6.4). Bound water cannot be tested by the conventional methods; in this regard, considerable difficulties arise in measuring the total moisture of oil. Deep drying of oil enables bound water to be removed, thereby significantly improving the oil characteristics. In addition to water, other low-molecular substances (formic, acetic, and naphthenic acids, and so on) affect the electric strength, the electrical conductivity, and the dielectric loss angle of the transformer oil. High-molecular substances (soaps, polar resins, and so on), being surface-active, increase the emulsion water content and hence the total water content in oils.

Moisture, like many other impurities, has essentially no effect on the pulsed electric strength of dielectric liquids at small pulse durations. Therefore, specifications on the quality of clearing the insulating liquids in high-voltage pulsed systems can be reduced to a minimum. In contrast, in equipment operating at ac and dc voltages with forced oil circulation, the possible moisture content is at most 0.001%. The stringent specifications on the moisture content of oil stem from the fact that significant wetting of solid electric insulating materials immersed in oil is impermissible.
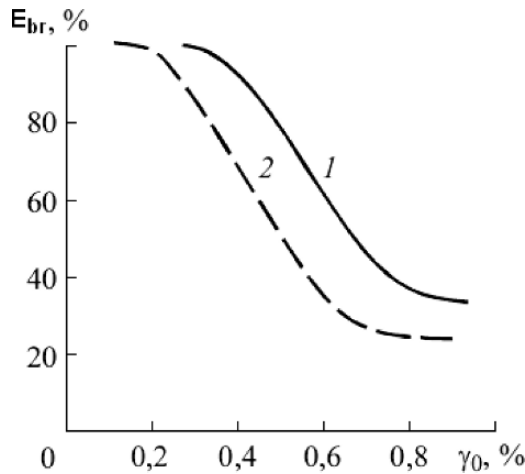
Fig. 6.25. Dependence of E_{br} on the relative humidity for technologically refined oil (*curve 1*) and oil with addition of 0.005% of cellulose fibers (*curve 2*) [73]

The electric strength of oil and composite insulation for dc and ac voltages decreases due to the wetting of solid impurities contained in oil, and the solid insulation itself becomes a source of oil wetting. However, the increase in the moisture content of solid insulation C influences only weakly the value of E_{br} of composite insulation if this increase is not accompanied by the corresponding increase in the moisture content of oil. Investigations of E_{br} of oil for different contents of solid impurities and different values of humidity controlled by the change in the temperature showed that the values of E_{br} depend on the relative oil humidity C_0 on which, in turn, the moisture content of solid impurities comprised in oil depends [48]. The values of E_{br} for commercially pure oil vary only slightly up to $C_0 \leq 0{,}4\%$, and then quickly decrease severalfold (Fig. 6.25) [73].

6.6 Discharge Gap Geometry and Conditions on the Electrodes

6.6.1 Macro- and Microgeometry of the Electrodes

An increase in the field nonuniformity in liquids as in other dielectric media causes U_{br} to decrease. The special feature of liquids in this respect in comparison with gases is a stronger dependence of the electric strength on the micro- and macrogeometry of the electrodes pointed out in many studies. This can be explained by the fact that during a pulsed discharge in the liquid, the pulse crown (whose space charge shields the electrode and distorts the field distribution specified by the geometry of electrodes even before pinching of the discharge channel) is absent, as well as by high density of liquids,

because of which local fields acting in small volumes can initiate a discharge. Moreover, as demonstrated in Chap. 4, changes in the end radius of the tip electrode can radically change the discharge mechanism.

One of the main components of the discharge time lag is the discharge ignition time lag t_{ign} that for the given liquid is determined by the electrode micro- and macrogeometry and the voltage rise time in the discharge gap. Obviously, the effect of the geometry of electrodes on the electric strength of the discharge gap will be maximum when t_{ign} makes a significant part of the total discharge time, that is, when the discharge gap length and the field nonuniformity decrease and the rate of voltage rise (overvoltage) increases. The available experimental data confirm the conclusions based on the results of investigations of ignition and initial stages of discharge propagation. In [49] it was established that the breakdown voltage of discharge the tip-plane gaps ($d = 3$–9.7 cm) in oil for $1.2/50$ and $1.2/450\,\mu$s pulses decreases on average by 25–40% when the end radius of the tip electrode decreases by more than two orders of magnitude (from 2.5 to 0.01 mm). Our measurements demonstrate that for 50–60 ns rectangular pulses and interelectrode distances of $\sim$1 mm, an increase in r_0 from microns to hundreds of microns causes U_{br} to increase by a factor of 1.5–2.

The microgeometry of the electrodes that affects U_{br} in short gaps with uniform or weakly nonuniform fields is determined by the quality of surface machining and the crystal structure of electrode metal. As demonstrated in [50], the electric strength of dielectrics (gases and capacitor oil) increases substantially (by a factor of 1.5–3) with the use of electrodes manufactured from single crystals.

It is well known that one of the methods of elimination of local field amplification centers on the electrodes manufactured from polycrystalline metals is their training by discharges. This operation (sometimes called conditioning) is widely used in experiments on vacuum breakdown and in some electrovacuum devices. In a number of studies, training of electrodes was used to measure the electric strength of liquids. The effect of previous discharges on the electrodes is aimed at raising E_{br} and reducing the scatter of E_{br} and t_d. In different studies, radically different regimes of conditioning are recommended. For example, the number of recommended training discharges lays in the limits 5–100. An analysis of the available experimental data and mechanisms of air-conditioning demonstrate that this effect depends on many factors, including the material of electrodes, their areas, quality of surface treatment, voltage duration, amount of energy and rate of its liberation in the spark channel, and properties of the liquid. Moreover, the positive effect is observed not for all liquids. Only in liquefied gases it is always positive (Fig. 6.26) [51]. An increase and stabilization of the discharge time (for $E = $ const) in pure water was observed after 15–20 discharges. In transformer oil, as can be seen from Fig. 6.27, the effect of air conditioning it is not observed for the examined number of discharges [2]. The sphere-sphere electrode systems ($d = 0.8$ cm) and Rogowski electrodes ($d = 2.6$ cm) were used; the electrodes were manufactured of stainless steel.
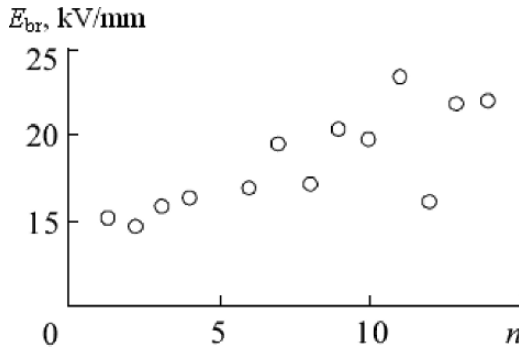
Fig. 6.26. Dependence of E_{br} of liquid nitrogen on the serial number of breakdown. Plane electrodes were fabricated from stainless steel, the interelectrode distance was 0.5 mm, and the electrode area was 1963 mm^2 [51]

During training, the liquid was replaced after each breakdown by pumping from the interelectrode gap and addition of a portion of fresh liquid into the chamber. It can be assumed that air-conditioning in oil was not observed due to the fact that during training discharges, alongside with the destruction and melting of microbulges, products of hydrocarbon decomposition are settled on the electrodes thereby precluding the stabilization of properties of the electrode surface. This is in agreement with the notion that weak elements on the electrodes where the discharge initiation (ignition) occurs for the least values of U_{ign} or t_{ign}, are not only geometrical inhomogeneities but also adsorbed impurities, structural defects of the surface, an so on. In this regard,
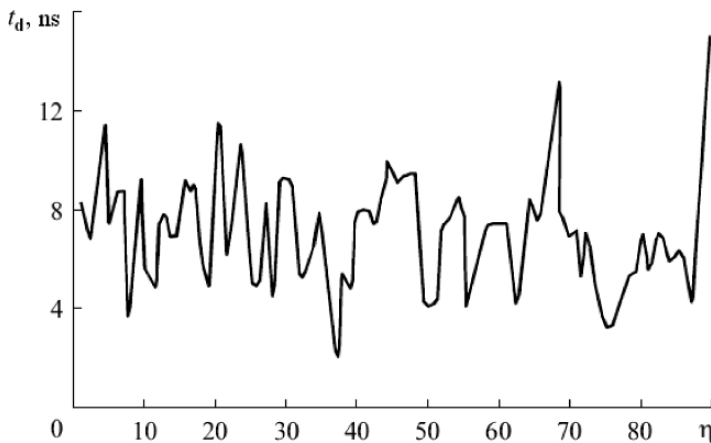
Fig. 6.27. Dependence of the discharge time lag on the number of nanosecond pulses applied to the gap with a transformer oil replaced after each breakdown ($E_{br} = 2.78$ MV/cm, $d = 1.5$ mm, and spherical electrode diameter of 8 mm) [2]

sites with the maximum local field strength not always are the most probable regions of discharge initiation. It was demonstrated both theoretically [52] and experimentally [53] that this effect for the cone-plane electrode configuration causes the discharge initiation from the lateral cone surface rather than from the apex of the conic electrode. Theoretical analysis is based on a multifractal model of discharge distribution over the electrode surface in which weak elements are taken into account through changes in the local field strength near the electrode surface.

The value of U_{br}, the number of breakdowns, and the distribution of coordinates (radii) of points of breakdown initiation over the electrode surface (erosive craters) were measured in experiments. The high-voltage electrode was shaped as a cone with a base diameter of 60 mm and rake angle β ranging from 90° to 170°. The grounded electrode was shaped as a plane with rounded end 100 mm in diameter. The discharge gap length was 5 mm. A voltage pulse with positive polarity, rise time of 1.5 μs, and pulse duration of 50 μs was used.

For small rake angles of the cone ($\beta \approx 90$–135°), points of discharge initiation are concentrated at the cone apex in the region with a radius of 1–2 mm. For $\beta \geq 135°$, the probability of discharge initiation from points on the lateral electrode surface increased, and for $\beta \sim 150°$, it exceeds 50%. In this case, the breakdown gap length can exceed twice the minimum interelectrode distance. For large β, additional peaks are observed on the erosive crater distributions that do not belong to the cone apex. For high impurity concentrations in a liquid and inhomogeneities on the electrode surface, the distribution is smoothed, but its character remains unchanged. (The former was achieved for the breakdown of oil preliminary aged by a series of breakdowns, and the latter was observed when going from the polished electrodes to grinded ones). By the way, the $t_d - E_{av}$ dependence obtained for this model coincides with the experimentally established one (for example, in [54]).

The foregoing demonstrates that training of electrodes with the help of breakdowns is ineffective method of increasing the value of E_{br} of liquids chemically unstable to the action of a spark discharge. For liquid dielectrics, training regimes without breakdowns are more promising.

The phenomenon of increase in the electric strength of liquid dielectrics with preliminary voltage application to the insulation gap was revealed already in the 40s. It continues to draw attention of researchers due to the opportunity to investigate with its help the processes of polarization, emission, injection, and relaxation of charge carriers, their transfer, etc. In practice of system operation, this effect has not found application. The researchers try to take it into account when estimating the operating conditions of insulation exposed to sign-variable voltage pulses or voltage of complex shape (for example, pulses superimposed on a constant voltage).

In liquids with increased conductivity, preliminary voltage exposure is accompanied by stronger effects, including those that under certain conditions cause the electric strength to increase. In [55] it was suggested to

raise the electric strength of strongly conducting liquids, in particular, water preliminary heating the electrodes by currents of pre-breakdown electrical conductivity. Golubeva et al. [55] consider that the effect of increase in the pulsed electric strength is due to an increase in the electrical conductivity of liquid upon heating and a decrease in the field strength near microbulges where the current density and temperature are maximum. Figure 6.28 shows the pulsed electric strength of pure water after preliminary passage of a direct current through the gap [56]. The test pulse duration was $1.5\,\mu s$, the interelectrode distance was $1\,cm$, and the plane electrode areas ranges from 30 to $150\,cm^2$. The positive direction of the abscissa in Fig. 6.28 coincides with the direction of current for which the positive terminal of the dc source is connected to the anode of the examined interval, and the negative direction coincides with the current direction for which the positive terminal of the source is connected to the cathode. As can be seen from Fig. 6.28, there exist optimal conditions under which E_{br} of water increases approximately by a factor of 1.7, and the scatter of the breakdown voltage decreases by a factor of 2–3. Komin and Morozov [56] explain this effect by accumulation of a homocharge near the electrodes as well as by the formation of conducting near-electrode layers due to an increase in the concentration of charge carriers there. When the current density is greater than the optimal one, E_{br} decreases because of the development of electrohydrodynamic instabilities and outgassing due to electrolysis.
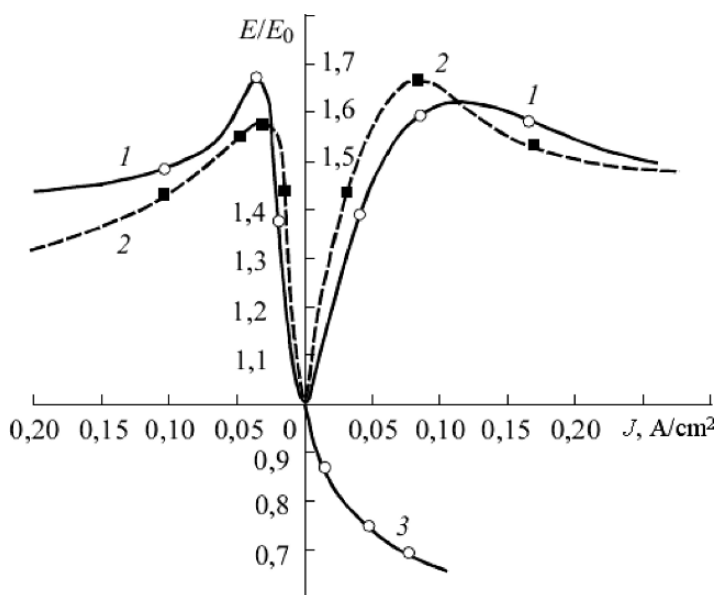
Fig. 6.28. Dependence of E/E_0 on the current density for the electrodes fabricated from stainless steel (*curve 1*), titan (*curve 2*), and aluminum (*curve 3*) [56]

6.6.2 Dielectric Electrode Coatings

In some cases, a more efficient method of decreasing the effect of electrode microgeometry and increasing E_{br} of liquids is electrode coating with a thin layer of high-strength solid dielectric. In most cases, the stable positive effect of coatings is observed for dc and ac voltages. For pulsed voltages, when the electric strength of liquids approaches that of solid dielectrics and impurity bridges are not formed, this effect is manifested only weakly. Investigations into the influence of electrode coating (vinyl film with a thickness of $50 \pm 15 \, \mu m$) on the pulsed flashover voltage of spacer isolators fabricated from various dielectrics in a system of plane electrodes show that such an influence is within the measurement error [57]. The sample heights were 5 mm, their diameters were 12 mm, and the slope of the oblique leading edge was $25 \, kV/\mu s$. The average breakdown field strength of transformer oil for coated and uncoated electrodes was 470–480 kV/cm, the flashover voltage of polycarbonate samples was 450–460 kV/cm, and for pressboard it was 400 kV/cm. However, there are publications in which U_{br} of transformer oil and U_{fl} of solid dielectrics in weakly inhomogeneous fields increased by 20–25% for microsecond pulses and electrodes coated with dielectric layers up to $150 \, \mu m$ thick.

A variety of lacquers are traditionally used for coatings, and cable or capacitor paper and polymeric films are used for simple electrode geometry. Table 6.8 summarizes data on the influence of plane electrode insulation methods on the electric strength of transformer oil for pulsed $(1.2/50 \, \mu s)$ and ac (60 Hz) voltages [58]. Plane brass electrodes with rounded edges created a uniform field in a 1.3×1.3 cm region. The interelectrode distance was 1.9 mm. Kraft paper (KP) and calendered polyamide paper (PAP) 0.125 mm thick were used for insulation. The KP breakdown voltage was 19.1 kV for a pulsed voltage and 8.8 kV (effective value) at 60 Hz. For PAP it was 20.4 and 10 kV, respectively. In tests both at 60 Hz and pulsed voltage, U_{br} it was measured with a 10% increment between test steps. The 60-Hz voltage duration at each step was 1 min, and the pulsed voltage was applied 3 times per step. It can be seen from Table 6.8 that electrode insulation increases the breakdown voltage U_{br} by ∼50% for a pulsed source and by 30% for 60-Hz ac. This increase is essentially independent of the number of insulating layers. When a single KP layer was used for insulation, a wide spread in U_{br} was observed to result from defects in the paper. It also follows from the table that both electrodes must be insulated to increase pulsed U_{br}. The positive effect of electrode insulation intensifies when aromatic additives (for example, anthracene) are injected into the oil. In liquids with large ε and γ (especially water), the dielectric coating appears to be overloaded by the field, and its breakdown can initiate breakdown of the whole insulation gap.

6.6.3 Interelectrode Distance

The scaling effect, that is, the dependence of electric strength on the interelectrode distance, electrode area, and volume of the insulating medium exposed

Table 6.8. Influence of electrode insulation on the breakdown characteristics of transformer oil

Insulation system and test type	Number of tests	U_{br}, kV	σ, %	E_{br}, kV/cm
		Pulsed tests		
Uninsulated electrodes	85	87.5	11	45.9
Two insulated electrodes:				
single KP layer	40	120.8	20	67.1
two KP layers	25	119.6	13	71.8
single PAP layer	20	121	16	66.3
two PAP layers	15	110	11	64
		Tests at 60 Hz		
Uninsulated electrodes	75	38.1	18	20
Two insulated electrodes:				
single KP layer	31	49.1	17	27.3
two KP layers	25	46.5	16	27.9
Single PAP layer	15	40.6	16	27.9
Two PAP layers	15	43.3	14	25.2

to an electric field, is a common property of all insulating media. In insulation systems, it shows up as a decrease in the average breakdown field strength with increasing overall dimensions of the system and increasing number of individual insulation units. The electric strength of all dielectrics increases with decreasing interelectrode distance, all other conditions remaining the same. Only for solid insulation containing defects might E_{br} decrease with d when the interelectrode distance becomes comparable in size to defects.

Classical explanation of the strong increase E_{br} for short gaps is based on an exponential dependences of the number of electrons in an avalanche on the distance passed by it: $n = n_0 \exp(\lambda d)$.

From this formula it follows that for short interelectrode distances, a higher electric field is required to produce in the avalanche the critical space charge necessary for avalanche transformation into a streamer. In condensed media, this factor is most probably acts for micron interelectrode distances. Numerous experimental data demonstrate an increase in E_{br} with decreasing d (for example, see [59, 62]). This effect is most strongly pronounced for interelectrode distances smaller than $100\,\mu$m [63, 65].

The increase in the electric strength for interelectrode distances less than $100\,\mu$m is observed for the bubble mechanism of breakdown from cathode. In this case, it is doubtful to explain this effect in the context of the theory of collision ionization. The increase in the electric strength can be due to

a decrease in the local electric field near the electrode surface that affects the process of electric discharge initiation. This enables us to give a simple and evident explanation to the shift of the boundaries of different breakdown types toward higher average field strengths and transition from the breakdown from anode to breakdown from cathode (for constant E) with decreasing interelectrode distance (See Chap. 3).

The d dependence of E_{br} is also caused by some other factors. The increase in d for the same electrode area is accompanied by an increase in the dielectric volume in the strong field region and in the number of weak elements that facilitate the breakdown. This effect is manifested for breakdown of liquids, solids, and composite dielectrics.

Under actual experimental conditions, the increase in d results in either increase in the electrode area when the field inhomogeneity coefficient remains unchanged, or and increase in the field inhomogeneity if the electrode area remains unchanged. In both cases, E_{br} decreases with increasing d.

The decrease in E_{br} with increasing d for large interelectrode distances follows from the consideration of the physical pattern of the discharge propagation under these conditions. The breakdown voltage for long gaps in liquids is largely determined by the leader stage of the discharge. The propagation velocity of the initial channel as though heading the leader channel is determined mainly by the field strength in the channel head. It, in turn, depends on the voltage applied to the gap and the voltage drop across the initial and leader channels. The voltage drop increases with d and discharge channel length; to compensate for this voltage drop, the voltage applied to the gap must be increased. However, the increase in the gap and discharge channel lengths and hence its propagation time results in the channel heating and decreases its longitudinal potential gradient. This means that the voltage increase needed to compensate the voltage drop across the gap is nonlinearly related to the gap length.

In generalized form, a dependence of the breakdown voltage on the interelectrode distance for all dielectric media can be written as

$$U_{\mathrm{br}} = Bd^{n},$$

where B and n are constants that depend on the properties of the dielectric medium and breakdown conditions. Moreover, n can be set equal to unity only for d changing in narrow limits. In most cases, $n < 1$.

It should be noted that the dependence $E_{\mathrm{br}} = f(d)$ is not so simple for submillimeter gaps, and the absolute values of E_{br} obtained by various authors differ strongly. This can be explained by the fact that in addition to the factors indicated in the beginning of this paragraph and causing electric hardening, impurity bridges are formed in the gap when d decreases faster and the field strengths are lower, the effect of electrode microgeometry on E_{br} also changes, and the probability of breakdown on foreign impurities (solid particles, microinclusions, and moisture) increases. With decreasing d, the conditions of

development of electrohydrodynamic, convective, and thermal processes, accompanied by breaking of the continuity of the medium and reduction of its electric strength, also change. As in gases, changes of d are accompanied by changes of the mechanism and laws of discharge propagation. In particular, the leader discharge is not observed when going from millimeter and longer gaps to submillimeter ones. The site of discharge initiation in the gaps with a uniform field changes when going to micron gaps (Chap. 3). In summary, we conclude that under conditions of minimum influence of secondary processes (careful preparation to liquid and electrode tests and for pulsed voltage) the decrease in E_{br} with increasing d is observed in the entire examined range of interelectrode distances.

In particular, Fig. 6.29 from [2] shows data on the nanosecond electric strength of transformer oil and distilled water obtained by different authors for gaps with a uniform field and different lengths. For microsecond pulses, the dependence of the electric strength of distilled water on the length of the gap with a uniform field is shown in Fig. 6.30 [66].

6.6.4 Electrode Area

The effect of the electrode area, that is, the dependence of the electric strength of the interelectrode medium on the electrode area, similar to the effect of total voltage, that is, the d dependence of E_{br}, is universal for all dielectrics. For long voltage duration, impurity bridges the breakdown conditions for which or along which are facilitated can be formed in the gap. For microsecond (and longer) pulses, when the impurity particles can be considered fixed, they have time to be polarized (including the processes of slow polarization), thereby resulting in local field distortions and decreasing the electric strength. Hence, in this case the scaling effect is caused by the joint effect of the electrode area and volume of the liquid in the strong electric field. For nanosecond
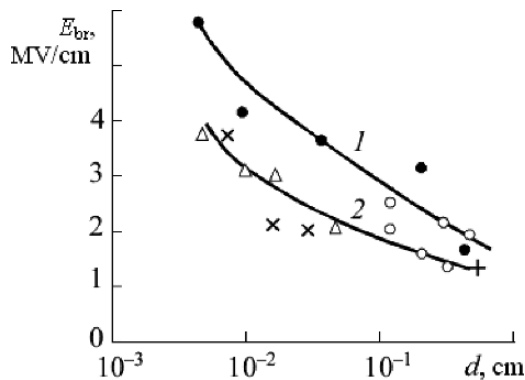
Fig. 6.29. Dependence of U_{br} on d for $t_d = 10\,\text{ns}$ in a transformer oil (*1*) and distilled water (*2*) in a uniform field [2]
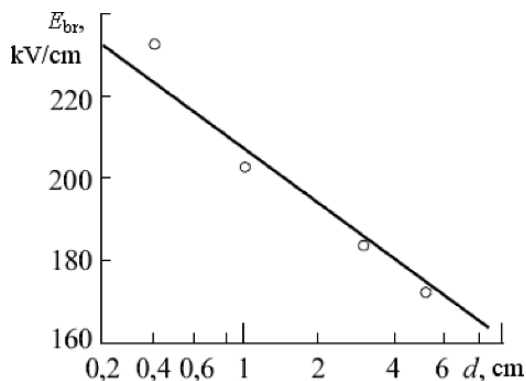
Fig. 6.30. Dependence of E_{br} of water under exposure to a single on the distance between the plane electrodes [66]

breakdown, the main role in the effect of the electrode area is played by weak elements of the electrode surface, and this effect is observed only when S changes over a wide range.

The general relation between electric strength and electrode area is given by an empirical relation of the form:

$$E_{br} \approx S^{-n} , \qquad (6.11)$$

where n is a coefficient depending on the dielectric type and breakdown conditions.

Figure 6.31 shows the generalized dependence of the pulsed electric strength of a transformer oil on the electrode area that changed within the limits of five orders of magnitude [67]. The dependences were generalized as follows: 1) all electrodes were similar (to this end, the field inhomogeneity coefficient μ was introduced), 2) to construct the dependences, a monotonically increasing pulse was used with duration t_{eff} determined as the rise time of voltage
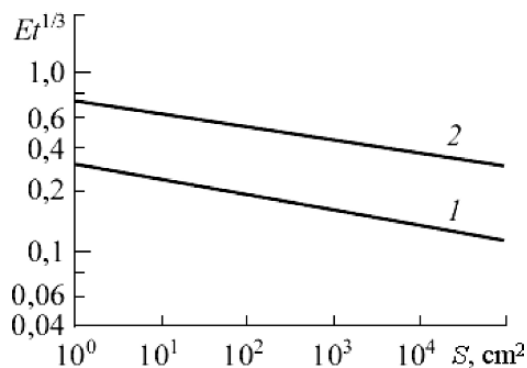
Fig. 6.31. Dependence of $Et^{1/3}$ on S for a transformer oil in weakly nonuniform (*curve 1*) and uniform fields (*curve 2*) [67]

from $0.63E_{br}$ to E_{br}. The value of the coefficient n in (6.11), according to these data, was 0.1. In the next few years, the value of this coefficient was repeatedly refined in numerous studies devoted to investigation of the electric strength of liquids (mainly of transformer oil and pure water) under conditions corresponding to their use as insulation for coaxial and strip shaping lines of high-power high-voltage generators for accelerators and x-ray sources. For water and microsecond voltage pulses, the value $n = 0.1$ was given, in particular, in [2, 66, 68]. For water and nanosecond voltage pulses $(7 \cdot 10^{-9}$–$3 \cdot 10^{-8}$ s), $n = 0.06$ [69]. In [67], $n = 0.1$ was recommended for transformer and castor oils, ethylene, methyl alcohol, water, and glycerin with allowance for the effect of electrode area.

From this brief consideration we can conclude that quantitatively the effect of electrode area is independent (or depends very weakly) of the individual properties of liquids of approximately identical degrees of cleanliness and decreases with voltage duration. The agreement between the experimental results and power-law approximation (6.11) is illustrated by Fig. 6.32 [66]. The results analogous to the foregoing normal liquids were also obtained for cryogenic liquids.

6.6.5 Liquid Dielectric Volume in the Interelectrode Gap

The significant influence of the volume of liquid dielectric in a strong electric field on the electric strength results from the fact that the in the bulk of the liquid strongly affect the discharge initiation near the electrodes, and subsequent propagation within the interelectrode gap. The relationship between electric strength and liquid volume depends heavily on the elemental composition of the liquid, the prevalence and nature of impurities, the discharge gap configuration, the electric field, and the exposure time of the liquid.
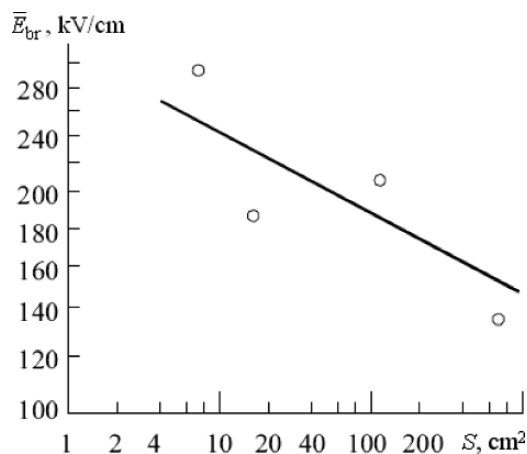
Fig. 6.32. Dependence of $\bar{E}_{br}$ of water under exposure to a single pulse on the electrode area S in a uniform field at $d = 1\,\mathrm{cm}$ [66]

Figure 6.33 [47] shows the typical dependences of the electric strength and its spread as functions of the dielectric volume for transformer oil of two types. The tests were carried out for voltages at the mains frequency by a stepwise method of voltage application, with ten or twenty voltage rises at each step and 1-min exposure. The voltage at the initial step was 30% of the predicted breakdown voltage, and the voltage was raised by increments equal to ∼5% of the breakdown voltage.

As follows from Fig. 6.33a, E_{br} was halved when the dielectric volume in the strong electric field increased by two orders of magnitude. The experimental dependences $E_{br}(V)$ and $\sigma(V)$ are described well by the empirical equations

$$E_{10\%} = 8.95V^{-1/7} + 2.33,$$

$$\sigma = 3.25V^{-1/6} \text{ for oil of type I,}$$

$$\sigma = 2.36V^{-1/7} \text{ for oil of type II,}$$

where E is in kV/cm and V is in cm^3.

Effects on E_{br} due to dielectric volume and electrode area. were also compared experimentally The results in (See Table 6.9) demonstrate that E_{br} increases by approximately 22% when the oil volume in a strong electric field doubles with electrode area remaining unchanged, that is, the influence of dielectric volume in a strong electric field is greater than that of electrode area.

For voltage pulses, when many processes responsible for the behavior $E_{br}(V)$ under long-term voltage exposure can be neglected, the most important factor is the increasing probability of occurrence of weak regions with increasing liquid dielectric volume. In this case, an attempt has been made [70] to use the distribution function of the breakdown field strength probability obtained in [39] for solid dielectrics.
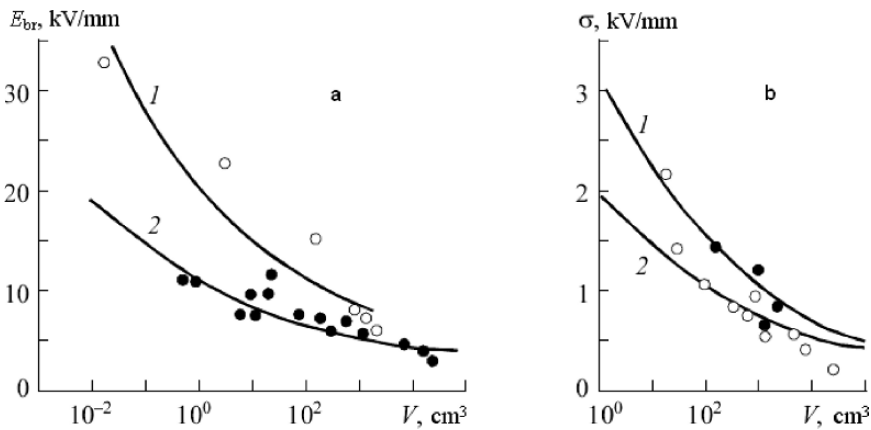
Fig. 6.33. Dependence of E_{br} (**a**) and its scatter (**b**) on the type I (*curve 1*) and II stressed oil volumes (*curve 2*) [47]

Table 6.9. Influence of dielectric volume on E_{br} of transformer oil (electrode areas held constant)

Interelectrode distance, mm	Electrode areas, cm³	Oil volume enclosed between electrodes, cm³	Number of tests	Breakdown voltage, kV/mm, for breakdown probability, %	
				10	50
8	1120	900	50	7.74	8.73
16	1120	1800	50	5.60	5.79

After some simplifications for a coaxial electrode system, the dependence of the maximum breakdown field strength on the liquid dielectric volume in a strong electric field assumes the form

$$E_{max}^{-0.82} = A + B \log \left(lr^2 \ln \frac{R}{r} \right) , \qquad (6.12)$$

where A and B are parameters describing the properties of the dielectric, l is the electrode length, and r and R are the radii of the inner and outer electrodes, respectively.

The applicability of the statistics of extreme values to a description of $E_{br}(V)$ for voltage pulses was tested for three coaxial electrode systems ($R = $ 19, 28, and 40 mm, $r = $ 2–30 mm, and $l = $ 70 mm) and commercially pure transformer oil. Breakdowns were initiated at the front of a single voltage pulse of positive polarity with a slope of 1700 kV/µs. Figure 6.34 shows the
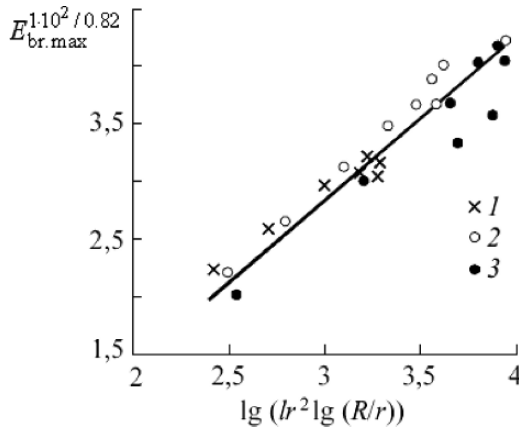
Fig. 6.34. Influence of the volume on $E_{br.max}$ of a transformer oil for $R = 19$ (*1*), 28 (*2*), and 40 mm (*3*) [70]

resulting measurements. In coordinates chosen according to (6.12), they are satisfactorily approximated by a straight line, which confirms the validity of (6.12). In this case, $A = -0.0161$ and $B = 0.0147\,\mathrm{kV/mm}$.

References

1. V. V. Bagin and V. Y. Ushakov, Investigations of the electric strength of dielectrics with application to insulation of nanosecond high-voltage equipment, Elektrichestvo, No. 4, 76–79 (1972).

2. V. Y. Ushakov, Pulsed Electric Breakdown of Liquids, Publishing House of Tomsk State University, Tomsk (1975).

3. I. P. Kuzhekin and A. A. Nersesyan, Electric strength of water in a uniform field at small interelectrode distances, in: Reports at the Scientific-Technical Conf. on the Results of Scientific Research in 1968–1969, Moscow Power Institute, Moscow (1969), pp. 95–101.

4. W. H. Bostik, V. Nardi, and O. S. F. Zucker, eds., Energy Storage, Compression, and Switching, Plenum Press, New York–London (1975).

5. E. M. Bazelyan, E. N. Brago, and I. S. Stekolnikov, A decrease in the discharge voltage of insulation of power systems for switching voltages of some types, Elektrichestvo, No. 7, (1962).

6. V. Y. Ushakov, Investigation of distilled water breakdown under exposure to oblique pulses of positive polarity, in: Breakdown of Dielectrics and Semiconductors, Energiya, Moscow (1964), pp. 207–211.

7. V. Y. Ushakov, Discharge propagation in liquid dielectrics under the effect of oblique voltage waves, Zh. Tekh. Fiz., **35**, No. 10, 1844–1847 (1965).

8. V. Y. Ushakov, To calculation of voltage-time characteristics of some liquid dielectrics, Izv. Vyssh. Uchebn. Zaved., Energ., No. 1, 15–19 (1966).

9. I. I. Kalyatskii and V. F. Panin, Investigation of pulsed strength of a transformer oil under the effect of switching overvoltages, Izv. Vyssh. Uchebn. Zaved., Energ., No. 6, 22–26 (1966).

10. G. Maier, Neure Ergebnisse uber die electrishe Festigkeit von Isolierol bei Wechselspannung, Schaltspannung und Normstoss, Brown Boweri Mitt., **54**, No. 7, 368–376 (1970).

11. W. Hauschild, Zur Abhangigkeit der Durchschlagspannung inhomogener Olisolierstrecken von Stirnzeit und Wirkdauer eines Impulsspannung, Elektrie, No. 7, 244–246 (1970).

12. V. A. Butenko and V. Y. Ushakov, Surface discharge in a transformer oil under exposure to oblique voltage pulses, Izv. Vyssh. Uchebn. Zaved., Energ., No. 1, 31–35 (1973).

13. O. Lesaint and P. Gournay, A study of the initiation of positive prebreakdown phenomena in liquid hydrocarbons, in: Proc. 11th Int. Conf. on Dielectric Liquids, Baden-Dattwil (1993), pp. 284–288.

14. J. Kucera and L. Valenta, Pevnost transformatoraveho olej v nehomogennim poli pri razovch prepetich ruzneho tvaru, Bull. EGU, Nos. 5–6, 26–29 (1968).

15. J. K. Nelson and I. F. M. Mashad, Frequency dependence of stress-induced cavitation in fluorocarbon liquids, in: Proc. 5th Int. Conf. on Conduction and Breakdown in Dielectric Liquids, Delft Univ. Press (1975), pp. 41–44.

16. K. Yoshino, K. Ohseko, M. Shiraishi, et al., Dependence of polarity effect of dielectric breakdown on molecular structure of liquids, in: Proc. 7th Int. Conf. on Conduction and Breakdown in Dielectric Liquids, Berlin (1981), pp. 236–240.

17. A. Beroual and R. Tobazeon, Effect de la pression hidrostatique sur les phenomenes de preclaquage dans les dielectriques liquids, C. R. Acad. Sci., Ser 2, **303**, No. 12, 1081–1084 (1986).

18. G. J. Fitz Patric and E. O. Forster, Effect of pressure on the pre-breakdown events in toluene, 1986 Annual Report Conf. El. Insul. Diel. Phenomena, IEEE #86CH2315-0 (1986), pp. 299–303.

19. R. E. Hebner, E. F. Kelley, G. J. Fitz Patrick, et al., The effect of pressure on streamer inception and propagation in liquid hydrocarbons, in: Proc. 9th Int. Conf. on Conduction and Breakdown in Dielectric Liquids, Salford (1987), pp. 27–39.

20. H. Yamashita, E. O. Forster, and M. Pompili, Streamer formation in perfluoropolyether under impulse conditions, IEEE Trans. El. Insul., **28**, No. 3, 324–329 (1993).

21. P. Gournay and O. Lesaint, Evidence of the gaseous nature of positive filamentary streamers in various liquids, in: Conf. El. Insul. Diel. Phenomena, Arlington (1994), pp. 834–839.

22. V. P. Borodin and V. F. Klimkin, Influence of pressure on mechanisms of electrical breakdown of n-hexane, Pis'ma Zh. Tekh. Fiz., **14**, No. 9 802–805 (1988).

23. E. M. Hizal and S. Dincer, Breakdown time lag and pre-breakdown in a transformer oil, effect of hydrostatic pressure, J. Electrostatics, **12**, 333–343 (1982).

24. J. Fuhr, H. M. Jones, and T. Aschwanden, Electrical breakdown in highly pressurized water, in: Conf. Record, 9th Int. Conf. on Conduction and Breakdown in Dielectric Liquids, Salford (1987), pp. 411–415.

25. G. I. Skanavi, Physics of Dielectrics (Region of Strong Fields), State Physical and Mathematical Press, Moscow (1958).

26. Y. Katsumi, Dependence of dielectric breakdown of liquids on molecular structure, IEEE Trans. El. Ins, **15**,No. 3 (1980), pp. 186–200.

27. N. P. Mel'nikov, G. A. Ostroumov, and M. Yu. Stoyak, Electric breakdown propagation in aqueous electrolits, in: Breakdown of Dielectrics and Semiconductors, Energiya, Moscow (1964), pp. 246–248.

28. N. B. Trofimova, Investigation of breakdown of conducting nondegassing liquids, in: Breakdown of Dielectrics and Semiconductors, Energiya, Moscow (1964), pp. 219–224.

29. J. Nakao and S. Sakamoto, Research on underwater spark discharge, El. Eng. Jpn., **87**, No. 5, 83–90 (1967).

30. V. J. Ushakov, O. P. Semkina, V. V. Ryumin, and V. V. Lopatin, On a nature of pulsed electric breakdown of aqueous electrolits, Elektr. Obrab. Mater., No. 44, 48–54 (1972).

31. A. T. Chepikov, B. V. Semkin, and A. M. Mironov, Impulse breakdown of electrolytes at small voltage exposure times, Izv. Tomsk. Politekhn. Inst., **149**, 152–157 (1966).

32. A. V. Valter and L. G. Inge, Electrical breakdown of liquid dielectrics, Zh. Tekh. Fiz., **4**, No. 9, 1668–1687 (1934).

33. E. Musset, A. Nikuradse, R. Ulbrich, Uber die Durchbruchfeldstarke in dielektrischen Flussigkeiten, verchiedener molekularen Zusammensetzung, Z. Angew. Phys., **8**, No. 1, 8–15 (1956).

34. D. D. Ryutov, Diffusion electrodes for investigation of liquid dielectric breakdown, Zh. Prikl. Mat. Teor. Fiz., No. 4, 186–187 (1972).

35. V. V. Vorobjev, V. A. Kapitonov, E. P. Kruglyakov, et al., Investigation of water breakdown in a system with diffusion electrodes, Zh. Tekh. Fiz., **50**, No. 5, 993–999 (1980).

36. S. N. Komin, G. S. Kuchinskii, and E. A. Morozov, Investigation of the influence of different substances on the electric strength of water in the microsecond range, Elektrichestvo, No. 12, 13–17 (1987).

37. R. J. Gripshover and D. B. Fenneman, Water/glycol mixtures as dielectric for pulse forming lines in pulse power modulators, in: Conference Record of the 15th Power Modul. Symp., New York (1982), pp. 174–180.

38. J. A. Kok, Der Elektrische Durchschlag in Flussigen Isolierstoften, Philips Techn. Bibliothek, Eindhoken, (1963).

39. V. S. Dmitrevskii, Calculation and Design of Electrical Insulation, Energoizdat, Moscow (1981).

40. M. P. Tonkonogov, S. V. Kim, and V. Y. Ushakov, Special features of pulsed electric breakdown of suspensions. Polarization breakdown mechanism, Elektr. Obrab. Mater., No. 5, 20–25 (1970).

41. A. O. Hirai and K. Arii, The Effect of contaminant in breakdown time lag of uniform electric field using impulse breakdown in mineral oil, in: Proc. 13th Int. Conf. on Dielectric Liquids, Nara (1999), pp. 207–210.

42. G. S. Kuchinskii and G. S. Kalentjev, Influence of mechanical impurity on the electric strength of a transformer oil and oil-barrier insulation for the voltage at the industrial frequency, in: Overvoltages in Electric Systems and Electric Strength of High-Voltage Insulation, Novosibirsk (1985), pp. 121–129.

43. L. D. Samat, Micro-particles in a transformer oil and dielectric withstand effect, Asthom Rev., No. 11, 47–57 (1988).

44. M. Ikeda, Measurement of the number of suspended particles in a transformer oil and study of the influence of these particles on insulation breakdown voltage, Trans. Inst. Elec. Eng. Jpn., **B118**, No. 11, 1277–1283 (1998).

45. E. F. Kelley, R. E. Hebner, G. J. Fitz Patrick, and E. O. Forster, The effect of pressure on streamer initiation in *n*-hexane, in: Proc. of the 1986 IEEE Int. Symp. on Electrical Insulation (1986), pp. 66–68.

46. H. Kishida, H. Isono, H. Mitsui, et al., Influence of moisture on electrical properties of dielectric liquids, in: Conf. Record of the 9th Int. Conf. on Conduction and Breakdown in Dielectric Liquids, Salford (1987), pp. 229–233.

47. T. I. Morozov and V. I. Antonov, Experimental research of the influence of oil volume on the electric strength of transformer insulation, Elektrotekhnika, No. 3, 41–43 (1986).

48. W. G. Chadband and T. M. Sufian, Experimental support for a model of positive streamer propagation in liquid insulation, IEEE Trans. El. Insul., **2**, 239–246 (1997).

49. P. Nikolopoulos, Einfluss veschiedener Parameter auf den Durchschlag in Isolierol bei Beanspruchung mit Stoss, ETZ, **A87**, No. 7, 239–244 (1966).

50. J. L. Stankevich and V. G. Kalinin, Influence of the cathode surface state on the electric strength of gaseous and liquid dielectrics, Zh. Tekh. Fiz., **39**, No. 7, 1264–1271 (1969).

51. L. Centurioni, G. Molinari, and A. Viviani, Statistical analysis of the dielectric breakdown in liquid nitrogen under uniform field conditions, in: Proc. of the 5th

Int. Conf. on Conduction and Breakdown in Dielectric Liquids, Delphi (1975), pp. 217–220.

52. M. D. Noskov, V. R. Kukhta, and V. V. Lopatin, A correlation of the electric strength with multifractal charge distributions over the electrode surface, Izv. Vyssh. Uchebn. Zaved., Fiz., No. 11, 96–99 (1993).

53. V. R. Kukhta, V. V. Lopatin, and M. D. Noskov, A correlation of discharge initiation sites with the field nonuniformity on the electrode, Izv. Vyssh. Uchebn. Zaved., Fiz., No. 4, 32–35 (1995).

54. N. K. Kapishnikov and V. Y. Ushakov, Influence of the electrode material on the discharge time lag in liquid dielectrics, Elektr. Obrab. Mater., No. 6, 9–11 (1979).

55. E. E. Golubeva, A. V. Kalenikov, I. P. Kuzhekin, et al., Increase in the electric strength of aqueous insulation, in: Abstracts of Reports at the Third All-Union Conf. on Pulsed Energy Sources, Moscow (1989), pp. 27–28.

56. S. N. Komin and E. A. Morozov, A method of increasing the pulsed electric strength of water, Certificate of Copyright No. 1618292, Bull. No. 48 (1990).

57. R. J. Taylor, Effect of permittivity matching on the flashover of solid/liquid interfaces, Proc. IEEE, **124**, No. 10, 899–904 (1997).

58. Z. C. Hosticka, Dependence of uniform/nonuniform field a transformer oil breakdown on oil composition, IEEE Trans. El., **14**, No. 1, 43–50 (1979).

59. A. A. Vorobjev, V. J. Ushakov, and V. V. Bagin, Electric strength of liquid dielectrics with application of pulsed voltage of nanosecond duration, Elektrotekhnika, No. 7, 55–57 (1971).

60. K. Yoshino, Dependence of dielectric breakdown of liquids on molecular structure, IEEE Trans. El. Insul., **EI15**, No. 3, 186–200 (1980).

61. D. W. Swan and T. J. Lewis, Influence of electrode surface conditions on the electrical strength of liquified gases, J. Electrochem. Soc., **107**, No. 3, 38–43 (1960).

62. B. A. Srebrov, L. P. Dishkova, and F. I. Kuzmanova, Investigation of electric breakdown of a short gap filled with distilled water, Pis'ma Zh. Tekh. Fiz., **16**, No. 2, 66–69 (1990).

63. K. S. Kao and J. B. Higham, The effect of hydrostatic pressure, temperature, and voltage duration on the electric strengths of hydrocarbon liquids, J. Electrochem. Soc., **108**, No. 6, 522–528 (1961).

64. N. S. Rudenko and V. I. Tsvetkov, Investigation of the electric strength of some liquid dielectrics under application of voltage pulses of nanosecond duration, Zh., Tekh. Fiz., **35**, No. 10, 1840–1843 (1965).

65. V. F. Klimkin, On mechanisms to increase electric strength of n-hexane in micron gaps, in: Proc. of the 11th Int. Conf. on Conduction and Breakdown in Dielectric Liquids, Baden Dattwil (1993), pp. 405–409; On a mechanism of increasing the electric strength of n-hexane in micron gaps, Zh. Tekh. Fiz., **63**, No. 5, 127–131 (1993).

66. E. S. Kuchinskii, E. E. Lysakovskii, A. E. Monastyrskii, et al., Electric strength of liquid dielectrics under voltage pulses of microsecond duration, Elektrichestvo, No. 10, 41–44 (1981).

67. J. C. Martin, Nanosecond pulse techniques: Preprint, Aldermoston, Berks (1970).

68. V. J. Ushakov, N. K. Kapishnikov, and V. R. Kukhta, Electric strength of liquids and working strength of insulation gaps of high-voltage pulsed device, in: Impulse Discharge in Dielectric, Nauka, Novosibirsk (1985), pp. 114–134.

69. J. Van Deveder, Water breakdown field strength under exposure to short pulses, in: High-Power Pulsed Systems, Mir, Moscow (1981), pp. 48–55.
70. V. S. Dmitrevskii and G. E. Kurtenkov, Influence of volume on the electric strength of a transformer oil, in: High-Voltage Engineering and Converters, Sverdlovsk (1977), pp. 51–54.
71. I. I. Kalyatskii and V. V. Krivko, Investigation of impulse electric breakdown of water at increased pressures and temperatures, in: Breakdown of Dielectrics and Semiconductors, Energiya, Moscow (1964), pp. 29–39.
72. V. Y. Ushakov, Insulation of High-Voltage Equipment, Springer-Verlag Berlin Heidelberg (2004).
73. V. V. Sokolov, Elaboration of methods increasing the efficiency for diagnostics of insulation state of high-power high-voltage transformers, Candidate's Dissert. In Technical Sciences, Kiev (1982).
74. V. V. Bagin, V. V. Ryumin, and V. Y. Ushakov, Influence of some physical and chemical parameters of liquid hydrocarbons on their nanosecond electric strength, in: High-Voltage Engineering, Publishing House of Tomsk State University, Tomsk (1973), pp. 25–27.

7

Physical Discharge Initiation (Ignition) Mechanisms

A great volume of experimental data on the electric breakdown of liquids that have been accumulated by the present time confirms repeated statements that there are several different breakdown mechanisms that cannot be described in the context of a unified theory.

For the discharge ignition stage, at least four mechanisms of discharge initiation can be identified: 1) *bubble*, 2) *microexplosive*, 3) *ionization*, and 4) *electrothermal*.

In *the first case*, the main role in discharge ignition is played by the gas that has already existed on the electrodes and in the liquid before field application. Ionization inside of gas bubbles results in their deformation and initiation of primary plasma channels. This discharge initiation mechanism is most probably realized in nondegassed liquids for voltage exposure times ranging from units to hundreds of microseconds and at standard or reduced hydrostatic pressure.

For the *microexplosive* discharge initiation, the events develop in the following sequence: electron emission into the liquid (the discharge from cathode) or ionization of liquid molecules (the discharge from anode) – fast local heating of the liquid by the current of induced charge carriers – shock wave generation and propagation – explosive vaporization behind the shock wave front – ionization of gas-vapor bubbles – initiation of a plasma channel. The main condition for realization of this discharge initiation mechanism is the high field strength near the electrode that can be achieved for nanosecond voltage pulse durations. Among the factors favorable for the realization of this discharge initiation mechanism are also a small tip radius of the initiating electrode (from units to tens of microns) and small (submillimeter) interelectrode distance.

The *ionization* discharge initiation mechanism implies the origin of the plasma channel due to autoionization of liquid molecules (anode initiation) or collision ionization (cathode initiation). In this case, energy liberation, first-order phase transition, and shock wave generation are among the secondary processes. The conditions for realization of this discharge initiation mechanism

are even more stringent than in the previous case: extremely high electric field strengths (more than 10^7 V/cm) and very short voltage pulses (10^{-8} s and shorter). In this case, the field strength is sufficient for ionization of liquid molecules, but the exposure time is insufficient for the first-order phase transition. The realization of this discharge type is favored by the increased hydrostatic pressure.

By the *electrothermal* discharge initiation mechanism is meant the following sequence of phenomena: high-voltage conduction current running under the effect of the electric field – heating up of the liquid in the near-electrode regions with maximum field strength – boiling up of the liquid – ionization of vapor-gas cavities – formation of a plasma channel.

This mechanism can be realized at large values of the product of the electrical conductivity of the liquid (γ) into the voltage pulse duration (τ). Since for pulsed voltages τ does not exceed several hundreds of microseconds, this initiation mechanism is most probable for liquids with large γ values, primarily for electrolytes.

According to the above-described classification and the logic prompted by the nature of the phenomenon itself, we now try to describe quantitatively the pre-discharge and discharge processes (some insight into which have already been gained by us or other researchers) or restrict ourselves to their physical interpretation. Exception is the electrothermal mechanism of the discharge ignition and propagation for which we only estimate the conditions of realization in Sect. 8.5. We have already presented experimental data on the electrothermal discharge in high-conducting liquids (in Sect. 4.2.4) and on the liquid electric strengths (Sect. 6.5.2).

This is explained by the fact that the authors of the monograph virtually did not investigate the electrothermal breakdown of liquids. We are not aware of the corresponding publications over the last 15–20 years. The computational models and experimental data were published previously (see References to the Foreword and Chaps. 4 and 6).

7.1 Bubble Discharge Initiation Mechanism

The significant dependence of the electric strength on the external pressure observed under a certain combination of breakdown conditions (see Chap. 6) gave us grounds to assume the important role of gases in liquid breakdowns. Physical models have been developed based on the processes describing the evolution of the gas already existed in the liquid or produced under the effect of the electric field. They considered the liquid breakdown under long-term exposure to dc or ac voltages. This approach to the pulsed breakdown caused serious objections mainly for three reasons:

1) Pulsed electric strength for a wide range of experimental conditions was independent of the pressure (Chap. 6).

2) The processes of gas bubble nucleation and evolution were considered slow with their time constants exceeding the applied voltage pulse duration.
3) There were no direct observations of gas bubbles in the process of discharge ignition and propagation.

These observations started when modern equipment with high spatial and temporal resolution and high optical sensitivity came into being. For example, the phenomenon described in [1–4] and called in [4] the electrode positive slow streamer that was observed under conditions when neither thermal nor hydrodynamic effects were realized could be identified with evolution of gas bubbles that have already existed in the liquid and on the electrode before electric field application.

Experimental data on the electric strength (Chap. 6) and space and time discharge characteristics (Chap. 3) versus the hydrostatic P enable one to determine even approximately the conditions under which the adsorbed and absorbed gas plays the important role in the breakdown initiation.

7.1.1 Physical Model of Discharge Initiation

The model developed by us was first briefly described in [5] and then in [6]. We consider that bubbles with sizes from units to tens of microns exist in the liquid mainly on the electrodes. Ionization processes (partial discharges) are initiated inside the bubble under the effect of the electric field once the voltage drop across the bubble has reached U_d. After the discharge, the electric field in the bubble decreases due to external field shielding by the attached charges. This results in the attenuation or termination of the ionization processes. The effect of the electric field on the attached charge results in bubble elongation along the field as well as in charge penetration into the liquids with the velocity determined by the mobility of charge carriers. In this case, two situations can be realized: sustained glow discharge or discharge termination [7].

In the first case, the voltage on the bubble obeys the Paschen law. In the second case, the voltage on the bubble increases, thereby resulting in a repeated discharge and motion of a new charge wave through the liquid. The determining parameter – the pressure on the bubble wall – is caused by the effect of the Coulomb forces on the injected and surface charges and the pressure increase inside the bubble due to gas heating. The discharge will be ignited in the liquid when the electric field strength near the bubble pole reaches the critical value.

The discharge will be initiated inside the bubble if electrons are generated by any mechanism. For long-term dc voltage exposure, the number of initial electrons is not so important, because by the breakdown voltage is meant the voltage at which the breakdown will ever be initiated, irrespective of the probability of generation and time of occurrence of the initial electrons. Under pulsed voltage exposure, the moment of generation of the initial electron is important, because it determines the moment of the discharge ignition. In this

case, the discharge time lag due to generation of the initial electron can be estimated from the expression [8]

$$t_{\text{lag}} = 1/\left[w\left(dn_e/dt\right)\right], \qquad (7.1)$$

where w is the probability that the avalanche initiated by the initial electron will cause a discharge in the bubble, and dn_e/dt is the number of initial electrons generated every $1\,\text{s}$. The w value can be set equal to unity, since electric fields inside the bubbles are strong enough in comparison with those characteristic of the conventional gas discharges. The number of initial electrons depends very strongly on the external conditions, and their contribution will be determining.

The estimate of charge carriers produced inside the bubbles under the action of cosmic ionized radiation demonstrates that t_{lag} can exceed several years under conditions of electrophysical experiments. Obviously, it cannot be responsible for the occurrence of free electrons inside the gas bubbles under the examined conditions. According to the modern concept, the most probable mechanism of electron generation is the decomposition of negative ions under the action of the temperature, electric field, and collisions with neutral gas molecules [9]. It can be demonstrated that the presence of negative ions inside the microbubbles is improbable even in the case of polar liquids. For the gas discharge it is assumed that ions can be produced as a result of desorption from the surface of electronegative molecules. Water and oxygen are the most frequent electronegative impurities for the breakdown of liquid dielectrics.

The mechanism of negative ion decomposition can be connected with the effect of the electric field. The estimated time of ion decomposition with allowance for the Schottky effect is units of microseconds. Still smaller decomposition times are characteristic of collisions of negative ions with neutral molecules, for example, in the reaction $O^- + N_2 \leftrightarrow N_2O + e$. The constants of these reactions have the order of 10^{-10}–$10^{-12}\,\text{cm}^3/\text{s}$. This means that at atmospheric pressure, electrons become free in units of nanosecond or several fractions of a nanosecond.

Thus, a comparison between the conditions of discharge ignition inside the bubbles located in the liquid volume and on the electrode suggests that the discharge will be initiated inside the bubble adjacent to the electrode. On the other hand, the analysis of generation of the initiating electrons demonstrates the important role of liquid degassing and electrodes in the discharge ignition.

We now consider in more detail a possible mechanism of microbubble breakdown. We assume that the breakdown is initiated in air at the characteristic values of the field strength ($100\,\text{kV/cm}$–$1\,\text{MV/cm}$). The pressure inside the bubble can be considered atmospheric. Then from the similarity law we can estimate E/p; we will use the system of units used in the gas breakdown, namely, V/cm for E and Torr for p, with $E/p \approx 100$–$1000\,\text{V}/(\text{cm} \cdot \text{Torr})$. It is well known [9] that for $E/p \approx 100$–$800\,\text{V}/(\text{cm} \cdot \text{Torr})$, the impact ionization coefficient α is well approximated by the expression

$$\alpha/p = A \cdot \exp\left[-B/\left(E/p\right)\right], \tag{7.2}$$

where $A = 15\,(\text{cm·Torr})^{-1}$ and $B = 365\,\text{V}/(\text{cm·Torr})$. Estimates based on this expression demonstrate that α ranges approximately from 700 to $8000\,\text{cm}^{-1}$. The determining parameter of the breakdown mechanism is the αd value which characterizes the number of electrons formed in the avalanche and the probability of avalanche conversion into a streamer. According to our estimates, $\alpha d \approx 2-3$ for microbubbles with diameter d ranging from a micron to tens of microns; this is much smaller than 18–20 characteristic of the avalanche-streamer transition. This means that the breakdown inside the microbubble should obey the Townsend mechanism. The breakdown criterion here is the condition

$$\gamma \cdot \left(e^{\alpha d} - 1\right) = 1, \tag{7.3}$$

where γ is the secondary impact ionization coefficient determining the occurrence of secondary avalanches initiated inside the bubble by photons or positive ions. This expression describes the Paschen curve [10] $U = f\left(p \cdot d\right)$ or in the other form $E/p = f\left(p \cdot d\right)$. From the Paschen curve, by inversion of (7.3), we obtain the coefficient $\gamma = 1/\left(e^{\alpha d} - 1\right)$. When the voltage on the bubble lies above the Paschen curve, at least two effective electrons are generated by a single avalanche, that is, the electron multiplication coefficient will be

$$\beta = \gamma\left(e^{\alpha d} - 1\right) > 1. \tag{7.4}$$

From here we can estimate the bubble breakdown time lag connected to the coefficient γ and the time of ion drift through the gap [10]:

$$\tau = 2 \cdot r/\left[b \cdot E\left(\beta - 1\right)\right]. \tag{7.5}$$

Here b is the ion mobility inside the bubble. Knowing the character of the dependence of the impact ionization coefficient on the electric field strength and taking into account that $\beta = 1$ on the Paschen curve and that the breakdown time lag is equal to ∞, we can estimate the bubble breakdown time lag given that the voltage exceeds only insignificantly the value specified by the Paschen curve. We take advantage of the typical procedure for calculating changes in the function β in the vicinity of 1 when the electric field strength increases from E_0 to E:

$$\beta \approx \beta(E_0) + \frac{\partial \beta}{\partial E}(E - E_0). \tag{7.6}$$

Calculating the derivative of β with respect to E from expressions determining β and α, we obtain

$$\beta \approx 1 + \frac{\alpha \cdot d}{\gamma} \cdot \frac{B \cdot p}{E} \cdot \frac{\Delta E}{E}. \tag{7.7}$$

Substituting concrete values of the parameters, we obtain, for example, that $\beta - 1 \approx 13 \cdot \Delta E/E$ for an electric field strength of $100\,\text{kV/cm}$ and

$\beta - 1 \approx 66 \cdot \Delta E/E$ for an electric field strength of $200\,\text{kV/cm}$. This means that when the electric field strength exceeds by 10% the value specified by the Paschen curve, the bubble breakdown time lag will be negligibly small compared to the characteristic values of the breakdown time lag. We now estimate τ for an electric field strength of $100\,\text{kV/cm}$ and a 20-μm bubble. Setting the mobility $b \sim 1\,\text{cm}^2/(\text{V·s})$ and neglecting the field gain inside the bubble, we obtain that the breakdown time lag is equal to $2\,\text{ns}$. These considerations remain valid for bubbles with smaller size. We can also neglect the microbubble breakdown time lag.

To estimate the effect of discharges on the bubbles, we consider that the discharges are initiated when the voltage on the gas inclusion reaches a certain value U_d that depends on the product of the pressure inside the bubble P into the bubble diameter $d = 2r$. The Coulomb force acting on the attached charge during the bubble breakdown results in the displacement of the bubble wall and the detachment of the charge carriers from the wall. All this results in an increase in the voltage drop across the bubble, repeated breakdowns, increase in the Coulomb force, and further displacement of the wall.

It should be noted that after the discharge initiation inside the bubble, electrons penetrate into the liquid from the side facing the anode, and positive ions interact with the surface from the opposite side. Clearly, electrons and ions interact differently with liquid molecules. Apparently, ions should be attached to the surface, while electrons should penetrate deeper into the liquids and after thermalization, move according to their mobility. Therefore, the partial discharge (PD) inside the bubbles located on the electrodes should have different consequences for the bubble.

Let us estimate the force acting on the bubble wall after the partial discharge inside the bubble considering that the spherical bubble is discharged thereby charging the walls:

$$F = \frac{\int \sigma \cdot E \cdot ds}{2}. \tag{7.8}$$

From here we obtain the average pressure on the bubble wall: $P_\sigma = \varepsilon_0 \varepsilon E^2/2$, and the maximum pressure near the bubble pole: $P_{\max} = 3P_\sigma$.

Another component of the pressure acting on the wall results from the gas heating. Its amplitude can be compared with the Coulomb component; however, it can be easily demonstrated that the thermal conductivity and heat capacity of the liquid provide fast heat carrying away, and this component has less of an effect on the growth of the pre-breakdown bubbles.

One of the most complex points of the model is the character of the discharge inside the bubble. It is well known that the partial discharge in a gas inclusion into a solid dielectric results in charging of the inclusion walls and discharge termination. A repeated discharge can be initiated only when the voltage will be changed or the surface charge will be dissipated. Inside the bubble located in the liquid, the discharge can occur periodically or exist

quasi-stationary due to motion of charges arising in the liquid and on the bubble walls.

The periodic discharge inside the bubble is terminated once the bubble walls have been charged by the attached charges. The repeated discharge occurs only after restoration of the voltage on bubble. Here it is important to estimate the number of breakdowns within the time over which the pulse acts. It seems impossible to solve this problem analytically; therefore, we restrict ourselves to a physical estimate. In the zero-order approximation we can consider that the voltage on the bubble will be restored when charges in the liquids pass the characteristic distance $x \sim r$. Then the number of partial discharges within the time τ over which the pulse acts will be $N \approx \mu E \tau / r + 1$, where μ is the hydrodynamic mobility which takes into account the motion of both charge carriers and bubble walls: $\mu \approx (\varepsilon_0 \varepsilon / \rho)^{1/2} / 3$ [11]. The charge carriers injected into the liquid after each discharge move in it in separate layers. The forces acting on each layer are approximately identical; the total equivalent pressure exerted on the bubble wall can be obtained if we increase N folds the pressure generated after a single partial discharge:

$$P = 3\varepsilon_0 \varepsilon E^2 \left(\mu E \tau / r + 1 \right) / 2. \tag{7.9}$$

The bubble size r plays the important role in (7.9). It is of interest that a decrease in r should increase the pressure on the bubble wall, causing its stronger deformation and hence reducing the discharge ignition time lag. The least bubble size at which the discharge is still initiated is observed when the voltage drop across the bubble is equal to U_d. Therefore, the most dangerous from the viewpoint of electric breakdown is the bubble with the critical size

$$r_{cr} = U_d \left(2\varepsilon + 1 \right) / 6\varepsilon E. \tag{7.10}$$

For carefully degassed liquids, when bubbles of such sizes cannot be present near the electrodes, the discharge ignition time lag will increase. However, no abrupt qualitative changes in the electric strength are expected until bubble micronucleation centers are present in the liquid. Their sizes can reach the breakdown values in very short times $t \approx \left(10^{-9} - 10^{-8} \right)$ s, for example, due to near-electrode liquid stressed at the expense of injection of charges from the double electric layer. Neglecting the time of bubble growth to the breakdown size, we assume that bubbles with sizes close to r_{cr} always exist near the electrodes. Therefore, we substitute r_{cr} in (7.9) for the unknown r and obtain the expression for the average pressure on the bubble wall:

$$P_{p.d} = \frac{3\varepsilon_0 \cdot \varepsilon \cdot E^2}{2} \left(\frac{6\varepsilon \cdot \mu \cdot E^2 \cdot t}{U_d \cdot (2\varepsilon + 1)} + 1 \right). \tag{7.11}$$

For a *quasi-stationary* discharge inside the bubble, the discharge current should be maintained by the conduction current at the expense of motion of the charged bubble wall or injected or intrinsic ions. According to [13], the

multiavalanche gas discharge in the gas gap can be maintained by low enough currents $I \approx 10^{-10}$ A approximately equal to currents inside the bubbles. Here we can consider two limiting cases: a) charges move inside the liquid and do not interact with the bubble wall and b) charges are attached to the bubble wall and move only with the wall. It seems likely that pressure values for mobile charges are close to those described by (7.11). For the attached charge, the pressure on the bubble wall will rise in the process of bubble deformation in full conformity with (7.10). Moreover, bubble lengthening causes the field amplification in the vicinity of the bubble pole, thereby increasing the pressure on the bubble wall and causing its further deformation. For the equivalent pressure, the approximate expression

$$P_{\text{p.d}} = \frac{\varepsilon_0 \varepsilon \cdot (K \cdot E)^2}{6} \tag{7.12}$$

was derived, where K is the field gain (see below). We note that (7.12) is transformed into (7.11) for a spherical bubble.

To derive final expressions suitable for an analysis of the experimental data on liquid breakdowns and their comparison with the results of calculations for the given model, we now consider the bubble dynamics. In so doing, we consider the heat and mass exchange processes in the simplified form, in particular, disregarding the nonequilibrium character of evaporation and Joule heat liberation considered in [12]. In addition, we also neglect the bubble asperity considering that the pressure $P_{\text{p.d}}$ acts on the bubble wall. The equation of bubble wall motion in this case can be written by analogy with the well-known Rayleigh equation of bubble wall motion under the action of the pressure difference:

$$R\frac{d^2 R}{dt^2} + \frac{3}{2}\left(\frac{dR}{dt}\right)^2 + \frac{4 \cdot \eta}{\rho \cdot R}\frac{dR}{dt} + \frac{2 \cdot \sigma}{\rho \cdot R} = \frac{1}{\rho}\left(P_{\text{p.d}} + P_{\text{s}} - P_{\text{out}}\right). \tag{7.13}$$

Here η is the viscosity of the liquid, σ is the surface tension coefficient, P_{s} is the saturated vapor pressure, and P_{out} is the external pressure. Equation (7.13) is the main equation of the model. It can be used to calculate by numerical methods the bubble growth under the effect of the discharge initiated inside it, to obtain a dependence of the time of bubble growth on the external conditions and properties of the liquid for various bubbles located in the liquid and on the electrodes. In the particular case, an analytical solution can be obtained. It describes the evolution either of the bubble with a framework from surface-active molecules or (more roughly) of the bubble put in a nonwettable pore under exposure to rectangular voltage pulses with approximate allowance for the pressure exerted by the electric field on the bubble [13], electrostriction pressure [14], viscosity, and surface tension:

$$\Delta P_E \approx \frac{3\varepsilon_0 \left(\varepsilon - 1\right)\varepsilon \cdot E^2}{2\left(2\varepsilon + 1\right)}, \Delta P_{\text{str}} = \varepsilon_0 \rho \frac{\partial \varepsilon}{\partial \rho} \frac{E^2}{2}, P_\eta \approx \frac{4\eta \cdot \mu \cdot E}{R}, P_\sigma \approx \frac{2\sigma \cdot R}{r_0{}^2}.$$

When $\left(P_{\mathrm{out}} - P_{\mathrm{s}} - \dfrac{3\varepsilon_0\varepsilon \cdot E^2}{2} + \Delta P_e - \Delta P_\eta + P_\sigma \right) \geq 0,$

$$t_2 = \frac{(2\varepsilon + 1)\,\rho \cdot U_{\mathrm{d}}}{6\varepsilon_0\varepsilon^2\mu \cdot E^4} \left\{ \frac{9\varepsilon_0\varepsilon^2 E^4}{(2\varepsilon + 1)\,U_{\mathrm{d}}} \left(R - \frac{(2\varepsilon + 1)U_{\mathrm{d}}}{6\varepsilon \cdot E} \right) \right\}^{2/3}. \qquad (7.14)$$

For the inverse inequality,

$$\begin{aligned} t_2 = {} & \frac{(2\varepsilon + 1)\,\rho \cdot U_{\mathrm{d}}}{6\varepsilon_0\varepsilon^2\mu \cdot E^4} \left[\left(\frac{9\varepsilon_0\varepsilon^2 E^4}{(2\varepsilon + 1)\,U_{\mathrm{d}}} \left(R - \frac{(2\varepsilon + 1)U_{\mathrm{d}}}{6\varepsilon \cdot E} \right) \right)^{\frac{2}{3}} \right. \\ & \left. + \frac{2}{3\rho} \left(P_{\mathrm{out}} - P_s - \frac{3\varepsilon_0\varepsilon \cdot E^2}{2} + \Delta P_e + \Delta P_\eta + P_\sigma \right) \right]. \end{aligned}$$

Equations (7.14) specifie the dependence of the bubble deformation time on the external factors.

In the process of bubble elongation, the discharge will penetrate into the liquid phase. If we consider that the bubble after the discharge is transformed into a conducting ellipsoid of rotation with the ratio of semiaxes R/r_{cr}, the electric field at the bubble poles will be amplified: $E = E_0 K$. In principle, the bubble can have another shape, for example, it can be shaped as a cylinder or a quasi-cone with an end hemisphere. For all these cases, the field gain will fast increase with increasing ratio of the longitudinal to transverse bubble sizes. There is no principal difference between these variants, and for definiteness, below we consider the bubble shaped as an ellipsoid. Clearly, the field cannot increase infinitely, because the ionization processes will start in the liquid as well. As a criterion for the discharge ignition in the liquid, we consider the achievement of a certain critical field strength estimated from above by the value $E_{\mathrm{max}} \sim 10^8$ V/cm. Both avalanche electron multiplication and autoionization of liquid molecules can occur at this electric field strength. Obviously, the actual discharge will be initiated at lower electric field strengths. In calculations, E_{max} was taken from the range 10^7–10^8 V/cm.

Thus, based on the analysis of bubble existence in the liquid and their behavior under the effect of a strong electric field, we have suggested the discharge initiation mechanism in nondegassed liquids. It involves the discharge initiation inside the bubble once the critical voltage has been achieved, bubble deformation by the Coulomb forces, field amplification at the bubble poles, and discharge penetration into the liquid once the electric field strength has achieved the critical value. Since the degree of deformation depends on the external conditions and the properties of the liquid and interface, the model discharge ignition parameters (E_{ign}, U_{ign}, and t_{ign}) will also depend on these parameters. When the breakdown is determined mainly by the first stage, that is, by the discharge ignition, the model can be used to establish relationships of the electric strength with these parameters.

7.1.2 Comparison with Experimental Results

The electric breakdown in a uniform or weakly nonuniform electric field inevitably occurs after the discharge ignition which is the necessary and sufficient breakdown condition. Hence the stage of discharge propagation (formation) with the discharge formation time lag $t_{d.f}$ (the time over which the discharge channel crosses the gap), which is determined by the gap length d and the average channel propagation velocity V_d: $t_{d.f} = d/V_d$, is taken into account only as the additional component of the total discharge time lag. The final expression for the discharge time lag is then the sum of three components: $t_{lag} = t_1 + t_{cr} + t_{d.f}$, where t_1 is the time of bubble growth from the nucleus to the minimum size at which partial discharges arise, t_{cr} is the time of bubble growth to the critical size, and $t_{d.f}$ is the time of discharge propagation. In this case, $t_1 = 0$ when microbubbles are present on the electrodes, $t_{d.f}$ is small for short interelectrode distances, and t_{cr} gives the greatest contribution under experimental conditions. This allows us to neglect the other two components of the discharge time lag in calculations of the pulsed electric strength under above-indicated conditions.

It is obvious that a satisfactory agreement between the calculated and experimental dependences will enable us to demonstrate the role of bubbles in the breakdown, to refine the model parameters, and to estimate its applicability limits. Since above expressions (7.14) involve such parameters as external pressure, voltage exposure time, permittivity, density of the liquid, saturated vapor pressure, and viscosity, it is expedient to consider empirical dependences for which the effect of these parameters would be clearly pronounced. This primary concerns the experimental dependences of the electric strength on the *voltage pulse duration* and *external pressure.*

Since bubbles can have different shapes, several variants of the model must be examined to compare the theory with the experiment. The simplest case to be analyzed is an incompressible (but growing) bubble for which we can derive an analytical expression. Straightforward calculations from formulas (7.14) call for the determination of a single parameter E_{max} that characterizes the properties of the concrete liquid. This parameter can be adjusted by means of comparison of the calculated and empirical voltage-time dependences. The comparison makes sense for exposure times from several tenth of a microsecond to several tens of microseconds for which the bubble discharge ignition mechanism is most probable.

Figure 7.1 shows the discharge time lags calculated for E_{max} ranging from 5 to 85 MV/cm. It can be seen that the change in E_{max} in wide limits influences only slightly the voltage-time characteristic. If we chose the dependence in the form $1/t^n$ suggested by Martin in [64], the exponent n of t will change in narrow limits from 0.27 for $E_{max} = 5$ MV/cm to 0.31 for $E_{max} = 85$ MV/cm. If we chose E_{max} based on this exponent, the best value will be 85 MV/cm. If we chose the electric strength value for the 1-μs point [the analog of the constant in the numerator of (6.5)], we obtain $E_{max} = 5$ MV/cm. Below in calculations
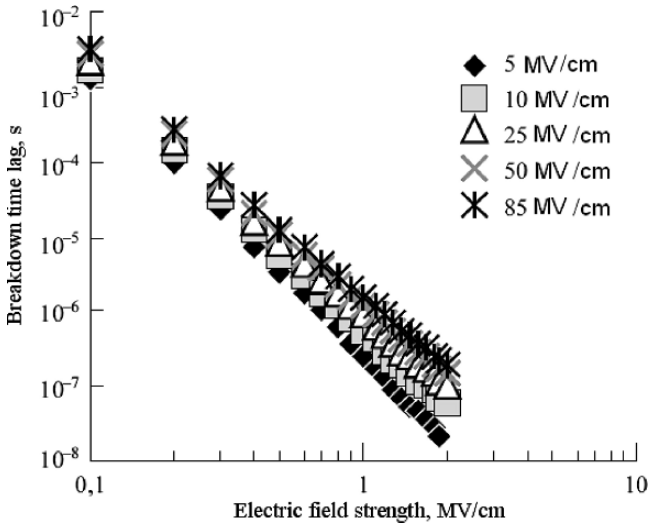
Fig. 7.1. Voltage-time dependence for hexane and the indicated values of the parameter E_{max}

we use $10\,\mathrm{MV/cm}$ for the critical field strength. More recently [66], this value was called the most probable discharge ignition field strength according to measurements and calculation estimates.

One more variant of the bubble, namely, a compressible bubble, is more realistic. In addition, this approach allows the breakdown dependences to be calculated for bubbles of different sizes rather than only for bubbles of critical sizes. In this variant, the second-order basic differential equation is solved. Calculations were carried out using the specially developed computer code *Bubbreak* that implements the Runge–Kutta–Merson method [20]. It is of interest to calculate the pulsed electric strength of large bubbles to show that they increase the discharge ignition time lag. Calculations were performed for bubbles with double and triple critical (most dangerous) radius in hexane. Figure 7.2 shows the calculated results. It can be seen that in weak electric fields (long exposure times), curves for bubbles of different sizes almost merge. In submicrosecond range, the most dangerous bubble results in a much smaller breakdown time lag.

One more point of the model that must be refined is the assumption that the transverse size of the bubble that grows along the field direction remains unchanged. In fact, it can decrease, since the deforming force acts in the field direction and causes the bubble to elongate in this direction; weak collapse forces caused by the external pressure and surface tension act on the bubble in the transverse direction. Therefore, the bubble can decrease its transverse size. In calculations, two limiting variants were examined: $V = \mathrm{const}$, that is, the bubble volume remains unchanged in the process of its elongation, and
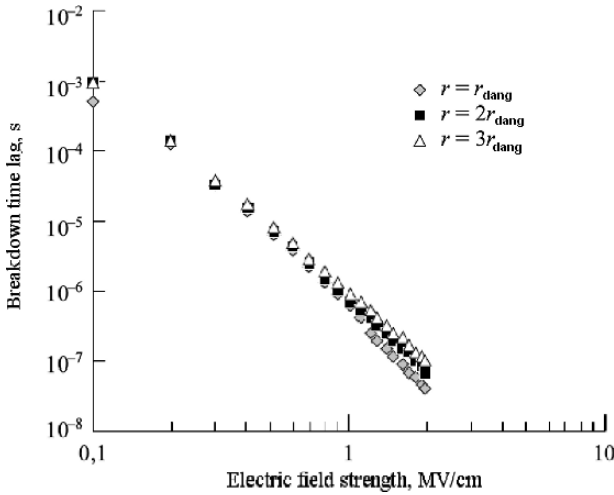
Fig. 7.2. Calculated voltage-time characteristic for the initiating bubbles with the indicated sizes

R_{tr} = const, that is, the transverse bubble size remains unchanged when the bubble is elongated. Figure 7.3 shows the calculated results. It can be seen that the form of the dependences remains essentially unchanged. Only for V = const the electric strength is smaller and the exponent of the power-law dependence reaches 0.33. However, in this case the dependence of the
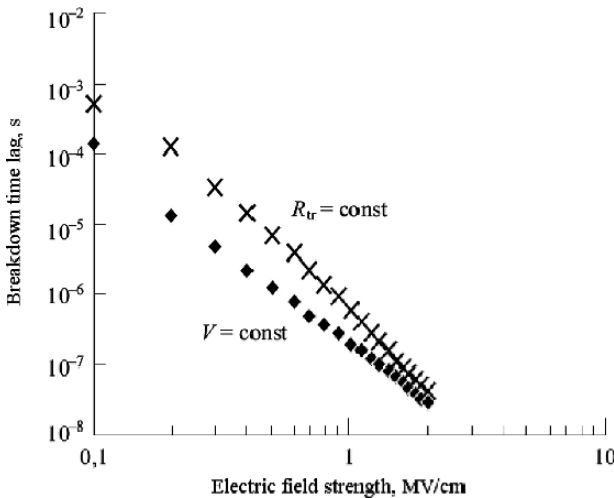
Fig. 7.3. Variants of bubble deformation at constant volume and constant transverse size

electric strength on the external pressure must disappear, which contradicts the available experimental data. In calculations below, we take $R_{tr} = $ const.

It is of interest to calculate the voltage-time dependences for different liquids with permittivity and viscosity changing in wide limits. Figure 7.4 shows the calculated dependences for the indicated liquids with different electrophysical characteristics. For calculations, we take $R_{tr} = $ const and $E_{max} = 10^7 \, \text{V/cm}$ for water, hexane, and glycerin and $E_{max} = 2 \cdot 10^7 \, \text{V/cm}$ for ethanol.

It can be seen that all voltage-time dependences follow the dependence $E \sim t^{-n}$, where $n = 0.33$ for water and ethanol, 0.29 for hexane, and 0.4 for glycerin. An explicit dependence of the electric strength of liquids on the permittivity and viscosity is also observed. If we exclude glycerin from our analysis, from Fig. 7.4 it can be seen that a lower electric strength is observed for a higher permittivity (see Sect. 6.5). For glycerin, its extremely high viscosity precludes the bubble growth and deformation, from which it follows that the required degree of deformation for identical voltage exposure times can be obtained only in stronger fields. In addition, this results in a stronger effect of the voltage pulse duration on the breakdown field strength E_{br}. We note that according to the calculated results, for viscous liquids like glycerin and hexachlorodiphenyl, the temperature dependence of the viscosity results in the temperature dependence of the pulsed electric strength. For low-viscosity liquids, the dependence $E_{br}(T)$ is pronounced only near the boiling point where $P_s \sim P_{out}$.

For water breakdown, the results calculated by the Martin empirical formula [64] (with the electrode area $S = 1 \, \text{cm}^2$) were compared with the theoretical dependence. Here $E_{max} = 10 \, \text{MV/cm}$ was chosen for the critical field
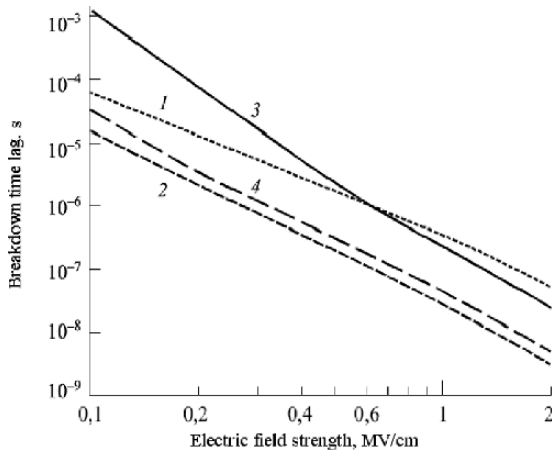
Fig. 7.4. Calculated voltage-time dependences for glycerin (*curve 1*), water (*curve 2*), hexane (*curve 3*), and ethanol (*curve 4*)

strength. The calculated and empirical dependences almost merge, though numerical coincidence must be considered occasional, since the electrode sizes were not taken into account in the model.

The voltage-time dependences differ for different pressures, in particular, in weak electric fields (large t). In strong electric fields, the curves almost merge (calculations were carried out for n-hexane at $P = 1$–100 atm).

The data [15] on the pressure dependence of the pulsed electric strength for various liquids demonstrate that the for liquefied noble gases of xenon type, it is not manifested for pressures up to 15 atm irrespective of the pulse exposure times. At the same time, in the case of breakdown of liquid nitrogen, an explicit dependence is observed for both microsecond ($t = 6\,\mu s$) and nanosecond pulses ($t = 100\,\text{ns}$); the dependence is weakened as the exposure time decreases. Gray circles in Fig. 7.5 show these special features of the breakdown of liquid nitrogen. Calculations were carried out for the following parameters. The breakdown bubble voltage was increased to $1{,}000\,\text{V}$ because of the increase in the gas bubble density at a liquefied nitrogen temperature of $88\,\text{K}$. The critical field was also increased to $20\,\text{MV/cm}$. Solid curves in Fig. 7.5 show the calculated results, symbols denote the results borrowed from [15]. A comparison of the data demonstrates that all experimental features are presented in the computational model.

Experiments [16] on hexane breakdown in a uniform field with registration of the breakdown time lag demonstrated that the normalized breakdown time lag, that is, $t(P)/t(1\,\text{atm})$ depends almost linearly on the pressure increasing from 1 to 15 atm. Figure 7.6 shows experimental data for electric fields of 1.3 and $1.9\,\text{MV/cm}$. Calculated results for these fields are also shown here by continuous curves. It can be seen that calculations yield the dependences close to linear and are in good agreement with the experimental data.
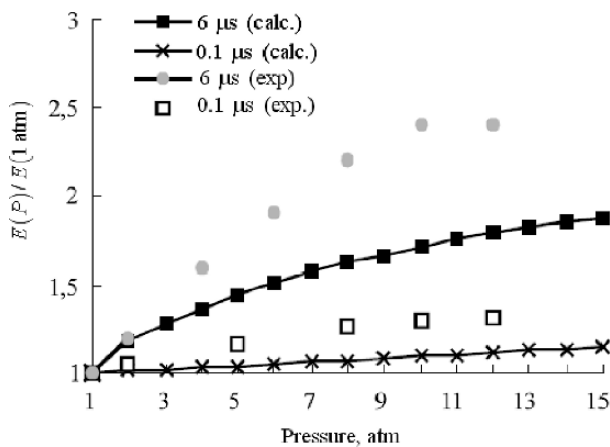
Fig. 7.5. Dependence of the normalized electric strength on the pressure for liquid nitrogen under exposure to 6- and 0.1-μs pulses
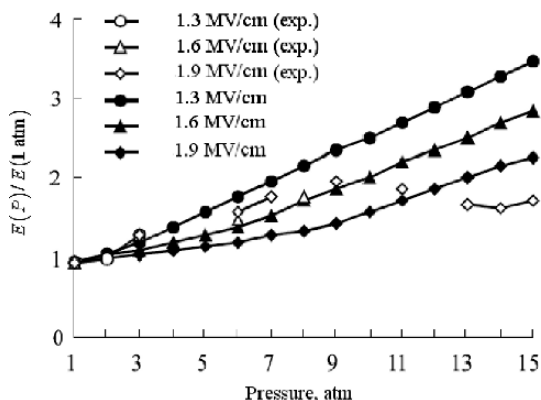
Fig. 7.6. Dependence of the normalized breakdown time lag for hexane on the pressure for electric field strengths of 1.3, 1.6, and 1.9 MV/cm

Of great interest for model verification is a comparison of experimental data on liquid breakdowns for oblique pulses, because for linearly increasing pressure, the breakdown of large bubbles occurs at the beginning of pulse application, and in the process of field strength increase, breakdowns occur in smaller and smaller bubbles. The bubble of intermediate sizes should have a minimum discharge ignition time, and the size of the most dangerous bubble will depend on the pulse slope. Figure 7.7 shows the discharge ignition times calculated for the most dangerous bubbles in hexane at pressures of 1 (open diamond) and 15 atm (open squares).
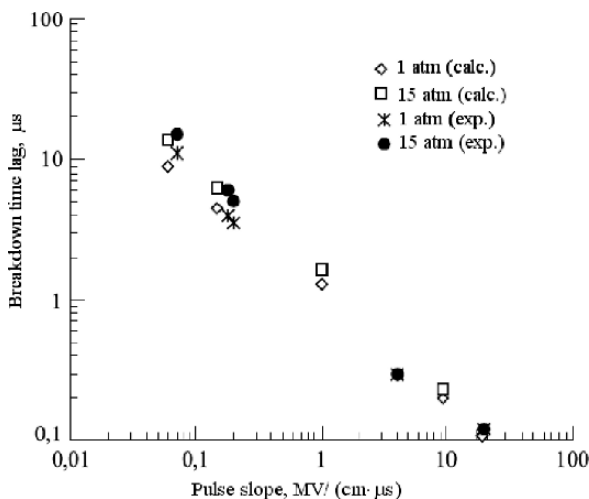
Fig. 7.7. Breakdown time lag for hexane and oblique wave at pressures of 1 and 15 atm

To carry out calculations, a subroutine for calculation of the dynamics of bubbles of different sizes was specially added to the computer code *Bubbreak*. Results of calculation were compared with the experimental data presented in [17] for *n*-hexane under exposure to pulses with slopes increasing from 0.05 to 20 MV/(cm · μs) that approximately correspond to the left branch of the voltage-time characteristic starting from the point of minimum (Figs. 6.3 and 6.4). The pressure in the liquid was atmospheric or increased approximately to 15 atm. It was demonstrated that for low rates of voltage increase, the discharge time lag depends strongly on the pressure, whereas it was independent of the pressure for high rates of voltage increase. From Fig. 7.7 it can be seen that the experimental data obtained at pressures of 1 (crosses) and 15 atm (closed circles) merge when the slope of the voltage pulse exceeds 4 MV/(cm · μs). The calculated results are in fairly good agreement with the experimental data; moreover, at high rates of voltage increase, the difference in the breakdown time lags was within the limits of the experimental data scatter and hence indistinguishable.

The effect of polarity on the discharge ignition for the bubble mechanism can be explained by two reasons.

According to [7], a cathode bubble breaks down as a result of a conventional partial discharge, and a quasi-stationary discharge is initiated in an anode bubble due to attachment of positive ions to the bubble wall and the wall motion. Figure 7.8 shows the results calculated for this case with the indicated values of E_{max}.

As already indicated above, the electric field strengths near the electrodes can differ from those calculated for the given electrode geometry. This is due to emission of charge carriers and double electric layers. These phenomena are
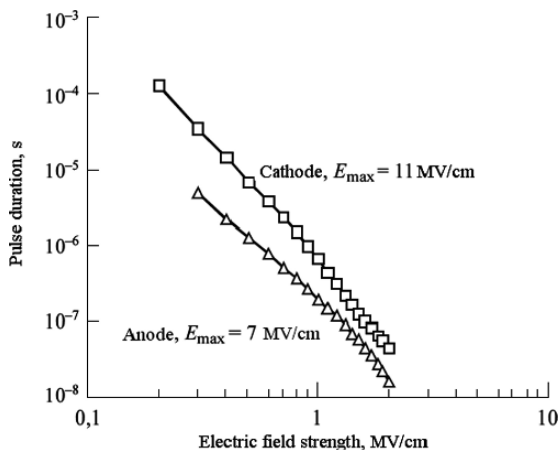
Fig. 7.8. Effect of polarity for hexane at the expense of different critical field strengths and different mechanisms of charge carrier interaction with the bubble surface

typically observed for polar liquids, and emission from cathode is dominant. Therefore, the conditions of discharge ignition are different in the space charge region near the cathode and in the geometrical field region near the anode. On the one hand, the Coulomb forces acting in the space charge region reduce the external pressure; therefore, this factor promotes the bubble growth and breakdown. On the other hand, the lower field strength decreases the intensity of discharges and hence the bubble deformation and precludes the discharge ignition. Electrode shielding was modeled in calculations by a decrease in the electric field strength near the electrode to the value of the emission strength. Results of calculations for water with non-emitting (analog of the discharge from anode) and emitting electrodes and electric field strengths of 0.2 and 0.3 MV/cm are shown in Fig. 7.9. The experimental data on the breakdown of water obtained in [18] with diffusion electrodes (see Sect. 6.5.3) are also shown in the figure. Curve *4* is for the discharge ignition from anode, and curve *5* is for the discharge ignition from cathode. A comparison of the dependences shown in the figure demonstrates that the curve for the discharge from anode is close to curve *1*, whereas the curve for the discharge from cathode has the same slope as the curve for the partially shielded electrode.

One more special feature of the polarity effect should be indicated, namely, that the dependence of the electric strength on the pressure for the discharge ignition from cathode is stronger than for the discharge ignition from anode (see [19] and Sect. 6.3). This fact can be easily explained with allowance for partial electrode shielding, since the hydrostatic pressure acts more strongly on the bubble in the attenuated near-electrode field. For high degree of shielding, the dependence tends to $E_{br} \sim p^{1/2}$.
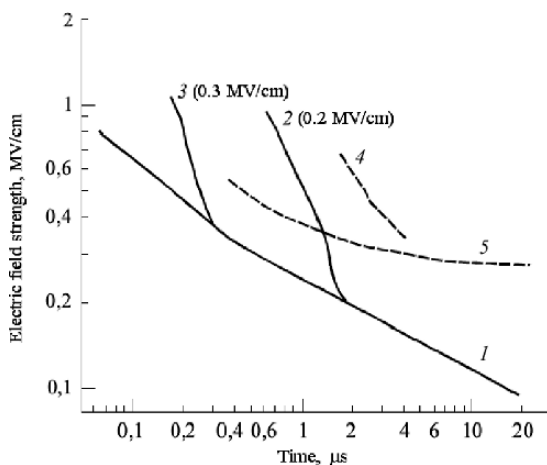
Fig. 7.9. Voltage-time characteristics of water calculated without (*curve 1*) and with emission (*curves 2* and *3*) and experimental dependences for the breakdown from anode (*curve 4*) and cathode (*curve 5*)

The dependence of the electric field strength on the *electrode area* is explained by the statistical character of weak elements of the electrode surface; the most important of the weak elements are gas bubbles that influence the discharge initiation (see Sect. 6.6.4). In this case, the probability of occurrence of bubbles with dangerous sizes depends on the electrode area. This results in different probabilities of the discharge initiation at the given electric field strength for different electrode areas and different breakdown probabilities the given electrode area for different electric field strengths. We can roughly estimate the effect of the electrode area as follows. If we consider that the probability density of bubble distribution over sizes is described by the function $f(r)$ and that the bubbles are uniformly distributed over the electrode area with number density n, the number of bubbles with sizes in the range from r to $r + dr$ will be $dN = nSf(r)\,dr$. Let us consider that the breakdown occurs with probability 1 for the given E and S, if the average number of bubbles with sizes greater than r_{cr} is no less than one, that is, $N(r > r_{\mathrm{cr}}) \geq 1$:

$$N(r > r_{\mathrm{cr}}) = \int n \cdot S \cdot f(r) \cdot dr \geq 1. \tag{7.15}$$

Since r_{cr} depends on E, this expression specifies the dependence of the electric field strength on the electrode area for a 100% breakdown probability. In this case, the pulse duration at which the breakdown is initiated is determined from the calculated voltage-time dependence. For $N < 1$, it can serve as an estimate for the probability of existence of bubbles with dangerous sizes. Then the above expression will determine the dependence of the electric field strength on the electrode area for the corresponding breakdown probability. Equation (7.15) can be transformed into

$$W = \int\limits_{r_{\mathrm{cr}}}^{\infty} n \cdot S \cdot f(r) \cdot dr, \quad S = \frac{W}{n \cdot F(r)}, \tag{7.16}$$

which allows us to analyze the dependence $S(E, W)$ and hence $E(S, W)$ in a more convenient form. In principle, an attempt can be made of more explicit (and rough) estimates of the sought-after dependences. To this end, an explicit form of the dependence $f(r)$ should be chosen. A log-normal distribution can be used for the first approximation. This distribution describes the particle sizes during their fractionation. If we consider that fractionation occurs along the inhomogeneities on the particle surface and that fractionation and electrode machining have analogous features (cleavage, fracture, presence of intercrystalline boundaries, etc.), the distribution of inhomogeneities over sizes of surface bulges and cavities (pores) can be considered similar to the distribution of particles during their fractionation. In turn, the distribution of surface inhomogeneities results in bubble distribution over sizes. This is the case for bubbles put inside pores. On the other hand, if microbubbles are formed near microbulges (due to emission of charge carriers plus the

Coulomb repulsion), the distribution of microbulges over sizes will result in a distribution of bubbles over sizes. Thus,

$$f(r) = \frac{1}{(2 \cdot \pi)^{1/2} \, r} \exp\left(-\frac{\ln(r/r_{\mathrm{av}})}{2 \cdot \sigma_s}\right), \tag{7.17}$$

where r_{av} is the logarithmically average bubble size and σ_s is its logarithmic variance. Substituting (1.17) into (7.16), after some manipulations we obtain

$$S = \frac{W}{n \cdot \left\{1 - \mathrm{erf}\left[\dfrac{\ln(r/r_{\mathrm{av}})}{2 \cdot \sigma_s}\right]\right\}}, \tag{7.18}$$

where $\mathrm{erf}(x)$ is the probability integral. It is difficult to analyze this expression, in particular, when $\mathrm{erf}(x)$ is close to 1. To simplify (7.18), we take advantage of the approximation, for example, in the form [20]

$$\mathrm{erf}(x) = 1 - \frac{1}{(1 + a_1 \cdot x + a_2 \cdot x^2 + a_3 \cdot x^3 + \cdots + a_6 \cdot x^6)^{16}} + \varepsilon(x),$$
$$|\varepsilon| \le 3 \cdot 10^{-7}, \tag{7.19}$$
$$S = \left(1 + a_1 \cdot x_c + a_2 \cdot x_c^2 + a_3 \cdot x_c^3 + \cdots + a_6 \cdot x_c^6\right)^{16} \cdot W/n,$$

where $a_1 = 0.0705230784$, $a_2 = 0.0422820123$, $a_3 = 0.0092705272$, $a_4 = 0.0001520143$, $a_5 = 0.0002765672$, $a_6 = 0.0000430638$,

$$x_c = \ln\left[\frac{U_{\mathrm{Pasch}} \cdot (2 \cdot \varepsilon + 1)}{6 \cdot \varepsilon \cdot E \cdot r_{\mathrm{av}}}\right] / 2\sigma_s.$$

Here U_{Pasch} is the breakdown voltage according to the Paschen curve.

To analyze mathematically, we express $x_{\mathrm{cr}} = \ln(E_{\mathrm{max}}/E)/2\sigma_s$ and consider different cases. Figure 7.10 shows the predicted dependences for E_{max}/E chosen arbitrary from the range 1000/10 and for $\sigma_s \approx 1$. This means that the dangerous bubble size exceeds 10–1000 times the average bubble size and that the bubble size distribution is narrow. It is difficult to comment the last assumption, but the first assumption is noncontradictory. If the dangerous bubble size ranges from units to tens of microns for electric field strengths of $1\,\mathrm{MV/cm}$–$100\,\mathrm{kV/cm}$, the most probable value of r_{cr} is several fractions of a micron. An analysis of the dependence obtained demonstrates that for almost any electric field strength, the dependence $E(S)$ can be described by a power-law function $E(S) \sim S^{-\kappa}$ with slightly varying exponent. Moreover, the dependence is weakened with increasing S (and intensifies with increasing E). For large S, the exponent $\kappa \sim 10$ and even greater; for small S, the exponent is less than 10. This is in good agreement with the available experimental data.

Thus, based on the analysis of bubble evolution in liquids and bubble behavior under the effect of a strong field, the bubble breakdown initiation mechanism has been suggested for liquid dielectrics. It involves a discharge
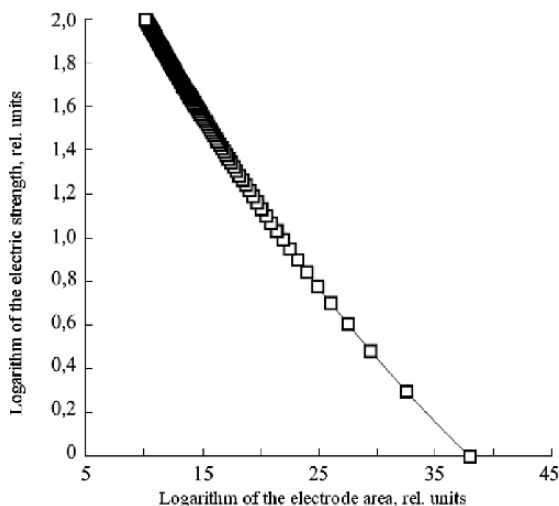
Fig. 7.10. Calculated dependence of the electric strength on the electrode area

in the bubble once the voltage applied to it has achieved the critical value, bubble deformation under the action of the Coulomb forces, electric field gain at the bubble poles, and discharge propagation into the liquid once the electric field strength has achieved the critical value. Since deformation depends on the external conditions and properties of the liquid and interface, an explicit dependence of the pulsed electric strength on these parameters arises in the model. The voltage pulse parameters (pulse slope and front) and electrode type and shape can also be taken into account in this model. The model can be further refined with allowance for the bubble statistics. This will provide the opportunity for taking into account the effect of the production technology on E_{br} as well as for a more correct allowance for the effect of the electrode area.

7.2 Microexplosive Discharge Initiation Mechanism

Significant differences in the mechanisms of charge carrier generation and subsequent behavior (Chap. 1), in characteristics and laws of discharge ignition from anode and cathode (Sects. 3.1–3.3, 4.1, and 4.2) call for their separate consideration and description.

7.2.1 Anode Initiation

To construct models of microexplosive anode and cathode discharge initiation, the processes of ionization and emission must be examined in more detail than in Chap. 1.

Autoionization at the Anode

For intermediate electric field strengths of $\sim 10^5$–10^6 V/cm characteristic of the nanosecond breakdowns of submillimeter gaps, the electric field strength at the end of bulges can be as great as $\sim 10^7 - 10^8$ V/cm. For these voltages, atoms can be ionized near the anode (due to electron emission from the liquid at the expense of tunnel transitions) with significant local energy liberation. These processes can be determining for the electric discharge initiation.

For liquids in which atoms or molecules interact via the weak Van-der-Waals forces (for example, for organic liquids), we can neglect splitting of the energy levels (their valence band width is $\sim 0.1 - 0.2$ eV) and consider electron tunneling for isolated atoms or molecules. Figure 7.11 illustrates changes in the potential energy of the valence electron of an atom or a molecule in a strong electric field. The potential barrier on the anode side is lower and, according to the principles of quantum mechanics, ionization is possible by means of electron tunneling through the potential barrier along the AB path. The probability D of electron tunneling through the barrier can be approximately determined by the Wentzel–Kramers–Brillouin method:

$$D = \exp\left[-2\left(2m/\hbar^2\right)^{1/2} \int_{r_1}^{r_2} (U - \chi)^{1/2} \, dr\right], \qquad (7.20)$$
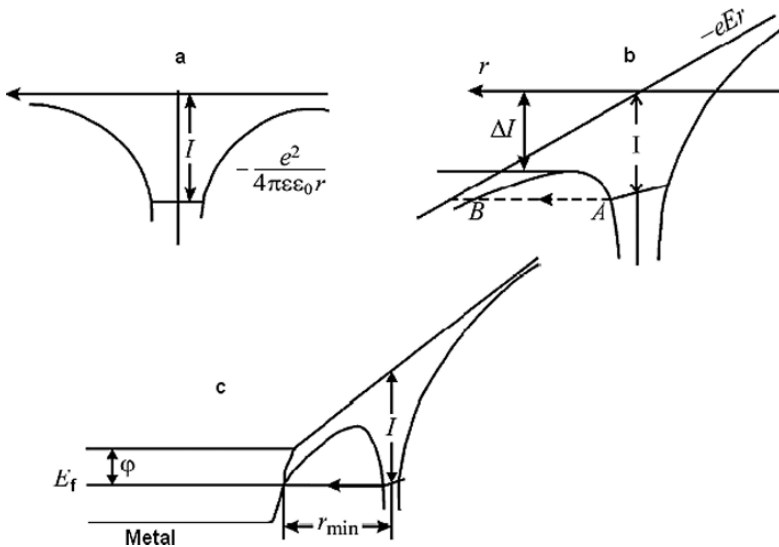
Fig. 7.11. Potential energy of the electron in an atom or molecule without (**a**) and with a strong electric field (**b**) and in the presence of a field near the metal surface (anode) (**c**). Here I denotes the ionization energy, E_F is the Fermi energy, and π is the metal work function

where m is the electron mass, $\hbar$ is Planck's constant divided by 2π, U is the potential electron energy, χ is the total electron energy, and r_1 and r_2 are the coordinates of the turning points.

Generally, the potential electron energy without external field cannot be described by a simple expression. In the approximation of the Coulomb potential in the field E, the total potential energy of the electron is

$$U = -\left(e^2/4\pi\varepsilon\varepsilon_0 r\right) - eEr, \qquad (7.21)$$

where ε is the relative permittivity and ε_0 is the permittivity of vacuum.

With allowance for (7.21), expression for the probability (7.20) can be expressed in the form [21]

$$D = \exp\left[-\left(6.8 \cdot 10^7 I^{3/2}/E\right)\theta\left(y\right)\right], \qquad (7.22)$$

where I is the ionization energy, in eV; E is the electric field strength, in V/cm; and $\theta\left(y\right)$ is the first-order correction to the Coulomb potential.

For $\theta\left(y\right) = 1$, probability (7.22) corresponds to a triangular potential barrier with height I and base I/eE. The correction $\theta\left(y\right)$ is analogous to the Nordheim function that takes into account the effect of the image potential on the field-induced electron emission from metals [22]. The parameter

$$y = 7.6 \cdot 10^{-4} E^{1/2}/\varepsilon^{1/2} I \qquad (7.23)$$

characterizes the ratio of the decrease in the ionization energy ΔI caused by the applied field to the absolute value of the electron energy I (see Fig. 7.11b).

When an atom or a molecule are on the conductor surface, the potential barrier decreases further under the action of the image forces (see Fig. 7.11c). The action of the image forces is equivalent to the electron attraction to the electron-ion dipole image on the conducting surface. Pauli's principle imposes the restriction on the least distance from the surface $r_{\min}$ at which autoionization can occur. If the atom is at the distance $r < r_{\min}$ from the surface, the electron energy level in the atom will lie below the Fermi energy level E_F in the metal, and the probability of tunneling will sharply decrease. If we neglect the ion-ion image potential and the polarizability of the initial atom (molecule) and ion it produces, the expression for $r_{\min}$ can be written as [21]

$$r_{\min} \approx \left(I - \pi\right)/Ee. \qquad (7.24)$$

In (7.24), π is the work function of the electron that escapes from the metal. For the probability D of tunneling of the electron from an atom or a molecule located at the distance $r_{\min}$ from the surface and for the electron current density j we obtain the following expressions [21]:

$$D = \exp\left\{-6.8 \cdot 10^7 \left[I^{3/2}\theta\left(y\right) - \pi^{3/2}\right]/E\right\} \qquad (7.25)$$

and

$$j = eN\nu \left(6.8 \cdot 10^7\right)^{-1} \frac{2}{3}\pi^{-1/2} \exp\left\{-6.8 \cdot 10^7 \left[I^{3/2}\theta\left(y\right) - \pi^{3/2}\right]/E\right\}, \quad (7.26)$$

where e is the electron charge, N is the number of atoms or molecules in unit volume, ν is the frequency the electron of the atom or molecule impinges on the potential barrier ($\sim 10^{15} - 10^{16}\,\mathrm{s}^{-1}$; it can be estimated from the uncertainty relation).

Table 7.1 tabulates the calculated ionization probability and the electron current density for n-hexane ($I = 8.6\,\mathrm{eV}$, $\varepsilon = 1.8$, $\pi = 4.5\,\mathrm{eV}$ (typical of metal electrodes), $N = 0.46 \cdot 10^{22}\,\mathrm{cm}^3$, and $\nu \sim 5 \cdot 10^{15}\,\mathrm{s}^{-1}$) versus the electric field strength. It can be seen that the ionization current arises once the electric field strength has reached a threshold value of $\sim (3 - 4) \cdot 10^7\,\mathrm{V/cm}$. The probability and current density depend strongly on the electric field strength. Even for rather small $D \sim 10^{-7}$, the electron current density is rather large ($\sim 10^3\,\mathrm{A/cm}^2$). We note that the decrease in the potential barrier height caused by the electron and ion images in metal was not taken into account in (7.25) and hence in (7.26). The image forces facilitate the transition through the potential barrier.

In liquids in which molecules interact via more efficient orientational forces (for example, in water and other polar liquids), each energy level of the isolated molecule is transformed into the energy band of finite width. Under the effect of an electric field, the energy bands of the liquid are tilted. The slope the stronger, the higher the field strength. Figure 7.12 illustrates the energy band diagram at the metal (anode) - liquid interface in a strong electric field. If the distance between points A and B is comparatively small (comparable to the de Broglie electron wavelength), electron tunneling can be observed from the valence band of the liquid through the potential barrier along the AB path to the free energy levels of the metal conduction band.

The analysis in this case results in the following expressions for the probability of tunneling D and the electron current density j [21]:

$$D = \exp\left\{-\left(\frac{I}{Eed}\right)\left[\ln\left(\frac{2I}{\tau}\right) - 1\right]\right\} \quad (7.27)$$

Table 7.1. Probability of ionization D and electron current density j for n-hexane versus the electric field strength E

Para-meters	Electric field strength E, V/cm						
	$4 \cdot 10^7$	$5 \cdot 10^7$	$6 \cdot 10^7$	$7 \cdot 10^7$	$8 \cdot 10^7$	$9 \cdot 10^7$	10^8
D	$2.5 \cdot 10^{-9}$	$3.7 \cdot 10^{-7}$	$1.0 \cdot 10^{-5}$	$1.1 \cdot 10^{-4}$	$6.8 \cdot 10^{-4}$	$2.7 \cdot 10^{-3}$	$1.1 \cdot 10^{-2}$
$j(\mathrm{A/cm}^2)$	$4.2 \cdot 10^1$	$6.3 \cdot 10^3$	$1.7 \cdot 10^5$	$1.9 \cdot 10^6$	$1.2 \cdot 10^7$	$4.7 \cdot 10^7$	$1.9 \cdot 10^8$
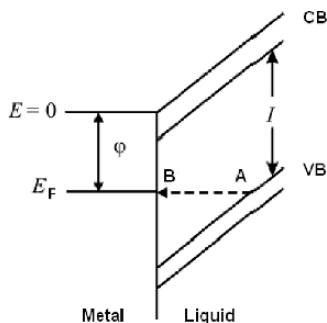
Fig. 7.12. Band energy diagram at the electrode (anode) - liquid interface in a strong electric field. Here E_F is the Fermi energy, π is the work function of the electron that escapes from the metal, VB denotes the valence band, CB denotes the conduction band, I denotes the gap width (ionization energy in the liquid phase)

and

$$j = \frac{N_e E e^2 d^2}{2h\left[\ln\left(2I/\tau\right) - 1\right]} \exp\left\{-\left(\frac{I}{Eed}\right)\left[\ln\left(\frac{2I}{\tau}\right) - 1\right]\right\}, \qquad (7.28)$$

where I is the gap width (the ionization energy in the liquid phase), E is the electric field strength, e is the electron charge, d is the spacing of liquid molecules, τ is the valence band width, and N_e is the number of valence electrons in unit volume.

In the literature, we have found no data on the valence band width τ for liquids. Its order of magnitude can be roughly estimated from the expression [23]

$$I = I_g + p_+ + v_0 - \tau/2, \qquad (7.29)$$

where I and I_g are ionization energies of the atom or molecule in the liquid and gas phases, respectively; p_+ is the polarization energy of the positive ion in the liquid ($\approx -1\,\mathrm{eV}$ for most liquids with $\varepsilon > 2$ [23]); v_0 is the energy at the bottom of the conduction band relative to the electron energy in vacuum. According to [24], $I = 8.76\,\mathrm{eV}$, $I_g = 12.6\,\mathrm{eV}$, and $v_0 = -1.3\,\mathrm{eV}$ for water, and taking $p_+ \approx -1\,\mathrm{eV}$, we obtain that the valence band width is $\tau \approx 3\,\mathrm{eV}$.

The ionization probability and the electron current density calculated for water ($d = 3 \cdot 10^{-8}\,\mathrm{cm}$, $N = 1.3 \cdot 10^{23}\,\mathrm{cm}^3$, and $\tau \sim 3\,\mathrm{eV}$) within the framework of the band model described by (7.27) and (7.28) are tabulated in Table 7.2 as functions of the electric field strength. A comparison of the data presented in Tables 7.1 and 7.2 demonstrates that the threshold field strength for ionization in water is approximately halved compared to that in n-hexane.

The examined models of the autoionization process are approximate. This is due to the difficulty of an exact problem solution. In particular, the assumption on the one-dimensional character of the tunneling process and the classical formula for the image potential near the metal surface are rough.

Table 7.2. Probability of ionization D and electron current density j for water as functions of the electric field strength E

Parameters	Electric field strength E, V/cm						
	10^7	$1.5 \cdot 10^7$	$2 \cdot 10^7$	$3 \cdot 10^7$	$4 \cdot 10^7$	$7 \cdot 10^7$	10^8
D	$2.2 \cdot 10^{-10}$	$3.7 \cdot 10^{-7}$	$1.5 \cdot 10^{-5}$	$6.1 \cdot 10^{-4}$	$4.1 \cdot 10^{-3}$	$4.2 \cdot 10^{-2}$	$1.1 \cdot 10^{-1}$
$j(\text{A/cm}^2)$	$6.7 \cdot 10^{-4}$	1.7	$9.3 \cdot 10^1$	$5.5 \cdot 10^3$	$5.0 \cdot 10^4$	$8.9 \cdot 10^5$	$3.3 \cdot 10^6$

However, the lack of a more realistic model of interaction of the liquid with the surface does not allow us to refine these simple models.

Autoionization of atoms was first observed by Muller [25] in gases. Autoionization in a strong electric field on the surface of positively charged tip electrode was also observed for liquefied gases [21], aromatic hydrocarbons [26], n-hexane [27], cyclohexane [28], and other liquids. It should be noted that an electric field strength of $\sim 2 \cdot 10^7$ V/cm is necessary for autoionization in n-hexane [27], which is in qualitative agreement with the results of theoretical considerations (see Table 7.1). The threshold electric field strength in cyclohexane is somewhat smaller [28]. For comparatively high values of the emission current ($> 10^{-9}$ A), its further growth is limited (deviation from theory) by the spatial charge formed in the liquid due to a finite velocity of charge carriers [27, 28].

Thus, autoionization of molecules in the liquid requires the electric field strengths that are actually achievable near the anode; in this case, the current density caused by the motion of arising charge carriers can cause phase transitions in the liquid.

Microexplosive Processes on the Anode. Discharge Initiation

The opportunity of homogeneous (spontaneous) vapor bubble occurrence as a result of local superheating of the liquid by ionization (emission) currents was demonstrated in [21, 29].

An attempt of quantitative estimation of the processes of local superheating of the liquid by ionization currents was undertaken in [30] to explain the mechanism of the electric discharge ignition from anode. We take advantage of the Dering–Volmer formula for the bubble nucleation frequency (rate) in unit volume of a superheated liquid [29, 31]:

$$S = N \left[\exp\left(-\frac{L}{kT} \right) \right] \left(\frac{2\sigma}{\pi m} \right)^{1/2} \exp\left(-\frac{16\pi\sigma^3}{3kT \left(p_s - p \right)^2} \right), \qquad (7.30)$$

where N is the number of molecules in unit volume, L is the vaporization heat of a single molecule, k is the Boltzmann constant, σ is the surface tension coefficient, m is the mass of the molecule, p_s is the saturated vapor pressure at temperature T of the superheated liquid, and p is the external pressure.

Because of the strong dependence of S on the depth of penetration into the metastable region (degree of liquid superheating), the boundary of the region of fluctuation bubble nucleation is sharp. The pressure and temperature of the first-order phase transition are related by the Clausius–Clapeyron equation:

$$dp_s = \frac{L(T) p_s}{kT^2} dT. \tag{7.31}$$

If the dependence of L on the temperature is known, (7.31) can be integrated and the coexistence curve can be found.

Let us assume that the average time of bubble nucleation $\bar{\tau}$ in volume V of a metastable liquid ($\sim r_0^3$, where r_0 is the characteristic radius of the energy absorption region) makes the main contribution to the average statistical discharge time lag,[*] that is, $\bar{\tau} \approx \bar{t}_{st}$. The parameters $S, \bar{\tau} (\bar{t}_{st})$, and $V (r_0^3)$ are related by the expression:

$$S r_0^3 \bar{t}_{st} = 1. \tag{7.32}$$

Formula (7.32) specifies the condition of the breakdown initiation, where the dependence of the average statistical time lag on the properties of the liquid, local electric field strength E_{loc} (characterizes the specific power deposited into the liquid and hence the achievable superheating), and external pressure is determined in terms of S by (7.30).

The energy balance equation (disregarding the thermal conductivity) has the form

$$j(t) E_{loc}(t) dt \approx C_p \rho(T) dT, \tag{7.33}$$

where $j(t)$ is the ionization current density, C_p is the specific heat, and ρ is the density of the liquid.

All thermodynamic characteristics included in computational formulas (7.30)–(7.32) are considered at the temperature T of the superheated liquid. This causes some difficulties, because the data on the properties of metastable liquids either are absent at all or are insufficient. The liquid density versus temperatures was found from a linear dependence $\rho(T)$. Values of the coefficient of surface tension of the liquid as functions of the temperature were determined by extrapolation of the available experimental data from the region far from the critical point toward $\sigma = 0$ at the critical temperature.

Values of the thermal-physical parameters were borrowed from handbooks of physical quantities. A very strong dependence of the last exponential term in (7.30) on the temperature and pressure makes errors in calculations caused by errors in the determination of the thermal-physical characteristics of the liquid insignificant.

Solid curves *1–3* in Fig. 7.13 show the dependences of the average statistical discharge time lag on the external pressure for *n*-hexane at the indicated temperatures of the metastable liquid calculated for model (7.11)–(7.13). Closed

---

[*] The physical meaning of this term for the discharge in liquids was explained in Chap. 2.
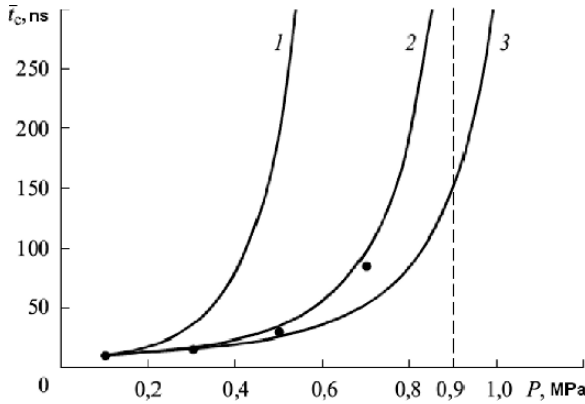
Fig. 7.13. Dependence of the average statistical discharge time lag for n-hexane on the external pressure. Solid *curves 1–3* show the results of calculations for the superheated liquid temperature T and the radius of the region of energy liberation r_0: *curve 1* is for $T = 210\,°C$ and $r_0 = 1.1 \cdot 10^{-7}$ cm, *curve 2* is for $T = 213°C$ and $r_0 = 4.6 \cdot 10^{-8}$ cm, and *curve 3* is for $T = 215°C$ and $r_0 = 3.5 \cdot 10^{-8}$ cm. Closed circles and the vertical dashed straight line show the experimental results for a complex electric discharge from anode ($E = 2.1\,\text{MV/cm}$ and $d = 100\,\mu\text{m}$)

circles here show the experimental data obtained from the statistical distributions of the breakdown time lag (Chap. 5) for the complex electric discharge from anode in the electric field $E = 2.1\,\text{MV/cm}$ for an interelectrode distance of $100\,\mu\text{m}$.

The vertical dashed straight line here indicates the pressure at which the complex electric discharge has no time to be formed, and transition to the ionization mechanism of breakdown from anode occurs.

The experimental points fall well on curve *2* calculated for the liquid temperature $T = 213\,°C$ and the characteristic radius of the energy liberation region $r_0 = 4.6 \cdot 10^{-8}$ cm. It can also be seen that with increasing pressure, points of curve *2* approach smoothly the asymptote at a critical pressure of $0.9\,\text{MPa}$.

The criterion for the breakdown is the liberation of the energy with volume density

$$W \approx C_p \int_{T_0}^{T} \rho\,(T)\,dT \tag{7.34}$$

near the anode, where T_0 is the initial temperature and T is the temperature of the superheated liquid.

To increase the temperature of n-hexane to $T = 213\,°C$ ($C_p = 2.26\,\text{J/g}\cdot\text{K}$ under normal conditions), the volume energy density $W \approx 250\,\text{J/cm}^3$ must be liberated. In this case, the homogeneous nucleation frequency is $S \sim 10^{30}\,\text{cm}^{-3} \cdot \text{s}$, and the mode of explosive or impact boiling up is realized [31].

It is exactly the high heating rate ($\geq 10^{10}$ K/s) in the very small liquid volume that provides deep enough penetration into the metastable region and intense fluctuation nucleation of bubbles even in the presence of the system of well-developed vaporization centers.

As demonstrated in Chap. 1, the system of electrodes with highly nonuniform field produces the electrostriction pressure in the liquid under exposure to pulsed voltage. An increase in the pressure is described by the formula [29]

$$\Delta p = \frac{(\varepsilon - 1)(\varepsilon + 2)}{24\pi} \left(\frac{E}{300}\right)^2 \cdot 10^{-6} \text{ [atm]} \tag{7.35}$$

analogous to formula (1.2), where ε is the relative permittivity of the liquid and E is the electric field strength, in V/cm. For n-hexane and field strengths near the tip electrode of $1 \cdot 10^7$ and $2 \cdot 10^7$ V/cm, the electrostriction pressures amount to 45 and 179 atm, respectively. A solution of the energy balance equation with allowance for the process of heat transfer in the stationary approximation demonstrates that the temperature distribution has a maximum at the distance $2R$ from the tip end, where R is the end radius of the tip [29]. The electric field strength at this distance from the tip decreases approximately 5 times (in the approximation of the conducting tip end shaped as a semi-ellipsoid of rotation), and hence the pressure decreases 25 times. With allowance for the electrostriction pressure $\Delta p \sim 2 - 7$ atm, the agreement of the theoretical dependence with the experimental data shown in Fig. 7.13 demonstrates that the increase in the temperature of the superheated liquid is greater than 6°C, and the radius of the region of energy liberation decreases by a factor of 1.5. It should be noted that the positive spatial charge formed in the liquid reduces the electric field strength near the tip electrode. This can decrease the effect of the electrostriction pressure on the bubble nucleation process.

The upper limit of the increase in the temperature of the liquid can be estimated from the formula [29]

$$\Delta T_{\max} = \frac{Ei}{32\pi\kappa}\alpha, \tag{7.36}$$

where E is the electric field strength at the tip end, i is the ionization current, κ is the thermal conductivity of the liquid, and $\alpha = 6.7$ is the coefficient that takes into account the spatial limitation of the emission current.

To increase the n-hexane temperature by $\Delta T_{\max} \sim 200$ °C ($\kappa = 0.15$ W/m·K at a temperature of 0°C and atmospheric pressure) for the field strength near the tip electrode $E \sim 2 \cdot 10^7$ V/cm, the emission currents $\geq 2 \cdot 10^{-7}$ A are required, that are greater than the emission currents at which the effect of the spatial charge is observed.

From the energy balance equation with allowance for (7.36), the time required for heating by $\Delta T_{\max}$ can be estimated [29]:

$$\Delta t \approx \left(2C_p R^2 \rho\right)/\kappa. \tag{7.37}$$

For n-hexane, $\Delta t \leq 2 \cdot 10^{-9}$ s for tips with end radii $R \leq 0.01$ μm.

The heating efficiency can be considerably increased due to conversion into heat of the energy lost by electrons in the process of elastic collisions with molecules of the liquid. Electron tunneling requires that the atom was separated from the emitter surface at the distance $\geq r_{\min}$ specified by (7.24). For n-hexane and $E \approx 2 \cdot 10^7$ V/cm, $r_{\min} \approx 20$Å. After passage of this distance, the electron cannot acquire the energy required for ionization of the molecule even in such strong electric fields. Therefore, the number of electrons in the liquid does not increase. After passage of a distance of $\sim 6 \cdot 10^{-8}$ cm equal to the average molecular spacing in n-hexane in a field of $\sim(1-2) \cdot 10^7$ V/cm, the electron will acquire an additional energy of ~ 0.6–1.2 eV. In the process of electron collisions with molecules of the liquid, its kinetic energy is transformed into the energy of vibrational and rotational degrees of freedom of the molecules. The most probable molecular vibrations in hydrocarbons such as n-hexane are oriented along the chemical bonds in the CH, CH_2, and CH_3 groups with normal frequencies of 1000, 1450 and 2960 cm^{-1} lying in the near infrared range of the spectrum [32]. The corresponding quantum energies are 0.12, 0.18, and 0.37 eV. The energy of vibrational degrees of freedom will be converted rather efficiently into heat in the process of collisions of molecules with each other. It should be noted that the liberated energy density $W \approx 250$ J/cm^3 corresponds to the average energy per a single molecule of 0.34 eV, which is close to the energy of excitation of stretching vibrations in the CH, CH_2, and CH_3 groups (0.37 eV).

Thus, the electron energy is converted into heat in small enough time and small enough volume. This leads to intense local superheating of liquids, explosive process of bubble formation, and generation of weak shock waves observed in the process of electric discharge initiation in n-hexane (see Sect. 3.1).

The first stable bubble nucleus arising in the superheated liquid and hence boiling up of the liquid are random processes. Under preset external conditions, the bubble nucleation time τ is described by the exponential Poisson distribution with the probability density [31]

$$f(\tau) = (1/\bar{\tau}) \exp(-\tau/\bar{\tau}), \tag{7.38}$$

where $\bar{\tau}$ is the average bubble nucleation time (the average lifetime of the superheated liquid). We note that the statistical time lag obeys an exponential distribution (Chap. 5).

Within the framework of the examined model, the statistical time lag for the complex electric discharge from anode involves electron emission from the liquid, fast local heating, and nucleation. Since the autoionization process is virtually inertialess, fluctuations of the statistical time lag are due to temporal fluctuations of energy dissipation and bubble nucleation processes.

The significant intensity of shock waves generated in water in the stage of discharge ignition allows us to estimate the minimum pressure level and some other parameters in the region of energy liberation on the electrode surface [33].

Their exact determination using the interpherometric methods is complicated by the fact that the propagation of shock waves in water with the velocity exceeding by a factor of 1.5–2 the sound velocity in unperturbed liquid causes significant changes in the pressure by $P_{fr} \approx (0.5 - 2.0) \cdot 10^9 \, \text{Pa}$ [44].

For the known changes in the refractive index in the shock wave front, the density and pressure can be determined for weak shock waves ($P \leq 10^8 \, \text{Pa}$) when temperature changes in the medium can be neglected. We now establish a relationship between changes in the refractive index of water and pressure. We take advantage of the condition of water isentropy for $P < 3 \cdot 10^8 \, \text{Pa}$ [34]:

$$\frac{P + B}{\rho^\alpha} = \frac{P_0 + B}{\rho_0^\alpha}, \tag{7.39}$$

where $B = 3.045 \cdot 10^8 \, \text{Pa}$ and $\alpha = 7.15$. Neglecting P_0 in comparison with B, for small density changes we obtain

$$P = B \left[\left(1 + \frac{\rho - \rho_0}{\rho_0} \right)^\alpha - 1 \right] \approx B\alpha \frac{\rho - \rho_0}{\rho_0}. \tag{7.40}$$

The dependence of the refractive index on the water density for weak shock waves ($P \leq 10^8 \, \text{Pa}$) has the form [35]

$$\Delta n = 0.322 \frac{\rho - \rho_0}{\rho_0}. \tag{7.41}$$

With the help of (7.40) and (7.41), we derive the expression used in experiments on the determination of pressure in water from the data of interferometric measurements:

$$P \approx 6.8 \cdot 10^9 \Delta n \; [\text{Pa}]. \tag{7.42}$$

The measurable range of pressures in the shock wave front P_{fr} for a characteristic spherical shock wave radius of $\sim 100 \, \mu\text{m}$ is $5 - 50 \, \text{MPa}$. Its lower limit is determined by the accuracy of measuring the displacement of the interference bands $\Delta k \sim 0.1$ and is also the estimate of the measurement error. Its upper limit is determined by a discontinuity of the interference band near the front and corresponds to $k \approx 1$. When the refractive index changes by $\Delta n \geq 2 \cdot 10^{-2}$, the interferometer yields a focused shadow image of stronger optical inhomogeneities.

Comparatively intensive shock waves were also investigated with a super-highspeed three-frame laser Schlieren system. Its sensitivity is estimated by the change in the refractive index $\Delta n \geq 10^{-2}$, which corresponds to the pressure in the shock wave front $P_{fr} \geq 70 \, \text{MPa}$ ($V_{fr} \geq 1.6 \cdot 10^5 \text{cm/s}$).

Let us consider now some concrete data on the dynamics of explosive processes in distilled water.

Figure 7.14 shows the time dependence of the shock wave front radius R_{fr} averaged over a large number of three-frame photographs (denoted by
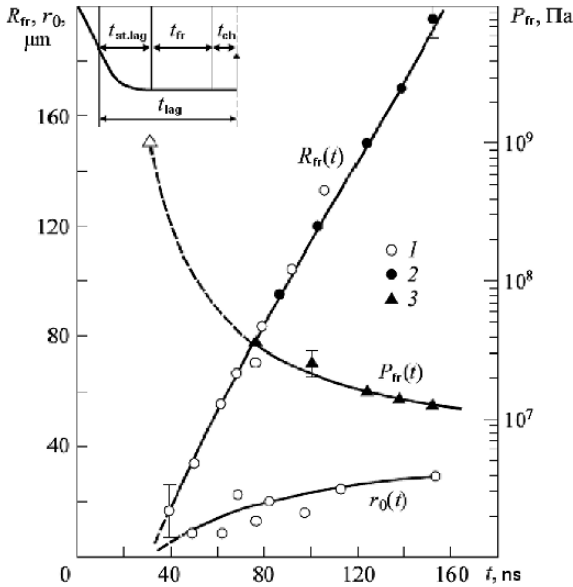
Fig. 7.14. Temporal dependence of the shock wave front radius R_{fr} (*curves 1 and 2*), pressure P_{fr} (*curve 3*), and initial perturbation radius r_0 for distilled water, a field strength of $0.6\,\text{MV/cm}$, and an interelectrode distance of $2\,\text{mm}$

figure *1*). Here the dependence $R_{\text{fr}}(t)$ obtained from the interferograms is also drawn (denoted by figure *2*) for time moments when they can be interpreted quantitatively. At the bottom of Fig. 7.14, the time dependence of the characteristic radius of the primary local perturbation region $r_0(t)$ is shown. At the top of the figure, the waveform of the voltage pulse is shown for $E = 0.3\,\text{MV/cm}$. Here t_{lag} is the average discharge time lag counted from the moment when the electric field strength achieved $E = 0.3\,\text{MV/cm}$ (the quasistatic breakdown field strength) to the breakdown moment (voltage cutoff), $t_{\text{st.lag}}$ is the average statistical breakdown time lag, and t_{ch} is the average time the plasma channel crosses the gap ($V_{\text{ch}} \sim 1.5 \cdot 10^7\,\text{cm/s}$). The sum $t_{\text{fr}} + t_{\text{ch}}$ can be treated as the discharge formation time $t_{\text{d.f.}}$.

Investigations with the three-frame Schlieren-system have demonstrated that the initial local optical inhomogeneities with characteristic sizes $\leq 10\,\mu\text{m}$ arise on the electrode surface in $t_{\text{st.lag}} \approx 20\,\text{ns}$. Further expansion of this perturbation and formation of a shock wave is observed.

A discharge channel arises at the moment of time $t = t_{\text{lag}} - t_{\text{ch}}$ (see Fig. 7.14) which corresponds to the characteristic size of the shock waves propagating with the average velocity $V_{\text{fr}} = R_{\text{fr}}/(t_{\text{lag}} - t_{\text{st.lag}} - t_{\text{ch}}) \sim 2 \cdot 10^5\,\text{cm/s}$. A more detailed analysis of the dependence $R_{\text{fr}}(t)$ shows that the initial channel propagation velocity is $V_{\text{fr}} \geq 2 \cdot 10^5\,\text{cm/s}$; then it decreases to $\geq 1.5 \cdot 10^5\,\text{cm/s}$ at $t \approx t_{\text{lag}}$. This means that the pressure in the region of local energy liberation can be $P_{\text{ch}} \geq 10^9\,\text{Pa}$ at the initial moment of time [34].

In the process of shock wave propagation, the pressure is described by the expression [36]

$$P_{\mathrm{fr}} \approx \rho_0 \frac{r_0^3}{\tau_0^2 R_{\mathrm{fr}}} g\left(\frac{t}{\tau_0}\right) \tag{7.43}$$

obtained for the spherical perturbation and the hydrodynamic model. Here ρ_0 is the density of water, r_0 is the characteristic perturbation radius, τ_0 is the characteristic time of energy liberation, and $g\left(t/\tau_0\right) \approx 1$.

The pressure in the perturbation region can be estimated with the help of the following relation:

$$P_{\mathrm{ch}} \approx \rho_0 \beta\left(\frac{t}{\tau_0}\right) \frac{r_0^2}{\tau_0^2}, \tag{7.44}$$

where β is a function of the parameter t/τ_0 that depends weakly on the Much number $M = r_0/\tau_0 C_0$. For $t = \tau_0$ and $\beta = 0.5$, from (7.43) and (7.44) we obtain

$$P_{\mathrm{fr}} \approx 2 P_{\mathrm{ch}} \frac{r_0}{R_{\mathrm{fr}}}. \tag{7.45}$$

If we assume that the pressure P_{ch} in the central region is maintained due to energy transferred from the arising primary ionization channels, from Fig. 7.14 it follows that by the moment of time $\tau_0 = t_{\mathrm{fr}} + t_{\mathrm{ch}}$, $R_{\mathrm{fr}} \approx 66\,\mu\mathrm{m}$ and $r_0 \approx 15\,\mu\mathrm{m}$; this yields $P_{\mathrm{ch}}\left(\tau_0\right) \approx 0.9 \cdot 10^8\,\mathrm{Pa}$ and $P_{\mathrm{fr}}\left(\tau_0\right) \approx 4 \cdot 10^7\,\mathrm{Pa}$.

Of interest is to compare the results obtained with the data of interferometric measurements. The experimental dependence $P_{\mathrm{fr}}\left(t\right)$ drawn in coordinates $\left(P_{\mathrm{fr}}, R_{\mathrm{fr}}\right)$ and denoted by figure 3 in Fig. 7.14 has the form $P_{\mathrm{fr}} = A/R_{\mathrm{fr}}$. The pressure reaches a value of $\sim 5 \cdot 10^7\,\mathrm{Pa}$ for $P_{\mathrm{fr}} \approx P_{\mathrm{fr}}\left(t_{\mathrm{lag}}\right)$, which is in good agreement with the result obtained by the Schlieren photography method. Using values of $P_{\mathrm{fr}}\left(R_{\mathrm{fr}}\right)$ for $R_{\mathrm{fr}} \sim 80 - 200\,\mu\mathrm{m}$, from (7.43) we obtain $r_0 \approx 15\,\mu\mathrm{m}$ for $\tau_0 = t_{\mathrm{fr}} + t_{\mathrm{ch}}$, which does not contradict the results obtained by the Schlieren photography method. For a maximum pressure in the region of energy liberation, the interferometric measurements yield

$$\mathrm{P}_{\mathrm{ch}} \approx 3\rho_0 \frac{r_0^3}{\tau_0^2} \approx 5 \cdot 10^8\,\left[\mathrm{Pa}\right]. \tag{7.46}$$

Thus, it can be seen that measurements of the main dynamic characteristics of the examined process by two independent methods, including measurements of $R_{\mathrm{fr}}\left(t\right)$ and $r_0\left(t\right)$ by the Schlieren photography method and measurements of $P_{\mathrm{fr}}\left(R_{\mathrm{fr}}, t\right)$ and $r_0\left(t = t_{\mathrm{lag}}\right)$ by the interferometric method, yield close values $P_{\mathrm{ch}} \sim (0.5 - 1) \cdot 10^9\,\mathrm{Pa}$ of the maximum pressure in the region of local energy liberation near the anode surface.

Assuming that the primary ionization process accompanied by the phase transition arises in this region, for the liberated energy density we have

$$W = R_{\mathrm{ch}}/\left(\gamma - 1\right) \approx (2 - 4) \cdot 10^3\,\left[\mathrm{J/cm}^3\right], \tag{7.47}$$

where $\gamma = 1.26$ is the effective adiabatic exponent for discharges in water [36].

At these W values, an intense phase transition arises in water, which causes the refractive index to change. These changes were registered by the optical methods.

It should be noted that for liberation of energy $\geq 4.10^{-6}$ J in the region with the characteristic radius $r_0 \approx 10\,\mu\mathrm{m}$ during $\tau_0 \leq 2 \cdot 10^{-8}$ s under exposure to voltage of $1.2 \cdot 10^5$ V, the current must be $\geq 1.5 \cdot 10^{-3}$ A, which is much greater than the autoionization current [21]. The additional energy required for explosive boiling up can be supplied through an increase in the conduction current in water in strong electric fields initiated by the special hopping motion of protons [37]. The proton H^+ forms the H_3O^+ complex (the hydroxonium ion) with the water molecule. This complex can transfer an excessive proton to the neighboring definitely oriented water molecule. This molecule turns into the H_3O^+ complex, and so on. In this case, the charge is transferred mainly via the displacement of electrons, while the proton passes only an insignificant distance. Thus, this mechanism is in many respects analogous to the hole mechanism typical of the semiconductors. In strong electric fields, the number of water molecules with favorable orientation sharply increases, and the mobility of charge carriers will also increase. Under assumption of independence of proton vibrations in molecular chains with hydrogen bonds, the mobility of positive charge carriers will be $\sim 1\,\mathrm{cm}^2/(\mathrm{V} \cdot \mathrm{s})$ [38]. When voltage is applied to the discharge gap, a positive surface charge, formed by electron vacancies, arises near the anode. In the field of these vacancies, the nearest waters molecules are polarized and displaced. This process is terminated by the transfer of electrons from these molecules to the anode. Ionization of water molecules results in the formation of hydroxonium ions near the anode by the scheme $H_2O^+ + H_2O \rightarrow H_3O^+ + OH$. Then the charge carriers move by the mechanism described above. Running of this quasi-hole current can cause fast heating of water near the anode and formation of microbubbles. Because of the electron mechanism of electrical conduction, this model is applicable for short voltage pulses, including nanosecond ones. However, the lack of more precise data on the mobility of charge carriers in strong electric fields and on the charge carrier concentration does not allow us to estimate the electrical conductivity of water and to compare it with the available experimental data to adopt or abandon the energy liberation model.

Generation of charge carriers in the process of autoionization is accompanied not only by phase transitions under the effect of liberated energy but also by a number of chemical transformations. For water, a mechanism of chemical transformation caused by the kinetic energy of electrons localized in the conduction band was suggested in [39]. It explains the main physical processes observed in the fast stage of electric discharge propagation. The H_2O^+ ions in water recombine with quasi-free electrons and form the $H_2O^*_{\mathrm{vib}}$ molecules in highly-excited vibrational state with energy of 6.26 eV. We note that the energy of the first electronically excited state of the water molecule (in the liquid phase) amounts to 8.4 eV. The vibrationally-excited molecules decompose through three schemes [39, 40]:

$$\{ H + OH + H_2O, \qquad (7.48)$$
$$H_2O^*_{vib} + H_2O \rightarrow \{ H_2 + 2OH, \qquad (7.49)$$
$$\{ 2H_2O + \Delta E_{dis} \qquad (7.50)$$

Scheme (7.50) describes dissipation of the excitation energy in the medium by the mechanism of vibrational-translational relaxation. Shock waves can be excited as a result of energy dissipation along the electron trajectory [41]. The $H_2O^*_{vib}$ state with the electron thermalization time equal to 10^{-13} s is excited in water. The vibrational-translational energy relaxation time for water is of the same order of magnitude (it is caused by a high density of molecules in the medium and hence a large number of collisions of molecules per second). In radiation chemistry, it is accepted that the electron energy in a condensed medium is absorbed in microregions (spurs) with linear sizes of $10 - 20$ Å [42].

When the energy $\Delta E_{diss} = 6.26$ eV is liberated in the region having the characteristic radius $r_0 = 7.5$ Å, the volume energy density in this region amounts to $W \approx 571$ J, and the temperature increases by $\Delta T = 179\,°C$. In this case, the condition of shock wave excitation (the condition of thermal peak localization) is satisfied, that is, the thermal relaxation time in the medium t_T ($t_T \sim (2r_0)^2/4D = 3.9 \cdot 10^{-12}$ s, where D is the thermal conductivity) is greater than the propagation time of hydrodynamic perturbation t_H($t_H \sim 2r_0/C_0 = 10^{-12}$ s, where C_0 is the velocity of sound in the unperturbed medium). As a result of fast local heating, temperature and pressure change abruptly, which causes the formation of the discontinuous front that propagates with the velocity exceeding the sound velocity. Calculations of the hydrodynamic parameters of shock waves yielded an initial pressure in the front of $\sim 3 \cdot 10^2$ MPa and a propagation velocity of $\sim 1.8 \cdot 10^5$ cm/s [41]. That is, the arising shock waves are weaker than those accompanying the electric discharge initiation, which is in qualitative agreement with the experimental data (see Sects. 3.1 and 3.2). As a result of attenuation, the shock wave velocity fast decreases to the sound velocity, and the shock wave is transformed into sound one. It should be noted that the above-considered mechanism of heat liberation provides the basis for operation of bubble chambers.

By virtue of competitive reactions (7.49) and (7.50), gas microbubbles are formed along with the excitation of shock waves in the region of the discharge channel initiation. In addition, reaction (7.48) competes with reactions (7.49) and (7.50), and some of the H atoms and hydroxyl radicals penetrate the gas microbubbles. Therefore, narrow hydrogen atom lines of the Balmer series are observed against the background of the continuous emission spectrum of molecules [43].

Natural luminescence of the perturbation region before pinching of the weakly ionized gas plasma channel can be explained by the reactions [39]

$$H + OH \rightarrow H_2O^*_{el}, \qquad (7.51)$$
$$H_2O^*_{el} \rightarrow H_2O + h\nu \qquad (7.52)$$

taking place in the gas bubbles.

Unlike reactions (7.48)–(7.50), these reactions are secondary. Therefore, the luminescence is observed with a certain time delay relative to the gas microbubble formation.

The characteristic radius r_0 can be estimated based on the Khristianovich solution [34]. The law of temporal pressure variations in the shock wave is typically characterized by an exponential dependence

$$P = P_{\mathrm{fr}} \exp\left[-t/t_0\right], \tag{7.53}$$

where the constant t_0 specifies the time during which the pressure decreases e times, and the time t is measured from the moment of wave arrival at the given point. Neglecting the deformation of the pressure profile with insignificant increase in the distance for $P_{\mathrm{fr}} \leq 3 \cdot 10^7\,\mathrm{Pa}$, we obtain for pressure variations behind the shock wave front

$$P = P_{\mathrm{fr}} \exp\left[-\rho/\rho*\right], \tag{7.54}$$

where $\rho*$ is the distance at which the pressure decreases e times and ρ is counted from the shock wave front R_{fr}.

For motion with spherical symmetry in water [34], we obtain

$$\frac{\rho*}{r_0} \approx \frac{t_0 \cdot C_0}{r_0} = \frac{1.92 \ln\left(17,000/P_{\mathrm{fr}}\right) - 1.11}{\sqrt{\ln\left(17,000/P_{\mathrm{fr}}\right) - 0.5}}. \tag{7.55}$$

Expression (7.53) gives the pressure level in the shock wave front P_{fr} and time constant of attenuation t_0 close to experimental ones for $P_{\mathrm{fr}} \leq 2.5 \cdot 10^7\,\mathrm{Pa}$.

Thus, the characteristic size of the energy liberation region for the given perturbation can be estimated from pressure variations in the narrow region adjacent to the shock wave front with the help of (7.55).

Figure 7.15 shows the refractive index variations behind the spherical shock wave front with radius $R_{\mathrm{fr}} \approx 170\,\mu\mathrm{m}$ in distilled water reconstructed from three interference bands [see Fig. 3.11a (1)]. Good agreement of the results in the region of maximum pressure level can be seen. Based on the estimate of the maximum pressure, we obtain $P_{\mathrm{fr}} \approx (1.4 \pm 0.3) \cdot 10^7\,\mathrm{Pa}$. Further different behavior of the profiles can be due to breaking of the spherical symmetry caused by the ionization processes that develop behind the shock wave front. The upper profile is described with good accuracy by an exponential dependence in the region adjacent to the shock wave front. From (7.55) for $P_{\mathrm{fr}} \approx 1.4 \cdot 10^7\,\mathrm{Pa}$ we obtain $\rho * r_0 \approx 4$. Determining ρ_* from the profiles shown in Fig. 7.15, we obtain for the radius of the energy liberation region $r_0 \sim 5-13\,\mu\mathrm{m}$. According to (7.43), for $P_{\mathrm{fr}} = 1.4 \cdot 10^7\,\mathrm{Pa}$, $R_{\mathrm{fr}} = 170\,\mu\mathrm{m}$, and $r_0 \sim 10\,\mu\mathrm{m}$ we obtain the characteristic time of energy liberation $\tau_0 \sim 2 \cdot 10^{-8}\,\mathrm{s}$.

Let us estimate the order of magnitude of the energy Q_0 liberated in the region with the characteristic radius $r_0 \sim 10\,\mu\mathrm{m}$ for the period $\tau_0 \sim 2 \cdot 10^{-8}\,\mathrm{s}$ [36]:

$$Q_0 \approx \frac{4\pi}{3} \frac{\rho_0}{\gamma - 1} \frac{r_0^5}{\tau_0^2} \approx 4 \cdot 10^{-6}\,[\mathrm{J}].$$
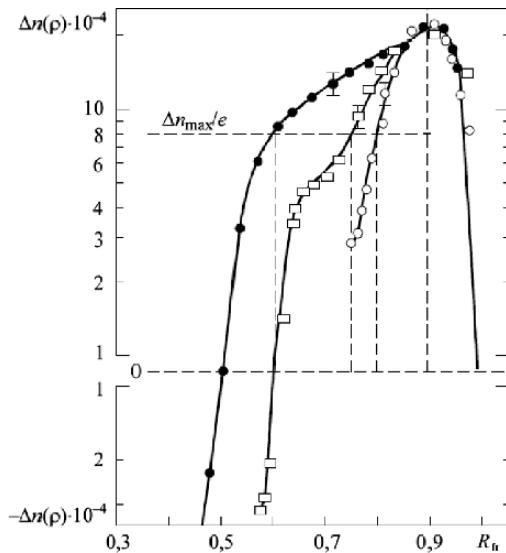
Fig. 7.15. Reconstructed refractive index distribution behind the spherical shock wave front with radius $R_{\mathrm{fr}} \approx 170 \, \mathrm{mm}$ for distilled water

Thus, for nanosecond voltage pulses, the electric discharge is initiated by the explosive processes characterized by liberation of the energy $Q_0 \geq 4{\cdot}10^{-6} \, \mathrm{J}$ in the region with radius $r_0 \sim 10 \, \mu\mathrm{m}$ during $\tau_0 \leq 2 \cdot 10^{-8} \, \mathrm{s}$.

The reconstruction of the profile behind the front of the propagating shock waves allows the pressure at the boundary of the initial ionization channel and hence inside the channel to be estimated. Figure 7.16 shows the refractive index distribution for perturbations in ether [see Fig. 3.11a and b (2)] calculated by the statistical regularization method [44].

Let us determine a dependence of the refractive index on the ether pressure. We take advantage of the data on isothermal compressibility of liquids. Quantitatively, the compressibility is characterized by the quantity X (the compressibility coefficient):

$$ X = -\frac{1}{V} \left(\frac{\partial V}{\partial p} \right) = \frac{1}{\rho} \left(\frac{\partial \rho}{\partial p} \right), \tag{7.56} $$

where ∂V ($\partial \rho$) specifies the volume (density) changes when the pressure changes by ∂p. For pressures lying in the range $\sim (1 - 2) \cdot 10^7 \, \mathrm{Pa}$ at a temperature of $273 \, \mathrm{K}$, the coefficient of ether compressibility is $\sim 1.2 \cdot 10^{-9} \, \mathrm{Pa}^{-1}$ [45].

A dependence of the refractive index on the density can be found from the data on the derivative of the refractive index (at $\lambda = 589.3 \, \mathrm{nm}$) and density with respect to the temperature at atmospheric pressure [46] :

$$ \frac{dn}{d\rho} = \frac{dn}{dT} \bigg/ \frac{d\rho}{dT} \approx 4.8 \cdot 10^{-4} \, \left[\mathrm{m}^3/\mathrm{kg} \right]. \tag{7.57} $$
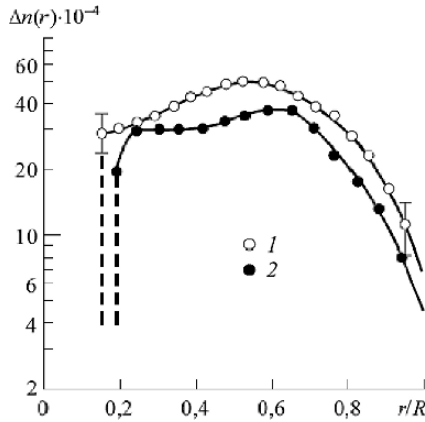
Fig. 7.16. Calculated radial distribution of the refractive index for ether and perturbations with cross sectional radii $R = 70\,\text{mm}$ (○) and $R = 60\,\mu\text{m}$ (●). Vertical dashed straight lines indicate the channel boundary

From (7.56) and (7.57), we obtain the expression which allows us to determine pressure from the changes in the ether refractive index:

$$p \approx 2.4 \cdot 10^9 \Delta n \; [\text{Pa}].$$

The results of interferogram interpretation shown in Fig. 7.16 demonstrate that the pressure on the channel boundary is $\sim (5-7) \cdot 10^6\,\text{Pa}$. This value can serve as an estimate of the lower pressure limit in the channel (the characteristic channel radius is about $10\,\mu\text{m}$).

Thus, the fast local energy liberation in the liquid near the electrode, formation of shock waves and microbubbles in the region with negative pressure behind the shock wave front can be considered as the initial phase of the discharge ignition. The intensity of these processes depends strongly on the near-electrode electric field strength and properties of the liquid.

The initial shock wave velocity in deionized water is $\geq 2 \cdot 10^5\,\text{cm/s}$, the pressure in the shock wave front reaches $\sim 2.5 \cdot 10^9\,\text{Pa}$, and the temperature of water increases by $\sim 130\,°\text{C}$ [36].

In n-hexane, the specific energy liberation accompanying the discharge ignition is approximately by an order of magnitude smaller than in water. Therefore, weaker and fast decaying shock waves are formed in n-hexane.

The development of ionization processes in microbubbles is the next phase of the discharge ignition. Thus, the discharge ignition is maintained by the shock wave, and the ionization processes develop in the shock wave front.

According to the streamer theory of gas breakdown, the parameters of arising microbubbles meet the empirical H. Raether condition [8]

$$(\alpha/p)\,px_{\text{cr}} \sim 20, \tag{7.58}$$

where α is the first Townsend ionization coefficient, p is the gas pressure, x_{cr} is the critical length of the avalanche (corresponds to the avalanche conversion into a streamer). As is well known, the ratio α/p is an unambiguous function of E/p. If local water heating results in the formation of a vapor cavity with pressure $p_0 \sim 10^9\,\mathrm{Pa}$, the temperature of molecules can be estimated from the formula $p_0 \approx n_0 k T_0$. For the particle concentration $n_0 \sim 3.3 \cdot 10^{22}\,\mathrm{cm}^{-3}$, the temperature will be $T_0 \sim 2 \cdot 10^3\,\mathrm{K}$. Under assumption of adiabatic cavity expansion from the initial radius r_0 to r, the pressure p inside the cavity will decrease in accordance with the formula $pV^\gamma = \mathrm{const}$ or $p = p_0 \left(r_0/r\right)^4$ with the adiabatic exponent $\gamma = 4/3$. Once the cavity size achieves $r \approx 5r_0 \approx 50\,\mu\mathrm{m}$, the temperature inside it will be $T = T_0 \left(r_0/r\right) \sim 4 \cdot 10^2\,\mathrm{K}$, and the concentration of molecules will be $n = n_0 \left(r_0/r\right)^3 \sim 3 \cdot 10^{20}\,\mathrm{cm}^{-3}$. This yields the equivalent pressure reduced to room temperature $p_{eq} \sim 1.2 \cdot 10^6\,\mathrm{Pa}$. This fact must be taken into account, because the ionization in an expanding cavity will be determined by the particle density rather than by the pressure inside it, that is, by p_{eq}. The parameter E/p_{eq} that determines the value of the ionization coefficient α, with allowance for the field gain inside the bubble equal to ~ 1.5 for the electric field strength $E \sim 1 - 2\,\mathrm{MV/cm}$, will be $E/p_{eq} \sim 100 - 200\,\mathrm{V/(cm \cdot Torr)}$. Since in this range the value $\alpha/p_{eq} \sim 1 - 5\ (\mathrm{cm \cdot Torr})^{-1}$ [25], from condition (7.21) it follows that $x_{cr} \sim (0.5 - 2) \cdot 10^{-3}\,\mathrm{cm}$. Even if we take the lower limit $\alpha/p_{eq} \sim 1$, the pressure for the critical avalanche length $x_{cr} \sim 10^{-3}\,\mathrm{cm}$ will be $p_{eq} \sim 3 \cdot 10^6\,\mathrm{Pa}$.

From the foregoing analysis it follows that the ionization processes resulting in the formation of the discharge channel will develop inside an expanding cavity only when the pressure decreases to the level $< 10^7\,\mathrm{Pa}$. Since the secondary microbubbles arise somewhat later and have the characteristic sizes $r_0 \leq 10^{-3}\,\mathrm{cm}$, the pressure inside them will be $p_{eq} \geq (1 - 3) \cdot 10^6\,\mathrm{Pa}$. This is in qualitative agreement with the results of interferogram interpretation. In addition, due to the channel lengthening, the field gain can noticeably increase.

The ionization in the secondary microbubbles promotes the energy inflow into the discharge channel being formed; for this reason, the characteristic branched structure is observed behind the shock wave front [Fig. 3.8 (2)]. Starting from a certain moment, the electrical conduction of the channel reaches such a value that the potential of the high-voltage electrode (anode) is transferred through the channel to the shock wave front.

In this case, the third stage of the electric discharge arises when the ionization processes are propagated ahead of the shock wave front with the high velocity $\geq 10^7\,\mathrm{cm/s}$.

7.2.2 Cathode Initiation

For cathode discharge initiation and propagation under conditions of the electric mechanism of liquid breakdown, a model have been developing for many

decades according to which electrons emitted from the cathode or from the head of the discharge channel are accelerated and produce collision ionization of the substance in the liquid phase (see Introduction). The subsequent development of the experimental technology and physics of the condensed state of substance gives us grounds to assume that such mechanism of the discharge initiation and propagation from cathode is realized only at very high electric field strengths ($\sim 10^8$ V/cm) near the electrode and head of the propagating channel (see Sect. 7.3). For moderate electric field strengths and moderately short voltage pulses, the emitted electrons moving in the liquid result in its local superheating, boiling up (nucleation), and expansion. When the density of the substance decreases to values at which free paths of electrons allow them to acquire the energy sufficient for collision ionization, avalanches are formed and avalanche-streamer conversion is observed by analogy with the discharge in gases. This mechanism differs from the anode initiation by the nature of the initial electrons (emitted from the metal in one case and from the liquid in the other case) and the direction of the field gradient along which they move (the increasing field for the anode initiation and the decreasing field for the cathode initiation).

The physical model of this process with well substantiated quantitative estimates for water and liquefied noble gases under exposure to submicrosecond voltage pulses was developed in the series of works (for example, see [7,47,48]).

The given model has four stages:

1) Formation of the region of spontaneous gas nucleation centers near the cathode. The required energy density is 10^9 J/m^3 for water and 10^8 J/m^3 for liquefied argon.
2) Expansion of this region until the density of substance decreases to the value at which the collision ionization begins; the size of this region must be no less than the critical avalanche length.
3) Development of an electron avalanche and its conversion into an ionized front.
4) Front propagation at the expense of three processes indicated above but ahead of the ionized front.

The model of discharge ignition and propagation is based on the assumption that the collision ionization coefficient α is equal to zero at $E = E_{\mathrm{br}}$ and on the experimental dependences of the breakdown time τ_{br} on the hydrostatic pressure P, electrical conductivity γ, and interelectrode distance d.

Since according to the available experimental data it follows that the low-voltage conductivity of liquids has essentially no effect on the breakdown characteristics, it is assumed that the role of the ion current is negligibly small. The electron autoemission from cathode plays the key role in the energy liberation and formation of the gas-phase nucleation centers.

In [29, 49] it was demonstrated that the Fowler–Nordheim equations for the probability D of electron tunneling through the potential barrier and the autoelectronic emission current density j from metal to vacuum describe well

the autoelectronic emission in dielectric liquids if π has been replaced by the work function of the electron from metal to the liquid $\pi_{\text{liq}} = \pi + v_0$, where v_0 is the energy of the ground state of the quasi-free electron, and the relative permittivity of the medium ε has been taken into account in the expression for the potential and hence in the argument y described by (7.61).

With the first-order correction for the image forces (the Schottky effect), these expressions assume the form [50]

$$D = \exp\left[-\left(6.8 \cdot 10^7 \pi^{3/2}/E\right)\theta\left(y\right)\right] \qquad (7.59)$$

and

$$j = 1.5 \cdot 10^{-6}\left(E^2/\pi\right)\exp\left[-\left(6.8 \cdot 10^7 \pi^{3/2}/E\right)\theta\left(y\right)\right], \qquad (7.60)$$

where π is the work function, in eV; E is the electric field strength, in V/cm; and j is in A/cm^2. The correction $\theta\left(y\right)$ is the Nordheim function. The parameter

$$y = 3.8 \cdot 10^{-4} E^{1/2}/\varepsilon^{1/2}\pi \qquad (7.61)$$

specifies a decrease in the work function due to the Schottky effect (that is, the image forces) for the electron with the given energy. The function $\theta\left(y\right)$ was tabulated by Nordheim; therefore, D and hence j can be easily calculated.

For n-hexane, $v_0 \approx 0$ and $\pi_{\text{liq}} = \pi \approx 4.5\,\text{eV}$ for the tungsten emitter (at the temperature $T = 293\,\text{K}$) [27]. Table 7.3 tabulates the calculated D and j values for emission into n-hexane ($\varepsilon = 1.8$) versus the electric field strength E for the indicated work functions π for the electron that escape from the metal. It can be seen that the electric field strength for the autoelectronic emission must be $\geq 10^7\,\text{V/cm}$ depending on the work function of the electron that escapes from the metal. Attention is drawn to the extraordinary fast increase in the transparency with the field and to the high currents at very small D values. The latter is explained by the fact that the number of electrons bombarding per second the barrier wall is so great what even for insignificant probabilities

Table 7.3. Probability of electron tunneling D and autoelectronic emission current density j for n-hexane versus the electric field strength E for the indicated values of the work function π of the electron that escapes from the metal

E, V/cm	$\pi = 4.5\,\text{eV}$		$\pi = 3.0\,\text{eV}$		$\pi = 2.0\,\text{eV}$	
	D	j, A/cm^2	D	j, A/cm^2	D	j, A/cm^2
$9 \cdot 10^6$			$3 \cdot 10^{-16}$	$1.2 \cdot 10^{-8}$	$2 \cdot 10^{-8}$	1.2
10^7	$1.6 \cdot 10^{-27}$	$5.3 \cdot 10^{-20}$	$1.3 \cdot 10^{-14}$	$6.3 \cdot 10^{-7}$	$1.5 \cdot 10^{-7}$	$1.1 \cdot 10^1$
$2 \cdot 10^7$	$1.5 \cdot 10^{-13}$	$2 \cdot 10^{-5}$	$4.1 \cdot 10^{-7}$	$8.2 \cdot 10^1$	$1.8 \cdot 10^{-3}$	$5.5 \cdot 10^5$
$3 \cdot 10^7$	$5.5 \cdot 10^{-9}$	1.6	$1.2 \cdot 10^{-4}$	$5.5 \cdot 10^4$	$3.6 \cdot 10^{-2}$	$2.5 \cdot 10^7$
$4 \cdot 10^7$	$1.0 \cdot 10^{-6}$	$5.3 \cdot 10^2$	$2.2 \cdot 10^{-3}$	$1.8 \cdot 10^6$	$1.9 \cdot 10^{-1}$	$2.3 \cdot 10^8$
$5 \cdot 10^7$	$2.5 \cdot 10^{-5}$	$2.1 \cdot 10^4$	$1.2 \cdot 10^{-2}$	$1.5 \cdot 10^7$		
$6 \cdot 10^7$	$2 \cdot 10^{-4}$	$2.4 \cdot 10^5$				

of the electron escape, high currents are recorded. From Table 7.3 it can be seen that the emission current density increases rather fast with decreasing work function, because $\pi^{3/2}$ is under the exponent sign in (7.60).

A comparison of the data presented in Tables 7.1 and 7.3 demonstrates that the emission currents are by several orders of magnitude higher than the ionization currents for the same electric field strengths. That is, lower electric field strengths are required for the electron emission from the metal to n-hexane than for ionization, which is confirmed by the experimental results [27].

The autoelectronic emission in a strong electric field was observed near the negatively charged tip surface in liquefied gases [29], n-hexane [27], cyclohexane [28], and other liquids. For example, the electric field strength $E \approx 2 \cdot 10^7$ V/cm was necessary for cold electron emission into cyclohexane. For emission currents $> 10^{-9}$ A, the deviation from the Fowler–Nordheim equation (7.60) was observed. This is due to the effect of the spatial charge formed in liquids because of the low mobility of charge carriers.

As already indicated above, the running emission current can result in fast local superheating of liquids and spontaneous bubble generation [7, 29]. We now try to invoke the processes of local liquid superheating by emission currents to explain the mechanism of the electric discharge initiation from cathode for n-hexane in a quasi-uniform electric field. We note that under conditions of n-hexane breakdown from cathode, a strong influence of the external pressure on the electric discharge was revealed (see Fig. 3.16 in Sect. 3.4). Comparatively low external pressures prevented the breakdown formation.

The solid curve in Fig. 7.17 shows the dependence of the average statistical discharge time lag on the external pressure for n-hexane calculated for model (7.30)–(7.32) with the temperature of the metastable liquid $T = 210\,°C$ and characteristic radius of the energy absorption region $r_0 = 5.1 \cdot 10^{-8}$ cm. Here closed circles show the experimental results obtained from the statistical distributions of the breakdown time lag (Chap. 5) for the electric discharge from cathode, the electric field strength $E = 1.3$ MV/cm, and the interelectrode distance $d = 100\,\mu$m. The vertical dashed straight line here indicates the pressure starting from which the breakdown is not formed. It can be seen that the experimental data are in qualitative agreement with the calculated dependence. With increasing pressure, points of the curve smoothly approach the asymptote corresponding to a critical pressure of 0.4 MPa. According to (7.34), the breakdown criterion is the liberation of the volume energy density $W \approx 245$ J/cm^3 near the cathode. It should be noted that the temperature of the superheated liquid, characteristic radius of the energy absorption region, and the specific energy liberation are close to values observed for the electric discharge initiation from anode for n-hexane. Therefore, the above estimates of the required emission currents by (7.36) ($\geq 10^{-7}$ A) and of the characteristic liquid heating time by (7.37) ($\sim 10^{-9} - 10^{-7}$ s) for the tip electrodes with end radii of $\sim 0.01 - 0.1\,\mu$m remain valid here.

The given model is in qualitative agreement with the electrooptical investigations of pre-breakdown phenomena in nitrobenzene for microsecond voltage
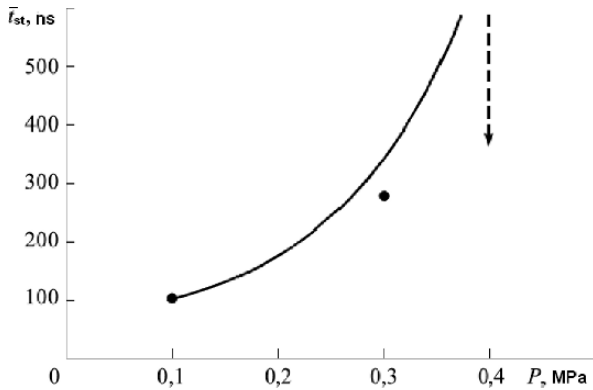
Fig. 7.17. Dependence of the average statistical discharge time lag for n-hexane on the external pressure. The solid curve shows the calculated results at the superheated liquid temperature $T = 210°C$ and the radius of the energy liberation region $r_0 = 5.1 \cdot 10^{-8}$ cm. Closed circles and the vertical dashed straight line show the experimental results for the electric discharge from cathode ($E = 1.3\,\mathrm{MV/cm}$ and $d = 100\,\mu\mathrm{m}$)

pulses [51]. In [51] it was demonstrated that the emission of charge carriers from the electrodes precedes the microbubble occurrence.

The thermal mechanism of microbubble formation is confirmed by the experimental data reported in [52, 53]. In these works, the formation of vapor bubbles near the tip cathode was investigated for cyclohexane and other hydrocarbon liquids. It was established that the microbubble occurrence and subsequent growth near the electrode were observed after running of a current pulse. Moreover, the external pressure did not influence the current running mode and affected only the bubble dynamics. This proves that the bubble results from the current pulse. Since the bubble is generated only when the pressure is below the critical level for the liquid, the mechanism of bubble formation is local boiling of the liquid due to high power density. Fast and local electric energy liberation results in intensive heating of the liquid near the tip and its subsequent nucleation. A high degree of correlation between the microbubble occurrence near the tip cathode and the current was also confirmed by the experimental results obtained in [54] for n-hexane.

If the liquid density decreases as a result of heating and nucleation to the critical value $\rho = \rho_{\mathrm{cr}} = 10^{20}\,\mathrm{cm}^{-3}$, avalanches will be developed. According to [55], electrons are localized in water for $\rho > \rho_{\mathrm{cr}}$. The avalanches are no longer developed if the space charge field becomes comparable with the external field E_{ext}. Electron avalanches moving from the cathode continue to heat the liquid and to decrease its density ρ to values smaller than ρ_{cr}. New avalanches forming an ionized channel can be observed in this region. The contribution of energy to this region of the liquid depends on the channel resistance that must be low enough to provide an energy inflow from the

external electric circuit. This cycle of liquid heating, decrease in its density, avalanche growth to the critical size, and conversion of the avalanche into an ionized channel provides the propagation of the ionized front to the opposite electrode.

In this case, the discharge (breakdown) time lag τ_{br} is expressed as the sum of four components:

$$\tau_{\mathrm{br}} = \tau_{\mathrm{nucl}} + \tau_{\mathrm{exp}} + \tau_{\mathrm{cr}} + \tau_{\mathrm{c.p}},$$

where τ_{nucl} is the time of gas phase formation (nucleation), τ_{exp} is the time of expansion of the region and decrease in ρ to ρ_{cr}, τ_{cr} is the time of avalanche growth to the critical size, and $\tau_{\mathrm{c.p}}$ is the time of avalanche conversion into a streamer and streamer crossing of the interelectrode gap.

By analogy with the gas discharge, τ_{nucl} can be identified with the statistical discharge time lag τ_{st}, and the sum of three terms $\tau_{\mathrm{exp}} + \tau_{\mathrm{cr}} + \tau_{\mathrm{c.p}}$ can be identified with the discharge formation time τ_{f}.

The breakdown criterion for the given model is obtained by quantitative estimation of each of four τ_{br} components.

To estimate τ_{br}, it was assumed that the necessary (but insufficient) condition of breakdown initiation is the formation of a single heated region with volume r_{t}^3 [29] during τ_{nucl}. According to [29], the nucleation rate can be found from (7.30).

The time τ_{nucl} was calculated from (7.11)–(7.13) for $E_{\mathrm{br}} = 660\,\mathrm{kV/cm}$, $E = 700E_{\mathrm{br}}$ (with allowance for the field gain by surface cathode microinhomogeneities), $j = 7 \cdot 10^2\,\mathrm{A/cm}^2$ (for typical emission current $\approx 9 \cdot 10^7\mathrm{A}$ and the above-indicated electric field strength [7]), and the characteristic radius of the energy absorption region $r_0 = 2 \cdot 10^{-5}\,\mathrm{cm}$.

The calculated τ_{nucl} values are in good agreement with the values measured in [47] (Figs. 7.18 and 7.19).

The character of the dependence of τ_{nucl} and external pressure P_{ext} on E_{br} can be explained if we consider the energy that must be liberated in the
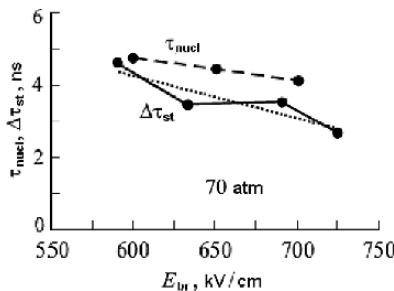
Fig. 7.18. Dependence of the time of forming gas phase nucleation centers τ_{nucl} and difference between the statistical time lags τ_{st} for degassed and nondegassed water on the electric field strength [48]
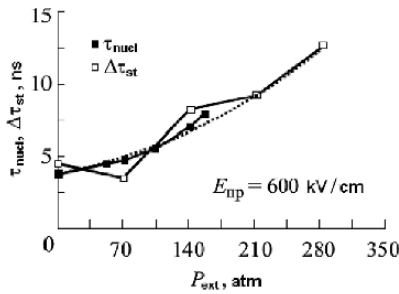
Fig. 7.19. Dependence of the time of forming gas phase nucleation centers τ_{nucl} and difference between the statistical time lags τ_{st} for degassed and nondegassed water on the external pressure

liquid at the expense of the emission current to increase the saturated vapor pressure P_v and hence nucleation S. Thus, an increase in τ_{lag} with $P_{ext}(E)$ is partly explained by the increase in τ_{nucl} with $P_{ext}(E)$.

Results of calculations of τ_{exp} were presented in [7]. For $E_{br} \approx 600\,\text{kV/cm}$ and the parameters the same as for calculations of τ_{nucl}, τ_{exp} turns out to be smaller than 1 ns.

The time of avalanche development to the critical size was calculated based on the assumption that this event occurs in the gas (vapor) phase. According to [7], the impact ionization coefficient for water vapor can be found from the expression:

$$\alpha/P_v = 12.9e^{-289P_v/E} \tag{7.62}$$

valid for $150 \leq E/P_v \leq 1000$ (where P_v is in mm Hg and E is in V/cm).

The Clausius– Clapeyron equation used to obtain the dependence of the vapor pressure $P_v\,[T(\tau)]$ at time τ after bubble nucleation shown in Fig. 7.20 demonstrates that E/P_v is well described by (7.62) when $\tau = 0.1\,\text{ns}$.
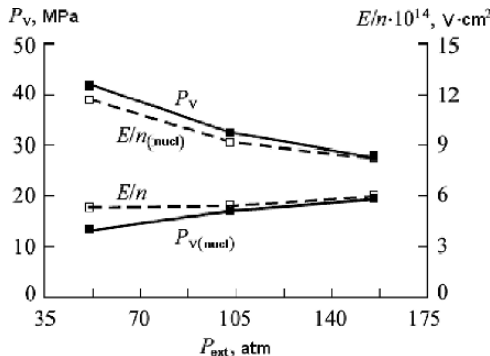
Fig. 7.20. Dependences of the vapor pressure P_v, pressure in the region of gas phase nucleation $P_{v(nucl)}$, and ratio E/n [E/p used in (7.62)] on the external pressure

Thus, (7.62) characterizes the maximum rate of increase in the electron density. It remains exponential until the field strength of the space charge $E_{\text{s.c}}$ acquires the same order of magnitude as E_{br}. At this moment of time, the total field $E_{\text{br}} + E_{\text{s.c}}$ inside the ionization region decreases with accompanying increase at the region boundary and the corresponding higher rate of electron density increase. By analogy with the avalanche-streamer transition in gases, the electron density increase will slow down at $\alpha r_{\text{cr}} = 18$. For concrete values of E and n in the heated region, $\alpha r_{\text{cr}} = 18$ determines the critical size r_{cr} of the region with reduced density in which the increased rate of the subsequent expansion and collision ionization is observed mainly in the direction of the field amplified by the space charge field. The dependence of r_{cr} on P_{ext} was found for the parameters corresponding to those of Figs. 7.18 and 7.19, and the P_{v} value was taken for a gas bubble. For the examined P_{ext} values, the equality $\alpha r_{\text{cr}} = 18$ is satisfied for $r \approx 10^{-6}$ cm, which is less than r_{cr}, because the avalanche becomes critical inside the region with $n \leq n_{\text{cr}}$. The time of avalanche growth to the critical size appeared much less that 1 ns [7].

Electrons from the avalanche head are injected into the liquid through the gas (vapor) - liquid interface and produce local heating of the liquid reducing its density. New avalanches develop in this region with $n \leq n_{\text{cr}}$. Due to this sequence of events, the ionization front propagates toward the anode.

7.3 Ionization Mechanism of Discharge Initiation

As already pointed out in Sects. 3.1 and 3.5, the so-called homogeneous electric discharge is observed for nanosecond voltage pulses, which exists and competes with the conventional discharge, that is, with the discharge ignited by the microexplosive mechanism. It is characteristic that the first rather slow phases of the discharge ignition (formation of shock waves – gas formation in the process of collisions – ionization inside microbubbles – origin of a plasma channel) are not observed for it. In this case, the first registered event is a brightly luminous rudiment of the discharge channel. The fact that the first-order phase transition does not participate in the formation of the initial discharge stages is also confirmed by the absence of the effect of external pressure. This mechanism becomes dominant for nanosecond voltage pulses and elevated pressures.

There are grounds to suggest that the initiation and propagation of the homogeneous electric discharge from anode is caused by the autoionization processes in the liquid, that is, the ionization discharge ignition mechanism is realized. In this case, the discharge ignition time lag is analogous to the statistical time lag (Chap. 2). The high field strength necessary for ionization of molecules in the liquid is provided by both large potential difference withstand by the liquid under exposure to a nanosecond pulse (Sect. 6.1) and high field gain near the microinhomogeneities on the electrode surface (Sect. 6.6.1).

Generation of intensive local electric fields due to structural fluctuations inside the dielectric can play the important role in the liquid ionization.

Based on the results obtained in [56, 57], the fluctuation model of ionization of liquid dielectrics was suggested in [58] and developed in [65]. The growth of the discharge channels was approximately described by a threshold-type criterion. If the local field (depending on the potential and radius of the channel head) is

$$E_{\mathrm{loc}} > E^* + \delta, \qquad (7.63)$$

a new conducting phase region arises in this place. Here E^* is the characteristic of the substance whose physical meaning is the threshold breakdown field for the ideal dielectric and δ specifies the random fluctuations of this field caused by many reasons. One of them is that the field acting on a polarizable liquid molecule changes the field magnitude and direction because of thermal fluctuations in the position of the neighboring polarized particles. This effect is analogous to the Holtsmark fluctuations of microfields in the plasma. On the other hand, states with vibrational degrees of freedom and electron configurations are excited with a certain probability because of interaction of molecules with each other during their thermal motion. Therefore, there is a noticeable probability of ionization of molecules in the distant wing of the Boltzmann distribution in the electric field. The spatial inhomogeneities of the dielectric itself also influence the field fluctuations. All this makes the breakdown a stochastic process. It is clear that the negative δ fluctuations play the determining role.

The fluctuations of the statistical time lag result from the temporal fluctuations of the substance state near sharp microbulges on the anode surface.

The main experimental features of the electric discharge are:

– fractal character of the electric discharge with the well-developed branched structure,
– dependence of the electric discharge structure on the electric field strength,
– threshold breakdown character and strong dependence of the statistical discharge time lag and discharge formation time on the field strength,
– opportunity of initiation and development of several discharge structures.

They all are well reproduced and explained in the context of the fluctuation model [59].

This testifies to the important role of the probabilistic processes that are taken into account in the given model through fluctuations in the local threshold breakdown condition. A more detailed physical explanation of the fluctuation breakdown model can be found in [60].

In conclusion, it should be noted that the discharge ignition by the microexplosive and ionization mechanisms realized in gaps for high overvoltages are accompanied by melting and even sublimation of metal of tip electrode with small r_0 and microbulges on the electrode surface with large area of stressed surface [62, 63]. The most reliable quantitative data on this

phenomenon were obtained for tip electrodes with small rake angles (8–30°) and end radii (1–10 μm). Depending on the experimental conditions (electrode geometry, liquid type, and electric field strength), the mass of the metal carried away from the tip electrode during a single interrupted discharge was within the limits $\sim 10^{-10}$–10^{-5} g. A part of this mass was transferred to the opposite electrode (for millimeter and submillimeter gaps). This phenomenon confirms once again the explosive character of the processes in the discharge ignition stage for the liquid under exposure to short pulses.

The authors of this monograph recognize that at present the subdivision of the processes that provide the basis for the discharge ignition under conditions when the *bubble* and *electrothermal* mechanisms cannot be realized into *microexplosive* and *ionization* is to some extent hypothetic. This is caused by insufficiently exact determination of the boundaries of their existence and distinctive parameters. Only further careful studies will allow the problem of the number and boundaries of applicability regions of different discharge initiation mechanisms to be solved. These investigations are continued, and some results have already been reported at the 2005 IEEE International Conference on Dielectric Liquids, Coimbra, Portugal, June 26 - July 1, 2005 (for example, see [67] and the references therein).

References

1. I. M. Gavrilov, V. R. Kukhta, V. V. Lopatin, et al., Formation of a pulsed discharge in water, Russ. Phys. J., No. 1, 88–92 (1989).
2. V. Kukhta and V. Lopatin, Discharge propagation in water in a non-uniform field, in: Proc. 12th Int. Conf. on Conduction and Breakdown, Rome, (1996), pp. 259–262.
3. I. M. Gavrilov, V. R. Kukhta, and V. V. Lopatin, The effect of heating and EHD events on breakdown in water, in: Proc. 10th Int. Conf. on Conduction and Breakdown in Dielectric Liquids, Grenoble, (1990), pp. 593–598.
4. V. R. Kukhta and V. V. Lopatin, Inception and development of prebreakdown cavities in water, in: Proc. 13th Int. Conf. on Conduction and Breakdown, Nara, (1999), pp. 473–476.
5. S. M. Korobeynikov and E. V. Yanshin, Model of prebreakdown processes in liquid dielectrics under pulse voltage, in: Conf. Record of the 9th Int. Conf. on Conduction and Breakdown in Dielectric Liquids, Salford (1987), pp. 398–402.
6. S. M. Korobeynikov, On the role of bubbles in liquid electric breakdown, Teplofiz. Vys. Temp., No. 3, 362–367 (1998).
7. H. M. Jones and E. E. Kunhardt, Pre-breakdown currents in water and aqueous solutions and their influence on pulsed dielectric breakdown, J. Appl. Phys., **78**, No. 5, 3308–3314 (1995).
8. J. M. Meek and J. D. Craggs, Electrical Breakdown of Gases, Oxford at the Clarendon Press, (1953).
9. Yu. D. Korolev and G. A. Mesyats, Physics of Pulsed Breakdown in Gases, Ekaterinburg: URO – press, (1998).

10. E.M. Bazelyan, Yu P. Raizer, Spark Discharge, CRC Press, N̲o̲ 4, Roca, Raton, (1997), 294 P.

11. N. Felici, Electrostatics and hydrodynamics, J. Electrostat., **4**, 119–139 (1978).

12. V. V. Glazkov, O. A. Sinkevich, and P. V. Smirnov, A spherical bubble in liquid dielectric with an electric field, Teplof. Vys. Temp., **29**, No. 6, 1095–1102 (1991).

13. S. M. Korobeynikov, Effect of the electric field on the boiling point of liquids, Inzh.-Fiz. Zh., No. 6, 1131–1134 (1981).

14. S. M. Korobeynikov and E. V. Yanshin, Dynamics of the electrostriction pressure near the spherical electrode, Zh. Tekh. Fiz., **53**, No. 10, 2101–2111 (1983).

15. K. Yoshino et al., Pressure dependence of dielectric breakdown in liquid nitrogen, Jpn. J. Appl. Phys., 2051–2057, (1981).

16. V. P. Borodin and V. F. Klimkin, Effect of pressure on the mechanisms of n-hexane electric breakdown, Pis'ma Zh. Tekh. Fiz., **14**, No. 9, 802–805 (1988).

17. K. Kao and J. McMath, Time-dependent pressure effects in liquids, IEEE Trans. El. Insul., **EI5**, 64 (1970).

18. E. P. Kruglyakov et al., Investigation of diffusion electrodes in water breakdown, Zh. Tekh. Fiz., **50**, No. 5, 993–998 (1980).

19. K. C. Kao and J. B. Higham, The effect of hydrostatic pressure, temperature and voltage duration on the electric strength of hydrocarbon liquids, J. Electrochem. Soc., **108**, 252 (1961).

20. M. I. Abramovitz and I. M. Stegun, eds., Handbook of Mathematical Functions, U.S. Govt. Printing Office, Washington (1972).

21. B. Halpern and R. Gomer, Field ionization in liquids, J. Chem. Phys., **51**, No. 3, 1048–1056 (1969).

22. A. Sommerfeld, H. Bethe, Electronentheorie der Metalle, 2nh edn., Springer Verlag, Berlin, (1933).

23. W. F. Schmidt, Electrons in non-polar dielectric liquids, IEEE Trans. El. Insul., **EI26**, No. 4, 560–567 (1991).

24. I. G. Kaplan, A. M. Miterev, and V. Ya. Sukhonosov, Modeling of the primary water radiolysis stage on irradiation by fast electrons, Khim. Vys. Energ., **23**, No. 5, 392–397 (1989).

25. E. V. Myuller, Autoionization and autoionization microscopy, Usp. Fiz. Nauk, **57**, No. 3, 481–552 (1962).

26. W. F. Schmidt, Electronic conduction processes in dielectric liquids, IEEE Trans. El. Insul., **EI19**, No. 5, 389–418 (1984).

27. K. Dotoku, H. Yamada, S. Sakamoto, et al., Field emission into nonpolar organic liquids, J. Chem. Phys., **69**, No. 3, 1121–1125 (1978).

28. A. Denat, J. P. Gosse, and B. Gosse, Electrical conduction of purified cyclohexane in a divergent electric field, IEEE Trans. El. Insul., **EI23**, No. 4, 545–554 (1988).

29. B. Halpern and R. Gomer, Field emission in liquids, J. Chem. Phys., **51**, No. 3, 1031–1047 (1969).

30. V. E. Klimkin, Bubble generation model for initiating breakdown from anode in n-hexane with quasi-uniform electrical fields, in: Proc. of the 13th Int. Conf. on Dielectric Liquids, Nara, 199–202 (1999).

31. V. P. Skripov, E. N. Sinitsyn, P. A. Pavlov, et al., Thermal Physics Properties of Liquids in the Metastable State, Atomizdat, Moscow (1980).

32. T. J. Lewis, Electronic processes in dielectric liquids under incipient breakdown stress, IEEE Trans. El. Insul., **EI20**, No. 2, 123–132 (1985).

33. V. F. Klimkin and A. G. Ponomarenko, Investigation of the initial discharge stage in liquid dielectrics by optical methods, in: Proc. of the 14th Int. Congress on High-Speed Photography and Photonics, Moscow, 385–389 (1980).
34. Yu. S. Yakovlev, Hydrodynamics of Explosion, Sudpromgiz, Leningrad (1961).
35. H. S. Yadav, D. S. Murty, S. N. Verma, et al., Measurement of refractive index of water under high dynamic pressures, J. Appl. Phys., **44**, No. 5, 2197–2200 (1973).
36. K. A. Naugol'nykh and N. A. Roi, Electrical Discharges in Water, Nauka, Moscow (1971).
37. E. V. Yanshin, I. T. Ovchinnikov, and Yu. N. Vershinin, A mechanism of pulsed breakdown of water, Dokl. Akad. Nauk SSSR, **214**, No. 6, 1303–1306 (1974).
38. V. Y. Ushakov, Electrical conductivity and breakdown propagation in liquid dielectrics, Russian Phys. J., No. 1, 105–121 (1979).
39. V. Ya. Sukhonosov, A mechanism of physical and chemical processes of a pre-discharge stage of electrical breakdown of liquid water, Khim. Vys. Energ., **28**, No. 5, 473–474 (1994).
40. L. T. Bugaenko, V. M. Byakov, and S. A. Kabakchi, A mechanism of water radiolysis, Khim. Vys. Energ., **19**, No. 4, 291–302 (1985).
41. V. Ya. Sukhonosov and I. G. Kaplan, Excitation of shock waves in water under irradiation by fast electrons, Khim. Vys. Energ., **28**, No. 3, 214–217 (1994).
42. V. V. Saraeva, Radiolysis of Hydrocarbons in the Liquid Phase, Publishing House of Moscow State University, Moscow (1986).
43. J. S. Clements, M. Sato, and R. H. Davis, Preliminary investigation of pre-breakdown phenomena and chemical reaction using a paused high-voltage discharge in water, IEEE Trans. Ind. Appl., **23**, No. 2, 224–234 (1987).
44. V. F. Klimkin and V. V. Pikalov, On the possibilities of microinterferometry in the study of nonstationary processes, Prikl. Mekh. Tekh. Fiz., No. 3, 14–26 (1979).
45. I. K. Kikoin, ed., Tables of Physical Quantities, Atomizdat, Moscow (1976).
46. N. M. Baron, E. I. Kvyat, E. A. Podgornaya, et al., Handbook of Physicochemical Quantities, Khimiya, Leningrad (1972).
47. H. M. Jones and E. E. Kunhardt, Development of pulsed dielectric breakdown in liquids, J. Phys., **D28**, 178–188 (1995).
48. H. M. Jones and E. E. Kunhardt, Evolution of cathode-initiated pulsed dielectric breakdown in polar and nonpolar liquids, in: Proc. of the 12th Int. Conf. on Dielectric Liquids, Roma, (1996), pp. 365–368.
49. V. Y. Ushakov, Pulsed Breakdown of Liquids, Publishing House of Tomsk State University, Tomsk (1975).
50. M. I. Elinson and G. F. Vasiljev, Autoelectronic Emission, Publishing House of Physical and Mathematical Literature, Moscow (1958).
51. E. V. Yanshin, K. V. Yanshin, and S. M. Korobeynikov, Space charge and pre-breakdown bubble formation near point electrodes under pulse voltage, in: Conf. Record of the 8th Int. Conf. on Conduction and Breakdown in Dielectric Liquids, Pavia, (1984), pp. 194–198.
52. R. Kattan, A. Denat, and O. Lesaint, Generation, growth and collapse of vapor bubbles in hydrocarbon liquids under a high divergent electric field, J. Appl. Phys., **66**, 4062–4066 (1989).
53. R. Kattan, A. Denat, and N. Bonifaci, Formation of vapor bubbles in non-polar liquids initiated by current pulses, IEEE Trans. El. Insul., **EI26**, No. 4, 656–662 (1991).

54. K. L. Stricklett, C. Fenimore, E. F. Kelly, et al., Observation of partial discharge in hexane under high magnification, IEEE Trans. El. Insul., **EI26**, No. 4, 692–698 (1991).

55. V. Giraud and P. Krebs, The onset of electron localization in subcritical water vapor, Chem. Phys. Lett., **86**, 85–90 (1982).

56. V. F. Klimkin, Mechanisms of electrical breakdown of water from tip anode in the nanosecond range, Pis'ma Zh. Tekh. Fiz., **16**, No. 4, 54–58 (1990).

57. V. F. Klimkin, A mechanism of electrical breakdown of n-hexane in the nanosecond range, Zh. Tekh. Fiz., **60**, No. 6, 161–163 (1990).

58. A. L. Kuperstokh, A Fluctuation model of liquid dielectric breakdown, Pis'ma Zh. Tekh. Fiz., **18**, No. 19, 91–96 (1992).

59. V. F. Klimkin and A. L. Kupershtokh, Statistical lag time in fluctuation model of liquid dielectric breakdown and experimental results, in: Proc. of the 11$^{\text{th}}$ Int. Conf. on Conduction and Breakdown in Dielectric Liquids, Baden-Dattwil, (1993), pp. 395–399.

60. A. L. Kupershtokh, Propagation of streamer top between electrodes for fluctuation model of liquid dielectrics breakdown, in: Proc. of the 12th Int. Conf. on Conduction and Breakdown in Dielectric Liquids, Roma, (1996), pp. 210–213.

61. E. F. Kelley and R. E. Hebner, The electric field distribution associated with prebreakdown phenomena in nitrobenzene, J. Appl. Phys., **52**, No. 1, 191–195 (1981).

62. V. M. Muratov and V. Y. Ushakov, Phenomena on the electrodes in pulsed breakdown of electrolytes in micron gaps, in: High-Voltage Engineering, Publishing House of Tomsk State University, Tomsk, (1973), pp. 31–33.

63. V. V. Lopatin, V. Y. Ushakov, and V. P. Chernenko, Ignition and propagation of a nanosecond discharge in liquids, Russ. Phys. J., No. 3, 100–105 (1975).

64. J. C. Martin, Nanosecond pulse technique, Preprint, Aldermoston, Berks (1970).

65. A. L. Kupershtokh and D.I. Karpov, Models of Pulse Conductivity of Streamers Propagating in Dielectric Liquid, 2005 IEEE Intern. Conf. on Diel. Liquids, Portugal, Coimbra, June 26-July 1, (2005), pp. 87–90.

66. M. Kim, S. D. Reedy, and R. E. Hebner, The incipient mode of streamers in a dielectric liquid as a function of electric field, in: Proc. 2005 IEEE Int. Conf. on Dielectric Liquids, Coimbra (2005), pp. 71–74.

67. O. L. Hestad, S. Ingebrigtsen, and L. E. Lundgaard, Streamer initiation in cyclohexane, Midel 7131 and Nyrto 10X, in: Proc. 2005 IEEE Int. Conf. on Dielectric Liquids, Coimbra (2005), pp. 123–126.

8

Mechanisms of Discharge Propagation and their Applicability Limits

For the stage of discharge propagation, three mechanisms (three discharge types) can be considered essentially different: 1) *fast* (supersonic), 2) *slow* (subsonic), and 3) *electrothermal*.

In the first case, the breakdown of liquids is usually called *ionization* bearing in mind that the initial phase state of the liquid is disturbed (changes) as a result of ionization processes in the liquid itself (in the liquid phase). In the second case, it is called *bubble* emphasizing that the propagation channel is connected with the formation of gas (vapor) bubbles. Their ionization provides the channel grows (elongation). Electron emission from the plasma channel into the liquid is accompanied by energy liberation in the liquid near the channel head and formation of new bubbles. Noticeable contribution comes from the gas bubbles that have already existed in the liquid before the field application (in the case of discharge in non-degassed liquids).

In most cases, the discharge from anode propagates as a *fast* discharge, while the discharge from cathode propagates as a *slow* discharge.

When the electrothermal mechanism of discharge initiation is realized (which is a rather rare case for pulsed breakdown of liquids), breakdown involves the following stages: heating of the liquid (mainly by ion currents), boiling up of the liquid with the formation of gas-vapor cavities, and ionization inside the cavity. The discharge channel is elongated at the expense of motion of the region of local heating to the opposite electrode and boiling up of the liquid. In [1] the maximum rate of channel elongation in water was calculated for this mechanism under assumption that energy liberation is caused by the ion current. Its dependences on the temperature and field strength are described by the Plumley equation. The maximum rate of channel elongation was equal to $5 \cdot 10^4$ cm/s, that is, was somewhat greater than the value measured in experiments on breakdown of electrolytes for long voltage pulses. The discrepancy can be explained by the assumptions used in calculations [1]. Taking into account that this breakdown for the pulsed voltage is a rare (even exotic) phenomenon and that it has already been described in [1] and in the references to the Introduction, we will not dwell on it here.

Since the fast channels from anode and the slow channels from cathode are most clearly pronounced, fast channels are described on the example of positive discharge, and slow channels are described on the example of negative discharge. In so doing, it is important to bear in mind that both slow and fast channels can be observed for one electric breakdown. As a rule, the first channels are transformed into the second ones. However, under certain conditions the sequence of events can be opposite (see Chaps. 3 and 4).

Causes and effects of a large variety of spatial structures of the figures formed by growing discharge channels (bush-like, treelike, umbrella-like, etc.) have already been discussed in ample detail in Chap. 4.

8.1 Propagation of the Fast (Anode) Channel

Intense luminescence registered with photomultipliers and ICC and accompanied by current pulses is taken to mean the discharge channel initiation. This indicates a rather high intensity of ionization processes and high electrical conductivity inside channels. Measurements of the electric field distribution with the help of the Kerr effect technique in nitrobenzene [2] confirmed high electrical conductivity of the channel already at early stages of its propagation registered by other methods (Chap. 4). For the cylindrical model of the conducting channel with the hemispherical end radius $r \sim 5\,\mu$m (see Sect. 3.1), the field amplification in the channel head is ≥ 20. Even higher values will be observed for ellipsoidal channel. For average values of the field strength in the gap equal to $\sim (0.5–1)\cdot 10^6$ V/cm, the electric field strength near the channel head can exceed $(1–2)\cdot 10^7$ V/cm, which is sufficient for the onset of autoionization in the liquid (see Table 7.2), in particular, with allowance for structural fluctuations. This mechanism is in qualitative agreement with strong influence of additives that have low ionization energies and with the absence of influence of additives that trap the electrons on the velocity of positive discharge channel propagation in various liquids (see Sect. 4.1.3).

The physical pattern of the positive initial discharge channel propagation is the following. The ionization processes develop in the liquid due to high electric field strength near the discharge channel head. The electrons are generated in front of the head in the process of autoionization and move toward the head under the effect of the field. They enter into the positively charged channel head and leave behind a new region of positive spatial charge. The generation and motion of charge carriers in a strong electric field provides intensive liberation of thermal energy. This translates the liquid into the supercritical state accompanied by virtually instantaneous formation of gas phase centers with high pressure and temperature. This is followed by fast (supersonic) expansion accompanied by the formation of a shock wave, decrease in the temperature and pressure, and initiation of a gas channel (Fig. 8.1) [3]. The channel column expands with slow (subsonic) velocity $\approx 10^3$–10^4 cm/s [4, 5]. The basic
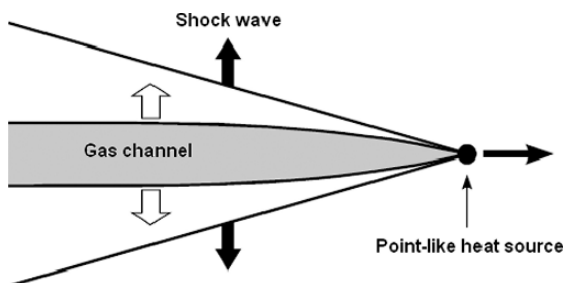
Fig. 8.1. Mechanical model of the initial channel propagation with the head in the form of a point heat source [3]

mechanism of the initial channel elongation is a *continuous creation* of the gas-liquid interface rather than its *motion.*

For an incomplete discharge, the expansion of the channel is followed by its collapse and transformation into a chain of gas bubbles, thereby terminating the initial channel propagation.

Some characteristic parameters, in particular, the scattered power ($\sim$10 W) were estimated in [3], where it was demonstrated that the dynamics, sizes, and lifetime of the initial channel were determined mainly by the inertia of the liquid (the Rayleigh model).

In this case, the influence of electric forces on the dynamics of the initial channel was negligibly small in comparison with the influence of inertia forces.

The full description of the initial channel propagation must take into account several different experimental parameters:

– electric phenomena near and inside the channel head (generation and motion of charge carriers) that depend on the liquid and impurity (additives) properties and the electric field strength
– characteristics of the initial channel (dynamics, internal pressure, lifetime, etc.) that depend mainly on the mechanical parameters: hydrostatic pressure, liquid density and viscosity, etc.
– generation and transport of charge carriers in the initial channel column that determine the electrical conductivity of the channel and depend on the hydrostatic pressure, additives, gas composition in the channel, etc.

Unfortunately, nowadays it is impossible to present a rigorous mathematical description of the processes in the liquid near the head and inside the column of the initial channel. Therefore, a mathematical description of the processes in the liquid near the initial channel head development by us in [1] and for the model suggested more recently in [6] are based on some simplifying assumptions and hence can give only estimates of the parameters.

For the approach suggested in [6], we now calculate the velocity of the initial channel propagation being the most precisely measured parameter of the discharge channel.

The channel is considered as a thin conducting filament with radius of the head and the channel behind it r_0. The number of charge carriers generated in unit time is written as

$$Z = \pi r_0{}^2 n v, \tag{8.1}$$

where n is the electron and positive ion concentration and v is the channel propagation velocity. On the other hand, Z can be expressed as

$$Z = \int\limits_{r_0}^{\infty} 2\pi r^2 N \gamma dr, \tag{8.2}$$

where N is the number of molecules in unit volume and γ is the probability of autoionization in unit time. In (8.2), the hemispherical shape of the channel head is taken into account, and the integral is taken over the entire region before the front. With allowance for the expression for the frequency of electron collisions with the potential barrier [7] and (7.27) for the probability of electron tunneling in unit time, we obtain

$$\gamma = \frac{Eed}{h} \exp \left\{ - \left(\frac{I}{Eed} \right) \left[\ln \left(\frac{2I}{\tau} \right) - 1 \right] \right\} . \tag{8.3}$$

Here E is the electric field strength, I is the gap width (the ionization energy of the liquid phase), τ is the valence band width, d describes spacing of molecules in the liquid, e is the electron charge, and h is Planck's constant. Considering that the field is spherically symmetric, for $r \geq r_0$ we obtain

$$E(r) = E_0 \frac{r_0{}^2}{r^2} = \frac{U r_0}{r^2}, \tag{8.4}$$

where E_0 and U are the field strength and the potential in the channel head, respectively. Combining expressions (8.1)–(8.4), for the velocity we obtain

$$v = \frac{2N E_0 e d}{hn} \int\limits_{r_0}^{\infty} \exp \left\{ - \left(\frac{I r^2}{E_0 r_0{}^2 e d} \right) \left[\ln \left(\frac{2I}{\tau} \right) - 1 \right] \right\} dr . \tag{8.5}$$

At the initial moment of time for $r = 2r_0$ (the front is displaced at the distance of the order of the head radius r_0), the channel propagation velocity is

$$v \approx \frac{2N e d}{h} \left(\frac{E_0 r_0}{n} \right) \exp \left\{ - \left(\frac{2.25 I}{E_0 e d} \right) \left[\ln \left(\frac{2I}{\tau} \right) - 1 \right] \right\} . \tag{8.6}$$

Here the exponent comprises the average distance $\bar{r} = 1.5 r_0$.

Expression (8.6) establishes the dependence of the channel propagation velocity on the head field strength (potential) and physical characteristics of the propagation medium. It can be seen that the velocity increases with decrease in the molecular ionization energy and liquid density (through the multiplier d with allowance for a stronger dependence of the exponential multiplier),

which is in qualitative agreement with the majority of experimental results. According to (8.6), the velocity v is proportional to the head radius r_0 determined actually by sizes of the initial discharge channel (the high-conductivity nucleus). Relationships among the parameters E_0, r_0, and n determine the rate of ionization processes in the given medium.

Having substituted the measured values of the initial channel parameters (see Table 4.8) and some tabulated physical constants into formula (8.6), we obtain $v = 1.4 \cdot 10^7$ cm/s, which is in good agreement with the measured value typical of the fast discharge mode. (Calculations were performed for charged particle concentration $n \sim 3 \cdot 10^{16}$ cm^3, specific conductivity of $\sim 0.1\,\Omega^{-1}$ cm^{-1}, current density of $\sim 2 \cdot 10^3$ A/cm^2, $N = 3.3 \cdot 10^{22}$ cm^{-3}, $d = 3 \cdot 10^{-8}$ cm, $I = 8.76$ eV, $\tau = 3$ eV (for water), $E_0 = 2.15 \cdot 10^7$ V/cm, $n = 3 \cdot 10^{16}$ cm^{-3}, and $r_0 = 5\,\mu$m).

To confirm the autoionization mechanism of charge carrier generation, the electrical conductivity of substance behind the initial channel head and the velocity of the initial channel propagation in the first stage of the leader process in long gaps were calculated in [1]. To estimate the field strength in front of the channel head, it was approximated by a hyperboloid of rotation. Taking into account that its radius r_0 is much less than the interelectrode distance d, we can write

$$E_{\max} = \frac{U - \Delta U}{1.15 \cdot r_0 \log \dfrac{4d}{r_0}}, \tag{8.7}$$

where U is the tip electrode potential and ΔU is the voltage drop across the discharge channel equal to

$$\Delta U = E_{\mathrm{lead}}^{\mathrm{av}} \cdot l_{\mathrm{lead}} + E_{\mathrm{in.ch}}^{\mathrm{av}} \cdot l_{\mathrm{in.ch}} . \tag{8.8}$$

Here l_{lead} and l_{ch} are lengths of the leader and initial channels at the examined moment of time and $E_{\mathrm{lead}}^{\mathrm{av}}$ and $E_{\mathrm{in.ch}}^{\mathrm{av}}$ are the average longitudinal field gradients in the leader and initial channels, respectively.

Setting $r_0 = 1.5 \cdot 10^{-4}$ cm, $U = 1.25 \cdot 10^5$ V, $E_{\mathrm{lead}}^{\mathrm{av}} = 5 \cdot 10^3$ V/cm, $E_{\mathrm{in.ch}}^{\mathrm{av}} = 1.6 \cdot 10^4$ V/cm, $d = 5$ cm, $l_{\mathrm{lead}} = 2$ cm, and $l_{\mathrm{in.ch}} = 0.3$ cm in accordance with the data presented in Tables 4.8 and 4.9 for the discharge in transformer oil and a positive aperiodic pulse whose shape is close to the standard one for $U = U_{50\%}$, from (8.7) with allowance for (8.8) we obtain $E_{\max} \approx 1.3 \cdot 10^8$ V/cm.

In the majority of studies, the critical (threshold) electric field strength in the liquid, that is, the minimum field strength at which the discharge processes are initiated near the tip electrode, is taken to be $(0.7\text{–}11) \cdot 10^7$ V/cm [8,9], that is, close to the value found from (8.7). This value was used in our calculations. According to [10], the probability of autoionization for condensed media in unit time W can be written as

$$W(E) = 4.6 \cdot 10^{-13} \cdot A \cdot \frac{E^{10/3}}{I_o^{5/2}} \cdot 10^{-1.75 \cdot 10^7 \cdot B \cdot I_o^{3/2}/E}, \tag{8.9}$$

where A and B are constants of about unity and I_0 is the ionization potential.

Equation (8.9) can be used to analyze the autoionization processes in liquids because of the existence of the near order in the structure to which the band theory, developed for solid dielectric, has been extended. In [11] the probability of autoionization in the liquid was calculated for the band model of noninteracting molecules. It was established that results of calculations for the band model provide the best agreement with the experiment and give the equation analogous to (8.9).

Time variations of the charged particle concentration due to autoionization can be expressed through the probability W and the concentration of neutral particles in the liquid n_0 as

$$\frac{dn}{dt} = n_o \cdot W\left(E\right) . \tag{8.10}$$

Using the continuity equation for the charge

$$\frac{\partial \rho}{\partial t} + div_j = 0, \tag{8.11}$$

where $\rho = \frac{\varepsilon}{4\pi} \cdot di \cdot VE$ and $j = e \cdot nV$ is the current density created by excessive charge moving with the velocity V.

Equation (8.11) can be written as

$$\frac{dE}{dt} + \frac{4\pi j}{\varepsilon} = 0 . \tag{8.12}$$

Since $V = \sqrt{\frac{2e\lambda}{m}}E$ in a strong electric field, (8.12) assumes the form

$$\frac{dE}{dt} = -\frac{4\pi}{\varepsilon} \ln \sqrt{\frac{2e\lambda}{m}} E, \tag{8.13}$$

or, designating $\frac{4\pi}{\varepsilon} e \sqrt{\frac{2e\lambda}{m}} = C$, we obtain

$$\frac{dE}{dt} = -Cn\sqrt{E} . \tag{8.14}$$

Equation (8.14) can be written as

$$\frac{dE}{dn} \cdot \frac{dn}{dt} = -Cn\sqrt{E} . \tag{8.15}$$

Substituting (8.10) into (8.15), we obtain

$$\frac{dE}{dn} = -\frac{C \cdot n\sqrt{E}}{n_o \cdot W\left(E\right)} . \tag{8.16}$$

Upon integration of (8.16), we obtain

$$n^2 = -2\frac{A_1 \cdot n_o}{C} \int\limits_{E_o}^{E} E^{17/6} \cdot \exp\left(-\frac{B_1}{E}\right) dE, \qquad (8.17)$$

where

$$A_1 = 4.6 \cdot 10^{-13} \cdot I_0^{-5/2} = 4.6 \cdot 10^{-15.5} \left[\frac{\text{cm}^{10/3}}{\text{V}^{10/3} \cdot \text{s}}\right],$$

$$B_1 = 1.75 \cdot 10^7 \cdot 2.3 \cdot I_0^{3/2} \approx 4 \cdot 10^{8.5} \,[\text{V/cm}]\,,$$

$$C = \sqrt{300}\frac{4\pi}{\varepsilon}e\sqrt{\frac{2e\lambda}{m}} \approx 1 \cdot 10^{-2} \left[\frac{\text{V}^{1/2} \cdot \text{cm}^{5/2}}{\text{s}}\right]. \qquad (8.18)$$

Here λ is determined from the expression

$$\lambda = \frac{1}{\sigma_{e\mathcal{M}} \cdot N_\mathcal{M}}, \qquad (8.19)$$

where σ_{em} is the cross section of the electron interaction with the hydrocarbon molecule and N_M is the concentration of molecules. According to [12], σ_{eM} is given by the expression

$$\sigma_{e\mathcal{M}} = 2r \cdot l \,(n - 1) \qquad (8.20)$$

Here $r = 2.45 \cdot 10^{-8}$ cm is half the distance between the molecular axes, $l = 1.23 \cdot 10^{-8}$ cm is the C–C bond length projected onto the cylinder axis, and n is the number of carbon atoms in the molecule.

Taking into account that the average molecular weight of the transformer oil is $\sim$280 [13] and hence $n \approx 20$, we obtain $\sigma_{\text{eM}} = 1.15 \cdot 10^{-14} \,\text{cm}^2$.

Then from (8.19) we obtain

$$\lambda = \frac{1}{1,15 \cdot 10^{-14} \cdot 1,86 \cdot 10^{21}} \approx 4,7 \cdot 10^{-8} \,\text{cm}$$

After integration of (8.17) for $E = E_0$ (before the onset of autoionization, that is, at $t = 0$) and $n = 0$, we obtain

$$n^2 = \tfrac{2A_1 \cdot n_0}{CB_1} \left[E_0^{29/6} \cdot \exp\left(-\frac{B_1}{E_o}\right)\left(1 - \frac{29}{6} \cdot \frac{E_0}{B_1} + \frac{29 \cdot 35 \cdot E_0^2}{6^2 \cdot B_1^2}\right) - \right.$$
$$\left. - E^{29/6} \cdot \exp\left(-\frac{B_1}{E}\right)\left(1 - \frac{29}{6} \cdot \frac{E}{B_1} + \frac{29 \cdot 35}{6^2 \cdot B_1^2}\right) \right] \qquad (8.21)$$

The concentration of the charged particles inside the initial channel head can be found from (8.21) neglecting the second term in square brackets, because $E = E_{\text{in.ch}}^{\text{av}}$ is much less than E_0:

$$n^2 \approx \frac{2A_1 \cdot n_0}{CB_1} E_0^{29/6} \left(1 - \frac{29}{6} \cdot \frac{E_0}{B} + \frac{29 \cdot 35 \cdot E_0^2}{6^2 \cdot B_1^2}\right) \exp\left(-\frac{B_1}{E_0}\right) \qquad (8.22)$$

Knowing the charged particle concentration, the electrical conductivity of the substance averaged over the initial channel cross section can be determined from the equation

$$\gamma = \frac{n_1 \cdot e^2 \cdot \overline{\lambda_1}}{2m\overline{V_1} \cdot 9 \cdot 10^{11}} \ \left[\Omega^{-1} \cdot \mathrm{cm}^{-1}\right] \ . \tag{8.23}$$

Here m is the electron mass, $\overline{\lambda_1}$ is the electron free path in the substance of the initial channel, and $\overline{V_1}$ is the average velocity of thermal motion of electrons at temperature $T[\mathrm{K}]$:

$$\overline{V}_1 = \sqrt{\frac{8kT}{\pi m}} \ . \tag{8.24}$$

To calculate $\overline{\lambda}_1$, $\overline{V}_1$, and n_1, the temperature of the substance inside the initial channel must be known.

For a liquid volume near the initial channel head, where the autoionization is observed, that is, where the field strength E is

$$E = E_0 \left(1 - \frac{2E_0}{B_1}\right), \tag{8.25}$$

the energy balance can be written as

$$\frac{\varepsilon \cdot \varepsilon_0 \cdot E_0^2}{2} = C_v' \cdot \Delta T, \tag{8.26}$$

given that the energy losses from this region are absent.

Physically, condition (8.25) means that n calculated from (8.22) decreases e folds at the boundary of the volume so determined. For $\varepsilon = 2.3$, $E_0 = 1.3 \cdot 10^8\,\mathrm{V/cm}$, $C_V' \approx 2.98\,\mathrm{J/cm}^3 \cdot \mathrm{deg}$, we obtain $\Delta T = 530\,\mathrm{K}$ and $T = 823\,\mathrm{K}$. Here C_V' is the heat capacity of the transformer oil at constant volume [13].

It is obvious that owing to the high temperature of the substance inside the initial channel head exceeding the critical temperature of the liquid, it must expand, and the temperature of the substance inside the initial channel near its head will differ from the temperature calculated from (8.26). Considering that the process is adiabatic, we can find the temperature change from the equation

$$T_2 = T_1 \left(\frac{V_1}{V_2}\right)^{\sigma - 1} \ . \tag{8.27}$$

Here the subscripts 1 and 2 of the temperature T and volume V designate their values before and after expansion, respectively, and σ is the adiabatic exponent for the gas.

Because we are not aware of the literature data on σ values for the gas formed from the transformer oil, we take it equal to that of the ionized gas

formed from water with allowance for the similarity of the examined phe-
nomenon of the initial channel propagation in these liquids. According to [14],
$\sigma = 1.26$.

Considering that V_1 is approximately equal to the volume of a cone,
that is,

$$V_1 = \frac{1}{3}\pi r_1^2 \cdot \Delta l, \tag{8.28}$$

$$V_2 = \pi r_0^2 \cdot \Delta l, \tag{8.29}$$

where Δl is the increment to the channel length, r_0 is the initial channel
radius, $r_1 = r_0 \cdot \sin\Theta$, the angle Θ can be determined from the equation

$$E = E_0 \cdot \cos\Theta = E_0 \left(1 - \frac{2E_0}{B_1} \right) . \tag{8.30}$$

From (8.28), (8.29), and (8.30) we obtain $\frac{V_1}{V_2} = 0.12$.

From (8.27) we obtain $T_2 = 823 \cdot 0.12^{0.26} \approx 475\,\text{K}$.

Using the data on the expansion of the initial channel head region and
on the temperature presented above, we now determine $\overline{\lambda}_1$, $\overline{V}_1$, and n_1 of the
initial plasma channel and hence γ from (8.23). Calculations of v_1, $\overline{\lambda}_1$, and n_1
for these parameters of the initial channel substance give $v_1 = 1.36 \cdot 10^7\,\text{cm/s}$,
$\overline{\lambda}_1 = 3.9 \cdot 10^{-7}\,\text{cm}$, and $n_1 = 3 \cdot 10^{16}\,\text{cm}^{-3}$. Then the electrical conductivity
of the initial channel substance will be equal to $0.121\,\Omega^{-1} \cdot \text{cm}^{-1}$, and the
current density $j = \gamma \cdot E_{av}$ will be equal to $2.18 \cdot 10^3\,\text{A/cm}^2$.

In spite of the fact that the impact ionization by electrons behind the ini-
tial channel head (and inside the cahnnel column), recombination, diffusion
of charge carriers from the initial channel, and other possible effects unknown
to us have been disregarded, the agreement of the main calculated parame-
ters with the experimental data is satisfactory. Thus, according to [15], the
temperature of the substance in the initial channel is 473–573 K.

According to [16], the electron density in the streamer in the initial propa-
gation stages (that is, in the initial channel) is $10^{16}\,\text{cm}^{-3}$. As already pointed
out above, the discrepancy between j and γ values calculated for our model
and values presented in [4, 17] is caused by the different values of the initial
channel radius used in calculations.

The assumption about the main role of autoionization in the formation
of charge carriers in front of the positive initial channel head requires both
further proofs and refinements to reveal and to consider the processes that
may reduce the critical electric field strength required for autoionization and to
refine the electric field strength in the region of the initial channel ionization.

It should be noted that accumulation of proofs for the benefit of autoioniza-
tion as a main mechanism of the initial ionization processes in the liquid phase
is being continued. Whereas 30–40 years ago the assumption about the au-
toionization mechanism of charge carrier formation resulting in the subsequent
initiation of the positive discharge channel was perceived as exotic, it has been
perceived as a reality by many researchers over the last decade [4, 8, 9, 18, 19].

8.2 Propagation of the Slow (Cathode) Channel

After discharge ignition on the cathode, electrons are emitted into the liquid from the plasma of the initiated discharge channel rather than from the metal cathode.

The energy density in front of the head of the propagating channel and hence the rate of its growth depend on the electrical conductivity of the channel for the galvanic coupling of the ionization region with the electrode. This means that the time of local heating of the liquid τ_h depends on the channel dynamics. Therefore, to describe the propagation of the ionization front, a self-consistent analysis of the channel and front dynamics is required.

As follows from the foregoing (Sect. 7.2.2) and [19], the contribution of the components τ_{nucl}, τ_{exp}, and τ_{cr} to τ_{br} is equal to 1–10 ns, 1 ns, and <1 ns, respectively. Thus, $\tau_{cp} \approx \tau_{br} - \tau_{nucl}$. This means that τ_{cp} is the main component of τ_{br} ($\tau_{br} \approx 10 - 80$ ns for measurements [19]). Since $d \ll r_{exp} + r_t$, $v_F \approx d/\tau_{cp}$. Results for $E_{br} = 600$ kV/cm and $d = 0.11$ cm demonstrate that $v_F < v_d$ in stronger fields (Fig. 8.2). This result allows us to conclude the following.

The degree of the electron density increase on the front is determined by the ionization time $\tau_i \approx 1/\alpha v_d$ (here v_d is the electron drift velocity on the front in the amplified field). Under conditions of interest to us, τ_i amounts to several tens of picoseconds. Considering that the front is displaced at the distance $\approx r_c$ during $3\tau_i$, its velocity must be slightly greater than the drift electron velocity ($\approx 10^7$ cm/s).

Since the experiments demonstrate that v_F may be much less than 10^7 cm/s, this means that additional time is necessary to increase the degree of substance ionization inside the channel and hence to decrease its resistance. Therefore, the process that gives the main contribution to τ_r results in an increase in the electrical conductivity that provides the energy inflow to the ionization front.

If the electrical conductivity of the channel is sufficient to provide the potential on the front the same as the potential of the cathode, $\tau_{exp} < 1$ ns.
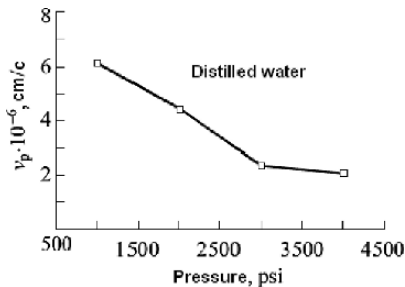
Fig. 8.2. Influence of pressure on the velocity of the ionization front propagation for $d = 0.11$ cm [19]

Therefore, the degree of change of the electrical channel conductivity determines the v_F value. Unlike the breakdown of gases, the initial ionization front in the liquid phase cannot propagate without deposition of energy necessary to decrease the substance density below n_c and to provide the high conductivity of the propagating channel. Thus, the change in τ_{cp} accompanying changes in P_{ex} and electrical conductivity is determined by their influence on heating and conductivity of the channel.

The results presented here demonstrate that $\tau_{ex} + \tau_{br} \ll \tau_{nuc} + \tau_{cp}$. Moreover, the critical radius $r_c < r_{ex}$, so that the discharge formation accompanying the decrease in n to n_c and the corresponding bubble size are sufficient for the ionization front propagation. To initiate a breakdown, it is sufficient to nucleate bubbles bearing in mind that the voltage pulse duration is greater than τ_{br}, the condition $\alpha r = 18$ is satisfied, and there is enough time for the front to flashover the entire gap. For the given degree of heating, there exists a minimum time necessary for the breakdown completion. A relationship between this time τ_{nuc} and the required energy density $E_d = \overrightarrow{j} \cdot \overrightarrow{E} \cdot \tau_{nuc}$ was derived in [19]. For water $E_d \approx 10^9 \, \text{J/m}^3$, and $E_d \approx 10^8 \, \text{J/m}^3$ for liquefied argon. This criterion is satisfied for a wide range of variations of the power density and P_{ex} for microsecond and submicrosecond voltage pulses.

Relatively small differences in spatial structures and main parameters of cathode discharges in liquids that differ by physical and electron properties indicate the common nature of the discharge processes. A lot of experimental data, including the bubble structure of discharge channels, subsonic velocity of channel propagation, strong dependence of discharge processes on the external pressure and independence of the electron properties of the liquid demonstrate the determining role of the vapor-gas phase in discharge initiation and propagation. An analysis of energy of the processes observed in the discharge gap demonstrates that not only for water (liquid with high intrinsic electrical conductivity) but also for classical dielectric liquids like n-hexane, transformer oil, etc. the processes of gas formation and subsequent ionization of gas bubbles can be realized.

For example, in experiments described in Sects. 3.1 and 3.2, the critical bubble radius determined from the condition of equilibrium between the liquid pressure on the bubble wall and the pressure caused by forces of surface tension, on the one hand, and the pressure of the vapor inside the bubble, on the other hand:

$$P_S = P + \frac{2\sigma}{r_{cr}},$$

is $r_c \sim 2 \cdot 10^{-7}$ cm for n-hexane (the field strength $E = 1.3 \, \text{MV/cm}$, interelectrode distance $d = 100 \, \mu\text{m}$, temperature of the liquid $T = 210 \, °\text{C}$, and saturated vapor pressure $p_s \approx 2.1 \cdot 10^6 \, \text{Pa}$). The volume density of energy liberated near the cathode is $W = 245 \, \text{J/cm}^3$, which yields the specific power $\rho_{sp} \approx 2.3 \cdot 10^9 \, \text{W/cm}^3$ for the characteristic heating time $\bar{t}_c = 105 \, \text{ns}$. Under

assumption of constant specific power, the rate of bubble expansion can be estimated from the formula

$$v = \frac{dr}{dt} = \left(\frac{jEt}{2\pi\rho} - \frac{2P}{3\rho} \right)^{1/2},$$

where v is the rate of bubble growth, r is the bubble radius, P is the external pressure, and ρ is the density of liquid.

The rate of bubble growth in 115 ns (10 ns after formation of viable nucleus) reaches $v \approx 2.5 \cdot 10^4$ cm/s, and its radius is $r \approx \Delta r = 2.4\,\mu$m. The radius can be determined from the previous equation upon integration over r from r_c to r and over t from $\bar{t}_c$ to t:

$$\Delta r = r - r_c = \frac{4\pi\rho}{3jE} \left[\left(\frac{jEt}{2\pi\rho} - \frac{2P}{3\rho} \right)^{3/2} - \left(\frac{jE\bar{t}_c}{2\pi\rho} - \frac{2P}{3\rho} \right)^{3/2} \right].$$

Let us estimate the current. For the characteristic bubble radius $r \sim 1\,\mu$m, the electric energy supply is approximately equal to $w \approx \rho_{sp} r^3 t \approx 2 \cdot 10^{10}$ J, and the transferred charge will be $Q = w/u \approx 10^{-14}$ C, where $U = 13$ kV is the potential difference between the electrodes and the current $i = Q/t \sim 10^{-7}$ A is equal to the emission one. After bubble ionization (that is, breakdown) its further expansion occurs under the effect of the electrostatic pressure. The rate of bubble growth in the stage of the development of ionization processes inside it can be estimated from the formula

$$v = \left(\frac{2\varepsilon\varepsilon_0}{3d^{1/2}\rho} \right)^{1/2} \frac{\left(r^{3/2} - r_1^{3/2} \right)}{r^{3/2}} \cdot U$$

derived by equating the work of the electrostatic force to the kinetic energy of the liquid (the work against the external pressure and the work of gas expansion inside the bubble are neglected).

The bubble expansion rate in n-hexane is $V \sim 10^4$ cm/s for $U = 13$ kV and interelectrode distance $d = 100\,\mu$m. This value is in qualitative agreement with the available experimental data. As indicated above, a more detailed analysis calls for a consideration of an increase in the pressure inside the bubble caused by gas heating and field amplification at the bubble pole caused by the bubble elongation under the action of the Coulomb forces that lead to an increased deformation rate.

Once the bubble achieves a characteristic size of $\sim 10 - 15\,\mu$m, the electric discharge channel is initiated which propagates with approximately constant velocity and has a complex shape. The study of its structure upon intensive laser illumination demonstrates that it consists of microbubbles with sizes of $\sim 10\,\mu$m. Of interest are the details of the electric discharge at the vapor-liquid interface that resemble initial cone-shaped perturbations on the cathode and the initiation of new channels at the instability boundary

(see Chaps. 3 and 4). This demonstrates that the discharge propagation from cathode is a multiphase process similar to the stage of cathode discharge ignition.

Small concentrations of electronegative additives influence the shape and propagation velocity of negative discharge channels in various liquids [6,20,21]. The discharge channels become more filament-like and faster. At the same time, additives with low ionization energy do not influence the propagation velocity of negative channels [6]. Spectral analysis of light emitted in the process of negative channel propagation into some organic liquids indicates the presence of hydrogen and carbon atoms and molecules [22]. This means that the electron processes are also involved in the breakdown mechanism.

Optical visualization with simultaneous high-speed measurement of current demonstrates that the propagation of negative discharge channels is accompanied by flashes of discrete increasing current pulses [6, 23–25]. The transition from the initial microbubble (with a diameter of $\sim 10 - 15\,\mu m$) to the channel was investigated in ample detail in [23, 26]. It was established that in the process of generation of subsequent current pulses, new growing microbubbles were observed ahead of the previous ones. Moreover, an increase in the external pressure results in the fast decrease of the number and amplitude of discrete current pulses [20, 27]. This suggests that the subsequent current pulses testify to the occurrence of electric discharges in the vapor phase and injection of energy into the liquid resulting in the formation of new microbubbles [23, 24, 28]. As suggested in [28], after partial discharge hot electrons move toward the bubble pole opposite to the cathode and enter into the liquid forming a space charge layer. The electric field inside the bubble decreases due to shielding by the attached charges and amplifies in the vicinity of the pole. This results in the termination of the discharge in the bubble. The electric field, acting on the charge injected into the liquid, results in the charge penetration into the liquid depth. The liquid is heated and evaporates as a result of dissipation of the electric energy. The voltage in the expanding gas phase increases, thereby leading to a new partial discharge and causing motion of a new portion of charges in the liquid.

Within the framework of the examined model, a mathematical expression for the velocity of channel propagation was derived in [20]. The injected electric energy can be spent for evaporation of the liquid, chemical decomposition, work against the surface tension, propagation of the discharge channel, and ionization [28,29]. Let w_{pr} be the portion of the total electric energy w spend for propagation of the discharge channel, so that

$$w_{\mathrm{pr}} = \beta w, \ 0 < \beta \leq 1 \ . \tag{8.31}$$

Based on the energy considerations, for an arbitrary time moment we can write

$$\frac{\rho v_j^2}{2}\pi r_j^2 dl_j = \beta q_j E_j dl_j, \tag{8.32}$$

where $\rho v_j^2/2$ is the volume density of mechanical energy (neglecting viscosity), v_j is the channel velocity, r_j is the radius of the channel head, dl_j is the channel displacement, q_j is the electric charge injected into the liquid, and E_j is the electric field strength in the discharge channel head. If we assume that the channel propagation is independent of the liquid motion, ρ will be the density of the gaseous phase. Thus, for the velocity of each elementary displacement dl_j of the channel we obtain

$$v_j = \left(\frac{2\beta}{\pi\rho r_j^2}q_j E_j\right)^{1/2}. \tag{8.33}$$

The electric field corresponding to each elementary charge q_j can be estimated with the help of the Gauss theorem:

$$E_j = \frac{\sigma}{\varepsilon\varepsilon_0} = \frac{q_j}{2\pi\varepsilon\varepsilon_0 r_j^2}, \tag{8.34}$$

where σ is the surface charge density in the discharge channel head (for the hemispherical shape of the head with radius r_j), q_j is the elementary charge corresponding to the current pulse i_j.

With allowance for (8.34), for velocity (8.33) we obtain

$$v_j = \left(\frac{\beta}{\varepsilon\varepsilon_0\rho}\right)^{1/2}\frac{q_j}{\pi r_j^2}, \quad q_j = \int i_j dt . \tag{8.35}$$

Formula (8.35) establishes the relation between the channel propagation velocity and the current pulse (injected charge).

For the characteristic values $r_j \sim 5\,\mu m$ (see Sect. 3.4) and $q_j \sim 10^{-11}\,C$ [20], the electric field strength in the channel head, for example, in n-hexane ($\varepsilon = 1.8$) will be $E_j \sim 4 \cdot 10^7\,V/cm$. As indicated above, energy density of about $280\,J/cm^3$ is required for heating and evaporation of n-hexane at atmospheric pressure. For the channel radius $r_j \sim 5\,\mu m$, the required linear energy density is $\sim 2 \cdot 10^{-4}\,J/cm$. Electric energy deposited per unit length is $q_j E_j \sim 4 \cdot 10^{-4}\,J/cm$, which is sufficient for liquid evaporation. For the density of the gas phase in the channel $\rho \sim 10^{-2}\,g/cm^3$ (the pressure $p \sim 5 \cdot 10^5\,Pa$ and the temperature $T \sim 500\,K$) and the channel propagation velocity $v \sim 10^5\,cm/s$, from (8.35) we obtain $\beta \sim 0.01$ (with the same values of r_j and q_j). Thus, the largest portion of the injected electric energy is spent for liquid heating and evaporation.

For average channel propagation velocity we generally have [20]

$$\bar{v} = \frac{1}{\sum\limits_{j=1}^{n} t_j} \cdot \sum\limits_{j=1}^{n} v_{pj} t_{pj}, \tag{8.36}$$

where $t_j = t_{pj} + t_{0j}$, t_{pj} is the current pulse duration, t_{0j} is the time interval to the next pulse, and v_{pj} is determined by (8.35). According to (8.35), the average propagation velocity increases with q_j.

When t_{0j}/t_{pj} increases (the repetition frequency of current pulses decreases), the time interval between two successive partial displacements of the channel increases, and it propagates in steps. The average velocity of channel propagation decreases and depends on q_j. With increase in the applied voltage, t_{0j}/t_{pj} decreases (the repetition frequency of current pulses increases), and the time between two successive partial displacements of the discharge channel decreases. The channel propagates quasi-continuously, and its average velocity increases. It seems likely that exactly this type of negative discharge channels was observed in our experiments.

The branching of the electric discharge channel in the process of its propagation can be due to the development of the electrohydrodynamic instability [30] caused by the action of the Coulomb force on the charge attached to the boundary and resulting in the elongation of the bubble wall. This results in the occurrence of a complex bush-like structure consisting of a large number of thin discharge channels. Once one of the channels is in contact with the opposite electrode, a high-power ionization wave arises in short gaps with strong overvoltage, resulting in the completion of the electric discharge propagation. In long gaps, the initial channel must be transformed into a highly conducting leader to complete the breakdown.

Thus, the propagation of the electric discharge from cathode is caused by the development of ionization processes in the vapor-gas phase and fast and repeated injection of electric energy (hot electrons) into the liquid leading to its heating and evaporation. Apparently, this results in the formation of shock waves that are especially clearly seen when the electric discharge from cathode propagates in distilled water [31].

For the models described above, the role of photoionization in the liquid due to channel emission is disregarded despite the fact that photoinjection and photoionization have been used for a long time to generate electrons in the liquid. This is explained by both the general notion about the photon processes in liquids and the experimental data about the velocity of channel propagation in liquids which for most experimental conditions does not exceed the drift electron velocity, that is, $\sim 10^7$ cm/s.

However, in some cases the rate of elongation of the discharge channel in the liquid can exceed by an order of magnitude the velocity of electron motion. Thus, discharge propagation velocities of $\sim 2 \cdot 10^8$ cm/s were registered in [32,33] for very long gaps in transformer oil and $U = 1$–10 MV. Close velocities were recorded in the final stage of the discharge for smaller interelectrode distances and lower voltages. This gives us grounds to suggest that photoionization can play a noticeable role in the formation of charge carriers in the liquid phase and in the ionized gas filling the channel under some specific conditions of the discharge propagation.

8.3 Boundaries of the Regions of Existence of Slow and Fast Discharges

In addition to the diagram of Fig. 4.32 showing the regions of existence of discharge figures with different spatial structures, we now consider regions of existence of slow (subsonic) and fast (supersonic) discharges.

The diagram in the $U_0 - r_0$ coordinates that illustrates the regions of existence of the three main discharge types (slow, fast, and very fast, see Sect. 4.1) was presented in [4] for liquids similar to the transformer oil that contained easily ionized molecules for voltage pulses with short fronts in the $+T-P$ electrode system. It is reproduced in Fig. 8.3. In the diagram, the following designations are used: U_0 for the voltage pulse amplitude, r_0 for the end radius of the tip electrode, $U_{ign} = E_c \cdot r_0 \cdot f$ for the initiation (ignition) voltage of the fast discharge (E_c here is the electric field strength at which the onset of the ionization processes in the liquid is observed, and f is the dimensionless coefficient that depends weakly on r_0 and is about 1), U'_{ign} is the same as U_{ign}
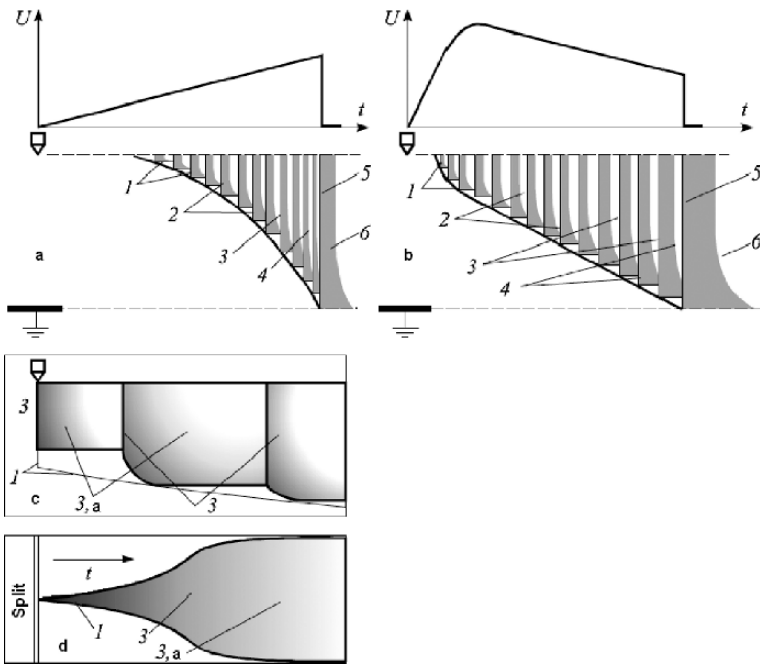
Fig. 8.3. Conventionalized pattern of the discharge in a liquid for oblique (**a**) and standard pulse (**b**): high-speed scanning (**c**) and streak scanning (**d**). Here *1* denotes the initial channel, *2* denotes the section of the initial channel transformed into leader one, *3* denotes a light flash of the leader channel during the step, *3a* and *4a* denote luminescence of the leader channel between flashes, *5* denotes the main channel, and *6* denotes the arc [1]

but with allowance for the field amplification to E_c on the electrode microinhomogeneities, U_d^{min} is the minimum voltage of discharge initiation, and r_c is the maximum end radius of the tip electrode at which the discharge ignition (initiation) does not result in its propagation.

Of interest is the fruitful attempt of Biller [34] to systematize the influence of the main experimental conditions on the observed discharge type based on this diagram in which the fundamental nature of the discharge processes is manifested.

For example, the special features of the discharge phenomena and the electric strength for the breakdown under *oblique pulses with different slopes* can be explained from these positions. In models of discharge propagation (Sects. 8.1 and 8.2), the limiting case was examined in which the pulse front duration was much less than the discharge time lag and less than the characteristic times of the majority of processes taking part in the discharge initiation. Of interest is to consider another limiting case in which the pulse front duration is much greater than the discharge time lag and is comparable with a quarter of the period of the ac 50- or 60-Hz voltage. Under these conditions, the shielding action of space charge accumulated due to emission or ionization is vividly manifested. Curves in the diagram of Fig. 8.3 are bent strongly upwards in the region of small r_0. It was established experimentally that fast channels were not observed for $r_0 \leq 0.2\,\mu m$. The other effect of low rate of voltage increase is that it becomes impossible to jump over a mode as for pulses with a steep front. This means, for example, that for $r_0 < r_c$ and $U_0 > U_d^{min}$, the pulse with a steep front initiates directly a fast channel, whereas the pulse with a gently sloping front initiates a slow channel. Only after collapse of this slow channel and voltage rise to the level exceeding U_d^{min}, a fast channel is initiated. If the front duration is less than the discharge propagation time to the opposite electrode, the slow channel can be transformed into a fast one. This will occur if the rate of increase of the initiating electrode potential provides the required liquid ionization rate in front of the channel head.

For high enough rate of voltage increase, the fast channel can be transformed into a very fast channel.

The absence of easily ionized *impurities* in the liquid causes U_{ign} to increase. In this case, the E_c value cannot be precisely established; it is a complex function of the electric field strength, impact ionization coefficient, and coefficient of electron capture. The electron density n_e is also variable. This, in turn, leads to generalization of the condition $U > \varepsilon E_c^2/en_e$ for the voltage in the channel head which must be solved as self-consistent one for the electric field strength in the channel head E. The field in the head changes in the process of channel propagation; therefore, the drift electron velocity and the velocity of channel propagation will change with the gap length. Even if there is no opportunity to establish the boundaries of alternation of thin discharge mechanisms because of the lack of data about the ionization processes,

electron energy levels, etc., the diagram specifies the approximate boundaries of slow, fast, and very fast channels.

As already indicated above, the *pressure* and *temperature* affect most strongly the slow channel. The curve determining the mode of Trichell pulses from a slow channel is displaced as P and T change. Since the bubble expansion is complicated for increased P, the region of existence of slow channels is reduced, and at very high P, it vanishes completely. The effect of the temperature is opposite.

For fast channels for which the ionization processes in the liquid are primary and the dynamics of the gas phase is secondary, the effect of P and T is much weaker. According to [1], it is manifested through the change of the discharge channel state and, in particular, longitudinal gradients of the potential.

The effect *of polarity of the initiating electrode* is manifested through the fact that slow and very slow (electrothermal) mechanisms of the discharge are most frequently (that is, over a wider range of changes of the experimental conditions) realized in gaps with the cathode being the initiating electrode. Accordingly, the fast channel is usually observed for positive polarity of the tip electrode, and the slow channel is observed only for a certain combination of the experimental conditions. This is primarily explained by the different natures of the initial electrons (emission in one case and autoionization in the other) and by different conditions of their existence in the liquid. In the case of cathode, they move in an attenuating field, and in the case of anode, they move in an amplifying field. In the first case, they generate a charge shielding the cathode or channel head field; in the second case, they promote intensive thermal emission and formation of a partly ionized channel of small radius.

The transformation of the initial channel into a highly conductive leader channel favors the realization of the *fast* discharge, because in this case almost all potential of the initiating electrode is transferred to the initial channel head.

For very high overvoltages (for high rates of voltage increase), not only fast, but also very fast channels can be observed for both polarities of the initiating electrode.

8.4 Conversion of the Initial Channel into the Leader (Formation of the Leader Step).

Generalizing the results of experimental investigation of the discharge propagation for microsecond pulses in long discharge gaps, the discharge pattern can be constructed (Fig. 8.4) with the following qualitative description.

The discharge is initiated as a leader process with two essentially different stages of propagation. The first stage is a continuous (or quasi-continuous) propagation of initial channels several microns in diameter from the electrode into the gap. These channels can propagate both as *fast* and *slow* discharges.
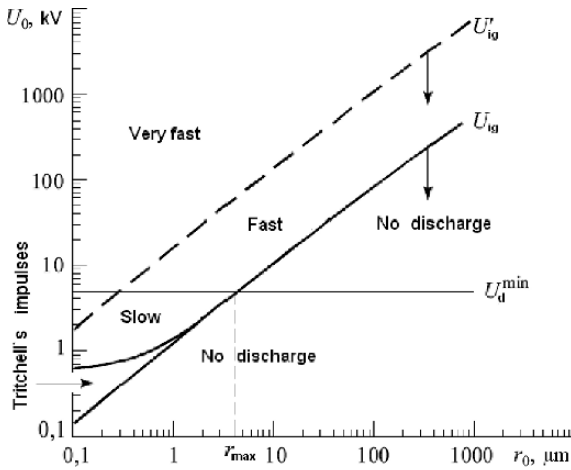
Fig. 8.4. Diagram of three discharge types: slow, fast, and very fast [40]

Their velocity can be both subsonic and exceeding supersonic many times. The initial channel propagation in dielectric liquids is accompanied by current of $\sim 10^{-4}$–10^{-3} A; the current density is $(1$–$8)\cdot 10^3$ A/cm^2 (according to [1]) or 1.5–10^2 A/cm^2 (according to [4, 17]), the average longitudinal gradients of the potential are $(15$-30 kV/cm), and the specific conductivity of the initial channel substance is 0.1–$0.8\,\Omega^{-1}\cdot$cm^{-1} (according to [1]) or $1.3\cdot 10^2\,\Omega^{-1}\cdot$cm^{-1} (according to [4, 17]). In the process of the initial channel propagation, some critical conditions are formed in its base resulting in impact channel expansion with a velocity of $(1$–$6) \cdot 10^5$ cm/s to 50–$120\,\mu$m (Fig. 8.4d), increase in the current by 3–4 orders of magnitude, and bright flashes of the channel (2 and 3). The transformation of the initial channel in the second stage of the leader process propagates from the initial channel base to its head with a velocity of $(1$–$3) \cdot 10^7$ cm/s (Fig. 8.4c). The first step of stepwise propagation of the leader channel (3 and $3a$) with longitudinal potential gradient of 2–11 kV/cm and specific substance conductivity of 2–$10\,\Omega^{-1} \cdot$ cm^{-1} (according to [1]) or $10^2\,\Omega^{-1} \cdot$ cm^{-1} (according to [4, 17]) is terminated. Then the initial channel propagates from the leader channel head, and its transformation into a leader channel occurs by analogy with above-described. The velocity of the initial channel propagation, time intervals between the leader steps and hence the effective rate of the leader channel elongation depend on the properties of the liquid, parameters of the voltage pulse, and field configuration in the discharge gap.

Obviously, a theoretical description of this process and hence the theory of pulsed breakdown of liquids in moderately short gaps must include a description of such successive discharge stages as 1) discharge ignition, 2) initiation of the initial channel, 3) transformation of the initial channel into a leader channel providing the transfer of the high-voltage electrode potential deep into the gap.

Possible approaches to a description of the processes in the stage of ignition and propagation of the initial channel have already been discussed above. An attempt of the theoretical description of transformation of the initial channel into a leader is made below.

Despite a better understanding of the structure of the gas discharge plasma, the mechanism of forming the leader channel in air has not yet been completely understood.

In particular, in [35] it was pointed out with reference to the leader discharge in air that the streamer-leader transition is the most difficult theoretical problem, the least investigated, and in many respects even incompletely understood; at the same time, it is one of the most important stages of the leader process. Under the streamer-leader transition is meant the leader initiation near the electrode in column of the initial flash of the pulsed crown as well as the formation of a new leader fragment from streamers of the streamer zone. According to [35], during $\sim 10\,\mu s$ time period between the flash of the initial crown and the inception of the leader channel, the plasma density in the crown column decreases by approximately two orders of magnitude (to $\sim 10^{12}\,cm^{-3}$). At such low plasma density, the field increasing due to the voltage rise will penetrate inside the column. As a result, the *secondary ionization wave* will propagate through the column initiating a leader. It was demonstrated that the processes of inception of the leader and subsequent reproduction of the channel in the leader head are more or less similar.

We have developed nearly the same approach in [1] for the discharge process in long gaps in liquids. The model of transformation of the initial channel into a leader is based on the assumption about the main role of the increase in the potential gradient in the initial channel owing to the recombination of the charge carriers to the value sufficient for the development of intensive impact ionization in the initial channel considered as a poorly ionized gas channel. Brighter luminescence of the leader channel head in comparison with its column is in agreement with this model and indicates that the leader channel grows where the longitudinal gradients of the electric field are high and where the intensity of collisions accompanied by ionization and excitation of molecules is high.

Let us estimate a change in the temperature of the substance inside the initial channel during its propagation as a reason for the subsequent hydrodynamic processes.

Owing to a low plasma temperature in the initial channel head ($\sim 475\,K$), losses of energy on radiation can be neglected. The losses of energy on the convective heat elimination can also be neglected, because due to small times characteristic of the examined phenomena, heat is eliminated only in the process of impact expansion of the initial channel. Actually, as demonstrated above, in the phase of mild propagation (before the impact transformation into the leader channel), the velocity of the initial channel expansion lies in the range 10^3–$10^4\,cm/s$. In this regard, we must assume that the basic

mechanism of energy losses from the initial channel is heat elimination due to the thermal conductivity.

With allowance for heat elimination, the time variations of the initial channel temperature T can be written as [48]

$$T = \frac{\gamma \cdot E^2 \cdot r_0^2}{4k} \left(\ln \frac{4\tau}{\delta} + \frac{1}{2\tau} + \frac{1}{2\tau} \ln \frac{4\tau}{\delta} + \dots \right), \tag{8.37}$$

where γ the electrical conductivity of plasma of the initial channel, $E = E_{\text{in.ah}}^{\text{av}}$ is the longitudinal gradients of the potential in the initial channel of radius r_0, k is the coefficient of heat conductivity of the liquid, $\delta = e^Z = 1.78$ (Z is Euler's constant), $\tau = \frac{\chi \cdot t}{r^2} + \tau_0$ (χ is the thermal diffusivity coefficient, t is the current time, and τ_0 is a constant determined from the initial condition: $T = T_0$ at $t = 0$).

Let us estimate T at the onset of the transformation of the initial channel, taking $T_0 = 475$ K, $t = 3 \cdot 10^{-6}$s, $\chi = \frac{K}{\rho \cdot C_V} = 8 \cdot 10^{-4}$ cm^2/s ($K = 1.27 \cdot 10^{-3}$ J/cm·s·deg, $\rho = 0.85$ g/cm^3, and $C_V = 1.88$ J/g), and $r_0 = 1.5 \cdot 10^{-4}$ cm. Under these conditions, $\tau_0 = 8.25$ and $T = 514$ K. Thus, the temperature of the initial channel increases in the process of its propagation only by ~40 K. Obviously, this temperature rise cannot cause thermal ionization or noticeable increase in the pressure inside the channel and cause its expansion. The most probable process resulting in the transformation of the initial channel into a leader is an increase in the potential gradient in the initial channel base due to recombination of charge carriers and a decrease in the electrical conductivity caused by it in the process of propagation of the initial channel head deep into the gap.

Due to recombination, the electron escapes from the conduction band into both low and high energy levels. A change in the electron concentration at the expense of recombination into the ground energy level is described by the equation

$$\frac{dn_e}{dt} = \alpha n_a \cdot n_e - \beta n_e^2 \cdot n_+, \tag{8.38}$$

where n_e, n_+, and n_a are the concentrations of electrons, positive ions, and atoms (molecules); α is the ionization rate constant, and β is the recombination rate constant.

According to [36],

$$\alpha = \sigma_e \cdot \overline{V}_e \left(\frac{I_0}{kT_e} + 2 \right) \exp \left(-\frac{I_0}{kT_e} \right), \tag{8.39}$$

where V_e is the average electron velocity, σ_e is the effective interaction cross section,

$$\beta = 1.1 \cdot 10^{-11} \frac{g_a}{g_+} \left(\frac{I_0}{kT_e} + 2 \right) C, \tag{8.40}$$

g_a and g_+ are the statistical weights of the atom (molecule) and ion, respectively, and C is a constant equal to ~$5 \cdot 10^{-17}$.

For a very nonequilibrium plasma of the initial channel, the estimate of α yields $\sim 10^{-100} \, \text{cm}^3/\text{s}$, and $\beta \approx 3 \cdot 10^{-28} \, \text{cm}^6/\text{s}$. For these α and β values, a solution of (8.2) has the form

$$n_e = \frac{n_{e_0}}{\sqrt{1 + \beta n_{e_0}^2 \cdot \tau}} . \tag{8.41}$$

Let us write $\beta n_{e_0}^2 = \frac{1}{\tau_0}$; for $n_{e_0}^2 \sim 10^{17} \, \text{cm}^{-3}$ characteristic of plasma of the initial channel, $\tau_0 \approx 3.3 \cdot 10^{-7} \, \text{s}$. During the initial channel propagation time ($\sim 3 \cdot 10^{-6} \, \text{s}$), the electron concentration decreases to $3.16 \cdot 10^{16} \, \text{cm}^{-3}$ due to recombination into the ground energy level. Such changes of the concentration will cause no essential increase in the longitudinal gradients, that is, cannot be determining for the mechanism of forming the leader step.

At the same time, the electrons most probably escape from the conduction band into high energy levels, that is, into the energy levels of excited states of atoms and molecules. As demonstrated in [36], the number of recombination events into these levels is

$$Z_{\text{rec}} = \beta_1 \cdot n_e^2 \cdot n_+ \left[\frac{1}{\text{cm}^3 \cdot \text{s}} \right] , \tag{8.42}$$

where

$$\beta_1 = \frac{5.2 \cdot 10^{-23}}{T^{9/2}[\text{thou. deg}]} \left[\frac{\text{cm}^6}{\text{s}} \right] . \tag{8.43}$$

Having substituted (8.42) into (8.38) and omitting the first term, we obtain the equation coinciding with (8.41):

$$n_e = \frac{n_{e_0}}{\sqrt{1 + \beta_1 \cdot n_{e_0}^2 \cdot \tau}} . \tag{8.44}$$

In this case, the estimated τ_0 value is $\sim 8.4 \cdot 10^{-14} \, \text{s}$, and the electron concentration in the conduction band of the initial channel plasma will decrease to $1.67 \cdot 10^{13} \, \text{cm}^{-3}$ in $3 \cdot 10^{-6} \, \text{s}$. It should be taken into account that the electron transition into the excited energy levels can be called recombination only when it will be followed by radiative electron transition to the ground energy level. The lifetime of this excited level, according to equation [36]

$$\tau^* = \frac{N^5}{1.6 \cdot 10^{10}} , \tag{8.45}$$

where N is the serial number of the level which can be determined as

$$N = \sqrt{\frac{I_0}{kT}} ,$$

is $4.5 \cdot 10^{-5} \, \text{s}$ at $T = 500 \, \text{K}$ and $1.4 \cdot 10^{-6} \, \text{s}$ at $T = 2000 \, \text{K}$.

Owing to a high rate of electron escape from the conduction band into the excited levels, the potential gradient and the temperature inside the initial channel increase, thereby resulting in two competing effects, namely, a decrease in the rate of transition into the excited energy levels and an increase in the rate of electron escape into the ground energy level due to a decrease in τ^*.

Once the potential gradient increases to the critical value ($\sim$(1–5) $\cdot$ 10^6 V/cm), the impact ionization starts in the plasma of the initial channel together with intensive heating probably to the temperature of thermal ionization. In this case, the concentration of electrons in the channel N_e and the kinetic plasma temperature T increase by an order of magnitude and even more. Thus, according to [37, 38] and the references therein, in the 1st mode streamer channel (in the initial channel according to our terminology), $N_e = (0.5\text{–}1) \cdot 10^{17}$ cm^{-3} and $T \approx 400$ K, whereas in the channel of the 2nd mode streamer (in the leader channel), $N_e = (1\text{–}8)\cdot10^{18}$ cm^{-3} and $T \approx 3000$ K. These values obtained from an analysis of the discharge channel emission spectra for different propagation regimes are in good agreement with our estimates [1]. An increase in the current density and pressure inside the channel causes its impact expansion. This is the termination of forming the leader step. Further these processes repeat with the frequency depending on the applied voltage and rate of its time change, current running through the channel (including the capacitive current), and some other parameters.

Analogous assumption that the channel between the leader steps loses the electrical conductivity because of plasma cooling and recombination of charge carriers resulting in the restoration of the electric field or its redistribution in the channel to the value sufficient for a repeated discharge was made in [39]. Each leader step is reminiscent of the arc discharge by the current (up to 20 A in very long discharge gaps) and luminescence brightness.

The other model of the initial channel transformation into the leader was suggested in [40]. The periodic character of the initial channel transformation into the leader was connected with the hydrodynamic nature of the channel interaction with the surrounding liquid. The transition from the initial channel (streamer according to the terminology [41]) to the leader occurs when the chain of gas bubbles in the initial channel is transformed into a continuous gas channel. Because of small electric strength of gas, a discharge is initiated in the gas channel, that is, the first or subsequent step of the leader is formed. This discharge is fast suppressed (within 50–100 ns), since the pressure in the channel fast increases because of virtually incompressible liquids. In the process of gas discharge decay, the longitudinal potential gradient is restored to the value equal to the electric strength of the gas inside the channel. A discharge accompanied with a current pulse and light flash is initiated in the channel. Typical time intervals between the successive steps of the leader – units of microseconds – have the same order of magnitude as the lifetime of the gas bubbles several millimeters in diameter estimated for the Rayleigh model.

Thus, the periodic discharges in the gas channel in both models fulfill two functions: prevent the channel collapse by virtue of the energy liberation in it and transfer the potential of the initiating electrode deep into the gap. The letter provides realization of the mechanisms of the initial channel propagation in the liquid. The discharge propagation can terminate if the electric field strength near the head is less than the critical value. This will take place if the potential of the high-voltage electrode is too small and the voltage drop across the channel is too large to provide the required potential of the channel head.

8.5 Conditions of Realization of the Leader Process

For high average field strengths in the discharge gap (for small interelectrode distances and short voltage pulses), the transformation of the low conductive initial channel into a highly conductive channel occurs either continuously or with high frequency. In this case, the luminescence on the streak photographs is perceived as continuous, but on the oscillograms of current accompanying it short-term pulses with high repetition frequency are registered almost always. The absence of two clearly distinguishable stages of the discharge – the initial channel propagation and periodic fast transformation into a leader (stepwise elongation of the highly conductive channel with large diameter) under these conditions makes it different from the leader discharge in gases and hence prevents the use of this term for its designation.

In the most general form, the two main conditions for realization of the two-phase leader process are the following: long gaps and nonuniform fields. The concepts of *long gap* and *nonuniform field* as conditions for realization of the leader process were refined and considered in ample details in [17].

For the initiation of the leader channel and its subsequent steady-state propagation, three more so-called field conditions must be satisfied:

– The electric field strength at the point of discharge origin (ignition) and in the head of the propagating channel must be no less than the critical value E_c.
– The volume of the liquid in which the electric field strength E is greater than or equal to E_c must be no less than a minimum volume of $\sim 4 \cdot 10^{-2}\,\mathrm{cm}^{-3}$.
– The average field strength in the interelectrode gap E_c^{av} must be no less than $(0.55–4.2) \cdot 10^5\,\mathrm{V/cm}$.

The limiting value E_c^{av} increases and E_{ign} decreases as the degree of the field nonuniformity decreases due to an increase in the end radius of the initiating electrode (or a descrease in the interelectrode distance).

In gaps with highly nonuniform fields, these conditions are met at the stage of leader channel initiation, that is, formation of the first leader step

due to the formation of a sphere from numerous channels leveling the field in the interval between the sphere and the flat electrode near the tip electrode (see Sect. 4.1). According to [17], the formation of the first step of the positive leader in transformer oil is analogous to the formation of the branch of the pulsed crown in a long air gap which is considered to be the first leader step. For the transformer oil, the role of crown branches is played by numerous (several tens) initial channels, one of which will be transformed first into the leader channel with a length of 0.2–0.7 mm and a diameter of several tens of microns.

In more recent publication [42], Yu. Torshin called this element of the discharge the initial channel. (Probably, by analogy with the similar element of pulsed breakdown of solid dielectrics detected in [43] and called initial channel in [44]). The use of the term *initial channel* for the radically different element (the first leader step) caused confusion. In addition, Yu. Torshin [42] used this fact as an argument against the leader process pattern suggested by us in [1] and confirmed by practically everyone who studied the space-time pattern of the discharge propagation in dielectric liquids in long gaps with nonuniform fields. The same pattern was described in some other studies. In particular, in [41, 45, 46] the length of the filamentary channel that can be considered as a leader step was several tenths of a millimeter in gaps 0.2–2.54 cm long in n-hexane, transformer oil, ether, and distilled water.

When the above-mentioned basic conditions are not satisfied, the discharge either propagates in the form of the initial channel or is not ignited and does not propagate at all.

References

1. V. Y. Ushakov, Pulsed Electric Breakdown of Liquids, Publishing House of Tomsk State University, Tomsk (1975).
2. E. F. Kelley and R. E. Hebner, The electric field distribution associated with pre-breakdown phenomena in nitrobenzene, J. Appl. Phys., **52**, No. 1, 191–195 (1981).
3. O. Lesaint, Propagation of positive discharges in long liquid gaps, in: Proc. 12th Int. Conf. on Dielectric Liquids, Roma (1996), pp. 161–166.
4. Yu. V. Torshin, Monochannel Propagation Mechanism in Transformer Oil at Low Breakdown Probabilities, in: Proc. 12th Int. Conf. on Dielectric Liquids, Roma (1996), pp. 230–233.
5. P. Gourny and O. Lesaint, Study of the dynamics of gaseous positive streamer filament in pentane, in: Proc. 11th Int. Conf. on Dielectric Liquids, Baden-Dättwil (1993), pp. 289–293.
6. J. C. Devins, S. J. Rzad, and R. J. Schwabe, Breakdown and pre-breakdown phenomena in liquids, J. Appl. Phys., **52**, No. 7, 4531–4545 (1981).
7. H. M. Jones and E. E. Kunhart, Evolution of cathode initiated pulsed dielectric breakdown in polar and nonpolar liquids, in: Proc. 12th Int. Conf. on Dielectric Liquids, Roma (1996), pp. 365–368.

8. R. Tobazon, Pre-breakdown phenomena in dielectric liquids, in: Proc. 11th Int. Conf. on Dielectric Liquids, Baden-Dättwil (1993), pp. 172–183.

9. O. Lesaint and P. Gournay, A study of the initiation of positive pre-breakdown phenomena in liquid hydrocarbons, in: Proc. 11th Int. Conf. on Dielectric Liquids, Baden-Dättwil (1993), pp. 284–288.

10. W. Franz, Dielektrisher Durschlag, Springr-Verlag. Berlin (1956);

11. B. Halpern and R. Gomer, Field emission in liquids, J. Chem. Phys., No. 51, 1031–1047 (1969).

12. I. Adamczewski, Ionization, Conductivity, and Breakdown in Dielectric Liquids, Taylor and Francis, Ltd. London, (1969).

13. R. A. Lipshtein and M. I. Shakhnovich, Transformer Oil, Energiya, Moscow (1968).

14. K. A. Naugolnykh and N. A. Roy, Electric Discharges in Water (Hydrodynamic Description), Nauka, Moscow (1971).

15. P. K. Watson, T. Sufian, and W. G. Chadband, A Thermal Model of Positive Pre-breakdown Streamers in Insulating Liquids, in: Proc. 11th Int. Conf. on Dielectric Liquids, Baden-Dättwil (1993), pp. 229–233.

16. P. Brmann and A. Sunesson, In-situ spectroscopic measurements of streamer properties (electron density and temperature) in dielectric liquids, in: Proc. 12th Int. Conf. on Dielectric Liquids, Roma (1996), pp. 197–200.

17. N. V. Torshin, To the problem of existence of the leader process for pulsed electric breakdown of transformer oils, Elektrichestvo, No. 5, 4–16 (1993).

18. W. G. Chadband, The ubiquitous positive streamer, IEEE Trans. Electr. Insul., **EI23**, 697–706 (1988).

19. H. M. Jones and E. E. Kunhardt, Development of pulsed dielectric breakdown in liquids, J. Phys., **D28**, 178–188 (1995).

20. A. Beroual, Electronic and gaseous processes in the pre-breakdown phenomena of dielectric liquids, J. Appl. Phys., **73**, No. 9, 4528–4533 (1993).

21. A. Beroual and R. Tobazeon, Prebreakdown phenomena in liquid dielectrics, IEEE Trans. Electr. Insul., **EI21**, No. 4, 613–627 (1986).

22. P. P. Wong and E. O. Forster, The dynamics of electrical breakdown in liquid hydrocarbons, IEEE Trans. Electr. Insul., **EI17**, No. 3, 203–220 (1982).

23. R. Kattan, A. Denat, and O. Lesaint, Generation, growth and collapse of vapor bubbles in hydrocarbon liquids under a high divergent electric field, J. Appl. Phys., **66**, 4062–4066 (1989).

24. O. Lesaint and R. Tobazeon, Streamer generation and propagation in transformer oil under ac divergent field conditions, IEEE Trans. Electr. Insul., **EI23**, No. 6, 941–954 (1988).

25. E. F. Kelley, M. Nehmadi, R. E. Hebner, *et al.*, Measurement of partial discharges in hexane under dc voltage, IEEE Trans. Electr. Insul., **EI24**, No. 6, (1989), pp. 1109–1119.

26. R. Kattan, A. Denat, and N. Bonifaci, Formation of vapor bubbles in nonpolar liquids initiated by current pulses, IEEE Trans. Electr. Insul., **26**, No. 4, 1109–1119 (1991).

27. A. Beroual and R. Tobazeon, Effects de la pression hydrostatique sur les phenomenes de preclaquage dans les dielectriques liquids, C. R. Acad. Sci., **303**, No. 12, 1081–1084 (1986).

28. N. J. Felici, Blazing a fiery trail with the hounds, IEEE Trans. Electr. Insul., **EI23**, No. 4, 497–503 (1988).

29. A. Beroual, C. Marteau, and R. Tobazeon, Behavior of streamers in liquids under step voltage in point-plane geometry, IEEE Trans. Electr. Insul., **EI23**, No. 6, 955–959 (1988).

30. P. K. Watson, W. G. Chadband, and M. Sadeghzadeh-Araghi, The role of electrostatic and hydrodynamic forces in the negative-point breakdown of liquid dielectrics, IEEE Trans. Electr. Insul., **EI26**, No. 4, 543–559 (1991).

31. V. F. Klimkin, High-speed optical and statistical investigation of prebreakdown phenomena in liquid dielectrics in the nanosecond region, in: Proc. of the 13th Int. Conf. on Dielectric Liquids, Nara 152–155 (1999).

32. M. L. Watkins and P. P. Budenstein, Ann. Rep. CEIDP.-NAS-NRC, Washington DC (1988).

33. K. L. Stricklett, C. Fenimore, E. F. Kelley, *et al.*, Observation of partial discharge in hexane under high magnification, IEEE Trans. Electr. Insul., **EI26**, No. 4, 692–698 (1991).

34. P. Biller, A simple qualitative model for the different types of streamers in dielectric liquids, in: Proc. 12th Int. Conf. on Dielectric Liquids, Roma (1996), pp. 189–192.

35. E. M. Bazelyan and Yu. P. Raizer, Spark Discharge, CRC Press, No 4, Roca, Raton, (1997), 294P.

36. Ya. B. Zeldovich and Yu. P. Raizer, Physics of Shock Waves and High-Temperature Hydrodynamic Phenomena, Nauka, Moscow (1966).

37. J. Nieto-Salazar, N. Bonifaci, A. Denat, and O. Lesaint, Characterization and spectroscopic study of positive streamers in water, in: Proc. 2005 IEEE Int. Conf. on Dielectric Liquids, Coimbra, Portugal (2005), pp. 91–94.

38. A. Denat, High field conduction and pre-breakdown phenomena in dielectric liquids, in: Proc. 2005 IEEE Int. Conf. on Dielectric Liquids, Coimbra (2005), pp. 57–62.

39. D. Linhjell, G. Berg, and L. Lundgaard, Streamer propagation in long point-plane oil gaps, in: Proc. 11th Int. Conf. on Dielectric Liquids, Baden-Dättwil (1993), pp. 268.273.

40. N. G. Trinh and A. Saker, Interpretation of the physical mechanisms in the breakdown of long gaps in transformer oil, in: Proc. 12th Int. Conf. on Dielectric Liquids, Roma (1996), pp. 287–291.

41. W. R. Thomas, An ultra-high speed laser schlieren technique for studying electrical breakdown in dielectric liquids, in: Annual Rep. Conf. on Electric Insulation and Dielectric Phenomena, (1973), pp. 130–133.

42. Yu. V. Torshin, Peculiarities of formation of the impulse discharge in liquids: To the existence of transition zone attached to a potential electrode, in: Proc. 2005 IEEE Int. Conf. on Dielectric Liquids, Coimbra (2005), pp. 79–82.

43. A. A. Vorobjev and G. A. Vorobjev, Electrical Breakdown and Destruction of Dielectrics, Vysshaya Shkola, Moscow (1966).

44. Yu. N. Vershinin, Electron Thermal and Detonation Processes in the Electric Breakdown of Solid Dielectrics, Publishing House of the Ural Branch of the Russian Academy of Sciences, Ekaterinburg (2000).

45. J. C. Devins, S. J. Rzad, and R. S. Shwabe, Pre-breakdown phenomena in sphere-sphere electrode configuration in dielectric liquids, Appl. Phys. Lett., **31**, No. 5, 313–315 (1977).

46. V. F. Klimkin, F. N. Popyrin, and R. I. Soloukhin, Optical Methods of Registration of Transient Processes, Nauka, Novosibirsk (1980).

47. V. J. Ushakov, V. A. Butenko, and Yu. I. Kuznetsov, A comparison of elec-
trophysical characteristics of the pulsed discharge in various dielectric media,
Elektronn. Obrab. Mater., No. 2, 44–54 (1970).
48. H. S. Carslaw, J.C. Jaeger, Conduction of heat in solids. Clarendon Press.
Oxford. (1973).

Conclusions

Summing up the generalization of the experimental and theoretical studies de-
voted to the discharge initiation (ignition) and propagation in liquids, we must
point out that, despite significant progress in understanding of the breakdown
mechanisms that has been made over the last 1.5–2 decades, some fragments
of this complex phenomenon remain "white spots."

The most complex for a quantitative (and even qualitative) description
are the processes in the head of the propagating discharge channel and in
the region of transition to the discharge plasma filling the channel column.
Exactly these processes provide the transformation of the liquid dielectric
medium into the plasma.

It is pertinent to note that these processes are considered to be the most
complex ones in the study and the least clearly understood for the electric
breakdown of other dielectric media – gases and solid dielectrics. Some cita-
tions from [35] (Sect. 8.3) convincingly confirm this thesis for the discharge in
long air gaps.

For solid dielectrics, the main efforts have been concentrated over many
decades on the definition of the criterion for the buildup impact ionization
of the valence band which is identified with the breakdown condition. Recent
achievements in the field of solid-state physics and data on the space-time
mechanisms of the discharge propagation in optically transparent solid di-
electrics have allowed Vershinin [44] to develop an alternative approach to a
description of breakdown of solid dielectrics. The discharge channel prop-
agation in them is connected with the occurrence and motion of the 1st
order phase transitions. For the discharge from cathode, this is the solid-
melt transition; this is the solid - dense plasma transition for the discharge
from anode. The cathode discharge with subsonic velocity is associated with
electron-thermal processes, and the supersonic anode discharge is associated
with electron-detonation processes. To calculate these processes, Yu. Vershinin
addressed other branches of science and used data from quantum mechan-
ics, electrochemistry of melts, detonation theory, solid-state physics, nonideal
dense plasma, etc.

This approach has allowed author [44] to derive analytical expressions that
relate the individual properties of solid dielectrics and the parameters of high-
voltage pulse to the space-time discharge characteristics.

We believe that the approach developed in [44] can be extremely useful for a description of phase transitions and, finally, formation and propagation of the discharge channel in the liquid. This is provided by far-reaching analogies in mechanisms of discharge propagation in these media emphasized by many authors including us [47].